

University of Nottingham
UK | CHINA | MALAYSIA

Optical fibre-based time resolved Brillouin scattering

Salvatore La Cavera III

Thesis submitted to the University of Nottingham for the degree of
Doctor of Philosophy

April 27, 2021



OPTICS & PHOTONICS
UNIVERSITY OF NOTTINGHAM

Sarah, this is for you...

Acknowledgements

I would first like to thank my family, who has supported me on this journey 5,353 miles from home. I cannot begin to thank my parents for everything they have done for me and taught me. My brothers for their friendship and motivation. And of course my grandparents for their enthusiasm and support. Lastly, thank you to Sarah, without whom none of this is possible, and whose tolerance of me is astounding.

My deepest gratitude goes to my supervisors: Matt, Richard, and Fernando. For your patience, enthusiasm, brilliance, persistence, and dare I say friendship. I am especially appreciative for all of my colleagues who have contributed to my post-graduate experience over these fun/arduous years. Rafael, Sidahmed, Rikesh, Victoria, Wenqi, Don, Paul, Shakila, Will, Mengting, Mina, and Tania, (and others I am forgetting) thank you! I look forward to working together in the future.

Dissemination

Publications

- **Phonon imaging in 3D with a fibre probe**. Salvatore La Cavera, Fernando Pérez-Cota, Richard J. Smith, Matt Clark. *Light: Science & Applications*, **10**, 91 (2021). https://doi.org/10.1038/s41377-021-00532-7
- **Time resolved Brillouin fiber-spectrometer**. Salvatore La Cavera, Fernando Pérez-Cota, Rafael Fuentes-Domínguez, Richard J. Smith, Matt Clark. *Optics Express*, 27, 25064-25071 (2019).
- **Picosecond ultrasonics for elasticity-based imaging and characterization of biological cells**. Fernando Pérez-Cota, Rafael Fuentes-Domínguez, Salvatore La Cavera, William Hardiman, Mengting Yao, Kerry Setchfield, Emilia Moradi, Shakila Naznin, Amanda Wright, Kevin F. Webb, Alan Huett, Claire Friel, Virginie Sottile, Hany M. Elsheikha, Richard J. Smith, and Matt Clark. *Journal of Applied Physics*, 128 (16), 160902, October 2020.
- **Apparent attenuation by opto-acoustic defocus in phonon microscopy**. Fernando Pérez-Cota, Salvatore La Cavera, Shakila Naznin, Rafael Fuentes-Domínguez, Richard J. Smith, and Matt Clark. *Photoacoustics*, 19, 100180, September 2020.
- **Thickness measurement of polymer thin films with high frequency ultrasonic transducers**. Richard J. Smith, Salvatore La Cavera, Fernando Pérez-Cota, Leonel Marques, Matt Clark. *AIP Conference Proceedings*, 2102, 040015 (2019).

Presentations

Invited talks

- **Imaging and spectroscopy with GHz phonons**. *Japan Society of Applied Physics*, Division of Applied Physics, Hokkaido University, Japan (2019).

- **Endoscope-compatible probes using GHz ultrasound**. *Salon for intracavity technology and application for urological tumor*, Wuhan, China (2019).

Oral presentations

- **Endoscope-compatible probes using GHz ultrasound**. *RCNDE Technology Transfer event*, London, UK (2020).
- **Biological NDE with GHz phonons**. *RCNDE Early Stage Researcher event*, London, UK (2019).
- **In vivo medical and on-wing aerospace diagnostics: laser ultrasonic fibre-transducers**. *Laser Ultrasonics 2018*, Nottingham, UK (2018).
- **Laser Ultrasonic Endoscopy**. *RCNDE Technology Transfer event*, London, UK (2018).

Poster presentations

- **Needle-compatible GHz acoustic spectrometer**. *International Congress on Ultrasonics 2019*, Bruges, BE (2019).
- **Thickness Measurement of Polymer Thin Films with High Frequency Ultrasonic Transducers**. *Laser Ultrasonics 2018*, Nottingham, UK (2018).

Recognitions

- Runner-up: best presentation, *RCNDE Early Stage Researcher event*, 2019.
- Engineering Showcase finalist, *University of Nottingham*, 2019.
- Engineering Showcase finalist, *University of Nottingham*, 2018.

Abstract

In this thesis, the first single-mode optical fibre ultrasonic probe for the GHz frequency regime is introduced. In many liquids and solids, including biological material, the acoustic wavelength in the GHz portion of the ultrasonic spectrum is shorter than optical wavelengths in the visible portion of the electromagnetic spectrum, and therefore presents an opportunity for high resolution. The *phonon probe* described here delivers ultrashort pulses of light into a nanometric metallic transducer which acts as a $\sim 100\ GHz$ bandwidth source of acoustic waves. This nano-transducer is fabricated onto the tip of a $125\ \mu m$ diameter single mode optical fibre, containing a $5\ \mu m$ diameter active region. Through the phenomenon of time resolved Brillouin scattering, a second pulse of light interferometrically detects and reconstructs GHz frequency acoustic waves travelling in the probed materials. Characteristics of a detected wave, such as the variations in amplitude and frequency, provide access to both spatial information and material properties. In addition to the phonon probe instrumentation, a signal processing methodology was developed in order to extract this information and allows the phonon probe to perform parallelised Brillouin spectroscopy and 3D imaging.

The performance of the phonon probe as a time-resolved Brillouin spectrometer is characterised using a variety of liquids and environmental parameters. From these demonstrations, it is shown that the device can identify liquids such as glycerol and polystyrene based on their unique elastic signature, i.e. the Brillouin frequency. What's more, it can also detect chemical and physical fluctuations in the desired medium; it is capable of detecting variations in water salinity with a sensitivity of $41 \pm 3\ MHz/\%wt$, and variations in water temperature with a sensitivity of $2.5 \pm 0.6\ MHz/^{\circ}C$. The fibre-spectrometer proves capable of measuring minute Brillouin frequency shifts down to $9 \pm 2MHz$.

Beyond spectroscopy, the probe can be converted into an optical fibre-based ultrasonic 3D imaging tool with a unique set of resolving capabilities. Spatial resolution is enabled by mechanically scanning the fibre or the specimen in the two dimensions that are parallel to the sample plane. The acoustic time-of-flight signal captured by the phonon probe is alone capable of providing spatial resolution along the longitudinal direction.The decay signature of this time-of-flight signal can be used to produce a proximity measurement between the fibre-tip and any object or boundary that exists

within the sensing region. Using these spatial resolution mechanisms, the device was capable of non-contact 3D profilometric imaging of the absolute or relative topography of polymer microstructures.

The lateral resolution of the device is determined by the $2.5\ \mu m$ radius optical spot of the pump and probe beams emitted from the optical fibre core. Axially, the probe utilises $\sim 300\ nm$ acoustic wavelengths to achieve a proximity measurement precision of $55\ nm$ and a profiling accuracy of $30\ nm$ compared with optical profilometry. While imaging, the probe is simultaneously acting as a spectrometer by measuring the Brillouin frequency shift of the probe beam within the imaging object; this measurement provides access to quantitative measurements of *viscoelasticity* inside the object.

It is shown that the underlying mechanisms of the tool can be extrapolated from a single-mode fibre to a multi-mode channel within a fibre imaging bundle containing 18,000 channels. Ultimately this capability paves the way for wide-field imaging with GHz frequency ultrasonic probes; it will also greatly simplify the scanning motion of the device since the bundle can be held stationary and the optical beams scanned across the input-end. This technology finally delivers acoustic microscopy-like capabilities in a portable instrument. Without micro-lenses and additional facilities on the tip of the fibre, the device dimensions are compatible with the majority of hypodermic needle gauges, which is particularly promising for tissue spectroscopy. To this end, its continued development holds great promise for application to *in vivo* needle biopsies, label-free cell profilometry/elastography, and label-free imaging of superficial tissue with resolution comparable to confocal laser endomicroscopy.

Contents

I Introduction **17**

1 Context & motivation **18**

1.1 Endoscopy 18

1.1.1 Optical fibre 21

1.1.2 Optical fibre-based imaging 22

1.1.3 Discussion 27

1.2 Ultrasound 29

1.2.1 Endoscopic ultrasound 33

1.2.2 Acoustic microscopy 34

1.3 Photoacoustics 36

1.3.1 Photoacoustic microscopy 37

1.3.2 Photoacoustic endoscopy 39

1.4 Discussion, device concept, and thesis outline 43

2 Background & modelling **48**

2.1 Brillouin scattering 48

2.1.1 Physical basis 49

2.1.2 Brillouin microscopy 55

2.1.3 Brillouin fibre probe 59

2.2 Picosecond laser ultrasound 61

2.2.1 Optical modelling 65

2.2.2 Opto-thermo-acoustic modelling 70

2.3 Time resolved Brillouin scattering 80

2.3.1 PLU-based microscopy 83

2.4 Discussion 89

II Methods **92**

3 Opto-acoustic fibre-transducers **93**

3.1 Transducer substrate: optical fibre 94

3.2 Transducer design 103

3.3 Fabrication and characterisation . . . 111
3.4 Discussion . . . 119

4 Pump-probe measurement system 122
4.1 Experimental set up . . . 123
4.1.1 Time resolution . . . 123
4.1.2 ASOPS pump-probe optical system . . . 128
4.2 Data processing . . . 137
4.2.1 Standard signal processing . . . 137
4.2.2 Time-frequency analysis: wavelet transform . . . 143

III Results 152

5 Spectroscopy: time resolved Brillouin fibre-spectrometer 153
5.1 Optical fibre TRBS configuration . . . 154
5.2 Spectroscopy applications . . . 160
5.2.1 Material characterisation . . . 160
5.2.2 Thermometry . . . 166
5.2.3 Solute sensing . . . 174
5.3 Discussion and conclusions . . . 181

6 Imaging: three-dimensional phonon imaging probe 183
6.1 Experimental design . . . 184
6.2 In-depth measurement process . . . 186
6.2.1 Initial boundary localisation . . . 186
6.2.2 Proximity measurement . . . 191
6.3 Polymer phantom imaging . . . 199
6.3.1 Imaging experiments . . . 201
6.3.2 Three-dimensional profiling . . . 206
6.3.3 Brillouin imaging . . . 212
6.4 Discussion . . . 216
6.4.1 Sources of systematic error . . . 216
6.4.2 Resolution . . . 223
6.4.3 Conclusions . . . 227

7 Future work 229
7.1 Phonon imaging bundle . . . 229
7.2 Fabry-Pérot transducer . . . 238
7.3 IR Brillouin scattering . . . 240
7.4 Super-resolution acoustic lens . . . 242

IV Conclusion **246**

8 Conclusion **247**

8.1 Summary of thesis 248

8.2 Outlook 254

A Green's function **258**

B Finite element thermal model **260**

C Fluence damage threshold **263**

D Polymer phantom fabrication **266**

E Profilometry methodologies **268**

List of Figures

1.1 Imaging examples from state of the art optical endoscopy 20
1.2 Basic architecture and working principle of an optical fibre 21
1.3 Diagram of an imaging bundle based confocal laser endomicroscope and example image 23
1.4 Diagram and imaging examples for a single fibre based confocal laser endomicroscope 24
1.5 Working principle and example images for a multi-mode fibre imaging tool. 25
1.6 Example images and diagrams of side-view optical fibre imaging tools . 26
1.7 Basic principles of ultrasonography 30
1.8 Performance qualities, modalities, and example images for endoscopic ultrasound 33
1.9 Device architecture, characteristics, and example images for an acoustic microscope 35
1.10 Working principle and example images for a photoacoustic microscope 38
1.11 Device architectures and *in vivo* images for photoacoustic endoscopes . 40
1.12 Device concept and example vasculature imaging of an all-optical photoacoustic probe 42
1.13 Laser ultrasonic optical fibre probe and example swine cardiac tissue imaging 45

2.1 Diagram of Bragg diffraction and illustration of Brillouin scattering 53
2.2 Instrumentation and signal processing for spontaneous Brillouin spectroscopy 57
2.3 Cell and tissue imaging examples for Brillouin microscopy 58
2.4 Device diagrams and example spectroscopy from a spontaneous Brillouin fibre probe 61
2.5 Diagram and early experimental work for picosecond laser ultrasonics . 63
2.6 Basic diagram and geometry for electric field propagation in multi-layers 67
2.7 Calculating electric field amplitude in multi-layer structures 69
2.8 Example spectra for a Fabry-Pérot optical cavity 70
2.9 Geometry, initial conditions, and optical properties throughout a multi-layer structure 71

2.10 Flow chart for the thermoelastic generation process 73
2.11 Geometry and boundary conditions for a scattering acoustic field 74
2.12 Generation bandwidth for picosecond strain pulses 76
2.13 Optical interference process for time resolved Brillouin scattering 82
2.14 Examples of a basic transducer and time resolved Brillouin scattering signals 83
2.15 Geometry and imaging examples for a single-layer picosecond ultrasonic transducer 86
2.16 Geometry and optical spectra for a cavity-based picosecond ultrasonic transducer 87
2.17 Signal performance comparision between various picosecond ultrasonic transducer styles 88
2.18 Example cell imaging using phonon microscopy 89

3.1 Ray diagrams for a basic optical fibre channel 95
3.2 Electric field solutions in a single-mode optical fibre 98
3.3 Demonstration of breaking single-mode cut-off in optical fibres 101
3.4 Wavelength performance for a single-mode optical fibre 102
3.5 Device concept for a GHz frequency opto-acoustic fibre transducer . . . 104
3.6 Optical transmission spectra and extinction coefficients for various metals 106
3.7 Geometry, simulated signal, and frequency spectrum for a fibre transducer107
3.8 Signal performance as a function of material and layer thickness 108
3.9 Laser absorption damage thresholds for various metals and thicknesses 110
3.10 Picture and diagram of facilities used for sputter coating 113
3.11 Picture, diagram, and spectrum for a white light spectrometer 115
3.12 Demonstration of metallic thin-film thickness measurement 116
3.13 Calibration curves for the sputter coating facility 118
3.14 Deposition speeds for the sputter coating facility 119
3.15 Final device geometry for the phonon probe prototype 121

4.1 Basic example of time-sampling for a detected acoustic wave 124
4.2 Instrumentation for mechanical and electronic pump-probe delay lines . 125
4.3 Comparison of acquisition speed for mechanical and electronic delay lines127
4.4 Experimental diagram for time resolved pump-probe spectroscopy using blue and red wavelengths 129
4.5 Experimental diagram for time resolved pump-probe spectroscopy using two red wavelengths 131
4.6 Illustration of the sample plane for pump-probe based microscopy . . . 132
4.7 Experimental demonstration of SNR as a function of signal averaging . 133

4.8 Experimental diagram for time resolved pump-probe spectroscopy using fibre optics . . . 135
4.9 Fibre optic network for the pump-probe system . . . 136
4.10 Flow chart for processing an experimental time resolved Brillouin scattering signal . . . 138
4.11 Demonstration of signal averaging for time resolved signals . . . 140
4.12 Example of measuring the attenuation coefficient of a signal . . . 142
4.13 Geometry and simulated signals for a heterogeneous measurement volume . . . 144
4.14 Demonstration of using wavelet analysis on a time resolved signal . . . 146
4.15 Relationship between time resolution and frequency resolution in wavelet analysis . . . 147
4.16 Scaling the mother wavelet . . . 148
4.17 Effect of mother wavelet scaling on signal transformation . . . 149
4.18 Application concept of wavelet analysis to a heterogeneous measurement volume . . . 151

5.1 Simple diagram for the phonon probe optical system . . . 155
5.2 Transducer diagram for the phonon probe prototype used in experiment 156
5.3 Time resolved signal and frequency spectrum for the phonon probe device 157
5.4 Demonstration of using the phonon probe as a Brillouin spectrometer . 158
5.5 Experimental demonstration of the acquisition speed of the phonon probe 159
5.6 Phonon probe Brillouin spectroscopy on heterogeneous liquid mixtures 161
5.7 Brillouin spectroscopy of liquid polystyrene . . . 163
5.8 Brillouin spectroscopy of sheep's blood plasma . . . 164
5.9 Brillouin spectroscopy of heated gelatin . . . 165
5.10 Thermo-optic and thermo-acoustic coefficients for water . . . 167
5.11 Using the phonon probe to measure water temperature . . . 168
5.12 Finite element model of steady-state heating by the fibre transducer . . 170
5.13 Calculation of the phonon probe's sensitivity to temperature . . . 172
5.14 Investigating axial variations in water temperature with the phonon probe 173
5.15 Salino-optic and salino-acoustic coefficients for water . . . 175
5.16 Measuring fluctuations in water salinity with the phonon probe . . . 176
5.17 Quantifying the smallest frequency shifts measured by the phonon probe 178
5.18 Interpolating the experimental Brillouin spectrum with zero-padding . . . 179
5.19 Breakdown of measuring the interpolated frequency resolution of the phonon probe . . . 180

6.1 Experimental diagram for the phonon probe in 3D imaging mode . . . 185

6.2 Illustrating the engagement of the phonon probe with a sample and the device response . . . 188
6.3 Initial demonstration of measuring proximity with the phonon probe . . . 190
6.4 Flow chart demonstrating how a quantitative measurement of proximity is obtained with the phonon probe . . . 192
6.5 Proximity measurement criteria . . . 195
6.6 Experimental proximity measurements between the phonon probe and a petri dish . . . 196
6.7 Simulated proximity measurements between the phonon probe and a petri dish . . . 197
6.8 Collating experimental and simulated proximity measurements with signal averaging . . . 198
6.9 Microscope image of polymer microstructures used for 3D profilometry . 200
6.10 High magnification images of the polymer microstructures used for 3D profilometry . . . 201
6.11 Visualisation of how the phonon probe interacts with an object during imaging . . . 202
6.12 Microscope image of the phonon probe engaged with an imaging target 204
6.13 Different types of signals obtained when scanning a polymer microstructure 205
6.14 Image processing techniques used to convert a proximity map into a height map . . . 207
6.15 Demonstration of 3D profilometry on an object whose height is beyond the dynamic range of the phonon probe . . . 209
6.16 Demonstration of 3D profilometry on an object whose height is is nearing the dynamic range of the phonon probe . . . 210
6.17 Demonstration of 3D profilometry on an object whose height is within the dynamic range of the phonon probe . . . 211
6.18 Measuring the Brillouin frequency of a polymer microstructure in 3D . . 213
6.19 Material and geometric requirements for measuring the Brillouin frequency of an object with the phonon probe . . . 215
6.20 Demonstrating the theoretical compatibility of the phonon probe with biological specimens . . . 216
6.21 Characterisation of the systematic measurement error due to the z-piezo stage . . . 218
6.22 Estimation of the systematic error due to sample/fibre tilt . . . 219
6.23 Approximating the contribution of transducer heating to systematic error 221
6.24 Theoretical and experimental examples of spatial resolution and measurement precision . . . 224

7.1 Picture of an imaging bundle distal end-face and the transmission spectrum of the product . . . 230
7.2 Experimental diagram and illustrations of the phonon imaging bundle prototype . . . 231
7.3 Experimental time resolved Brillouin scattering signals from the phonon image bundle prototype . . . 232
7.4 Signal amplitude and Brillouin frequency maps from the phonon imaging bundle . . . 233
7.5 Optimisation of the pump-probe scanning protocol for the imaging bundle 234
7.6 Signal amplitude and Brillouin frequency maps after optimising the acquisition speed of the phonon imaging bundle system . . . 235
7.7 Signal processing method for improving the signal amplitude of the phonon bundle device . . . 236
7.8 Simulating the performance of a Fabry-Pérot cavity-based fibre-transducer239
7.9 Theoretical demonstration for increasing acoustic penetration depth by using longer probe wavelengths . . . 241
7.10 Design and ray diagram simulations for an acoustic lens to increase the lateral resolution of the phonon probe . . . 244

8.1 Device concept for phonon endomicroscopy . . . 257

B.1 The geometry utilised for simulating steady-state heating with finite element method . . . 262

D.1 Picture of polystyrene microspheres at various stages of the melting process . . . 267

List of Tables

1.1 Performance metrics for current state of the art optical fibre imaging tools 27
1.2 Comparison of performance metrics for state of the art photoacoustic endoscope technology 46

2.1 Summary of current capabilities for Brillouin microscopes and endoscopes 90

6.1 Comparison of performance metrics for atomic force microscopy, optical profilometry, and the phonon probe 226

8.1 Phonon probe performance metrics 253

C.1 Material parameters used for simulating the laser absorption damage threshold of metallic thin-films 265

Part I

Introduction

Chapter 1

Context & motivation

This work presents the design, development, and proof of concept for an ultrasonic optical fibre imaging device which is capable of both spectroscopy and microscopic resolution imaging. This *phonon probe*, draws inspiration from two well-established fields of study: optical fibre imaging systems and high frequency ultrasonics. Extremely high frequency acoustic waves, e.g. in the GHz regime, are capable of exchanging energy with visible frequencies of light through the phenomenon of Brillouin scattering. This mechanism serves as a basis for optically detecting acoustic events that occur on length scales of $\sim 100\ nm$ and time scales of $\sim 1\ ps$. When pairing this concept with the light-guiding principles of a compact and flexible optical fibre, a pathway to ultra-high resolution acoustic endoscopy emerges, and will be explored here. In particular, this chapter will lay out the two pillars upon which the phonon probe is built: optical fibre-based endoscopy and endoscopic ultrasonics.

1.1 Endoscopy

Optical endoscopes are so ubiquitous in society that anyone with an internet connection or a local DIY-shop can procure one. The working concept is very simple: create a thin channel that conveys light - and therefore the components of an image - in and out of environments which are beyond line-of-sight for conventional imaging tools, e.g. the human eye, a magnifying glass, telescope, or microscope. Their utility spans an immense range of applications, from the trivial, e.g. checking a drain for blockage, to the life-saving, e.g. diagnosing colorectal cancer.

The first endoscopes emerged at the turn of the 19^{th} century and consisted of a long open-ended rigid tube, with a 45° mirror placed at the input, or *proximal*, end [1]. The object or environment that was under inspection at the *distal* end of the tube was illuminated by simple candle-light or gas-lamp that passed light from the mirror, down the tube, onto the object, and relayed the image back into the tube-mirror system for viewing. However, it wasn't until the advent of electricity, and with it the light bulb,

that endoscopes began to provide enough illumination for expert physicians to inspect sub-surface cavities of the human body. By the start of the 20^{th} century, applications for the rigid-endoscope were beginning to strongly focus on its use in gastrointestinal inspection; in this context it adopted the name: gastroscope. For the first time highly skilled physicians could characterise basic physiological responses of the oesophagus and stomach; more importantly, gastrointestinal diseases could finally be investigated *in vivo*, such as gastritis and pyloric tumours [2].

Despite these major advances at the time, widespread adoption of the device was stunted by how clearly dangerous and discomforting the long rigid endoscope was to patients [3]. At the time, the most significant strides in gastroscopic procedural development were made using sword-swallowers as test subjects [1, 2]. However, by the mid-20^{th} century, the single biggest breakthrough in endoscopic innovation was provided by the newly realised *optical fibre* (introduced in following section). Replacing the rigid and semi-rigid gastroscopes with thin and flexible, yet robust, glass fibres meant that endoscopic instrumentation could be made drastically thinner, and therefore safer.

Once the potential for this technology was realised, techniques were quickly developed to organise hundreds of $\approx 25\ \mu m$ diameter fibres into a $1\ mm$ diameter bundle [4], a *fibrescope*, which was the precursor of the modern *imaging bundle*. The medical implications for using the fibrescope as a truly non-invasive gastroscope were all too clear to the leading gastroenterologists; when presenting the inventor of the first optical fibre gastroscope (Basil Hirschowitz) the president of the American Gastroscopic Society remarked: “I shall forego my prerogative of boring you with a Presidential address so that Dr. Hirschowitz may at half past 8 o’clock tell you about what I understand to be a new principle of gastroscopy. I hear that fiber glass conducts light around corners and that Dr. Hirschowitz has used this material in a new type of gastroscope” [3].

What has since followed is a development boom for endoscopic instrumentation, enabling less invasive diagnosis, albeit still with a strong reliance on the experience and subjectivity of the endoscopist [1]. In particular, modern endoscopy provides unprecedented access to the oesophagus, stomach, pancreas, colon, and the abdominal cavity (laparoscopy) [2]. This progress has been enabled by the commercialisation of the technology, driven by companies such as Olympus, Pentax, and Fujifilm, who have brought the endoscope into the Digital Age with standard features such as: charge-coupled device (CCD) imaging sensors, ultra high definition viewing monitors, efficient high power light sources (e.g. LED), video processors, and various computational imaging and machine learning tools (e.g. computer-aided diagnosis) [5–7]. Furthermore, numerous optical modalities have emerged that enhance contrast and magnification, beyond what is provided by simple white-light illumination and miniaturised objective lenses, e.g. fluorescence imaging, narrow band imaging, multi-band imaging, chromoendoscopy, confocal laser endomicroscopy, and endocytoscopy (for examples

see Figure 1.1) [8–10].

The current gold standard for diagnosing a broad spectrum of diseases and cancers is *histopathology*, which requires extracting a biopsy (tissue) sample from the patient; when the tissue samples are inspected under a microscope, the cellular morphologies and groupings are indicative of the existence and grade of disease [11]. Unsurprisingly, there is immense interest in developing *in vivo* histological techniques to overcome the invasiveness of biopsies as well as the potential need for repeat procedures. In the journal series *Moments in Surgical History*, a review on endoscopy concluded with the following open-ended query: "Is it possible that instruments capable of determining cellular structure and biological behaviour will supplant devices capable of mere visual appreciation of mucosal structure?" [2]. It is this question, and the corresponding path to high resolution, that this thesis seeks to answer, yet from the perspective of acoustics which will be introduced shortly. Interestingly, despite strong commercial development of imaging bundle-based endoscopes, the path to ever-increasing endoscopic resolution is returning to the single optical fibre, which will be the topic of the next two sections.

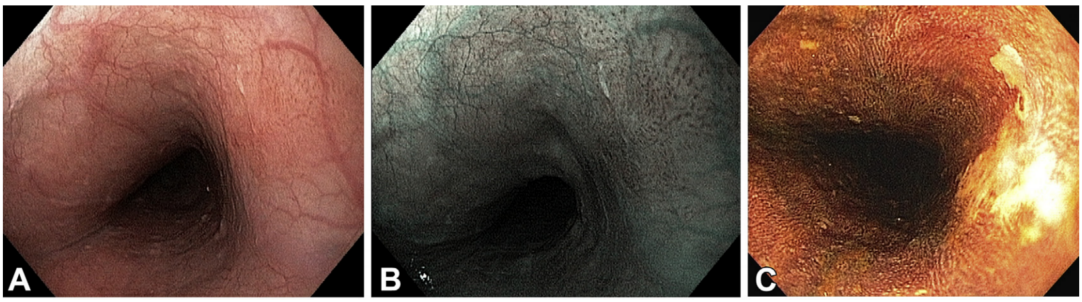


Figure 1.1: Examples of the most prevalent modalities for optical endoscopy. (a) White light endoscopy (WLE) uses the entire visible portion of the electromagnetic spectrum and therefore closely resembles human eyesight; it is the most universal modality and allows basic visualisation, guiding, sizing, etc. (b) Narrowband imaging (NBI) utilises blue and green wavelengths which are preferentially absorbed and reflected by blood vessels and mucosal tissue therefore enhancing contrast of these objects; this provides access to subsurface features of lesions and better visualisation of vasculature. (c) In chromoendoscopy the tissue is chemically stained to artificially create contrast between lesions and healthy tissue; this has been used in the picture to identify malignant lesions of oesophageal squamous cell carcinoma [12]. Reprinted from Gastrointestinal Endoscopy, 85, Adriana Vaz Safatle-Ribeiro, Elisa Ryoka Baba, Sheila Friedrich Faraj, et al., Diagnostic accuracy of probe-based confocal laser endomicroscopy in Lugol-unstained oesophageal superficial lesions of patients with head and neck cancer, 1195-1207, Copyright (2017), with permission from Elsevier.

1.1.1 Optical fibre

An optical fibre can be simply described as a thin glass rod - e.g. similar in diameter to a human hair - which internally supports the propagation of light. The general mechanism at work, is *total internal reflection*, which was discovered as early as the mid-19^{th} century. The phenomenon (described more thoroughly in Section 3.1) allows light to remain contained inside an object, even if the object is transparent and curved. At the time of discovery, this sensation was visually captured by public displays called "light fountains" in which light was made to totally internally reflect down a falling stream of water [13]. This basic phenomenon now underpins an entire global telecommunications network in addition to its central role in optical endoscopy.

Wide-scale adoption of optical fibre technology did not manifest until the mid-20^{th} century, due to the following developments: the introduction of an outer *cladding* layer which surrounds the glass rod, and the improvement in the purity of the fibre glass (and therefore its optical transmission) [14, 15]. Figure 1.2a presents the basic architecture of the modern optical fibre. In general the main components are the *core*, in which the light propagates, and the optically insulating *cladding*. These layers are designed such that the cladding allows light to propagate at a higher velocity than does the core, that is, the cladding has a lower refractive index $n = c/v$ where c is the constant speed of light in vacuum, and v is the speed of light in the particular medium. This contrast in refractive index causes the light propagating in the core to completely reflect without entering the cladding (for certain incidence angles), as shown in Figure 1.2b.

The above describes the operating principle of a *multi-mode* optical fibre. As light enters the core region at differing angles, such as the black and violet light rays in Figure

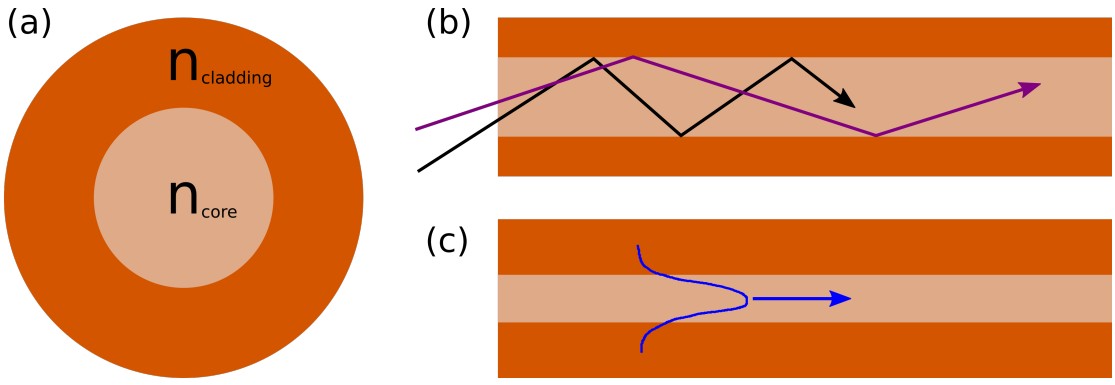


Figure 1.2: (a) An optical fibre consists of two main features, a cylindrically symmetric core layer in which the light propagates, and an outer cladding layer. The refractive index of the cladding ($n_{cladding}$) is typically lower than that of the core (n_{core}) which in part permits total internal reflection of the light in the core. (b) Light rays that enter the core at different angles carry different reflection angles down the core, which gives rise to multiple propagation modes within the fibre. (c) Under certain conditions the core will only permit a single mode to propagate, e.g. with a Gaussian-like intensity profile, which does not change along the length of the fibre.

1.2b, the rays totally internally reflect at different angles, thus giving rise to different *modes* of propagation within the fibre-core. Since the two modes travel with different angles, their path lengths down the fibre are therefore different as are their timings when they finally exit the fibre; this effect is referred to as *intermodal dispersion* in mutli-mode fibres. On the other hand, if the diameter of the core is reduced, or the refractive index contrast between the core and cladding is reduced, the electric field in the core interferes with itself in such a way that only a single mode can propagate: a *single-mode* optical fibre as shown in Figure 1.2c [15, 16]. These simple concepts, which will be treated more rigorously in Section 3.1, are the key ingredients for transmitting the information that constructs an image in endoscopy. Traditionally this is achieved with a bundle of fibres, where each fibre acts as an imaging pixel, however, in the following section recent advances will be discussed that enable a single fibre to be used as a powerful stand-alone imaging device.

1.1.2 Optical fibre-based imaging

There are many forms of optical endoscopy, the most common of which is white light endoscopy (WLE). For decades this modality has been used with magnifying miniature lenses and chemical staining procedures (chromoendoscopy) in an effort to maximise resolution and contrast. Within the last decade this branch of endoscopy has broken the barrier of cellular resolution imaging, with a tissue-contact imaging technique called *endocytoscopy* which utilises high resolution micro-objective lenses and fluorescent chemicals to dye the tissue (discussed in Section 1.1.3) [17]. However, the more common and clinically relevant route to cellular resolution endoscopy is provided by a narrowband laser technique, confocal laser endomicroscopy (CLE), or endomicroscopy for short [10, 18]. Confocal laser endoscopy is a collection of techniques which utilise a single wavelength laser light source. In general, a confocal pinhole is used to reject out of focus light thereby enhancing resolution and contrast while scanning the imaging system along the optical axis for in-depth imaging. Typically short wavelengths (e.g. UV) are used to both increase resolution and excite fluorescence for added contrast (Section 1.1.3) [10]. Within CLE there are further ways to categorise the range of techniques; one of the most common distinctions is between a single-fibre device and a fibre imaging bundle. Both CLE and non-CLE strategies for high resolution endoscopy will be discussed in the following sections in the context of single-fibre or multi-fibre devices.

Imaging bundle

In the 1954 seminal paper on fibre imaging bundles a clear description of the utility of a bundle is provided: “each [fibre] could convey light from one element of the image formed on it to the other end of the bundle. This is a principle which we propose to call

'static scanning' in contrast to ordinary (dynamic) scanning" [4]. Consequently, the bundle can remain in a fixed position and the illumination sequentially scanned from fibre to fibre across the proximal end of the device, and the intensity of the each pixel recorded at the sensor/detector. A caveat is that the object image becomes pixelated by the core-to-core spacing of the bundle, and thus the resolution of the device is limited. The imaging resolution can also be reduced if light from one channel of the bundle leaks into a neighbouring channel (cross talk). Despite these limitations, fibre bundle CLE systems have already achieved impact in clinical settings, and are a leading candidate for the first "optical biopsy" tool which makes possible *in vivo* histology, and therefore *in vivo* diagnostics. Cellular resolution commercial devices have been developed [19] which are capable of identifying gastrointestinal pathology - such as Barrett's oesophagus - with greater accuracy than WLE alone (see Figure 1.3) [10, 20, 21].

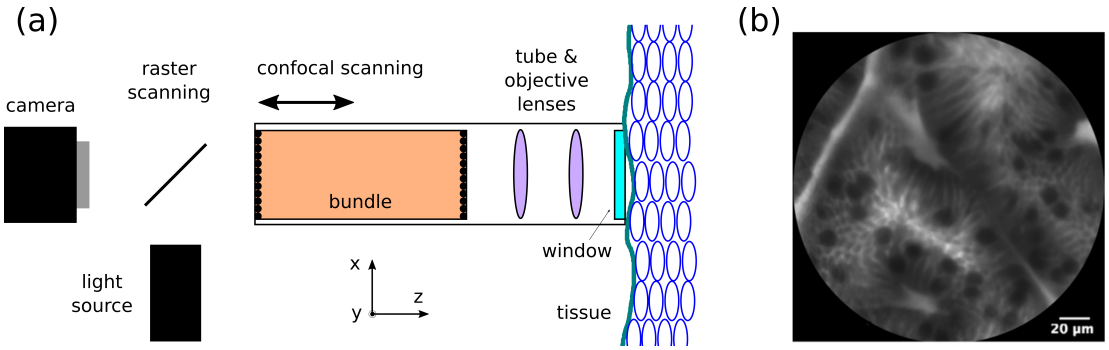


Figure 1.3: (a) Simplified diagram for an imaging bundle-based CLE instrument. The imaging bundle enables spatial resolution by scanning the input beam across the proximal end in the x/y directions. A miniaturised imaging system enables cellular resolution and the bundle is scanned in the z-direction for depth resolution. (b) Bundle-based CLE as performed in the oesophagus allows clinicians to investigate neoplasia at the cellular level in patients with potential Barrett's oesophagus. [21]. Reprinted from Gastrointestinal Endoscopy, 74, Prateek Sharma, Alexander R. Meining, Emmanuel Coron, et al., Real-time increased detection of neoplastic tissue in Barrett's oesophagus with probe-based confocal laser endomicroscopy: final results of an international multicenter, prospective, randomized, controlled trial, 465-472, Copyright (2011), with permission from Elsevier.

Single fibre

Single-fibre devices provide a more direct path to cellular resolution since the pixelation of the bundle is avoided. There are two ways in which single-fibre devices realise this increased resolution: (1) scanning the distal end of a single-mode fibre in x, y, and z, and (2) using each mode in a multi-mode fibre as a separate imaging pixel. Scenario (1) is a well-established configuration for CLE, however, it is implemented at the cost

of integrating miniaturised raster-scanning instrumentation into the distal housing of the endoscope (Figure 1.4a). There are a variety of ways in which the fibre can be scanned, e.g.: place a miniature piezoelectric tip-tilt mirror beyond the fibre (sample is orthogonal to fibre direction), piezoelectrically actuate the fibre such that it vibrates in a spiral pattern, or linearly actuate the fibre in the x, y, and z plane [18, 22]. In particular the latter of these has been adopted by industry in cellular resolution endomicroscopy [23], and similar to the case of the bundle, has resulted in endoscopists being equipped with a new resolution of insight for *in vivo* gastrointestinal diagnostics (Figure 1.4b-e) [10, 24].

Single-fibre scenario (2) - using a single multi-mode fibre - enables a return to quasi-static scanning. The underlying principle for this concept is that the spatial intensity distribution of light after it has scattered from an object can then be encoded by the modes of the fibre which will produce an image at the sensor. However, even starting with a well-behaved Gaussian profile illumination at the input end of the multi-mode fibre, intermodal dispersion and turbidity will scramble the illumination field at the output of the fibre creating a random *speckle* pattern or field [26]. To make matters worse this

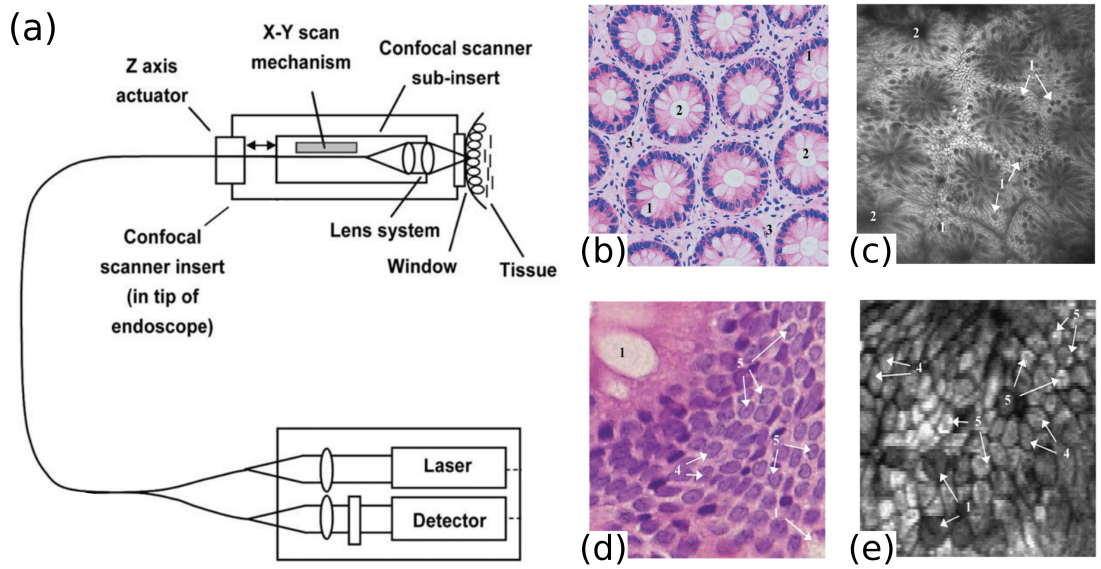


Figure 1.4: (a) Device concept for a single fibre CLE system. Spatial resolution is achieved by actuating a single fibre in $x/y/z$ and the lens system reduces the illumination spot size at the specimen. The fibre acts as the confocal pinhole in the system which allows high resolution and contrast for in-depth sectioning. (b-c) The CLE device is capable of imaging cellular structures *in vivo* in the colonic mucosa (c) which would normally only be accessible through histology (b) (FOV 500 μm). (d-e) High magnification in CLE enables sub-cellular resolution; similar to histology (d), the uptake of fluorophores by the tissue results in variations in fluorescence intensity between cells (e) (FOV 80 μm) [24]. Reprinted from Gastrointestinal Endoscopy, 62, Adrian L. Polglase, Wendy J. McLaren, Stewart A. Skinner, et al., A fluorescence confocal endomicroscope for in vivo microscopy of the upper- and the lower-GI tract, 686-695, Copyright (2005), with permission from Elsevier.

happens twice in multi-mode fibres, once as the illumination is propagated from the proximal to distal end, and then after the light has interacted with the imaging-target as the light travels from distal to proximal end (and on to the detector). Leading techniques solve this by calibrating the speckle fields, i.e. calculating the transmission matrix of the fibre, as the illumination field is varied in space, and applying these transformations to unscramble an object field (Figure 1.5) [25, 27]. This holds tremendous promise for biomedical endoscopy because wide fields of view can be attained ($\sim$ 100 μm) while maintaining sub-micrometre resolution; all this with a single fibre (and no lens), which reduces the footprint by an order of magnitude compared with a typical fibre bundle. A caveat remains in that the scrambling-effect changes as the position of the fibre is altered, and grows in complexity as the fibre is lengthened to practical lengths, however, numerical modelling and exotic fibre geometries have begun to emerge which are robust to such influences [28, 29].

All of the above techniques are classified as *front-view* probes, that is, the distal end of the fibre is end-on from the imaging target. For the internal imaging of luminal structures - such as vasculature - a *side-view* probe provides superior access to the

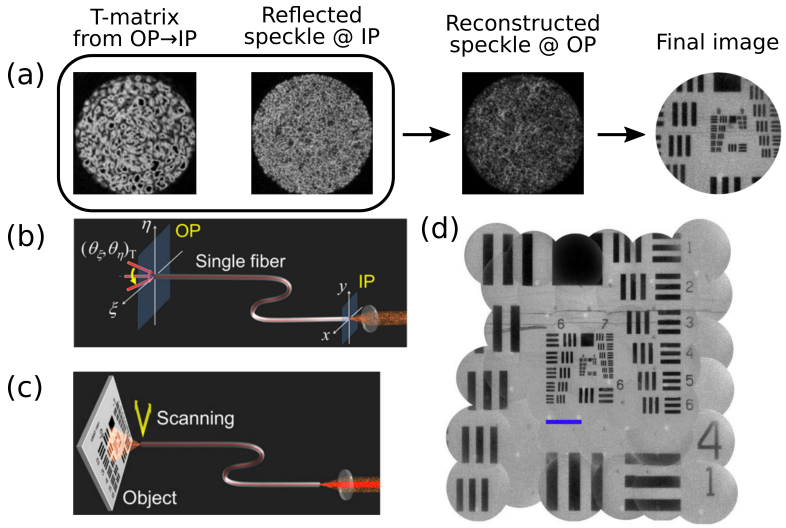


Figure 1.5: Demonstration of one approach to single fibre multi-mode imaging. Using the set-up in (b), light is sent in reverse through the system (from the object plane (OP) on the left to the input plane (IP) on the right) as a function of illumination angle. At each angle, the speckle pattern at the IP is recorded and serves as the transmission matrix of the system. (c) Then the system is operated the correct way around: illumination from IP, reflection from an object in OP, and transmission back through the fibre to the IP and camera. (a) The T-matrix operates on a speckle pattern measured at the IP to reconstruct the speckle field at the OP; averaging this speckle field over all illumination angles recovers the final image of the object. (d) Scanning the fibre allows wide fields of view (Scale bar 100 μm) [25]. Reprinted figures with permission from Youngwoon Choi, Changhyeong Yoon, Moonseok Kim, et al., Physical Review Letters, 109, 203901, 2012. Copyright (2012) by the American Physical Society. DOI: https://doi.org/10.1103/PhysRevLett.109.203901

lumen-wall provided that the probe transmits light orthogonally from its distal end (e.g. using a prism). Spatial resolution is enabled using miniaturised lenses coupled to the fibre (or bundle) and by distally scanning the endoscope (Figure 1.6a) [30]; as a result cellular resolution imaging of mouse vasculature, oesophagus, and colon has been performed with sideview CLE (Figure 1.6b) [31]. This configuration is also central to the endoscopic branch of optical coherence tomography (OCT) which uses an optical fibre-based Michelson interferometer to track changes in the optical scattering of tissue (Figure 1.6c-d). As an alternative to distal scanning, angled diffraction gratings can be used to spatially disperse broadband light therefore achieving static line-scanning [32]. In the following section, these endoscopic technologies will be discussed in the greater context of cell imaging.

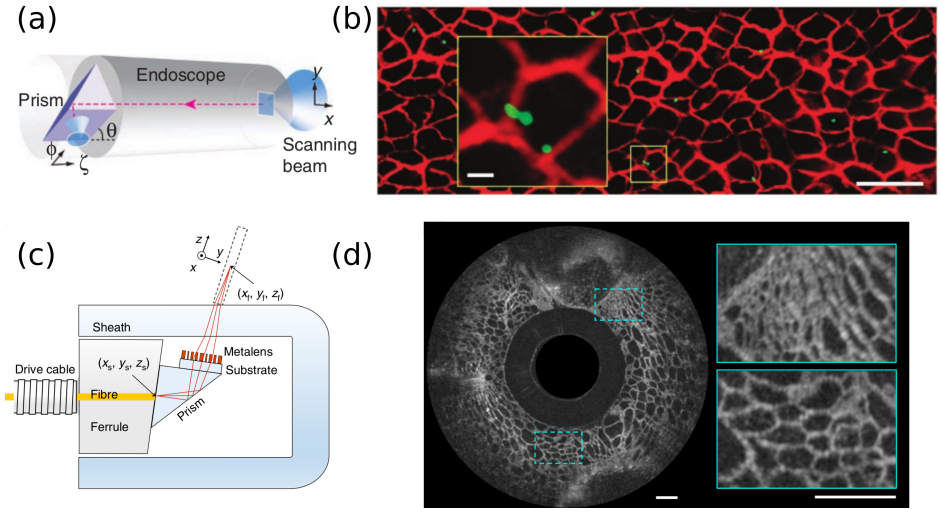


Figure 1.6: Side-view optical fibre imaging technologies. (a) A CLE-based sideview instrument which is scanned in the z-direction and rotated along the z-axis to achieve spatial resolution. (b) Fluorescence imaging of the vasculature in the colonic mucosa of a mouse; inset shows the ability to image T_{reg} cells (green) (Scale bars 200 μm and 20 μm for inset) [31]. (c) Configuration for an endoscopic OCT device using a single-mode optical fibre. A metalens structure is embedded onto the prism to achieve optical focusing in the tissue; (d) the same distal scanning paradigm as (a) is used to visualise tissue structure in a grape and even cell walls (insets) (Scale bars 500 μm) [33]. (a-b) Reprinted/adapted by permission from Springer Nature: Springer Nature, Nature Methods, In vivo wide-area cellular imaging by side-view endomicroscopy, Pilhan Kim et al., Copyright (2010). DOI: https://doi.org/10.1038/nmeth.1440. (c-d) Reprinted/adapted by permission from Springer Nature: Springer Nature, Nature Photonics, Nano-optic endoscope for high-resolution optical coherence tomography in vivo, Hamid Pahlevaninezhad et al., Copyright (2018). DOI: https://doi.org/10.1038/s41566-018-0224-2.

1.1.3 Discussion

Aside from the single-fibre multi-mode imaging devices, all other techniques discussed above are reliant on attaching a miniaturised optical lens onto the distal facet to allow light to converge at a distance away from the end-face. The two most prevalent lens-types are miniaturised convex lenses (placed a focal length away from the fibre-tip) and graded index (GRIN) fibres (can be attached directly to tip) [18, 24]. The latter makes use of a quadratic variation in refractive index along the radial cross-section of the fibre-core, which refracts light similarly to a curved lens. By using combinations of these miniature lenses, the magnification (and resolution for non-bundles) of the systems can be further increased at the cost of imaging depth and field of view. Furthermore, as 3D printing and lithography techniques continue to advance, a new class of bespoke micro- and nano-optics will facilitate a more efficient route to high resolution [33–35].

Table 1.1 collates the current capabilities of the optical endoscopic systems introduced in this Section, and will serve as a future reference for other endoscopic technologies discussed in this report. In general, a single fibre provides superior resolution compared with the pixelation of an imaging bundle, and penetration depth (e.g. into biological tissue) is dependent on the confocal geometry or the optical wavelength used. The rise of multi-mode single-fibre imaging tools holds great promise for this field since high resolution is maintained (and even potential for super-resolution [36]) while the device diameter is reduced by an order of magnitude.

One of the bedrocks of modern microscopy, and by extension optical endoscopy, is *fluorescence*, the phenomenon of an atom absorbing a photon and re-emitting a lower energy photon. Nearly all of the endomicroscopy techniques above (other than OCT) are dependent on fluorescence in a biological context. Biological cells are composed of 70% water molecules, and live in aqueous environments [40]; as a result of the similarity

Optical endomicroscopy specifications						
Technique	diameter (μm)	lateral resolution (μm)	axial resolution (μm)	field of view (μm)	penetration depth (μm)	frame rate (Hz)
Bundle endomicroscopy [37]	800	4.4	–	800	$>100^{\dagger}$	33
GRIN-lens endomicroscopy [38]	350-1000	0.85	–	60-250	$270^{\dagger}$	2.6
Confocal endomicroscopy* [24, 31]	1250	1	10	250	50	1-30
Endocytoscopy [39]	3000	4.2	–	300	30	30
Spectrally encoded endoscopy* [22, 32]	350	145	7	$\sim$1000	†	30
Multi-mode endomicroscopy* [25]	230	1.8	13	200	†	1
Endoscopic OCT* [33, 35]	2500 (sheath)	6.53	315	$\sim$1000	500	1

Table 1.1: Table comparing the performance of various micro-endoscopy techniques. * 3D imaging capable either using confocal microscopy or time-resolved modalities. † This value is dependent on fluorescence modality applied.

in optical properties (i.e. refractive index) between cell and medium, very little intrinsic optical contrast exists for cell microscopy/endoscopy. Aside from purely optical means of increasing contrast, such as phase contrast microscopy, fluorescent chemicals have drastically increased the contrast and sensitivity of cell imaging techniques for a very simple reason: “an image can be better differentiated and fine structures are more easily discernible if the object itself emits light” [41].

Despite revolutionising microscopy, and providing a path to sub-diffraction limit resolution [42, 43], the fluorescent agents (fluorophores) upon which the collection of techniques rely can pose certain risks to living biological specimens. For example, one of the key ingredients for the boom in fluorescence microscopy - the green fluorescent protein (GFP) which was originally derived from jellyfish [44] - has been known to directly contribute to apoptosis (cellular suicide), mitotic arrest, and gene mutation [45]. As the fluorophore absorbs the excitation light, reactive oxygen species free radicals are produced, which are directly toxic to key cellular molecules and disturb cellular homeostasis [46]. This problem is exasperated by: (1) photobleaching that is commonly associated with fluorophores, (2) multiple prolonged exposures associated with imaging modalities such as confocal microscopy, and (3) using short excitation wavelengths (e.g. UV) [46, 47]. Current ways of mitigating these toxic effects are by controlling the total light dosage and by utilising lower energy fluorescence mechanisms such as two-photon microscopy [18, 45]. Beyond fluorescent proteins, a variety of chemicals are used within chromoendoscopy to stain biological tissue (human and otherwise) for superior contrast; in a similar way, toxicity is strongly (and non-linearly) dependent on dosage, and has been shown to manifest in a variety of pathologies from nausea and chaotic fluctuations in blood pressure to carcinoma in the small intestine, pancreas, and lungs [48, 49].

The above examples should be taken as limiting cases for the overall toxicity of fluorophores. There also exist a number of low-risk fluorophores with minor side-effects and exceedingly rare fatalities after decades of use and testing [50]. Two such dyes, Fluorescein and Indocyanine green are both approved by the U.S. Food and Drug Administration, and as such, pose negligible risk when concentration is controlled [51]; however, for the case of Fluorescein, it has been reported that toxic effects may be more pronounced in cell culture compared with typical patient uptake [50].

Along the path to high contrast and high resolution endoscopy in biology, an interesting alternative to fluorescence imaging is the contrast natively provided by using sound instead of light. In the following section the field of ultrasonics will be introduced. Throughout the rich history of this non-destructive imaging modality which underpins sectors of clinical healthcare, the development of cellular imaging systems has not evolved from microscope to endoscope, a reality which will motivate the work presented here.

1.2 Ultrasound

Generally speaking, *acoustics* is the study of mechanical vibrations in an object or material. This basic phenomenon is most often interpreted in the form of *sound*, i.e. disturbances in the pressure, or the displacement, of air molecules which are perceivable by the human ear [52]. Given the tangibility of sound, and its role in sensing, communication and musical expression, the study of its properties dates back millennia; in particular, over the last several centuries, the development of the mathematical framework of acoustics has led to a diverse understanding about the fundamental unit of an acoustic vibration. In the regime of classical mechanics, occupied by everyday macroscopic objects such as a violin string, the acoustic vibration can be treated as a wave which oscillates between high pressure and low pressure. After the quantum revolution of the early 20^{th} century, it was shown that just as there exists a wave-particle duality for light, that an elastic wave can also be described in terms of discrete *quanta* of energy. This quasi-particle came to be known as the *phonon*, and is used to describe the free vibrations within lattices of atoms, and therefore is a foundation of modern thermodynamics and related fields [53].

The frequency of an elastic wave is one of the central themes when discussing acoustics. Elastic waves such as the surface wave of an earthquake, oscillate with a frequency of $\sim 0.1\ Hz$. As the frequency of the wave increases, the vibrations become audible to humans, e.g. in the frequency range of $20 - 20,000\ Hz$ [54]. Above this audible threshold, the acoustic waves are said to be *ultrasonic*. In the late 18^{th} century it was discovered that bats utilise ultrasonic frequencies to map their surroundings by sending out acoustic pulses and listening for echoes, i.e. *echolocation*, a characteristic which can be attributed to many animals [55].

As is often the case throughout human history, the development of ultrasonic technology was greatly accelerated by wartime efforts. Pierre Curie's discovery of the piezoelectric effect, i.e. the mechanical deformation of an object under the influence of an electric field (and vice versa), led to his doctoral student, Paul Langevin, developing the first ultrasonic transducer for use in World War I submarine detection using the echolation principles of SOund NAvigation and Ranging (sonar) [55, 56]. This worked in the following way: when a voltage pulse was applied to the piezoelectric crystal (such as quartz) of the transducer, the crystal would "expand and contract violently for a short period of time, thus producing a mechanical wave" which radiates into the surrounding water [57].

By the onset of World War II, ultrasonic transducers (Figure 1.7a) were widely used in sonar-detection, and interestingly, were developed into tools capable of detecting flaws in the solid/metallic components of naval ships and aircraft [58]. In principle this was similar to sonar, a pulse of ultrasound was sent from the transducer, and if a flaw existed in the metal, the sound pulse would prematurely echo from the change in

material density produced by the flaw and return to the transducer (now acting as a receiver). These flaw detectors made use of two critical aspects of ultrasound:

1. as with optics, the energy (E) of the wave is proportional to its frequency (f),

$$E = hf = h\frac{v}{\lambda} \tag{1.1}$$

   where h is Planck's constant, λ is the wavelength in medium, and v is the sound velocity. Therefore a $5\ MHz$ ultrasound wave travelling at $\sim 10^3\ m/s$ will deliver roughly eight orders of magnitude less energy than a $\lambda = 500\ nm$ optical wave (green) travelling at $\sim 10^8\ m/s$. Furthermore, when compared with a gold standard of diagnostics, X-ray radiography, ultrasound is upwards of 13 orders of magnitude less energetic and is non-ionising.

2. sound has the capability to penetrate deep into solid and optically opaque objects (e.g. in the visible portion of the electromagnetic spectrum). For example, one can hear a baby crying through the wall of the nursery even though one cannot see through the wall.

These principles are ideally suited for inspecting the collection of soft tissues (high opacity yet high sonic transmittance) that comprise the human anatomy; the industrial flaw detectors were finally adapted for biomedical use in the 1940's-50's by Karl Dussik, John Wild, George Ludwig, and Douglas Howry, among others [55, 60]. Early work

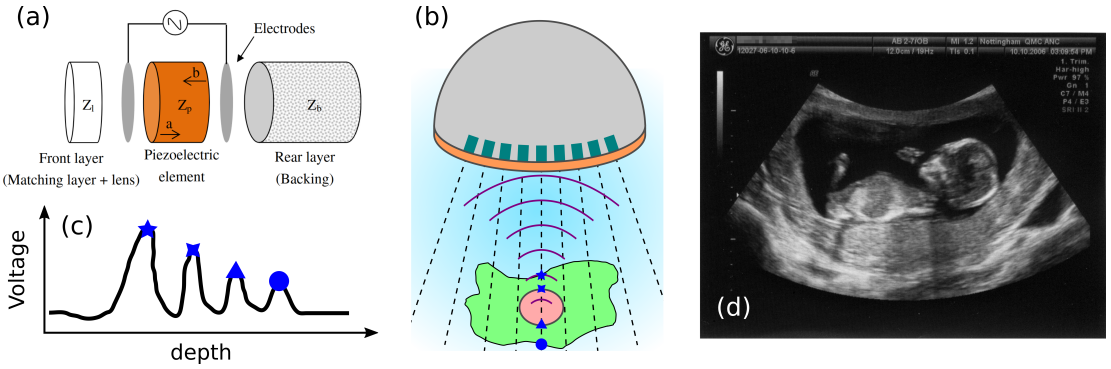


Figure 1.7: Basics of ultrasonics. (a) The central feature of an ultrasonic transducer is the piezoelectric element which expands and contracts under an applied voltage thus creating pressure waves [59]. A layer between the piezoelectric component and the sample aids in index matching such that sound is transmitted into the medium. (b) Transducer arrays (dark green) and acoustic lenses (orange) allow focusing and beam steering; (b-c) when acoustic waves encounter boundaries in acoustic impedance (blue symbols) a partial reflection occurs and an echo is recorded by the transducer (acting as a receiver). (d) One of the most prolific uses of ultrasonography is the inspection of fetal development. Reprinted from Progress in Materials Science, 56, Qifa Zhou, Sienting Lau, Dawei Wu, K. Kirk Shung, Piezoelectric films for high frequency ultrasonic transducers in biomedical applications, 139-174, Copyright (2011), with permission from Elsevier.

centred on measuring the velocity of sound through various tissues, and importantly on achieving proof of concept that sound will echo from the boundary between tissues of different densities (Figure 1.7b-c). In a testament to the role that the military-industrial complex played in ultrasound's upbringing, one of the big breakthroughs occurred when Ian Donald brought biological specimens into a nuclear plant to achieve proof of concept for using an industrial flaw detector on biological tissue; he later went on to perform the first ever measurements on the human fetus and established ultrasound as a technique for detecting early pregnancy and monitoring fetal development (Figure 1.7d) [60].

In the same way as optical endoscopy, commercial entities such as Olympus, Pentax, Siemens, and RCA (now owned by GE) have guided and accelerated the adoption of ultrasonography in a clinical setting. Despite the change in scenery over the last several decades from testing pathological samples next to a nuclear boiler, to a sterile hospital room with refined ultrasonic equipment, there has been one constant: contrast. When an acoustic wave encounters a change in material density, e.g. at the interface between fat and muscle, the wave will partially reflect and partially transmit; this is equivalent to the concept of refraction at interfaces in refractive index in optics. From the very beginning of ultrasonic diagnostics, this contrast mechanism was immediately used to investigate the acoustic difference between healthy tissue and cancerous tumours [57]. When pioneer John Wild performed ultrasonic measurements on gastric carcinoma, brain tumours, and breast tumours, he realised that the ultrasonic echoes differed drastically compared with the echoes from normal tissue [60].

Throughout the development of ultrasonic technologies and procedures, there has been a general perception that the energy delivered by ultrasonic waves is non-destructive to biological tissue. However, if energy is deposited at extremely high rates, in a highly concentrated way, or over long periods of time it is possible for acoustic power to induce potentially damaging effects in biological tissue such as heating and cavitation [61]. Such effects have reportedly led to cell death, lung tissue damage, or intestinal hemorrhage in animal studies, yet were not reproducible in human subjects [62]. Nevertheless, ultrasonographic equipment and technicians must adhere to exposure thresholds called thermal and mechanical indexes (TI and MI, respectively) which track the probability of potentially dangerous heating and cavitation events occurring.

As technology has progressed, ultrasonography has become a sophisticated diagnostic tool that is used in a wide range of medical procedures. The advent of transducer arrays (Figure 1.7b) and computer-based image processing algorithms have led to increasingly powerful imaging modalities such as 3D imaging and Doppler-based motion tracking [63, 64]. Consequently, ultrasound plays an integral role in clinical diagnostics with applications in visualising cardiovascular disease [65, 66], breast cancer tumour masses [67], liver cirrhosis [57, 68], and gynecological cancers [69], in addition to ap-

plications in therapeutics [70] and surgical guiding [71]. Many of these techniques are based on transcutaneous ultrasonography (TU) (clinician using the transducer to image objects inside the body through a layer of skin), which is inherently challenged in certain procedures for the following reason: the existence of fat, bones, and gas introduces significant acoustic attenuation.

The damping of acoustic waves generally occurs due to the internal friction of a medium. In other words, the acoustic wave performs work on the medium in the form of heating or molecular re-organisation, thereby reducing the amplitude of the propagating acoustic wave [72]. The concept of attenuation is universal to wave propagation in matter, and is generally known to be a dispersive quantity. For example in optics it is well established that the refractive index of an electromagnetic wave is complex, depending both on the phase velocity ($n = c/v$) and the extinction coefficient of the material (κ):

$$\tilde{n}(\lambda) = n(\lambda) + i\kappa(\lambda) \tag{1.2}$$

This is also the case for the propagation of an mechanical wave, e.g. in terms of the wavenumber $k = 2\pi n/\lambda$ and the angular frequency $\omega = 2\pi f$ [73]:

$$\tilde{k}(\omega) = k(\omega) + i\alpha(\omega) \tag{1.3}$$

where α is defined to be the *attenuation coefficient*. The challenge of deriving a universal analytical expression for α as a function acoustic frequency - while considering the wide range of relaxation processes for numerous materials and states of matter - has persisted for several decades [74]. However, there is overwhelming experimental consensus that the attenuation coefficient in general obeys a power law of the form:

$$\alpha(\omega) = \alpha_0 \omega^n \tag{1.4}$$

where the parameters α_0 and n are material dependent [73]. Empirically, it is well-established that many bulk liquids can be described by $n = 2$ leading to the frequency-squared attenuation paradigm in acoustics [74]. Unsurprisingly, the phenomenon of attenuation will further complicate as environments become increasingly heterogeneous, leading to additional sources of attenuation such as scattering. The above effects carry serious implications for TU inspections - in which the acoustic line of sight from the skin-layer to an intra-cavity organ may contain significant variations in density or scattering objects - and ultimately motivated the development of endoscopic ultrasound 40 years ago.

1.2.1 Endoscopic ultrasound

Just as spatial resolution is dependent on the optical wavelength in optics, so too is the case in acoustics (Figure 1.8a-b). Therefore in order to increase the resolution, and thus the level of detail, from an ultrasonic image, the acoustic wavelength must be decreased (increase in frequency). In principle this can be achieved by reducing the thickness of the piezoelectric layer in the transducer, as its resonant frequency is inversely proportional to its thickness [59]. However, as discussed previously, this presents an additional challenge for TU imaging since high frequency ultrasound is attenuated more strongly than low frequency and therefore requires that the source of high frequency ultrasound be closer to the imaging object. Similar reasoning was proposed as the reason that TU inspection of pancreatic cancer was only 80% sensitive and specific [75]. Consequently, endoscopic ultrasound (EUS) was identified as a potential path to high resolution ultrasonography; since layers of skin and fat would no longer impede the imaging volume, higher frequency transducers could then be used to increase resolution.

Other than the housing of the measurement apparatus and the increase in transducer frequency, there is essentially no fundamental difference between TU and EUS

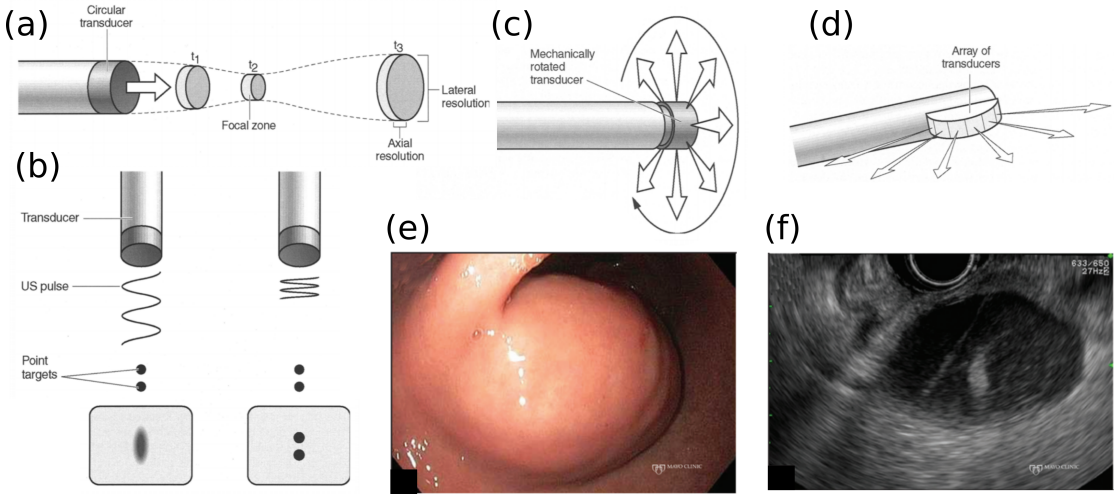


Figure 1.8: Characteristics of endoscopic ultrasound (EUS). (a) Similar to lateral resolution in optics, resolution is defined in acoustics by the acoustic wavelength and the power of the lens, whereas axial resolution is more strictly defined by the acoustic wavelength (b). (c-d) Visualisation of two common EUS configurations: rotational/radial and linear/convex arrays [76]. (e-f) Optical and acoustic endoscopic views of a gastrointestinal stromal tumour; (f) the thin track of a needle can be seen in the sub-surface volume of the tumour from which blood is pooling (bright spot in middle) [77]. (a-d) Reprinted from Techniques in Gastrointestinal Endoscopy, 2, Steven M. Shaw, Michael B. Kimmey, General principles of endoscopic ultrasonographic imaging, 50-55, Copyright (2000), with permission from Elsevier. (e-f) Reprinted from Endoscopic Ultrasound, 3, Larissa L. Fujii, Michael J. Levy, Basic techniques in endoscopic ultrasound-guided fine needle aspiration for solid lesions: Adverse events and avoiding them, 35-45, Copyright (2014).

devices. Although probe-type ultrasonic transducers had been tested beforehand, the real breakthrough in EUS came in the early 1980's when ultrasonic transducers were combined with the optical endoscope [78]. This mainly provided the ability for the endoscopist to visualise the intracavity environment optically before identifying the region in which they wanted to perform high resolution ultrasound measurements. Following the development of hybrid EUS devices, it was shown in a clinical trial that pancreatic tumours could be diagnosed with 99% sensitivity and 100% specificity, compared with the 80% mark previously attained [79].

In addition to the acoustic wavelength, maximum resolution for EUS systems is also dependent on the aperture size of the transducer, numerical aperture of an acoustic lens (if used), and the density of the transducer array (equivalent to situations in which the pixel spacing limits resolution in optical microscopy) [76, 78]. State of the art EUS equipment sold by Olympus, Pentax, and Fujifilm - which come in a variety of side-view, rotational, and forward viewing configurations (Figure 1.8c-d) - contain operating frequencies in the range of $5 - 12\ MHz$ [80], with prototypical devices containing as high as $20\ MHz$ [81]; among these devices the maximum achievable lateral and axial resolution is on the order of $1\ mm$ and $0.2\ mm$, respectively [76, 78, 81]. Despite having relatively low imaging resolution, the long penetration depths ($\sim$4 cm) and video-rate acquisition speeds allow EUS to play a crucial role in a wide range of procedures, including diagnostics for gastric, pancreatic, rectal, and oesophageal cancer (Figure 1.8e-f) [75, 78]. However, further improving the resolution of an ultrasonic endoscopic will serve to expand the power and usefulness of acoustics, especially in a diagnostic capacity. In the following sections the paths to sub-mm, and even sub-micron resolution will be introduced.

1.2.2 Acoustic microscopy

In the 1970's it was realised that a high frequency piezoelectric transducer, e.g. $f > 100\ MHz$, could be turned into a microscope for acoustic waves. The key enabler of this acoustic microscope was fabricating an acoustic lens with the following properties: (1) is fixed in direct contact with the transducer, (2) is highly transmissive of the acoustic waves, and (3) contains at its output a concave surface with spherical curvature which uses refraction to focus ultrasound into the subsequent water volume [82]. Early designs utilised two transducer/lens combinations, one for exciting ultrasound, and the other placed on the opposite side of the sample plane (compared to the source) for detecting the amplitude of the transmitted ultrasound at a single pixel [82]; later on, the microscope was adapted to work in reflection mode and therefore use a single transducer as source and detector (Figure 1.9a) [83].

The radius of curvature (ROC) for the acoustic lens is similar in principle to the numerical aperture (NA) of an optical lens. High radius of curvature allows higher spatial

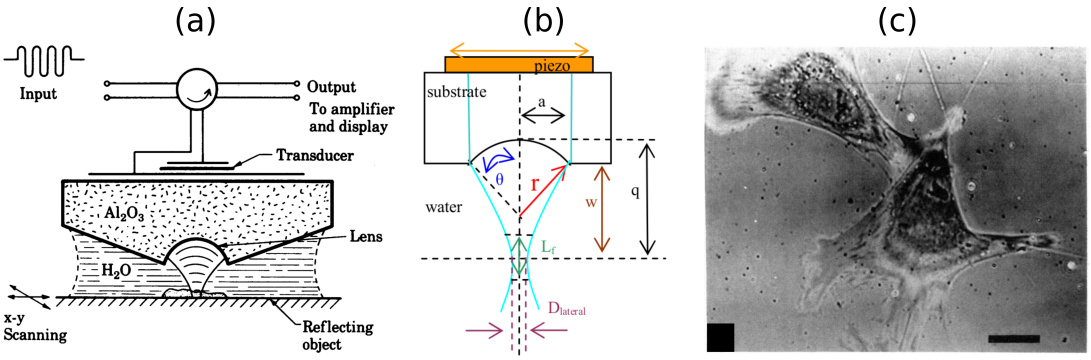


Figure 1.9: Device concept for the scanning acoustic microscope (SAM). (a) A concave acoustic lens is fashioned out of an acoustically transmissive material, such as sapphire and fixed to a high frequency piezoelectric transducer [85]. The transducer acts as both the transmitter into the coupling medium/sample, and after a quiescent state, acts as the receiver for acoustic echoes from acoustic impedance boundaries of the specimen. (b) Lateral resolution ($D_{lateral}$ in image) is determined by the resonant frequency of the transducer, and the lens aperture (a) and radius of curvature (r) [86]. (c) SAM image of a chicken heart fibroblast cell showing the ability for resolving subcellular features (Scale bar $20\ \mu m$) [85]. (a,c) Reprinted from Proceedings of the National Academy of Sciences of the United States of America, 78, J A Hildebrand, D Rugar, R N Johnston, and C F Quate, Acoustic microscopy of living cells, 1656-1660, Copyright (1981). (b) Reprinted from 2009 IEEE International Ultrasonics Symposium, A. Jakob, M. Bender, T. Knoll, et al., Comparison of different piezoelectric materials for GHz acoustic microscopy transducers, Copyright (2009).

frequencies to be produced, yet at the cost of a shortened focal length (Figure 1.9b). Therefore the resolution of the microscope will depend on the lens ROC as well as the acoustic wavelength. An early design of the acoustic microscope with a $160\ MHz$ transducer ($9.4\ \mu m$ wavelength in water) and $1.59\ mm$ ROC was capable of a resolution of $10\ \mu m$ in water [82]. Following initial development, acoustic microscopy was quickly applied to the imaging of biological cells where the intrinsic variation in the mechanical properties of sub-cellular features produced high contrast images. This was first performed on fixed cells [84], and later living cells (Figure 1.9c) [85]; in both cases the vitality of the cells appeared unaffected by the high frequency acoustic waves, especially in contrast with the equivalent violet and ultraviolet wavelengths in the electromagnetic spectrum.

In order to increase resolution, either a shorter acoustic wavelength is required (higher frequency transducer), or a smaller radius of curvature. A caveat to further increasing resolution with higher frequency transducers, is that the attenuation of acoustic waves increases with the square of the acoustic frequency, and therefore drastically reduces the practical working distance of the microscope [82]. In the 1980's the solution to this obstacle was to replace water as the coupling material and instead choose a material which lowers the acoustic velocity, and therefore the wavelength, given a constant frequency. As it turned out, the most natural candidates for this material were

cryogenic liquids. By making the switch from water to supercooled liquid argon, nitrogen, and helium the acoustic wavelength could be reduced by 2 to 4 times; these shorter wavelengths could then be used to achieve higher resolution while keeping ROC and frequency fixed (attenuation), or a fixed resolution could be maintained with an increased ROC (focal length). Consequently, by increasing transducer frequency to $630\ MHz$, an acoustic wavelength of $360\ nm$ was achieved in cryogenic helium, which allowed the resolving of $400\ nm$ features in a resolution target [83].

In the context of developing a micrometre resolution ultrasonic device that could be compatible with endoscopic instrumentation, there are difficulties presented by acoustic microscopy technology. Since, the resonance frequency of the piezoelectric transducer will inversely scale with the thickness of the piezoelectric element, an increasingly fragile transducer needs to be fabricated and electrically driven, e.g. on the order of $1-10\ \mu m$ film thickness. Conventional piezoelectric transducer materials, such as ZnO (zinc oxide), are capable of being deposited to such dimensions, however, at frequencies at and above $1\ GHz$, there is severe insertion loss resulting in acoustic amplitudes that are too low for use [86]. Additional materials and thin-film deposition techniques have been explored, yet issues still centre on achieving a thin-film of sufficiently high quality; if the fabrication procedure introduces inhomogeneity or stress into the film, it is likely to crack under electrical excitation [59]. Furthermore, there is the complication of miniaturising and implementing the surrounding electrical system. One potential solution to these issues was identified in the mid 1980's: instead of using electro-acoustic systems, why not use opto-acoustic? In addition to simplifying the electrical obstacles of acoustic microscopy, this also presents an opportunity to utilise optical microscopy as a route to high resolution.

1.3 Photoacoustics

The field of photoacoustics (sometimes referred to as optoacoustics) had its beginning in the late 19^{th} century with Alexander Graham Bell and his assistant Summer Tainter. They discovered that by shining light onto an object, the object was capable of producing sound. In a description of one of their seminal experiments, Bell remarked: "a beam of sunlight was focussed into one end of an open tube, the ear being placed at the other end. Upon interrupting the beam, a clear, musical tone was heard, the pitch of which depended upon the frequency of the interruption of the light and loudness upon the material composing the tube" [87]. Bell then proposed that this effect could be explained in the following way (using the pigment lamp-black as an example): "when a beam of sunlight falls upon this mass the particles of lamp-black are heated, and consequently expand... When the light is cut off the converse process takes place" thus implying that the rapid modulation of these processes give rise to audible sound

waves [87]. This process of creating elastic waves from a thermal gradient is known as *thermoelastic*. It was then Bell's ambition to prove that this *photoacoustic effect* was in fact a property that was "common to all matter." Following these important experimental breakthroughs, C.V. Raman and Léon Brillouin indeed discovered a more intimate (and quantitative) relationship between light and sound [88, 89]. In the following chapter the discoveries and developments enabled by Brillouin will be introduced and utilised for application to high frequency ultrasonic imaging.

1.3.1 Photoacoustic microscopy

The usefulness of the photoacoustic effect became more apparent with the advent of the laser, and especially pulsed lasers in the mid-20^{th} century, the latter inherently providing "interruptions" to the optical beam at rates of thousands to millions of interruptions per second. By the 1970's the potential for utilising the photoacoustic effect as an imaging mechanism was realised; the inventors of the scanning acoustic microscope [82] integrated a focusing lens into their system for this purpose thus creating the first photoacoustic microscope (PAM) [90]. The lens would focus short pulses of light onto the sample, resulting in: optical absorption, thermal expansion (and contraction with cooling), and radiation of mechanical vibrations, which would then propagate to a conventional piezoelectric transducer for detection (Figure 1.10-B1).

The curiosity that dark pigments could generate photoacoustic waves was eventually applied to highly absorbing biological materials, e.g. chromophores [93]. Despite the low optical absorption in biological tissue, endogenous chromophores such as haemoglobin, DNA, RNA, melanin, and mitochondria (among others) by contrast exhibit significant absorption [94]. Through this mechanism, biological specimens themselves act as label-free photoacoustic sources; in this context PAM provides the following capabilities:

- potential for optical lateral resolution - when the optical spot size (and thus the size of the photoacoustically excited region) is smaller than the focal spot of the acoustic transducer [94]. The inflexibility of acoustic lenses with fixed focal length/spot size can be replaced with an interchangeable optical lens while providing spatial resolution equivalent to an optical microscope [90].

- reduced acoustic path length (and therefore attenuation) - compared with techniques that use a transducer as an acoustic source. Since the specimen itself acts as the acoustic source, acoustic attenuation which would normally occur from the piezoelectric transducer source to the sample is avoided (replaced by optical attenuation) [95].

- high contrast - imaging contrast is provided by changes in optical absorption as opposed to optical transmittance or reflectance [94, 96]. For common endoge-

nous chromophores absorption of visible wavelengths can be 4 to 8 orders of magnitude stronger than water alone [95].

- broadband ultrasonic frequency performance - the optical penetration depth of the absorbing material, the size of the object, the sound velocity, and the pulse width of the generation laser will determine the frequency response of the system [97–99]. Due to the wide range in size and absorption profile of various absorbers, photoacoustic waves spanning from the $kHz - GHz$ range can be generated allowing a range of axial resolutions [100].

- long acoustic penetration depth - with wideband frequency performance comes a

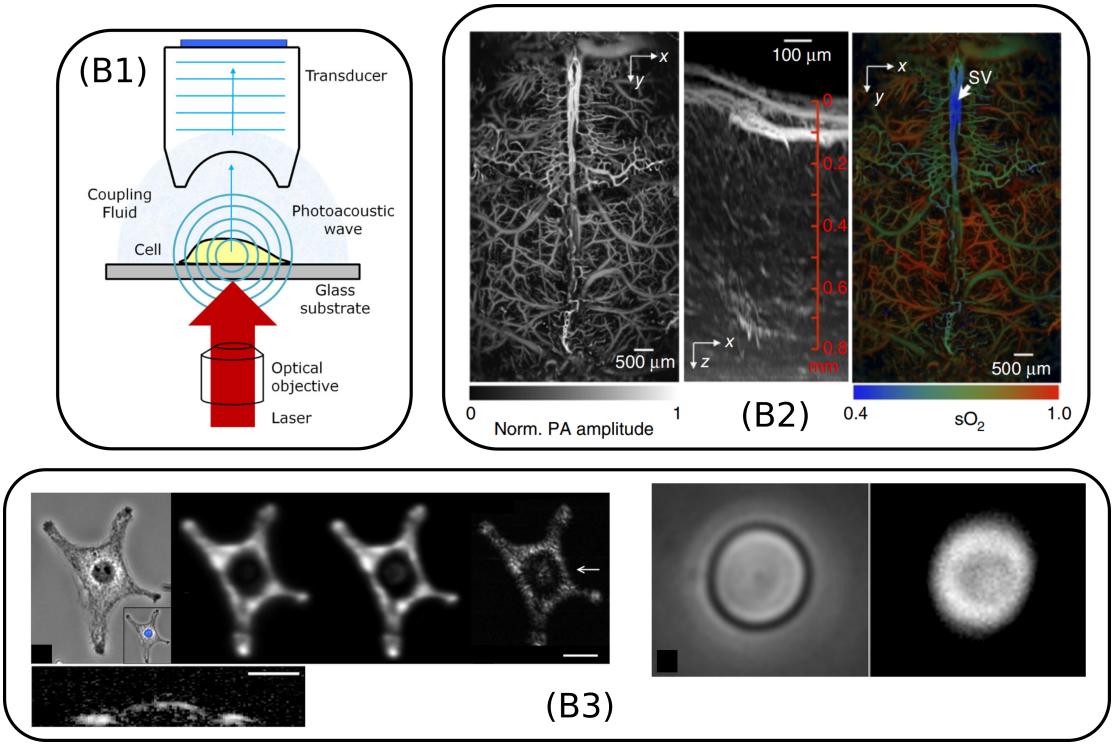


Figure 1.10: Working principle and imaging capabilities of photoacoustic microscopy (PAM). (B1) In general the sample is illuminated by a pulsed laser, and the acoustic waves generated by optical absorption in the specimen are detected by a piezoelectric receiver [91]. (B2) PAM imaging of the vasculature network of a mouse brain. (left-middle) Normalised acoustic amplitude for lateral and longitudinal cross-sections; (right) using excitation beams with different pulse-widths multiple chromophores can be targeted and used for spectral imaging of blood oxygenation [92]. (B3) PAM imaging of single cells: (left) melanoma cell and (right) red blood cell (FOV 15 μm). (left) Bright-field and fluorescence showing the cell nucleus, followed by PAM images showing the increasing image resolution as the detection-transducer frequency is increased (scale bar 30 μm); (bottom) in-depth imaging, scale bar 15 μm [91]. (B1,B3) Reprinted from Photoacoustics, Eric M. Strohm, Elizabeth S. L. Berndl, and Michael C. Kolios, High frequency label-free photoacoustic microscopy of single cells, Copyright (2013). (B2) Reprinted by permission from Springer Nature: Spring Nature, Nature Methods, High-speed label-free functional photoacoustic microscopy of mouse brain in action, Junjie Yao et al., Copyright (2015).

wide range of acoustic attenuations. For the low frequency end of the ultrasonic spectrum, e.g. $5\ MHz$, this results in penetration depths on the order of $\sim 10\ cm$; the attenuation that occurs over this distance is equivalent to the amount experienced by a $50\ MHz$ wave in $\sim 1\ cm$ [100]. Furthermore, NIR wavelengths of light will achieve maximum penetration on the order of $\sim 1\ cm$ [101] as they scatter much more significantly than for low frequency ultrasound [97, 98].

Using these principles PAM has been established as a powerful tomography and microscopy technique for inspecting biological specimens with high contrast, penetration depth, and resolution. It is especially ideal for biological subjects with high concentrations of endogenous chromophores; consequently, it is a vital modality for investigating a variety of physical and chemical conditions within the cardiovascular network, composed of the endogenous contrast agent haemoglobin (Figure 1.10-B2) [92, 97]. When used with high numerical aperture microscope objectives PAM enables cell imaging with photoacoustic contrast and optical (and even super-optical) resolution [94, 102, 103]. It is worth noting that this is typically carried out on cell-types that carry high concentrations of chromophores, such as red blood cells or melanocytes (Figure 1.10-B3); this condition is commonly not the case for other cell-types which necessitate exogenous photoacoustic contrast agents such as dyes and nanoparticles [94].

Beyond the bench-top implementation of PAM, there has been a great deal of development in photoacoustic endoscopy (PAE), which enhances the clinical adoption of photoacoustics. In the following section, these technologies will be briefly described.

1.3.2 Photoacoustic endoscopy

Given the optical excitation mechanism of photoacoustic microscopy, it is natural to translate the technology from using bench-top optical microscopy equipment to optical fibre-based equipment that is compatible with conventional endoscopes. Early implementations of this concept utilised a relatively conventional EUS transducer, with an optical window surrounding the acoustical axis. Excitation light was illuminated external to the sample through to the acoustical axis for photoacoustic excitation and ultrasonic detection [104]. Soon after fully endoscopic designs emerged which placed an optical fibre - used to deliver light into the imaging volume for photoacoustic excitation - through the same channel occupied by the mechanical scanning and piezoelectrical wiring (Figure 1.11-B1) [105–107]. This work led to a great leap in pre-clinical relevance for PAE through the 3D volumetric *in vivo* imaging of the lower and upper gastrointestinal tract vasculature (rabbit) [96]. The breakthrough was enabled by designing the probe such that a single piezoelectric transducer could act as a receiver for 3 excitation events: piezoelectric transducer excitation, and two separate optical fibre photoacoustic excitations (Figure 1.11-B1). In this way, the device simultaneously performed EUS and 2-channel PAE; the latter achieved by using 2 separate optical wavelengths with which

2 different optical absorption peaks and therefore chromophores could be targeted.

Similar to bench-top PAM, the spatial resolution of a photoacoustic endoscope can be improved by minimising either the optical spot size (generation) or the acoustical spot size (detection), with the region of overlap between the two ultimately setting the lateral resolution. However, the only way to improve axial resolution is by maximising the upper frequency of the piezoelectric transducer [109]. Currently the photoacoustic endoscope (with piezoelectric transducer detection) with the highest spatial resolution

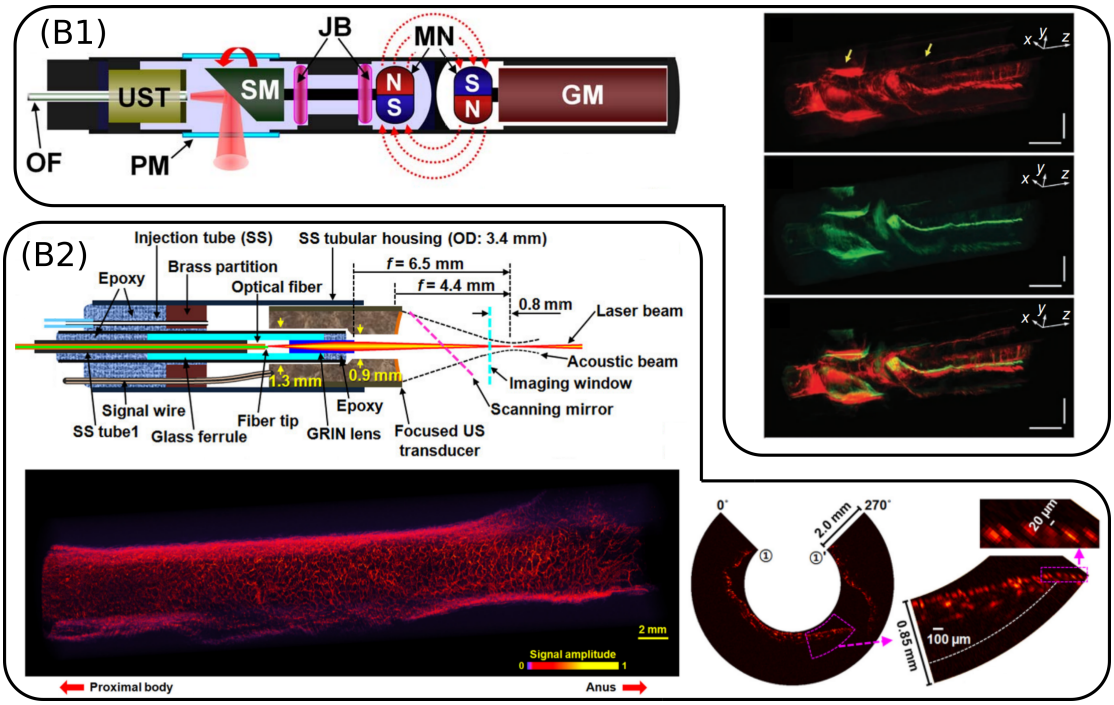


Figure 1.11: Illustration of state of the art photoacoustic endoscopes (PAE). (B1-left) the measurement apparatus consists of a piezoelectric ultrasonic transducer (receiver) with an optical fibre running through its centre (photoacoustic excitation source) [105]. The transducer can also be used for parallel ultrasonography, by exciting and detecting its own acoustic waves (at different times compared with its acquisition of the PA signal). Optical beam is scanned radially by electromagnetically rotating the optical-acoustic mirror (SM) along the long axis of the endoscope; the probe is withdrawn along the long axis of the device to achieve transverse spatial resolution. (right) *In vivo* PAE imaging of rabbit oesophagus: (top) photoacoustic amplitude, (middle) all-ultrasonic image, (bottom) overlay of PA and ultrasonic (horizontal and vertical scale bars $2\ cm$ and $5\ cm$ respectively.) [96]. (B2-top) Optical-resolution PAE device which achieves optical focusing by coupling a GRIN lens to the tip of the photoacoustic excitation fibre. (bottom-left) 3D volume rendering of a rat colorectum imaged *in vivo*; (bottom-right) given the optical and acoustic focusing of the device a radial resolution of $10\ \mu m$ is possible allowing fine tissue structure to be resolved [108]. (B1-L) Reprinted from Optics Letters, Joon-Mo Yang, Konstantin Maslov, Hao-Chung Yang, et al., Photoacoustic endoscopy, Copyright (2009). (B1-R) Reprinted by permission from Springer Nature: Spring Nature, Nature Medicine, Simultaneous functional photoacoustic and ultrasonic endoscopy of internal organs in vivo, Joon-Mo Yang et al., Copyright (2012). (B2) Reprinted from Biomedical Optics Express, Joon-Mo Yang, Chiye Li, Ruimin Chen, et al., Optical-resolution photoacoustic endomicroscopy in vivo, Copyright (2015).

is achieved using a GRIN-lens optical fibre for photoacoustic excitation, which produces a lateral resolution of $10\ \mu m$ and an in-depth resolution of $50\ \mu m$ (Figure 1.11-B2) [108]; similar resolutions have also been demonstrated by other optical-excitation and acoustic-detection configurations [110, 111].

The PAE devices discussed thus far can be classified as being side-view probes, i.e. the line-of-sight for the probe is orthogonal to the surface normals of the optical fibre (excitation) and piezoelectric transducer (receiver). Side-view configurations achieve spatial resolution by acquiring a series of photocaoustic measurements along the radial direction, and then mechanically rotating the probe in order to interrogate the adjacent region. This scheme is ideal when the probe is used for inspecting luminal objects, such as arteries, the oesophagus, and the colon [96]. However, for procedures such as needle biopsies and gastric mucosal inspection a device which looks forward into the target is more desirable. The path to forward-viewing for piezoelectric PAE devices is made difficult by the need to scan the transducer in the x/y direction in order to achieve spatial resolution. This is achievable in principle as seen with endomicroscopy; however, the footprint of piezoelectric PAE devices is already dominated by the transducer (typically on the $\sim mm$ scale), and providing additional space for range of motion will drastically increase the device size. Alternative solutions to this obstacle are made difficult by the fact that: piezoelectric transducers decrease in sensitivity as their active area decreases, and high-performance transducers are generally optically opaque which presents challenges for the placement of the excitation optical fibre [100].

All-optical photoacoustic endoscopy

Piezoelectric transducers operate via electrical sensitivity to mechanical vibrations. An alternative to this mechanism, is to design a transducer which is *optically* sensitive to mechanical vibrations. An ideal tool with which this detection scheme can be achieved is an optically resonant cavity, such as a Fabry-Pérot interferometer (discussed in the following chapter). In such cavities the reflection and transmission of light through the device is strongly dependent on cavity thickness, which provides an opportunity for optical power modulation under mechanical strain. This innovation meets the challenges outlined in the previous section, especially in the following aspects:

- by fabricating an optical receiver onto an optical fibre, the lateral dimensions of the probe can be reduced by nearly an order of magnitude (compared with piezoelectric detectors). This reduction in size drastically improves the prospects for implementing the device into standard endoscope instruments where space is restricted.

- the dimensions of the transducer can be reduced to thicknesses which would normally break under high voltage application (for a piezo-electric transducer) [59].

This makes available standard thin-film fabrication techniques such as physical vapour deposition and dip-coating. These considerations become relevant when seeking to increase the bandwidth of the receiver, but more importantly when attempting to detect ultra-high frequency ultrasound.

- arrangement of ancillary components for piezoelectric detection, such as wiring, electrical isolation, pre-amplifiers is no longer required (nor is the space they consume), especially when replaced by a simple optical fibre.
- the optical cavities can be designed such that they are transparent at the wavelength used for photoacoustic excitation, thus allowing a consolidation of excitation and detection channels
- by consolidating excitation and detection channels, previous difficulties in co-aligning the piezoelectric transducer axis with that of the optical axis are avoided or simplified [107].
- endoscope-compatible optical fibre scanning techniques are well-established, either distally [24, 112] or proximally by using a static optical fibre imaging bundle; both being capable of optical microscopy resolution.

Within an all-optical paradigm of PAE, the prospect of achieving spatial resolution by scanning the detection laser across the proximal end of an imaging bundle is especially promising. This negates the use of complicated miniaturised distal scanning units

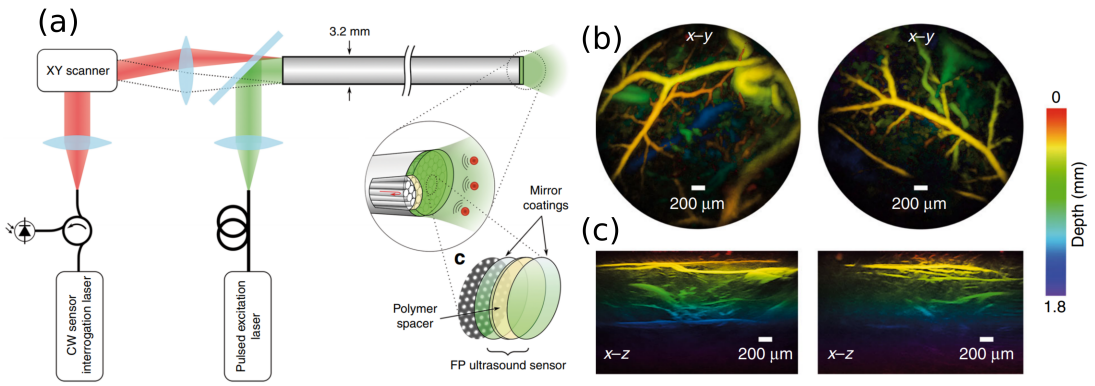


Figure 1.12: All-optical forward viewing photoacoustic probe. (a) The device consists of an optical fibre imaging bundle; just as with conventional PAE, the fibre is used to deliver the excitation laser to the sample. A Fabry-Pérot optical cavity is fabricated onto the distal end of the bundle; the cavity is designed such that its optical reflectivity (of a second probe laser) is sensitive to the mechanical deformations caused by the photoacoustic waves of the sample. Photoacoustic-based depth imaging of vasculature in mouse abodominal skin both in the lateral (b) and longitudinal (c) directions [113]. Reprinted from Light: Science & Applications, Rehman Ansari, Edward Z. Zhang, Adrien E. Desjardins and Paul C. Beard, All-optical forward-viewing photoacoustic probe for high-resolution 3D endoscopy, Copyright (2018) under Creative Commons license Attribution 4.0 International (CC BY 4.0).

(rotational or linear), which add to the footprint of a PAE system. The leading work on this particular solution has been carried out by fabricating a Fabry-Pérot interferometer directly onto the distal end-face of a coherent imaging bundle [113]. The cavity is designed such that it is transparent for the excitation wavelength, and sensitive to vibration for the detection wavelength (Figure 1.12a). The device contains maximum lateral and axial resolutions of $45\mu m$ and $31\mu m$ respectively, which were used to attain images of vasculature in *ex vivo* duck embryo and mouse abdominal skin (Figure 1.12b-c). Recently, an alternative design has been proposed, in which a GRIN-lens is fixed to the bundle distal facet to increase the resolution and field of view [114].

In the following section, the preceding advancements in photoacoustic endoscopy will be brought into context within the landscape of high resolution imaging tools with endoscopic dimensions. A particular focus will be applied to the prospects of the highly miniaturisable all-optical ultrasonic imaging techniques, and how these might be developed to the point where biological cell imaging is possible.

1.4 Discussion, device concept, and thesis outline

This chapter has introduced the history, working principle, and technological developments of optical, acoustic, and photoacoustic endoscopy. The trajectory laid out by optics - from microscopy to endoscopy - has inspired similar innovation for the younger field of ultrasonics, and the even newer field of photoacoustics. Compared with optical techniques, and even conventional ultrasound, photoacoustics provides superior contrast due to the stark difference in optical absorption throughout biological tissue, as opposed to contrast achieved via refractive index or acoustic impedance mismatches. This provides further value due to the fact that optical absorption is chromophore-specific, and therefore high specificity and spectroscopic accuracy can be obtained. However, the path to microscopic resolution is less trivial in photoacoustics than for optical endomicroscopy. Aside from distal scanning units (if required) and focusing micro-optics, optical endomicroscopy is without additional complexity and therefore space can be used to increase pixel density. For photoacoustics, the reliance on optical, acoustic, electrical, and mechanical instrumentation results in complicated payloads at the distal facet which are exclusively on the order of $> 1\ mm$ in total diameter [109].

Currently, the most reliable way to shrink PAE's appears to be via optical detection of ultrasound, i.e. all-optical ultrasonics. In this way, the pitfalls of reduced piezoelectric transducer sensitivity and bulky distal scanners are avoided, and replaced by a wideband/high-sensitivity optical cavity combined with the $\sim 10\ \mu m$ channel of an optical fibre, e.g. in an imaging bundle with tens of thousands of channels. Even if a convetional PAE device could be sufficiently miniaturised, one of the strengths of PAE is also a relevant limitation: a close reliance on optical absorption. When there exists

weak intrinsic optical absorption, e.g. as in many cells, the technique becomes reliant on extrinsic labels, or must change excitation wavelength to photoxic UV [115, 116]. For this reason, most cell imaging in PAM is reported with cells that exhibit strong absorption (red blood cells) or labelled cells [94]; this could also provide an explanation for the lack of dedicated cell imaging technology for PAE thus far.

Instead of relying on strictly the optical absorption (and thermoelastic) characteristics of the imaging target itself, there is the possibility of mechanically exciting the target with ultrasound that was generated by the endoscope. In other words, the device would rely on the historic concepts of pulse-echo ultrasonography, where the piezoelectric transducer is both a transmitter and receiver of ultrasound; however, the device would be all-optically driven. What has been described are effectively the principles of *laser ultrasonics*, a technology which has been widely applied in materials science and industrial applications [117]. In laser ultrasonics, an optically absorbing (often polymeric or metallic) transducer layer is used to generate ultrasound through the same photoacoustic effect described earlier, and the time-of-flight of the wave can be optically monitored through interferometry. These principles have already been successfully applied to *ex vivo* and *in vivo* imaging of swine vascular tissue (Figure 1.13) [118, 119] using an optical fibre terminated with carbon nanotube-based polymer composites for thermoelastic generation and a neighbouring fibre as a detection interferometer [120].

Despite significant progress in PAE, and now laser ultrasonic fibre imaging, the prospect of cellular resolution imaging (akin to cell imaging in endomicroscopy and endocytoscopy) still eludes the wide range of acoustics-based endoscopy modalities. The following are proposed as reasons as to why this has not yet happened:

- high lateral resolution requires tightly focused light - with micro-optics this is routine for optics (if the optical excitation spot size is being used to set the resolution of PAE). However, achieving this acoustically requires shortening the acoustic wavelength which requires more fragile high frequency transducers with acoustic lenses (if the acoustic detection spot size is being used to set the resolution of PAE). Furthermore, as the lateral resolution of the device is increased this will demand greater resolution for the mechanical scanning elements (more easily accomplished using a fibre bundle with proximal scanning).

- high axial resolution requires high frequency ultrasound (e.g. $> 100\ MHz$) - this is inherently difficult for acoustic-detection PAE since high frequency transducers would be compulsory. This can be more readily achieved with optical detection since the Fabry-Pérot sensor can be fabricated such that it is sensitive over a greater bandwidth.

- higher acoustic frequency means greater attenuation - consequently, both the working distance and penetration depth of the device will be more significantly

limited than typical $20 - 40\ MHz$ frequency PAE techniques.

- decreased field of view - using a high numerical aperture micro-objective lens or acoustic lens will reduce the imaging field of view which then places greater demand on the scanning mechanism.

However, these are rather similar challenges faced by endomicroscopy and endocytoscopy which provide *in vivo* imaging capability with resolutions that are comparable with histology. If these qualities could be realised for acoustics, microscopic resolution and acoustic contrast could then be applied to medical and industrial applications in which there is no conventional line-of-sight and would normally require extraction for inspection. This would extend the utility of acoustics:

- the life sciences would gain a new label-free tool with which mechanical pro-

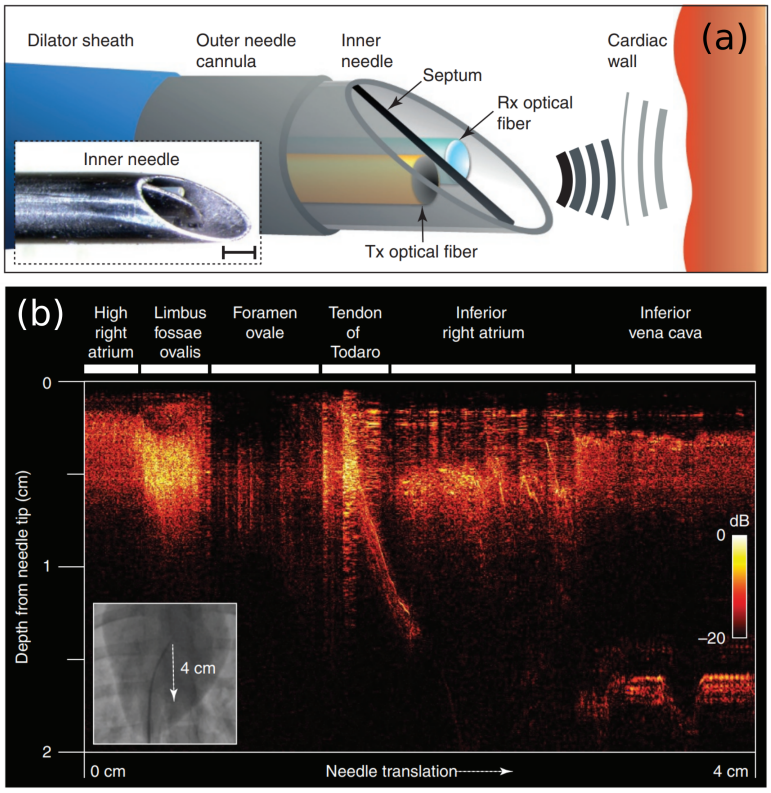


Figure 1.13: Device concept for an all-optical laser ultrasonic fibre imaging device. (a) The system consists of two fibres: a multi-mode fibre capped with a carbon nanotube polymer composite for photoacoustic excitation, and a single-mode fibre capped with a Fabry-Pérot interferometric detection cavity. The two are placed adjacently in a cardiac needle which is mechanically articulated in $x/y/z$ to achieve spatial resolution. (b) *In vivo* brightness mode (B-mode) imaging (in the lateral and longitudinal dimensions) as the probe is translated along swine cardiac tissue. By tracking the amplitude of acoustic echoes at impedance changes, the probe is capable of resolving the topography and anatomical features of the cardiac wall [119]. Reprinted from Light: Science & Applications, Finlay, M., Mosse, C., Colchester, R. et al., Through-needle all-optical ultrasound imaging in vivo: a preclinical swine study, Copyright (2017) under Creative Commons license Attribution 4.0 International (CC BY 4.0).

cesses in the microstructure of biology (cells and tissue) could be investigated

- this could lead to new tools for pathology where acoustic spectroscopy and imaging could search for micro-mechanical signatures of disease for less invasive high throughput biopsies
- the above concept could also be applied to non-biological specimens, for example in on-wing aerospace diagnostics or precision manufacturing monitoring
- compatibility with standard endoscopes, needles, catheters, etc, would change the concept of an ultrasonic payload.

Therefore, it is the intent of this thesis to create an all-optical fibre-based imaging device which delivers microscopic resolution, label-free contrast, and portability, utilising optical lateral resolution and ultra-high frequency ultrasound (e.g. $\sim GHz$) for axial resolution. The devices discussed above will serve as references, and their relevant characteristics are reported in Table 1.2.

One prospect which could meet the outlined needs for the phonon probe, is a derivative of laser ultrasonics called *picosecond ultrasonics* (PU) or *picosecond laser ultrasonics* (PLU). By using ultrashort pulse-width lasers (e.g. $\leq 1\ ps$) and optical absorbers with nanometre-scale skin-depths, ultrasonic frequencies from $GHz - THz$ can be photoacoustically generated [121]. In water, acoustic waves with these frequencies possess wavelengths that span $1500\ nm$ down to $1.5\ nm$, and therefore provide an opportunity for ultra-high axial resolution and optical lateral resolution provided that

Photoacoustic endoscopy specifications						
Technique	diameter (mm)	lateral resolution (μm)	axial resolution (μm)	field of view (mm)	penetration depth (mm)	A-scan rate (Hz)
AR-PAE† [96, 105]	4.2	230	47	25	3	1000
OR-PAE† [108]	3.8	10	50	20	2	1000
all-optical PAE #1 [113]	3.2	39	31	3.5	2	30
all-optical PAE #2 [114]	2.4	10	68	3.5	0.38	–
all-optical LU [118, 119]	0.5*	88	64	$\sim 10^{\bullet}$	25	50
all-optical phonon probe^{+}	0.125	$\sim$1	$<$1	–	–	–

Table 1.2: Table comparing the specifications of current state of the art Photoacoustic endoscope-type devices. AR - acoustic resolution, meaning that the size of the acoustic spot size used for detection is smaller than the optical spot size used for excitation and thus sets the lateral resolution. OR - optical resolution, optical spot size (detection) sets the lateral resolution. †The technique is in a side-view configuration and therefore relies on a combination of linear and rotational scanning mechanisms; all other listed configurations are front-view. *This value represents the total diameter of the 2 optical fibres, however, the total diameter of the integrated needle device is $1.08\ mm$ [119]. •This technique is distal scanning so the field of view is acquired over a series of spatially resolved point measurements. $^{+}$ Specifications proposed by this work.

an optical detection cavity is fabricated within the desired bandwidth. Furthermore, by utilising acoustic wavelengths that are on the order of NUV-NIR optical wavelengths, an alternative way of optically detecting acoustic waves becomes available. Under these conditions, the acoustic wave itself becomes an interferometer. Through the effect of Brillouin scattering, the mechanical vibrations of an atomic lattice (phonons) are capable of resonantly reflecting or transmitting light (photons), which provides the necessary modulation in detected optical power. Brillouin scattering and PLU are both well-established fields of study which are growing in maturity for biology and microscopy oriented applications, yet are both without viable endoscopic imaging technologies; these concepts will be introduced more quantitatively in the next chapter.

Following the context and motivations described in this chapter, with the end goal of achieving proof of concept for a phonon probe, the remainder of this report will be organised in the following way. Chapter 2 will introduce, derive, model, and discuss background material underpinning the concept for the phonon probe. Here the scope of the report will narrow towards the phenomena of PLU and Brillouin scattering, and how they will be leveraged in order to create an ultra-high resolution optical fibre ultrasonic imaging device. In Chapter 3 the design concept, specific working principles, performance modelling, and fabrication methods for the device will be addressed, followed by the experimental methods in Chapter 4. Proof of concept results for both spectroscopy and imaging will be presented in Chapters 5 and 6. Lastly, Chapter 7 presents the future developments and outlook for the device and is followed by a summary and closing remarks in Chapter 8.

Chapter 2

Background & modelling

In this chapter the fields of Brillouin spectroscopy and picosecond laser ultrasonics (PLU) will be introduced and analysed. Compared with the piezoelectric and photoacoustic systems described in the previous chapter, Brillouin scattering and PLU are driven by physical processes that occur on a picosecond time scale, and therefore provide access to GHz, and even THz frequencies of the ultrasonic spectrum. Both techniques have the benefit of being non-contact, and importantly, they are inherently all-optical and therefore present an opportunity for imaging with high spatial resolution and without bulky electrical components in the measurement volume. Given the all-optical nature of the systems, translation to endoscopy via fibre optics is especially promising. For PLU in particular, spatial resolution can be even further improved since GHz frequency ultrasound contains wavelengths similar to NUV optical wavelengths in biological media. Coupling this with an optical fibre that delivers and collects the light, the fierce attenuations of GHz frequency ultrasound can be somewhat mitigated by a substantial improvement in the portability of the measurement system. The following section will introduce Brillouin light scattering, followed by PLU, and finally the marriage of these concepts: time resolved Brillouin scattering.

2.1 Brillouin scattering

In the late 19^{th} century there was great interest in using the newly discovered theory of electromagnetism, organised by James Clerk Maxwell, to describe a wide variety of optical effects. The most obvious of these was describing the transmission of light through the atmosphere, and the resulting range of colours. Lord Rayleigh developed a theory of *elastic scattering* where he posited that small molecules in the atmosphere scatter blue light much more intensely than red light, and used this to describe the blue colour of the day-time sky [122, 123]. The process is elastic since the electric dipoles of the atmospheric molecules are in resonance with the illuminating light, and therefore re-radiate the same wavelength [16]. Following these discoveries it was then realised

that since “the molecules of the atmosphere are in thermal motion, with velocities in uncorrelated directions, the wavelength of the radiation scattered from them will thus vary within a range of 10^{-6} of itself” [124, 125]. In other words, if the scattering processes are *inelastic*, where energy is exchanged between scatterers, the light will exchange energy in a manner similar to the Doppler effect.

This concept of inelastic scattering was extended to the inherent thermal motions of molecules in crystal lattices by C.V. Raman. It was also becoming more apparent that these thermal perturbations were equivalent to miniature acoustic waves (phonons) that propagate both intra- and inter-molecularly. The former constituting high frequency oscillations (optical phonons) and the latter encompassing lower frequency oscillations of the collective lattice (acoustic phonons). Similar to Raman, Leon Brillouin first theorised the Doppler shift in frequency that should be experienced by light scattering with an acoustic phonon. For the case of Raman and Brillouin scattering, as they came to be known, the optical frequency shifts are directly related to the phonon frequency and the geometry of the scattering interaction. Therefore techniques that are capable of quantifying these shifts, serve as spectrometers for the mechanical identity and behaviour of a substance from macroscopic to molecular levels, in a wide range of materials from condensed matter to biological tissue [126, 127]. The development path of Brillouin scattering in particular will be discussed in this section, beginning with a quantitative treatment of the scattering process.

2.1.1 Physical basis

Maxwell's equations

Light fundamentally consists of electric (**E**) and magnetic (**B**) fields (bold implying vectors). These fields arise from the existence of electric charges and currents that permeate a given material. Mathematically the fields obey Maxwell's equations, which in a material with free charge density ρ_f and free current density $\mathbf{J_f}$ are represented as [128]

$$\nabla \cdot \mathbf{D} = \rho_f \qquad (2.1) \qquad\qquad \nabla \cdot \mathbf{B} = 0 \qquad (2.2)$$

$$\nabla \times \mathbf{E} = -\frac{\partial \mathbf{B}}{\partial t} \qquad (2.3) \qquad\qquad \nabla \times \mathbf{H} = \mathbf{J}_f + \frac{\partial \mathbf{D}}{\partial t} \qquad (2.4)$$

In Equations 2.1-2.4, **D** is known as the electric displacement and considers the portion of the total electric field that arises due to the electric polarisation (**P**) of the material itself:

$$\mathbf{D} = \epsilon_0 \mathbf{E} + \mathbf{P} \qquad (2.5)$$

where ϵ_0 is the electric permittivity of free space. Similarly, the contribution to the magnetic field from the magnetisation ($\mathbf{M}$) of the material is given by $\mathbf{H} = \frac{1}{\mu_0}\mathbf{B} - \mathbf{M}$ where μ_0 is the magnetic permeability of free space. The electric polarisation encodes the capacity for interaction between light and matter, and can be defined as the density of electric dipoles ($\mathbf{P}$) induced by the electric field:

$$\mathbf{P} = \epsilon_0 \chi \mathbf{E} \tag{2.6}$$

where χ is defined as the (first order) electric susceptibility and is related to the relative permittivity of the medium:

$$\epsilon_r = 1 + \chi \tag{2.7}$$

which in turn determines the speed of light in the medium (non-magnetic material), and therefore the refractive index $n = \sqrt{\epsilon_r}$.

An electromagnetic field that exists, and therefore propagates in space and time, must self-consistently solve Maxwell's equations. The consolidation of these laws comes in the form of the electromagnetic wave equation (e.g. with $\rho_f = J_f = 0$):

$$\nabla^2 \mathbf{E} = \frac{\epsilon_r}{c^2} \frac{\partial^2 \mathbf{E}}{\partial t^2} \tag{2.8}$$

For the case of a plane wave, Equation 2.8 is generally solved by a complex exponential with amplitude E_0 that oscillates in space (e.g. z) and time (t)

$$\mathbf{E} = \mathbf{E}_0 e^{i(kz \pm \omega t)} \tag{2.9}$$

with wavenumber $k = 2\pi/\lambda$ and angular frequency $\omega = 2\pi f$ which are further related by the fundamental relationship between velocity (v), frequency (f), and wavelength (λ)

$$v = \lambda f \tag{2.10}$$

Due to the symmetry between electric and magnetic field solutions, it is usually sufficient to describe a light wave in terms of the electric field alone.

Light-matter interaction

To determine the capacity for interaction between an optical wave and an acoustic wave which are both propagating within an arbitrary piece of matter, it is necessary to define an acoustic (plane) wave oscillating in space and time, manifesting as modulations in the density of the material:

$$\Delta\rho = \mathbf{A}_0 e^{i(k_a z \pm \omega_a t)} \tag{2.11}$$

where A_0 is the wave amplitude and k_a and ω_a are the wavenumber and angular frequency of the acoustic wave. Density fluctuations like this are intrinsically present in any thermodynamic system, as energy states surrounding the average energy level of the system (e.g. thermal equilibrium) are occupied and are interpreted as thermal fluctuations (phonons) [53]. Also the fluctuations can arise by external means: an acoustic wave pumped into the medium through a transducer. In any case, changes in mass density give rise to a modulation in the permittivity (Lorentz-Lorenz relation) and therefore optical properties of the material [126], i.e. a refractive index grating:

$$\Delta\epsilon_r = \frac{\partial\epsilon_r}{\partial\rho}\Delta\rho \tag{2.12}$$

Therefore, using the Taylor series expansion for the permittivity, a more complete expression can be constructed:

$$\epsilon_r' = \epsilon_r + \Delta\epsilon_r \tag{2.13}$$

where ϵ_r' contains now the unmodulated and modulated permittivities for the medium. Utilising Equation 2.7, the modulation in electric susceptibility induces the following change in the polarisation

$$\Delta\mathbf{P} = \epsilon_0\Delta\chi\mathbf{E} \tag{2.14}$$

and contributes to the total polarisation in the medium [129]

$$\mathbf{P} = \mathbf{P}_0 + \mathbf{\Delta P} = \epsilon_0\mathbf{E}(\chi + \frac{\partial\chi}{\partial\rho}\Delta\rho) \tag{2.15}$$

where $\mathbf{P}_0$ is now the unmodulated polarisation (Equation 2.6).

Now it is necessary to further define the applied field $\mathbf{E}$ as the incident field $\mathbf{E}_i$ that is probing the density fluctuation in the medium:

$$\mathbf{E}_i = \mathbf{E}_{i0}e^{i(k_i z \pm \omega_i t)} \tag{2.16}$$

Evaluating Equation 2.15 for the incident field, and including the contribution from the acoustic field (Equation 2.11) then gives the final field that has scattered with the perturbed medium

$$\mathbf{P}_{tot} = \epsilon_0\chi\mathbf{E}_{i0}e^{i(k_i z - \omega_i t)} + \epsilon_0\gamma\mathbf{A}_0\mathbf{E}_{i0}e^{i\left((k_i \pm k_a)z - (\omega_i \pm \omega_a)t\right)} \tag{2.17}$$

where the coefficient γ has been introduced for the change in optical properties due to a perturbation in density, $\gamma = \frac{\partial\chi}{\partial\rho}$. The first term on the right-side of Equation 2.17 is the elastic component of the field that oscillates with the same frequency as the input field. Conversely, it is apparent that the second term is an inelastic scattering process,

as shown by the shift in frequency (and wavenumber) with respect to the incident field

$$f_s = f_i \pm f_a \tag{2.18}$$

$$k_s = k_i \pm k_a \tag{2.19}$$

(given $\omega = 2\pi f$), a process known as Brillouin scattering [123, 129, 130]. The positive/negative sign for the acoustic wavenumber denotes whether the wave is co-propagating or counter-propagating with the direction of the optical wave. Equations 2.19 and 2.18 serve as expressions for momentum and energy conservation, respectively. A scattered optical field that has gained energy with respect to the incident beam is said to have undergone an anti-Stokes shift ($+f_a$), and a field that has lost energy - a Stokes shift ($-f_a$). In the context that the acoustic field occupies a moving reference frame, the two scenarios can be interpreted as Doppler shifts. Ultimately, this shift in frequency (and therefore wavelength) is the end result of Brillouin scattering, and serves as the basis for a field of Brillouin spectroscopy whose aim is to construct a spectrometer that is capable of measuring these small shifts in the spectrum of light which will be discussed in Section 2.1.2.

Bragg condition

As the acoustic wave travels in space with wavelength λ_a, the optical field will scatter at successive positions of the acoustic wavefront (Figure 2.1). Therefore, just as with diffraction gratings, the relationship between the phase of the acoustic wave and the phase of the optical wave will determine whether the scattered optical wavefronts either constructively or destructively interfere. In order for constructive interference to occur, a photon that scatters from acoustic wavefront $\#1$ must have an $m2\pi$ (integer value m) phase difference with a photon that scatters from acoustic wavefront $\#2$. Consequently photon $\#2$ travels an additional distance L $(2d)$ compared with photon $\#1$, which is related to the acoustic wavelength by (see Figure 2.1):

$$L = 2\lambda_a \cos\theta \tag{2.20}$$

This requires that photon $\#2$ acquires an additional phase that is an integer multiple of 2π

$$\Delta\phi = nkL = \left[nk2\lambda_a \cos\theta = m2\pi\right] \tag{2.21}$$

where k is optical and θ the angle of incidence of the optical field with respect to the acoustic field. Equation 2.21 is an expression of Bragg's law, which was originally derived for predicting X-ray diffraction patterns through the atomic lattices in crystals [126]. By simplifying the terms in the brackets in Equation 2.21, Bragg's law can be

alternatively expressed as

$$\lambda_a = \frac{\lambda_{probe}}{2n\cos\theta} \tag{2.22}$$

where λ_{probe} is the optical probing wavelength ($k = 2\pi/\lambda_{probe}$) and for the case of the fundamental diffraction order ($m = 1$). Applying this to the case of the acoustic wave travelling with velocity v the phase matching condition for Brillouin scattering between the optical and acoustic fields can be written:

$$f_B = \frac{2nv}{\lambda_{probe}}\cos\theta \tag{2.23}$$

For the special case of normal incidence, the expression reduces to

$$f_B = \frac{2nv}{\lambda_{probe}} \tag{2.24}$$

which relates the optical frequency shift to the optical wavelength and the material properties refractive index and sound velocity (Figure 2.1b). Given a coherent monochromatic light source in the NUV-NIR range, and a typical biological material (e.g. $n \approx 1.33$ and $v \approx 1500\ m/s$), the Brillouin shift and associated acoustic waves will be in the GHz frequency range. Equation 2.23 serves as the central design equa-

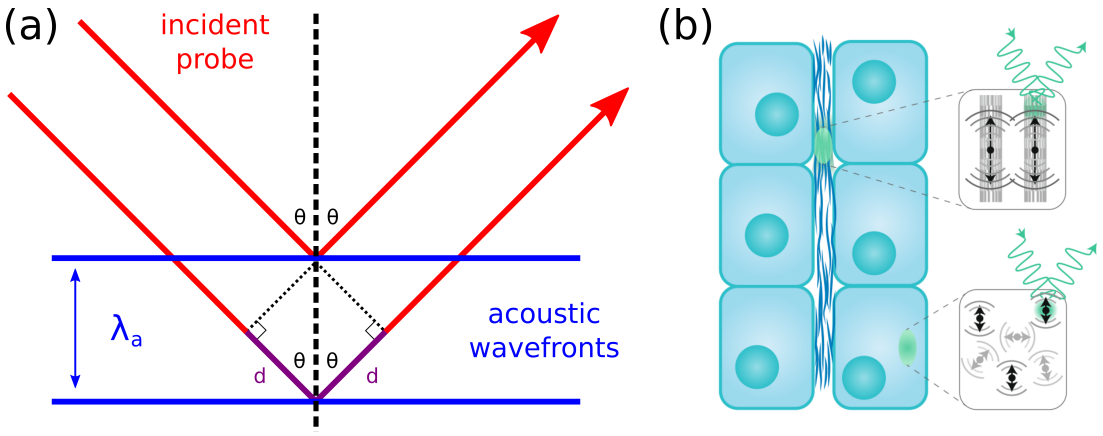


Figure 2.1: Bragg's law applied to the Brillouin scattering interactions (a). As photons Brillouin scatter with an acoustic wave, photons scattered by successive acoustic wavefronts will experience different phase shifts as they travel an additional distance $2d$ (purple). In order for light to constructively interfere after scattering, the additional $L = 2d$ should produce a $m2\pi$ phase shift (Equation 2.21). This condition is fulfilled given the relationship between the optical and acoustic wavelengths in Equation 2.22. (b) Visualisation of the Brillouin scattering interaction in matter; normal probe incidence dictates that longitudinal phonons will be sampled. When the optical probe (green spot) irradiates a stiff material with high sound velocity (central column), the light will experience a greater frequency shift than for softer materials (bottom right). Materials with high viscosity (bottom right) will attenuate the acoustic fluctuation more quickly (shorter acoustic path length) [131] (b) Reprinted by permission from Springer Nature: Springer Nature, Nature Methods, Brillouin microscopy: an emerging tool for mechanobiology, Robert Prevedel et al., Copyright (2019).

tion for any optical system that seeks to measure Brillouin scattering. It shows that by choosing the optical probe wavelength, the incidence angle of the probe beam, and a material with properties [n,v], that the system will be able to measure inelastic photons that have shifted by f_B.

Quantifying viscoelasticity

By measuring the Brillouin frequency shift of an object or environment, one is able to quantify the product nv. Going further, if the system contains a well-known and/or characterisable refractive index, the f_B measurement then directly quantifies the sound velocity. This provides access to quantitatively measuring the elasticity of the material, in the form of the real-valued longitudinal modulus:

$$M_r = v\rho^2 \tag{2.25}$$

where ρ is the mass density of the object. Similar to the refractive index, M_r, can only be considered quantified if the mass density is measured or known *a priori*. However, for the case of weakly absorbing materials, the Lorentz-Lorenz approximates that $n^2 \sim \rho$ and thus $f_B = 2\sqrt{M_r}/\lambda_{probe}$ [131]. Using the example of biological cells, tomographic phase microscopy and optical diffraction tomography can be used to map subcellular refractive index and approximate mass density, quantities which show little variation intracellularly due to the domination of water content (60-80%) [132, 133]. Experiments performed on HeLa cells showed that refractive index varies by less than 1% intracellularly, while mass density typically varies by less than 10% between major subcellular components such as nucleoplasm/cytoplasm and nucleoplasm/perinuclear cytoplasm (with the exception of the nucleoplasm/nucleoli which vary by 50%) [134].

It is useful to interpret the Brillouin frequency in terms of longitudinal modulus since this quantity provides insight on the dynamic response of a material undergoing stress; also, elastic moduli are already ubiquitous in metrology, material science, and clinical settings. The *stiffness* or *elasticity* that Brillouin spectroscopy quantifies must be conceptually differentiated from another standard modulus: the Young's modulus (E). Young's modulus can be defined as the ratio between the uni-directional stress and the resulting strain, given that the volume of the object is conserved [131, 135]. This is the modulus typically accessed by atomic force microscopy (AFM), and normally achieves units with $\sim kPa$ order of magnitude. In contrast to this, the longitudinal modulus corresponds with compressions/expansions under which volume is not conserved, and therefore is related to elasticity on ultrafast time scales generally producing values in the GPa range.

In addition to measuring elasticity, Brillouin scattering-based measurements also provide access to the rate at which the elastic wave is attenuated by the medium,

and therefore its viscosity. This ties back to a complex expression for the longitudinal modulus

$$M = M_r + iM_i \tag{2.26}$$

where the loss modulus, $M_i = 2\pi f_B \eta$, is related to the medium's resistance to displacement, i.e. its (longitudinal) viscosity $\eta = 2\alpha\rho$ where α is the attenuation coefficient (see Figure 2.1b) [131]. The methods for measuring and qualifying these measurements will be discussed in the following sections.

A major advantage of Brillouin scattering is that acoustic properties of a material can be measured using an optical system. When the system is capable of spatially resolving elasticity throughout a sample, the technique turns into a powerful label-free microscopy technique which obtains unique elastic information as a contrast mechanism. Currently, there are two primary ways of achieving this: detecting the Brillouin scattering spectrum in the frequency domain, or acquiring the acoustic wave itself in the time-domain. The former of these will be discussed in the following section.

2.1.2 Brillouin microscopy

The concept of Brillouin microscopy is simply to measure viscoelasticity at one pixel in a specimen, and then translate the specimen to a new pixel. Repeating this process across the area of a specimen generally results in two maps: one of M_r and another of M_i. In form, a Brillouin microscope is nearly identical to an optical microscope. Lateral spatial resolution is determined by the optical wavelength and the numerical aperture (NA) of the objective lens(es) used to deliver and collect light from the sample. Similarly axial resolution is determined by the depth of focus of the optical system. In general a continuous wave (CW) laser is illuminated onto the specimen with an objective lens; the angle of incidence created between the illumination field and an arbitrary acoustic wavevector will dictate the scattering angle, which equals the incident angle with respect to the acoustic wavevector (Figure 2.1a). Consequently, the choice in collection lens angle (with respect to the incident light) will dictate which acoustic wavevector, and therefore which phonon frequency, is sampled; for conventional transmission or reflection configurations the sampled phonons will be longitudinal.

The key difference between optical and Brillouin microscopy is that instead of using a scientific camera to record the optical intensity of a pixel, it instead captures the Brillouin spectrum. The role of the Brillouin spectrometer is to map spectral dispersion into spatial dispersion such that sub-GHz Brillouin shifts in optical frequency can be detected, a capability not provided by conventional optical spectrometers. The early method for achieving this was to send the Brillouin scattered light through an etalon, i.e. a Fabry-Pérot interferometer [136]. As will be discussed in Section 2.2.1, the spacing of the cavity serves as a bandpass filter at the optical frequency that is resonant. Original Brillouin spectrometers then scanned the distance between the cavity mirrors,

effectively producing a serial readout of the Brillouin spectrum (across the range of frequencies scanned by the cavity) captured by a single pixel detector [136].

By the early 2000's Brillouin spectrometers had begun to take on a new form. Non-scanning interferometers were created by using an etalon that sits at an angle with respect to the incident light. Consequently, each wavelength will refract out of the etalon at a unique angle, and therefore the various frequency components of the Brillouin spectrum are spatially dispersed across a line of pixels in a CCD camera [137]. This methodology improved upon the slow acquisition speeds of the etalon-based spectrometers - that needed to be mechanically scanned - and led to the first 2D imaging of heterogeneous samples [138]. However, these etalons were still too inefficient for practical acquisition times because the entrance to the etalon was highly reflective and therefore vastly reduced the number of Brillouin scattered photons making it to the detector. In 2008 a significant breakthrough in Brillouin spectroscopy was achieved by using a virtually imaged phased array (VIPA) to achieve both spatial and spectral dispersion (see Figure 2.2a) [127]. The transparent entrance aperture of the VIPA made a 100-fold increase in efficiency possible and was used to Brillouin image biological materials (*ex vivo* and *in vivo*) in 3D using a confocal microscope [127, 139]. The main attractions for Brillouin microscopy are that it is non-contact unlike AFM or elastography [140], provides label-free contrast of mechanical properties, and accesses elasticity on time-scales that are relevant for small objects like cells.

Following these developments, Brillouin microscopy has been increasingly applied to the life sciences (Figure 2.3). Opthoalmology has been a key application for Brillouin microscopy, primarily due to the optical transparency of the eye anatomy thus allowing light to penetrate more deeply into and out of the tissue. The change in cornea stiffness for patients with keratoconus has been demonstrated experimentally showing the promise for Brillouin spectroscopy as a diagnostic tool [141]. Furthermore, applications for detecting changes in stiffness due to the presence of a tumour or plaque-buildup are particularly promising as the technology continues to develop [142, 143]. Brillouin microscopy has also been adapted for cell imaging where it was capable of demonstrating the transformation in stiffness of a 3T3 fibroblast cell undergoing hyperosmotic shock [144]. However, so far the technique has primarily been applied to the study of transparent zoological tissue, such as zebrafish and mouse embryo [145–147].

The technologies discussed thus far all make use of spontaneous Brillouin scattering (SBS), i.e. detecting the natural density fluctuations that arise in samples. Figure 2.2 demonstrates a typical SBS spectrum acquired by a Brillouin microscope. Due to the combined spatial and spectral dispersion provided by the VIPA, the Brillouin spectrum (at a single spatial position on the sample) is projected across a row of pixels on a scientific camera (Figure 2.2b). The spectrum is composed of three primary features: the central Rayleigh peak, a Stokes peak, and an anti-Stokes peak. The Rayleigh peak

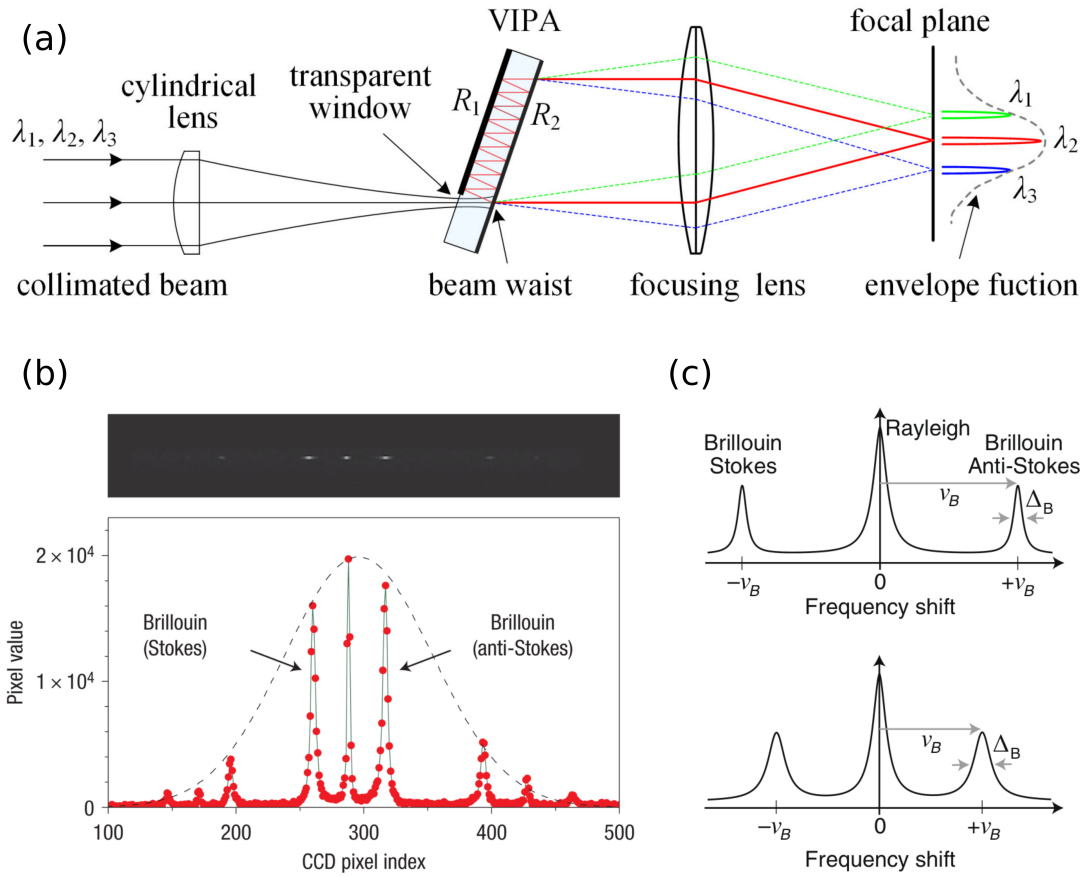


Figure 2.2: (a) Operational principles for a virtually imaged phased array (VIPA). Polychromatic light enters the VIPA, which sits at angle, through a transparent window in order to improve coupling efficiency. High reflectivity (R1) and lower reflectivity (R2) mirrors enable the incident light to be spatially dispersed. Due to the semi-transparency of R2 light is partially refracted at a frequency dependent angle providing spatial dispersion [148]. The spatially dispersed Brillouin spectrum can then be imaged onto a CCD sensor (b) where the different frequency components occupy different pixels [127]. (c) The Brillouin spectrum consists of an elastic Rayleigh scattered peak neighboured by two inelastic peaks which have been Brillouin shifted ($f_B = \nu_B$ in this report); anti-Stokes and Stokes correspond with whether the photon gained or lost energy after scattering respectively. The linewidth of the Brillouin peaks corresponds with the attenuation of acoustic energy within the sample [131]. (a) Reprinted from Optics Express, 23, Xinrong Hu, Qiang Sun, Jing Li, et al., Spectral dispersion modelling of virtually imaged phased array by using angular spectrum of plane waves, 1-12, Copyright (2015). (b) Reprinted by permission from Springer Nature: Springer Nature, Nature Photonics, Confocal Brillouin microscopy for three-dimensional mechanical imaging, Giuliano Scarcelli and Seok Hyun Yun, Copyright (2007). (c) Reprinted by permission from Springer Nature: Springer Nature, Nature Methods, Brillouin microscopy: an emerging tool for mechanobiology, Robert Prevedel et al., Copyright (2019).

contains a mixture of elastically scattered (no frequency shift) light that originates from Rayleigh scattering within the specimen, Mie scattering within the specimen, or stray reflections from elements along the optical path. This is a relevant challenge of SBS as the peak is often orders of magnitude stronger than the Brillouin scattering interactions,

and may overlap with the spectral band of interest for small frequency shifts [127]. The Stokes and anti-Stokes represent the negative and positive Brillouin frequency shifts respectively. The real longitudinal modulus - which relates to elasticity - is obtained by simply measuring the frequency shift of the peak maxima (Figure 2.2). The attenuation - the imaginary portion of the longitudinal modulus - of the sampled phonon is measured by fitting and calculating the linewidth of the Brillouin peak.

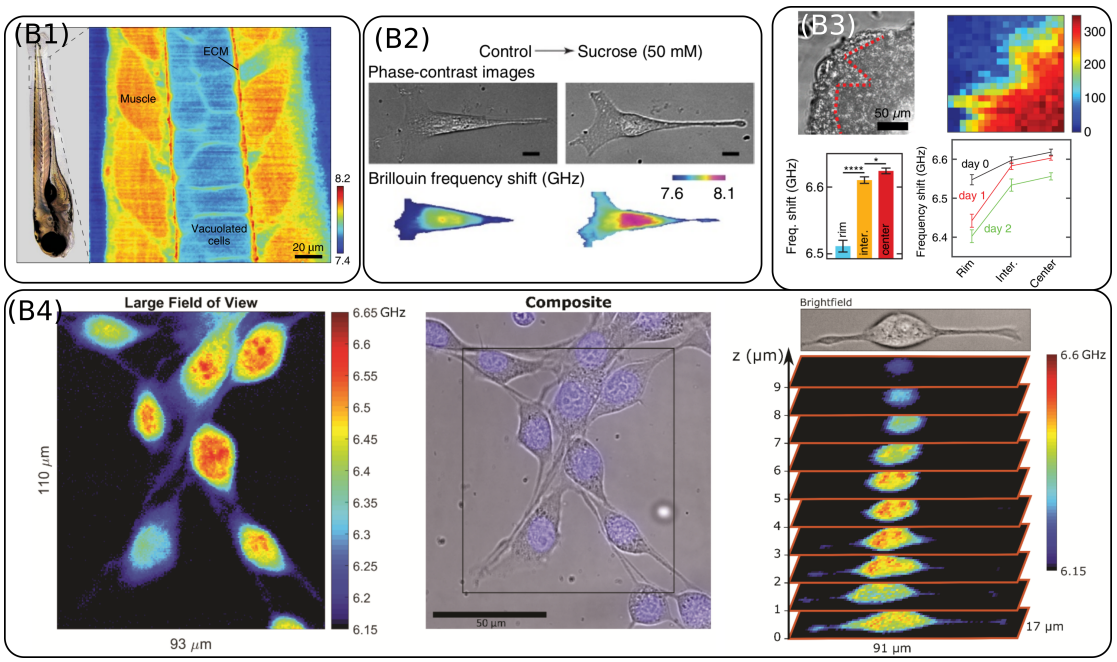


Figure 2.3: (B1) Brightfield and Brillouin microscopy of tissue from a living zebrafish larva. Brillouin microscopy reveals the mechanical properties of the extra-cellular matrix (ECM) lining the vertebra which dictates organ development and repair [146]. (B2) Cell imaging using SBS, revealing that osmotic shock changes the stiffness of 3T3 fibroblast cells [144]. (B3) Optical and Brillouin images of a HCT116 tumour spheroid revealing the stiff central region compared with the periphery of the spheroid. (bottom right) Following treatment, it is shown that the centre of the tumour becomes less stiff more slowly than the other regions [142]. (B4) (left) Brillouin microscopy of 3T3 fibroblast cells revealing the stiffness of the nuclei as confirmed by fluorescence (centre); (right) Confocal sectioning allows in-depth reconstruction [149]. All colour bars are in units GHz, with the exception of (B3) (MHz). (B1) Reprinted from Biomedical Optics Express, 10, Carlo Bevilacqua, Hèctor Sánchez-Iranzo, Dmitry Richter, et al., Imaging mechanical properties of sub-micron ECM in live zebrafish using Brillouin microscopy, 14201431, Copyright (2019). (B2) Reprinted by permission from Springer Nature: Springer Nature, Nature Methods, Noncontact three-dimensional mapping of intracellular hydromechanical properties by Brillouin microscopy, Giuliano Scarcelli et al., Copyright (2015). (B3) Reprinted figures with permission from Jérémie Margueritat, Angèlique Virgone-Carlotta, Sylvain Monnier, et al., Physical Review Letters, 122, 018101, 2019. Copyright (2019) by the American Physical Society. DOI: https://doi.org/10.1103/PhysRevLett.122.018101. (B4) Reprinted from Biomedical Optics Express, 10, Milos Nikolic and Giuliano Scarcelli, Long-term Brillouin imaging of live cells with reduced absorption-mediated damage at 660nm wavelength, 1567, Copyright (2019).

There are two common challenges as it pertains to Brillouin microscopy and SBS: parsing viscoelasticity within the optical PSF, and the inherent weakness of the spontaneous scattering process. In heterogeneous samples it is possible for the PSF to encounter multiple sub-volumes with different viscoelasticity. This results in complex Brillouin spectra where the Brillouin shifts from each sub-component can either add or average together depending on the path length of the acoustic excitation [131, 150]. Heterogeneity also introduces difficulties when measuring acoustic attenuation; if the acoustic wave encounters a sub-volume with different mechanical properties the wave could prematurely attenuate, therefore introducing error to the viscosity measurement. Furthermore, since the collection objective lens produces a range of spatial frequencies, a range of Brillouin shifts are collected (Equation 2.23) producing peak broadening that is unrelated to viscosity. Finally, due to the spontaneous nature of the density fluctuations, only 1 out of approximately 10^{12} photons are Brillouin scattered, which places an upper limit on the theoretical acquisition speed achievable with Brillouin microscopes [127, 131]. This, in addition to the strength of the elastically scattered components of the signal, contributes to the reality that Brillouin spectroscopy is so far limited to the investigation of largely transparent biologically tissue. Recently, techniques have begun to emerge that circumvent this scattering efficiency limit by using non-linear electrostriction processes [151] or laser ultrasonic transducers to actively generate GHz acoustic waves. Nevertheless, the inherent inefficiency of the scattering process becomes a relevant limitation when seeking to translate SBS from microscopy to endoscopy.

2.1.3 Brillouin fibre probe

The Brillouin microscope has demonstrated that fundamental mechanical information can be obtained in a way that is non-contact and label-free. Naturally, the utility of this technique can be further extended if the technology is translated into an endoscope. Brillouin spectroscopy would no longer be limited to samples placed on a bulky microscope stage. Endoscopic technology would also simplify an element of Brillouin imaging that is related to the opto-acoustic properties of the specimen.

The strength of Brillouin scattering varies according to a particular property of the scattering medium: its *photoelasticity*. The influence of this property can be found in the constant γ in Equation 2.15, and represents the amount by which the refractive index shifts given a unit change in density (e.g. when a material is stressed). Many transparent materials show a strong propensity for high photoelasticity, which partially explains the focused application of Brillouin spectroscopy and microscopy to transparent specimens. If a Brillouin endoscope was successfully realised, bulk optical transparency would no longer be a strict requirement, as the endoscope could be manoeuvred through opaque tissue towards a target with higher photoelasticity.

Coincidentally, the most useful tool for translating a microscopy technique into an

endoscopic one - the optical fibre - is composed of a highly photoelastic material (fused silica). For spontaneous techniques this means that the system will need to contend with Rayleigh scattering from the pre-existing system (discussed above), Rayleigh scattering from the optical fibre, and now Brillouin scattering from the optical fibre, all which reduce the sensitivity needed to characterise the Brillouin peaks of a specimen.

As a consequence of these challenges, there are only two known optical fibre-based Brillouin probe prototypes [152, 153]. The first device was originally designed using a single optical fibre to deliver the probe wavelength through a GRIN lens which focuses into the sample, and then the Brillouin back-scattered light is collected using the same optical fibre. However, the Brillouin shifts of the test samples could not be measured due to the following reason. Since the path length of the optical fibre is on the order of $\sim m$, and the depth of focus of the GRIN lens is on the order of $\sim 10\ \mu m$, the likelihood that light will scatter in the fibre-glass is 5 orders of magnitude greater than in the sample (the ratio of the path lengths). In order to circumvent this, the design was modified such that one fibre is used for delivery and another used for collection (both terminated with the GRIN lens) as shown in Figure 2.4a. This avoids the Brillouin scattering in the glass, since photons and phonons that co-propagate in glass do not meet the phase matching criterion for forward scattering [130]. However, the dual-fibre solution for improving the dominance of the glass material introduces another source of signal loss. The $\sim 125\ \mu m$ offset between the optical axes of the fibres means that their focal planes after the GRIN lens will also be offset. Due to this lack of overlap, the region in which Brillouin scattering is taking place will be collected inefficiently by the detection fibre.

Recently, in order to solve these issues, replacing the two fibres with a single hollow-core fibre has been proposed [153]. Still terminated with a GRIN lens, this single-fibre approach improves the collection efficiency of the device while still avoiding the issue of Brillouin scattering in conventional fibre glass (Figure 2.4c). These improvements have allowed the device to achieve 1D line scanning of the Brillouin frequency of hydrogels on the mm scale (Figure 2.4d), yet on the order of 45 minutes per line due to the inherent weakness of the scattering process.

Following the advent of Brillouin microscopy, a number of techniques have been developed in parallel which could offer a solution to the above issues. A particularly intriguing solution is provided by laser ultrasonics which has also proved capable of accessing the phenomenon of Brillouin scattering. Through the use of an optoacoustic transducer, much higher amplitude acoustic waves can be driven through a specimen compared with the random thermal fluctuations on which SBS relies. This results in greater mechanical stress experienced by the probed volume, and therefore a greater photoelastic response. In the following two sections, laser ultrasonics will be introduced and discussed in the context of Brillouin microscopy and endoscopy.

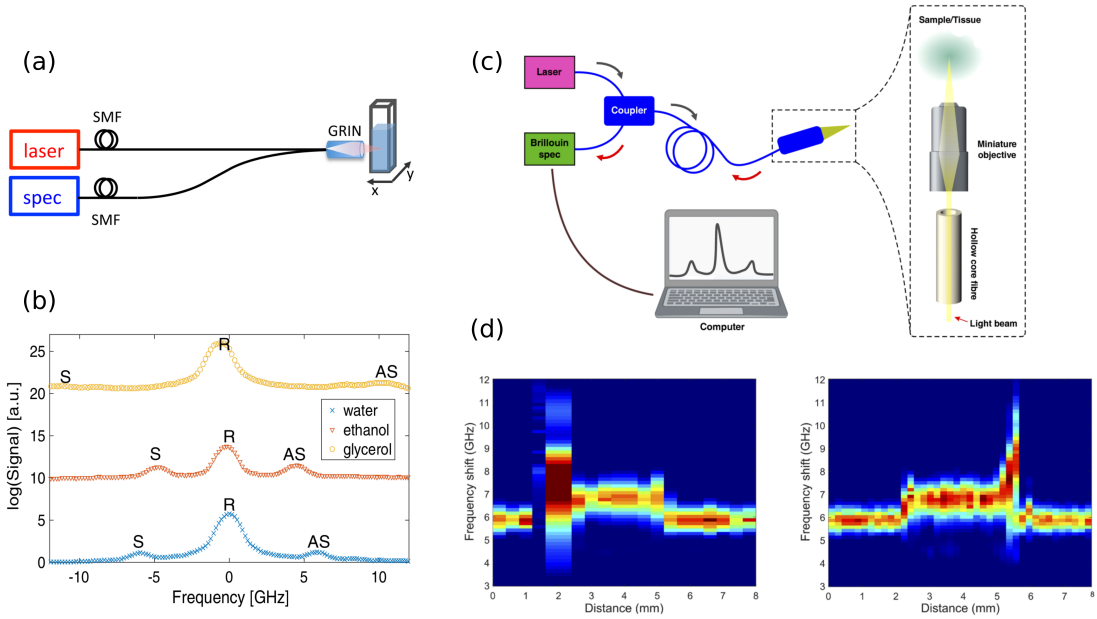


Figure 2.4: (a) Initial design for the SBS-based fibre-probe; since backwards Brillouin scattering in the glass of the fibre dominates the probe, a second fibre is required for detection with both fibres coupled directly to a GRIN lens. Using separate channels results in spatially mismatched focal volumes for each fibre resulting in lower detection efficiency. [152] (b) Brillouin spectroscopy of various liquids using the set-up in (a). (c) SBS-based fibre-probe which instead uses a hollow-core fibre in order to avoid Brillouin scattering in glass and focal mismatch. Using this configuration higher SNR spectra are achieved which has enabled 1D profilometry of hydrogels (d) [153]. (a-b) Reprinted from Journal of Innovative Optical Health Sciences, 10, Irina V. Kabakova, YuChen Xiang, Carl Paterson and Peter Torok, Fiber-integrated Brillouin microspectroscopy: Towards Brillouin endoscopy, 1742002, Copyright (2017). (c-d) Reprinted from Biomedical Optics Express, 11, YuChen Xiang, Carin Basirun, Joshua Chou, et al., Background-free fibre optic Brillouin probe for remote mapping of micromechanics, 6687-6698, Copyright (2020).

2.2 Picosecond laser ultrasound

Photoacoustics and laser ultrasound share the same basic excitation mechanism for a given material: (1) optical absorption, (2) heat generation, (3) thermal expansion and contraction, (4) which launches acoustic waves into the surrounding environment. The key difference between the two is that with laser ultrasonics, a special absorbing layer is used to control the properties of the acoustic waves; whereas photoacoustics is reliant on the optical and mechanical properties of the specimen itself. For laser ultrasonics in general, the light source (e.g. a laser) used to instigate this process, is called the *pump* laser. This pump will encounter the absorbing material, which in this report, will be referred to as a *transducer*, i.e. a structure which is capable of transducing light and sound. Typically the pump laser is pulsed, such that the excitation event is switched on and off, similar to the use of pulsing in photoacoustics. In order to optically detect the propagation of the acoustic waves, a second *probe* laser is used;

the presence of the acoustic wave will alter the optical properties of the transducer and/or the surrounding environment which will be encoded on the probe laser and recorded by an optical detector. For the probe laser, it is common to use both CW and pulsed lasers; when using a pulsed laser, the timing of the probe pulse needs to be progressively delayed with respect to the periodic pump pulse. This will allow each successive probe pulse to detect a thin slice of the acoustic phenomena it is interacting with. This can be accomplished by making the optical path of the probe variably longer than the pump, and will be discussed in Section 4. The generation and detection scheme described above is referred to as a *pump-probe* system, and the technique: pump-probe spectroscopy.

In the 1980's it became apparent that if ultrashort pulses of light were used in pump-probe spectroscopy, e.g. pulse widths on the order of $\leq 1\ ps$, that there was sufficient time-discretisation to detect ultrafast phenomena. The application of this concept to high frequency acoustics (e.g.$f > 1\ GHz$) was coined picosecond laser ultrasonics (PLU) or picosecond acoustics. Early development in this field stemmed from the work of Thomsen *et al* in 1984. At that time it was known that the absorption of short laser pulses by metals creates an excited electronic state within the material which in turn causes a transient change in the absorbance of the material [121]. Thomsen *et al* then noted that in addition to this electronic excitation, that the absorption of the (pump) laser pulse causes a heat rise and thermal expansion within the metal (see Figure 2.5a for transducer diagram); however, the heated region is localised to the optical skin depth of the metal, which is on the nanometre-scale. Consequently, the thermal relaxation process is carried out by phonons with wavelengths on this scale, corresponding to acoustic frequency phonons ($\sim GHz - THz$) [121]. Furthermore, if the excitation spot is large with respect to the optical absorption depth, the generated phonon field can be approximated as coherent, since it propagates primarily in the longitudinal direction.

A key realisation for Thomsen *et al* was that the propagation of these high frequency stress waves causes strain within the metal. The presence of strain has two key effects: (1) physical displacement of the metal boundaries (changes in thickness) and (2) modification of the optical properties of the metal through the photoelastic effect [154]. Initial experiments in the field of PLU focused on the first effect: after the generation of coherent phonons with a pump laser (with a *a*-As_2Te_3 layer), a time-delayed probe laser was made to transmit through this mechanically oscillating layer. The periodic changes in thickness caused the overall probe-absorbance of the layer to also modulate, creating oscillations in the probe intensity at the detector (see Figure 2.5b) [121]. When thicker metal layers were used, the period of these oscillations increased (Figures 2.5b-c), since the strain pulses had to travel a longer distance to displace the boundary (as they echo back and forth within the layer).

As the field developed, it became apparent that the second strain-induced effect:

photoelasticity, could also be detected optically. As the probe beam travels through a photoelastic material undergoing picosecond mechanical vibrations, the beam will scatter at the position of the propagating strain pulse, i.e. the position where the optical properties of the film are perturbed. In this way the probe intensity at the detector is

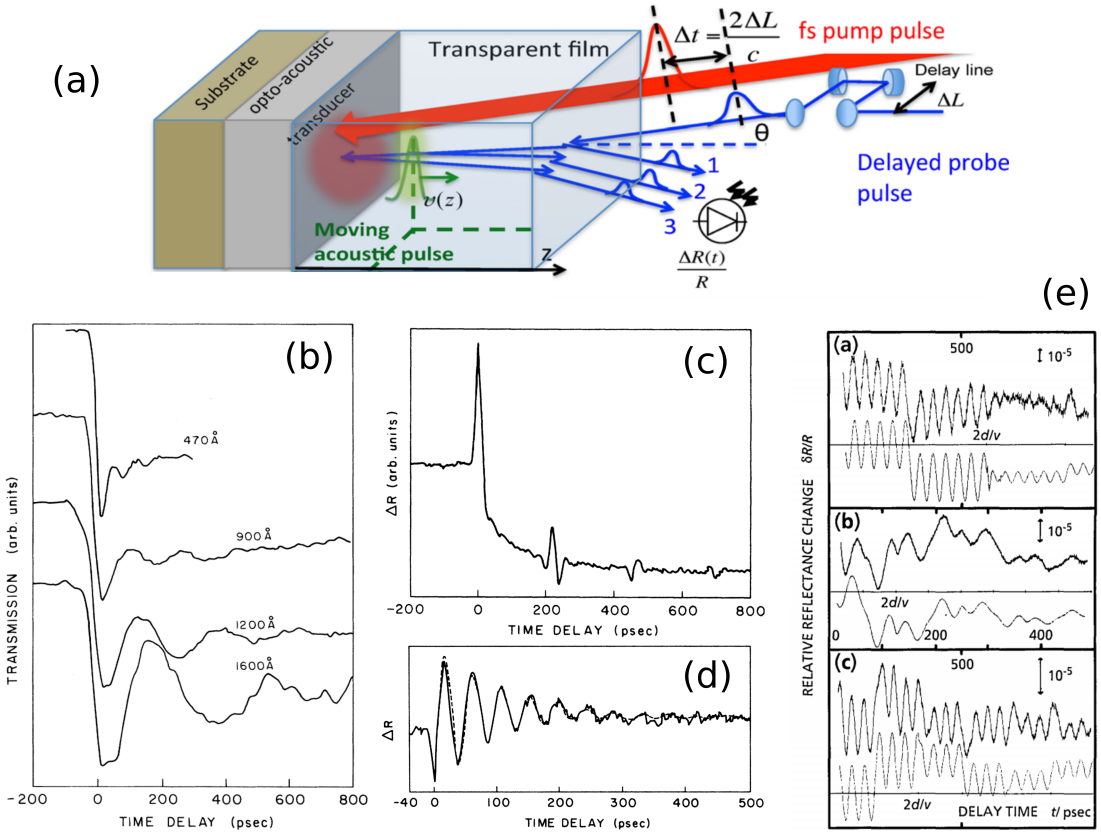


Figure 2.5: Introduction to picosecond ultrasonics. (a) Diagram demonstrating the basic geometry for PLU: an opto-acoustic transducer generates strain pulses through the absorption of a pump pulse; a time-delayed probe pulse is sensitive to boundary displacement and photoelasticity [155]. (b-c) Monitoring strain pulse echoes through the optical transmissivity (b) and reflectivity (c) of the probe beam (respective thicknesses $d = 47,\ 90,\ 120,\ 160,\ 220\ nm$ of a-As_2Te_3) [121, 154]. All signals contain a fast spike at time delay zero due to electronic excitation, followed by a series of slower acoustic events. (d) Modulation in optical reflectivity due to photoelasticity in a-As_2Se_3 (TRBS) [154]. (e) Simultaneous detection of TRBS (fast oscillations) and acoustic echoes (step changes) in a-Ge ($d = 1600\ nm$), Cr ($d = 350\ nm$), and Cr ($d = 900\ nm$) from top to bottom. (a) Reprinted from V.E. Gusev and P. Ruello, Advances in applications of time-domain Brillouin scattering for nanoscale imaging, Applied Physics Reviews, 5(3), 031101, (2018), with the permission of AIP Publishing. (b) Reprinted figures with permission from C. Thomsen et al., Physical Review Letters, 53, 989-992, 1984. Copyright (1984) by the American Physical Society. DOI: https://doi.org/10.1103/PhysRevLett.53.989. (c-d) Reprinted figures with permission from C. Thomsen et al., Physical Review B, 34, 4129-4138, 1986. Copyright (1986) by the American Physical Society. DOI: https://doi.org/10.1103/PhysRevB.34.4129. (e) Reprinted from Optics Letters, O.B. Wright and T. Hyoguchi, Ultrafast vibration and laser acoustics in thin transparent films, Copyright (1991).

modulated by the propagation of the acoustic wave itself, and represents the acoustic time of flight at a particular acoustic frequency (will be discussed in this Chapter). This mechanism ultimately led to the realisation that Brillouin scattering could be observed in the time domain through interferometric means, and was first demonstrated on semiconductor and transparent films (Figure 2.5d) [154, 156]. This manifestation of PLU is called time resolved Brillouin scattering (TRBS), or time domain Brillouin scattering.

These developments inspired further milestones in the field of PLU, achieved by Wright *et al*, who demonstrated that both surface displacement and Brillouin scattering could be observed simulataneously in a transparent thin film [157]. This breakthrough showed that the film thickness and sound velocity could be measured in parallel; the thickness could be obtained from the timing of the strain pulse echoes, and the sound velocity could be extracted from the frequency of the acoustic wave measured through time-resolved Brillouin scattering (will be discussed in this Chapter). Wright also first demonstrated that the spectrum of the phonon field resonating within the transducer layer, could be detected through ultrafast surface vibrometry, and provides access to mechanical information on an atomic or molecular scale [158]. This leads to a greater realisation about PLU, that phonon and electron dynamics can be studied at room temperature, as previous state of the art required superconducting equipment and environments [154].

Leading up to the year 2000, significant effort was dedicated to establishing the mathematical formalism for PLU [121, 154, 157, 159]. In general, this required partitioning the physics of PLU into two components: the elastic process and the optical process. In reality these processes play out in three spatial dimensions; however, in order to more easily model the phenomena it was important to introduce simplifying assumptions, such as the requirement that the optical spot sizes ($\mu m - mm$) be much greater than the thickness of the metallic transducer (easily realised in practice since the optical skin depth of metals is nanometric and therefore $\sim 100\ nm$ thicknesses can be used). Such an assumption allows the problem to be reduced from 3D to 1D, i.e. acoustic and optical plane waves. The aim is to then solve for the acoustic and electric field solutions (quasi-independently), and ultimately couple the two processes to model the optical signal one would expect from a PLU experiment. A source of complexity when modelling this interaction is considering the effects of multiple optical reflections/transmissions in a structure. For this reason most theoretical work in the field focused on 1-layer and 2-layer optical structures (e.g. a substrate layer and a transducer layer) [154, 160]. It was not until 2002, that Osamu *et al* developed a formalism which successfully modelled PLU for an arbitrary number of optical layers [161].

This Chapter will now turn to exploring and mathematically approximating the elastic and optical processes for PLU and TRBS, primarily using the formalism of Osamu

et al. This will lead to the creation of an analytical model which simulates the design and theoretical performance for the phonon probe and its optimisation. It will also provide a framework for modelling future transducers with added complexity (Chapter 7). Initially a method for approximating optical plane wave field solutions will be explored, followed by the propagation of strain pulses (acoustic waves), and finally the coupling of acoustics and optics.

2.2.1 Optical modelling

The aim of this section is to identify a method for solving the electric field at every point in (one-dimensional) space in an arbitrary transducer-structure surrounding by arbitrary media. Once the fields within the system are defined, the optical absorption of the transducer can be modelled which will ultimately determine the generation of elastic waves. Furthermore, by solving for the electric fields throughout space, the optical detection system can then be propagated through the system in time; as this probe beam encounters modulations to the optical properties of the structures, the elastic behaviour of the material will be transduced into the optical detection system. These principles will define the operation of the device proposed by this report, which will allow its performance to be simulated and optimised.

As an incident optical wave ($\mathbf{E}_i$) encounters a change in dielectric (non-magnetic) material (from material 1 to 2), part of the field will reflect ($\mathbf{E}_r$) and part will transmit ($\mathbf{E}_t$). For simplicity, it is assumed that the fields are plane waves travelling in the z-direction, are polarised in the $\hat{\mathbf{x}}$ direction, and are time averaged such that $e^{-i\omega t}$ is constant, resulting in the fields:

$$\mathbf{E}_i = \mathbf{E}_{i0} e^{ik_1 z} \tag{2.27}$$

$$\mathbf{E}_r = \mathbf{E}_{r0} e^{-ik_1 z} \tag{2.28}$$

$$\mathbf{E}_t = \mathbf{E}_{t0} e^{ik_2 z} \tag{2.29}$$

where $+z$ in the exponent implies travelling in the positive direction (forward), and $-z$ in the negative direction (backward). When a field that is polarised tangentially ($\hat{\mathbf{x}}$) to the plane of incidence ($\hat{\mathbf{z}}$) encounters a boundary, both the field amplitudes and derivatives of the incident and scattered components must exhibit continuity, resulting in the following boundary conditions [128]

$$\mathbf{E}_i + \mathbf{E}_r = \mathbf{E}_t \tag{2.30}$$

$$n_1 \mathbf{E}_i - n_1 \mathbf{E}_r = n_2 \mathbf{E}_t \tag{2.31}$$

Equations 2.30 and 2.31 can then be combined, and the following relationships are

found between the ratio of the incident and reflected/transmitted field amplitudes:

$$r_s = \left(\frac{E_{r0}}{E_{i0}}\right)_s = \frac{n_1 - n_2}{n_1 + n_2} \tag{2.32}$$

$$t_s = \left(\frac{E_{t0}}{E_{i0}}\right)_s = \frac{2n_1}{n_1 + n_2} \tag{2.33}$$

the well known Fresnel coefficients. Similar solutions are obtained for fields that are polarised in parallel with the plane of incidence (r_p and t_p). Evaluation of the transmitted and reflected power is attained by taking the squared magnitude of the Fresnel coefficients:

$$R = r_s^* r_s \tag{2.34}$$

$$T = t_s^* t_s \tag{2.35}$$

$$A = 1 - R - T \tag{2.36}$$

where A is the absorbance. The fields thus far have been assumed as normally incident to the boundary, which will be the case for the study in the report, however, the case of oblique incidence yields [16, 128]:

$$r_s = \frac{n_1 \cos\theta_i - n_2 \cos\theta_t}{n_1 \cos\theta_i + n_2 \cos\theta_t} \tag{2.37}$$

$$t_s = \frac{2n_1 \cos\theta_i}{n_1 \cos\theta_i + n_2 \cos\theta_t} \tag{2.38}$$

The above demonstrates the transmission and reflection for the simplest geometry of a single interface between two semi-infinite materials; if the input field $\mathbf{E}_i$ is known it is straight forward to determine the reflected and transmitted fields. However, for the case of a multi-layer structure, the situation becomes more complex since the total field in any single layer will also be composed of multiple reflections and transmissions from all layers in the structure. In a geometry consisting of N-layers of arbitrary materials, the total field in the mth layer can be expressed as the superposition of the forward and backward propagating fields with amplitudes A_m and B_m respectively (both fields are polarised in $\hat{\mathbf{x}}$)

$$E_m = A_m e^{ik_m z_m} + B_m e^{-ik_m z_m} \tag{2.39}$$

where z_m is the relative z-position within the mth layer of thickness d_m and positive and negative signs indicate forward and backward travel respectively.

Solving for the field amplitudes A_m and B_m for each layer will then allow the total field in the structure to be calculated. Consider the simple case of a structure containing two layers, m and $m+1$. Within layer $m = 1$ of thickness d_1, the following four nodes are defined (see Figure 2.6)

1. A_1^L - forward propagating (left to right) field amplitude at left hand side (LHS) of

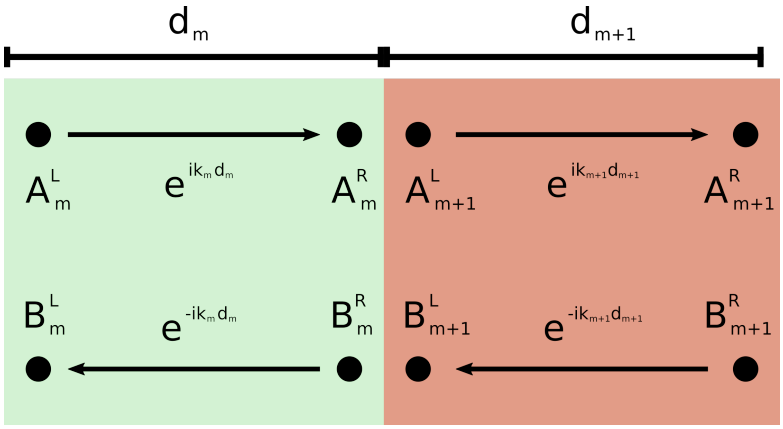


Figure 2.6: Visualisation of the electric field propagation in two materials m and $m+1$ with thicknesses d_m and d_{m+1}. For a field travelling from left to right (forward), the field at the end of a layer (A^R) will have undergone a phase shift over the path length $k_m d_m$ compared with the field at the beginning of the layer (A^L). Conversely, for a backward travelling field, the left hand side of the layer will have been shifted in phase by $-k_m d_m$.

layer

2. A_1^R - forward propagating field amplitude at right hand side (RHS) of layer
3. B_1^L - backward propagating (right to left) field amplitude at LHS of layer
4. B_1^R - backward propagating field amplitude at RHS of layer

The change in field from the LHS to the RHS of the layer will be set by the propagator $e^{\pm ik_1 d_1}$ which produces the following system of field equations:

$$E_1^L = A_1^L + B_1^L \tag{2.40}$$

$$E_1^R = A_1^R + B_1^R = A_1^L e^{ik_1 d_1} + B_1^L e^{-ik_1 d_1} \tag{2.41}$$

which can be expressed more compactly using matrix notation:

$$\begin{pmatrix} A_1^R \\ B_1^R \end{pmatrix} = \begin{pmatrix} e^{ik_1 d_1} & 0 \\ 0 & e^{-ik_1 d_1} \end{pmatrix} \begin{pmatrix} A_1^L \\ B_1^L \end{pmatrix} = P_1 \begin{pmatrix} A_1^L \\ B_1^L \end{pmatrix} \tag{2.42}$$

and P_1 can be defined as the propagation matrix for material/layer 1. Now when the total field in material 1, $E_1 = A_1 e^{ik_1 z_1} + B_1 e^{-ik_1 z_1}$, encounters the boundary between materials 1 and 2, the boundary conditions in Equations 2.30-2.31 must be applied for both the forward (A) and backward (B) propagating field components (on the LHS and RHS of the boundary):

$$A_1 + B_1 = A_2 + B_2 \tag{2.43}$$

$$n_1 A_1 - n_1 B_1 = n_2 A_2 - n_2 B_2 \tag{2.44}$$

or in matrix format:

$$\begin{pmatrix} 1 & 1 \\ n_1 & -n_1 \end{pmatrix} \begin{pmatrix} A_1 \\ B_1 \end{pmatrix} = \begin{pmatrix} 1 & 1 \\ n_2 & -n_2 \end{pmatrix} \begin{pmatrix} A_2 \\ B_2 \end{pmatrix} \tag{2.45}$$

The field amplitudes in the second layer can now be solved by simplifying Equation 2.45:

$$\begin{pmatrix} A_2 \\ B_2 \end{pmatrix} = \begin{pmatrix} 1 & 1 \\ n_2 & -n_2 \end{pmatrix}^{-1} \begin{pmatrix} 1 & 1 \\ n_1 & -n_1 \end{pmatrix} \begin{pmatrix} A_1 \\ B_1 \end{pmatrix} = D_2^{-1} D_1 \begin{pmatrix} A_1 \\ B_1 \end{pmatrix} = D_{12} \begin{pmatrix} A_1 \\ B_1 \end{pmatrix} \tag{2.46}$$

where the scattering matrix D_{12} is defined and is equivalent to the Fresnel coefficients for materials 1 and 2 [162]

$$D_{12} = \frac{1}{t_{12}} \begin{pmatrix} 1 & -r_{12} \\ -r_{12} & 1 \end{pmatrix} \tag{2.47}$$

Using this *transfer matrix method* (TMM) the field amplitudes in material 3 can be computed in terms of the amplitudes in material 1: (1) scatter from material $1 \rightarrow 2$, (2) propagate through 2, and (3) scatter from material $2 \rightarrow 3$

$$\begin{pmatrix} A_3 \\ B_3 \end{pmatrix} = D_{12} P_2 D_{23} \begin{pmatrix} A_1 \\ B_1 \end{pmatrix}$$

This process can be further generalised for a multi-layer structure of N layers, where layer 0 is the incident medium and layer $N+1$ is the output medium [162]

$$\begin{pmatrix} A_{N+1} \\ B_{N+1} \end{pmatrix} = D_{01} P_1 D_{12} P_2 D_{23} ... P_N D_{N(N+1)} \begin{pmatrix} A_0 \\ B_0 \end{pmatrix} \tag{2.48}$$

where the product series can be defined as the transfer matrix, M:

$$M = D_{01} P_1 D_{12} P_2 D_{23} ... P_N D_{N(N+1)} \tag{2.49}$$

Also, the inverse of Equation 2.48 can be written

$$\begin{pmatrix} A_0 \\ B_0 \end{pmatrix} = \bar{M} \begin{pmatrix} A_{N+1} \\ B_{N+1} \end{pmatrix} \tag{2.50}$$

where $\bar{M} = M^{-1}$.

The power of the TMM is fully realised when at least two of the field amplitudes A_0, B_0, A_{N+1}, B_{N+1} are known, in addition to the thicknesses and refractive indexes of each material in the structure. The most intuitive set of boundary conditions can be defined for the case where light of amplitude 1 is incident to the structure from the 0^{th} layer (LHS in Figure 2.7):

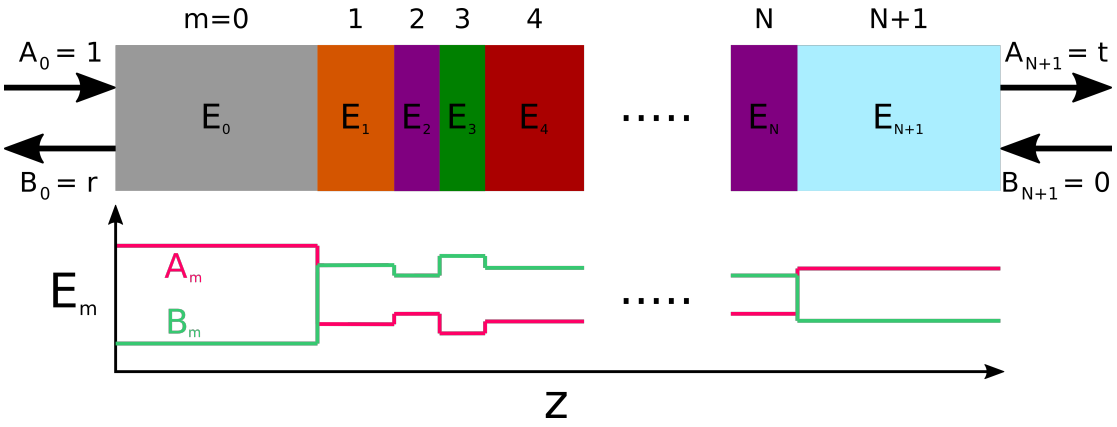


Figure 2.7: Visualisation of an arbitrary multi-layer structure containing $N + 2$ layers. In order to determine the electric field amplitude that will occupy each individual layer (e.g. when the structure is illuminated), any two of the field amplitude values at the boundaries are required (A_0, B_0, A_{N+1}, or B_{N+1}). Subsequently the TMM is used to calculate the forward and backward propagating amplitudes in the m^{th} layer.

1. $A_0 = 1$ - forward propagating incident field set to amplitude 1
2. $B_0 = r$ - backward propagating field on the side of incidence is simply the total reflectance of the structure
3. $A_{N+1} = t$ - forward propagating field output from the structure is the total transmittance of the structure
4. $B_{N+1} = 0$ - since incident field is on the LHS there is no backward propagating light on the output side of the structure.

These conditions lead to the following relationship

$$\begin{pmatrix} 1 \\ r \end{pmatrix} = \bar{M} \begin{pmatrix} t \\ 0 \end{pmatrix} = \begin{pmatrix} \bar{M}_{11} & \bar{M}_{12} \\ \bar{M}_{21} & \bar{M}_{22} \end{pmatrix} \begin{pmatrix} t \\ 0 \end{pmatrix} \tag{2.51}$$

where the total reflectance and transmittance are defined as [161–163]

$$r = \frac{M_{21}}{M_{11}} \tag{2.52}$$

$$t = \frac{1}{M_{11}} \tag{2.53}$$

which allow the Fresnel coefficients of an arbitrary optical structure to be determined (see Figure 2.8). Using TMM, the field amplitudes in any layer can be computed by simply halting the series in Equation 2.48 at the desired layer (Figure 2.7). Given knowledge of the initial boundary conditions, the total field at every point in the structure (Equation 2.39) can be determined; the above has derived this for the case of normal incidence and *s*-polarised light.

Figure 2.8 demonstrates an example of the TMM applied to modelling the optical response of a Fabry-Pérot cavity which has been mentioned previously. The cavity is defined by two partial mirror layers (silver in example) spaced by a highly transparent cavity layer (glass in example). When the illuminating wavelength of light undergoes 2π phase shifts for each round trip, constructive interference occurs giving rise to resonant transmission and reflection. In Figure 2.8 this is shown by transmission/reflection minima and maxima at characteristic cavity thicknesses given a fixed wavelength $\lambda = 800\ nm$. The TMM will be used in the following section to model the absorption of the pump beam by the transducer, and the scattering of the detected probe beam. Furthermore, the Fabry-Pérot cavity will be revisited in transducer-form in Section 2.3.

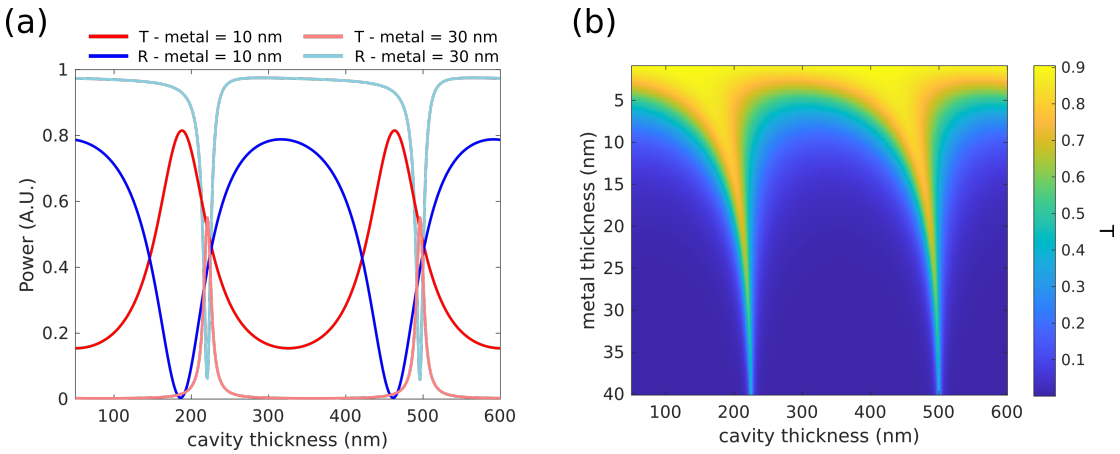


Figure 2.8: Optical modelling of a Fabry-Pérot cavity using the TMM. (a) Given an illumination wavelength of $\lambda = 800\ nm$, a mirror material of Ag, and a cavity material of glass the total transmissivity (T) and reflectivity (R) of the cavity is calculated as a function of glass thickness. When the Ag mirror thickness is increased from $10\ nm$ to $30\ nm$ (increased reflectivity), the number of round trips within the cavity increases; for cavity thicknesses where phase matching is not optimised cavity-interference will become increasingly destructive with time. This results in a more narrow cavity bandwidth and a higher *finesse*. (b) The modelling process is extended to iterate the thickness of the mirror layer providing a way to comprehensively simulate a wide range of possible cavity dimensions and parameters.

2.2.2 Opto-thermo-acoustic modelling

Generation

Now that the optical fields can be described in an arbitrary transducer, the photoacoustic effect that is responsible for converting absorbed pump light into mechanical vibrations can be analytically modelled. First the initial conditions of the transducer geometry and optical pump field need to be defined, e.g. in Figure 2.9:

- a planar geometry is assumed, consisting of N layers, and if desired 2 additional layers representing the materials that are in direct contact with the transducer (layers 0 and $N+1$).

- the optical pump wavelength, λ_{pump} is set (with free-space wavenumber $k_0 = 2\pi/\lambda_{pump}$), and is used to determine the complex refractive index in the $m = 0, 1, 2, ...N+1^{st}$ layer: $\tilde{n}_m(\lambda_{pump})$ where the complex refractive index is defined as the complex sum of the refractive index (n) and extinction coefficient (κ)

$$\tilde{n} = n + i\kappa = \sqrt{\epsilon_r} \tag{2.54}$$

  (note that the wavenumber is $k_m = \tilde{n}k_0$).

- the orientation of the structure is determined with respect to the incident pump beam, which determines the initial boundary conditions for the TMM calculation of the pump field throughout the structure. For example: $A_0 = 1$ and $B_0 = r$ for a pump field that is incident from the $z = 0$ side of the transducer.

Then the TMM is used to evaluate the forward and backward propagating pump fields in each layer in the form of Equation 2.39. Subsequently, the work done by the pump field on each layer in the structure results in the volumetric heating rate of the material

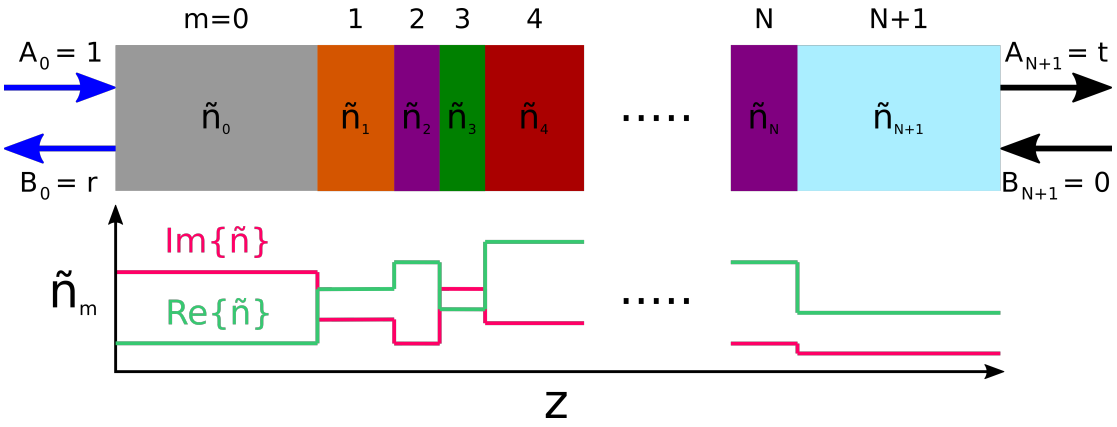


Figure 2.9: Initial geometry and conditions for simulating strain wave generation through optical absorption of the pump beam. A planar 1D geometry is assumed which consists of an N-layer transducer, substrate ($m = 0$), and external medium/sample ($N+1$). The thickness and complex refractive index of each layer (at the pump wavelength) is predetermined for the optical system. Boundary conditions for the system are selected, e.g.: pump field with amplitude 1 incident from the substrate-side of the system (top blue arrow), and the total field that occupies the LHS of the system is the system's total reflectivity (bottom blue arrow). Once initialised TMM is utilised to solve for the field amplitudes in each layer.

[161]

$$\dot{Q}(z) = -\nabla\langle \mathbf{S} \rangle = \epsilon_0 \omega n_m \kappa_m \big(|A_m|^2 e^{-2\kappa_m k_0 z_m} + |B_m|^2 e^{2\kappa_m k_0 z_m} + A_m B_m^* e^{2in_m k_0 z_m} + A_m^* B_m e^{-2in_m k_0 z_m}\big) \tag{2.55}$$

(note the simplification of the exponents when evaluating the complex conjugates for each summed term) where $\langle \mathbf{S} \rangle = \frac{1}{2v}\mathbf{E}^*\mathbf{E}$ is the time-averaged Poynting vector, i.e. the power density carried by the field [128]. Equation 2.55 represents the initial instantaneous heat rise throughout the space of the structure; after applying the volumetric specific heat capacity of each layer (C_m) the instantaneous temperature rise (due to the absorption of the pump beam) throughout the structure is calculated:

$$\Delta T(z) = \frac{Q(z)}{C_m} \tag{2.56}$$

Due to the short pulse-width and high peak power of ultrashort pulses, the peak power density experienced by the transducer can be several orders of magnitude higher than a CW laser with similar average power. Consequently, much greater quantities of electrons are excited within the atomic lattice of the structure resulting in electron-electron collisions at ballistic velocities [164]. Eventually through electron-phonon coupling and then phonon-phonon collisions, the phonons begin to diffuse the absorbed energy (heat) into the lattice away from the hot spot [165]. In other words, the heat rise creates thermal stress within the structure which relaxes in the form of strain pulses that propagate throughout the system [121]. The initial strain profile ($\eta_0(z)$) (i.e. thermal expansion) within the system will follow the temperature rise profile (Equation 2.56) due to pump absorption [161]

$$\eta_0(z) = \frac{3B\beta\Delta T(z)}{\rho v^2} = \gamma \Delta T(z) \tag{2.57}$$

where B is the bulk modulus, β the linear thermal expansion coefficient, ρ the mass density in the layer, v the sound velocity in the layer, and γ has been introduced for discussion in Figure 2.10. The propagation of this strain distribution for time $t > 0$ is equivalent to an acoustic field of the form:

$$\eta(z,t) = f(z - vt) + g(z + vt) + \eta_0(z) \tag{2.58}$$

where f and g represent the forward and backward propagating waves respectively, and η_0 is the time-independent initial strain owing to the thermally expanded state of the sample [121]. For the special case of $t = 0$, the initial strain is distributed in both longitudinal directions

$$\eta(z,0) = f(z) + g(z) = -\eta_0(z) \tag{2.59}$$

and therefore $f(z) = g(z) = -\eta_0(z)/2$ [163]. Following this, the evolution of the strain distribution over the time window of interest is computed by iterating $t = [0, t_{end}]$ in Equation 2.58; e.g., for the path length of a $\sim GHz$ phonon the time of flight will typically be on the order of $t_{end} \sim 10\ ns$. This general process from optical absorption to strain generation is visualised in Figure 2.10.

When a strain pulse encounters a boundary in acoustic impedance (ΔZ), $Z = \rho v$, the acoustic wave will partially reflect and transmit just as with optics. Therefore at time t_j at the z-positions z_{i-1} and z_i straddling the boundary between the mth and (m+1)st layer ($z = z_{m,m+1}$), the boundary values for the forward and backward propagating terms in Equation 2.58 will be composed of reflected and transmitted terms from the previous time step (reference the diagram in Figure 2.11):

$$f(z_i, t_j) = T_{m,m+1} f(z_{i-1}, t_{j-1}) + R_{m+1,m} g(z_i, t_{j-1}) \tag{2.60}$$

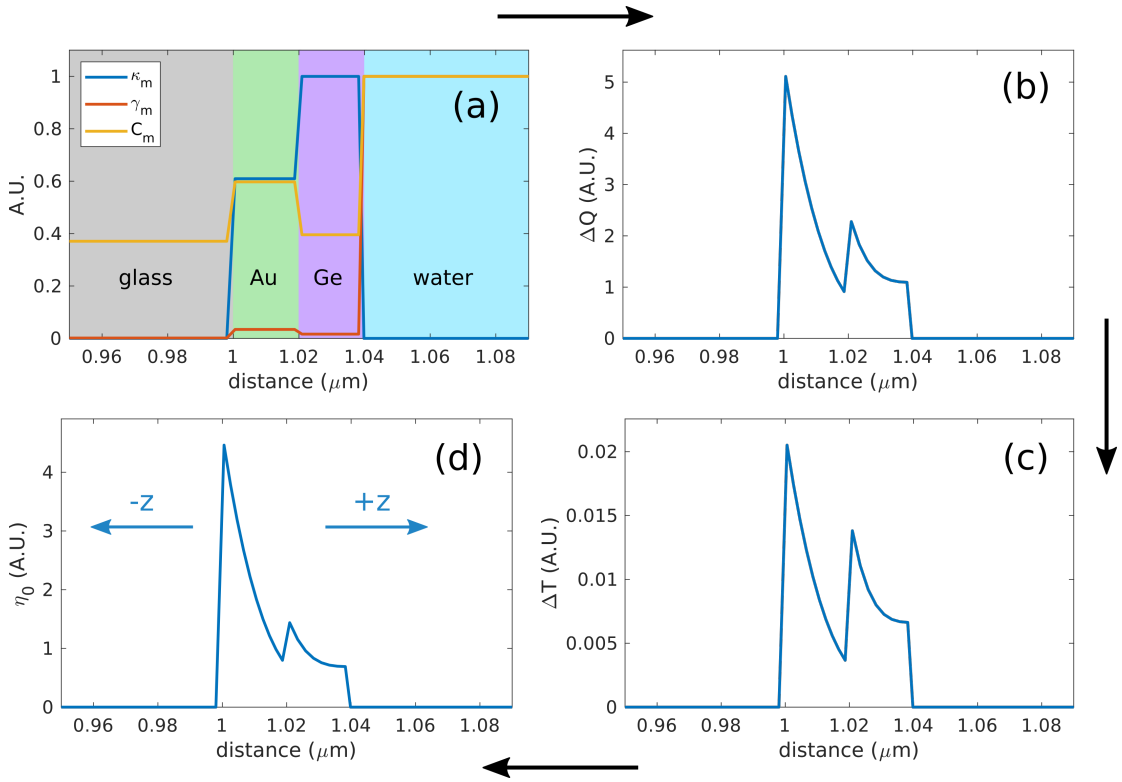


Figure 2.10: Process flow from absorption of the pump beam to the initial strain distribution within the structure using the the example of a glass/Au/Ge/water geometry. (a) The relevant material properties of each layer are predetermined: extinction coefficient (κ_m) which dictates optical absorption, γ_m a consolidation of mechanical constants (see Equation 2.57), and C_m the volumetric specific heat capacity. (b) The optical power transferred from the pump field to the structure leads to a distribution of the heat rise throughout the structure (function of κ_m) which is used to simulate the relative temperature rise (c) (function of C_m). Finally the constant γ_m converts temperature to the initial strain distribution within the structure (d). For time $t > 0$ this strain distribution propagates in the positive and negative directions thus generating the acoustic field.

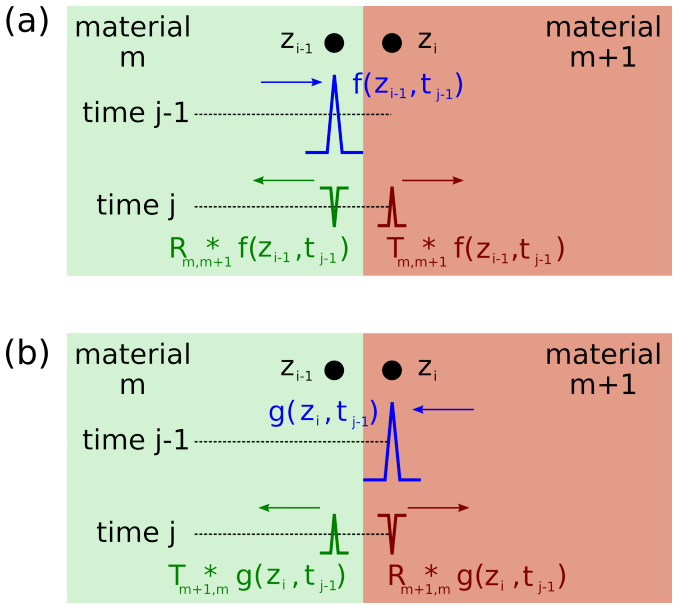


Figure 2.11: Calculating the transmission and reflection of strain when an acoustic impedance boundary between material m and $m+1$ is encountered. Spatial node z_{i-1} occupies the m^{th} side of the boundary, the z_i node occupies the $(m+1)^{st}$ side.(a) At time t_{j-1} a forward propagating strain pulse located at z_{i-1} is described by $f(z_{i-1}, t_{j-1})$. At time t_j the pulse will have partially transmitted (to position z_i) and reflected (to position z_{i-1}) according to the scattering coefficients (Equations 2.62-2.63). (b) The same process is carried out for the backward propagating strain pulse in material $m+1$. At a single spatial node z_i, the forward and backward propagating terms at time t_j are superimposed through Equations 2.60-2.61 and ultimately Equation 2.58.

$$g(z_{i-1}, t_j) = T_{m+1,m} g(z_i, t_{j-1}) + R_{m,m+1} f(z_{i-1}, t_{j-1}) \tag{2.61}$$

where $T_{m,m+1}$ and $R_{m,m+1}$ are the acoustic transmittance and reflectance:

$$T_{m,m+1} = \frac{v_m}{v_{m+1}} \frac{2Z_m}{Z_m + Z_{m+1}} \tag{2.62}$$

$$R_{m,m+1} = \frac{Z_{m+1} - Z_m}{Z_m + Z_{m+1}} \tag{2.63}$$

Once the strain amplitude at the boundary has been calculated using the acoustic scattering coefficients, these reflections and transmissions then propagate through the system until they encounter another boundary. In this way, acoustic interference can be used to design cavities which are mechanically resonant [166, 167].

The existence of longitudinal strain in an object results in its deformation, and therefore a displacement u of its interfaces:

$$\eta = \frac{\partial u}{\partial z} \tag{2.64}$$

where ∂z represents the discretisation of the spatial vector occupied by the object. Consequently, for a multi-layered structure, the longitudinal strain in any one layer (at

any instant in time) will result in the displacement of both that layer and the entire attached structure. Therefore the total strain (Equation 2.58) within the (m-1)st layer has a cumulative effect on the total strain experienced by the mth layer (all the way through to the N^{th} layer) ultimately causing displacement of the mth layer:

$$u_m(t) = \int_0^{z'} \eta(z', t) dz' \tag{2.65}$$

(at every time step t) where z' is the spatial vector of the structure from $z = 0$ up to the mth layer (dz' will vary according to the sound velocity of each layer material) [161].

The above has described the generation and propagation of strain pulses in a multi-layered structure given the following qualifiers: (1) the spot size of the pump beam is much larger than the thickness of the multi-layer transducer, and (2) that the structure is infinite in the x and y dimensions. With these two conditions a 1D analytical model is set up where the elastic waves described above can be approximated as longitudinal plane waves travelling in the $\pm z$ direction. This greatly simplifies the calculation of the acoustic fields since the longitudinal strain $\eta = \eta_{zz}$ is the only non-zero component of the elastic strain tensor [154].

The generation bandwidth of the acoustic field will be dictated by the axial extent of the strain pulse(s). Since the initial strain distribution follows the optical absorption profile of the pump laser, the absorption length can be used to determine the upper frequency limit of the transducer. Considering the extinction coefficient (κ) from the complex refractive index (Equation 2.54), the absorption coefficient of the material can be written:

$$\alpha = \frac{4\pi\kappa}{\lambda_{pump}} \tag{2.66}$$

which produces an absorption length of $\zeta = 1/\alpha$. Consequently, the acoustic frequency spectrum in medium m will peak at

$$f_p = \frac{v_m}{2\zeta} \tag{2.67}$$

As an example, for a $150\ nm$ gold film transducer and $\lambda_{pump} = 390\ nm$, an absorption length of $\approx 16\ nm$ will produce a strain pulse with peak frequency $f_p \approx 120\ GHz$. When this pulse propagates into an adjacent water layer the frequency spectrum reveals a frequency peak at $f_p \approx 40\ GHz$ and a $3dB$ bandwidth of $\Delta f_{3dB} \approx 135\ GHz$ which has a $3dB$ cut-off at $f_{3dB} \approx 140\ GHz$. This is confirmed by using the analytical model in this section to simulate the strain pulse in water (Figure 2.12a) and its Fourier transform (Figure 2.12b).

Thus far the mechanism for generating GHz frequency acoustic plane waves has been discussed. A generalised approach was outlined using a structure with an arbitrary number of planar layers of arbitrary materials. Often times a single metallic layer

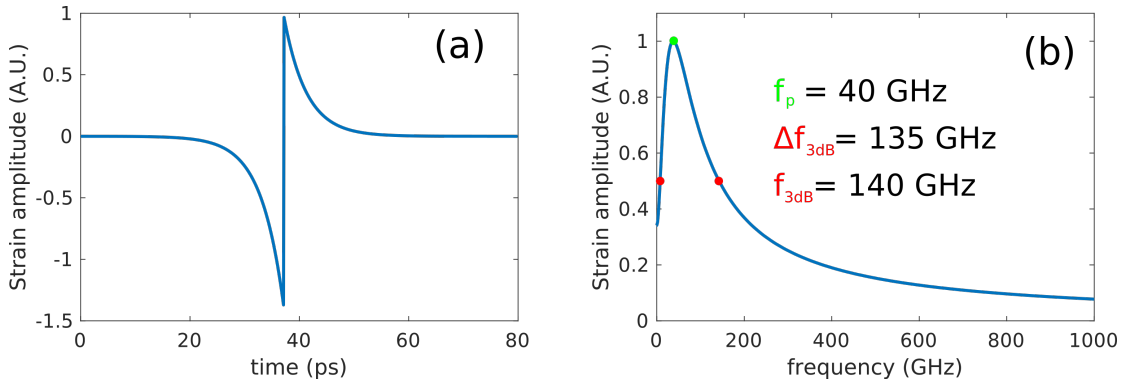


Figure 2.12: Frequency content of a high frequency strain pulse in water. The geometry for this example is a 150 nm gold layer preceded by a glass substrate and followed by a water medium. The unipolar strain pulse reflects at the glass/gold interface producing the bipolar strain pulse. (a) Total strain over the first 80 ps experienced at the boundary between gold and water due to the propagation of a bipolar strain pulse. (b) Fourier transform of the strain pulse reveals its frequency content: $f_p \approx 40\ GHz$, $\Delta f_{3dB} \approx 135\ GHz$, and $f_{3dB} \approx 140\ GHz$.

is sufficient for photoacoustic generation, as will be shown in future sections. However, the N-layer approach demonstrates the working principles and capabilities of the 1D mechanical model presented. In the following section, the optical detection mechanisms for high frequency ultrasound will be discussed.

Detection

A picosecond strain pulse can be optically detected if it perturbs the optical properties of the material(s) in which it travels; when this occurs the reflection and transmission of a probe beam will be modulated (Equation 2.32-2.33) and recorded by a photodetector. In order to model this phenomenon the probe electric field should be solved for two scenarios: before the transducer is perturbed and during perturbation, i.e. in terms of the electromagnetic wave equation (Equation 2.8)

$$\frac{\partial^2 E}{\partial z^2} = -\frac{\omega^2}{c^2}\left[\epsilon + \Delta\epsilon\right]E \tag{2.68}$$

where $\Delta\epsilon$ is the permittivity perturbation [154]. Equation 2.68 can be rearranged and relabelled in the following way

$$\left[\frac{\partial^2}{\partial z^2} + k^2\epsilon_h(z)\right]E(z) = -k^2\epsilon_{ih}(z)E(z) \tag{2.69}$$

where $\epsilon_h(z) = \epsilon(z)$ is the (unperturbed) bulk values along the stack and $\epsilon_{ih}(z) = \Delta\epsilon(z)$ is defined as a perturbation (source of inhomogeneity). Equation 2.69 is analogous to solving Maxwell's equations (Equations 2.1-2.4) for the case of a non-zero charge density (ρ_f) and/or current density ($\mathbf{J_f}$). Inhomogeneous differential equations of the

form in Equation 2.69 are commonly solved by using *Green's method* to rewrite the equation in the form

$$\Big[\frac{\partial^2}{\partial z^2} + k^2\epsilon_h(z)\Big]G(z,z') = -\delta(z-z') \tag{2.70}$$

where the source (in this case $\epsilon_{ih}(z)$) is treated as a delta function centred at position z' (position of the strain pulse); solving Equation 2.70 for the Green's function $G(z,z')$ (discussed in Appendix A) then provides a solution for the field in space $E(z)$ (Equation 2.69).

At this point the mechanisms through which the electric permittivity are perturbed (ϵ_{ih}) need to be identified. The first effect is photoelasticity: the modulation of the complex refractive index due to the presence of strain in an object. For the material in the mth layer the permittivity will vary by:

$$\epsilon_p(z) = P_m\eta(z) \tag{2.71}$$

where $P_m = \partial\tilde{n}/\partial\eta$ is the photoelastic constant of the mth layer. The second contribution to the modulation in optical properties of a material is when the material changes in thickness, e.g. due to the propagation of strain within the material. In PLU this typically amounts to thickness variations on the order of $\sim pm$, which for a 10 nm thin-film would be on the order of 0.01% change in thickness. Consequently, the effect can instead by approximated by a change in permittivity only when $z = z_m$ at the mth boundary [163]:

$$\epsilon_d = \begin{cases} \epsilon_m - \epsilon_{m+1} & \text{for } u_m > 0 \ ; \ z_m < z < z_m + u_m \\ \epsilon_{m+1} - \epsilon_m & \text{for } u_m < 0 \ ; \ z_m + u_m < z < z_m \\ 0 & \text{otherwise} \end{cases} \tag{2.72}$$

where the sign of the variation depends on whether the boundary displacement is positive (expansion) or negative (contraction). Finally the total perturbation in permittivity can be written

$$\epsilon_{ih} = \epsilon_p + \epsilon_d \tag{2.73}$$

Recall the basic mechanism of optical detection with PLU: (1) a strain pulse is generated by the transducer due to the absorption of a pump pulse, (2) a probe pulse samples the excited region at one instant in time (t_1), and (3) repeat steps (1-2) but with the probe pulse time-delayed such that it samples instant t_2 in time ($t_2 > t_1$). Then through the relationship $z' = v_m t$ the electric field value at every instant in time can be reconciled with the position of the strain pulse (z') that moves with velocity v_m in material m. Now an analytical expression for the total reflected field $E(z)$ at every instant in time/space can be solved by combining Equations 2.73 with the field solutions for the homogeneous and inhomogeneous contributions (see Equations A.6 and A.9 in

Appendix A) [161]

$$E(z) = A_0 e^{ik_0 z} + B_0 e^{-ik_0 z} + \frac{ik_0 e^{-ik_0 z}}{2k_0 A_0}\Bigg[\int_z^0 P_0\eta(z')[A_0 e^{ik_0 z'} + B_0 e^{-ik_0 z'}]^2 dz' + \sum_{m=1}^{N+1}\int_0^{d_m} P_m\eta(z' + z_{m-1})[A_m e^{ik_m z'} + B_m e^{-ik_m z'}]^2 dz' + \sum_{m=1}^{N+1}(A_m + B_m)^2[\epsilon_{m-1} - \epsilon_m]u_{m-1}\Bigg] \quad (2.74)$$

This is for the case that the $m = 1^{st}$ layer of the transducer begins at $z = 0$ and that the detector lies somewhere $z < 0$ in the $m = 0$ region. Note that the first two terms in Equation 2.74 represent the homogeneous solution in the $m = 0$ layer for the unperturbed structure (E_0). The first term in the brackets containing P_0 represents the electric field contribution due to the photoelastic effect in the $m = 0$ layer, and the following summed term containing P_m represents the total contribution from all $m > 0$ layers at position $z' = vt$ in time. The final term, represents the contribution to the field made by the movement of the interfaces for each layer.

After considering that the detector is at some arbitrary position $z = z_{det}$ in the region $z < 0$ the relative change in the reflection coefficient of the probe due to the propagation of strain waves - $\delta r/r_0 = (r - r_0)/r_0$ - can be written [161]

$$\frac{\delta r}{r_0} = \frac{ik_0}{2A_0 B_0}\Bigg[\int_z^0 P_0\eta(z')[A_0 e^{ik_0 z'} + B_0 e^{-ik_0 z'}]^2 dz' + \sum_{m=1}^{N+1}\int_0^{d_m} P_m\eta(z' + z_{m-1})[A_m e^{ik_m z'} + B_m e^{-ik_m z'}]^2 dz' + \sum_{m=1}^{N+1}(A_m + B_m)^2[\epsilon_{m-1} - \epsilon_m]u_{m-1}\Bigg] \quad (2.75)$$

(recall r in Equation 2.32) where $r_0 = b_0/a_0$ is the reflection coefficient of the unperturbed structure which is determined by Equation 2.52. A field solution similar to Equations 2.74 and 2.75 can also be written for the case of the transmitted portion of the probe beam, which can be detected in the $N+1^{st}$ layer ($z > z_N$ region) of the structure. At the detector the optical signal described by Equation 2.75 will register as an intensity; consequently, the experimental signal can be modelled by calculating the relative change in reflectivity:

$$\frac{\Delta R}{R_0} = 2 \cdot \mathrm{Re}\Big(\frac{\delta r}{r_0}\Big) \quad (2.76)$$

Since this analytical model retains the relative optical phase of the probe field, the imaginary portion of Equation 2.75 can also be utilised; a suitable interferometric detection scheme can be modelled by considering $2 \cdot \mathrm{Im}(\delta r/r_0)$.

The signal presented in Equation 2.76 is referred to as the *modulation depth*. This is

distinct from solely the modulated (shorthand: AC) portion of the signal (ΔR); normalising the AC component of the signal by the mean (shorthand: DC) reflectance of the structure (R_0) allows transducer structures with different optical properties to be compared in terms of their sensitivity to strain propagation. Following the instantaneous temperature rise due to pump absorption, Equations 2.75 and 2.76 model the reflected probe signal for each successive instant in time that the strain pulses propagate, e.g. from $t = [0, 10]\ ns$. When using this analytical PLU-model to make experimental predictions or design planar transducers it is useful to identify relationships between the input optical intensities of the pump and probe beams and the following parameters. Notice in Equation 2.75 that the probe signal field is proportional to the strain and displacement terms, η and u_m, (which are proportional to each other), and through Equations 2.55-2.57 are found to be proportional to the intensity of the pump beam

$$\frac{\Delta R}{R_0} \sim u \sim \eta \sim I_{pump}$$

where η and u are synonymous with the acoustic amplitude A_{ac}. Furthermore, Equation 2.75 reveals that the final modulation depth signal is proportional to the intensity of the probe beam:

$$\frac{\Delta R}{R_0} \sim I_{probe}$$

Therefore, the following relationships can be drawn:

$$\frac{\Delta R}{R_0} \sim A_{ac} I_{probe} \sim I_{pump} I_{probe} \tag{2.77}$$

which given a shot-noise limited photodetector results in the following relationship between beam power density and the final SNR of the TRBS signal

$$SNR \sim I_{pump} \sqrt{I_{probe}} \tag{2.78}$$

A crucial outcome from the above operating principles, is that just like spontaneous Brillouin scattering, PLU is inherently sensitive to the photoelasticity of a specimen. Unlike spontaneous Brillouin scattering, PLU has the advantage that the excited transducer actively pumps broadband strain pulses into the medium/specimen of interest. In principle a spontaneous Brillouin spectrometer should be capable of detecting the inelastic wavelength shifts in a photoelastic region that has been excited by the PLU generation mechanism. However, the following section will show that the PLU-detection mechanisms are capable of obtaining similar information to a Brillouin spectrometer. This has been exploited by the emerging field of time resolved Brillouin scattering which synergises Brillouin spectroscopy with PLU.

2.3 Time resolved Brillouin scattering

Now that the principles of PLU have been revealed through the mathematical formalism of Osamu *et al* [161], this section will revisit and expand upon the concept that PLU is capable of observing Brillouin scattering in the time domain, first discussed in Section 2.2. Unlike spontaneous Brillouin spectroscopy which detects spectral shifts in optical frequency, PLU is insensitive to the spectral information of the detected probe light. Instead, PLU must interferometrically observe the time-of-flight of the propagating phonon from which the probe beam scattered [156, 159]; this process is aided by the built-in ultrasonic generation process for PLU. By actively generating coherent phonon fields, PLU avoids the reliance on the random thermal fluctuations of incoherent phonons that naturally arise in a specimen. The PLU-based approach to observing Brillouin scattering has been coined time resolved Brillouin scattering (TRBS), or time domain Brillouin scattering (TDBS), and operates in the following way.

Recall that the total reflected electric field in Equation 2.74 is set up when a time-resolved pump-probe optical system (discussed in Chapter 4) is used to excite a laser ultrasonic transducer and monitor the modulation of the probe beam that has interacted with the excited environment. Evidently, according to the second summed term in Equation 2.74 containing the variable P_m, the field variation from the mth layer is determined by: the integration of the photoelastic perturbation in permittivity (Equation 2.71) and the intensity of the probe field. However, it becomes apparent that the electric field contains an additional phase term $\sim e^{\pm i2k_m z}$ (after taking the squared sum of the fields). Compared with the wavevector of the optical probe, this phase term differs by a factor of $2n$

$$\lambda_{signal} = \frac{\lambda_{probe}}{2n} = \lambda_a \tag{2.79}$$

which is identical to the phase matching condition for the Bragg diffraction process that occurs during Brillouin scattering between an optical wave λ_{probe} and acoustic wave λ_a (Equations 2.22 and 2.23, for the case of normal probe incidence). Subsequently, the solution for the scattered probe field will contain a total wavevector of

$$e^{-ik_0 z} \cdot e^{\pm ik_a z} \sim e^{-i(k_0 \pm k_a)z}$$

where $e^{-ik_0 z}$ has come from the term preceding the brackets in Equation 2.74. This is the same result as conventional Brillouin spectroscopy shown in Equation 2.15: the Brillouin scattered beam will experience a wavelength shift with respect to the incident light.

PLU detection of Brillouin scattering is still inherently challenged by the fact that only 1 out of $\sim 10^6$ photons Brillouin scatter with the acoustic wave [168]. Despite the 6 orders of magnitude improvement in scattering efficiency over spontaneous Brillouin scattering, the TRBS process is still a relatively weak process, and is dominated by the

DC portion of the field $E_{DC} = E_0$. Consider the simplified version of Equation 2.74 into DC and AC portions

$$E_{det} = E_{DC} + E_{AC}$$

At the detector the intensity will then be

$$I_{det} = E_{DC}^2 + E_{AC}^2 + 2E_{DC}E_{AC}$$

where $E_{DC} >> E_{AC}$. Due to the existence of both elastic and inelastic light at the detector, TRBS naturally provides a mechanism for heterodyne detection as demonstrated by the interference term $2E_{DC}E_{AC}$. Now the detected intensity is normalised to achieve modulation depth (Equations 2.75-2.76) and the appropriate phases applied

$$\frac{I_{det}}{I_{DC}} \sim \frac{2E_{DC} \cdot e^{ik_0 z} E_{AC} \cdot e^{i(k_0 \pm k_a)z}}{E_{DC}^2 \cdot e^{i2k_0 z}} \sim \frac{E_{AC}}{E_{DC}} e^{\pm k_a z} \tag{2.80}$$

to reveal that probe signal intensity will be modulated at the phonon frequency, which, as expected is the beat frequency for the interference of the DC and AC terms. This outcome is easily seen in the expression for the modulation depth in Equation 2.75, with the wavevector of the signal being $e^{i2k_m} = e^{ik_a}$.

Figure 2.13 shows an example of this intrinsic heterodyne process created with PLU detection for the case of a non-attenuating $f_a = 5.11\ GHz$ frequency phonon in water ($\lambda_a = 293\ nm$) and a $f_{probe} = 380\ THz$ ($\lambda_{probe} = 780\ nm$) probe field. The elastically reflected light (orange) propagates at frequency f_{probe}, while the inelastically scattered light (yellow) propagates at frequency $f_{probe} + f_a$ (Equation 2.18). The superposition between the two fields at the detector (last term in Equation 2.80) results in an interference pattern (blue) with beat frequency f_a, which is characterised by fast Fourier transform (FFT).

As a result of the above TRBS detection process, a unique feature of PLU becomes apparent. Since the instantaneous phase of the detected propagating phonon is encoded on the phase of the optical signal, TRBS is capable of reconstructing the acoustic time of flight. Crucially, this time-domain signal can be analysed in the frequency domain through FFT, in order to characterise the Brillouin frequency shift (Equation 2.24) and elasticity. Furthermore, viscosity can be accessed by measuring the amplitude decay of the phonon in the time-domain, rather than relying on ambiguous spectral linewidths. A key benefit to TRBS compared with conventional Brillouin spectroscopy, is that axial resolution is provided by the acoustic wavelength ($\sim 100\ nm$) instead of the optical depth of focus of a Brillouin microscope ($\sim 10\ \mu m$). This axial resolution can then be used to resolve changes in phonon frequency (i.e. elasticity) or instantaneous phase below the optical diffraction limit while still maintaining optical lateral resolution through the use of microscope objective lenses.

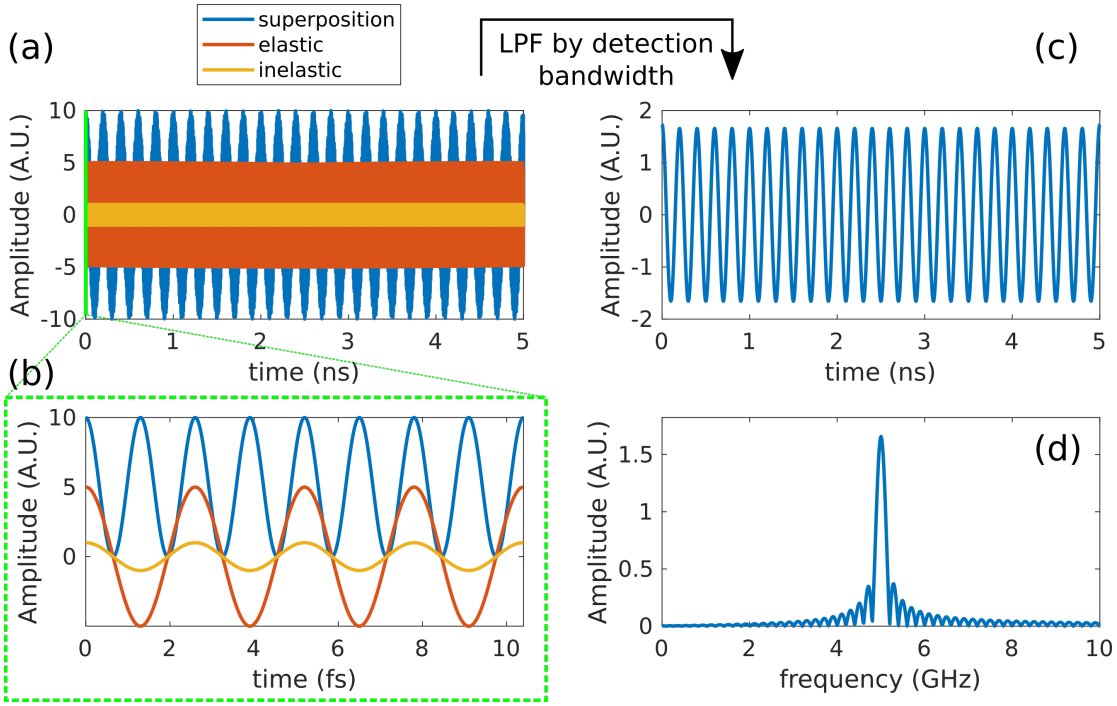


Figure 2.13: Simplified demonstration of the heterodyne detection process for TRBS in water with a probe wavelength of $\lambda_{probe} = 780\ nm$. (a) Inelastically scattered light (yellow) has shifted in frequency by $\Delta f \approx 5\ GHz$ with respect to the elastically scattered light (orange). This shift is unnoticeable in the zoomed-in time of flight for the optical field (b). However, the superposition of the elastic and inelastic fields (blue in (a-b)) will be modulated by a lower frequency beating between the two fields. (c) Through low pass filtering this low frequency oscillation is isolated and its frequency characterised by FFT as the sampled phonon frequency $f_B \approx 5\ GHz$.

Figure 2.14 demonstrates using the PLU-model to simulate TRBS (Equations 2.75-2.76). A single metallic thin-film is irradiated by a pump pulse to produce strain which travels into the surrounding medium. The refractive index and sound velocity in the medium (e.g. water or polystyrene) dictates the measured Brillouin frequency. A second probe beam Brillouin scatters as it propagates through the medium, and produces the TRBS signal shown in Figure 2.14a containing the frequency spectra (FFT) for each medium in Figure 2.14b.

Following the above developments in the theory of PLU and TRBS, the potential for using these techniques as a basis for microscopy was soon realised. In particular, the technologies showed promise for application to bio-imaging since they could be implemented with non-contact, label-free, and high resolution operation. However, significant development in instrumentation was needed to realise this potential; especially with regards to the acquisition speed of the pump-probe measurement system which will be introduced and discussed in Section 4.1. In the following section the application of PLU, and in particular, TRBS to microscopy will be discussed.

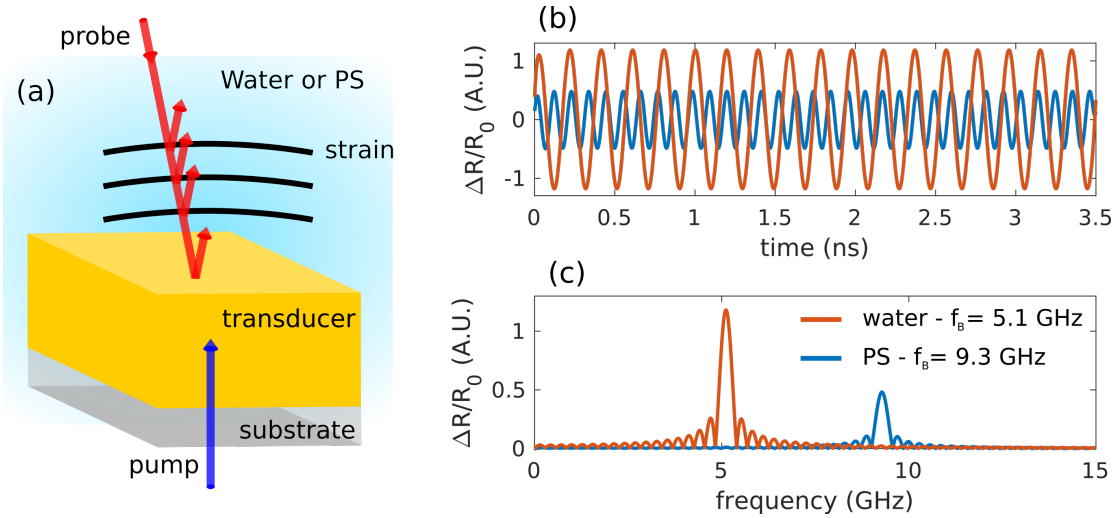


Figure 2.14: Basic example of using the PLU-model to simulate TRBS with a transducer and the external medium: water or polystyrene (PS). (a) Geometry assumed for the simulation: the pump beam is incident from the substrate side of the system and the probe beam from the medium side, and the optical probe wavelength is set to $\lambda_{probe} = 780\ nm$. The optical beating between the elastic and inelastic photons gives rise to the modulation depth shown in (b). (c) FFT is used to cast the time-resolved signals in (a) into the frequency domain. Due to the differences in refractive index and sound velocity between water and PS, the measured Brillouin frequency (frequency position of the peaks) will differ when either medium acts as the external medium.

2.3.1 PLU-based microscopy

The first single-point TRBS measurements were performed on a sub-cellular scale in the early 2000's [169]. This was achieved using a bulk titanium substrate as an opto-acoustic transducer, on top of which sat onion cells. A high NA objective lens was used to direct the pump and probe pulses through the top of the cell and create a $\sim 1\ \mu m$ diameter spot for the thermoelastic generation process and high spatial resolution. The degree of overlap between the pump and probe spots overlap is crucial since the probe field will experience maximum modulation where the strain amplitude per unit volume is maximised [161]. The spatial resolution for the microscope was sufficient to measure TRBS in sub-cellular components such as the nucleus and vacuole. In these organelles, the measured Brillouin frequency shifts differed by over $1\ GHz$, which under the assumption of homogeneous refractive index, corresponds with approximately a $400\ m/s$ variation in measured sound velocity (Equation 2.24). Additionally, quantities such as the attenuation of the acoustic wave could be measured with $\sim 250\ nm$ axial resolution using the acoustic wavelength. These initial experiments pointed towards TRBS' ability to measure viscoelastic-related properties of biological media and motivated the first 1D scanning of Brillouin frequency across onion cells [170].

As instrumentation continued to improve, the first images of cells using PLU soon followed [171–173]. From these measurement systems, two general approaches to

PLU-based microscopy evolved:

1. single-layer metallic transducer $\rightarrow$ { A. all-optical GHz ultrasonography; B. TRBS imaging }
2. Fabry-Pérot cavity transducer $\rightarrow$ A. TRBS imaging

Case $\#1$ represents the most widespread transducer architecture: a single metal-layer typically fabricated of Ti and with thickness $> 100\ nm$ [174]. The transducer is usually fabricated onto a sapphire substrate, which along with the transducer thickness, is meant to optimise thermal conduction following the pump-induced heat rise [171]. In all cases the pump beam is illuminated from the beneath the substrate/transducer which houses the specimen on top; due to the thickness of the transducer, the pump is absorbed within the first ten's of nanometres of the layer and generates a broadband phonon field with frequencies up to $\sim 100\ GHz$ [171, 172]. This broadband packet then travels from the bottom of the transducer to the top interface with the cell where it reflects and transmits into the specimen. Cases $\#1A$ and $\#1B$ represent two detection mechanisms used in this configuration; in $\#1A$ the probe pulse is also delivered from beneath the transducer. As strain pulses reflect from the transducer/cell interface and impinge on the substrate/transducer interface, the displacement of the layer modulates the reflectivity of the probe beam. By analysing the amplitude of the reflected echo as a function of frequency, the technique is capable of measuring surface variations in cellular acoustic impedance and adhesion [171].

In case $\#1B$, the single Ti layer is again used as a thermoelastic source of broadband ultrasound, yet the probe beam is made to pass through the specimen and partake in TRBS. Imaging is performed by measuring the TRBS signal at a single position in the cell, which is then scanned in x and y. Elasticity-related properties such as the Brillouin frequency are attained by Fourier transforming the time-domain signal into the frequency domain; which when done recursively for each pixel creates a 2D Brillouin frequency map. The time-domain signal can also be subjected to time-frequency analysis (Section 4.2.2), to extract Brillouin frequency in the axial direction [172, 175]. Through Bragg's law (Equation 2.22), this allows z-sectioning of the specimen with sub-optical wavelength phonons. Regarding the experimental set-up for case $\#1B$, it is possible for the pump beam to be delivered either from beneath the substrate [172, 176] or through the cell [175]; whereas due to the optical opacity of the $> 100\ nm$ Ti transducer, it is compulsory to deliver the probe through the cell in order to measure cellular Brillouin scattering. In both instances, one or both of the following caveats emerge: (1) the cell is directly exposed to fs-radiation often with phototoxic NUV wavelengths [172], or (2) difficulty aligning overlap between oppositely incident pump and probe spots.

Hybrid systems have also been developed that are capable of performing cases $\#1A$ and $\#1B$ in parallel [174]. The microscope is configured such that the pump and

probe can both be delivered from above the cell and beneath the cell/transducer (see Figure 2.15). This allows simultaneous impedance imaging (when both beams are incident from beneath) and Brillouin imaging (probe beam from above the cell) [177]. Measuring impedance and Brillouin frequency enables a unique ability to measure an approximation of cell density at the cell/transducer interface. This is particularly relevant for Brillouin scattering-based imaging in general, as refractive index and density are quantities which must be unambiguously measured in order to quantify elasticity (longitudinal modulus). Nevertheless, this novel capability has only been proven for the case of dehydrated cells which demonstrate greater impedance mismatches compared with live cells in medium.

State of the art transducer design for PLU-based imaging was limited to single (quasi-bulk) layers of metal until the emergence of Case $\#2A$, a technique called phonon microscopy which focused on TRBS imaging. This design replaced the single layer with a low order Fabry-Pérot cavity, known as an opto-acoustic transducer (OAT), made from two Au partial mirrors spaced by a indium tin oxide (ITO) cavity (Figure 2.16a) [166]. By carefully designing the thicknesses of the Au and ITO layers, the degree of optical interference within the cavity can be controlled; this results in specific wavelengths resonating in the cavity leading to strong transmission and reflection characteristics. From this perspective the transducer cavity was initially designed using the TMM to solve for the Fresnel coefficients (Equations 2.32-2.35) over a range of mirror/cavity thicknesses at pump and probe wavelengths of $\lambda_{pump} = 390\ nm$ and $\lambda_{probe} = 780\ nm$. This Fresnel model was utilised to optimise the following properties:

- maximise transmission of the NIR probe wavelength (see Figure 2.16b)
- minimise the transmission (Equation 2.35) of the phototoxic NUV pump wavelength to prevent cell exposure (see Figure 2.16c)
- ensure that the cavity spacing still sufficiently absorbs the blue which corresponds with high amplitude strain pulses (Equation 2.77).

If all the above is realised, it is then possible to deliver both pump and probe beams from beneath the transducer/specimen; since the probe is resonantly transmitted through the cavity, it can then pass through the specimen and Brillouin scatter with the phonon wavefronts and ultimately continue onward to a collection lens and detector. This is enabled due to the semi-transparency of the cavity, made possible due to the transmission resonance and transparency of the ITO cavity layer. All designs discussed thus far integrate the transducer directly into a brightfield microscope configuration which allows specimens to be located optically before performing PLU. With quasi-bulk Ti layers, brightfield imaging is limited to reflection configuration only and must contend with strong reflections from the metal which leads to low contrast and camera saturation. With a semi-transparent cavity greater flexibility for brightfield imag-

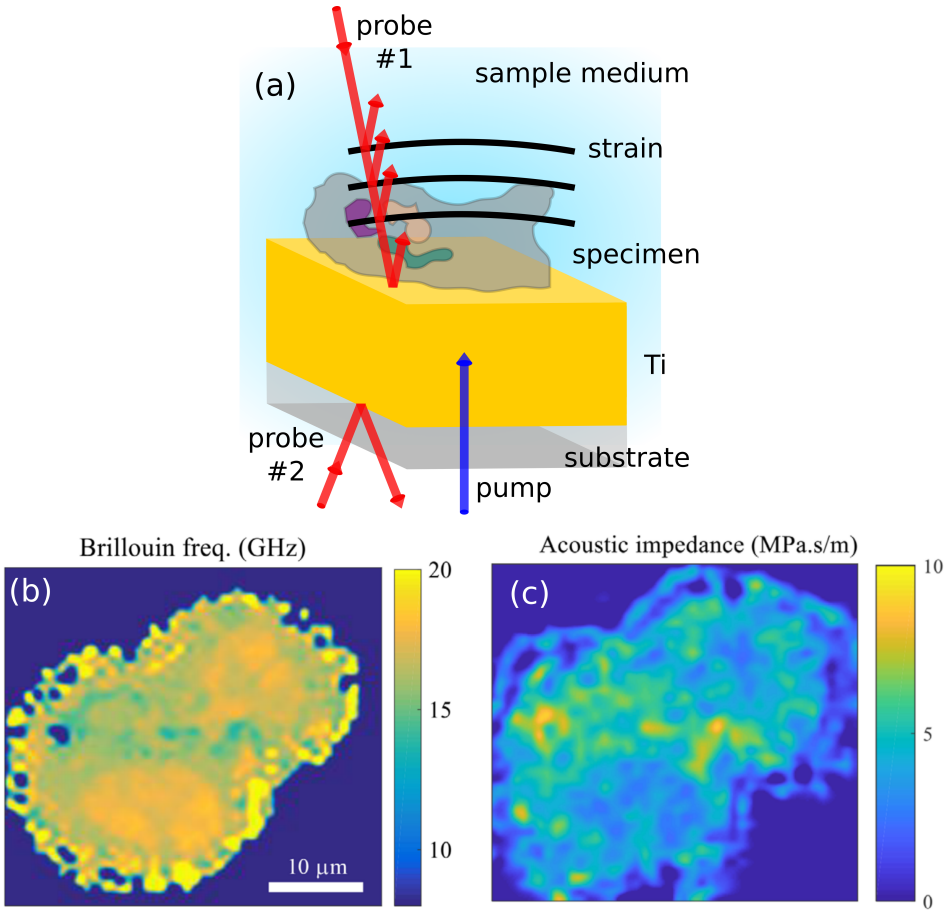


Figure 2.15: Example of a coventional TRBS transducer and imaging capabilities. (a) Typically a quasi-bulk layer of Ti is used for thermo-elastic generation with the pump beam incident from beneath the transducer. The probe can be configured to impinge the transducer/specimen from below or above the transducer. When incident from above the specimen (probe $\#1$) the system is capable of mapping cellular Brillouin frequency (b). Alternatively, when the probe is incident from beneath the transducer (probe $\#2$) the acoustic impedance mismatch at the transducer/cell interface is measured as strain modulates the optical response of the transducer (c). Due to the opacity of the transducer, probe $\#2$ is unable to participate in Brillouin scattering through the sample. (b) and (c) are examples from a hybrid TRBS microscopy in which probe paths $\#1 - 2$ are run in parallel (iPOM) [177]. (b-c) Reprinted from Journal of Biophotonics, 12, Bertrand Audoin, Marie-Christine Durrieu, Laurent Plawinski, et al., Label-free multi-parametric imaging of single cells: dual picosecond optoacoustic microscopy, 11, Copyright (2019).

ing is enabled since illumination can be collected in reflection or transmission mode, while also increasing overall contrast. Furthermore, since pump and probe are delivered to the sample through the same objective lens, the overlap between pump-probe spots is greatly simplified leading to more efficient TRBS.

Following these innovations, phonon microscopy was among the first techniques to report the successful imaging of biological cells (3T3 fibroblasts) using PLU [173]. Compared with competing TRBS-imaging techniques, the cavity produces heat at a much lower rate than single Ti-layer transducers where NUV is delivered through the

cell, and similar heating characteristics to techniques where only NIR is delivered through cell (see Figure 2.17) [178]. Furthermore, the PLU-model can be used to simulate the TRBS signal strength (Equation 2.77 or the analogus $\Delta T/T_0$) of the various transducer types; the generation and detection efficiency of the Fabry-Pérot appears to show the highest SNR normalised for input beam power [178]. Combining the SNR with the lack of UV exposure has allowed phonon microscopy to become the first TRBS transducer technology that is capable of imaging living cells (alive before and after scanning) (Figure 2.18) [168]. What's more, it was shown that the instantaneous Brillouin frequency along the signal time-of-flight could be used to z-section the specimen

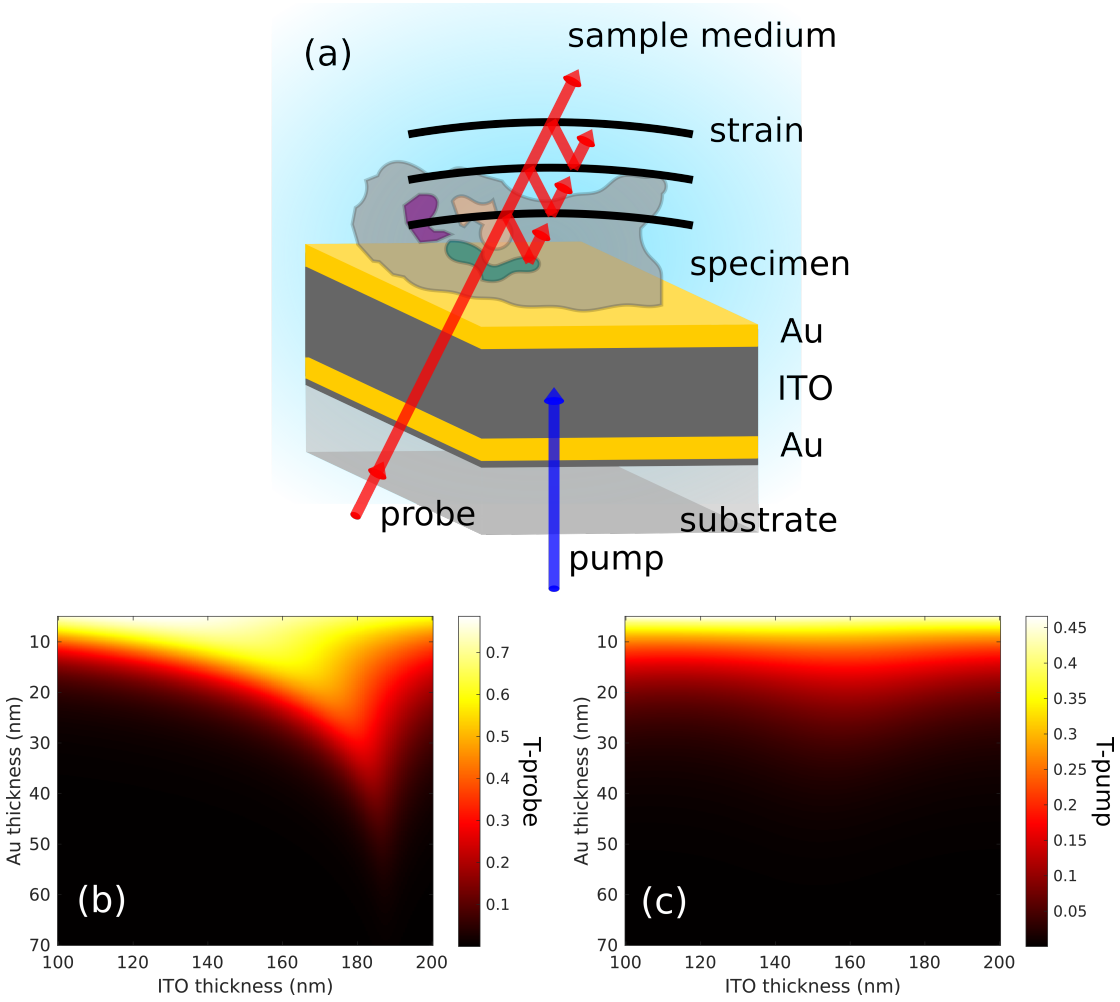


Figure 2.16: Device concept for the OAT. (a) The OAT geometry is a nanometric Fabry-Pérot cavity consisting of gold partial mirrors (20 nm) spaced by the transparent material ITO (transparent at thickness 140 nm). Both the pump and probe wavelengths are incident from beneath the transducer; due to the partial transparency of the cavity the probe beam is capable of performing TRBS and is collected for detection above the specimen. This configuration for the beams simplifies spatial overlap for the pump and probe. (b-c) Transmission spectra for the probe and pump wavelengths ($\lambda_{probe} = 780\ nm$ and $\lambda_{pump} = 390\ nm$ respectively) as a function of Au/ITO thicknesses. The OAT dimensions are selected to maximise T_{probe} and minimise T_{pump}.

with using sub-optical wavelength phonons [168].

PLU and TRBS imaging techniques are relatively young with the earliest proof of concept being first demonstrated in 2015 [171–173]. As such, the exploration for applications of the technology is still in its early stage. To date PLU has been applied to a number of cell types: human mesenchymal stem, osteoblastic, osteosarcoma, cardiac, 3T3 fibroblast, Toxoplasma-infected cells, adipose, HeLa, Acanthamoeba castellani, and PC12 (neuron-like) (Figure 2.18) [168, 171, 173, 176, 178–180]. Many of these experiments have quantified novel elastic signatures of the nuclear mechanical network [179] or the process of encystation [180]. One of the main challenges that faces PLU-based cell imaging is increasing the acquisition speed of the instrumentation (Section 4) to allow real-time operation. On a similar note of applicability, PLU and TRBS are without endoscopic/optical fibre-based technology, which will be discussed in the next section.

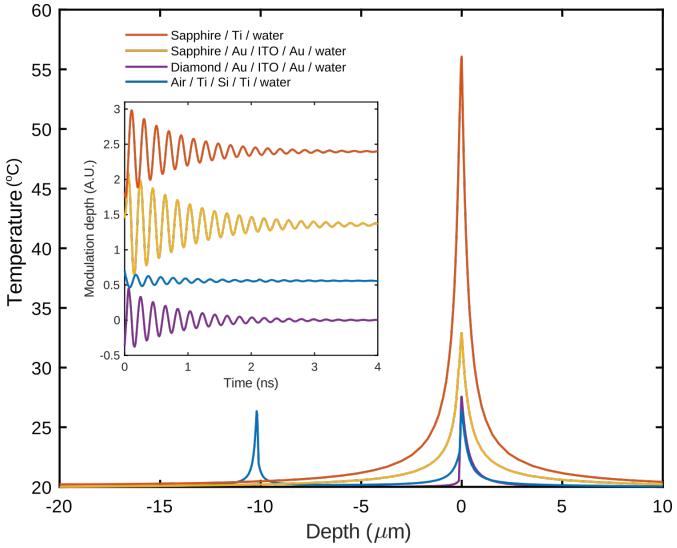


Figure 2.17: Comparison of the OAT with other conventional PLU transducers used in TRBS microscopy. (outer) Finite element method was used to simulate the steady-state temperature rise (at the transducer/specimen interface) produced by the transducer type shown in Figure 2.15 (orange and blue curves) and the OAT (yellow-sapphire substrate and purple-diamond substrate). The temperature rise measured by the blue curve (conventional) achieves the lowest specimen heating since it uses Si instead of sapphire (approximately 7 times more thermally conductive). (inset) Comparison of TRBS signals for each transducer type using the PLU-model, showing the combination of generation and detection efficiency of the resonant OAT device [178]. Reprinted from Fernando Perez-Cota, Rafael Fuentes-Dominguez, Salvatore La Cavera, et al., Picosecond ultrasonics for elasticity- based imaging and characterization of biological cells. Journal of Applied Physics, 128 (16):160902, 2020, with the permission of AIP Publishing.

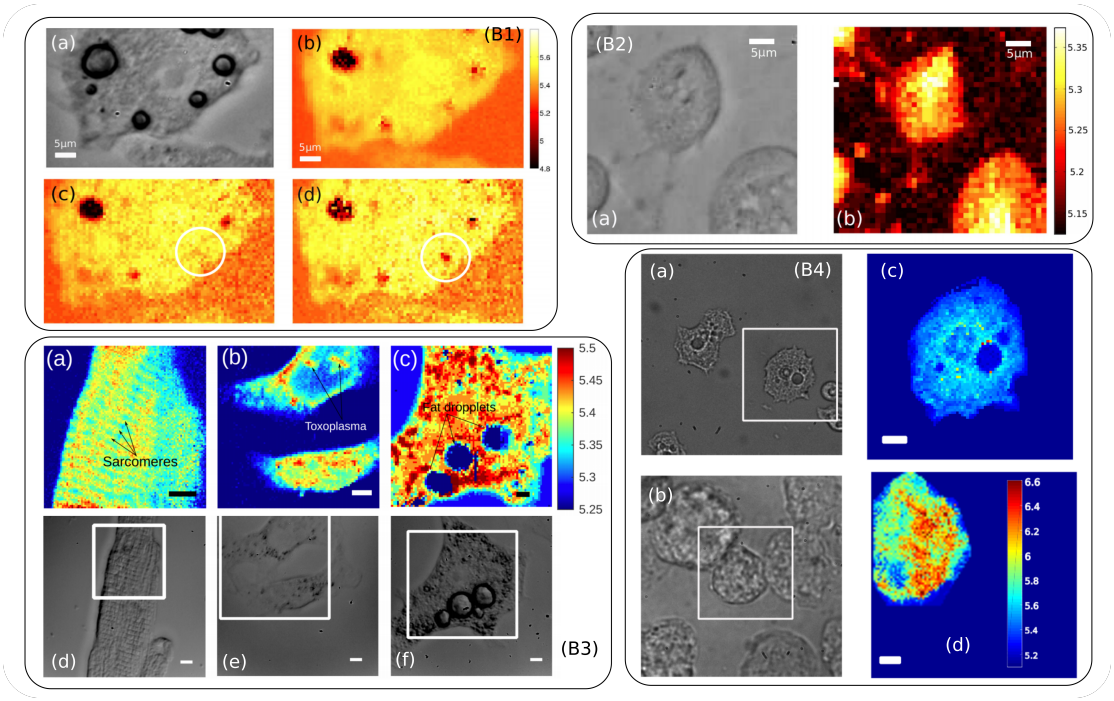


Figure 2.18: Imaging capabilities of phonon microscopy and the OAT design. (B1) Brightfield (a) and Brillouin frequency maps of an adipose cell. (c-d) In-depth sectioning capabilities of the phonon microscope using 280 nm wavelength phonons [168]. (B2) Brightfield (a) and Brillouin frequency maps (b) of living 3T3 fibroblast cells [168]. (B3) Phonon microscopy applied to cardiac muscle cells (a,d), Toxoplasma gondii cellular infection (b,e), and stem cell differentiation into adipose cells (c,f) [178]. The sensitivity of phonon microscopy to cellular elasticity is exemplified by imaging the transformation of Acanthamoeba castellani (c) into a hardened cyst (d) [180]. All colour bars are in GHz. (B1-B2) Reprinted from Nature Scientific Reports, 6, Perez-Cota, F., Smith, R., Moradi, E. et al., High resolution 3D imaging of living cells with sub-optical wavelength phonons, 39326, Copyright (2016). (B3) Reprinted from Fernando Perez-Cota, Rafael Fuentes-Dominguez, Salvatore La Cavera, et al., Picosecond ultrasonics for elasticity-based imaging and characterization of biological cells. Journal of Applied Physics, 128 (16):160902, 2020, with the permission of AIP Publishing. (B4) Reprinted from Biomedical Optics Express, 10, Fernando Perez-Cota, Richard J. Smith, Hany M. Elsheikha, and Matt Clark, New insights into the mechanical properties of Acanthamoeba castellanii cysts as revealed by phonon microscopy, 2399-2408, Copyright (2019).

2.4 Discussion

In this chapter the fields of Brillouin scattering and picosecond ultrasonics have been introduced, modelled, and discussed in the context of imaging systems. These fields merge in the form of time resolved Brillouin scattering which drives coherent phonons into the region of interest and is capable of recording the actual acoustic time-of-flight rather than strictly a frequency domain measurement. This offers a unique opportunity to characterise Brillouin frequency, acoustic attenuation, and depth-resolved information. With regard to latter, TRBS accesses in-depth information using the acoustic

wavelength (sub-optical), as opposed to the depth of focus utilised by Brillouin microscopy. In order to make use of the TRBS concept, the mechanisms for photoacoustic excitation of a transducer and all-optical detection of elastic waves were derived. Two analytical models from this chapter will be utilised to simulate TRBS throughout the remainder of this study: the transfer matrix method (also referred to as the Fresnel model) and the PLU-model.

From the perspective of opto-acoustic imaging modalities, both Brillouin microscopy and TRBS microscopy provide access to viscoelastic properties and behaviours of biological systems on a subcellular level. Both techniques are sensitive to the same elastic regime: low frequency acoustic phonons ($\sim GHz$ frequencies). This regime is important to investigate since natural mechanical fluctuations within cells take place on this time scale and ultimately dictates key cellular processes such as division, migration, differentiation, and apoptosis [131]. Conversely, gold standard tools for mechano-biology, such as the AFM cannot provide access to these frequencies as they are limited to $Hz - kHz$ deformations.

Both imaging mechanisms are less than two decades old; therefore technological innovation is a key driver of maturation for the techniques and their future application beyond university laboratories. Each form of microscopy has strengths and weaknesses (Table 2.1). Brillouin microscopy has long penetration depth, yet the Brillouin signal must contend with elastic scattering. TRBS is limited to near-field measurements ($< 20\ \mu m$), yet does so with better than optical axial resolution. One of the main drawbacks limiting widespread adoption of both technologies, e.g. in clinical healthcare settings, is low acquisition speed. This is due to the scarcity of the Brillouin scattering interaction, especially for spontaneous scattering methods. Despite having superior scattering efficiency TRBS still remains slow due to the time-resolved mechanisms of pump-probe spectroscopy (e.g. oscilloscope averaging, or scanning the delay between the pump and probe). However, solutions to these bottlenecks are already starting to

Brillouin imaging		
	Microscopy	Endoscopy
Spontaneous	• optical lateral resolution • optical axial resolution • long penetration depth*	• optical lateral resolution • currently no depth resolution • long penetration depth • currently not imaging capable
Coherent	• optical lateral resolution • acoustic axial resolution • short penetration depth$^{\circ}$	• does not yet exist • developed in this study

Table 2.1: Table outlining the comparative strengths and weaknesses between spontaneous and coherent Brillouin scattering imaging technologies. Endoscopy for this discussion is loosely defined as an optical fibre-based probe, and not a robust endoscope. $*$ Penetration depth limited by diffuse optical scattering. $\circ$ Penetration depth limited by acoustic attenuation.

emerge, such as stimulated Brillouin scattering [151] or single-shot pump-probe spectroscopy [181]. A second limitation towards applicability is the lack of robust endoscopic technologies for each technique (Table 2.1). An optical fibre probe has been produced for spontaneous Brillouin scattering, however, thus far it is only capable of one-dimensional profiling. Applying the principles of PLU to a Brillouin endoscopic device is promising since actively driving strain into the sample results in six orders of magnitude higher Brillouin scattering efficiency. In PLU, high amplitude elastic waves are localised to the region surrounding the transducer and decay exponentially away from the transducer. As a result, Brillouin scattering interactions occur over an acoustic path length of $\sim 10\ \mu m$ as opposed to $\sim 1\ m$ with the SBS fibre-probe and will allow PLU to utilise standard single-mode optical fibres instead of expensive photonic crystal fibres [153]. Interestingly, PLU and TRBS are currently without any viable optical fibre-based technology. In the following report, the first ever PLU optical fibre device will be introduced.

Part II

Methods

Chapter 3

Opto-acoustic fibre-transducers

This chapter will introduce the design, fabrication, and characterisation of an opto-acoustic transducer. With the future aim of deploying this transducer endoscopically, an optical fibre will be utilised as the transducer substrate. In addition to supporting the transducer on its tip, the optical fibre acts a waveguide for both the pump and probe beams. Unlike in phonon microscopy and other PLU microscopy techniques, the fibre substrate can no longer be treated as a broadband optical window, e.g. like a glass coverslip slide in a free space experiment. The waveguiding behaviour of the optical fibre will impose restrictions on the experimental set-up; or conversely, the properties of the experimental set-up (presented in Chapter 4) will be used to select an optical fibre waveguide with specific compatible properties.

In principle the opto-acoustic transducer has one active role: to thermo-elastically generate a broadband pulse of coherent phonons (section 2.2). It also plays an equally important passive role, as it dictates the amount of probe light that is passed onto the sample of interest; the probe intensity within the scattering volume in part dictates the overall TRBS signal strength (Equation 2.77). In phonon microscopy, the measurement system is designed in the configuration of a transmission microscope, i.e. the probe light transmits once through the transducer, Brillouin scatters in the sample, and continues along the optical axis towards a photo-detector. In order for this technology to be implemented endoscopically, the phonon microscope must be converted from this transmission configuration, into a more conventional epi-configuration where back-scattered (reflected) light must transmit through the transducer a second time before detection. In order to realise these criteria, this chapter will focus on items in the following outline:

- define the relevant parameters for selecting a suitable optical fibre substrate
- establish a process for designing and optimising opto-acoustic transducers
- present the calibration, fabrication, and characterisation techniques for producing transducers.

3.1 Transducer substrate: optical fibre

Operating principles

In order to select an optical fibre substrate which is compatible with the existing optical system - femtosecond pulse-width lasers over the tuning range of $\lambda = 700 - 900\ nm$ (see Section 4) - it is relevant to cover the general operating principles of an optical fibre. In its simplest form, an optical fibre utilises Snell's law -

$$n_1 sin\theta_1 = n_2 sin\theta_2 \tag{3.1}$$

where n is the refractive index and θ is the incidence angle (with respect to the surface normal) - which dictates the angles at which light (and waves in general) refracts at the interface between materials 1 and 2. When light is incident upon the interface, such that the refracted angle occurs at $\theta_2 = 90°$, a phenomenon called *total internal reflection* (TIR) occurs. This can be interpreted using the Fresnel coefficients, which recall from Equations 2.32-2.33, determine the ratio of incident field to reflected and transmitted fields when incident from medium 1 to 2:

$$r_s = \left(\frac{E_r}{E_i}\right)_s = \frac{n_1 cos\theta_1 - n_2 cos\theta_2}{n_1 cos\theta_1 + n_2 cos\theta_2}$$

$$t_s = \left(\frac{E_t}{E_i}\right)_s = \frac{2n_1 cos\theta_1}{n_1 cos\theta_1 + n_2 cos\theta_2}$$

For the case of TIR, when $\theta_2 = 90°$, $r_s = 1$ and consequently $t_s = 0$ indicating that the incident field is totally reflected. This imposes a condition on θ_1 known as the critical angle:

$$\theta_c = \sin^{-1}\frac{n_2}{n_1} \tag{3.2}$$

and TIR holds for $\theta_1 > \theta_c$. Furthermore, when using the Pythagorean identity to express $\cos\theta$ in terms of $\sin\theta$, the Fresnel coefficients can be expressed in complex notation producing the following identity:

$$\cos\theta_t = \sqrt{1 - \sin^2\theta_t} = \sqrt{1 - \left(\frac{n_1}{n_2}\sin\theta_i\right)^2} = \pm i\sqrt{\left(\frac{n_1}{n_2}\sin\theta_i\right)^2 - 1} \tag{3.3}$$

where $\left(\frac{n_1}{n_2}\sin\theta_i\right)^2 > 1$ for $\theta_i > \theta_c$ (now $\theta_t = \theta_2$ and $\theta_i = \theta_1$) [16]. The result is an evanescent field which decays exponentially away from the interface plane, but propagates parallel to the interface plane.

Figure 3.1a presents a visualisation of TIR using an optical fibre, which consists of an optically slow core layer (n_1) wrapped with a relatively faster cladding layer (n_2), i.e. $n_1 > n_2$. Following Snell's law, a light ray which is incident from air ($n_0 = 1$) at angle θ_0 will arrive at the interface between the core and the cladding at an angle $\theta_2 = \theta_1 - \frac{\pi}{2}$. If

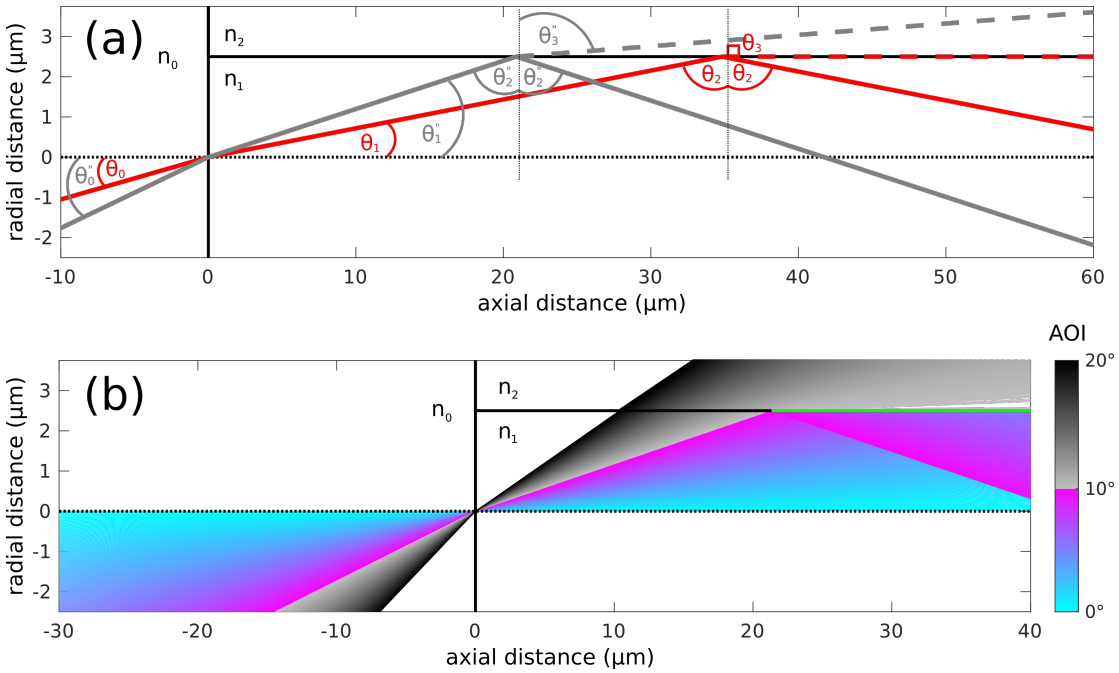


Figure 3.1: (a) Diagram of the basic operational principles of an optical fibre which consists of a slow core layer (n_1) and a fast cladding layer (n_2). Using Snell's law (equation 3.1), the path of the light ray can be traced as it refracts from air to core to cladding layers. If the incidence angle at the core:cladding interface is beyond a critical angle (θ_c), the electromagnetic field will fully reflect back into the core only leaving an evanescent field component (red dotted line). (b) Using core $n_1 = 1.46$ and cladding $n_2 = 1.45$ layers, the range of input angles which result in total internal reflection down the fibre are shown in blue-violet colours (evanescent component in green), and angles of incidence (AOI) which are incapable of total internal reflection are shown in gray-scale (rays reflected back into core not shown). A cutoff angle of $\approx 10°$ was calculated and corresponds to a fibre NA = 0.13.

$\theta_2 < \theta_c$, as is the case for the grey-coloured ray ($\theta_2^{"}$), the ray will not be totally internally reflected, and will therefore refract into the cladding layer (grey dotted line). However, when $\theta_2 > \theta_c$ total internal reflection will be maintained as shown by the red-coloured ray, in addition to the evanescent component which travels along the boundary (red dotted line). Initial incidence angles (θ_0) for which this condition is preserved are said to be within the cone of acceptance, or the acceptance angles of the optical fibre. The inverse can be said for light that is emitted from the core of a fibre, i.e. the numerical aperture of the fibre can be defined by the maximum acceptance angle:

$$NA = sin(\theta_{0_{max}}) = \sqrt{n_1^2 - n_2^2} \tag{3.4}$$

In Figure 3.1b the acceptance cone can be seen in colour, resulting in propagation down the fibre-core, whereas the rejected incidence angles (grey-scale) refract into the cladding. When designing the experimental set-up, a lens will be required to couple light from free-space into the acceptance cone of a fibre. If too high of NA is used, this will result in coupling inefficiency and therefore optical power attenuation within the

experiment.

Guided modes

Strictly speaking, geometric optics (e.g. ray diagram approach) is ill-equipped to describe the wave-phenomenon that occurs in optical fibre waveguides, especially when the radius of the light propagating region (the core) approaches the wavelength of light. At these length scales the transverse components of the wave interfere within the core and form standing wave patterns that do not change with propagation distance [15]. In the same way as a harmonic oscillator, there are discrete modes of oscillation (and even superpositions of modes) that arise which depend on the properties of the materials and boundaries. These modes will be solutions to the electromagnetic wave equation (Equation 2.8) - a complete formulation of Maxwell's equation.

To describe the modes of a waveguide it is useful to move beyond the single plane wave description of an electric field (as was treated throughout the previous Chapter), i.e., to now assume that the intensity distribution of the beam is no longer spatially uniform. In terms of solving the homogeneous wave equation (Equation 2.69 with RHS = 0), a non-uniform field amplitude (E_0) requires a solution of the (scalar) form:

$$E(x, y, z) = E_0(x, y, z)e^{-ikz} \tag{3.5}$$

when expressed in Cartesian coordinates (x, y, z), and assuming that the wave is propagating in the z-direction. After expanding and evaluating the spatial derivatives in Equation 2.69 the differential equation can be written:

$$\frac{\partial^2 E}{\partial x^2} + \frac{\partial^2 E}{\partial y^2} + \frac{\partial^2 E}{\partial z^2} - 2ik\frac{\partial E}{\partial z} = 0 \tag{3.6}$$

Now, if the beam E travels with a small angle relative to the optical axis (z), e.g. $< 30^\circ$, the second derivative with respect to z becomes effectively zero relative to the first derivative on the right [182]. In other words the diffraction of the wave in z is much slower than the propagation of the wave in z with wavenumber k. This concept is the well-known *paraxial approximation*, which after eliminating the $\frac{\partial^2}{\partial z^2}$ term in Equation 3.6 leads to a solution of the form [183]

$$E_0 = \exp\left\{ -i\left(P + \frac{k(x^2 + y^2)}{2q} \right) \right\} \tag{3.7}$$

Equation 3.7 and the paraxial approximation is the basis for the field of Gaussian Optics, and leads to well-known optical parameters such as the Gouy phase shift (related to P) and the Gaussian beam description (beam waist related to q). The paraxial approximation can then be generalised to higher-order mode solutions to the wave equation,

e.g., using Hermite polynomials, resulting in a family of modes called Hermite-Gaussian modes denoted by the symbol TEM_{mn} [182, 183]. The mode orders m/n correspond with unique spatial distributions of optical intensity in the two transverse dimensions (x/y) that are allowed to propagate in the waveguide/resonator. The most ubiquitous of these modes is the TEM_{00}, i.e. the fundamental mode, because it can be focused to a diffraction limited spot (with an approximately Gaussian profile) and it diffracts the most slowly [16].

Similar to the Hermite-Gaussian description of electric field modes, the paraxial approximation can be translated to a cylindrical coordinate system - which utilises axial symmetry and more closely describes the geometry of an optical fibre - using Laguerre-Gaussian mode decomposition. However, the paraxial approximation is not strictly needed to describe the modes of an optical fibre waveguide. In cylindrical coordinates (r, z, ϕ) the axially symmetric wave equation is described by [15]:

$$\frac{\partial^2 E_z}{\partial r^2} + \frac{1}{r}\frac{\partial E_z}{\partial r} + \frac{1}{r^2}\frac{\partial^2 E_z}{\partial z^2} + n^2 k_0^2 E_z = 0 \tag{3.8}$$

where E_z is the axial-component of the electric field, $n = n_{core}$ for $r \leq a$, and $n = n_{clad}$ for $r \geq a$ (core radius a). Equation 3.8 is in the form of the Bessel differential equation which is solved by the well known Bessel functions, and has separate solutions for the core and cladding [15]

$$E_z = \begin{cases} E_{core} = aJ_m(r\rho)e^{im\phi}e^{i\beta z} & ; \quad \rho = \sqrt{n_{core}^2 k_0^2 - \beta^2} \\ E_{clad} = cK_m(r\delta)e^{im\phi}e^{i\beta z} & ; \quad \delta = \sqrt{\beta^2 - n_{clad}^2 k_0^2} \end{cases} \tag{3.9}$$

where J_m and K_m are the m^{th} order of the Bessel function of the first kind and modified Bessel function of the second kind (respectively), and $\beta = k_{core}\sin\theta_2$ (θ_2 in Figure 3.1a) is the propagation constant, in other words the effective wavenumber of the wave as it propagates longitudinally down the fibre-core. The m^{th} order of the Bessel function solutions corresponds with the m^{th} order mode of the resonator. Figure 3.2 shows the first five core modes within an optical fibre with core $a = 2.5\ \mu m$, $n_{core} = 1.46$, $n_{clad} = 1.454$, and $\lambda = 850\ nm$ (cladding modes not shown). It is apparent that the radius of the core plays a vital role in determining the light intensity distribution: if a radius larger than $a = 2.5\ \mu m$ was used (with the same parameters) higher order modes will begin to contribute to the total distribution within the core. This is the case for multi-mode fibres which generally have diameters larger than $10\ \mu m$ and often in the $50 - 200\ \mu m$ range.

When choosing between using multi-mode or single-mode optical fibres in the context of PLU and TRBS, the following characteristics should be taken into consideration:
Multi-mode fibre:

- similar to free space techniques, the lateral resolution of the phonon probe is

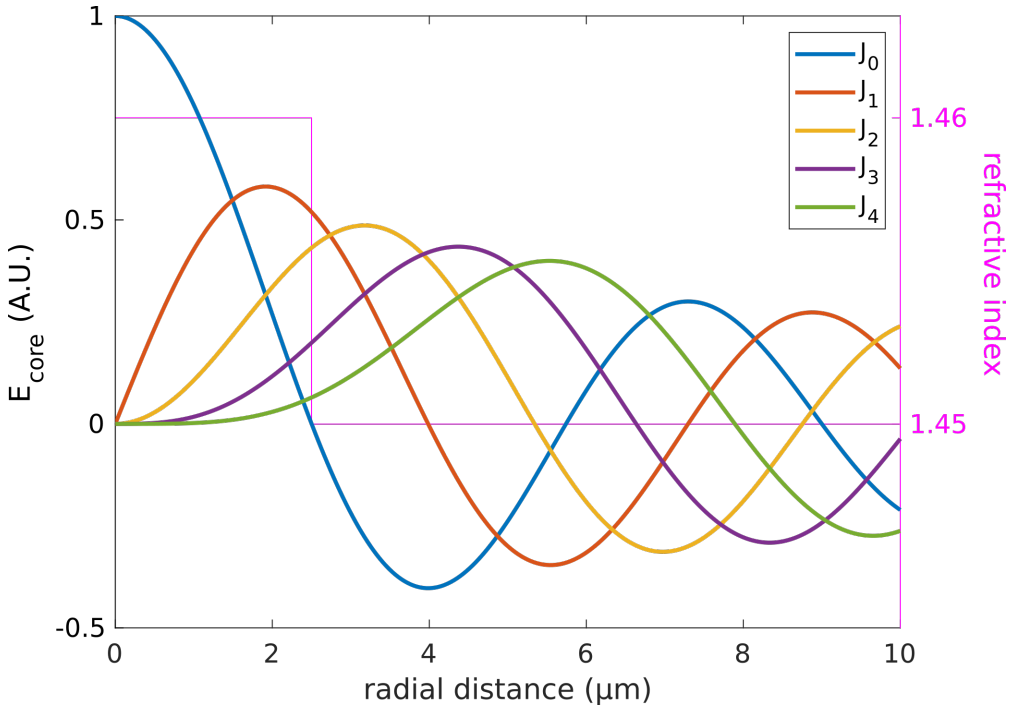


Figure 3.2: Analytical solutions (Equation 3.9) to the cylindrical wave equation (Equation 3.8) which dictates the electric field modes that are capable of propagating within an optical fibre (with $a = 2.5\ \mu m$, $n_{core} = 1.46$, $n_{clad} = 1.454$, and $\lambda = 850\ nm$). Presented are only the solutions for the field within the core (E_{core}), the boundary of which ($r = a$) is defined by the step index profile (pink line). The zeroth-order Bessel function of the first kind represents the fundamental mode of the fibre (blue line), with higher order modes (other colours) being relegated to the cladding. Exponentially decaying evanescent cladding modes (E_{clad}) not shown.

dependent on the pump-probe beam spot sizes. With wider diameter multi-mode fibres comes a decrease in resolution of the technique, especially in an imaging context.

- with larger core and spot diameters comes a reduced optical power density (given a fixed input power). Therefore in order to retain TRBS signal strength, the average beam power will need to increase to offset the a^{-2} reduction in power density.

- intermodal dispersion: due to the interferometric nature of the detection mechanism (explained in Section 2.3) if photons that scatter from the same acoustic wavefront (or a neighbouring cycle) travel different path lengths (and arrive at different times) there will be a loss of coherence with respect to the reference beam, which ultimately reduces signal amplitude. This will effect will worsen as the length of the fibre is increased.

- due to relatively large core diameters and high NA (more acceptance angles), light is generally more easily coupled into multi-mode fibres

- as will be discussed below, the wavelength bandwidth for transmitting down a

multi-mode fibre is higher and places less restriction on the wavelength of the light source.

Single-mode fibre:

- smaller core diameters to ensure that the 0-order (TEM_{00}), or fundamental, mode is dominant (blue line J_0 in Figure 3.2) negating the effects of intermodal dispersion.
- smaller cores also improve lateral resolution of the probe.
- small core diameter improves power density given a fixed input power
- single-mode fibres contain low attenuation rates (e.g. $\leq 4\ dB/km$) and therefore allow long distance propagation.
- small core size and low NA make light coupling more challenging.
- as will be discussed below, single-mode transmission is limited to a narrow band of wavelengths.

Both multi-mode and single-mode fibres are affected by the fact that silica is a dispersive medium, i.e. wavelengths of light will propagate at different velocities with respect to each other. When using $100\ fs$ pulses to excite and detect ultrafast phenomenon, this chromatic dispersion will effectively stretch the original pulse, as higher optical frequencies within the pulse travel at one speed, and lower optical frequencies another. The pure silica used in most single-mode optical fibres displays generally low rates of dispersion. As an example, a pulsed laser with a NIR wavelength of $\lambda = 800\ nm$, a linewidth of $\Delta\lambda = 5\ nm$, and a dispersion parameter of $D \sim 100\ ps/nm \cdot km$ would require $100\ m$ of fibre to broaden the pulses by $50\ ps$. Such broadening effects will effectively lower the peak power of the pulse, but more importantly have the potential to limit the temporal resolution and detection bandwidth of a pump-probe system (discussed further in Chapter 4).

Overall, single-mode optical fibre offers many desirable properties for adaptation to time-resolved pump-probe spectroscopy and imaging. One reality that must be confronted when choosing to work with single-mode fibres, is that the narrowband optical frequency performance of the fibre will limit the number of pump and probe wavelengths available for the device.

Wavelength performance

Phonon microscopy utilises NUV pump and NIR probe wavelengths for the following benefits:

- NUV photons carry roughly twice the energy of NIR photons, which enhances the thermo-elastic generation process.
- Short NUV pump wavelengths enable small spot sizes and therefore higher spatial resolution for imaging applications.
- the gold mirror layers of the opto-acoustic transducer reflect NUV wavelengths less efficiently than NIR wavelengths, which permits a higher percentage of the pump beam to be absorbed by the cavity.
- the separation in wavelength allows optical filtering (e.g. using a dichroic filter) which reduces the NUV shot noise contribution to the signal.

A benefit from using multi-mode optical fibres, which support a wider range of optical frequencies than single-mode, is that this separation in pump and probe wavelengths can be preserved. This will be less possible when choosing to use single-mode fibres, as only a narrowband of wavelengths are capable of single-mode behaviour. The general metric for how many modes are supported within the fibre core is provided by a quantity known as the normalised frequency (V) [15]:

$$V \approx \frac{2\pi a}{\lambda}\sqrt{n_{core}^2 - n_{clad}^2} = \frac{2\pi a}{\lambda} NA \tag{3.10}$$

When this parameter is $V < 2.405$ the waveguide can be considered single-mode, e.g. $V = 2.40$ in Figure 3.2. Wavelengths which defy this condition are said to be beyond the *cut-off wavelength* of the fibre, i.e. if used they will exhibit multi-modal behaviour. This can be confirmed by looking again to the Bessel functions which themselves describe the modes as a function of the optical wavelength and fibre geometry. Again, using the example of an NIR-type single-mode fibre (same parameters used for Figure 3.2) which possesses a cut-off wavelength of $\approx 730 \pm 30\ nm$ (Thorlabs 780HP), if the wavelength is reduced to $\lambda = 532\ nm$ ($V = 3.8$) higher order modes will begin to more strongly contribute to the total field within the core (as shown in Figure 3.3a). Similarly, if the wavelength is returned into the NIR $\lambda = 850\ nm$, yet the core radius is increased to $a = 25\ \mu m$ ($V = 3.24$), many more modes will now be converted from cladding to core modes as seen in Figure 3.3b (assuming that the NA is unchanged).

In order to choose the optimum single-mode optical fibre to act as the transducer substrate, the parameters of the experimental optical system are considered. As detailed in Chapter 4, the phonon probe will be designed around two fs pulsed lasers which are tunable over the range $\lambda = 700 - 900\ nm$. These systems can be frequency doubled to emit NUV light, but in order to maximise the penetration depth of the GHz acoustic waves, which scales as $\zeta \sim \lambda_{probe}^2 \sim f_B^{-2}$, the NIR window of the lasers will be targeted. Consequently, the Thorlabs 780HP single-mode fibre was identified as an optimum fit and has the following specifications:

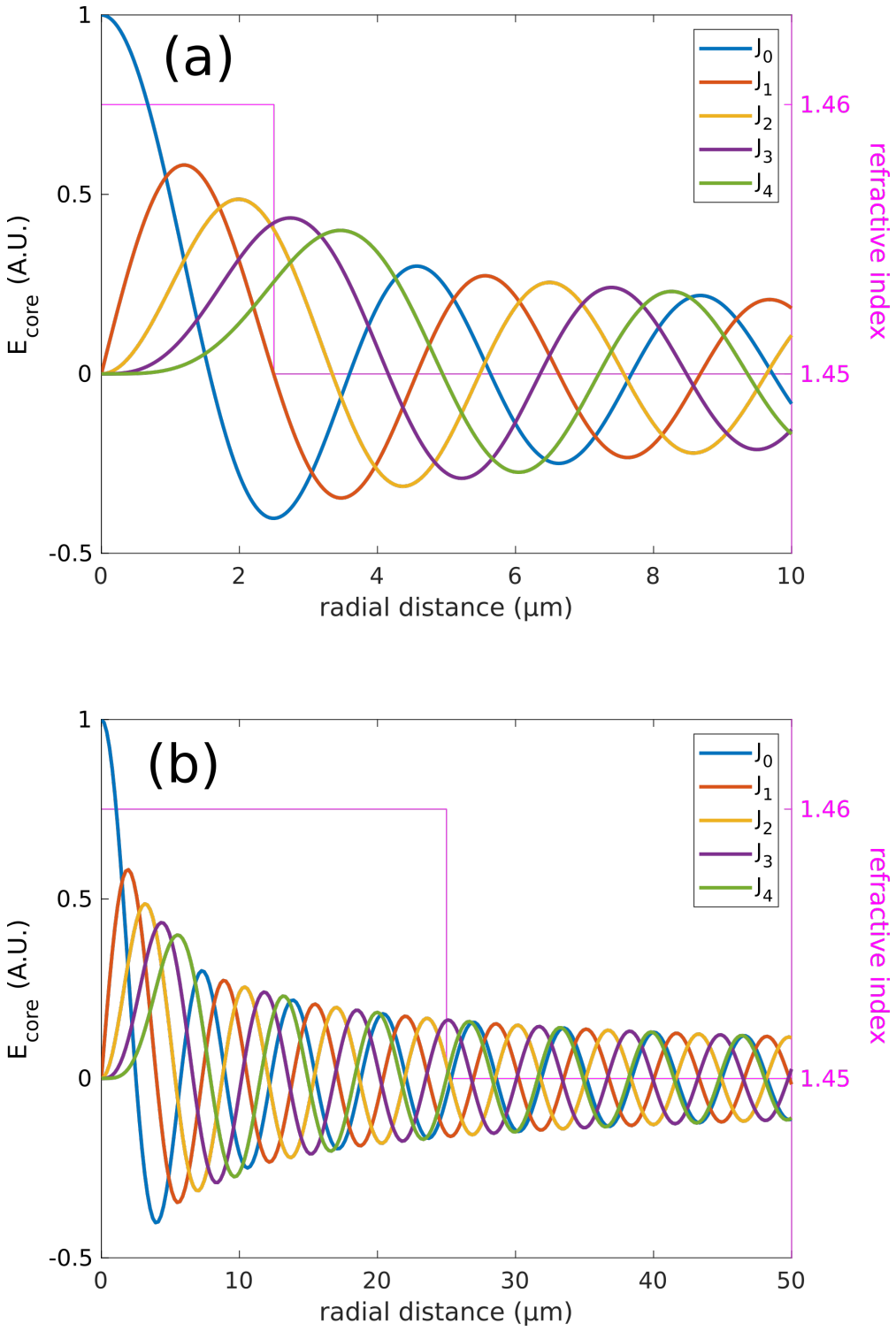


Figure 3.3: (a) Allowed modes of propagation for the optical fibre in Figure 3.2, except with an optical wavelength (532 nm) that is below the cut-off wavelength of the fibre ($\approx$ 730 nm). When compared with Figure 3.2, the prevalence of modes $m > 0$ increase indicating that they more heavily contribute to the total field confined to the core. The fibre has effectively become a multi-mode fibre, albeit with low order modes. (b) Similarly, as the core radius is increased, e.g. to $a = 25\ \mu m$, previous cladding modes are now promoted to core modes and strengthens the effects of intermodal dispersion.

- operating wavelength - $780 - 970\ nm$
- cut-off wavelength - $730 \pm 30\ nm$
- mode field diameter (MFD, the effective spot size) - $5 \pm 0.5\ \mu m$ (@ $\lambda = 850\ nm$)
- cladding diameter - $125\ \mu m$ which will determine the radial footprint of the phonon probe
- $NA = 0.13$
- $n_{core} = 1.46$ and $n_{clad} = 1.454$

This product covers a majority of the laser tuning range, contains a relatively high resolution spot radius (compared to optical fibre products) of $\approx 2.5\ \mu m$, and a low cut-off wavelength. Using fixed values for core:cladding refractive indices (i.e. not considering chromatic dispersion), the wavelength dependency of the fundamental mode can be calculated down to the cut-off wavelength, using E_{core} in Equation 3.9 and is presented in Figure 3.4. With nearly $200\ nm$ of both laser wavelength tuning range and single-mode fibre behaviour this product will provide flexibility in the experimental set-up. For

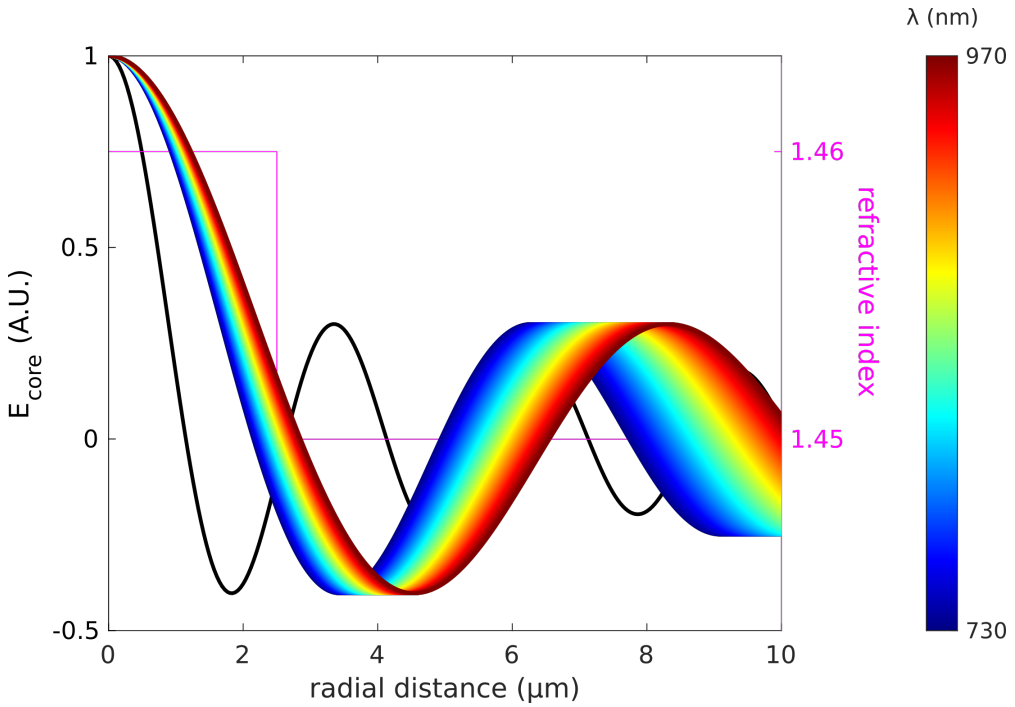


Figure 3.4: Slight variations in the fundamental mode as a function of wavelength for the Thorlabs 780HP single-mode fibre (E_{core} from Equation 3.9). The extreme blue side of the spectrum represents the approximate fundamental mode at the $\approx 730\ nm$ cut-off, and the extreme red end of the spectrum occurs at the maximum operating wavelength $\approx 970\ nm$. This result indicates that the $> 200\ nm$ range of single-mode wavelengths is strongly compatible with the tuning range ($700-900\ nm$) of the fs-pulsed lasers used in this study. The black curve demonstrates the multi-modality when using a NUV wavelength below single-mode cutoff; the first minimum now occurs within the core diameter.

example, two identical pump/probe wavelengths (e.g. $780\ nm$) can be simultaneously coupled into the same fibre, or even two separate pump/probe wavelengths (within $\sim 200\ nm$ of each other). Even if one of the lasers is tuned at or below the cut-off wavelength ($V = 2.8$), the core will still be dominated by the fundamental mode (blue extreme in Figure 3.4) with only a 5% reduction in the power of the fundamental mode (compared to $\lambda = 850\ nm$).

The 0.13 numerical aperture of this particular fibre product will become relevant in two ways: (1) this parameter will determine the divergence of the beam when making measurements in the axial direction; (2) in order to maximise the transfer of optical power from free-space to the single-mode optical fibre core, the mode of the (approximately) Gaussian free-space beam will need to be transformed to match the spatial characteristics of the fundamental mode of the fibre. Mode matching the input beam can be achieved using a lens with the correct focal length/numerical aperture - ideally matched to the NA of the fibre - to focus the larger free-space beam into the space defined by the MFD [183]; otherwise, mismatched mode diameters will result in inefficient coupling. Therefore, when designing the optical system in this thesis, a suitable fibre-coupling facility must be selected to ensure power is efficiently coupled into the TEM_{00} mode.

Now that an optimum optical fibre substrate has been identified, the discussion will turn to the design, fabrication, and characterisation process for the opto-acoustic transducer needed to generate ultrasound from the tip of the fibre.

3.2 Transducer design

Signal optimisation

In order to drive the device at ultrasonic frequencies greater than $1\ GHz$, an opto-acoustic transduction element is needed which exchanges optical photons for acoustic phonons. As described in Chapter 2, this process can be instigated thermo-elastically, i.e. a metallic thin-film should be used to absorb fs pump pulses which thermally generates picosecond strain pulses. Consequently, the performance of the metallic transducer will depend on its optical and thermal properties. As proven by phonon microscopy, a metallic:dielectric zero order Fabry-Pérot interferometer can be designed such that the cavity both optically and mechanically resonates while also shielding the specimen from transducer-heating [166, 173]. In order to achieve proof of concept, this study will instead design and utilise a single metallic layer, and will discuss and simulate the transition to a Fabry-Pérot transducer in Chapter 7.

The basic device concept of a single-mode optical fibre terminated with a single metallic thin-film transducer is presented in Figure 3.5. The central elements to this design are: (1) that there is maximal optical absorption at the pump wavelength, and

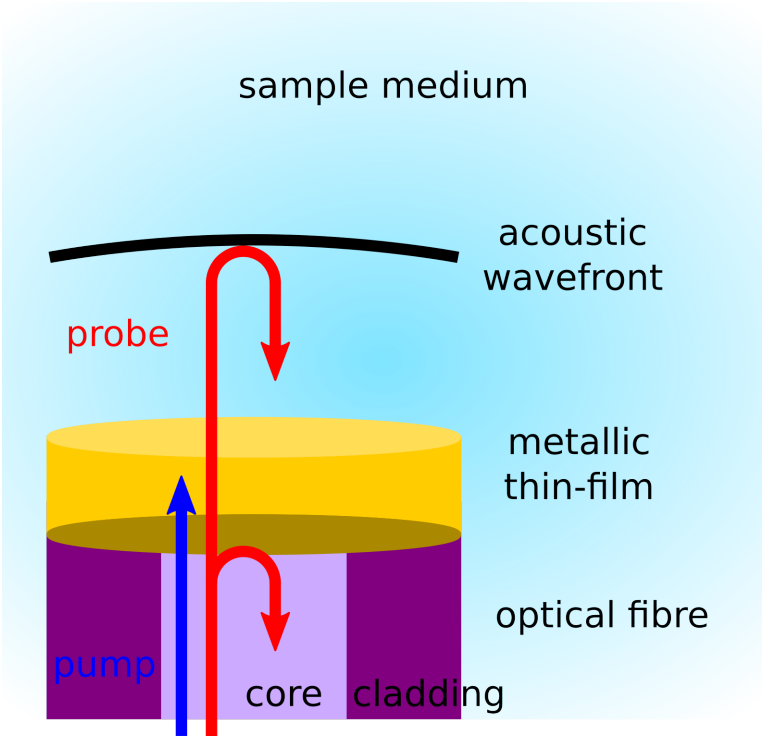


Figure 3.5: Basic device concept: a single-mode optical fibre substrate terminated with a single metallic thin-film. The sole purpose of the thin-film transducer is to thermo-elastically generate picosecond strain pulses through the absorption of the fs pulse-width pump beam. This proof of concept transducer will be designed to maximise pump absorption, but also to optimally transmit the probe beam before and after it has scattered with the acoustic wavefront. The transducer will also produce a DC reflection from the fibre/metal interface which acts as a reference beam in TRBS interferometric detection.

(2) that the transducer maximally transmits the probe wavelength. The latter will be especially crucial; the novelty of this device will rely on the ability for the probe to act as a *transceiver*, i.e. a transmitter and receiver of probe light. In order to achieve this, the probe beam will need to: (1) transmit through the transducer layer, (2) Brillouin scatter (reflect) with the phonon wavefront, and (3) transmit back through the transducer for detection. Therefore, optimising the proof of concept transducer will require the consideration of a range of materials, transducer thicknesses, and optical wavelengths.

A variety of metals display strong absorption characteristics in the VIS-IR portion of the electromagnetic spectrum, owing to the strength of the imaginary component (extinction coefficient κ) of the complex refractive index ($\tilde{n} = n + i\kappa$). For the basic case of a plane wave solution to the electromagnetic wave equation, the electric field travelling in the $+z$ direction within an arbitrary metal can be written and simplified [16]:

$$\mathbf{E} = \mathbf{E}_0 e^{ikz} = \mathbf{E}_0 e^{ik_0\tilde{n}z} = \mathbf{E}_0 e^{ik_0 nz} e^{-k_0\kappa z} \tag{3.11}$$

where k_0 is the wavenumber in vacuum. The final term in Equation 3.11 results in an

exponentially decaying attenuation of the electric field as a function of material thickness, which, due to dispersion, is a function of optical wavelength ($\tilde{n}(\lambda)$, Equation 1.2). This property of metals has an adverse effect on the transmission of light through the material. This reality is normally averted in conventional picosecond laser ultrasonic imaging techniques by settling on nearly bulk thicknesses of highly absorbing metal (e.g. Ti), and ultimately limiting the experiment by illuminating pump and probe directly onto the sample, or utilising pulse-echo [171, 172, 174]. However, by decreasing metal thickness to a degree such that a large portion of the field transmits through the layer, a thin-film transducer can be attained.

As introduced in Section 2.2.2, an analytical PLU-model was created (based on the work of [161, 163]) to simulate the generation and detection of picosecond strain pulses. However, before utilising this model, it is useful to simulate the static optical responses (calcualted with TMM) for a range of thin-films with different parameters; this is convenient because strain propagation is not required and thus the computation is accelerated compared with the PLU-model. Recall that probe transmission and pump absorption provide optimum TRBS interaction via Equation 2.77. Figure 3.6a presents the transmission spectra of six typical metals as a function of probe wavelength and metal thickness (refraactive index data [184–186]). The simulation consisted of an infinite glass substrate, the desired metal layer, and an infinite water layer with both beams incident from beneath the transducer with normal incidence. It is apparent that Au, Ag, and Cu display the strongest transmission, especially in the range of $10-20$ nm film thicknesses (blue box). The response to probe wavelength reveals that for most materials, transmission will be optimum for shorter NIR wavelengths.

Figure 3.6b visualises extinction coefficient (κ_{pump}) as a function of material, and indicates that Al shows very strong absorption qualities (also evidenced by its poor transmission in Figure 3.6a). It is worth noting that although the extinction coefficient provides an estimate of the optical absorption of a bulk material, it is not the sole determinant of optical absorption. For thin-film transducers where thickness is less than the optical coherence length, multiple reflections within the thin-film will interfere causing resonant transmission or reflection as discussed with Fabry-Pérot cavities in Figure 2.8. For this reason, a material with a relatively large extinction coefficient (e.g. Au at $\lambda = 900$ nm) may exhibit greater transmittance (Figure 3.6a) than a material with a relatively smaller extinction coefficient (e.g. Cr at $\lambda = 900$ nm). In this example a single trip through a 10 nm thick Au layer results in a $\Delta\phi \approx 0\%$ change in phase (for $\lambda = 900$ nm) leading to greater constructive interference, whereas the same trip through a 10 nm thick Cr layer results in a $\Delta\phi \approx 5\%$ change in phase leading to greater destructive interference.

Now in order to identify a transducer design which maximises probe transmission and strain amplitude, the PLU-model was run as a function of metal thickness, for the

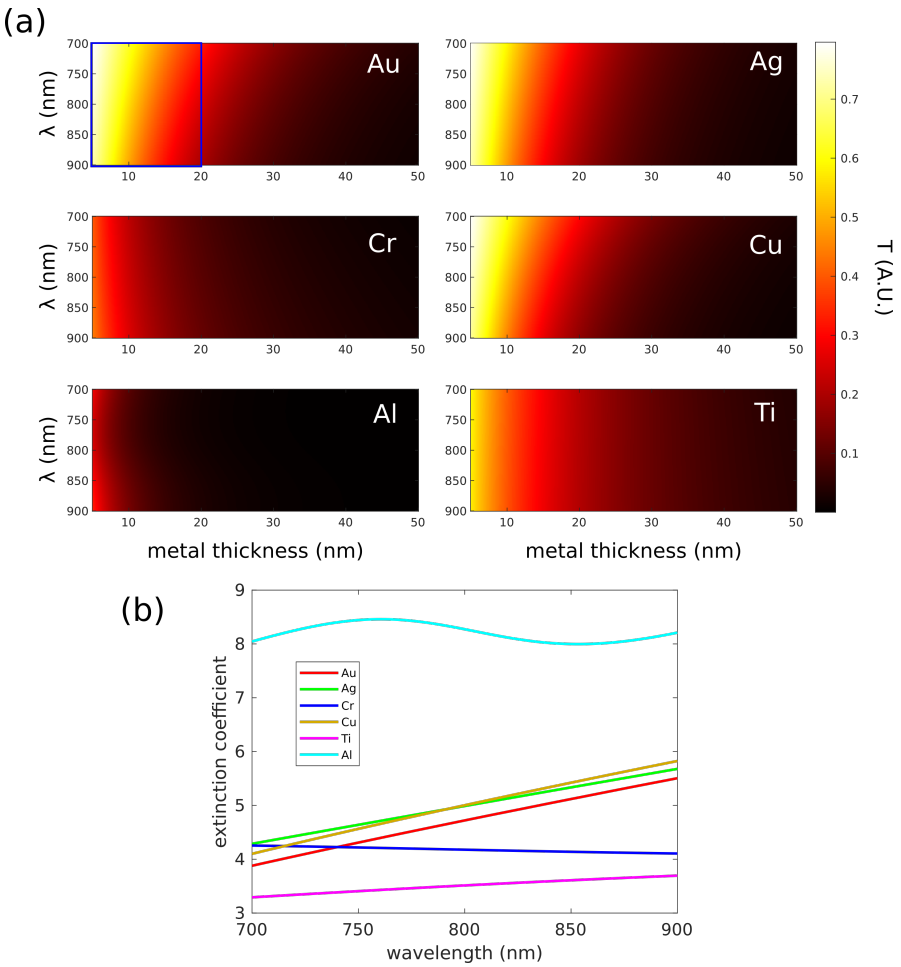


Figure 3.6: (a) A TMM model was utilised to determine the transmission coefficients of metallic thin-films as a function of pump/probe wavelength and film thickness. Gold, silver, chromium, copper, titanium, and aluminium films were modelled. As film thickness decreases transmittance (T) increases. Blue box indicates a region of interest where film thickness is conducive to high transmission. (b) The extinction coefficient κ at the pump wavelength will in part determine the absorption characteristics of the transducer layer and ultimately the amplitude of the acoustic field.

materials gold, silver, chromium, copper, titanium, and aluminium. Given the results of the Fresnel-model in Figure 3.6 a probe wavelength with high transmission was selected $\lambda_{probe} = 780\ nm$; for simplicity the pump wavelength was set equal to the probe. The simulation mesh consisted of the following: semi-infinite glass substrate, current thickness of metal, and semi-infinite water layer, with both beams being incident from the glass side of the mesh (diagram in Figure 3.7a). An example simulation output can be found in Figure 3.7 for the case of a gold film with $15\ nm$ thickness. The TRBS signal (in water) in Figure 3.7b was transformed into the frequency domain using fast Fourier transform (Figure 3.7c), and the frequency position containing the maximum amplitude was recorded for each combination of material and thickness (Figure 3.8a-b).

In addition to the modulation depth of the signal, it is important to consider the SNR performance of each prospective transducer. As shown in Equation 2.77, in the

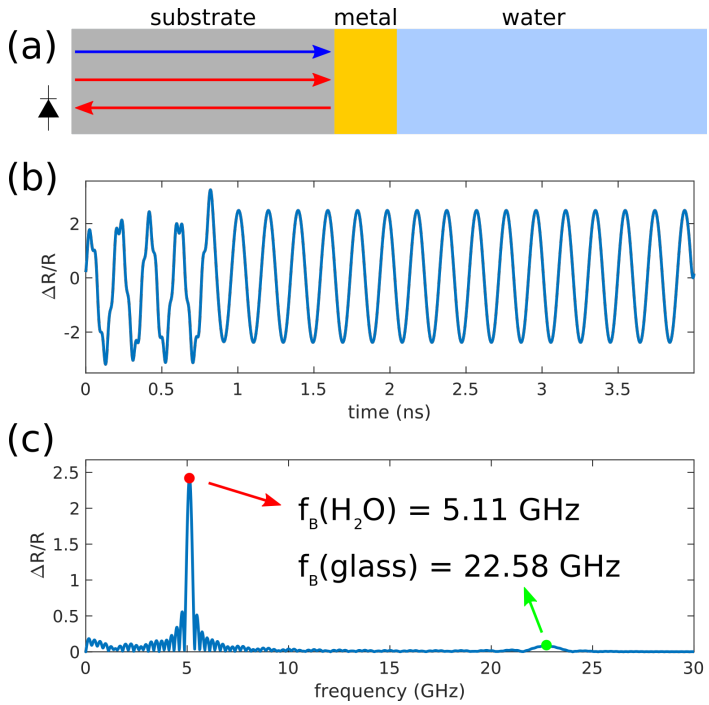


Figure 3.7: Example of simulated TRBS signal using the analytical PLU-model. (a) Simulation mesh consisting of semi-infinite glass substrate, metallic, and semi-infinite water layers. Both pump and probe were incident from the substrate side of the mesh, and the Brillouin scattered probe light was detected in reflection (substrate side) to emulate the configuration that will be carried out for an optical fibre transducer. (b) TRBS signal for the case of $\lambda_{pump} = \lambda_{probe} = 780\ nm$ and a $15\ nm$ thick layer of gold. (c) Fast Fourier transform of the signal in (b), which consists of frequency peaks at $5.11\ GHz$ and $22.58\ GHz$, the Brillouin frequencies of water and the glass of the substrate (green circle) at λ_{probe}. The amplitude of the frequency peak (for water) is used as a measure of the signal strength that the transducer is capable of producing for later comparison with other metals and thicknesses.

approximation that the detection system is shot noise limited, the signal SNR will scale with the square root of the probe intensity $\sqrt{I_{probe}}$. This can be approximated by the square root of the total reflectivity of the transducer (R) and is shown as a function of metal-material and thickness in Figure 3.8c. Now, the simulated TRBS signal strength can be scaled by the approximate SNR of the transducer material producing the plots in Figure 3.8d.

Overall, aluminium and titanium appear to show the highest amplitude designs, especially as film thickness decreases (as transmittance increases). In particular, Al exhibits nearly an order of magnitude difference in amplitude between the other metals. Among the lower-amplitude metals there are very similar signal amplitudes (Figure 3.8b), with gold having the advantage; comparing the TRBS·SNR amplitudes (Figure 3.8d), Au is approximately 10%, 25%, and 50% higher amplitude than Cu, Cr, and Ag respectively within the $10-20\ nm$ thickness range. While the results from this simulation provide crucial insight on the optimisation of the signal the phonon probe will generate,

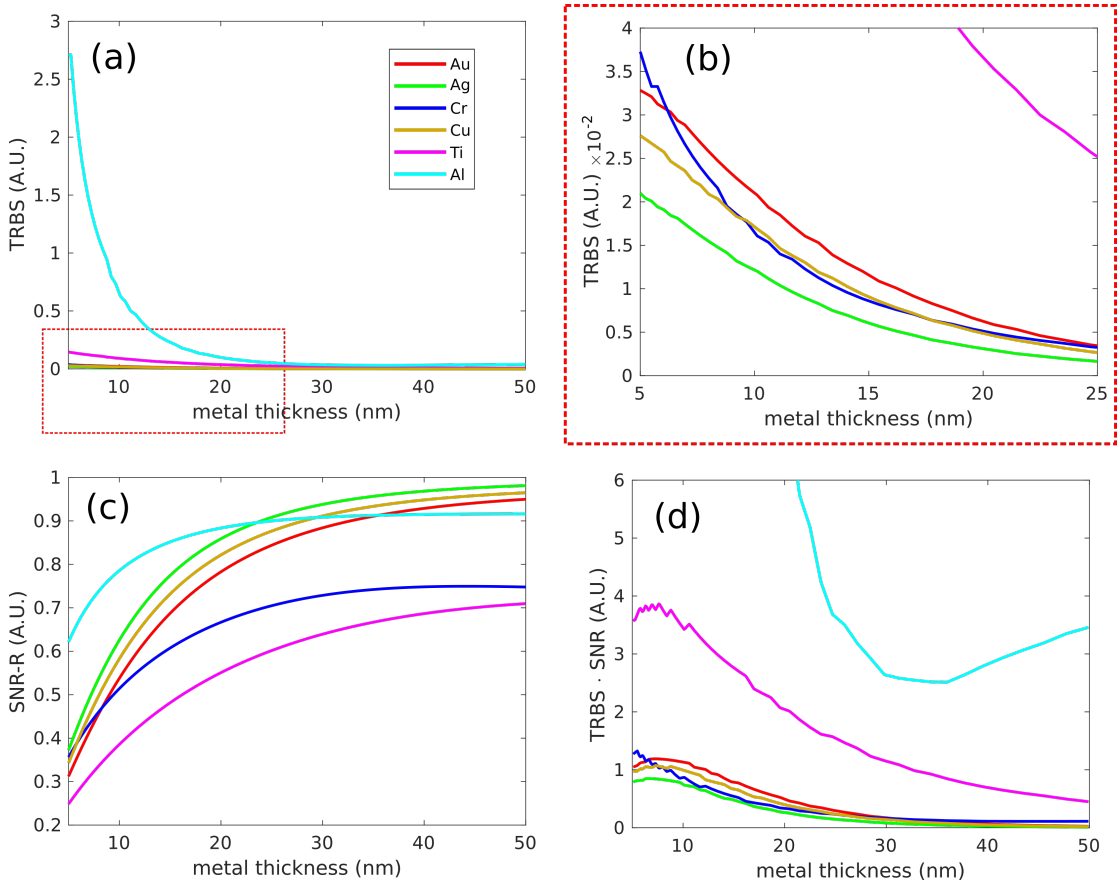


Figure 3.8: (a) TRBS signal amplitude using the PLU-model as a function of material and transducer thickness with $\lambda_{pump} = \lambda_{probe} = 780\ nm$. Aluminium and titanium show significantly higher signal amplitude compared with the other metals (b). This simulation indicates that signal amplitude is inversely proportional to transducer thickness, a relationship which will guide the design of the fibre transducer. (c) Approximation for the signal SNR due to shot noise, calculated as the square root of the transducer reflectivity ($\sqrt{R}$). (d) TRBS signal amplitude scaled by the shot noise contribution; for transducers with low DC reflectance the combination of modulation depth and SNR will be reduced.

there are other factors which should be considered before fabricating and testing fibre-transducers, namely how well the metal film manages heat and how easily it can be deposited.

Thermal performance

The absorption of short light pulses by a metallic structure has the potential to create a significant temperature gradient within the material (discussed in Section 5.2.2), which ultimately diffuses into the surrounding medium. The type of diffusion process that takes place has been reported to depend on the: (1) pulse-width of the illuminating light, (2) material properties, and importantly, (3) the thickness of the metal film [165]. Consequently, these parameters determine the damage threshold (e.g. melting, fracturing, ablation, etc.) of the film, which is critical for finding a viable design for the

phonon probe.

It has been shown, both theoretically and experimentally, that absorption of ns-pulses by metals results in a direct heating of the metal-lattice and the subsequent thermal diffusion properties are largely dictated by phonon-phonon ($ph - ph$) coupling interactions [187, 188]. However, when the thickness of the metal becomes shorter than the (phonon) diffusion length, the energy density required to melt the film decreases linearly as thickness decreases [165, 189].

This problem becomes more sensitive for the case of fs-pulse-width irradiation. In this sub-ps regime, optical absorption creates a highly non-equilibrium state between hot electrons and the lattice. In order for the system to reach thermal equilibrium, two additional diffusive processes must first take place: (1) electron-electron ($e - e$) collisions, followed by (2) electron-phonon collisions ($e - ph$) [165]. The ability for a metal to diffuse heat will then rely on the $e - e$ collision rate of a metal, and its $e - ph$ coupling strength (g). Therefore, for fs-pulses, it is the *electron* diffusion length which dictates damage threshold; e.g. the length at which hot electrons in gold equilibrate with the lattice is on the order $\sim 400\ nm$ [165]. As gold thickness falls below this, a constant fluence experiences increasing energy density, and as electron diffusion becomes increasingly constrained the layer is more easily melted.

In order to approximate the damage threshold of a single metallic thin-film as a function of film thickness and material, a thermal diffusion model was invoked from literature [189]. This model - which is described in Appendix C - computes the absorbed optical fluence (F_m, see Equation C.6) required to raise the temperature in the metal to its melting temperature within the time-span of a single optical pulse-width (single shot). The damage threshold fluence can be converted into a threshold for average absorbed optical power using the energy density within the optical spot (r):

$$P_m = F_m \cdot r_r \cdot \pi r^2 \tag{3.12}$$

given a laser repetition rate of r_r. Figure 3.9a simulates P_m for experimental parameters that will be used for the phonon probe in this study: approximate optical wavelength $\lambda \approx 780\ nm$, repetition rate $r_r = 80\ MHz$, and fibre core radius (optical spot size) $r = 2.5\ \mu m$. This process was repeated for the materials considered thus far (Figure 3.6) and for film thicknesses within the range $d = 1 \rightarrow 50\ nm$.

From Figure 3.9a it is evident that although aluminium and titanium appear to exhibit impressive TRBS signal amplitude, this comes with the risk of more easily destroying the transducer. It is important to note that this literature model applies the simplifying approximation of ns-pulse-width radiation, as opposed to the fs pulse-widths that will be utilised in this study. However, it has been demonstrated previously, that a similar dependence between damage threshold and metal thickness exists in the fs-regime compared with ns-pulses, and therefore allows first order approximation. In fact, the

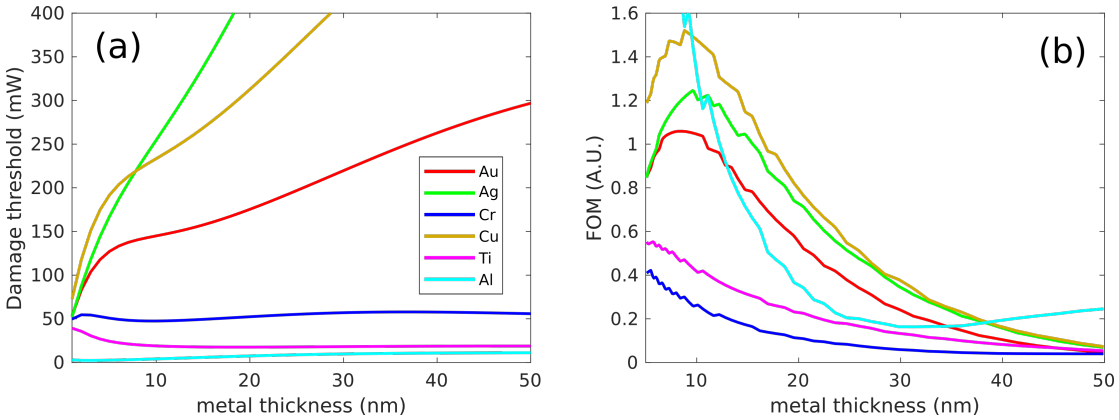


Figure 3.9: Damage threshold in units of average absorbed optical power approximated using an analytical model from literature (Appendix C). Gold, silver, chromium, copper, titanium, and aluminium are compared in the model, with the transition metals (Ti and Al) displaying lower damage thresholds than the noble metals (Ag, Au, Cu). The key result is that the threshold for damage (melting) decreases as metal layers become thinner; this puts restrictions on the maximum practical thickness achievable for each material. (b) The damage threshold is used to normalise the signal amplitude and signal SNR for each material/thickness combinations creating a figure of merit (FOM) shown in Equation 3.13. Metals with the lowest damage thresholds may require optical powers that are inefficient for TRBS. Note the limitations of the model as $d \to 0$ where bulk optical, thermal, and mechanical material properties are no longer valid.

damage threshold for metals such as Al and Ti will suffer even more so in the fs-regime; since hot electrons are no longer in equilibrium with the lattice, the stronger electron-phonon coupling for these metals results in greater energy transfer to the lattice [165]. Given these assumptions, the exact numerical values for the average power damage thresholds (Figure 3.9a) are not physically relevant, and are meant to reveal a general trend between optical power and damage.

The damage threshold trends for each metal/thickness combination can now be used to scale the TRBS·SNR performance of the transducers creating the figure of merit:

$$FOM = TRBS \cdot SNR \cdot F_{damage} \tag{3.13}$$

which is shown in Figure 3.9b. This effectively points to the TRBS and SNR performance at the approximate power damage threshold of the material (maximum usable power). Evidently, metals which appeared to produce high amplitude and high SNR TRBS signal (Figure 3.8), are indeed less practical once their damage thresholds are factored into the figure of merit. Conversely, Cu, Ag, and Au appear to provide strong power handling; at the damage threshold, the TRBS and SNR performance should then be superior to the other metals. Equation 3.13 is a simple order of magnitude approximation developed here to demonstrate that more thermally robust materials can be driven with greater power, thus resulting in better overall signal performance. As the phonon probe develops from prototype into certain application-specific forms, other

quantities may become more pertinent. For example, in future bio-imaging applications, minimising the temperature rise (T_{rise}) in the water/tissue adjacent to the transducer may become a priority, and the FOM can be adjusted ad hoc by factors such as T_{rise}^{-1} (or even given greater weighting, T_{rise}^{-2}). It is also important to note that the FOM, and in particular the PLU-model, break down in the limit that transducer thickness approaches $d \rightarrow 0$ (e.g. $d < 10\ nm$ in Figures 3.8a, 3.9b). This is likely because the bulk material properties used for modelling are no longer valid for sparse populations of atoms (ultrathin films) (let alone the limitations with fabricating homogeneous ultrathin films) [163, 190]. Now after modelling transducer performance, the fabrication of these metallic thin-films will be considered in order to finalise the transducer design for the phonon probe prototype.

3.3 Fabrication and characterisation

In order to form thin-films of the materials discussed above, the physical vapour deposition technique - *sputtering* - will be utilised which is capable of depositing a range of metals at a rate on the order of $\sim nm/s$. Prior to fabrication, the sputtering facility must be modified to accept the long aspect ratio of a fibre, and the fibre itself must be prepared. Once the fabrication procedure has been discussed, a simple spectroscopic method for characterising the thin-film thickness and optical properties will be introduced. Using this characterisation method, thin-film thickness measurements can then act as a feedback loop for calibrating the output of the sputtering process which leads to the final optical fibre transducer.

Fabrication

The precursor of the phonon probe is a custom Thorlabs 780HP patch cable, with FC/PC termination on the proximal end, and bare on the distal end. This particular product is optimum because the FC/PC connection (and ferrule) maintains a permanent bond with the optical fibre, yet the entire patch cable can still be easily swapped in and out of any fibre-optical system (containing FC/PC connectors). Furthermore, the bare end is left un-terminated allowing small structures, such as a transducer, to be fabricated on its tip. Also the $125\ \mu m$ diameter of this distal end sets the radial footprint of the measurement apparatus, which is novel compared with conventional pump/probe and Brillouin spectroscopy and imaging techniques.

Initially the bare end is stripped of its outer jacket using a stripping tool, in order to expose the cladding/core for cleaving. Then, the stripped end is cleaned using isopropyl alcohol and a lens cloth, and dried with a nitrogen gun. Next the stripped and cleaned end is placed into a manual fibre cleaver (Swift CL-03B), which cleaves the end-face at a nearly flat 0.5° angle to prevent strong back reflections. Now that the distal end is

free of contamination and the end-face flattened, a metallic thin-film transducer can be deposited.

A DC magnetron sputter coating facility (HHV BT300, pictured in Figure 3.10a) was used to coat metallic and dielectric films on the $nm - \mu m$ thickness scale. Noble metals are ideal for this type of thin-film deposition due to their resistance to oxidation and therefore their low resistivity. Moreover, noble metals require considerably less accommodations than metal-oxides and dielectrics, such as the need for: oxide cleaning cycles, ultra-low vacuums, high plasma currents, and argon modulation. The result is that nobles offer much higher deposition rates while requiring relatively low plasma currents. The device is capable of coating transparent dielectric layers, such as indium tin oxide (ITO). However, special considerations must be made to prevent the thermal shock of the plasma from breaking such targets. This BT300 has been modified to accept a water-cooling facility which prevents this issue.

In order to deposit metallic thin-films onto the flat end-face of the patch cable, there needs to be a way of fixing the optical fibres upright within the sputtering chamber. The diameter of the fibre-mount should be large enough so as to not overly stress the optical fibre coils, which could lead to breakages when mounting and dismounting the fibres. Furthermore, the mount should be light enough to still be easily spun by the motor that drives the specimen rotation stage (and thus homogenise the deposited layer). Figure 3.10b presents the design for this mount, which was prepared in the OpenSCAD software programme, and 3D printed in an Ultimaker 3 machine. PLA was used as the object material; this choice in material has the potential to: (1) introduce unwanted atmosphere into the sputtering vacuum chamber (due to the porosity of the PLA matrix) which can significantly lengthen vacuum pump-down times, and (2) become melted by the plasma that is irradiating the sample. These issues have been mitigated by: (1.1) printing the object with maximum infill density in order to reduce porosity, (1.2) leaving large holes in the structure to allow atmosphere to be pumped out, (1.3) storing the mount in vacuum, and (2) using the large volume of the vacuum chamber to maintain a safe distance between the top PLA surface and the plasma source. Small recesses in the vertical column of the mount were designed to accept small neodymium magnets, which attach to small metallic jaws that grasp the fibres upright. The magnetism of both the magnets and the jaws is small enough to not disturb the strong magnetic fields required for magnetron sputtering.

Once the sputtering target of the desired material is placed into the magnetron facility, the machine is pumped down to a vacuum of approximately $1 \times 10^{-4}\ mbar$. After achieving vacuum, argon gas (sputtering catalyst) is released into the chamber, and the combination of plasma current (current applied to the magnetron) and deposition time will determine the deposited thickness. This thickness will then need to be characterised in order to calibrate the deposition characteristics of the sputter

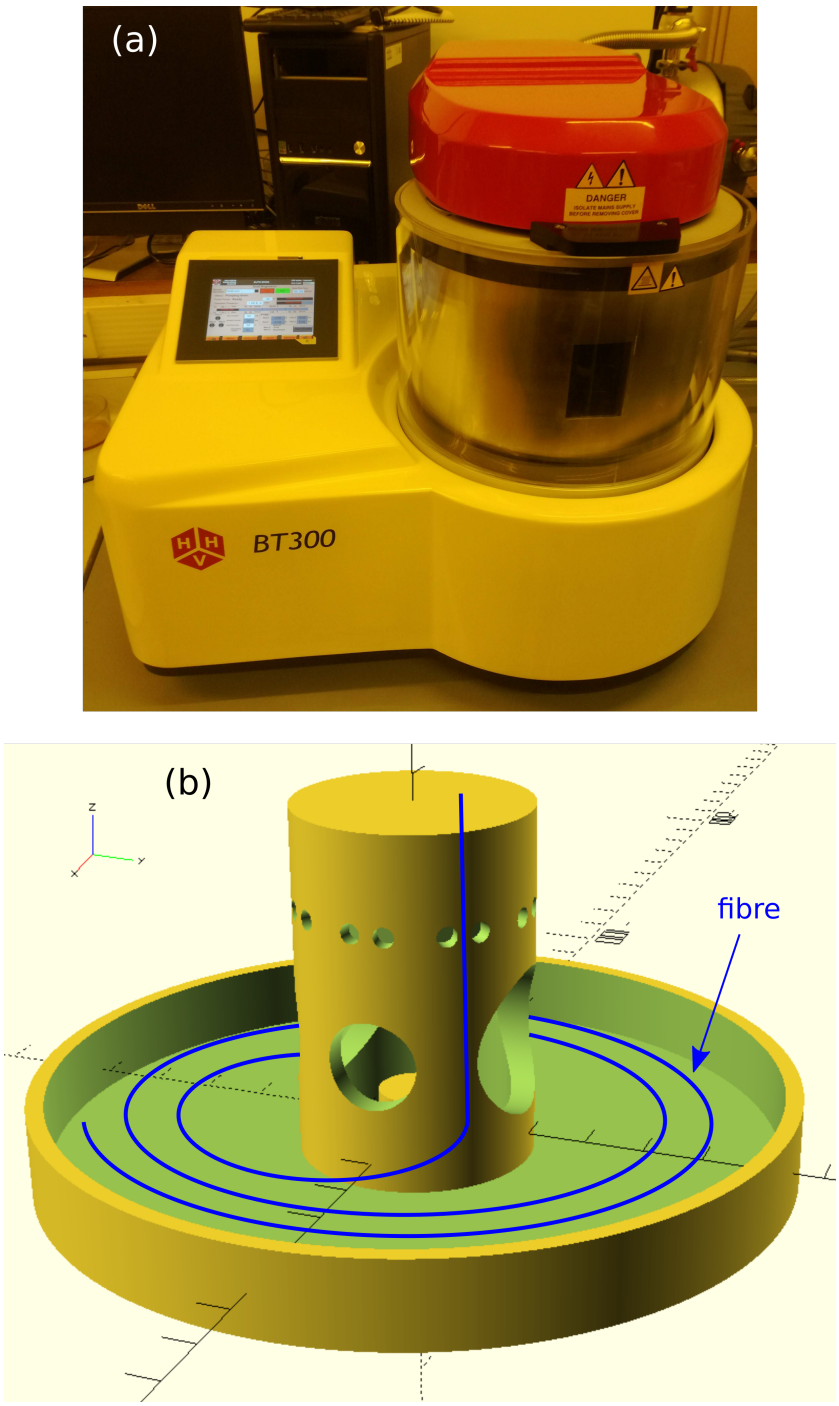


Figure 3.10: (a) HHV BT300 bench-top sputter coating machine with water-cooling. This device deposits a range of noble metals, metal-oxides, and dielectrics with sub-nm precision using DC magnetron technology and argon gas. The sputtering process is aided by the ability for the deposition chamber to be pumped down to low vacuum states (down to $\sim 10^{-5}$ *mbar*), which enhances uniformity of the thin-films. (b) The sputter coating specimen stage must be adapted in order to accommodate optical fibre samples. This design was selected to minimise fibre bending while allowing the end-face (transducer substrate) to be placed in a vertical position. 3D printed plastic was used for the fibre-stage; the porosity of the material slightly affects the vacuum pump-down time and the material appears to be unaffected by the plasma temperature.

coater. There are a host of techniques capable of measuring metallic film thickness: atomic force microscopy (AFM), stylus profilometry, ellipsometry, and X-ray photoelectron spectroscopy. However, the most convenient and cost-effective way to measure the film thickness of partially transparent layers is with simple white light spectroscopy.

White light spectroscopy

As detailed in Section 2.2.1, the optical resonances of a film or cavity can be uniquely attributed to: the wavelength of light, the optical properties of the material, the optical properties of the neighbouring materials, and the thickness of the desired material. If a broadband VIS light source is illuminated onto the film, light that is reflected or transmitted through the material can be captured and spectrally analysed using a VIS-NIR spectrometer (Ocean Optics USB2000+). The optical resonances captured by the spectrometer software can then be compared with theory, in order to find a matching film thickness.

A white light spectrometer was designed and constructed for this study, and is presented in Figure 3.11. The body of the device is a Meiji Techno IM7200 inverted microscopy body containing an x/y manual stage to control the sample plane (Figure 3.11a). Light is delivered from an Ocean Optics HL-2000 light source via multi-mode optical fibre patch cable, into an objective lens. This lens focuses the collimated light onto the sample plane, and after passing through the film is captured by a second objective lens. The light can then be directed into an imaging camera, or into the spectrometer by way of another multi-mode patch cable (Figure 3.11b) to record the transmission spectrum of the film structure (example in Figure 3.11c). The spectroscope is also capable of measuring the transmission and reflection spectra of structures on the tips of optical fibre samples. This is achieved by replacing the top objective lens with the optical fibre sample, and butt-coupling the source light directly into the fibre core whose optical axis is aligned with that of the spectrometer. A 1:2 coupler can be used to deliver light (from channel-2a) to the fibre sample (occupying channel-1), and the reflection spectrum can be captured in channel-2b.

In order to calibrate the deposited thickness of a material, an arbitrarily thin semi-transparent layer is deposited onto a glass microscope slide (which is set to the same height that the fibres will sit at). Its transmission spectrum is then measured using the above spectrometer, shown by the red curve in Figure 3.12a top. A Matlab script was written in order to determine the film thickness from the experimental transmission spectrum, which was normalised by the transmission spectrum of only the glass substrate. Using the assumption that the material identity of the film is known (e.g. gold), the optical properties of that material can be used to simulate theoretical transmission spectra (using the aforementioned Fresnel coefficient model) over a range of potential thicknesses (blue curves in Figure 3.12a top). The best matched theoretical

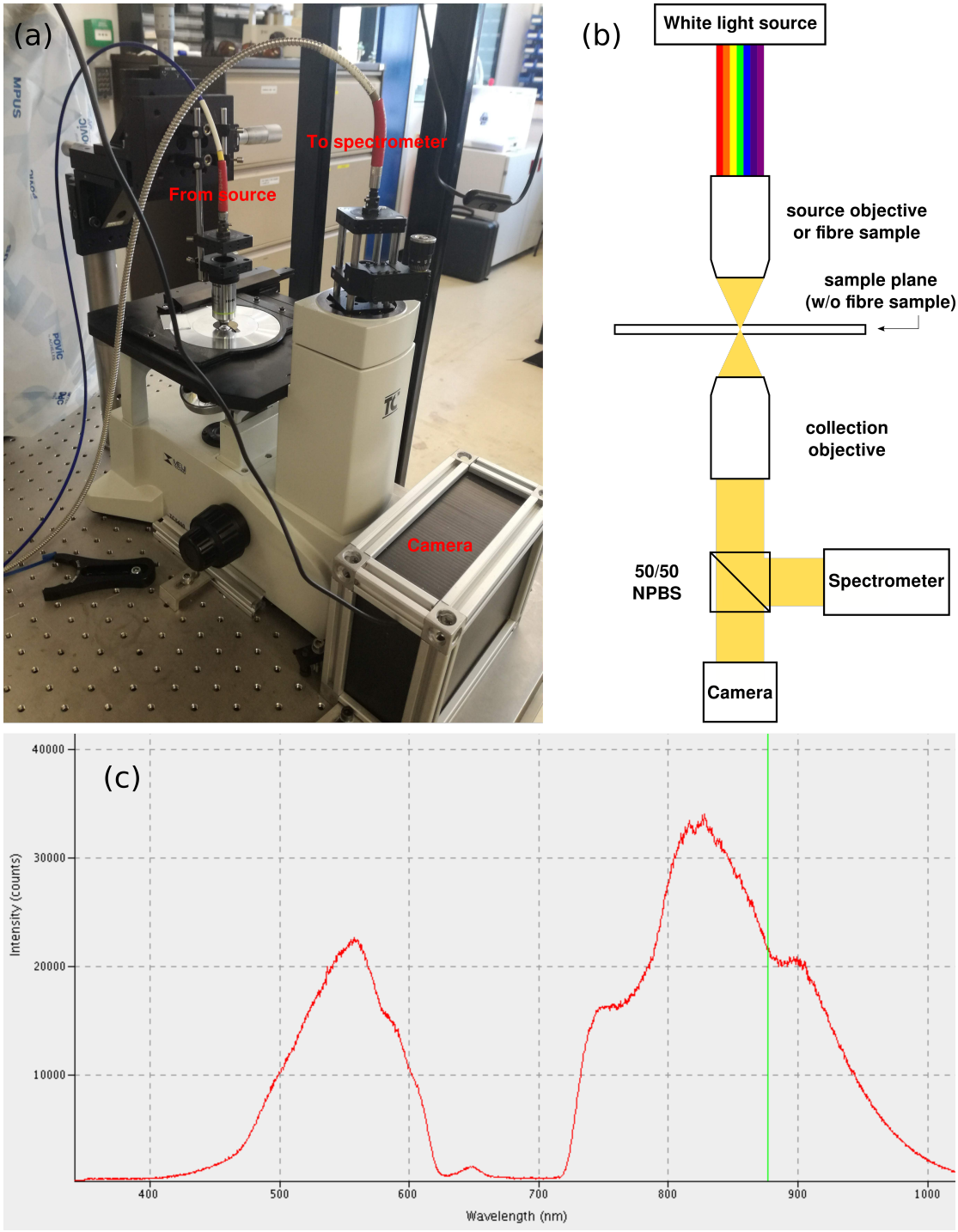


Figure 3.11: (a) Picture of the spectrometer that was built to measure reflection and transmission spectra of either planar or optical fibre samples. White light is delivered to and from the microscope body via optical fibre patch cables. There is also the option to use the body as a transmission or reflection microscope using the camera port at the bottom. (b) Schematic of the spectrometer optical design. Source light is brought to the sample plane either by objective lens or optical fibre, and is collected with an objective lens that relays the light for spectroscopy or imaging. For spectroscopy, the 50/50 non-polarising beamsplitter can be switched for a mirror. (c) Example transmission spectrum of a coloured polymer recorded by the Ocean Optics SpectraSuite software.

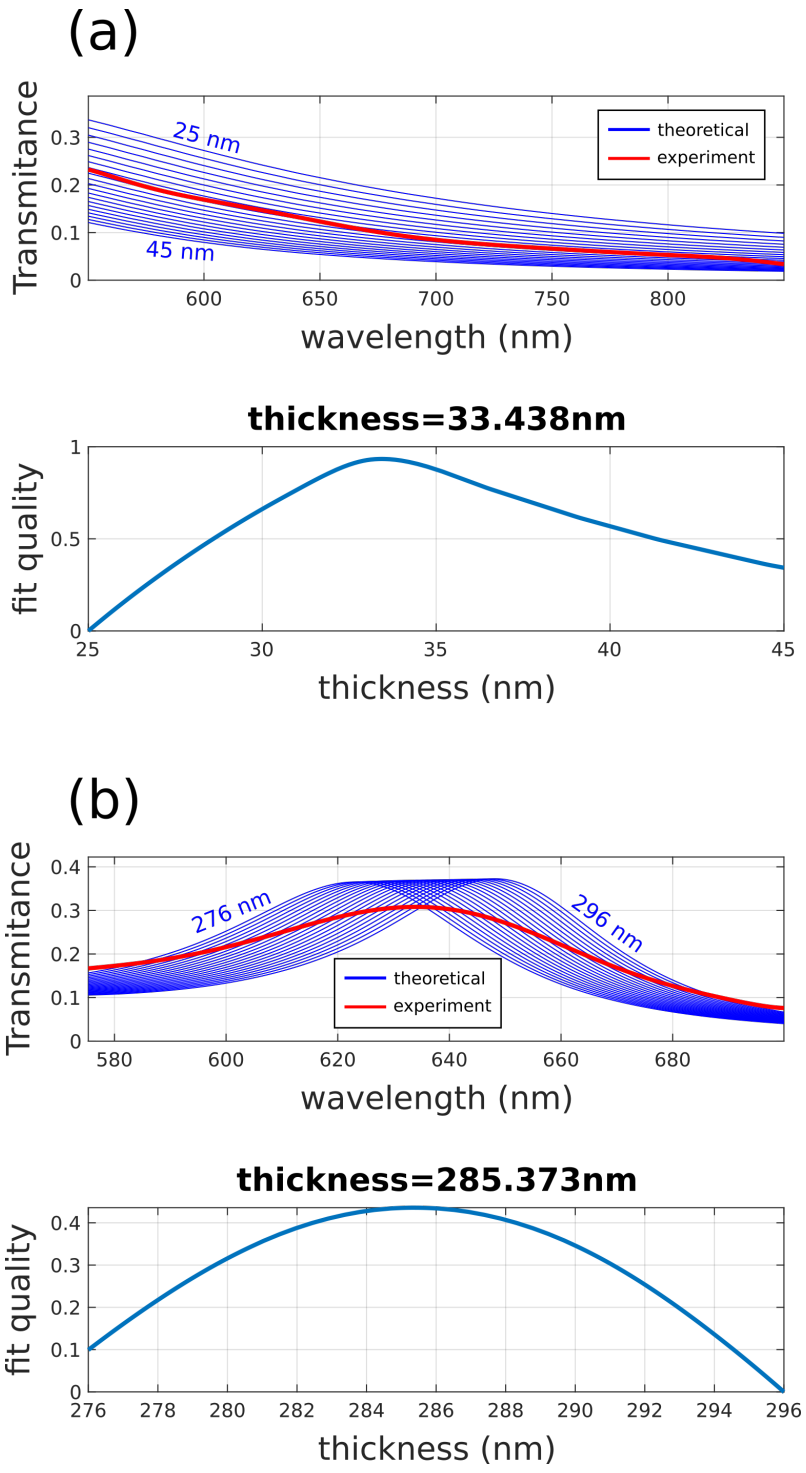


Figure 3.12: After measuring the thin-film (single layer or cavity) in the spectrometer, the transmission spectrum of the structure (red line in (a) and (b) top) is compared with theoretical Fresnel coefficients for a range of thicknesses (blue lines and text in (a) and (b) top) using the same wavelength range (or sub-range) as the light source. The closest match between experimental and theoretical spectra is considered to be the thickness of the film (x-position of peaks in (a) and (b) bottom). This technique applies to both single metallic thin-films (gold in (a)), and transparent dielectrics placed in cavities (ITO in (b)).

spectrum is located and assigned as the thickness measurement (fit quality in Figure 3.12a bottom).

This characterisation technique can also be applied to the measurement of transparent thin-film thickness, by depositing the film as the middle layer of a Fabry-Pérot cavity. The strong optical resonances produced by the cavity, are characteristic of the optical properties and thickness of the middle transparent layer. If the identity and thickness of the two mirror layers are known (measured as described for single semi-opaque layers), and the identity of the cavity layer is known (e.g. ITO), the same Fresnel curve fitting script can be used to measure the thickness of the cavity layer (Figure 3.12b).

Film thickness calibration

Following the deposition and spectroscopic-characterisation procedure, the deposition rate of the sputter coater can be determined by varying the deposition time that each separate glass coverslip experiences. Using gold as an example, the following parameters were kept fixed such that the only parameter which affects film thickness is the deposition time: plasma current $40\ mA$, working pressure $9 \times 10^{-3}\ mbar$, 40% valve position for argon gas, and $40\ rpm$ stage rotation. Gold was deposited with times between 20 and 90 seconds, and the resultant thicknesses were measured (plotted in Figure 3.13a). From these calibrations the mean gold deposition rate (for the parameters fixed above) can be characterised as $\approx 0.57\ nm/s$. This calibration data set can then be used to identify the deposition time required to achieve an arbitrary desired thickness. The same procedure was performed for ITO film thickness ($120\ mA$ plasma current) which was deposited at a rate of $0.82\ nm/s$ (Figure 3.13b).

The above example for calibrating thickness was then carried out on the metals that have been modelled and discussed in previous sections: Ti, Al, Cu, Ag, and Cr. The materials Ti, Al, and Cr were operated at higher plasma currents ($> 100\ mA$) in order to remove the oxide layers that naturally occur on these metals which effectively lowers electrical conductivity (required to generate sufficient magnetic fields). However, Cu and the noble metal Ag can be operated under similar conditions as gold ($40\ mA$). Figure 3.14 shows the time required for each material to deposit $\approx 20\ nm$. It is clear that good electrical conductors that are resistant to oxidation, such as Au and Ag demonstrate the highest sputtering rates, whereas materials such as Ti and Al require long deposition times. Figure 3.14 only represents the total time period in which the substrate is exposed to plasma; this does not take into consideration the required cooling intervals that interrupt the deposition. Cooling is initiated every ≈ 2 minutes which increases the total deposition time by roughly a factor of 2 (for materials which require longer than 2 minutes). Additionally, Al, Ti, and Cr demonstrated inconsistencies in forming plasma (especially Al) potentially due to imperfect removal of oxide layers, which further increases deposition time and decreases reproducibility. These findings

will be further discussed in the following section.

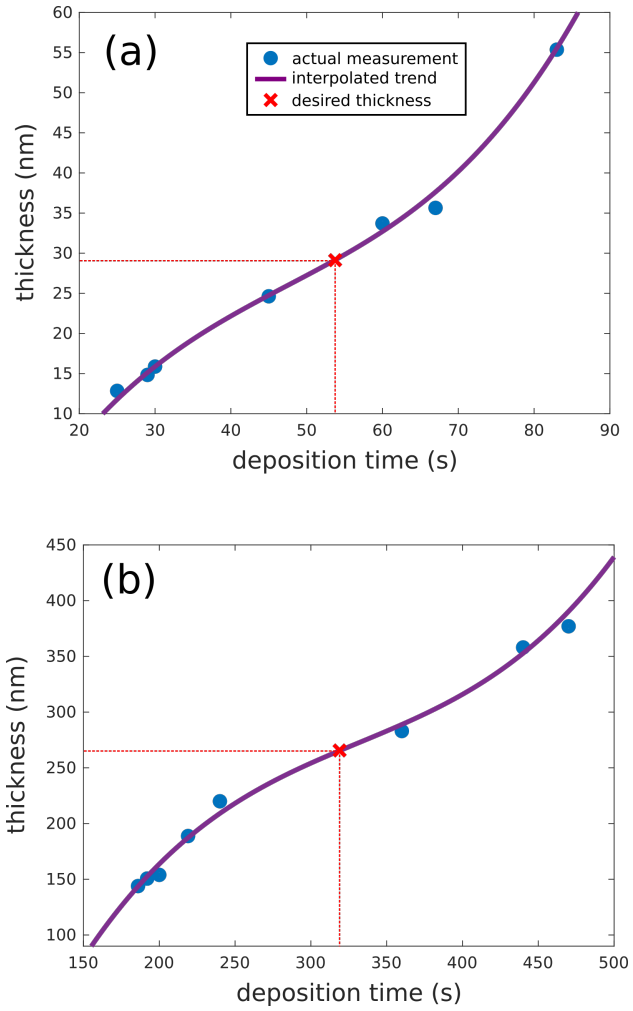


Figure 3.13: In order to calibrate the sputter coater, a number of blank glass coverslips are deposited onto for varying deposition times. Using the spectroscopy and characterisation procedures described in this section, an archive of film thickness as a function of sputtering time can be constructed for future use. (a) Calibration procedure for gold, and (b) the equivalent for ITO. Both materials were deposited with parameters of 9×10^{-3} $mbar$ working pressure, 40% valve position for argon gas, and 40 rpm stage rotation. Plasma currents for gold and ITO were 40 mA and 120 mA respectively, and mean deposition rates were 0.57 nm/s and 0.82 nm/s respectively.

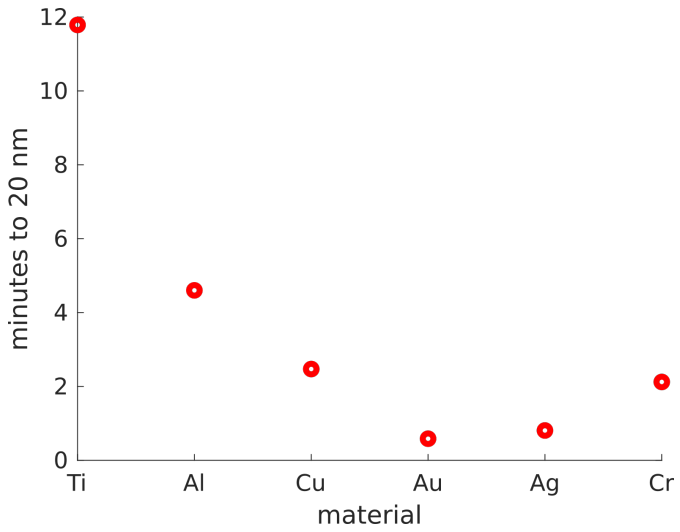


Figure 3.14: Time required for 20 nm of each metal to be deposited. Gold and silver exhibit the quickest deposition rates due to their electrical conductivity and chemical inertness. Oxidising metals such as Ti and Al require much longer deposition times and are less reproducibly deposited than the noble metals.

3.4 Discussion

This chapter has defined the parameters of an optical fibre which must be considered in the context of pump-probe experiments. As a result, the single-mode optical fibre has been identified as the optimum waveguide for the following reasons: high transmissivity, low dispersion, and a small core diameter which produces greater optical power density and higher spatial resolution. However, this comes at the cost of narrower wavelength bandwidth and more restrictive free-space-to-fibre coupling. The prospects of using multi-mode optical fibres in PLU experiments will be revisited in Chapter 7. The single-mode fibre selected for this study contains a core diameter of 5 μm, 125 μm cladding diameter, 780 nm centre wavelength, $730-970$ nm wavelength bandwidth (single-mode), and $NA = 0.13$.

A design for a thin-film transducer was proposed which centred on maximising transmission of the optical probe wavelength while maintaining high optical absorption for the thermo-elastic generation process. These processes were modelled using both optical TMM and PLU simulations. Initially, the materials Al and Ti exhibited the highest amplitude modulation depths (Figure 3.8a-b), which is a result of the combination in probe transmission and pump absorption. The contribution of the total reflectivity to the relative SNR of the signals was also estimated (Figure 3.8c) and used to normalise TRBS amplitude (Figure 3.8d).

The effect of thin-film damage due to the absorption of pulsed radiation was also considered (Figure 3.9a). In this regard, Al was identified as easily damaged through

melting or ablation; consequently, much lower optical powers would be required thus lowering the available signal amplitude and SNR. Figure 3.9b includes this effect to the metric of modulation depth and SNR. In Figure 3.9b it becomes evident that the majority of the metals demonstrate a peak response in the thickness range of $10 - 20\ nm$; this region is indicative of optimal performance given: high pump absorption, optimised combination of transmissivity (ΔR component) and reflectivity (R component), and low damage threshold. Furthermore, the discussion in this chapter on depositing the various thin-films through sputter coating has revealed that Ti, Al, and Cr are less conducive to high-throughput fabrication.

Considering the above findings, it is proposed that a $15\ nm$ layer of gold be used as the transducer layer. This represents a compromise between relatively high damage threshold (Figure 3.9a), high throughput thin-film deposition (Figure 3.14), and high modulation depth/SNR performance (Figure 3.8d). Gold contains a lower figure of merit performance compared with Cu and Ag ($\sim 35\%$ lower), however, operating the transducer in this near-damage regime will have consequences for sample heating which will be discussed in Section 5.2.2. Therefore the design of $Au = 15\ nm$ offers better performance per-mW with regards to $TRBS \cdot SNR$ when operated below damage threshold.

Single metallic thin-film transducers have been utilised in picosecond ultrasonics for several decades; however transducer-thicknesses that approach the ultrathin-film regime are scarcely discussed or demonstrated in literature. The Optics and Photonics Group at the University has pioneered a Fabry-Pérot cavity-based transducer design which uses a stack of two such thin-films [166, 173]; within the group a single-layer device within this ultrathin-film regime was proposed. Although single-layer thin-films are no longer novel, their adaptation to optical fibre substrates/systems are. It is this novelty to which I lay claim. Accommodating optical fibres to the thin-film fabrication facilities was a considerable challenge. Previous equipment did not contain a sufficient working distance between the hot plasma source and the transducer-plane, which resulted in high breakage rates for the optical fibre tips. I oversaw the specifications and purchasing of a custom sputter coating facility, which increased the plasma-stand-off distance by an order of magnitude, and then designed a novel mount to integrate optical fibre substrates (Figure 3.10) leading to a drastic reduction in breakage.

A key factor in the above transducer-design, is the fact that silica-based optical fibre substrates provide the most accessible and cost effective route for rapid prototyping. In the context of thin-film damage and potential specimen heating, a more thermally conductive substrate material may be desired for future optimisation. For example, if a single-crystal sapphire optical fibre was instead used as a substrate, the 30-fold increase in thermal conductivity (between sapphire and glass) would increase fluence damage thresholds for both the transducer and an adjacent specimen. It would

be ideal for this substrate to remain single-mode (to avoid intermodal dispersion) and small-diameter (e.g. $< 10\ \mu m$) to maximise lateral resolution. The fabrication of single-mode sapphire fibres is an area of great interest and current research [191]. These efforts are focused on etching to minimise core-diameters or engineering compatible optical claddings to minimise the mode-order of the waveguides [192]; however, currently these challenges are unmet in a way that is scalable and commercially viable. Beyond this, a possible compromise may be introducing thermal coatings [111] onto the tip of a silica optical fibre.

Now, after having calibrated the sputter coater (with microscope slides instead of fibre) and characterised thin-films using white light spectroscopy and Fresnel coefficients, the cleaned and cleaved custom patch cable can be placed into the fibre-mount facility of the sputter coater. Approximately $5\ nm$ of ITO was deposited which acts as an adhesion layer for the gold, followed by approximately $15\ nm$ of gold (Figure 3.15). This gold thickness is achieved with $30\ s$ of sputtering exposure and is reproducible with a precision of $\sigma_{Au} \approx 0.2\ nm$. With a prototype fibre-transducer now fabricated, the next chapter will introduce the experimental system which is capable of performing optical fibre-based time-resolved Brillouin scattering measurements.

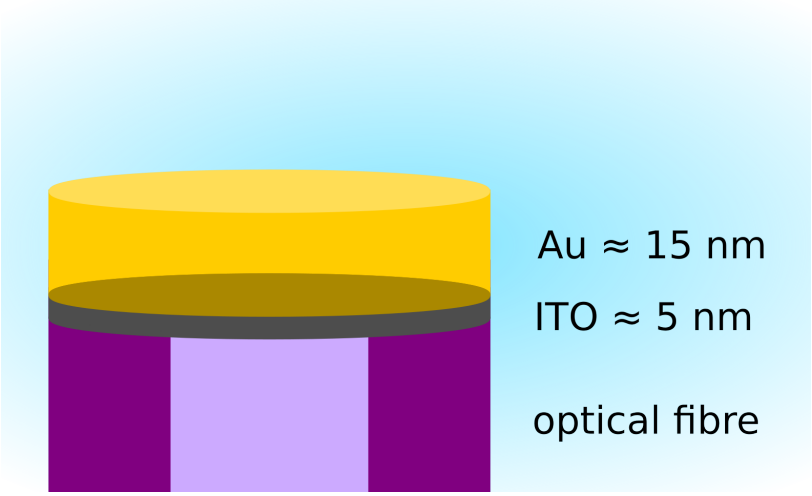


Figure 3.15: The fabrication and characterisation protocols outlined in this section were utilised to fabricate a metallic thin-film transducer onto the tip of a single-mode optical fibre. Using performance simulations discussed in Section 3.2, $15\ nm$ of gold was selected and is adhered to the substrate using a small amount of ITO. This prototype phonon probe will be used to perform high resolution spectroscopy and imaging.

Chapter 4

Pump-probe measurement system

In this chapter, a system for measuring $ps - ns$ time-scale phenomena, such as the time-of-flight of a GHz frequency phonon, will be detailed. The phonon probe concept is based on time-resolved pump-probe spectroscopy which has been described previously (Section 2.2). In short, the absorption of an ultrafast pump laser pulse by a material (e.g. opto-acoustic transducer) creates a non-equilibrium thermal state which relaxes in the form of strain pulses. These excitations have the potential to modulate the optical properties of the sample, for the case of time-resolved Brillouin scattering (TRBS) this occurs photo-elastically as the presence of strain modulates the refractive index of media such as water, polymers, and biological cells. Consequently, these events can be detected optically as fluctuations in the reflected (or transmitted) intensity of a second probe laser as it interrogates the excited region. In order to temporally resolve these events, the probe laser should consist of a pulse that is much shorter in time than the acoustic event; furthermore the arrival time of this pulse at the sample should be varied with respect to the stationary pump pulse. Then, by recording the optical intensity at each slice in time, the full transient event can be reconstructed and analysed.

The first half of this chapter will discuss the basic experimental pump-probe system used to make TRBS measurements, in particular the benefits of synchronising the pump and probe pulses with asynchronous optical sampling (ASOPS). The theme of the chapter will be less focussed on fibre optics, and the fibre-transducer, and will focus more so on the experimental foundation on which the fibre system can be integrated. A more rigorous presentation and discussion of the fibre-optic developments within the phonon probe system can be found in Chapter 5.

Once the instrumental framework of the experiment has been established, this chapter will turn towards defining the tools with which data processing and analysis can be performed. In particular, the transition from raw signal (on the oscilloscope) to final acoustic waveform will be detailed, followed by various treatments of the waveforms which can be used for performing parallelised spectroscopy and imaging.

4.1 Experimental set up

This section will focus on two themes: how the time-of-flight of a high frequency acoustic wave can be sampled, and the equipment capable of performing this task. The basic mechanism of PLU, and pump-probe spectroscopy in general, is that the absorption of the pump pulse is a periodic process which repeats at the repetition rate of the pulsed laser system. For each pump excitation pulse, there is one probe detection pulse that samples the reflectivity or transmissivity of the transducer/specimen at a discrete time position as the wave propagates. Due to the aperiodicity between pump and probe pulse timings, these generation-detection events are progressively staggered in time until a specific time window of the acoustic wave has been sampled and recorded. The remainder of this section will explore the common ways with which this *aperiodicity* is achieved and the supplementary optical components which facilitate measurement.

4.1.1 Time resolution

Sampling

Resolving a GHz frequency acoustic waveform requires careful control of the timing between pump and probe pulses. If considering an acoustic wave in water with centre frequency $f = 5\ GHz$ (e.g. the Brillouin frequency of water in the NIR), the period of each wavefront will be on the order of $200\ ps$. In order to effectively sample the frequency content of this wave, the Nyquist limit requires that each cycle of the wave contain at least two discrete samples, i.e. the maximum time difference between successive probe pulse positions should be $\Delta t_{max} = 100\ ps$ (in practice the sampling rate will be much faster than this). In order to increase the precision with which an acoustic frequency can be sampled, or the resolution with which two frequencies can be distinguished (discussed in Section 4.2), the number of wave-cycles detected should be increased, which requires that these $\sim ps$ sampling intervals should take place over the course of nanoseconds. Increasing the temporal sampling rate also serves to partially define the detection bandwidth of the system ($\sim 1/\Delta t$), i.e. when the sampling interval of the system is greater than the laser pulse width (of the probe beam in particular). This is achieved by using pulse widths in the sub-picosecond regime if a $\sim ps$ sampling rate is desired.

Figure 4.1 visualises the concept of temporal sampling; at the beginning of the excitation event, i.e. when the pump (blue pulse in figure) and probe (red pulses in figure) are synchronised in time at the sample (0 on signal clock). Subsequently, the timing of the two beams should be made asynchronous at a rate Δt, such that the probe pulse is increasingly delayed with respect to each pump pulse (Figure 4.1 top), thus sampling the optical response of the system (Figure 4.1 bottom). The time span of the acoustic wave that is capable of being detected is determined by the repetition rate

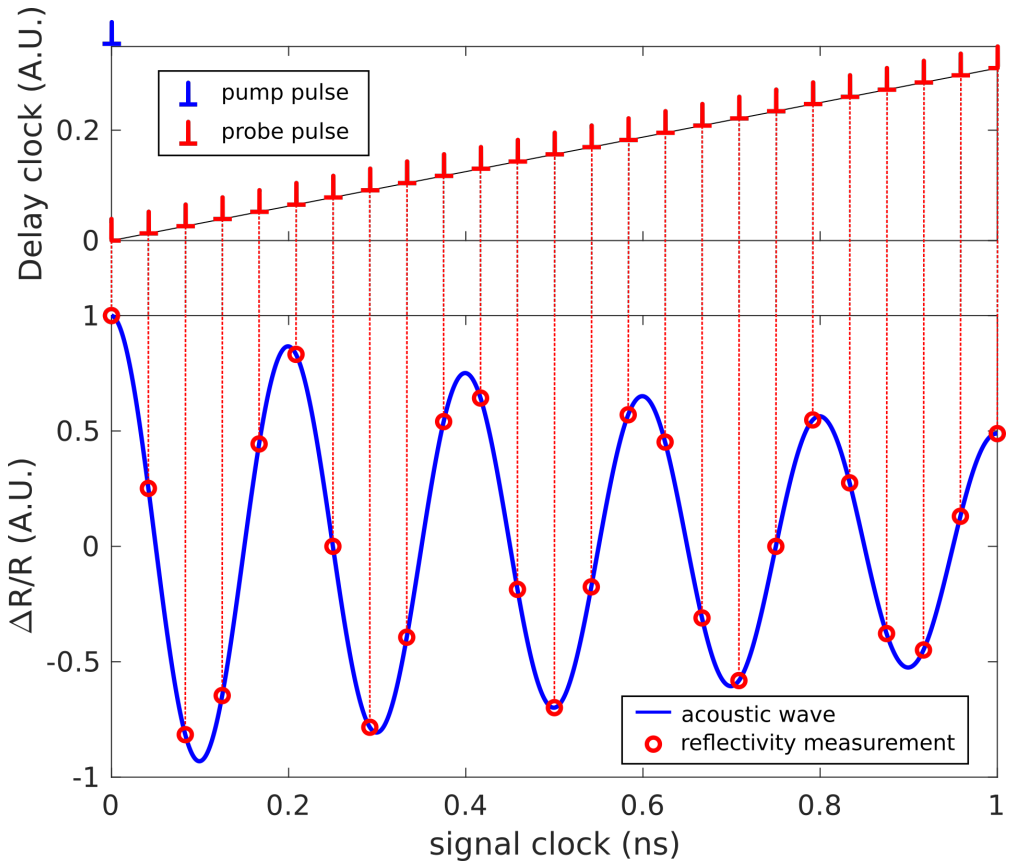


Figure 4.1: Following an initial excitation event - when the pump pulse (top blue spike) is absorbed by the sample - a second probe pulse (red spikes in top) should be progressively delayed with respect to the timing of the pump pulse, such that it samples a different time slice of the excited phenomenon. In order to reconstruct a $5\ GHz$ acoustic waveform (blue line in bottom window), the wave must be sampled at a minimum rate of twice per acoustic cycle, i.e. a probe delay period of $\sim 100\ ps$. Achieving full sampling of the acoustic amplitude will require many more samples than this; in this example, four samples per acoustic period is still insufficient to properly determine the full amplitude of the wave. Both plots share the same x-axis which is the real time signature of the wave; the total time required for the detection system to sample the wave is shown as the y-axis of the top figure, and is related to the delay mechanism of the pump-probe lasers.

(r_r) (of the pump pulses), while the total acquisition time is determined by the period of the asynchronisation mechanism ($\zeta = 1/\delta$ where δ is the delay rate/frequency), and the total number of samples is the product of these two $N = \zeta r_r$.

Optical delay line

Historically the most convenient method for varying the time delay between the pump laser pulse-train and the probe detection train, is to physically change the path length difference between the two lasers. In this *optical delay line* configuration, the path of one beam is redirected and contains two orthogonal reflective surfaces - often two perpendicular mirrors or a retroreflector - such that it experiences a time delay of $\Delta t =$

Lc where L is the round trip length of the delay line and c the speed of light (e.g. in air). By translating the position of these reflectors, and therefore varying the length of the delay path L, the progressively delayed probe pulse samples a subsequent position of the excited state. An example of a commercially available delay line system (Thorlabs ODL600) can be found in Figure 4.2a.

The relative simplicity of using an optical delay line, indeed comes at the expense of significant acquisition times. In order to achieve time discretisation on the picosecond scale, the linear translation stage must be capable of moving with micrometre precision; this is often easily achieved, even down to hundreds of nanometres. However, the rate at which the stage can be translated ultimately affects the delay period required to reconstruct an entire trace. Typically these mechanical devices can move at velocities up to $\sim$ 500 mm/s; however, it is normally impractical to operate mechanical stages at maximum velocities as mechanical vibrations will be introduced to the signal [193]. Moreover, mechanical delay lines often contain limited travel ranges reducing the total time window of the signal. Using the Thorlabs ODL600 product as an example - which is capable of reconstructing a total of 4 ns of time-of-flight, a maximum theoretical velocity

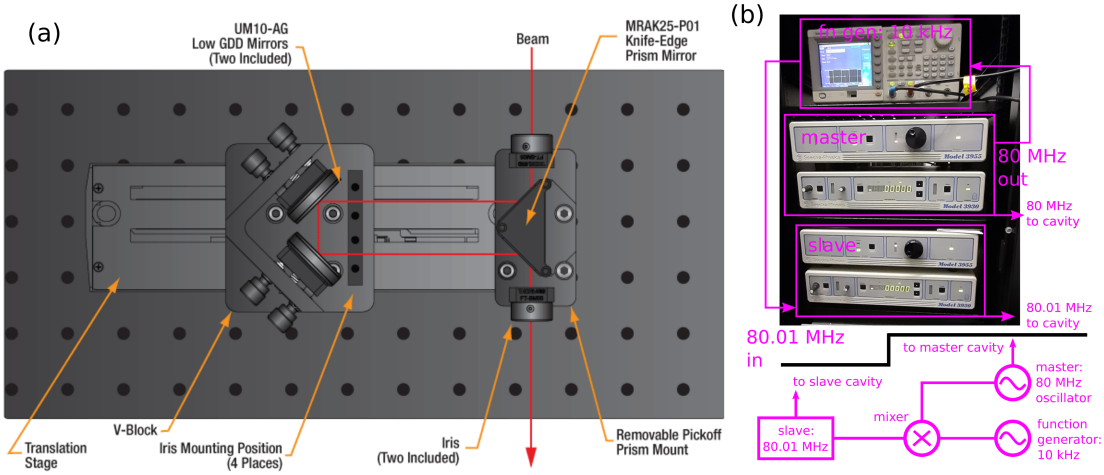


Figure 4.2: (a) An example of a commercially available conventional optical delay line (Thorlabs ODL600, photo taken from thorlabs.com). The normal path of one of the beams (e.g. the probe, red ray in figure) is diverted in order to impose a time delay of $\Delta t = Lc$ where L is the total round trip length of the diversion. The length of this optical cul-de-sac is then scanned by translating the reflecting elements, and results in an increasing Δt. This technique is limited by the length of travel of the translation stage (in part determines the detectable signal window), the velocity at which the stage moves (acquisition time), and the need to align additional (moving) optics. (b) The opto-electronic alternative to the optical delay line: asynchronous optical sampling (ASOPS) (control electronics pictured in top). Time resolution is achieved by simply using two lasers that have slightly different repetition rates, thus producing a progressive time-delay between pump and probe pulses. The 80 MHz clock signal of the master laser is mixed with a 10 kHz signal (function generator) to synchronise the slave laser clock (bottom). Without the need for moving optics, ASOPS provides orders of magnitude superior acquisition speeds compared with mechanically delaying the probe pulses.

of $400\ mm/s$, and a minimum resolution of $200\ nm$ - a time step of $1.5\ ps$ would be achieved by acquiring a time-point every $\sim 1\ ms$ ($470\ \mu m$ movement), with the full $4\ ns$ requiring $3\ s$ of acquisition (without additional averages). An example of this acquisition period can be seen in Figure 4.3a.

Asynchronous optical sampling

A powerful alternative to the mechanically driven optical delay line arose in the last few decades called asynchronous optical sampling (ASOPS) [194, 195]. This route to time-resolution is achieved by utilising two lasers with slightly different repetition rates. In doing so, the two pulses experience an incremental phase walk-out which repeats at the frequency of their repetition rate difference. For example if a master laser (pump) is set to $80\ MHz$, and the slave laser (probe) set to $80.01\ MHz$ (a delay rate of $\delta = 10\ kHz$), the slave laser will cumulatively step away from the master at a rate of $1.5\ ps$ per pulse. Using this technique, the entire $12.5\ ns$ time-of-flight between pump pulses ($1/r_r$) can be reconstructed in $100\ \mu s$, the beat period of the master/slave. Returning to the example used for the optical delay line, $4\ ns$ of signal at $1.5\ ps$ intervals would only take $30\ \mu s$ (neglecting the effect of detection electronics at first) given an $80\ MHz$ master and $80 + 0.01\ MHz$ slave (see Figure 4.3b).

In contemporary ASOPS systems the relative difference between the master and slave repetition rates can be controlled electronically. For example in Figure 4.2b-top, a master $80\ MHz$ oscillator (clock for the master laser) is used as the input to a function generator, which then mixes the $80\ MHz$ reference with its own $10\ kHz$ square wave (Figure 4.2b-bottom). The $80.01\ MHz$ output of the function generator is then used as the input for the clock of the slave laser. Then, the repetition rates of the master and slave laser cavities are monitored by fast photodiode, and the cavity lengths are modulated by a piezo-electric transducer mirror in a closed-loop such that the repetition rate for each cavity ultimately matches the respective master and slave clocks. This complex feedback network required to regulate the cavity lengths and repetition rates, leads to considerable financial cost for ASOPS-based systems, compared with the mechanical components needed for an optical delay line. Additionally, the mechanical vibrations of the moving cavity mirrors can introduce an error on pulse timings: *jitter*; a similar effect can also be caused by thermal fluctuations in the refractive index of the laser gain medium [196]. Jitter ultimately affects the temporal resolution of the measurement system and therefore the detection bandwidth. Such effects are also prevalent with the mechanically oscillated mirrors in optical delay line systems.

In spite of the above challenges, ASOPS provides several orders of magnitude improvement on the acquisition speed compared with mechanical delay lines; in the examples used above, this improvement is approximately 4 orders of magnitude. This level of improvement ultimately provides opportunities to (1) attain significant increases

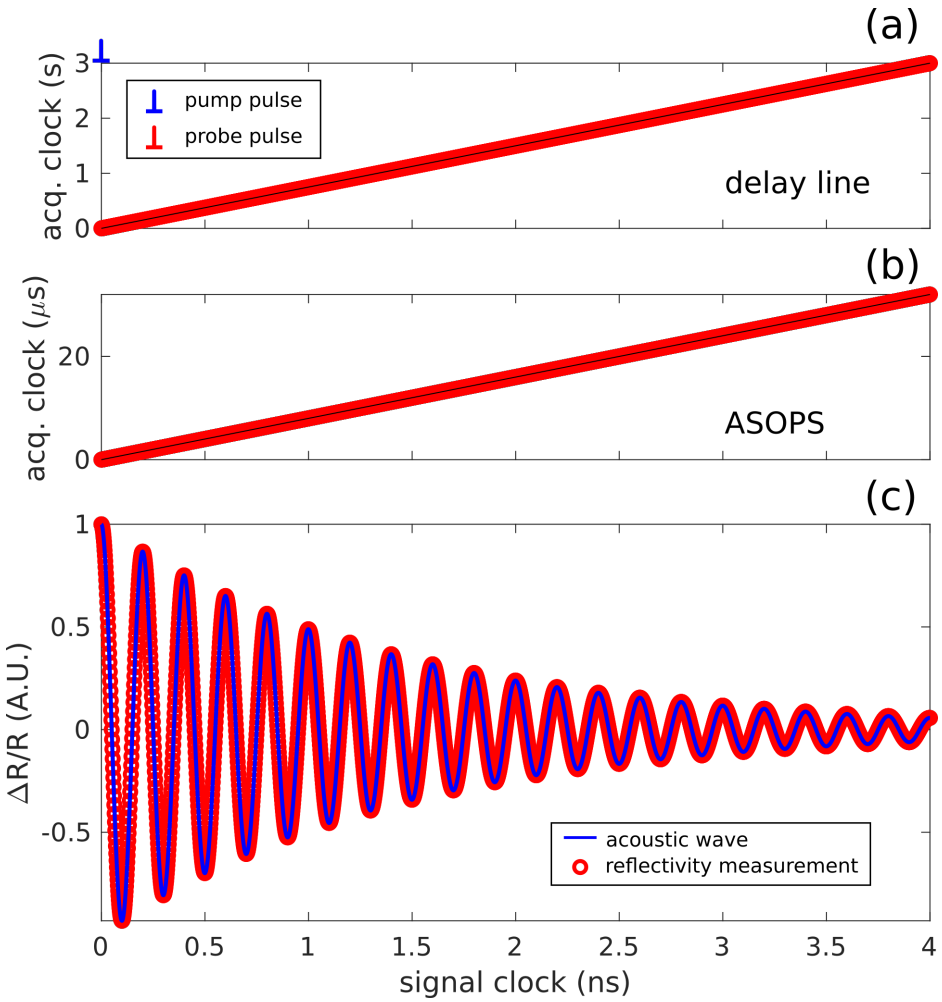


Figure 4.3: Comparison of detecting 4 ns of a 5 GHz acoustic wave (blue line in (c)) with 1.5 ps temporal resolution using an optical delay line (a) and an ASOPS laser system (b) (in both cases pump and probe have native $r_r = 80\ MHz$ repetition rates). (a) Using the Thorlabs ODL600 product as an example, at maximum stage velocity, a single time slice can be sampled every 1 ms, and therefore the entire time window can be detected in roughly 3 seconds (y-axis). Conversely, an ASOPS system shifts the repetition rate of one of the beams by $r_r' = r_r + \delta$. The shifted pulse will then sample a different slice of the wave, which is generated at a frequency of r_r. For $\delta = 10\ kHz$, the pump and probe will re-synchronise every 100 μs $(1/\delta)$ which in part determines the acquisition speed of the system. In the example here, 4 ns of signal is attained in $\approx$ 30 μs (neglecting memory and data transfer).

in SNR (per unit time), (2) increase acquisition speed towards real-time performance, or (3) scan much larger fields of view (per unit time). Furthermore, the lack of additional optical components (with ASOPS) negates the need to carefully align a variable length optical path, nor compensate for a changing optical spot size at the sample plane (e.g. due to imperfect beam collimation) [194].

The ASOPS laser system, and its powerful time resolving capabilities, will serve as the primary engine for the pump-probe experiment that will be described in the following section. The various optics and electronics required to make ultrafast acoustic

measurements will now be introduced, and discussed in the context of creating the first optical fibre implementation of time-resolved pump-probe spectroscopy.

4.1.2 ASOPS pump-probe optical system

Laser sources

Ultrashort pulsed lasers are central to the time-resolved pump-probe system on which the phonon probe is based. The lasers used for this study are the Tsunami Series by Spectra Physics. A Millennia eV $532\ nm$ pump laser is used to lase the titanium:sapphire gain medium within the Tsunami cavity over a bandwidth of $\sim 100\ THz$, resulting in a wavelength tuning range of $\Delta\lambda = 200\ nm$ over the NIR spectrum ($700 - 900\ nm$). The length of the Tsunami Fabry-Pérot cavity determines the repetition rate of the pulse train, which is inherently $80\ MHz$. Wavelength selectivity is achieved using a birefringent element within the cavity length, which when turned by a micrometre, selectively transmits according to wavelength. An acousto-optic modulator is used for active mode-locking and pulse compression down to the range of $100\ fs$. The $\tau = 100\ fs$ pulse width of the beams contributes to the overall time resolution of the measurement; with a delay rate of $\delta = 10\ kHz$ ($\Delta t = 1.5\ ps$), the condition $\tau < \Delta t$ is preserved implying that temporal resolution is not limited by the laser pulse width. Furthermore, the timing jitter produced by this laser system is on the order of $\leq 0.5\ ps$, and therefore does not limit bandwidth compared with the delay rate (bandwidth discussed later in the section).

Two such Tsunami cavities are used for the pump and probe laser pulse trains. For ASOPS configuration, their relative repetition rates are controlled electronically with a function generator (pictured on the top rack of Figure 4.2b) which synchronises the cavities relative to the master $80\ MHz$ oscillator (e.g. the pump laser). After achieving wavelength tuning and mode-locking, the output Gaussian beams from the laser cavities can achieve average powers on the order of $1 - 2\ W$, which translate to peak pulse powers of over $100\ kW$, and maximum pulse energies of $\sim 25\ nJ$.

The NIR output of one beam can be frequency doubled, using a second harmonic generation crystal, if NUV wavelengths are desired. This is the usual case for phonon microscopy, and ultrafast spectroscopy of metallic nanoparticles for which this optical system is used. A typical NUV-NIR configuration of the experiment is shown in Figure 4.4.

Optical elements

From the output aperture of the tuning cavities, the beams are directed by a high power turning mirror into the succession of downstream optics. In general, both NUV and NIR

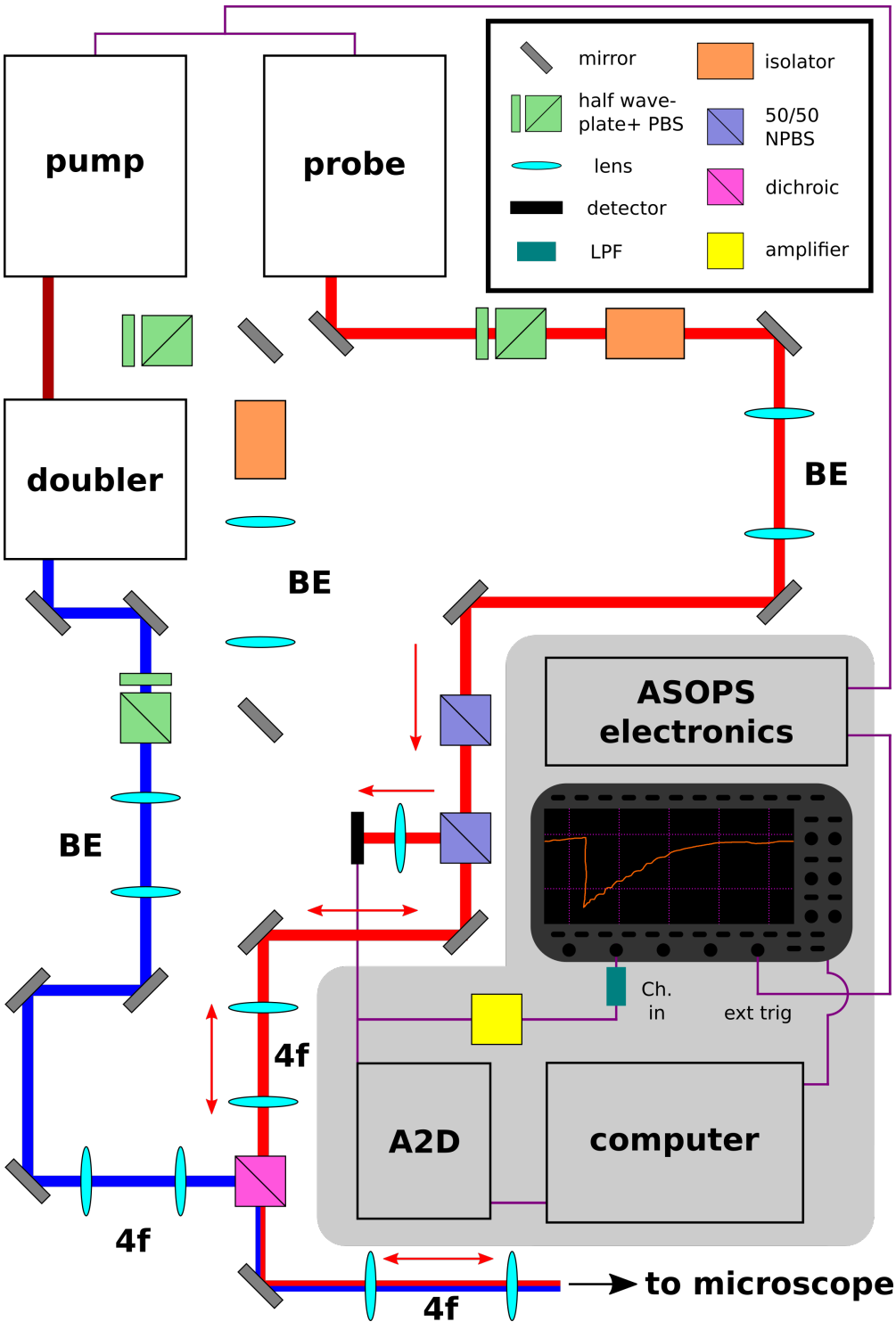


Figure 4.4: Schematic of the experiment used to perform pump-probe spectroscopy with NUV-NIR wavelengths. Two NIR femtosecond pulse width lasers are synchronised using ASOPS. One of NIR beams can be frequency doubled using a second-harmonic generation crystal. Each optical path contains: power attenuation, beam expansion, and 4f systems. Blue and red are combined using a dichroic before travelling to the sample plane. Double-sided red arrows indicate forward and back-reflected probe light. The detected signal passes through a detection chain of: DC capture, AC amplification and low pass filtering, AC digitisation from oscilloscope, and computer storage. BE - beam expander.

paths contain high reflectivity broadband dielectric mirrors, and achromatic lenses with wavelength-specific anti-reflection coating. In order to reduce $\sim W$ average power down to the mW range, the combination of a half wave-plate and a polarising beam-splitter are used to attenuate power as a function of the wave-plate rotation position. Faraday isolators are utilised to prevent back reflections from re-entering the Tsunami cavities and causing instabilities to the cavity modes. Newport Broadband Faraday Optical Isolators are used providing 90% transmission and $30\ dB$ isolation in the NIR.

Beyond this point, the optical elements are strictly for utilising the system to perform conventional pump-probe measurements in free-space. This will be briefly discussed since it is the foundation and reference point for adaptation to optical fibres. Each pump/probe path contains a beam-expander, two lenses with focal lengths $f_2 > f_1$, which allows the originally $< 2\ mm$ beam to expand to fill the back aperture of the downstream objective lens, and thus achieve the full numerical aperture. The expanded and collimated beams then pass through a final turning mirror (which can be used to adjust the overlapping between the pump and probe spots) before entering a 4f imaging system. The 4f systems ensure that adjustments of the turning mirrors are imaged onto the back focal plane of the objective lenses without clipping the objective aperture. Following the first 4f, NUV and NIR are combined with a dichroic beamsplitter which is followed by a fast scanning mirror. This allows simultaneous raster scanning of both pump and probe spots if desired. Additional 4f systems are used as the beams are periscoped up to the microscope body / objectives lenses where the sample is placed (see Figure 4.6).

The optical system can also be converted into a NIR-NIR configuration (NIR pump wavelength), by using a magnetic removable mirror in between the pump cavity and its doubler (Figure 4.5). This may be desirable when NUV phototoxicity is of concern, or if a particular nanostructure optically resonates in the NIR. This alternative NIR path contains the same basic set of optical elements, and is combined with the NIR probe-labelled beam using a 50/50 non-polarising beamsplitter (NPBS). However, in practice, the pump-probe roles of the two NIR beams are interchangeable.

Detection chain

For the NUV-NIR and NIR-NIR configurations discussed thus far, probe light that has transmitted through or reflected from the sample plane (Figure 4.6) can be detected in parallel. For the case of the reflected probe signal, the light will travel backwards through the optical systems shown in Figures 4.4-4.5, and will be tapped out by a 50/50 NPBS where a $50\ mm$ focal length lens focuses onto a photodetector. This equivalent process occurs for the transmitted portion of the signal above the microscope body.

The detector used in experiment is a Thorlabs Si Switchable Gain Detector (PDA36A) which operates over the wavelength range $350 - 1000\ nm$. A gain of $10\ dB$ is utilised

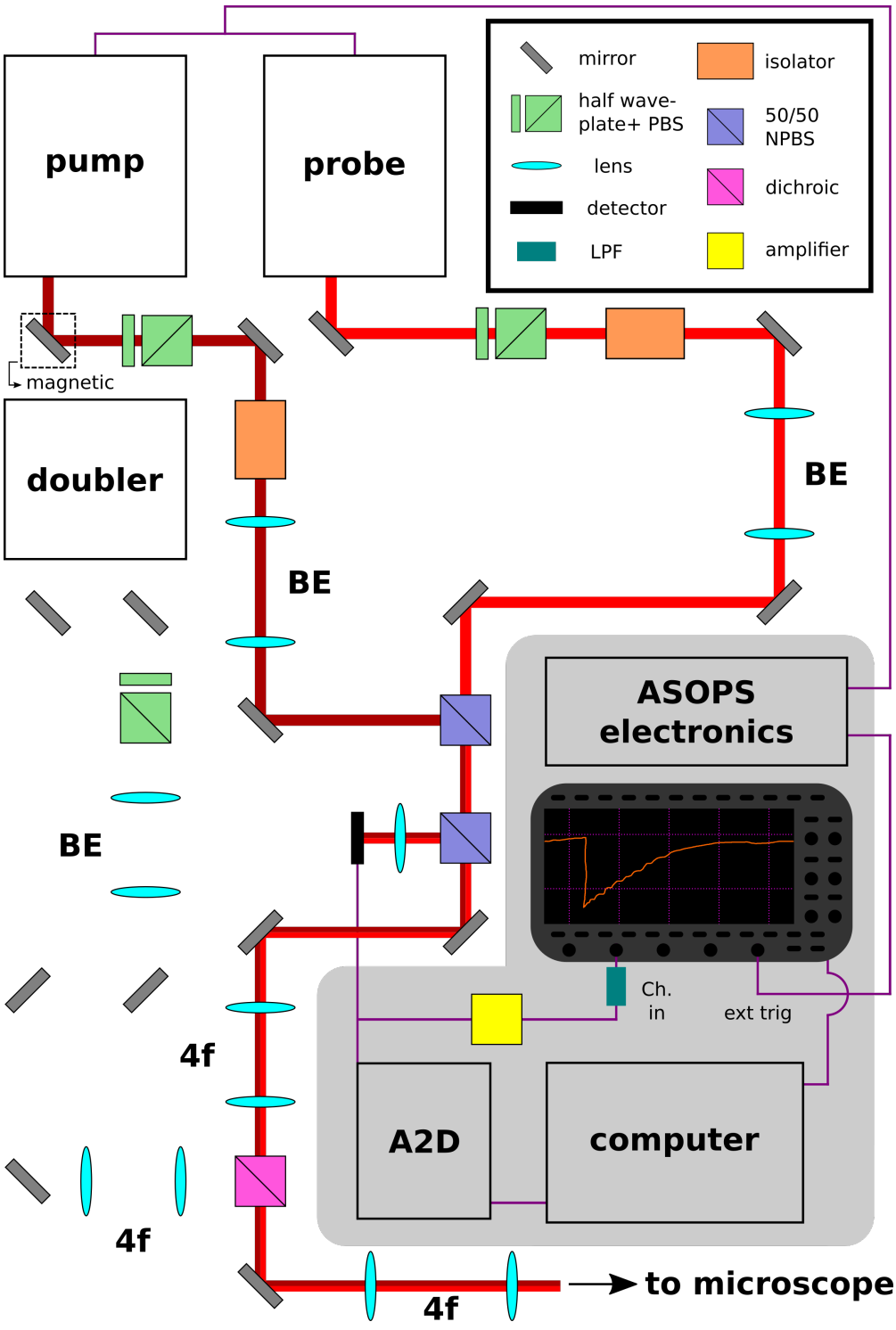


Figure 4.5: The optical system in Figure 4.4 can be modified to perform with two NIR wavelengths for the pump and probe. A magnetic removable mirror (shown as a dotted box in the top left) is placed between the pump laser and its frequency doubler, after which the light follows a similar path to the probe laser. Beam propagation follows the same directions shown in Figure 4.4. Both NIR beams can be directed to the detector, or one can be optionally long-pass filtered.

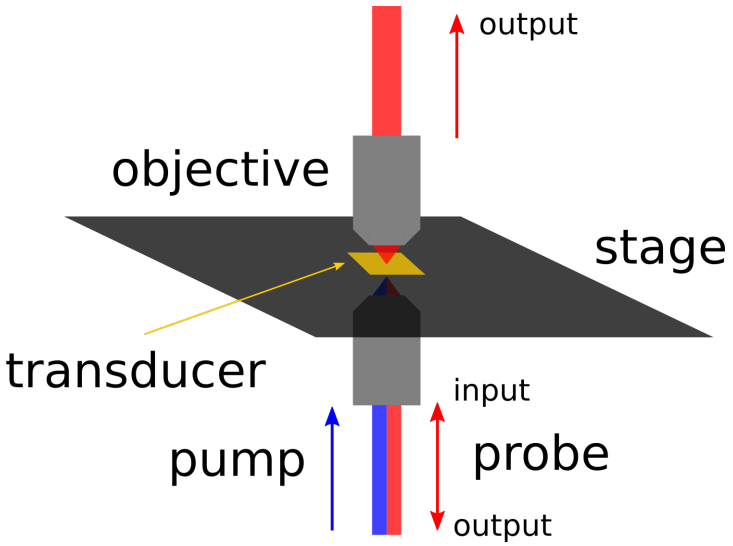


Figure 4.6: Basic diagram of the sample plane for the free-space implementation of the pump-probe system. Either a NUV-NIR or NIR-NIR pump-probe combination is directed through a series of 4f systems such that the beams can be translated in space while still being accepted into the back aperture of a microscope objective lens (bottom lens). After interacting with the transducer and sample, the probe light can be detected in two configurations: the signal light that has transmitted through the sample, and signal light that reflects from the transducer/sample and travels back through the optical systems in Figures 4.4-4.5. A mechanical stage can be used to control the x/y position of the pump-probe spots with respect to the sample for scanning and imaging.

which provides a detection bandwidth of $5.5\ MHz$. The offset between the $100\ \mu s$ acquisition period (given by $\delta = 10\ kHz$) and the $12.5\ ns$ signal window (given by $r_r = 80\ MHz$), also results in acoustic frequencies being downshifted by the same factor of 8000 in the detected signal. Therefore a $5.5\ MHz$ detector bandwidth translates to a frequency in the signal domain of roughly $50\ GHz$. This is far more limiting than the $\sim 1\ THz$ bandwidth provided by the time delays of the probe pulses ($\Delta t = 1.5\ ps$), and also less than the $\sim 0.1\ THz$ acoustic generation bandwidth of the pump laser absorption (Figure 2.12). Considering that the frequency band of interest for TRBS in liquids and biological media is in the $1 - 20\ GHz$ range, the $\sim 50\ GHz$ bandwidth of the system is sufficient.

After a signal is collected at the detector it is relayed by coaxial cable to: (1) a Mini-Circuits RF amplifier (ZFL-500LN-BNC)), and (2) a National Instruments analogue to digital converter BNC-2110. The latter digitises the photovoltage from the DC light level of the signal, for use in later signal processing. The output of the amplifier is then low pass filtered and passed to an input channel of a digital oscilloscope LeCroy HRO66Zi. The δ frequency waveform produced by the function generator (e.g. $\delta = 10\ kHz$) is set as the input/external trigger for the oscilloscope. The sampling rate of the oscilloscope can be varied up to 2 GS/s, however to avoid over-sampling, typically a value in near 100 MS/s is chosen to match the 80 MS/s discretisation of the ASOPS system (at

$\delta = 10\ kHz$).

Due to the inherent weakness of the TRBS process, where approximately 1 in 10^6 photons contributes to the AC component of the signal [168], the output modulation depth of the TRBS signal will require additional averaging. Linearly increasing SNR can be achieved by increasing the energy density of the pump beam, as this directly scales the amplitude of the phonon field. In the shot-noise limited case SNR can also scale as $\sqrt{N}$ by increasing the probe energy density. However, in both cases, additional heating and/or light exposure could lead to damaging the region of interest.

Performing averaging, either by integrating for longer time periods on the oscilloscope or by averaging measurements in post-processing, will also improve SNR at the cost of acquisition time and therefore longer potentially-damaging exposures. The rate of improvement of SNR as a function of averaging and acquisition time can be found in Figure 4.7, which uses the example of the amplitude of the detected Brillouin frequency in water using a $20\ nm$ gold layer transducer (signal processing in Section 4.2). The experimental rate of improvement for SNR (red circles) matches the theoretical relationship SNR $\sim \sqrt{N}$ (red line). Another compromise for increasing acquisition speed while maintaining higher averaging is to reduce the detection window from $100\ \mu s$ to $50\ \mu s$, which has the adverse affect of shortening the available time window from $12.5\ ns$ to $6.25\ ns$. In many cases this trade off is acceptable since high frequency acoustic signals

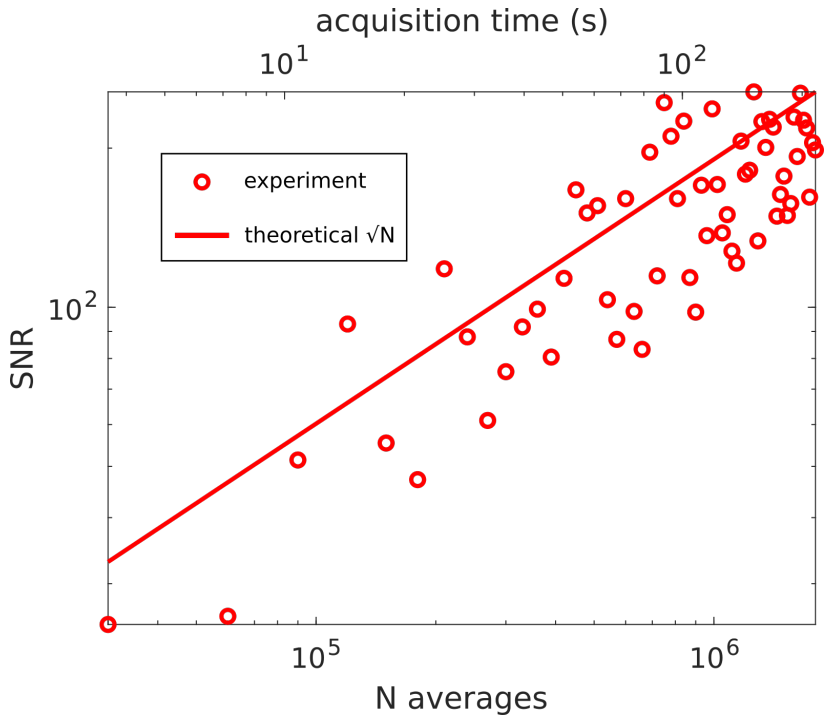


Figure 4.7: Signal-to-noise ratio of a TRBS signal in water as a function of total number of averages (averaged in post-processing, with a fixed number of averages on the oscilloscope per data point) and therefore acquisition time. In addition to signal averaging, SNR can also be scaled by increasing the pump and probe beam power density according to the relationship in Equation 2.78.

will attenuate within this time-span (discussed in Section 5.1). Reducing the time-base effectively shortens the time required to buffer the data from the previous just-acquired signal, i.e. $100\ \mu s$+buffer$_{100\mu s} > 50\mu s$+buffer$_{50\mu s}$. The ideal configuration for acquisition parameters will depend upon the desired measurand. For example if using the phonon probe as an *in situ* Brillouin spectrometer for liquids or polymers, additional optical power and/or heating may not be of concern and less averaging may be used for speed. Conversely, if the phonon probe is being used an endoscopic imaging tool on biologically relevant samples, reducing power and exposure may be more critical.

Future strategies for increasing acquisition speed will focus on overcoming the bottleneck created by the synchronisation of the pump and probe pulses. One possibility for this is converting the probe beam from a synchronised pulsed laser to a continuous wave laser (e.g. see [119]), which would require a photodetector and oscilloscope with analogue bandwidths that cover the signal band of interest, e.g. $f_{max} > 5\ GHz$ for TRBS in aqueous materials with NIR probe wavelengths. This and other potential strategies, such as encoding the TRBS signal onto a time-stretched rainbow pulse (e.g. see [181]), would lead to a drastically more cost effective optical system at the cost of developing novel signal processing and data-storage protocols.

Finally, a computer connects with both the A2D converter and the oscilloscope outputs in order to store the data. In addition to controlling the Millennia pump lasers, the entire experimental protocol is called from this PC, using the D-scan software programme that has been developed in the Optics and Photonics Group at the University of Nottingham. This provides storage of data in addition to controlling supplementary components, such as $x/y/z$ stages, CCD cameras and webcams, and solenoid beam shutters. Following this data acquisition procedure, the data will be conditioned and analysed using the signal processing protocols set out in Section 4.2.

Fibre adaptation

By adding three magnetic removable mirrors and two additional fibre coupling facilities, the paths of the pump-probe optical system described in the above section can be converted from free-space to optical fibre. With the system in NIR-NIR mode - to keep the pump and probe wavelengths within $200\ nm$ of each other for single-mode operation (Section 3.1) - mirrors are placed after the isolators directing the beams into unoccupied space on the optical bench (see Figure 4.8). Each beam is then aligned to enter a Thorlabs Achromatic FiberPort ($\lambda = 650 - 1050\ nm$) with normal incidence. The FiberPort contains a small lens at the front aperture which focuses the input collimated light to a fixed focal distance where an FC/PC-terminated 780HP single-mode patch cable is placed (NA of the lens matched to that of the fibre). The lens is placed in a cell that needs to be aligned in the x/y plane and three tip/tilt directions, in order to maximise the coupling efficiency and power output of the attached optical fibre. The placement

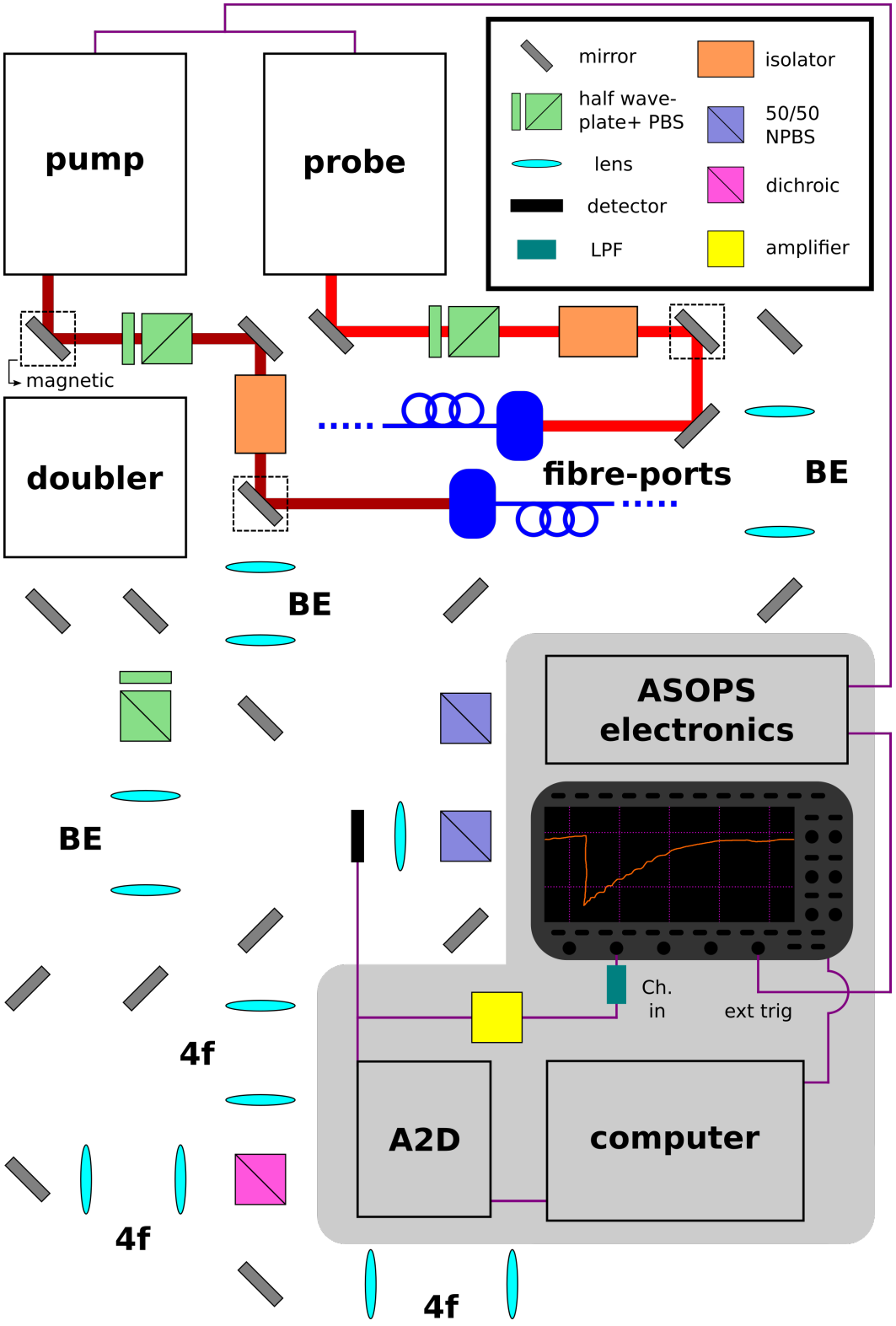


Figure 4.8: The experimental optical system can be adapted to convert free-space pump-probe beams into optical fibre. Removable magnetic-mount mirrors are placed into the beam paths which deliver light into Thorlabs FiberPorts: a small articulating lens which focuses light into the core of a connected optical fibre patch cable. Once fibre-coupled the pump and probe beams can be delivered into a common channel containing the transducer. The same photodetector as before will now be placed at one of the output fibre channels.

of the FiberPorts allows control to be maintained over the average powers of the beams (using the half wave-plate and PBS combination), and utilises the isolators to prevent strong reflections that might occur when placing additional optical fibre connections in series with this path.

Whereas the free-space configuration combines and separates pump-probe beams using a dichroic beamsplitter (for NUV-NIR wavelengths) or a NPBS (for NIR-NIR wavelengths), a similar solution will be required for the fibre variation of the system. After coupling both pump and probe into optical fibre patch cables, these cables should be joined into a common channel which is terminated by the fibre-transducer. Figure 4.9 shows a diagram of a basic way this can be carried out: two 1:2 optical fibre-couplers ($3dB$) in series with one another, the first used as the probe input and output channel, and the second used to combine the pump and probe beams (both NIR) into a common channel terminated by the transducer.

This section has introduced the fundamental optical system that is capable of exciting and detecting high frequency acoustic phenomena. An ASOPS configuration for the pump and probe femtosecond pulsed laser beams provides access to $ps - ns$ features within a signal, and more importantly does so with greater acquisition speed relative to the traditional optical delay line method. However, the modulation depths that this system intends to detect are still extremely faint. Additional averaging and integration time are typically required to generate high SNR signals creating a trade-off between SNR and speed. The following section will now detail the signal processing procedures which transform raw signals into useful acoustic waveforms.

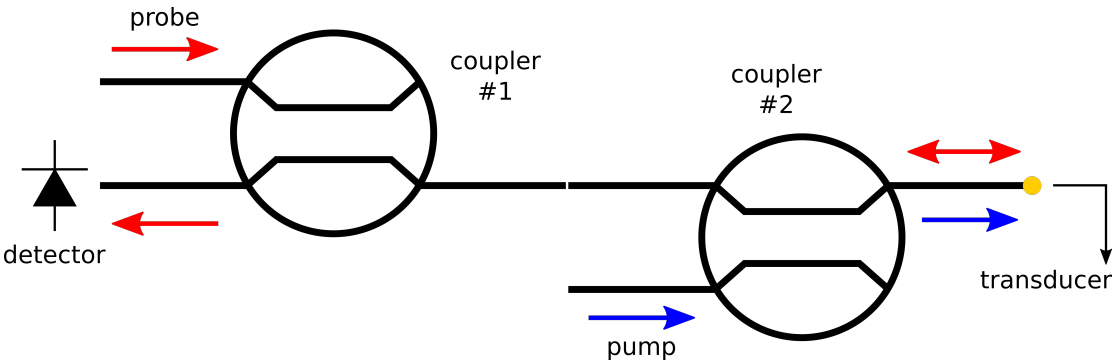


Figure 4.9: Diagram of the optical fibre analogue of beam combination and separation (required for pump-probe measurements) using two 1:2 $3dB$ fibre-couplers in series with one another. The first coupler acts as the input and output for the probe beam (terminated by a detector), similar to the (bottom purple-coloured) 50/50 NPBS in Figure 4.4. The second coupler acts as the combining element, similar to the (pink-coloured) dichroic beamsplitter in Figure 4.4.

4.2 Data processing

In this section the protocol for processing the experimental TRBS signal will be defined. This is primarily achieved using Matlab to organise, operate upon, and display the data. The waveform that is recorded by the oscilloscope must be treated to remove various unwanted features before obtaining the time-of-flight of the acoustic phenomena sampled by the ASOPS pump-probe system. Transformation of the time-domain signal into the frequency domain will enable Brillouin spectroscopy and therefore the characterisation of viscoelastic properties of the material in which the phonon probe is immersed. The discussion will then transition to measuring signal frequency as a function of time, i.e. time-frequency analysis. The latter will play a crucial role in utilising the phonon probe as a 3D imaging tool for microscopic objects.

4.2.1 Standard signal processing

Time domain

Prior to an experiment, the user generates a con-file containing the scan instructions - e.g. mechanical stage movements / number of measurements per point / etc - which is passed to the data acquisition software (D-scan). During and after an experiment, D-scan writes the experimental data to a series of files and file-types: dat-file which contains the raw oscilloscope output (AC), m-file containing the meta-data for the scan including names for file-bases and oscilloscope parameters, and a d-file containing the average photovoltage level(s) (DC). A custom Matlab script has also been developed by the Optics and Photonics Group (to which I have also contributed) to parse and process the raw data according to the methodology that will be presented below.

The experimental case study used for this discussion of signal processing, is a $20\ nm$ gold transducer (on a planar glass slide), topped with a droplet of water. The experimental set-up was that of the NIR-NIR free-space configuration shown in Figure 4.5, where the signal has been detected in transmission (top output in Figure 4.6). The target signal for this experiment is the time-resolved signal due to the probe beam Brillouin scattering with $f_B = 5\ GHz$ phonons in the water medium. Pump and probe wavelengths were 720 and $780\ nm$ respectively, with average powers of $8\ mW$ each (≈ 0.4 NA objective lenses on top and bottom). Oscilloscope averages were set to $30k$ per acquisition, which was performed a total of 60 times (60 counts), for a total of 1.8 million averages.

The raw AC time trace (ΔT) from the oscilloscope is shown in Figure 4.10a. Upon first glance, a sharp spike in the signal level is seen at around $t = 7\ ns$ followed by a high frequency oscillation. Initially, this AC signal is normalised by the DC-level (T) (Figure 4.10b) that was acquired using the A2D converter (it is worth noting that the DC measurement can also be made using an empty channel on the oscilloscope but adds

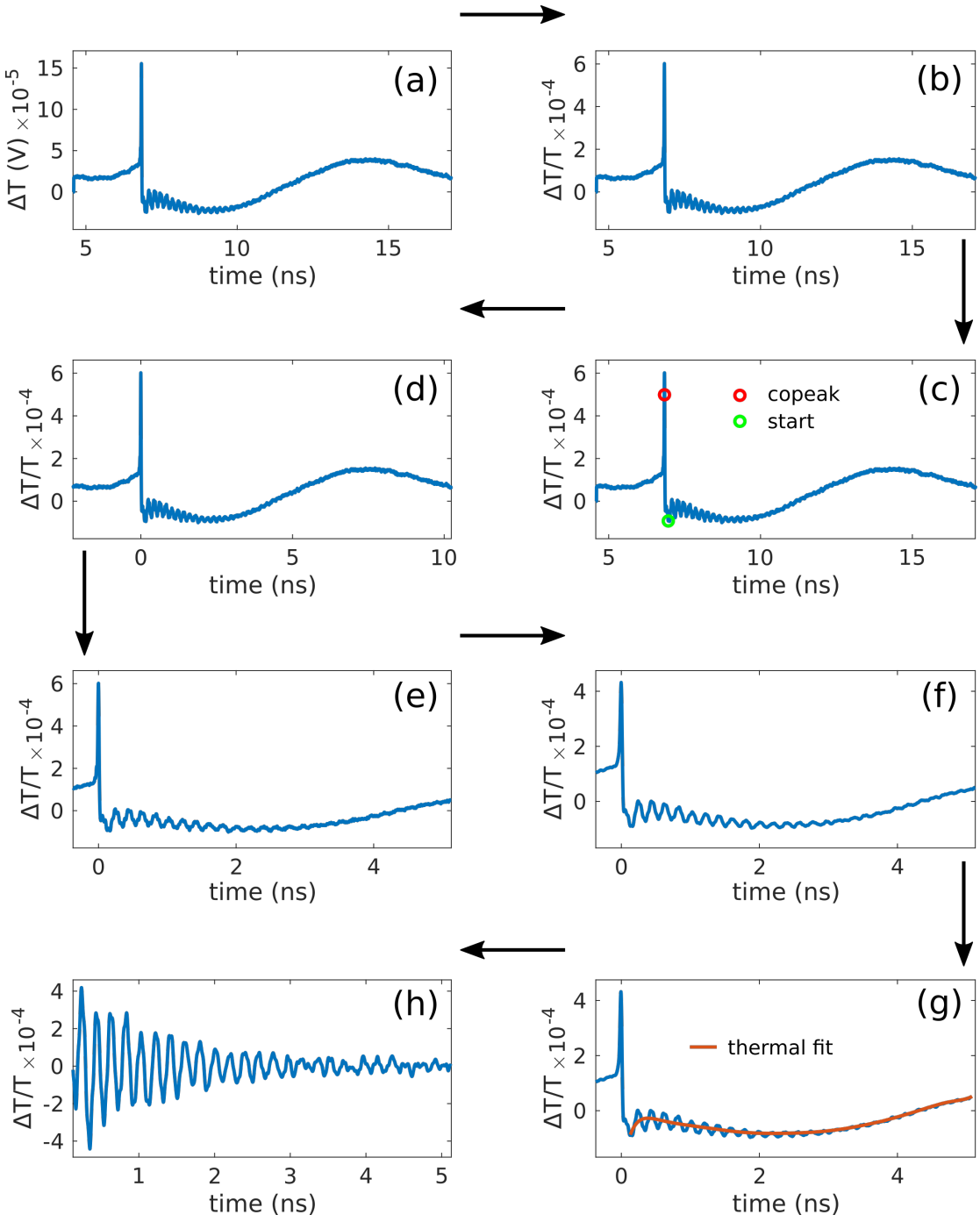


Figure 4.10: Logic diagram for the standard signal processing protocol. (a) Raw (transmittance) AC signal as output from the scope. (b) AC signal is normalised by the DC photovoltage as measured by the A2D converter (or a separate channel on the oscilloscope). (c) Location of the coincidence peak (red) which occurs when the pump and probe are synchronised; a user-defined offset (green) will be applied to indicate the onset of the region of interest. (d) Time-vector of the signal is shifted such that the coincidence peak is time zero. (e) Signal is cropped again to only consider the high SNR segment (e.g. $t = 0 - 5$ ns). (f) Signal is low pass filtered. (g) The slow thermal decay following the coincidence peak is fitted to a polynomial expression and subtracted. (h) Final modulation depth of the acoustic wave.

additional acquisition time). DC-normalising the signal (AC $\rightarrow$ AC/DC) provides a basis for comparing the signal across experiments, transducer types, or even environmental conditions.

When the pump and probe pulses overlap in time, an intense excitation process is instigated within the transducer. In this highly excited state, the existence of non-equilibrium electrons and lattice phonons (heat) are capable of affecting the optical properties of the transducer [121]. What results is a sudden spike, or a *coincidence peak*, in the optical response of the system, followed by a slower relaxation process. In order to begin removing this effect, the coincidence peak is first located by searching for the maximum change in transmittance/reflectance (Figure 4.10c), and the time-vector of the trace is shifted such that the coincidence peak occurs at $t = 0$ (Figure 4.10d). Then the trace is cropped to the length of signal time that is of interest to the user (Figure 4.10e), e.g. the 5 ns following time zero. At this point the trace is low pass filtered to accentuate the signal bandwidth of interest, which in the case of TRBS in water with a NIR probe wavelength is < 50 GHz. This is accomplished by filtering the time-signal in the Fourier domain with a Hann window whose width is determined by the desired cut-off frequency, followed by inverse transforming the filtered signal back into the time-domain (resulting in Figure 4.10f). A final step is performed in order to remove the slowly varying thermal decay that follows the initial excitation; this is achieved by a fitting a polynomial and subtracting it from the signal [197, 198] (Figure 4.10g) that has now been cropped to start at the coincidence peak position plus a user-defined offset (green circle in Figure 4.10c). What results is now the final modulation depth (i.e. AC/DC - $\Delta T/T$ or $\Delta R/R$) of the optically detected acoustic time-of-flight, found in Figure 4.10h.

Frequency domain

The frequency of an acoustic wave is related to the elastic properties of the medium in which it is travelling. The fields of TRBS and Brillouin spectroscopy/microscopy rely on measuring acoustic frequency - in the form of optical frequency shifts (Brillouin shifts) - to access to novel elastic information about a specimen [142, 180, 199]. For the case of TRBS, the original broadband phonon field that coherently emanates from the transducer is effectively bandpass filtered by the phase matching condition of the Bragg condition at the selected probe wavelength (and linewidth of the probe laser). This ensures that any acoustic wave sampled through TRBS will possess a wavelength of $\lambda_a = \lambda_{probe}/2n$ (Equation 2.22) and will oscillate with frequency $f_B = v/\lambda_a$. Therefore, in a single static material the TRBS signal will oscillate at a single Brillouin frequency. However, if the experiment takes place in a heterogeneous medium, across the space of multiple materials (e.g. glass and water), or in a dynamic environment (e.g. undergoing heating and cooling), variations in material properties will give rise to shifts in

the sampled acoustic wavelength. Consequently, multiple Brillouin frequencies will be present in the TRBS signal providing an opportunity for multiplexed material sensing or spatially resolved frequency measurements.

In order to characterise the frequency content of a detected acoustic wave, the time-of-flight signal is Fourier transformed using a fast Fourier transform algorithm (Matlab). The resulting frequency spectrum (Figure 4.11b) reveals the amplitude (Fourier coefficient) contributed by each frequency-bin in the Fourier series. The inherent frequency resolution (bin spacing) of a measurement will be determined by the temporal extent of the signal, i.e. if the entire $12.5\ ns$ time window is preserved the frequency bins should be spaced $80\ MHz$ apart. However, in practice the time window is often shortened, which decreases the frequency resolution (wider bins). This can be mitigated by zero-

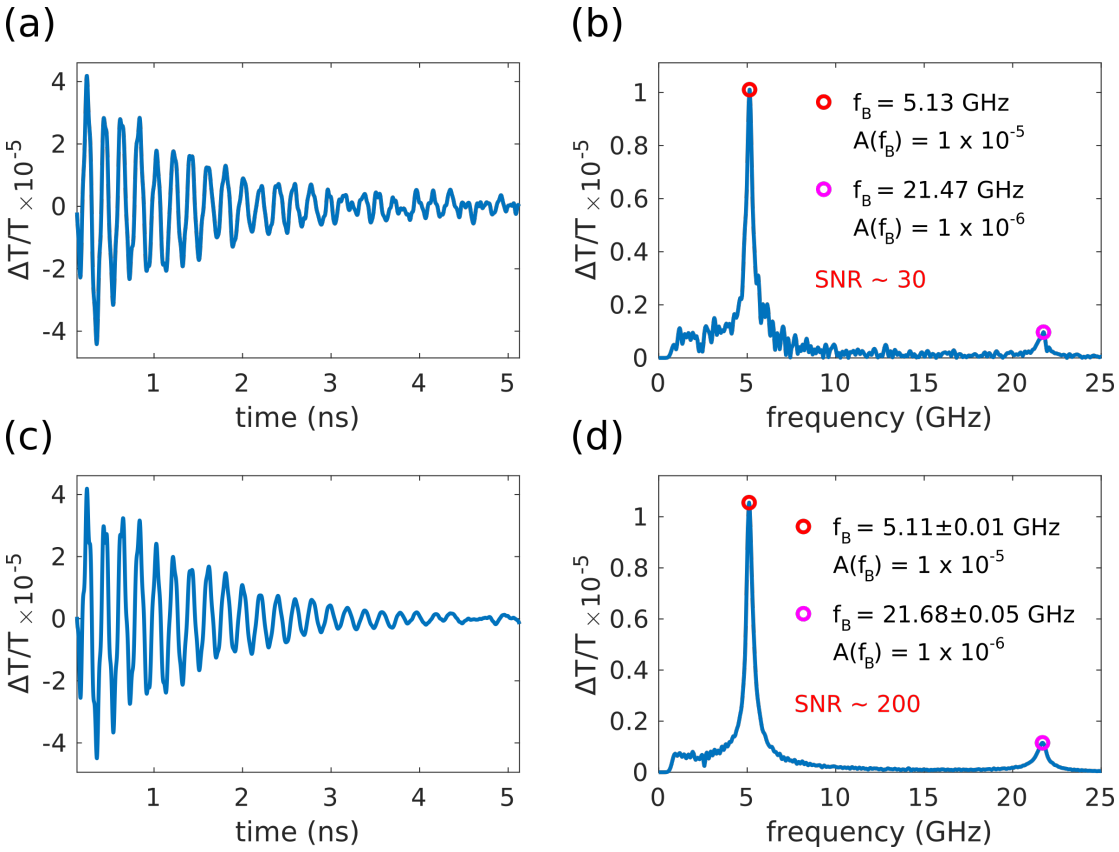


Figure 4.11: (a) Transmittance modulation depth using one count of $30k$ oscilloscope averages for demonstration purposes. (b) Fast Fourier transform of (a) which provides the frequency spectrum of the oscillation. Absolute (red circle) and local (pink circle) maxima can be located in order to characterise the elastic signature of the sample. In this example, $5.13\ GHz$ and $21.47\ GHz$ frequency peak ($A(f_B)$) locations have been identified and correspond to the Brillouin frequency shifts (f_B) in water and glass respectively. (c) Additional averaging of (a) using the mean signal of 60 sequential measurements. (d) The corresponding frequency spectrum to (c) displays similar amplitudes and f_B characterisations, $f_B(H_2O) = 5.11 \pm 0.01\ GHz$ and $f_B(SiO_2) = 21.68 \pm 0.05\ GHz$, as does (b); albeit the increased averaging has improved the SNR by a factor of ~ 7.

padding the signal to interpolate the frequency sampling rate, which will be discussed in Section 5.2.3.

Characterising the most prevalent amplitude in the frequency domain, is the equivalent of characterising the strongest amplitude phonon frequency. Experimentally this is achieved by simply searching the frequency spectrum of the signal in the window of interest, e.g. $0-30\ GHz$, for the maximum amplitude value using a basic max-locating algorithm (Matlab). This can also be aided by using a user-defined threshold below which max-amplitudes are not measured. Figure 4.11b reveals the frequency spectrum of the time-resolved signal in Figure 4.11a (same as Figure 4.10h) attained with a zero-pad of 2^{16}. Two separate windows - $f < 15\ GHz$ and $f > 15\ GHz$ - were used to find frequency peaks at $5.13\ GHz$ and $21.47\ GHz$ which displayed modulation depth amplitudes of approximately 10^{-5} and 10^{-6}. These two frequencies can be identified as the Brillouin frequency shifts ($f_B = 2nv/\lambda$) of the $\lambda = 780\ nm$ probe laser in water and the glass of the transducer substrate, respectively.

The modulation depth measurement in Figure 4.11a was attained using $30,000$ oscilloscope averages. This was repeated 60 times resulting in 60 separate measurements. These measurements can be averaged in post-processing to increase the SNR of the technique. Figure 4.11c shows the result of this operation, and its corresponding frequency spectrum in Figure 4.11d. By increasing the averaging from $30k$ to $1.8M$, the SNR of the f_B-water amplitude was estimated to increase by a factor of 7.1 which matches the expected value of $\sqrt{60} \approx 7.7$. Furthermore, the standard deviation of the 60 frequency peak location measurements can be calculated, resulting in Brillouin frequency shift characterisations of $f_B = 5.11 \pm 0.01\ GHz$ and $f_B = 21.68 \pm 0.05\ GHz$ for water and glass respectively.

Signal amplitude modulation

Once the dominant signal frequency has been identified (f_B), this can be used to extract additional information from the time domain as it pertains to the rate of signal decay. As recently demonstrated [200], signal attenuation in opto-acoustics can occur by both optical and acoustical means; therefore, one must exhibit caution when attributing the source of the attenuation effect. However, for the case of low NA provided by the optical fibre, signal attenuation will be dominated by acoustics [200]. In any case, the rate of generic signal attenuation can be estimated by using an iterative minimum-value search algorithm. The goal is to empirically construct an equation for the TRBS signal, which is assumed to be an exponentially decaying sinusoid:

$$S(t) = A + Bsin(2\pi f_B t + \phi)e^{-\alpha v t} \tag{4.1}$$

where A is a vertical offset, B the sinusoid amplitude, α the attenuation rate, and v the sound velocity in the medium (e.g. water). In order to numerically determine the parameters in Equation 4.1, a series of guesses are defined by the user for the following quantities: (1) experimental signal frequency ($f_B \approx 5\ GHz$), (2) offset ($A = 0$), (3) amplitude ($B =$ amplitude of modulation depth), (4) phase offset of the sinusoid ($\phi = \pi$), and (5) the decay rate ($\alpha \approx 0.5\ \mu m^{-1}$ [201]); the guesses for quantities (1) and (3) can be formulated through inspecting the FFT-spectrum, and even (5) as with conventional Brillouin spectroscopy. The algorithm then iterates through permutations of these parameters, until the minimum residual error is located between the experimental signal and Equation 4.1. Figure 4.12 shows the result of this process for the example of the modulation depth in Figure 4.10h (blue - experimental and cyan - fitted). Furthermore, the approximate signal attenuation rate α can be calculated $\alpha \approx 0.4\ \mu m^{-1}$ and is within reasonable agreement with literature [201].

The time domain signals presented thus far can be converted into the 1D spatial domain, i.e. $z = vt$ (x-axis in Figure 4.12), providing a ruler with which to make in-depth spatial measurements (in the direction perpendicular to the fibre end-face). The ticks on this ruler, and therefore the axial resolution, will be determined by the acoustic wavelength, which at GHz is sub-optical. If there is *a priori* information that there is only

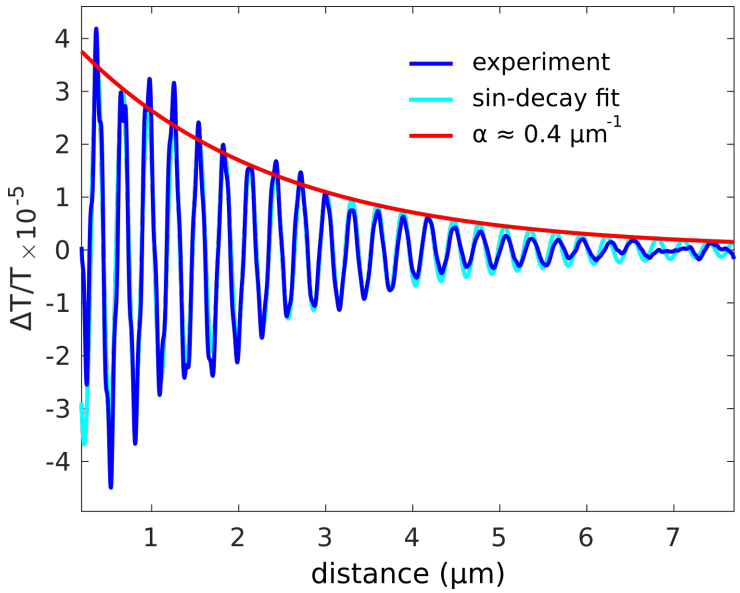


Figure 4.12: The attenuation of the TRBS signal can be determined by numerically deriving an expression for a decaying sinusoid which matches the characteristics of the experimental signal. The algorithm is passed a set of user-defined guesses for the signal expression in Equation 4.1, and then locates the combination of parameters which minimises the error between experiment (blue curve) and fit (cyan curve). The signal attenuation rate for this example was calculated to be $\alpha = 0.4\ \mu m^{-1}$ which agrees with values found in literature [201]. Time-domain has been converted into 1D spatial-domain using the fixed relationship between distance and time, $z = vt$ assuming that the sound velocity of the medium is known and constant.

a single medium within the measurement window, e.g. water, and the sound velocity of this medium is known, then the entire time-vector can be converted into an evenly spaced spatial-vector. However, if there exists a spatial variation in sound velocity, e.g. if there is a boundary between two materials, then the following criteria must be met:

- the two sound velocities must be measured by identifying Brillouin frequency peaks in the Fourier domain (given *a priori* information that refractive index is constant or characterised for each material).
- the position of the instantaneous change in velocity must be localised - such that the discretisation of the spatial domain in each material i can be defined $\Delta z_i = \Delta v_i t$.

The following section will introduce a time-frequency analysis technique with which these criteria can be met towards the application of the phonon probe to profilometry and 3D imaging.

4.2.2 Time-frequency analysis: wavelet transform

If the measurement volume of phonon microscopy, and now by extension the phonon probe, contains a transition in the local sound velocity and/or refractive index, this will manifest as a change in Brillouin frequency. This frequency modulation could be due to a change in material or a change in the state of a single material. The existence of this effect can be confirmed by simply taking the Fourier transform of the entire time-length of the TRBS signal, where multiple frequency peaks will be revealed and characterisable. For example, Figure 4.13 shows a result from the PLU-model, where beyond the transducer there lies a boundary between water and polystyrene (PS) (Figure 4.13a). The change in the frequency of the sampled phonon can easily be seen in the time-domain (Figure 4.13b), and is quantitatively confirmed by analysing the two frequency peaks in the Fourier spectrum (Figure 4.13c): $f_B(H_2O) = 5.1\ GHz$ and $f_B(PS) = 9.3\ GHz$. However, simply characterising the frequency peaks in the Fourier domain does not provide spatial information about the change in material, as is obvious in the time-domain.

In order to attain the time-dependency of the frequency-variation in the harmonic TRBS signals, a suitable time-frequency analysis tool should be used. In this study, the continuous wavelet transform (CWT) will be used to perform this type of analysis. Compared with other techniques, such as short-time Fourier transform (STFT) and zero-crossing analysis (ZCA), there are unique advantages to using CWT. The qualities of STFT and ZCA methods will be very briefly summarised:

- STFT - effectively the entire length of the signal is segmented into slices of Δt within which separate Fourier transforms are performed. The size of the Δt window determines the frequency resolution of the technique $\Delta f \sim 1/\Delta t$. Therefore

there exists a fixed trade-off between time-resolution and frequency-resolution [202].

- ZCA - very easily performed and understood method where the instantaneous period of a sinusoidal signal is determined by tracking when the oscillation crosses amplitude $A = 0$. This technique is easily contaminated by both high frequency noise (false zero-crossing events) and low frequency noise (mean peak-to-peak amplitude dislocating from $A = 0$). Furthermore, ZCA is only capable of providing frequency measurements and not the relative amplitude of the wave at the detected frequency [203].

CWT is a process by which a time-varying signal $f(t)$ (e.g. the TRBS signal) is band-

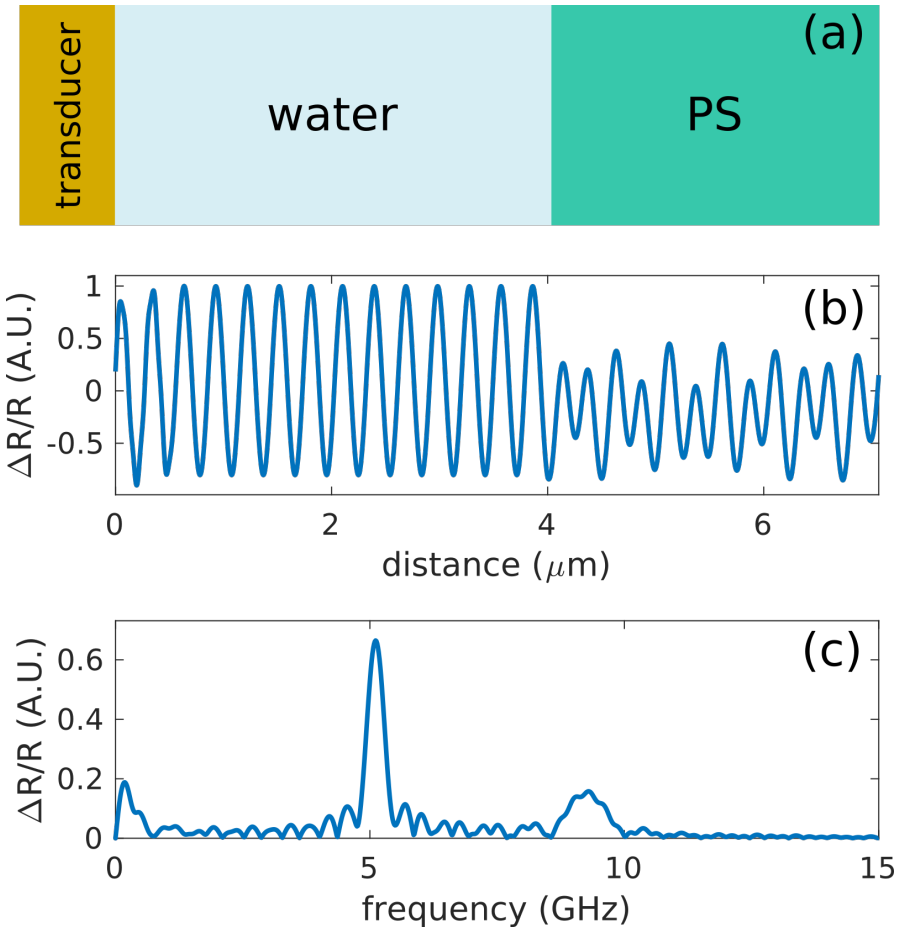


Figure 4.13: (a) Example of a sample volume in which a change in detected Brillouin frequency can be observed as the probe beam transitions from Brillouin scattering in the water to the polystyrene (PS). (b) The mesh architecture in (a) was used to simulate the reflectance TRBS signal (x-axis converted from time to axial distance) using the PLU-model. (c) FFT of the modulation depth in (b) revealing frequency peaks at $f_B = 5.1\ GHz$ and $f_B = 9.3\ GHz$ which are characteristic of water and PS respectively. The existence of multiple frequency components can be easily observed in the time/spatial (b) and frequency domains (c), however, time-frequency analysis allows the position of this transition to be quantitatively analysed.

pass filtered by the impulse response $\Psi_{a,b}(t)$ [202, 204]:

$$\Psi_{a,b}(t) = \frac{1}{\sqrt{a}}\Psi\Big(\frac{t-b}{a}\Big) \tag{4.2}$$

This impulse response, is referred to as the *mother wavelet* of the transformation. Starting with an arbitrary mother wavelet found in Figure 4.14a, the dilation parameter a will control the scale of the wavelet, i.e. the centre frequency (f_c) $a \sim f_c^{-1}$. This mother wavelet is then transformed with a signal of interest (blue line in Figure 4.14b) at each position in time as it translates across the trace (at a rate b). This transformation produces a set of wavelet coefficients (C_w), similar to how a Fourier transformation results in a set of Fourier coefficients:

$$C_w(a,b) = \int_{-\infty}^{\infty} f(t)\Psi_{a,b}(t)dt \tag{4.3}$$

The wavelet coefficient at each time position will then reflect the amplitude of the signal at f_c (Figure 4.14c); or if a range of scales a are passed through the transformation, the technique can produce a spectrogram of the time-varying frequency spectrum as presented in Figure 4.14d.

One of the main benefits of CWT, is the finite nature of the mother wavelet, as opposed to the series of infinite sine waves used in Fourier transforms (and STFT). As seen in Figure 4.14a, the envelope of the wavelet is non-zero for a finite duration in time. This allows the time-resolution of the technique to scale with the centre frequency of the wavelet, when the envelope is defined by a fixed number of cycles, unlike STFT. This concept is shown in Figure 4.15, where the time resolution (indicated by the full width at half maximum) of each wavelet increases as the wavelet centre frequency increases. Furthermore, as the envelope width of the wavelet varies with centre-frequency, so too does the frequency bandwidth of this envelope due to the reciprocal relationship between time and frequency $\Delta f \sim 1/\Delta t$. Therefore, as time-resolution increases, frequency-resolution decreases, and vice versa (Figure 4.15) [204, 205]. This is an especially useful feature of CWT which is unavailable to STFT and ZCA. However, there is a double-edged sword in that low frequencies cannot be measured with great time-resolution and measuring small changes in frequency at high frequencies will be sub-optimal (more detail below).

There exists a range of mother wavelet types, each suited to a particular set of applications. For the time-frequency analysis of harmonic signals, a mother wavelet with smoothly varying oscillation features (i.e. continuous derivatives) will be ideal as this will match the relatively smooth oscillations of a phonon field. One example that meets this criterion, and the wavelet of choice for this study, is the complex Morlet (cMor). The cMor is constructed by applying a Gaussian envelope to a complex exponential (as seen in Figures 4.16a-b):

$$\Psi_M(t) = \sqrt{\pi f_b} \cdot e^{-\frac{t^2}{f_b}} \cdot e^{i2\pi f_c t} \tag{4.4}$$

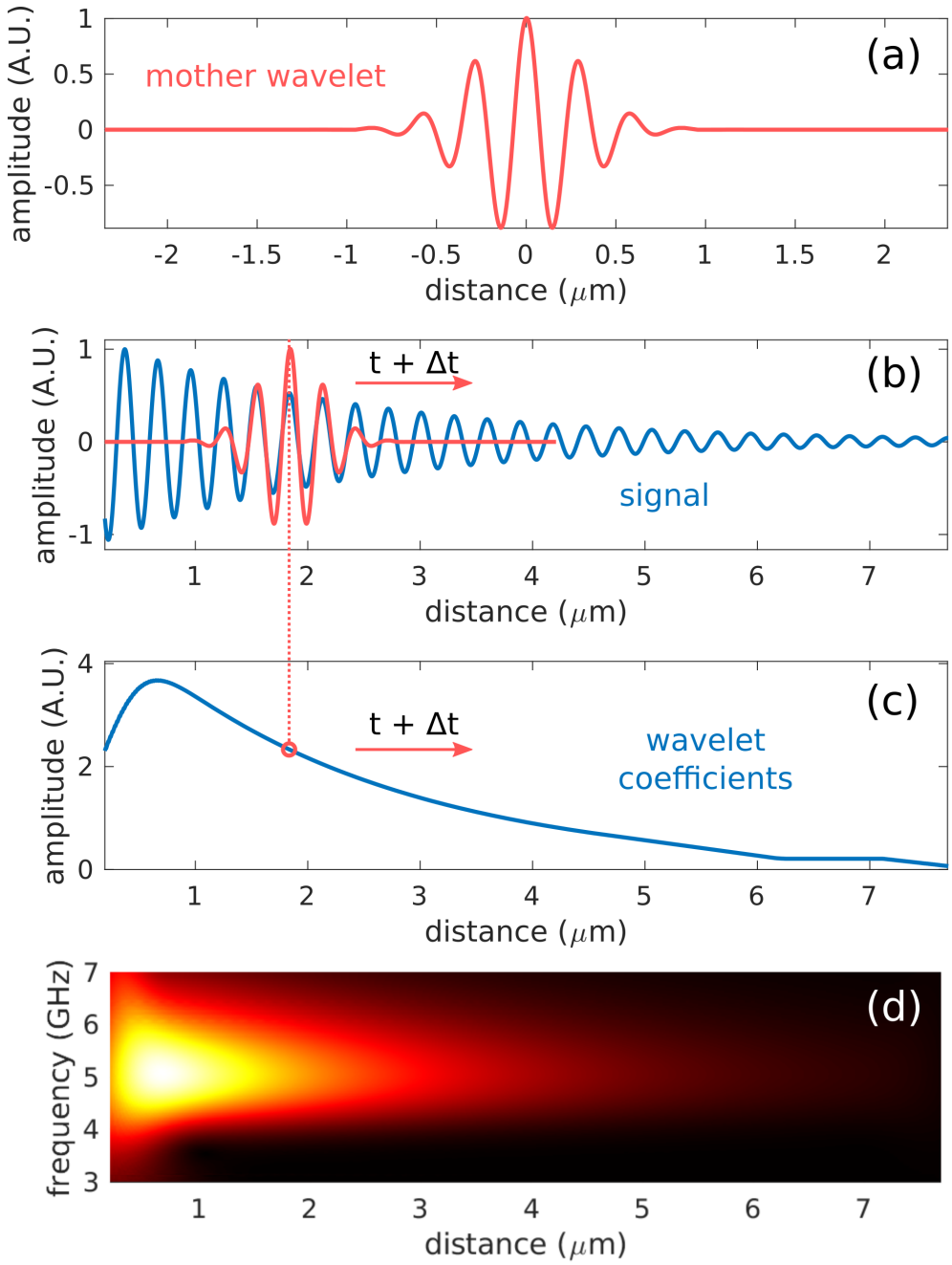


Figure 4.14: (a) Basic example of a mother wavelet used to wavelet transform the time-signal of interest. The centre frequency of this wavelet is scaled by a dilation parameter *a* which allows different variations of this mother wavelet to sample different frequency content within the time-signal. The transformation of this wavelet and the time-signal (b) is then translated across the temporal extent of the signal. The integral under the curve of the signal-mother product (at a single slice in time) can then be used to analyse the amplitude of the centre-frequency at that position in time (c). In this case, the amplitude decay at 5 GHz in Figure 4.12 (cyan line) is recovered. (d) Varying the dilation parameter produces a spectrum of frequency-amplitude as a function of signal time.

where f_c is the centre frequency and f_b is a bandwidth parameter for the wavelet, which is equivalent to the standard deviation of the Gaussian [205]. This family of wavelets also provides unique benefit in that the mother contains an analytical solution; the complex nature of the wavelet preserves the phase of the signal and transformation, whereas taking the complex magnitude of the wavelet coefficients reveals the amplitude roll-off in Figure 4.14c.

Consistent with the general definition of a wavelet in Equation 4.2, the cMor can be scaled in frequency (Figures 4.16c-d) in order to analyse the specified frequency window. The width of the Gaussian envelope of the cMor can also be used to change the bandwidth of the wavelet. As seen in Figures 4.16e-f, changing the bandwidth parameter of the mother wavelet permits more or less periods of the complex exponential to contribute to the transformation. This provides a route to to optimising time-frequency

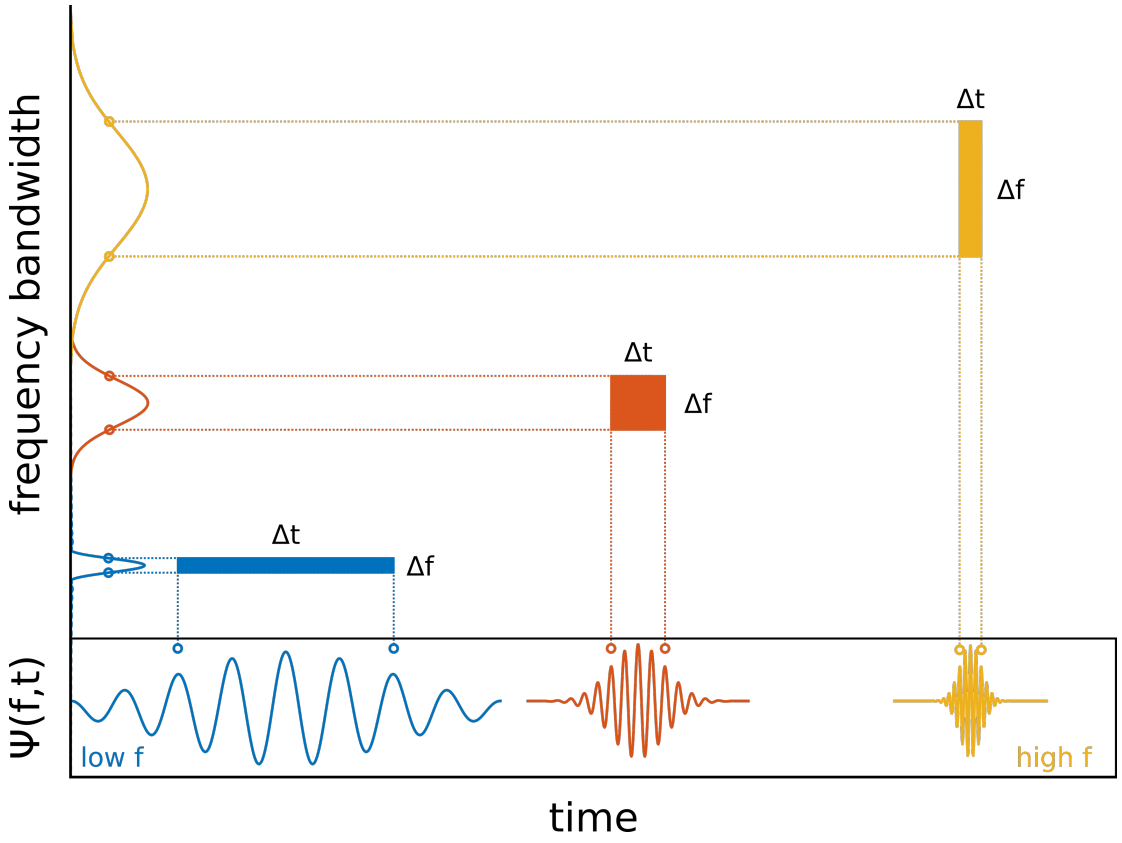


Figure 4.15: Visualisation of the time-frequency resolution relationships provided by continuous wavelet transforms. Since the mother wavelet spans a finite time-length, the time-resolution of the transformation scales with centre-frequency (length defined by fixed number of cycles). In other words, the more compact nature of a higher frequency wavelet (yellow wavelet) means that they can sample rapid variations in the signal frequency. However, this comes at the cost of frequency resolution. By taking the Fourier transform of the low-frequency envelope of each wavelet, the frequency-bandwidth of the wavelet is determined (y-axis) and reveals a reciprocal relationship between time and frequency resolution given an envelope width of a fixed number of cycles.

resolution, albeit with the same trade-offs as mentioned previously.

Using the experimental TRBS signal presented throughout this section (Figure 4.10h), the effect of mother wavelet bandwidth can be observed in Figure 4.17. In each row the wavelet bandwidth is fixed, and the centre frequency varied over the window $f_c = 3 - 7\ GHz$; when the mother wavelet contains fewer periods of oscillation (Figure 4.17a-b), the spectrogram rapidly responds to the amplitude decay of the signal along the x-axis, but does so with poorer frequency resolution as seen by the spread along the y-axis. Conversely, when the envelope of the mother is widened (Figure 4.17e-f) the frequency resolution in the spectrogram becomes noticeably narrower, yet the length of

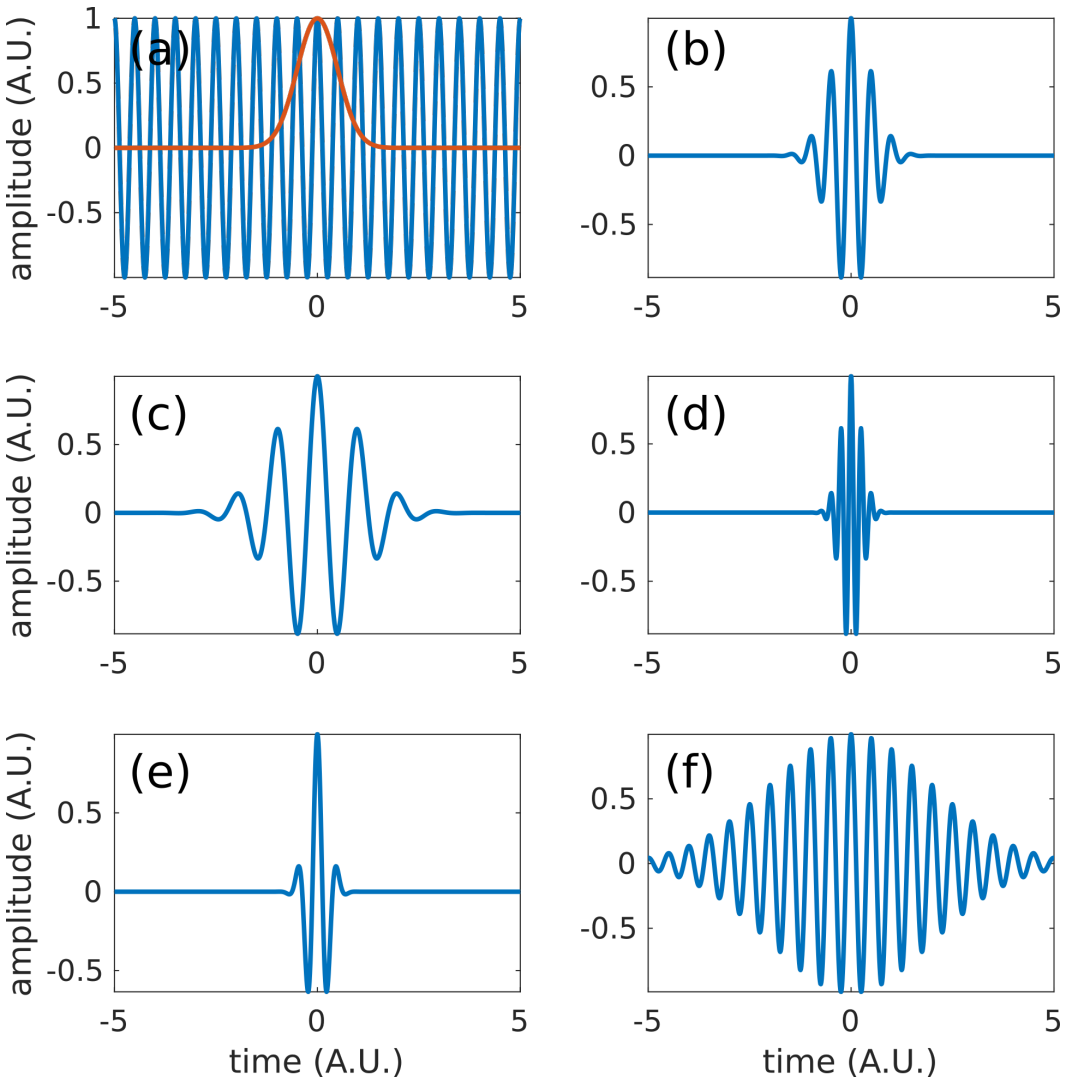


Figure 4.16: A complex Morlet mother wavelet is constructed by multiplying a Gaussian envelope (orange) with a complex exponential (blue, only real portion showed), resulting in the waveform found in (b). This wavelet can be stretched (c) or compressed (d) in the time-domain by changing the centre-frequency of the complex exponential and thus the wavelet, while maintaining a fixed number of cycles. Additionally, the centre-frequency can be fixed and the bandwidth of the waveform can be decreased (e) or increased (f) by changing the width of the Gaussian envelope, offering routes to increase time-resolution (e) or increase frequency resolution (f) for a given centre-frequency.

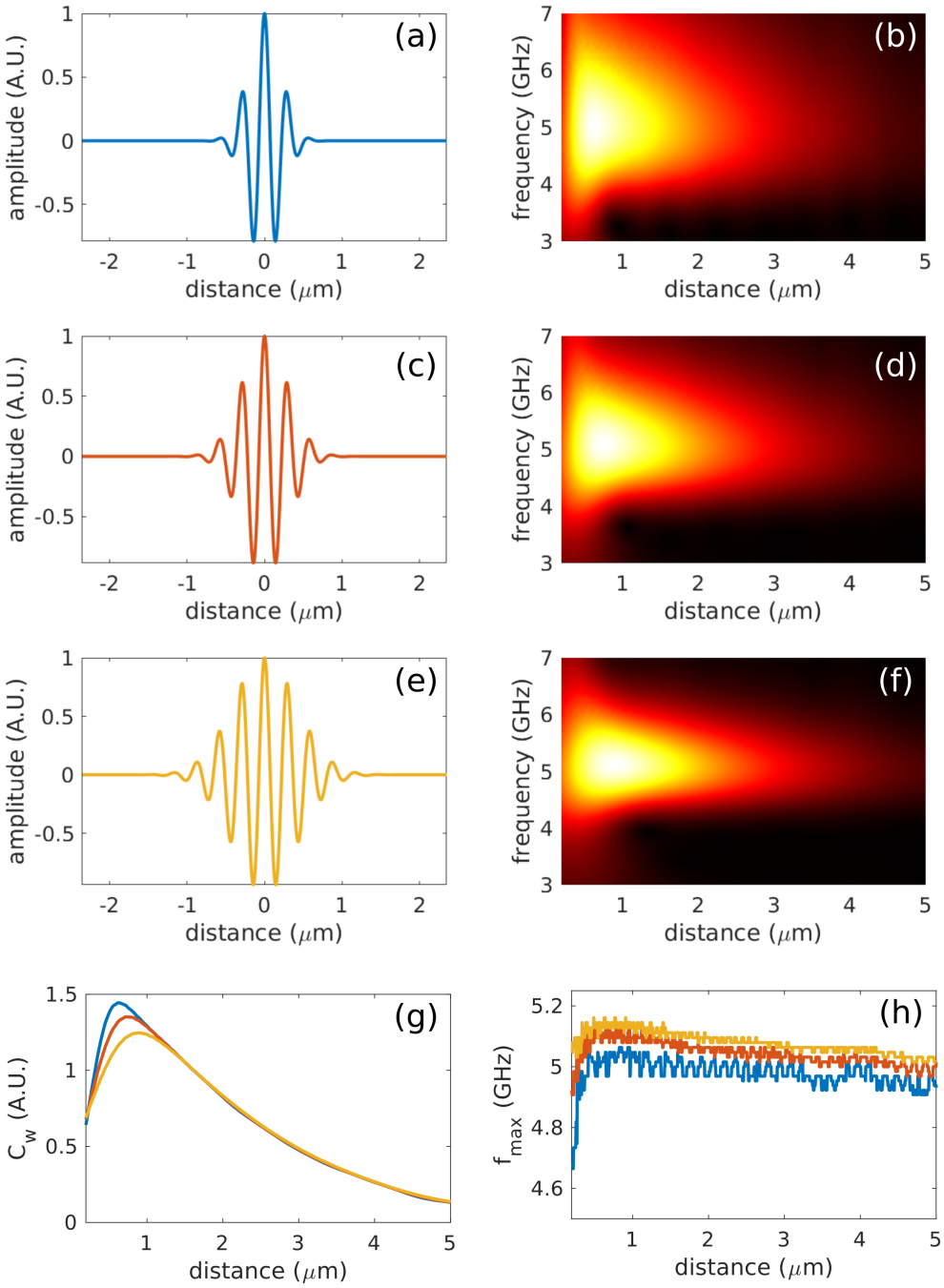


Figure 4.17: The effect of wavelet bandwidth, or the number of sinusoidal cycles, in time-frequency analysis of the TRBS signal in Figure 4.14b. The transition from using a mother wavelet with few cycles (a) to many cycles (e) corresponds to progressively worsening time resolution (and spatial resolution through $z = vt$), yet progressively improving frequency resolution as seen in the spectrograms in (b) through (f). (g) Tracking the change in amplitude (wavelet coefficient) of a single centre-frequency as a function of signal-time and wavelet bandwidth. (h) Tracking the change in frequency which contributes the maximum amplitude to the signal. Both (g) and (h) confirm that faster processes can be observed using a wavelet with fewer cycles, yet there is greater SNR and frequency resolution when using a wider wavelet.

the wavelet is less conducive to resolving sharp changes in amplitude. Figures 4.17g-h display: (g) the time-varying amplitude at the centre frequency of the signal (e.g. $\approx 5\ GHz$), and (h) the maximum amplitude frequency along the time-of-flight, both as a function of wavelet bandwidth. In both cases the shortest length wavelet (blue colour) provides the sharpest response to changes in amplitude. However, in both cases it does so with lower SNR, and thus less accuracy in characterising frequency, than does the wider wavelet (yellow colour). Ultimately, the optimum choice in mother wavelet parameters will depend on the question being asked by the user. If information about rapidly varying features of the acoustic wave is desired, and SNR can be sacrificed, then using more compact wavelets is ideal. If however, very precise frequency measurements are desired, especially towards the end of the signal (when SNR worsens with attenuation), then more dilated wavelets should be used.

Wavelet processing will allow the phonon probe to access in-depth information about an object or environment with unprecedented axial resolution compared with conventional optical and acoustic endoscopes. In particular, the information gained from wavelets will be used to observe physical processes that induce changes in the centre frequency of the signal or the amplitude of a single carrier frequency. Examples of these physical changes are: thermo-optic and thermo-acoustic changes in the Brillouin frequency as a function of axial-distance away from the probe, or, a sudden change in sound velocity and refractive index as one material transitions into another material (such as the modelled scenario in Figure 4.13). The latter is of particular interest, as the phonon probe is brought near to a photoelastic object (such as a biological cell or a polymer microstructure), the time-variations of the detected Brillouin frequencies provide a mechanism for imaging the object in 3D as well as characterising its elastic properties. An example of this potential is presented in Figure 4.18b-c; the decay of the low frequency carrier wave is accompanied by the rise in amplitude of a high frequency response from the polymer (seen in both the spectrogram and wavelet coefficient trace); both of these transition responses offer an opportunity to perform a distance measurement from the position of the fibre transducer tip to the object. In Chapter 6 these concepts will be more thoroughly defined and developed in an imaging context.

This section has introduced the basic signal processing methodologies for a time resolved Brillouin scattering experiment. The photodetector captures both elastically and inelastically scattered photons, the latter occurring through Brillouin scattering (not considering Raman scattering). Since only 1 out of every 10^6 photons captured by the detector are inelastic (and contain the desired TRBS signal), signal amplification and signal averaging are important tools for observing TRBS. The raw signal from the oscilloscope contains a number of artefacts which are treated in post-processing to isolate the time-of-flight waveform of the phonon that was sampled through TRBS; this

processed signal is called the modulation depth ($\Delta R/R$ or $\Delta T/T$), which has been normalised by the mean transmissivity or reflectivity throughout the exposure (elastically scattered light level). Quantities related to material properties, such as the Brillouin frequency and attenuation rate, can be extracted through Fourier transform and amplitude decay fitting, respectively. A key method for tracking the amplitude of the TRBS signal in the time-domain is by wavelet transforming the signal; this also allows the instantaneous Brillouin frequency along the time-of-flight to be analysed. These principles will be utilised, and in some cases further developed, in the following chapters for the purposes of spectroscopy and 3D profilometry.

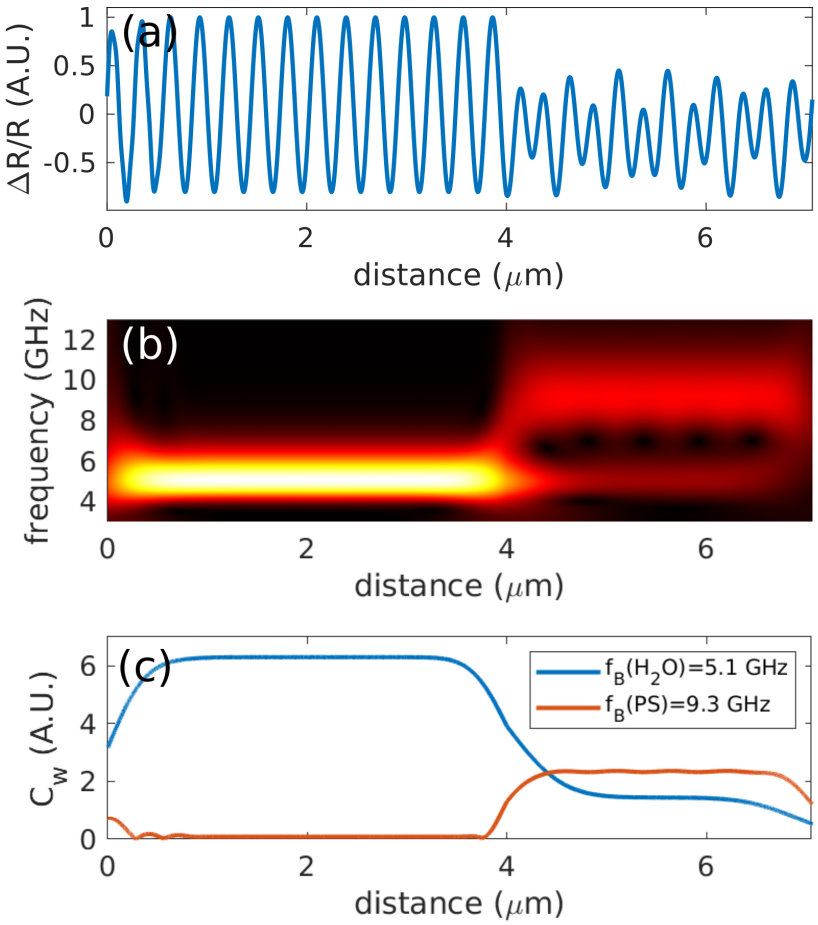


Figure 4.18: Continuous wavelet transforms and complex Morlet wavelets permit a time signal with variations in frequency (a), such as the modelled transition in TRBS signal from water to PS (in Figure 4.13), to be analysed in the time-frequency domain. (b) Spectrogram showing the spectrum of frequencies sampled from (a). The two peaks in the Fourier domain (Figure 4.13c) are replicated in the spectrogram. Acoustic impedance mismatch between the first and second material will cause reflections of the $5\ GHz$ mode which co-propagate in signal-time with the high frequency mode (seen as beats for $z > 4\ \mu m$ in (a) and a faint $5\ GHz$ band in (b)). (c) The relative signal amplitude at each frequency can be tracked independently and will be used in Chapter 6 as a mechanism for 3D imaging of microscopic objects. The initial rise and fall of the blue and orange curves at $z \approx 0$ occur when the wavelet has not fully entered the time-window.

Part III

Results

Chapter 5

Spectroscopy: time resolved Brillouin fibre-spectrometer

The field of Brillouin spectroscopy has begun to corroborate and reveal the importance of mechanical phenomena in biology. State of the art Brillouin spectrometers have been used to quantify changes in elasticity - in the human cornea [141], colorectal tumours [142], zebrafish spinal cord [145], Acanthamoeba cysts [180], and atherosclerotic plaque [143] - which govern the development and treatment of keratoconus, colorectal carcinoma, spinal cord repair, corneal infection, and Acute coronary syndrome, respectively. Among these techniques, *in vivo* operation has only been accomplished when the biological tissue of the specimen is sufficiently transparent to deliver and collect enough light to detect the faint effect of Brillouin scattering [139, 145, 146, 151]. Extrapolation of Brillouin spectroscopy to more diverse *in vivo* and clinical environments is challenged by $\sim 1\ cm$ maximum penetration depth of NIR-light in biological tissue (even shorter for $\lambda <$ NIR) [101].

Optical fibres are an ideal tool with which Brillouin spectrometers can be miniaturised and made portable; this would allow the measurement system to be deployed in standard medical equipments such as needles, endoscopes, catheters, and even scalpels which can be manoeuvred beyond optically opaque tissue barriers. However, the optical fibre presents inherent challenges for translating spontaneous Brillouin spectroscopy from microscope to endoscope. The strength of the Brillouin scattering process in the glass of the fibre itself dominates the response of the spectrometer. To solve this, multi-fibre and (recently) glass-less fibre configurations have been proposed using a GRIN lenses ($\approx 2\ mm$ diameter) [152, 153]. Currently these systems contain acquisition speeds on the order of $\sim 40\ s$ per spectrum and therefore are not readily applicable to real-time processes. Alternatively, TRBS uses the principles of laser ultrasound to increase the acoustic amplitude in the Brillouin interaction leading to greater scattering efficiency and a reduced scattering volume; the latter makes it possible to design a simple fibre-spectrometer with one single-mode fibre which is not dominated

by the glass response.

In this chapter proof of concept spectroscopy is demonstrated for a time-resolved Brillouin fibre-spectrometer. The device centres on the opto-acoustic fibre transducer designed and fabricated according to the principles outlined in Chapter 3. The experimental pump-probe ASOPS system described in Chapter 4 will facilitate the TRBS process which has been derived and modelled in Chapters 2 and 3 respectively. A novel fibre-optic system is presented as an extension of the pump-probe optical system described in Chapter 4. High resolution spectroscopic information from various liquids and environments will be extracted from TRBS signals using the processing techniques discussed in the previous chapter.

5.1 Optical fibre TRBS configuration

In Chapter 4.1.2 the basic pump-probe optical system (using ASOPS) was introduced; this general experimental design is utilised for cell imaging by phonon microscopy [168, 173, 180] and other TRBS-microscopy techniques [175]. Now the adaptation of this design for fibre optics will be discussed. After the pump and probe beams have been coupled from free-space to optical fibre (Thorlabs FiberPort), Thorlabs 780HP single-mode patch cables relay light into the remainder of the system. For the probe path, a splitter will be required to accommodate the following three ports: probe input channel (input port $\#1$), probe output channel with detector (input port $\#2$), and a common channel (output port). A Thorlabs 2:2 coupler (780HP single-mode fibre) was used for this purpose and carries the caveat that all through-transmission suffers a $3\ dB$ loss.

In order to combine the pump and probe beams into a common channel terminated by the fibre-transducer, a second splitter is required. Recall from Figure 4.9 that with two splitters the path for the probe beam is as follows: (1) transmission through splitter $\#1$, (2) transmission through splitter $\#2$ (now combined with pump) into fibre-transducer channel, (3) Brillouin scatter with sample, (4) back-reflected light re-enters the fibre, (5) transmission through splitter $\#2$, and (6) transmission through splitter $\#1$ where the detector is placed. To avoid a total $12\ dB$ loss for the probe beam (4 consecutive $3\ dB$ losses for a round trip through 2 splitters), a fibre-optic splitter containing a dichroic edge is desired. An optical fibre-based wavelength division multiplexer (WDM) from OZ Optics was identified which provided $< 1\ dB$ loss and a dichroic element with a transmission/reflection cut-off band of $\approx 720 - 740\ nm$. This solution requires that the pump and probe beams be sufficiently separated in wavelength to optimise the wavelength-dependent transmission and reflection through the WDM. Consequently, pump and probe wavelengths of $\lambda_{pump} = 730\ nm$ and $\lambda_{probe} = 780\ nm$ were selected; given the $\lambda = 700 - 900\ nm$ tuning range of the lasers (Chapter 4.1.2), the NIR side of the spectrum is preferred in order to combat acoustic attenuation (will be discussed

shortly). With the WDM, the probe beam can now make use of both input channels of the 2:2 coupler (probe in and probe out to detector), while efficiently coupling the pump beam, and outputting both to a common fibre (with transducer on tip). Furthermore, the WDM filters the pump wavelength from reaching the detector reducing its contribution to shot-noise. A simplified diagram of the optical system is shown in Figure 5.1.

A slight modification to the transducer design (compared with Figure 3.15 was made for the purpose of spectroscopy. A thin transparent layer of graphite was evaporated (carbon rod evaporation facility in the sputter coater) onto the top surface of the transducer in an effort to make the tip more hydrophobic, such that residual liquid did not linger on the tip when the transducer was placed in a dynamic environment, though this was not confirmed experimentally. This final design for the fibre-transducer is shown in Figure 5.2.

The first proof of concept for the fibre-spectrometer was achieved by simply dipping the tip of the fibre-transducer into a beaker of water. Initially 200 measurements (*counts*) were taken over the course of $\sim$12 minutes, with 10,000 averages per count (on the oscilloscope) at a rate of $\approx 3.5\ s$ per count, resulting in a total of two million averages. Figure 5.3 shows the averaged modulation depth for this experiment, and the corresponding frequency spectrum. The Fourier transform indicates that Brillouin scattering was detected at phonon frequencies of $5.223 \pm 0.004\ GHz$ and $22.0 \pm 0.1\ GHz$. These values are consistent with the Brillouin frequencies (Equation 2.24) for water and glass at the probe wavelength $\lambda_{probe} = 780\ nm$ and for normal probe incidence. The detection of $22\ GHz$ frequency phonons can be explained by TRBS that occurs for the

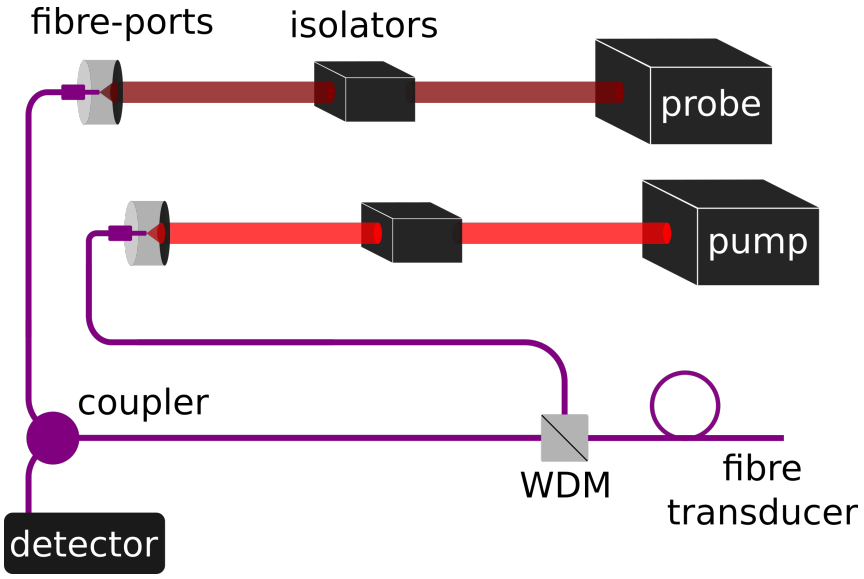


Figure 5.1: Optical design for the first time resolved Brillouin spectrometer containing a single optical fibre transceiver. Pump and probe wavelengths are coupled into a common channel using a 2:2 coupler and WDM in series. The probe signal (from the tip of the fibre) travels back through the system transmitting through the WDM and 2:2 ($3\ dB$ loss) before detection.

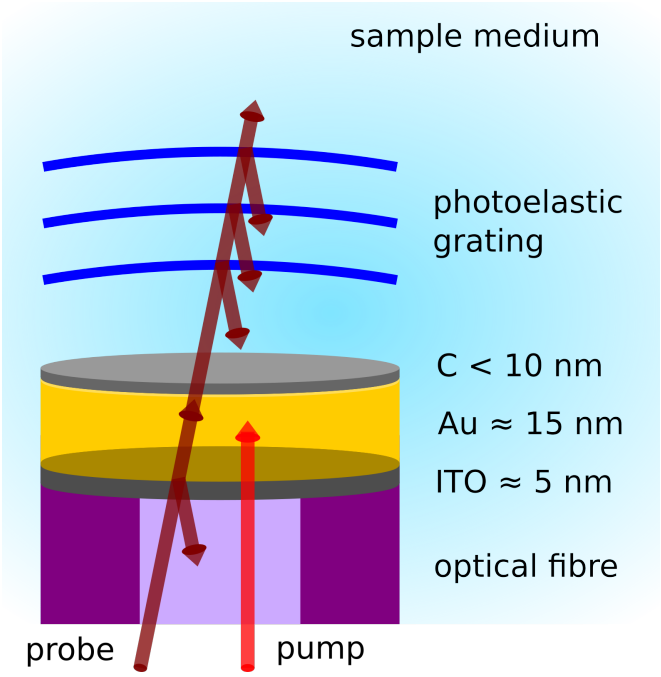


Figure 5.2: The original design for the phonon probe (Figure 3.15) was updated with a thin layer of graphite in an effort to make the fibre tip hydrophobic. Ultrasound is generated thermoelastically as the transducer absorbs the pump beam. The refractive index grating created through the photoelasticity of the sample medium causes Brillouin scattering with the probe beam (note the DC reflection from the glass/gold interface which serves as an interferometric reference beam in the TRBS detection scheme).

acoustic waves that travel from the transducer into the glass of the optical fibre core. In the frequency spectrum, the ratio between the amplitudes of the two Brillouin peaks is approximately 30; this can be explained by the relative difference in photoelasticity between the two materials, and the fact that the acoustic transmission coefficient between gold and water is greater than that of gold and glass.

In the ASOPS acquisition system, the signals are recorded in the time domain, with a total time window (per signal) of $12.5\ ns$. The measured Brillouin frequency can provide a measurement of the sound velocity assuming the refractive index is known ($n = 1.33$ for room temperature water): $v = 1532 \pm 1\ m/s$, which can be used to convert the time-domain of the signal to the spatial domain. Spatially, the acoustic wave propagates in water with a wavelength of $286\ nm$ (spatial period in the signal), which is in agreement with the Bragg condition $\lambda_{acoustic} = \lambda_{probe}/2n$.

The dark red line (in Figure 5.3a) represents the experimental material attenuation rate of the acoustic wave, $\alpha_{H_2O} = 0.369 \pm 0.002 \mu m^{-1}$, obtained using the fitting algorithm discussed in Figure 4.12. Acoustic penetration depth, and therefore the penetration depth of the TRBS signal, will strongly depend on this material attenuation rate, which in water has been reported as $\alpha = f^2 \cdot 19.1 \times 10^{-15} sec^2/m$ [201]; based on the experimental f_B the theoretical value for attenuation is approximately $0.5\ \mu m^{-1}$ which is within reasonable agreement with the experimental value. The light red shading behind

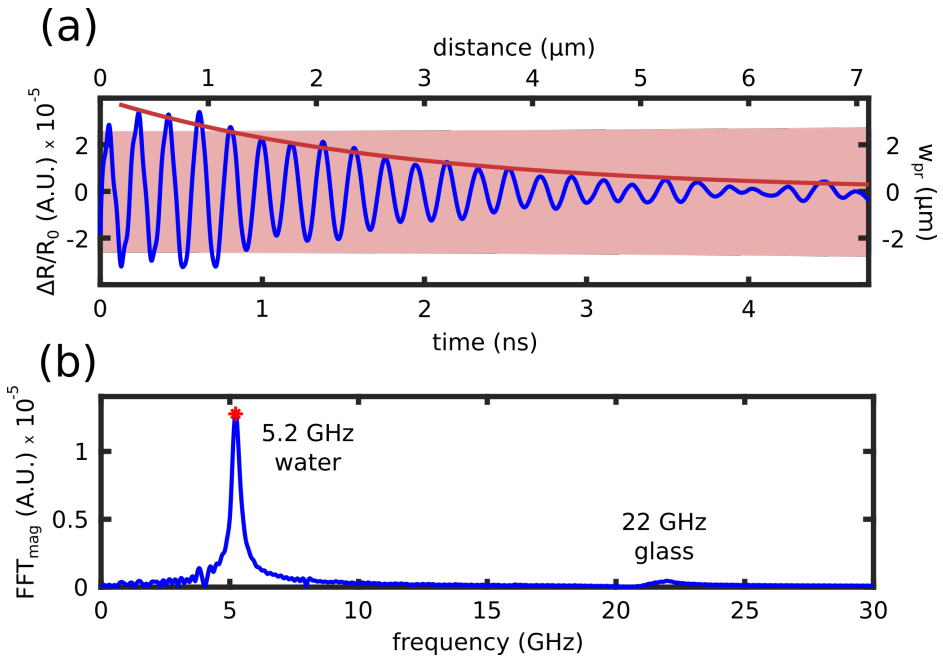


Figure 5.3: Proof of concept spectroscopy for the optical fibre based Brillouin spectrometer system. Performance was initially tested by dipping the fibre-tip into water. (a) The averaged modulation depth measured by the system. Red line indicates the experimental signal attenuation due to the inherent material attenuation of water: $\alpha_{H_2O} = 0.369 \pm 0.002\ \mu m^{-1}$. Light red shading and the right y-axis shows the divergence of the $780\ nm$ wavelength probe beam, which has exited an optical fibre with $N = 0.13$. (b) FFT of the above modulation depth showing spectroscopic measurements of $5.223 \pm 0.004\ GHz$ (characteristic of water) and $22.0 \pm 0.1\ GHz$ (glass). The red star shows the frequency location of the maximum FFT amplitude. Distance in (a) is measured using the Brillouin frequency, $v = 1532 \pm 1\ m/s$, i.e. the sound velocity of water.

the trace represents the slow divergence of the probe beam propagating away from the tip of the fibre-transducer. The low NA of the fibre $NA = 0.13$ ($\approx 46\ \mu m$ depth of focus) mitigates the effects of apparent attenuation - which occurs when the acoustic field propagates beyond the probe focal volume [200] - thus ensuring that only material attenuation limits the penetration depth.

Pump and probe average powers of $11\ mW$ and $3\ mW$, respectively, were used to perform this experiment, corresponding to an average power density of $\approx 0.7\ GW/m^{-2}$ in the $5\ \mu m$ diameter core. Since the pump beam is not hindered by a $3\ dB$ coupler, the power can be used to directly scale the SNR of the signal of interest. For the case of the water sample in Figure 5.3, an SNR of ≈ 60 was calculated. A particularly helpful by-product of designing an optical fibre-based pump-probe system, is the fact that both pump and probe beams are always “perfectly” overlapped ensuring the maximum signal level, thus avoiding overlap errors inherent to conventional free space systems.

It may appear as if it took 200 counts over 12 minutes to make a single spectroscopic measurement of water’s Brillouin frequency. However, the experiment can be reinterpreted as having made 200 spectroscopic measurements at an acquisition rate

of $\approx$ 3.5 seconds per count (time it takes for 10,000 oscilloscope averages). Using this approach, the frequency at which the maximum FFT amplitude occurs can be located for the signal of each count (the red star in the bottom of Figure 5.3), and tracked as a function of the total time of the experiment (12 minutes). Figure 5.4 shows the parsing of the frequency spectra data in Figure 5.3 allowing a read-out of the Brillouin frequency (blue line) versus experiment time.

In order to test the capabilities of the new Brillouin fibre-spectrometer, the device-tip was dipped in and out of water every 10 seconds while data were being acquired (see Figure 5.5). The oscilloscope was set to capture 1,000 oscilloscope averages every count, at an acquisition speed of $\approx$ 0.4 seconds over the course of roughly 80 seconds. Using the processing discussed above, the Brillouin frequency read-out oscillates between the frequency band at $5.24 \pm 0.02\ GHz$ (water) and the dimmer band at $22.1 \pm 0.2\ GHz$ (glass, which exists in all measurements, but only dominates the frequency spectrum when the tip is in air). The fibre-tip spent roughly 100 total measurements in water; after averaging these measurements an SNR of ~ 12 was calculated which is approximately $\sqrt{20}$ lower than the SNR obtained from the measurement

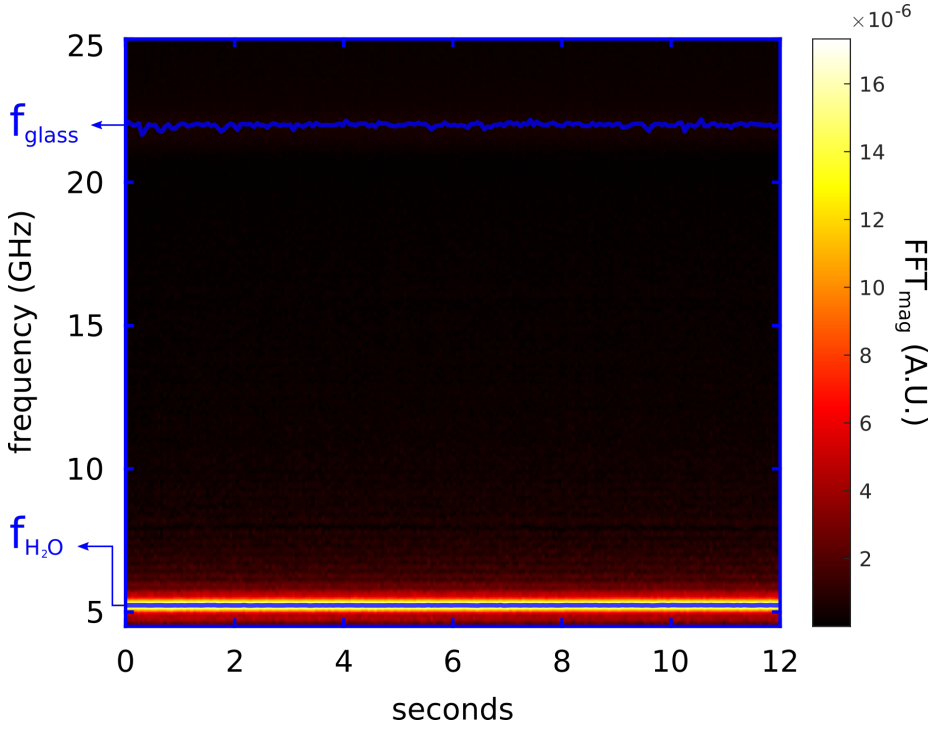


Figure 5.4: N averages can be used to provide a measurement with low uncertainty; however, the data can also be segmented into N spectroscopic measurements of the environment surrounding the tip of the fibre-transducer. This figure shows 200 slices of the Fourier spectra which contributed to the averaged spectrum seen in Figure 5.3 - frequency is now on the y-axis, experiment time on the x-axis, and colour as amplitude of each frequency spectrum. The semi-transparent blue line represents the location of the red star in Figure 5.3, the measurement of the Brillouin frequency as a function of time.

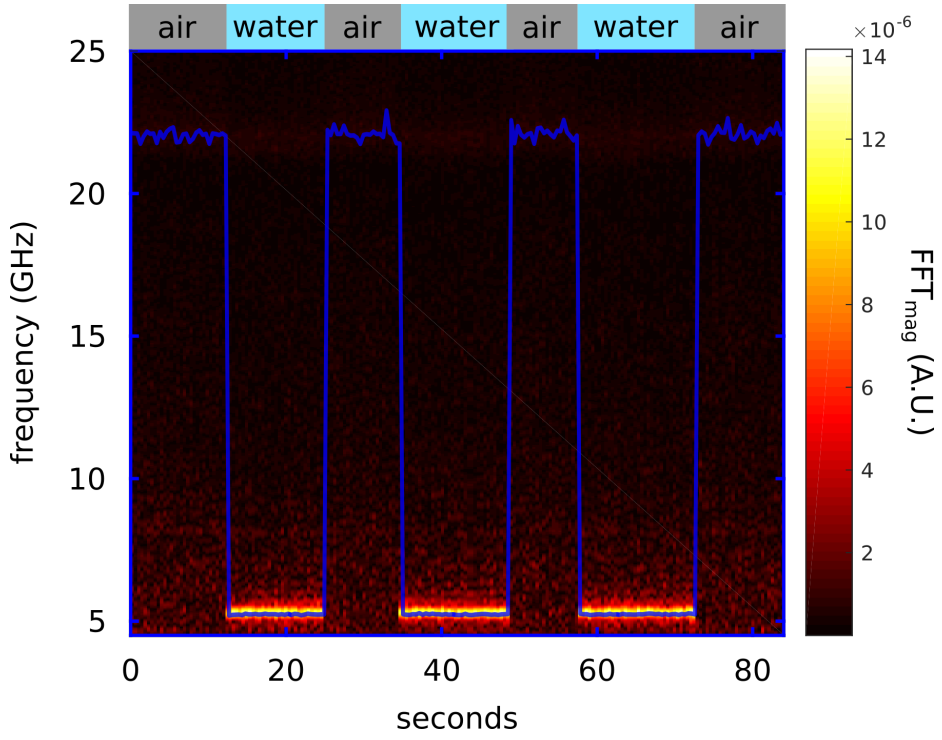


Figure 5.5: Processed frequency spectra of TRBS signals acquired at a rate of 0.4 seconds per measurement while the fibre-tip was repeatedly dipped and withdrawn from water. A lower number of averages was used in this result compared with previous experiments, which adversely affects the certainty of the measurement, but allows near real-time data acquisition for resolving phenomena which occur in shorter time-spans. When the tip is not immersed in water, the data processing interprets the always-present 22 GHz glass signal as being the detected Brillouin frequency.

in Figure 5.4. This highlights the trade-off between measurement precision and acquisition speed, which is now nearly real-time. Furthermore, the tip transition from water to air occurs in the frequency domain within the time of one count (0.4 s), which is a promising result for potentially spectroscopically resolving fast dynamic processes in the future.

This section has presented the first optical fibre system for the field of PLU. The introduction of the WDM to the fibre-optic system enables greater power transfer between input, sample, and detector than would otherwise be possible using 3 dB couplers. Further optimisations to the system are possible (discussed in 5.3) which could improve SNR for use when greater signal averaging is required or when acquisition speed is a priority. Proof of concept spectroscopy was performed in water with both high SNR and fast acquisition speed. The following section will focus on exploring different applications where the Brillouin fibre-spectrometer can be utilised to characterise various parameters related to the state of the medium or environment.

5.2 Spectroscopy applications

After demonstrating the feasibility of the optical fibre measurement system, it can now be applied to the probing of elasticity within liquid environments. With TRBS technology no longer limited to bulky microscope bodies, the measurement end of the phonon probe can be relocated into a wide range of environments without needing to adjust instrumentation. As it pertains to measurands, any process by which the refractive index and sound velocity of a medium is altered will induce a variation in the TRBS signal and Brillouin frequency measured by the device. Examples of processes which cause such optical and elastic fluctuations are changes in material identity, chemical changes, or fluctuations in the thermodynamic state of a system. This section will explore the performance of the probe for identifying and monitoring these phenomena.

5.2.1 Material characterisation

Recall from Chapter 2 that the optical frequency shift due to Brillouin scattering is given by Equation 2.24:

$$f_B = \frac{2nv}{\lambda_{probe}}$$

If either n or v are known beforehand, the experimental Brillouin frequency then provides a measurement of the other parameter. For example, many cellular media exhibit poor optical contrast due to homogeneity in refractive index; this permits the variation in sound velocity throughout the cell to be approximated by the Brillouin frequency shift. Similarly, if there exists *a priori* information about the state of the environment, e.g. that a particular solution is homogeneous and at room temperature, the experimental Brillouin frequency could serve as a signature for identifying certain photoelastic materials, provided that there is sufficient variation in the product $n \cdot v$ across materials (or states).

In order to test the sensitivity of the fibre-transducer in different media (other than water), a Brillouin cocktail was prepared (Figure 5.6b) consisting of glycerol and water (and air), which were poured and left to differentiate. The z-position of the fibre-transducer-tip was controlled via micrometre; during TRBS data acquisition (10,000 oscilloscope averages repeated over $\approx$ 24 minutes) the fibre tip was descended from air to water, water to glycerol, and then ascended back through the layers. The tip dwelled in each material layer for roughly five minutes in order to provide sufficient signal averaging; towards the end of the first water layer, the tip was slowly moved towards the glycerol layer in an attempt to resolve the change in Brillouin frequency. The time averaged TRBS signals from the first three layers of the cocktail can be found in Figure 5.6d, and the corresponding frequency spectra in Figure 5.6e. TRBS signals from all layers were processed using the same set of parameters, except for the polynomial order used to fit and subtract the thermal background response. For the first three layers the following Brillouin spectroscopic measurements were attained: 21.80 ± 0.04 GHz (Brillouin

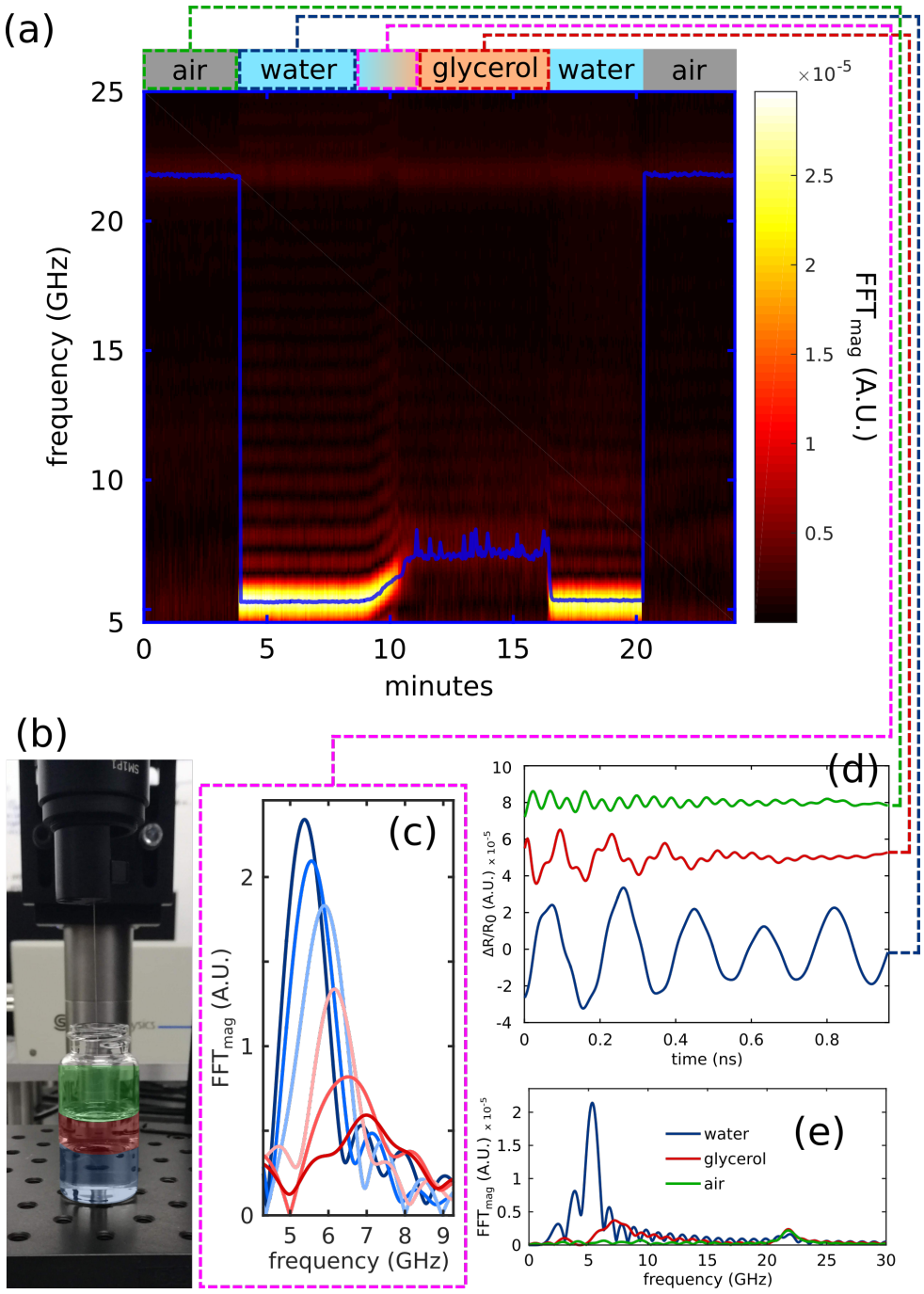


Figure 5.6: An experiment testing the dynamic performance of the fibre-transducer when presented with a sequence of different materials. The fibre-tip was continuously dipped from air to water to glycerol and back up. (a) TRBS signal frequency spectrum as a function of experiment time; light blue line represents the read-out of the Brillouin frequency, i.e. the position of the maximum FFT amplitude. (b) Picture of the fibre-spectrometer immersed in the Brillouin cocktail where the green, red, and blue false colours represent the air (glass), water, and glycerol layers respectively. (c) Successive frequency spectra as the tip transitions from water to glycerol. (d) Time-averaged TRBS signals from the first three layers of the cocktail and the respective frequency spectra; Brillouin frequencies of $21.80 \pm 0.04\ GHz$ (glass), $5.24 \pm 0.08\ GHz$ (water), and $7.20 \pm 0.28\ GHz$ were measured.

frequency of glass when the tip is in air), $5.24 \pm 0.08\ GHz$ (water), and $7.20 \pm 0.28\ GHz$. The latter of these measurements correlates with the theoretical value for the Brillouin frequency of glycerol, calculated (Equation 2.23) using refractive index and sound velocity data from literature [206, 207].

Tracking the TRBS frequency spectra versus experiment time (Figure 5.6a), and the frequency position of the maximum FFT amplitude (blue line), provides a read-out of the transient Brillouin frequency measurement. From Figure 5.6c, the transition of the frequency band centred on the Brillouin frequency is tracked as the probe tip is slowly moved from water to glycerol; a drop in amplitude can be seen along with a gradual shift to higher frequencies. A likely explanation for the gradual frequency shift, is that there exists mixing of the water and glycerol at the boundary, with the concentration of the faster glycerol increasing as the tip nears the bulk glycerol layer. Once in the more viscous glycerol layer, the acoustic waves attenuate rapidly - at an experimental rate of $\alpha_{gly} = 1.79 \pm\ 0.04\ \mu m^{-1}$ - which can also be seen as spectral broadening in the frequency domain.

In addition to glycerol, the transducer was tested in a $20\ \%wt$ solution of the common polymer polystyrene (PS) in toluene. As seen in Figure 5.7, the signal shares similar features with the $7.2\ GHz$ phonon measured in glycerol. Due to the viscosity of the solution, the amplitude of the sound wave dampens more quickly as the liquid resists deformation. A central Brillouin frequency of $4.67 \pm 0.27\ GHz$ and attenuation rate of $\alpha_{PS} = 1.75 \pm\ 0.07\ \mu m^{-1}$ were measured after one million total averages (of the TRBS signal); using values for the refractive index and sound velocity (as functions of concentration in toluene), the experimental Brillouin frequency expected was approximately $5.25\ GHz$ [208, 209]. The $0.58\ GHz$ deviation from the expected value could be due to a number of parameters: the molecular weight of the PS, under-sampling the wave due to attenuation, or perhaps an underestimation from values found in literature. For example, if the refractive index of 10,000 Mw PS in toluene ($20\ \%wt$) was confirmed to be 1.51, then the technique provides an experimental measurement of the sound velocity of $\approx 1206\ m/s$. However, in order for our measurement to provide quantitative value, information from at least one environmental condition should be known *a priori*, e.g. the refractive index, temperature, concentration, etc.

An interesting development path for the Brillouin fibre-transducer, is to determine whether it might be applicable to bio-liquids in various biomedical procedures. Such a device could have consequences in the performing of biopsies or surgical guiding (e.g. epidural procedures). As an initial proof of concept, anti-coagulated sheep's whole blood was purchased and subjected to measurement using the fibre-transducer. As the blood coagulated over time, the plasma started visibly differentiating from the rest of the cellular and platelet components. The transducer was immersed into this more transparent and aqueous plasma layer, and two million total averages of TRBS

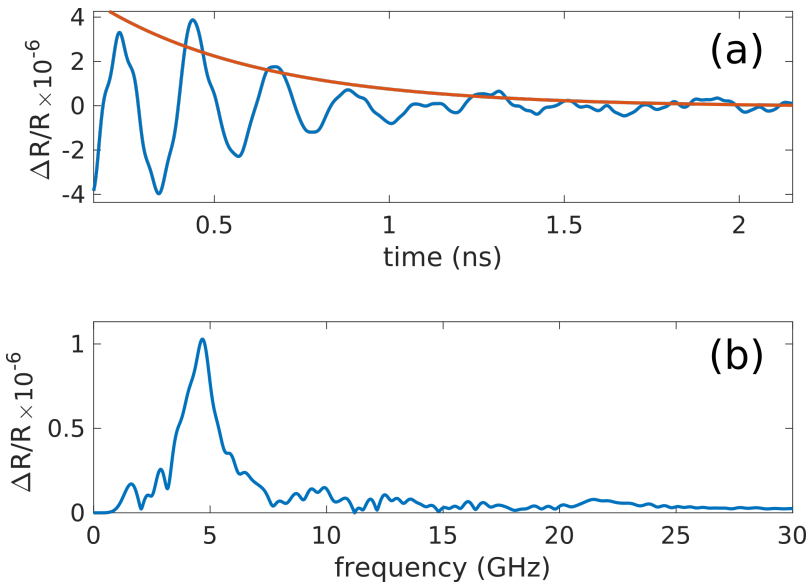


Figure 5.7: Spectroscopy performed from the tip of an optical fibre using time resolved Brillouin scattering on 20 $\%wt$ PS in toluene. (a) The viscosity of the solution results in a fast dampening of the TRBS signal (blue curve), at an attenuation rate of $\alpha_{PS} = 1.75 \pm 0.07\ \mu m^{-1}$ (orange line). (b) A Brillouin frequency of $4.67 \pm 0.27\ GHz$ was measured by the device.

signal was acquired over $\sim$ 12 minutes. Figure 5.8 shows the corresponding average modulation depth signal and Fourier transform, revealing an acoustic wave with centre-frequency of $5.5 \pm 0.2\ GHz$ and attenuation rate $\alpha_{plasma} = 0.7 \pm 0.3\ \mu m^{-1}$. Approximate values for the refractive index and sound velocity of blood plasma were taken from literature and used to calculate a theoretical Brillouin frequency of $5.34\ GHz$ [210, 211], which is within the experimental range of confidence. The short expanse of the time-vector in this signal was necessitated by the presence of a parasitic coincidence peak that occurs at $t \approx 1\ ns$ in the signal. This occurs when there exists an unwanted DC reflection within the fibre-optic path and can be mitigated through index-matching gel, or changing the length of fibre used in this specific phonon probe device. Consequently, there is increased experimental uncertainty and the true attenuation rate of the material is under-sampled. The fibre-transducer remains at an early stage of development, especially in the context of using it as a spectrometer in clinical applications; however even the limited success of this experiment reveals promise and a need to continue increasing SNR/acquisition speed and investigating compatibility with various liquids and tissues in the human body.

As a final example of the device's ability to detect Brillouin oscillations in various media, the transducer tip was dipped into a vial of gelatin-water solution during pump-probe exposure and data acquisition. Originally, the aim of the experiment was to evaporate the water over seven hours and look for shifts in the Brillouin frequency - e.g. from 5 to 7 GHz - as the gel matrix became stiffer and faster. Before the gelatin could fully harden, the fibre-tip rose above the level of the solution. When analysing

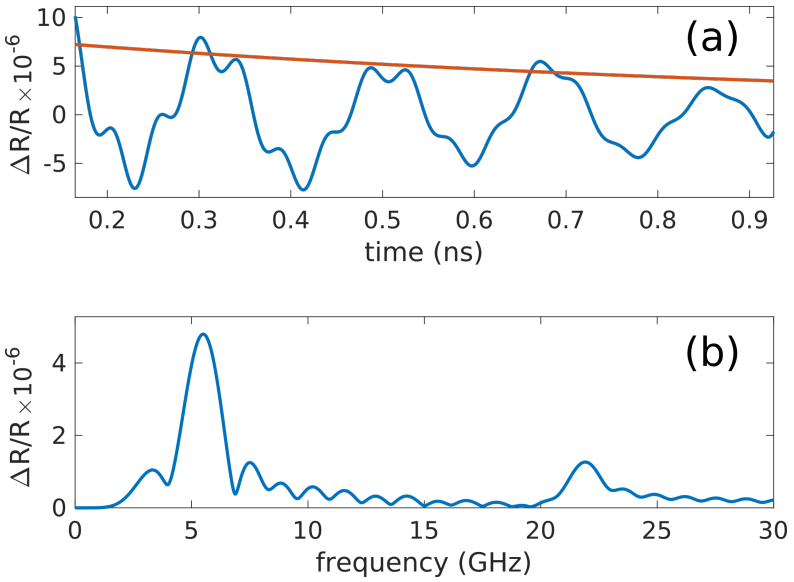


Figure 5.8: (a) Average modulation depth and frequency spectrum for the TRBS signals detected in blood plasma which had been differentiated from sheep's whole blood. The increased transparency and water content of the plasma, compared with anti-coagulated whole blood, makes for better detection of TRBS. (b) A Brillouin frequency of $5.5 \pm 0.2\ GHz$ was experimentally attributed to the blood plasma; an attenuation rate of $\alpha_{plasma} = 0.7 \pm 0.3\ \mu m^{-1}$ (orange line in (a)) was measured, however, this time trace was deliberately shortened in the time-domain due to the presence of an additional coincidence peak at $1\ ns$.

the TRBS signals up until the tip left the gelatin solution, an oscillating pattern in the detected Brillouin frequency emerged (shown in Figure 5.9a). This behaviour is dually seen in the B-scan of the modulation depth in Figure 5.9b. The most likely explanation for this 45 minute period variation in the experimental Brillouin frequency, is that the thermal cycling of the hot plate is imparting detectable changes on the refractive index and sound velocity of the aqueous solution (thermo-optic and thermo-acoustic effects, respectively). In the following section, the potential for utilising the Brillouin fibre-spectrometer as a thermometer will be explored further.

When the fibre-transducer enters a photoelastic medium with refractive index n_m and sound velocity v_m, the detected Brillouin frequency acts a type of signature for the identity of the material. This section has introduced the possibility of using the fibre-spectrometer as a tool for measuring unique differences in different materials, which could potentially be used for characterisation in the future. In this scenario, a catalogue of material identities and environmental parameters would be pre-arranged, and their respective refractive index and sound velocity data tabulated from literature. Then, by comparing the experimental Brillouin frequency with the literature values, an estimate can be made as to the identity of a Brillouin frequency. This method is not without caveats: sufficient uniqueness is required for the range of potential Brillouin frequencies, and certain environmental parameters must be well controlled. However,

for applications where the environment is closely monitored, or where contrast from a mean/expected value is of more importance, the device could be readily applied.

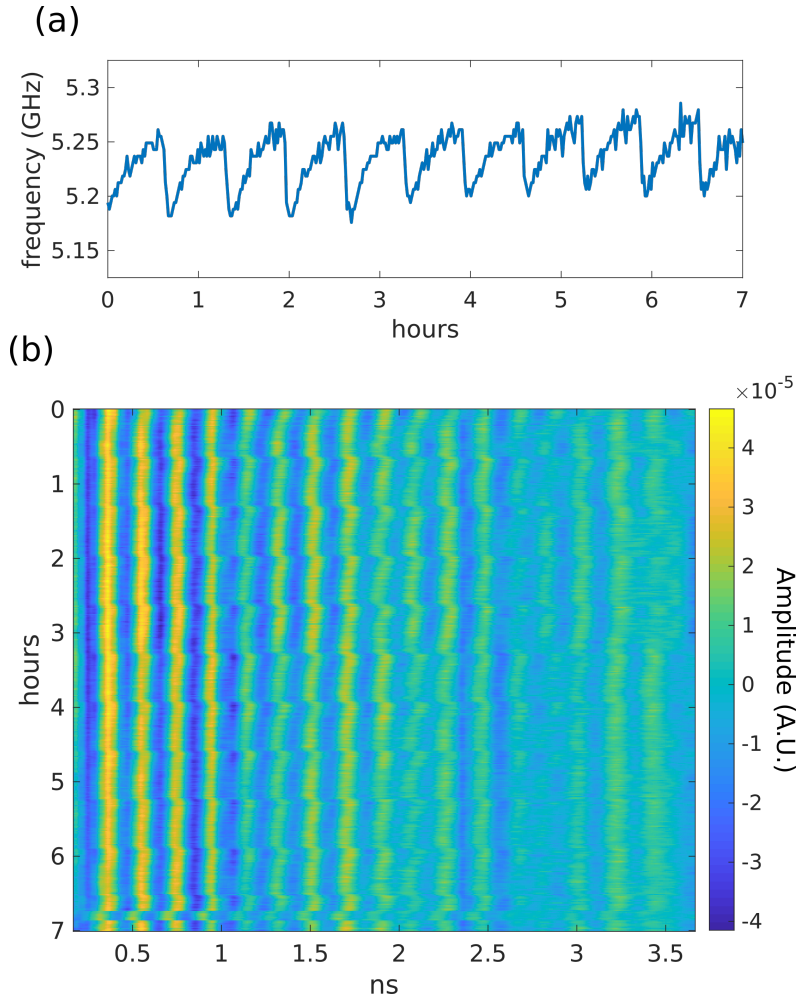


Figure 5.9: In an effort to use the Brillouin frequency versus time to resolve the change in phase from liquid gelatin to solid gelatin, the transducer tip was left dipped in a water-gelatin solution over a hot plate. The tip did not remain in the liquid gelatin long enough to measure a 2 GHz shift in Brillouin frequency, however the pattern in (a) emerged. This is also corroborated in the time domain (b): B-scan of the seven hour exposure where x-axis is the signal time window, y-axis the count number/experiment clock, and colour is the amplitude of the modulation depth. It is believed that these oscillations are the result of thermal cycling of the hot plate which ultimately modulates the detected Brillouin frequency.

5.2.2 Thermometry

It is well known that temperature affects the optical and mechanical properties of materials. Thermo-optic and thermo-acoustic effects are even accessible in daily-life: a mirage created by light refracting across thermal gradients, or sound travelling longer distances on colder days as it scatters from warmer layers above. With refractive index and sound velocity being two central parameters in Brillouin scattering, their thermal variations should correspond with the phonon frequency detected by a Brillouin spectrometer.

In order to test the sensitivity of the fibre-transducer to these effects, water was used as a case study. Thermo-optic and thermo-acoustic coefficients were extracted from literature [212, 213], and used to formulate a theoretical dataset of refractive index ($n(T)$ at $\lambda = 780\ nm$) and sound velocity ($v(T)$) versus temperature (T) (presented in Figure 5.10a-b). These literature-based models of the refractive index and sound velocity can be combined into a theoretical expression of the Brillouin frequency as a function of temperature (Equation 5.1)

$$f_B(T)' = \frac{2 \cdot n(T) \cdot v(T)}{\lambda_{probe}} \tag{5.1}$$

as revealed by Figure 5.10c. A theoretical measure of the sensitivity of the Brillouin frequency to temperature, $|\Delta f_B'/\Delta T| \approx 2MHz/^{\circ}C$, can also be calculated using a well-behaved region in the plot in Figure 5.10c (pink segment).

An experiment was devised where the fibre-transducer was immersed in a beaker of deionised water, which was placed on a hot plate. Furthermore, the beaker contained a magnetically spun propeller in order to promote thermal equilibrium throughout the sample. The leads of a K-type thermocouple (calibrated at the boiling point of water) were also immersed into the beaker in order to provide an external temperature measurement. TRBS data and thermocouple data (Pico Technology thermocouple data logger) were simultaneously acquired over the course of approximately 2 hours, at an averaging rate of 10,000 averages per count (678 total counts). The first 20 minutes of the experiment was spent at room temperature (RT measured as $\approx 19^{\circ}C$ by the thermocouple), after which the hot plate was increased to $50^{\circ}C$ for 1 hour and 10 minutes, followed by a final increase to $100^{\circ}C$ for the remaining 30 minutes. The TRBS data were processed according to the standard procedure outlined in Section 4.2.1 and then Fourier transformed from the time-domain to the frequency domain. The frequency position of the maximum FFT amplitude (f_B) was recorded for each count and overlaid (blue line) onto the colour-map of the time-varying frequency spectra (Figure 5.11). Initially it is evident that the measurement of the Brillouin frequency appears to fluctuate on the scale of minutes-hours, and that these fluctuations seem to be synchronised with the clock-readings at which the hot plate was manipulated. The temperature read-

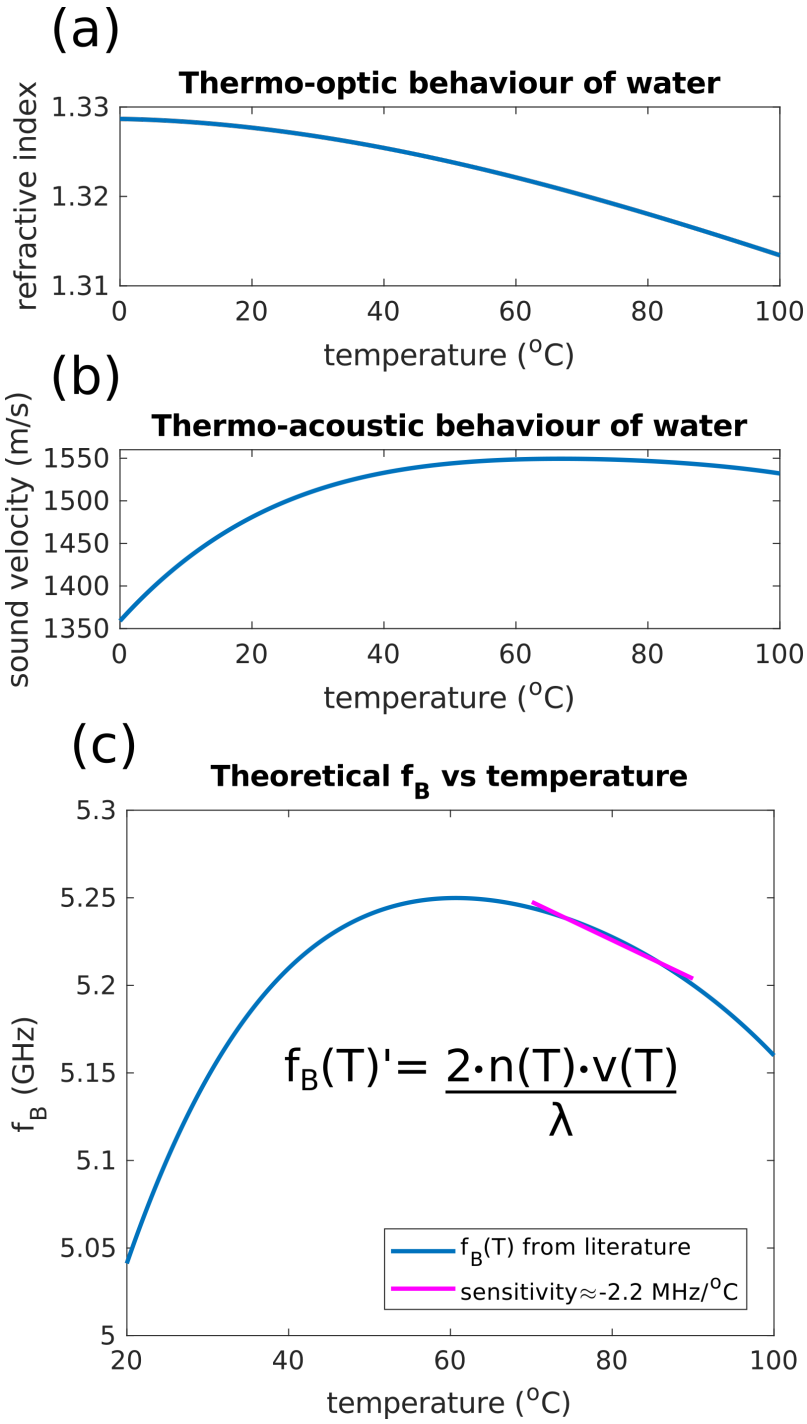


Figure 5.10: Organisation of literature-data to create a model-set of values for Brillouin frequency as a function of water-temperature. (a) Literature values of the refractive index (at $\lambda = 780\ nm$) as a function of water temperature. (b) Literature values of the sound velocity of water as a function of temperature. These curves were used to formulate a theoretical expression for the temperature-dependency of the Brillouin frequency (c). A first-order polynomial was fit to a well-behaved region of the curve (pink line segment) in order to provide an estimate of the theoretical sensitivity. An approximate value of $|\Delta f_B'/\Delta T| \approx 2.2 MHz/^\circ C$ will be compared with the sensitivity of the fibre-transducer experimental measurements.

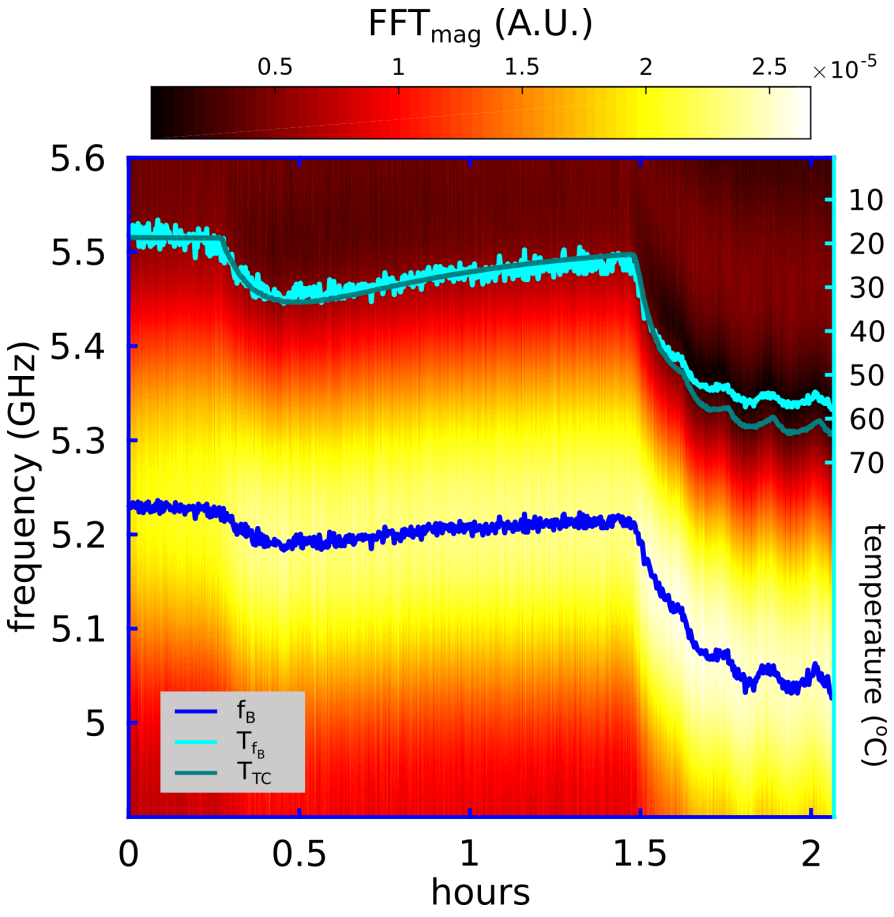


Figure 5.11: Using the phonon probe as a thermometer in water. The colour-map represents the amplitude of the frequency spectrum as a function of experiment time and water heating; blue curve reveals the frequency position of the maximum FFT amplitude, the Brillouin frequency (f_B, blue line). As the thermocouple measures variations in temperature (T_{TC}, teal line, with temperature as right y-axis), similar yet inverted variations can been seen in f_B. This inversion is a consequence of being in a negative sensitivity regime of the f_B vs T curve (Figure 5.10c). f_B can be converted to a temperature measurement via Equation 5.2 and parameters from literature; this temperature was found to be offset from T_{TC} due to transducer heating. Once this bias was accounted for, the Brillouin spectroscopic measurements of the temperature T_{f_B} (cyan line) corroborate the thermocouple data.

ings of the thermocouple (T_{TC}) are presented in the teal-coloured curve (temperature scale inverted on the right y-axis), and visually correlate with the trends of the Brillouin frequency.

Upon inspection, it becomes evident that as the thermocouple measures a continually increasing temperature, the curve of the Brillouin frequency appears to trend in the opposite direction. Returning to Figure 5.10c, $f_B(T)'$ displays negative slope when the temperature is beyond roughly $60°C$, which implicates that the experimental Brillouin frequency (f_B) is representative of this temperature range. Using $\approx 60°C$ as a threshold, the i^{th} experimental Brillouin frequency can be matched with the closest theoretical

value (from Figure 5.10c) by tracking the residual between the two:

$$\Delta f_{B_{i,all}} = |f_{B_i} - f'_{B_{all}}| \tag{5.2}$$

The value within the range 'all' at which $\Delta f_{B_{i,all}}$ is minimum, represents the closest match between experimental and theoretical Brillouin frequencies (when only considering temperatures above $60°C$). At this value of $f_B(T)'$, the theoretical temperature can be interpolated and extracted from Figure 5.10c. In this way the entire dataset of f_B can be converted into a temperature measurement, $T_{f_{B0}}$, albeit one that is offset from the thermocouple measurements.

At the beginning of the experiment - when the water sample is known to be at room temperature ($19°C$) as confirmed by the thermocouple measurement - the first experimental Brillouin frequency measurement was found to be $5.23\ GHz$, which converts to a temperature measurement of $80°C$. The $\Delta T_{RT} = 60°C$ offset between the room temperature measurement of the thermocouple and that of the fibre-transducer, would then represent the heating contribution by the transducer itself. When this offset is used to calibrate the experimental Brillouin temperature values:

$$T_{f_B} = T_{f_{B0}} - \Delta T_{RT} \tag{5.3}$$

the experimental measurement of the temperature (T_{f_B}, cyan line in Figure 5.11) appears to closely agree with the thermocouple data (teal line). This offset permeates all measurements of the f_B in water presented in this report; e.g. the measurement made in Figure 5.4 of $f_B = 5.235 \pm 0.004\ GHz$, which differs from the theoretical value of $f_B(RT) = 5.11\ GHz$.

In order to validate the measurement of the temperature rise in the water, finite element method (FEM) was used to model the steady-state heating by the transducer (model discussed in Appendix B). Pump and probe powers of approximately 7 and $1\ mW$, respectively, were measured at the output of the fibre-transducer. Using these input powers, the transfer matrix (TMM) optical model (Section 2.2.1) was then used to compute total average power absorbed by the transducer: $\approx 2\ mW$ which was designated as the steady-state heat source for the FEM COMSOL model. Figure 5.12 presents an axially symmetric map of the temperature rise in the space surrounding the tip of the fibre-transducer (core and cladding modelled as glass). Experimental Brillouin frequencies were determined using a signal length of $\sim 5\ \mu m$ in the axial direction, and given the $5\ \mu m$ core diameter, the average temperature rise within a 5 x 5 x 5 μm volume of water surrounding the tip was calculated by the FEM model as $\approx 55°C$. In addition to corroborating the $60°C$ offset measured by the fibre-transducer, this model informs that the reciprocal relationship between temperature and proximity to the transducer is of key importance when bringing the transducer close to thermally

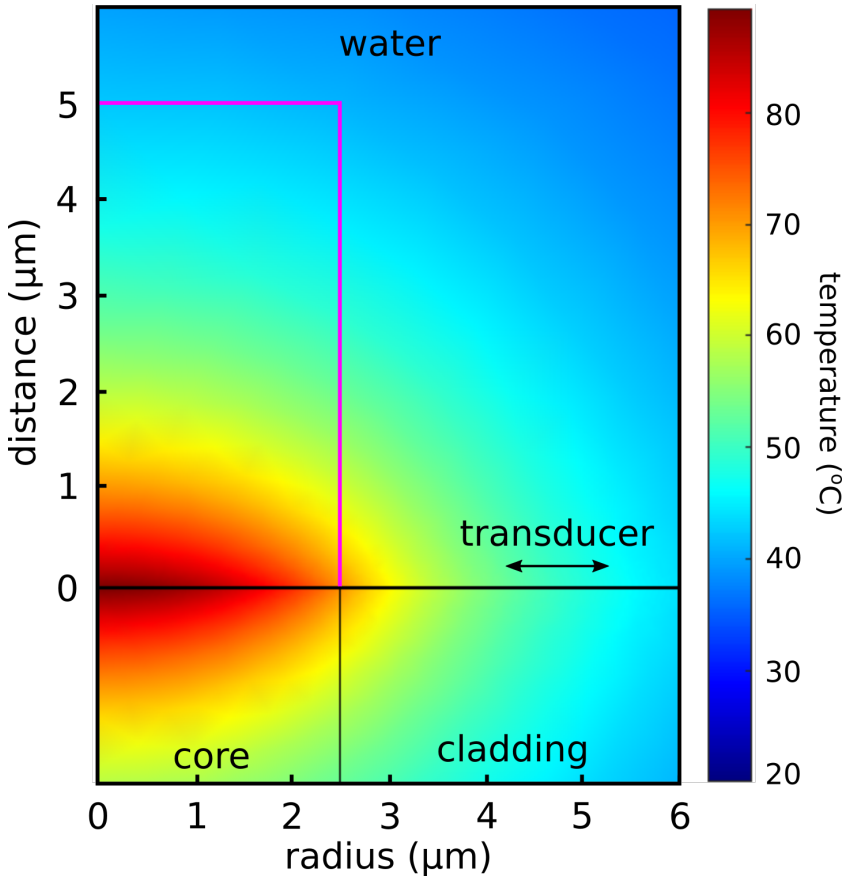


Figure 5.12: Finite element software (COMSOL) was used to model the axially symmetric temperature rise due to the transducer's absorption of the pump and probe beams. A steady-state heat source was utilised under the approximation that the total average optical power absorbed by the 15 nm gold layer had a one to one correlation with the source heating rate. A majority of the heating occurs within the vicinity of the core-region of the transducer; the peak temperature rise in this area is dramatic, however, this drops off aggressively as heat diffuses into the surroundings. An average temperature of 55°C was measured for the 5 x 5 x 5 μm volume area (outlined in pink) surrounding the core, which is in agreement with the 60°C temperature rise estimated using the Brillouin fibre-spectrometer.

sensitive specimens.

Quantitatively, the fibre-spectrometer is measuring the temperature change relative to the static temperature rise induced by the excited transducer. Since this background temperature is on the order of 60°C, and the calibrated fibre-spectrometer is measuring changes in water temperatures on the order of $60 - 70°C$, it is clear that the actual temperature of the water may be approaching or numerically surpassing the 100°C boiling point of water. This could be explained by the fact that the acoustic waves being generated by the transducer are effectively increasing the pressure of the sample volume, which increases the boiling point of water approximately logarithmically. However, there are additional complexities to consider, such as the dynamic state of the environment (e.g. undergoing convection, diffusion, turbulence, etc), and the overall accuracy of the

tabulated literature values for refractive index and sound velocity which break down as the boiling point is approached (and do not account for changes in pressure).

The possibility for approaching the vaporisation of water could also result in bubble formation within the measurement volume of the fibre-probe. As a result, the interfaces between gas and water and the corresponding mismatches in refractive index (both optically and acoustically) have the potential to scatter light and sound away from the measurement volume, reducing the sensitivity of the technique. The hydrophobic surface of the graphite-coated fibre-tip could also contribute to this, especially if the surface is of considerable roughness (nucleation sites for bubbles) [214]. These effects can be monitored in bench-top techniques by constructing an optical imaging system to monitor the fibre-tip (e.g. see Section 6.1). In this work bubble formation was not regularly observed, but the above effects can be mitigated by lowering the optical beam power of the technique (reducing the temperature rise), eliminating the hydrophobic layer, or by reducing the wetting contact angle through polishing (smoothing roughness) or tapering the tip.

The sensitivity of the device to temperature was calculated by separately considering the Brillouin frequency data and the thermocouple data. Figure 5.13 shows the experimental f_B and thermocouple temperature data both fitted with first order polynomials in well-behaved linear regions of the curves (fitted region in red, and the polynomial fit in green). The average of the slopes of the green curves was taken for both the numerator and denominator, resulting in an overall sensitivity of $\Delta f_B/\Delta T = 2.5 \pm 0.6\ MHz/^{\circ}C$. In addition, this sensitivity value and the confidence interval correlates with the sensitivity value from the literature-based model found in Figure 5.10c.

The study shown thus far has revealed that temperature fluctuations can be detected by monitoring the temperature induced Brillouin frequency shift over the course of minutes and hours. However, as shown in Figure 5.12, there also exists a significant temperature gradient in the space surrounding the transducer tip. As this heat diffuses and dissipates travelling axially and radially away from the transducer, this gradient will manifest as instantaneous Brillouin frequency shifts within the time window of a TRBS signal. Then, if time-frequency analysis is employed, such as continuous wavelet transform, this frequency transience can be converted into axial measurements of the temperature on the scale of microns. The protocol outlined in Section 4.2.2 was utilised to wavelet transform the TRBS signal for water (Figure 5.3a). A complex Morlet was selected as the mother wavelet (see Figure 5.14a) and contained the following parameters: (1) a bandwidth of approximately 8 acoustic wavelengths was chosen to improve the accuracy of the frequency characterisation, (2) the frequency at which the maximum FFT amplitude occurred (in Figure 5.3b) was assigned to be the centre frequency of the mother wavelet, and (3) the centre frequency was varied over the range

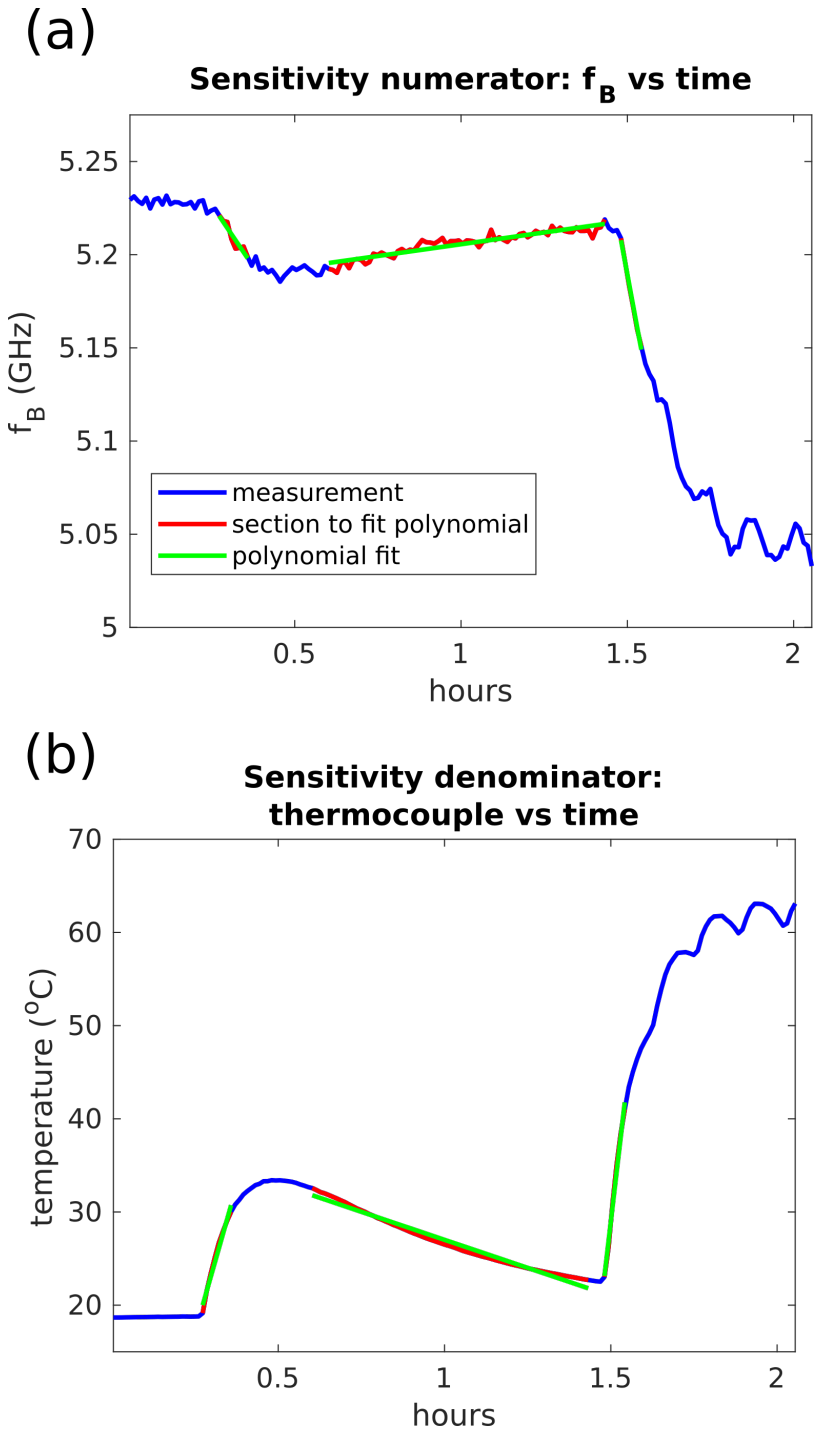


Figure 5.13: Plots used to calculate the sensitivity of the fibre-spectrometer to changes in water temperature. (a) Blue curve of experimental Brillouin frequency measurements. The three red segments were selected for their linearity, and a first-order polynomial was fitted to extract a slope measurement. (b) The same procedure was applied to the temperature measurement of the thermocouple. Sensitivity calculated as the mean of the green slopes in figure (a) divided by the mean of the green slopes in figure (b): $\Delta f_B/\Delta T = 2.5 \pm 0.6\ MHz/^\circ C$.

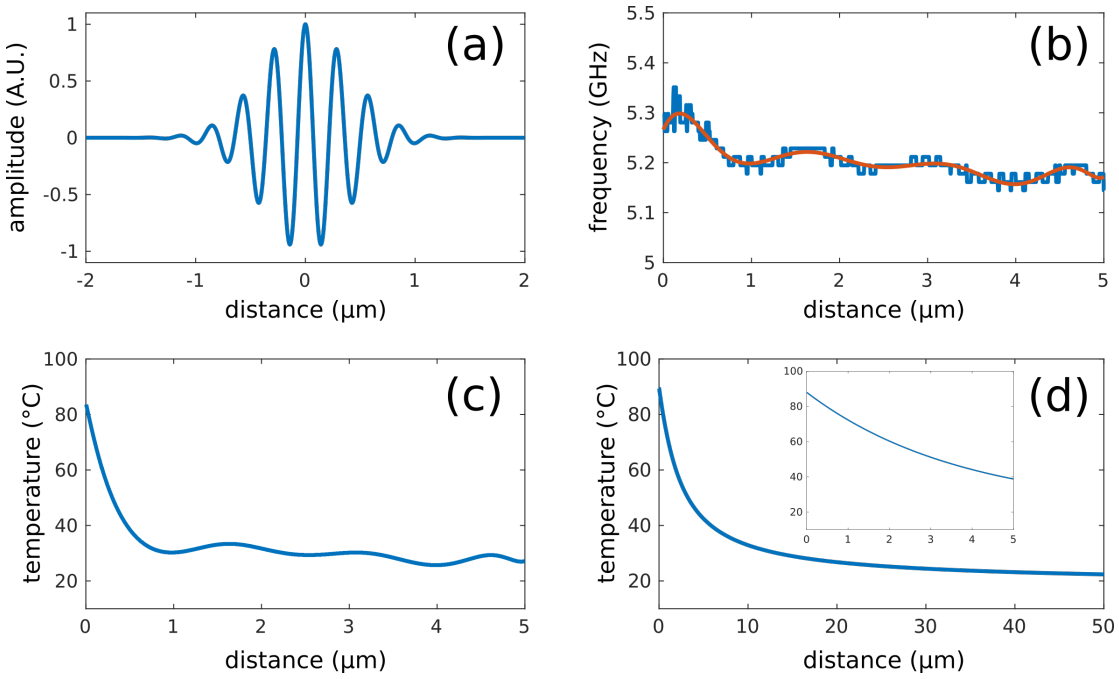


Figure 5.14: Using a single TRBS time trace (from Figure 5.3a) to measure the axial temperature variation after the initial heat rise of the transducer. A continuous wavelet transform was used - with a complex Morlet mother wavelet (a) - to find the instantaneous variation in signal frequency across the time window. At a given slice in signal time (or z through $z = vt$), the frequency at which the wavelet amplitude is maximised represents the instantaneous frequency measurement (b); the resulting trace was smoothed by fitting a polynomial. The literature model in Figure 5.10c allowed the instantaneous f_B to be converted to T as a function of axial distance (c). (d) Simulated temperature rise along the $r = 0$ cross-section. Compared with simulation, the experiment shows a much faster rate of equilibration (zoomed inset); this is partially explained by the experiment producing an average temperature measurement within the measurement volume, and the simulation being only along a single cross-section.

$4 - 7\ GHz$ in order to characterise experimental frequency shifts. A high order polynomial was then fit to the resulting trace of maximum amplitude Brillouin frequency versus z (Figure 5.14b). As with previous temperature measurements, literature values (Figure 5.10c) were used to match experimental f_B to the corresponding temperature measurement (Figure 5.14c). Figure 5.14d shows the simulated equivalent of this trend, which appears to corroborate the initial temperature rise at the gold:water interface, but diffuses at a much different rate. This can possibly be explained by the fact that the experimental f_B measurement represents an average measurement within the 5 x 5 x 5 μm measurement volume, whereas the simulation only represents the temperature rise along the $r = 0$ axis. Furthermore, the simulation represents a static environment, i.e. each node of water (molecule) is stationary in space. In experiment this is not the case due to the dynamic nature of the water reservoir which is undergoing convection, mechanical motion, and potentially even hydrodynamic cavitation. Therefore the

experimental temperature measurement appears to show a system which equilibrates quicker than simulation. However, further investigation is required to better understand the ways in which temperature is encoded into the instantaneous Brillouin frequency of the signal.

Similar to the case of using the fibre-spectrometer to perform material characterisation, optical and acoustic data can be tabulated from literature and used to convert TRBS data to quantitative measurements of local temperature. This capability is owed to the thermo-optic and thermo-acoustic effects, whereby refractive index, sound velocity, and ultimately Brillouin frequency are modulated by temperature. Initially the temperature measurements made by the device were found to differ substantially from the parallel measurement of a thermocouple, however, this provided an opportunity to confront the reality of the transducer heating the sample medium. By comparing experiment (f_B) with literature (f_B'), the experiment provided an estimated reading of this heating as $60°C$, which was also corroborated by FEM modelling. Once this contribution was taken into account, the transducer enabled accurate measurements of water temperature with a sensitivity of $2.5 \pm 0.6\ MHz/°C$. There still exist ambiguities related to the limitations of the experimental measurement; e.g. are literature values of $n(T)$ and $v(T)$ valid to extrapolate if the water local to the tip is heated towards boiling. This could be a possible explanation for the divergence of T_{f_B} and T_{TC} when the hot plate was increased at the 1.5 hour mark. In contrast, there could have existed a sufficient thermal gradient between the edge of the beaker (where the thermocouple was fixed) and the centre (where the fibre was fixed) such that the transducer and thermocouple registered different measurements at high temperatures. There are various potential options for mitigating the heating of the sample by the transducer, which will be discussed further in Section 5.3. If the Brillouin fibre-spectrometer is to be used as a temperature sensor, there will be a requirement for having *a priori* information about the constituents and initial state of the environment, much like previous results characterising the performance of the device. However, for the first time, the Brillouin spectroscopy of temperature has been performed with a measurement apparatus that is compact, flexible, remotely accessible, and portable.

5.2.3 Solute sensing

The refractive index and sound velocity of water can also be modulated by the presence of varying concentrations of salt. Similar to the experiments with temperature, this transitively modulates the Brillouin frequency and provides an opportunity to test the sensitivity of the fibre-transducer to a new measurand: salinity. Optical and acoustic properties, as functions of salt concentration (C) were drawn from literature [215, 216] (Figure 5.15a-b) and used to construct a theoretical dataset for Brillouin frequency

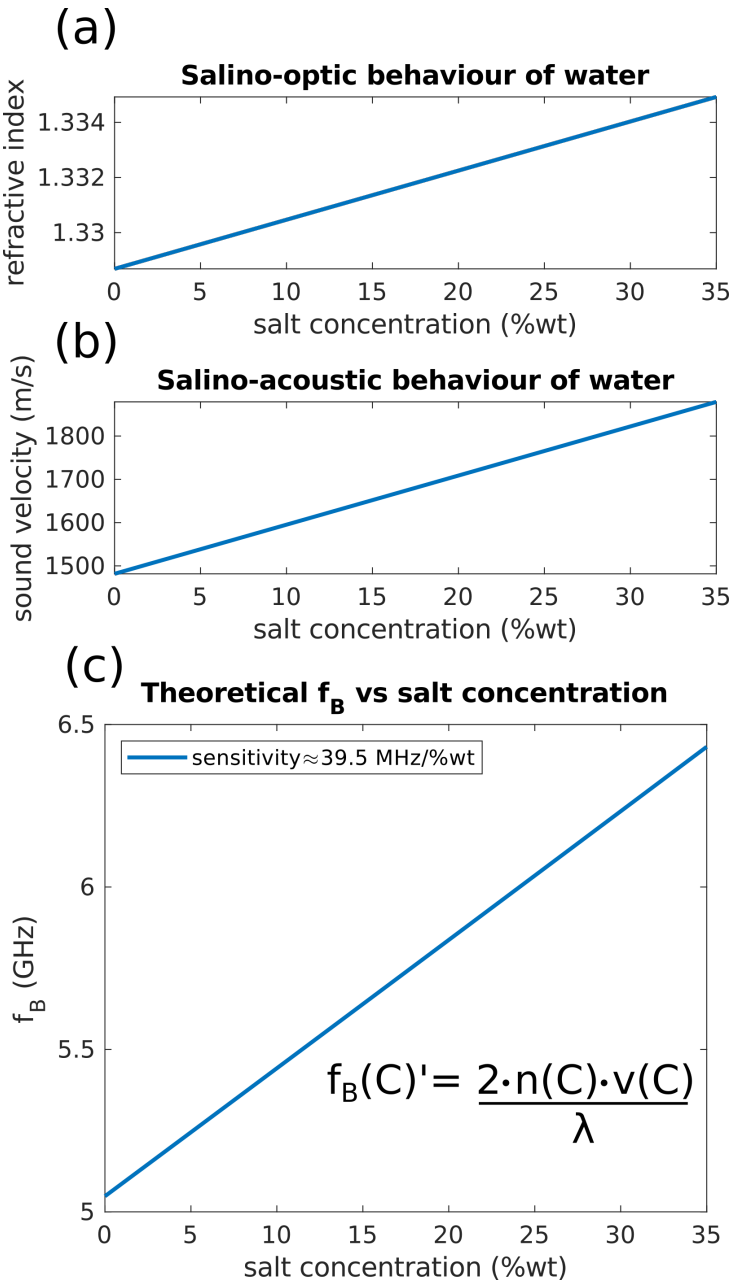


Figure 5.15: Organisation of literature-data to create a model-set of values for Brillouin frequency as a function of water-salinity. (a) Relationship between refractive index and salt concentration for water, taken from literature [215]. (b) Relationship between sound velocity and salt concentration [216]. (c) Combining (a) and (b) gives a set of theoretical/expected values for Brillouin frequency ($f_B(C)'$) as salinity fluctuates in water. This can be used to convert an experimental f_B measurement into a read-out of the current salt concentration. The slope, i.e. sensitivity of this analytical expression measures as $39.5\ MHz/\%wt$.

versus salinity (Equation 5.4), with theoretical sensitivity $39.5\ MHz/\%wt$ (Figure 5.15c).

$$f_B(C)' = \frac{2 \cdot n(C) \cdot v(C)}{\lambda_{probe}} \tag{5.4}$$

A pot of highly concentrated salt-water was prepared using store-bought table salt

(primarily NaCl). Concentrate was drawn from this solution and added to a vial of pure deionised water every two minutes such that the overall concentration (C) of the water solution grew in $\approx 1-2\ \%wt$ increments. Similar to previous experiments, TRBS data were acquired at a rate of 10,000 averages per count ($\approx$ 3.5 s) for 10 minutes. The first two minutes were spent at $0\ \%wt$ salt in order to provide a reference signal and Brillouin frequency measurement. Figure 5.16 presents the frequency spectrum as a function of experiment time, overlaid with the frequency position of the maximum FFT amplitude (blue line). The red stars along the blue curve represent additional averaging (of exper-

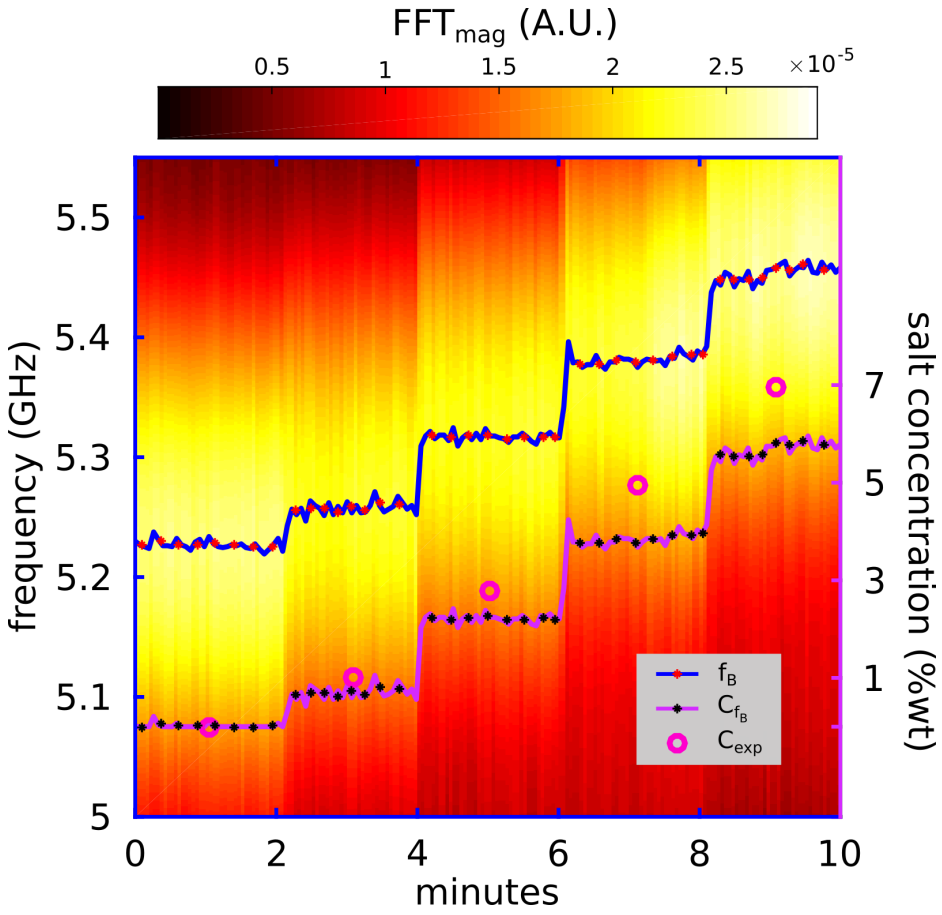


Figure 5.16: Experimental results which show the fibre-transducer's potential for performing spectroscopy on variations in water salinity. Colour-map represents the frequency spectra of the TRBS signals with respect to experiment time (x-axis). Frequency at which the maximum FFT amplitude occurs indicated by the blue curve. Red stars are additional averages of the f_B values; the original dataset (154 total measurements) was segregated into 41 bins with each step in concentration possessing approximately 8 bins. Outlying data-points were excluded from the bin-averaging, e.g. the over-shoot at the six minute mark. Averaging in this way increases certainty but also increases the time required to attain each measurement. The literature-model shown in Figure 5.15c was used to correlate each f_B with a concentration measurement (C_{f_B}, pink curve), where black stars represent bin-averaging. The experimental mass and concentration of salt added to the original water solution was noted during the experiment and used as a point of comparison (C_{exp}). From these measurements a sensitivity of $41 \pm 3\ MHz/\%wt$ can be attributed to the device.

imental f_B) which took place in the post-processing. For N = 154 total measurements and selecting $N_{bin} \approx 41$ total number of bins ($\approx$ 8 bins per step in concentration), the following expression yields the average Brillouin frequency measurement at the j^{th} bin:

$$\bar{f_{B}}_j = \frac{1}{n}\Big(\sum_{i=j-n/2}^{j+n/2} f_{B_i}\Big) \tag{5.5}$$

where $n = N/N_{bin} \approx 4$ is the number of counts in each bin and j is the bin number ($j = [1, N_{bin}]$). By increasing the number of counts per bin the certainty of the measurement can be increased, but at the cost of temporal resolution.

At $C = 0\ \%wt$ salt there existed a $\Delta f_{B_{0\%wt}} = 0.179\ GHz$ offset between literature ($f_B(0\%wt)' = 5.048\ GHz$) and un-calibrated experiment ($f_{B_0}(0\%wt) = 5.227 \pm 0.004\ GHz$), which could be a consequence of the literature values used, in addition to experimental transducer heating. This offset was used to calibrate the experimental measurements

$$f_B = f_{B_0} - \Delta f_{B_{0\%wt}} \tag{5.6}$$

which were then compared with the model dataset (Figure 5.15c); the model-value ($f_B(C)'$) at which the residual with experiment was minimised (see Equation 5.2) provided the concentration measurement (C_{f_B}) for a given f_B, represented by the pink curve in Figure 5.16. This salt concentration measured with the fibre-spectrometer can be validated by the user-added concentration which was noted during experiment (C_{exp}), as the two are in reasonable agreement. Binning and further averaging was also applied to the device's concentration read-out, shown as black stars Figure 5.16. Sensitivity of the fibre-transducer to changes in concentration was calculated by considering the bin-averaged f_B and C_{f_B} over time, and was found to be $\Delta f_B/\Delta C = 41 \pm 3\ MHz/\%wt$. This measure of the sensitivity is also in close agreement with the sensitivity provided by the literature-model dataset shown in Figure 5.15c.

A second experiment was performed, but instead of linearly increasing the salinity, each increment in total concentration was half of the preceding increment (e.g. $0\ \%wt$, $1\ \%wt$, $1.5\ \%wt$, $1.75\ \%wt$, etc). As the Brillouin frequency shift is measured with these diminishing changes in concentrations, eventually there will arise a limit of the device's frequency resolution, i.e. when a change in the input does not produce a detectable change in the output. Using the same data acquisition parameters as the previous experiment, TRBS data were acquired over the course of 16 minutes, initiated by two minutes at $0\ \%wt$ salt (presented in Figure 5.17). The same signal-processing protocol (use of calibration, bin-averaging, and model comparison) as Figure 5.16 was used to provide salt concentration measurements which are in agreement with the experimental values (C_{exp}) and reveal a sensitivity of $\Delta f_B/\Delta C = 43 \pm 5\ MHz/\%wt$.

Upon visual inspection Figure 5.17 appears to have a Brillouin frequency measurement which is saturating as the concentration-added of salt decreases. In order to

assign a quantitative measurement to these steps in frequency, a discussion of the frequency resolution of both the physical experiment and the signal processing is required. As discussed in Section 4.2, the intrinsic frequency resolution of the optical system is determined by the repetition rate of the pump laser, $80\ MHz$. However, this resolution limit is only achievable if the length of the TRBS signal encompasses the entire $12.5\ ns$ time window. In practice, the experimental set-up and signal processing typically dictate that the final TRBS signal is less than $12.5\ ns$, further reducing the frequency resolution. For example, if the TRBS signal in water from Figure 5.3 was processed such that the final trace length was $\approx 3.5\ ns$, the corresponding frequency discretisation would be $\approx 286\ MHz$, as seen in orange in Figure 5.18. Since the bandwidth of the $\sim 5\ GHz$ acoustic wave (in reality) is wider than the $80\ MHz$ fundamental frequency

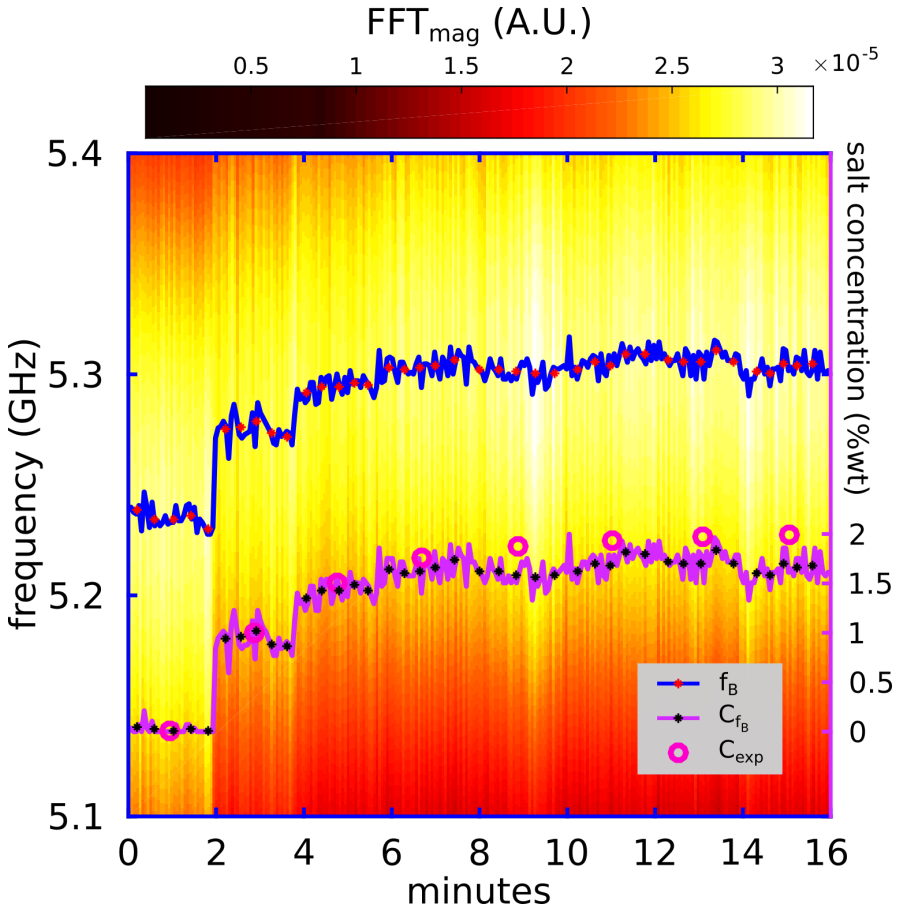


Figure 5.17: Same experiment as in Figure 5.16, but instead of linearly increasing the concentration of salt, total concentration was stepped in increments of 2^{-n} where $n = 0, 1, 2, ...$ Measurements of the experimental Brillouin frequency (f_B, blue line) can be converted into read-outs of the salt concentration (C_{f_B}, pink line) and compare favourably with the user-measurements of the concentration (C_{exp}). The precision of these measurements can be controlled by averaging f_B within a set of bins (red and black stars). 5 bins per step in concentration was utilised for this experiment to allow a more precise estimation of the frequency resolution to be achieved. This data yielded performance metrics of $\Delta f_B/\Delta C = 43 \pm 5\ MHz/\%wt$ (sensitivity) and frequency resolutions of 40, 19, and $9 \pm 2\ MHz$.

step - due to the attenuating nature of the acoustic waves - the original sampling rate in the frequency domain aliases the actual signal of interest. In order to combat this, zero-padding can be used to interpolate the spectra and increase the effective sampling rate. The blue histogram in Figure 5.18 displays this concept using data from Figure 5.3 and a zero-pad of 2^{16}, which produces frequency bins spaced $\sim 6\ MHz$ apart.

The results presented in figures 5.16 and 5.17 have already been re-sampled with a zero-padding of 2^{20}, in order to resolve small changes in the Brillouin frequency of the TRBS signals. After re-sampling, the minimum detectable step change in the Brillouin frequency should be limited by the precision of the measurement(s). A step in frequency can be considered resolved if the step is greater than half of the sum of the uncertainties in neighbouring steps. Figure 5.19 is a reproduction of Figure 5.17 where the frequency steps have been partitioned into average measurements of five bins each (green stars). Subsequently, the mean of each set of five bins can be measured with a lower uncertainty than that of the un-binned data. With the increase in precision, the

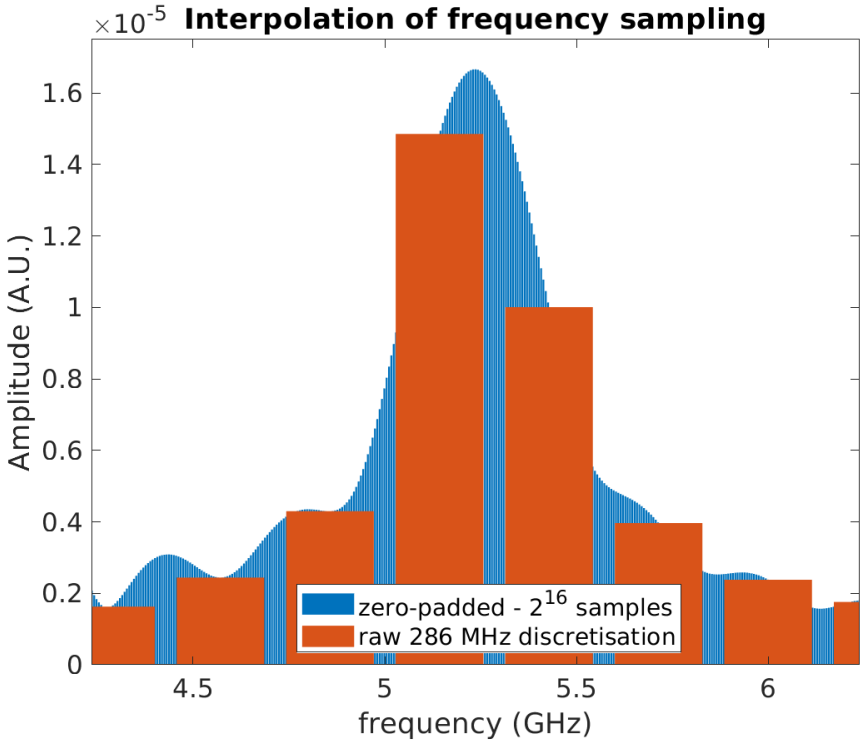


Figure 5.18: Frequency spectra of the TRBS signal presented in 5.3. This particular time trace only consumed a $\approx 3.5\ ns$ portion of the $12.5\ ns$ (after signal processing); in the frequency domain this expanse in time translates to a frequency resolution of $\approx 286\ MHz$, roughly 4 times the fundamental limit of $80\ MHz$ (if $12.5\ ns$ time window was used). If the bandwidth of the acoustic wave is greater than the spacing of the original frequency bins - e.g. due to acoustic attenuation within a given material - the signal can be anti-aliased by zero-padding the trace and therefore increasing the sampling rate in the frequency domain. The blue histogram is the orange spectrum re-sampled with 2^{16} bins, and reveals sub-repetition rate variation in the frequency content of the signal.

first three frequency steps can be resolved as 40, 19, 9 ± 2 MHz which correlate to changes in salt concentration of 0.91, 0.49, and 0.23 $\%wt$. Ultimately a sub-repetition rate frequency resolution of 9 MHz is possible in this experiment due to the interpolation provided by zero-padding, and the use of averaging to lower uncertainty; the latter ultimately effects the overall experiment time required, e.g. 10 bins of 6 counts each (600,000 averages) takes $\approx$ 3.5 minutes to acquire. Consequently, if there is a desire to measure the smallest shift in a sample's state, an increasingly long acquisition period will be required. This time-dependency can be lessened as further improvements are made to the optical system and fibre-transducer design (discussed in Section 5.3), thereby increasing SNR and native precision.

This section has shown that aside from material characterisation and temperature, the Brillouin fibre-spectrometer can also be used as a sensor for the concentration of a solute. These measurements still require that there is *a priori* information regarding the initial state of the sample environment; e.g. that the solution is primarily composed of water at room temperature. However, by tracking the direction and magnitude of the Brillouin frequency shifts, there exists potential to characterise unknown environ-

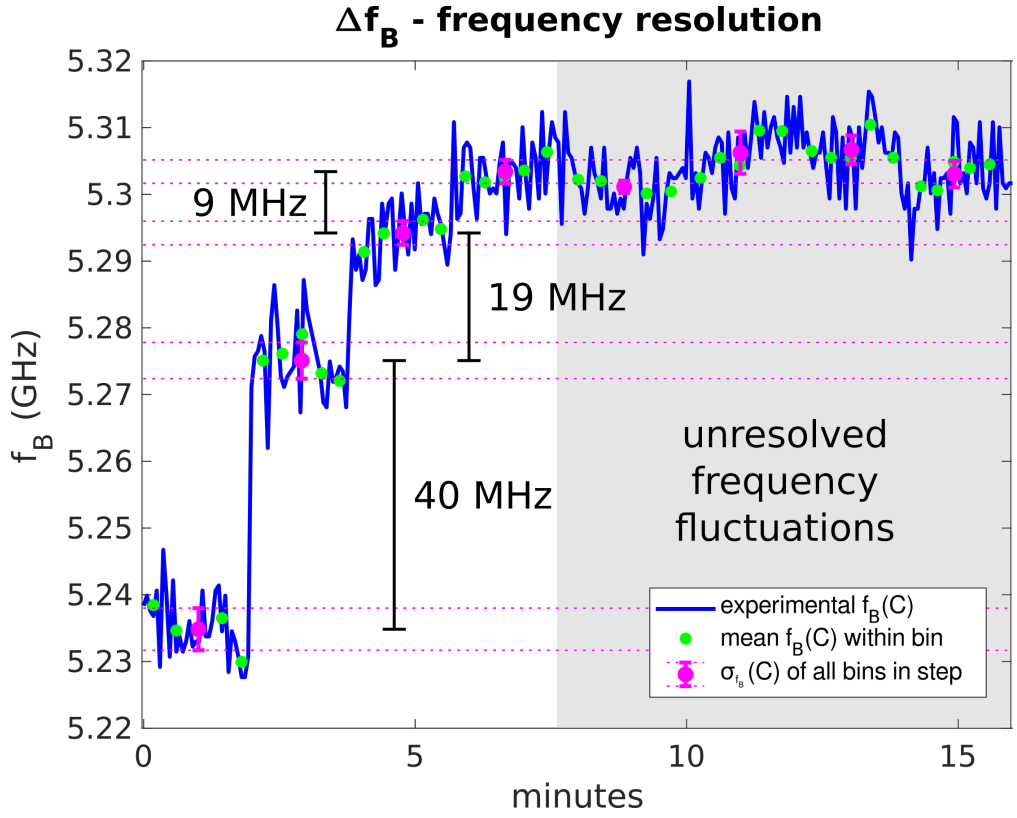


Figure 5.19: Closer look at the f_B data from Figure 5.17. Each two minute step in Brillouin frequency (due to increasing salt concentration) was partitioned into five bins and averaged according to bin (green stars); the mean f_B across these bins (pink circle) will possess a lower uncertainty than if the mean of the entire step was considered. Using this technique, only the first three steps in frequency can be measured with a precision that is sufficient for resolution: 40, 19, 9 ± 2 MHz.

ments once a sufficient library of measurements has been constructed. Finally, this section has also discussed the way in which small frequency shifts can be measured, and the limitations on this resolution imposed by the experimental system and signal processing.

5.3 Discussion and conclusions

This chapter has presented the concept, design, and proof of concept results for a novel time resolved Brillouin spectrometer which consists of a single-mode optical fibre topped with an opto-acoustic thin-film transducer. The device's viability in a range of materials such as water, glycerol, PS, gelatin, and sheep's blood plasma was demonstrated. The fibre-transducer also proved capable of measuring Brillouin shifts in water caused by temperature and salinity induced modulations of the optical and mechanical properties. Sensitivities of $2.5 \pm 0.6\ MHz/^{\circ}C$ and $41 \pm 3\ MHz/\%wt$ were reported for changes in temperature and salinity, respectively. Additionally, the underlying contributions to the device's frequency resolution have been discussed, and the minimum experimental frequency resolution was reported as $9 \pm 2\ MHz$.

An experimental design was targeted that utilised a fibre-based WDM which provides $< 1\ dB$ of loss for the pump wavelength. The WDM also provides $< 1\ dB$ of insertion loss for the probe wavelength, however, this beam experiences $3\ dB$ loss upon input (before the WDM) and another $3\ dB$ prior to detection (Figure 5.1). One key improvement which could be made to the design of the optical system for the Brillouin fibre-transducer, is updating the probe coupler from a 2:2 coupler, to a fibre optic circulator. With respect to the input probe beam, this would allow greater optical powers to be utilised at the sample without having to compensate for the 2:2 coupler. More crucially, replacing the $3\ dB$ loss before the detector with the $< 1\ dB$ of the circulator would immediately provide a $\sqrt{2}$ improvement in SNR (given the same input powers as used in this chapter). This gain in SNR could contribute towards increasing the acquisition speed of the system while maintaining similar levels of signal averaging.

The SNR improvement enabled by the circulator could also be used to reduce the heating supplied by the irradiation of the transducer: if the total average power absorbed can be decreased by a factor of two, the steady-state temperature rise would reduce to $30^{\circ}C$ according to the FEM model (Appendix B). Alternative means for reducing the transducer heating could include: (1) utilising an alternative optical fibre substrate with higher thermal conductivity, e.g. sapphire [168, 217], or (2) incorporating a thermally insulating layer to the design of the transducer, e.g. carbon nano-diamonds.

With regard to the exposure of short light pulses on biological samples, it has been reported that a peak power density of 10^{12} W/cm^2 of femtosecond-radiation inhibits Chinese hamster ovary cell division, and even higher intensity induces cell fragmen-

tation and death [218]. Furthermore, there is evidence that light absorption-induced damage in subcellular components can manifest as cellular-scale morphologies [149]. This damage mechanism has shown to correlate with total optical energy delivered to the sample - a function of wavelength, average power, and exposure time - with a critical energy of $249\ J$ being the damage threshold for $\lambda = 660\ nm$ (threshold would be larger at $\lambda = 780\ nm$). The current device and experimental parameters presented in this chapter is beneath the pulsed damage threshold above, and would require roughly 3.5 hours of cell exposure to break the second threshold mentioned. Therefore, the fibre-spectrometer shows great promise for being safely used on biological samples, especially in the context of adapting the device for imaging where longer exposures may be necessary.

Perhaps spectroscopy is at its most tangible when a series of spectroscopic measurements can be organised into an image which provides unique information about a specimen. This is the fundamental motivation and imaging mechanism for techniques such as phonon microscopy, and Brillouin microscopic techniques in general. The following chapter will introduce results that indicate that the fibre-transducer can be transformed into a GHz-frequency ultrasonic imaging probe.

Chapter 6

Imaging: three-dimensional phonon imaging probe

In optics and photoacoustics, the leap from bench-top to portable imaging systems has been met by the optical fibre. Specifically for the case of optical endoscopy, this transition has culminated in a collection of cellular resolution techniques called endomicroscopy, which is driven by miniaturised lens systems and fluorescent dyes [10, 18]. This same path towards sub-microscopic resolution optical fibre imaging tools has not been duplicated so far in the greater field of acoustics. For the branch of photoacoustic endoscopy [96, 113], this is partly due to the reliance on cell types with strong optical absorption, such as red blood cells [91, 108]. However, one of the key challenges for any acoustic imaging technique, is that high resolution requires short acoustic wavelengths, and therefore high acoustic frequencies. Since the attenuation of acoustic waves depends on the square of the frequency [201], the working distance of high frequency acoustic imaging systems is greatly restricted.

The field of spontaneous Brillouin spectroscopy avoids this challenge by neglecting to generate sound altogether. The frequency of random thermal phonons - in the GHz frequency range - within specimens can be detected remotely using the opto-acoustic phenomenon of Brillouin scattering which can be accessed with optical resolution [127]. This has inspired early prototypes for spontaneous Brillouin endoscopes which must contend with parasitic Brillouin and Rayleigh scattering in optical fibres, and thus far have only been capable of 1D profiling on the $\sim 100\ \mu m - mm$ scale [152, 153].

In this chapter the path towards using a single optical fibre ultrasonic tool to achieve microscopic resolution imaging will be presented for the first time. As described thus far, this imaging device utilises the principles of PLU and TRBS to generate and detect sub-micrometre wavelength acoustic phonons. This scheme provides two key benefits: (1) high amplitude strain pulses can be actively driven into the imaging target by a laser ultrasonic transducer, allowing low-background Brillouin scattering with single-mode optical fibre; (2) the interferometric nature of TRBS provides access to the acoustic

time-of-flight for sub-optical wavelength axial resolution. To enable these benefits, the chapter will initially revisit the experimental design in an imaging context. Next the process by which a TRBS signal is converted into a spatial measurement will be introduced, followed by extrapolation to 3D profilometry, with proof of concept imaging attained for polymer microstructures. All of this will be possible while still retaining the ability to perform parallelised Brillouin spectroscopy, initially presented in the previous chapter. Finally, the performance metrics and future applications will be discussed in the context of other profilometry techniques, such as atomic force microscopy (AFM), optical profilometry, and stylus profilometry.

6.1 Experimental design

With the aim of using the phonon probe as an imaging tool, the Brillouin spectroscopy set-up presented in Figure 5.1, Chapter 5.1, must be modified in order to allow scanning in three dimensions. Ideally the scanning behaviour would be performed solely by the phonon probe, as this is the basic operating principle for endoscopic procedures. However, in order to achieve proof of concept for the proposed imaging technique, the x/y scanning capabilities will be assigned to the sample instead. This is accomplished by fixing a specimen-platform to a double-stack of precision linear translation stages (PI M-605) with minimum incremental motion of $300\ nm$ and $1\ \mu m$ accuracy, as seen in Figure 6.1.

Scanning in the z-direction is realised by constructing a vertical column to which the phonon probe can be fixed, and from which the fibre-transducer tip can descend down towards the sample-plane. The column-assembly is comprised of an optical post, on top of which sit two perpendicular micrometres which allow manual adjustment of the fibre tip position in the x/y plane relative to the sample. An L-bracket is then used to create a vertical plane (with respect to the sample plane); fixed to the vertical surface of this L-bracket is an additional micrometre which allows manual adjustment of the fibre tip in the z-direction. Attached to the z-micrometre are a series of rods which support an SM1-threaded cage plate; this cage-plate is then coupled with a piezo nanopositioner (PI P-721 PIFOC). The positioner is conventionally used for axially scanning microscope objectives, and is capable of $5\ nm$ positioning resolution over a range of $100\ \mu m$. Finally, an SM1-threaded fibre clamp (Thorlabs SM1F1-250) is coupled to the z-piezo and houses the tip of the phonon probe which is now capable of motion with nm resolution in the z-direction and $\sim 100\ nm$ in the x/y directions.

The mechanical motions of the x, y, and z stages are controlled by computer using custom-written C-programming scripts. In particular, the z-stage is controlled by varying the output voltage (over $0-5V$) from a microcontroller (Phidgets PhidgetAnalog 4-Output 1002_0B) which is amplified by a factor of 20 (using PiezoDrive PDm200 Minia-

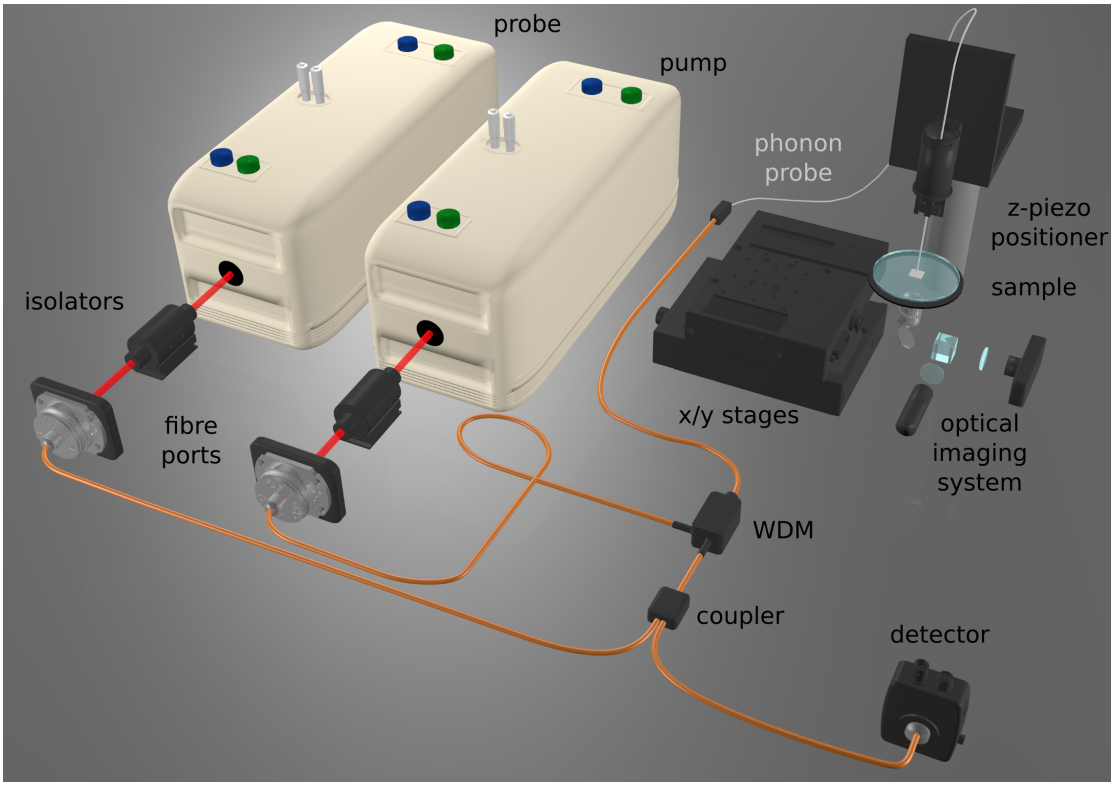


Figure 6.1: Illustration of the phonon probe system configured for 3D imaging. The sequence of pump/probe lasers, isolators, fibre ports, couplers, and detector are identical to the system presented in Section 5.1 used for Brillouin spectroscopy. This configuration has been modified to control the x/y positioning of a sample (e.g. microstructures on a glass coverslip slide) and the z-positioning of the phonon probe (using a z-piezo stage). A supplementary imaging system has been assembled beneath the sample plane to aid in finding regions of interest on the sample and for localising the fibre-tip when it is descended to the sample for TRBS measurements.

ture High Voltage Amplifier) and supplied to the z-piezo device. The piezo nanopositioner is run in an open-loop configuration and is specified to convert input voltage to output motion at a rate of $1\ V/\mu m$ ($50\ mV/\mu m$ considering pre-amplification).

Following the construction of the precision motion control facilities, an ancillary imaging system was assembled beneath the sample plane (see right side of Figure 6.1). The system consists of a red LED that is focused onto the back focal plane of an Olympus Plan Achromat Objective lens (RMS20X with 0.4 NA). The sample-reflected light is then imaged onto a CMOS webcam sensor. This provides the ability to quickly locate features in the sample plane before descending the phonon probe to the surface in a manner similar to stylus profilometry and atomic force microscopy. The imaging system aids in this process, as once the fibre-tip enters the focal plane of the objective, the system can be switched over from coarse movements (z-micrometre) to high resolution movements (z-piezo stage). This is done to ensure the phonon probe is not accidentally driven into the sample/substrate which would cause damage to the transducer, sample, or even break the fibre.

Aside from the additional elements described here, the remainder of the measurement system is identical to the optical set-up described in Section 5.1, and the detection chain described in Section 4.1.2. The pump and probe wavelengths utilised throughout this chapter are $\lambda_{pump} = 730\ nm$ and $\lambda_{probe} = 850\ nm$; these were selected since the dichroic edge of the WDM lies between them, and a longer probe wavelength (compared with Chapter 5) ensures that a relatively low frequency phonon is used as the carrier signal. The latter is important since the penetration depth of the technique will depend on the amount of attenuation experienced by the acoustic wave, a quantity which is frequency dependent [85, 201].

The following section will outline how the above experimental set-up will enable the phonon probe to act as a 3D imaging probe for microscopic objects.

6.2 In-depth measurement process

In order to perform imaging on microscopic objects, the objects must first be localised within the sensing region of the instrument. The process for achieving this will be defined and calibrated using the flat surface of a polystyrene petri dish. This calibration process will lead to the assembly of a signal processing package built from the methods outlined in Section 4.2, which will enable the device to make in-depth measurements of 3D objects.

6.2.1 Initial boundary localisation

If a photoelastic object that is immersed in water (the coupling medium) is brought within the penetration depth of the phonon probe, the transition in Brillouin frequency should be detectable by the device. Moreover, the position in time (and therefore axial distance) at which the frequency transition occurs can be localised through time-frequency analysis (e.g. continuous wavelet transform). This ultimately has the potential to provide both a *proximity* measurement to the photoelastic object, and a measurement of its elasticity by characterising its Brillouin frequency.

The most convenient test sample which would allow these concepts to be tested, is a common laboratory petri dish (plastic), which is made out of the photoelastic polymer polystyrene (PS). The petri dish was placed at the sample plane of the imaging system in Figure 6.1 and filled with water to allow for ultrasonic coupling. In addition to being photoelastic PS has the added benefit that it shares a similar acoustic impedance with that of water (discussed in Section 6.3.1), which should result in efficient coupling of acoustic waves between the water and the petri dish.

The phonon probe, placed in the vertical assembly above the sample, was manually descended into the water. Initial TRBS measurements were performed in the water, well away from the influence of any boundary. This will serve as a reference signal both

for the Brillouin frequency of the carrier medium (the water), and the signal amplitude decay only as a function of acoustic attenuation and not a physical boundary. It is useful to classify this type of measurement as NB, i.e. no boundary. Parameters for data acquisition were set to $10k$ averages per measurement on the oscilloscope ($3.5\ s$ per measurement), and was repeated for 100 counts, which allows up to $1M$ averages to be obtained in post-processing. The red TRBS signal in Figure 6.2b displays this reference signal, and was characterised to have a Brillouin frequency of $f_B = 4.81 \pm 0.01\ GHz$ as seen in the FFT in Figure 6.2c. In Chapter 5.2.2 it was demonstrated that the expected theoretical and experimental Brillouin frequencies in water differed by approximately $125\ MHz$ due to the effect of temperature; this same offset is found between the measurement in Figure 6.2b and the theoretical value of $f_B(\lambda_{probe} = 850\ nm) = 4.69\ GHz$.

Following this reference measurement (NB), the tip was descended towards the petri dish surface using the z-micrometre until the tip appeared within the focal plane of the imaging system. Then, the z-piezo stage was used to incrementally step the fibre tip closer to the dish surface in $1 - 2\ \mu m$ steps (during live TRBS data acquisition) until a visible change in TRBS signal on the oscilloscope was observed. If the position of the z-micrometre is such that the petri dish surface cannot be reached within the $100\ \mu m$ range of the z-piezo, the z-piezo is then retracted to position zero, and the z-micrometre is lowered by $100\ \mu m$, and the process is repeated.

Once this procedure produced a signal that clearly differed from the reference signal another $1M$ averages was recorded as exemplified by the blue signal in Figure 6.2b; this is now classified as the *with boundary* case, WB. Initially, the signal appears to clearly match the initial 3 cycles of the reference signal, after which the altered TRBS signal experiences a shift to a higher frequency. This is confirmed by analysing the frequency content of the wave in the Fourier domain (blue spectrum in Figure 6.2c), where the amplitude of the $f_B(H_2O)$ peak has substantially fallen and broadened, and is accompanied by a neighbouring frequency peak of $f_B = 7.9 \pm 0.1\ GHz$ that has emerged. The refractive index and sound velocity of polystyrene were collected from literature [219, 220] and used to calculate an approximation for the expected Brillouin frequency: $f_B = 8.7\ GHz$. Even though the theoretical value is outside of the confidence interval of the experimental measurement, the two values are within reasonable agreement and variations are expected between material properties reported in literature and commercial lab-ware.

The method for converting the original time-domain signal into the spatial-domain is central to using the phonon probe to perform in-depth measurements. This is achieved by first taking the FFT of the time-domain signal and recording the frequency position of the maximum amplitude, e.g. $f_B(H_2O) = 4.81\ GHz$ for the red-coloured signal in Figure 6.2c. Then, using the relationship between sound velocity and Brillouin frequency

(Equation 2.24), an experimental measurement of the sound velocity is obtained:

$$v_f = \frac{f_B \lambda_{probe}}{2n} \tag{6.1}$$

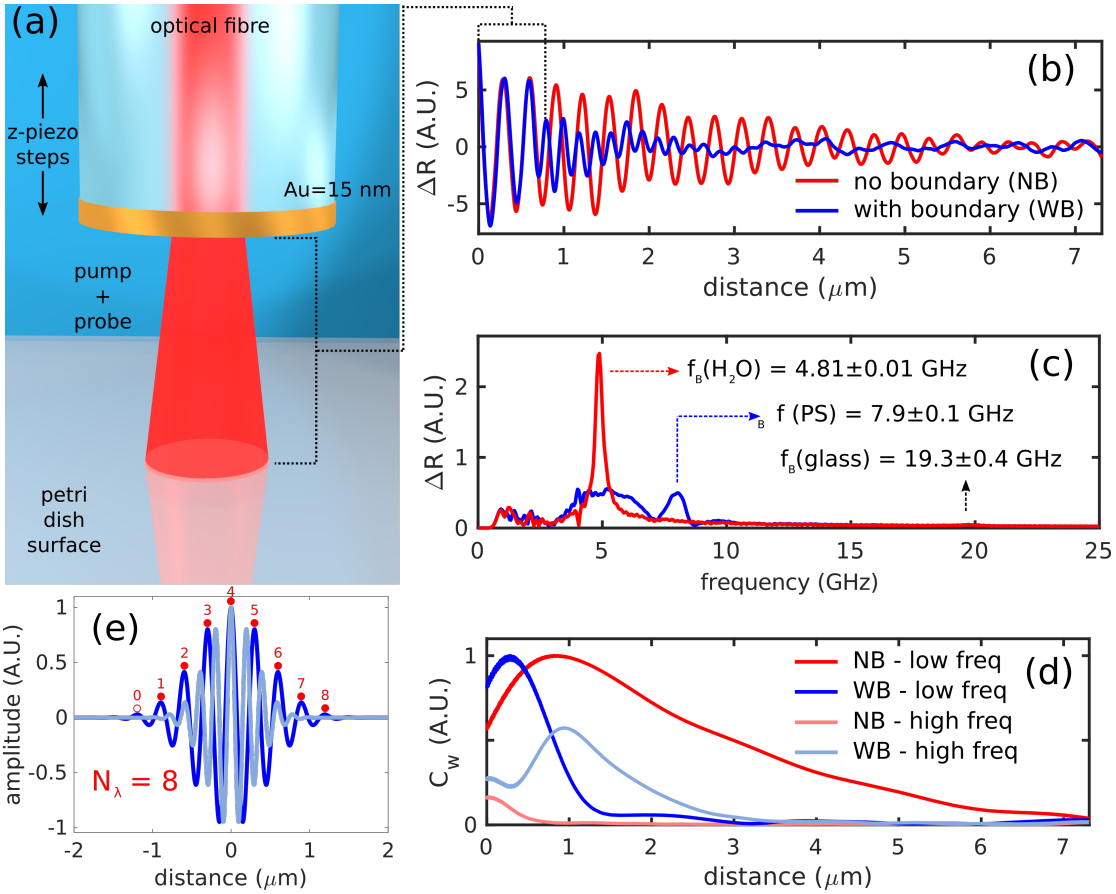


Figure 6.2: (a) Illustration of the phonon probe interrogating the surface of a polystyrene petri dish. The z-position of the probe-tip can be controlled manually via micrometre and with high resolution via nanopositioner stage. When the measurement volume is unimpeded (NB - no boundary), the device registers measurements of the background medium, in this case water, resulting in the red TRBS signal in (b). The blue signal in (b) is the result of the transducer tip and petri dish stand-off distance being within the penetration depth of the phonon probe (WB - with boundary). (c) FFT of the two cases in (b): the NB red measurement consists of a $f_B = 4.81 \pm 0.01\ GHz$ frequency peak (water), and the WB blue measurement reveals a broad low amplitude peak around 5 GHz (first $2-3$ low frequency cycles from the carrier medium) and a new high frequency peak at $f_B = 7.9 \pm 0.1\ GHz$ from the PS petri dish. (d) Wavelet analysis was performed on the time-domain signals in (b); the frequency peaks in (c) were used to assign centre frequencies to the complex Morlet mother wavelets shown in (e) (blue-low frequency, light blue-high frequency). (d) For the NB signal, wavelet analysis reveals a slowly varying amplitude decay at the carrier frequency (red), with virtually no contribution from higher frequencies (light red). Conversely, the WB signal displays a sharp attenuation of the low frequency carrier (blue) accompanied by a rise in amplitude at higher frequencies (light blue). (e) Red circles provide an estimate for the number of acoustic wavelength cycles in the wavelet width, e.g. $N_\lambda = 8$ which corresponds to a total width $w_\lambda \approx 2.5\ \mu m$.

where the refractive index of the couplant medium (medium in which the measurement is taking place) is assumed to be $n = 1.33$ and homogeneous. Now, using the experimental sound velocity, the spatial vector can be assembled $z = v_f t$ where t is the time-vector of the original signal. This spatial vector can now be used to visualise (Figure 6.2b) and measure (next section) the spatial propagation of the acoustic wave, which propagates with acoustic wavelength $\lambda_a = \lambda_{probe}/2n$. Below and in Section 6.4 the cases of multiple materials (multiple sound velocities) within a single signal (e.g. blue in Figure 6.2b) and sound velocities (in a single material) which fluctuate over signal-time will be discussed.

Now in order to evaluate the time-variation of the frequencies present in both the reference and boundary signals, wavelet transformations (Section 4.2.2) were performed on the signals using complex Morlet mother wavelets and a wavelet width of $N_\lambda = 8$ acoustic wavelengths ($w_\lambda \approx 2.5\ \mu m$ total width); this value is estimated by counting the number of cycles in the wavelet with approximately non-zero amplitude (red circles in Figure 6.2e). The frequency peaks that were characterised for the carrier wave and PS oscillations (red and blue spectra in Figure 6.2c) were used to set the centre frequency of two separate wavelets found in Figure 6.2e. The wavelet coefficients (C_w) resulting from transformation between the wavelets and the two signals can be found in Figure 6.2d. Upon inspection, the amplitude roll-offs of the low frequency carrier wave ($5\ GHz$) appear to occur at different rates between the reference and boundary signals. Following the peak amplitude of the C_w response (when the wavelet has completely entered the time window) the reference signal experiences a much slower amplitude decay when compared with the sharp response of the boundary signal. For the case of the higher frequency wavelet, the boundary signal contains a sharp rise in amplitude at approximately $z = 1\ \mu m$, whereas the same rise cannot be found in the carrier signal.

This initial observation of a change in TRBS signal when the phonon probe appears to be close to a boundary can be taken a step further by using the piezo-stage to incrementally step the fibre-tip away from the surface of the petri dish. If the altered TRBS signal is indeed a response from the dish boundary, the change in Brillouin frequency should occur progressively later in the time window. This experiment was performed by: (1) acquiring $1M$ averages at the current tip position, (2) step the z-piezo away from the surface by $50\ mV$ (which should correspond with $1\ \mu m$), (3) repeat steps 1-2. The TRBS signals produced by this experiment are found in Figure 6.3a, accompanied by the wavelet coefficient traces in Figure 6.3b. From these results the transition in frequency from the $5\ GHz$ carrier signal to the $8\ GHz$ object signal clearly occurs later in signal time (axial distance) as the fibre tip is stepped away from the surface (green bars, approximate position). The same phenomenon is observed for the low frequency amplitude of the wavelet coefficient traces (blue curves in Figure 6.3b), which have been normalised to each one's maximum amplitude. It is worth

noting that the amplitude of the Brillouin oscillations in the PS are noticeable in both the time-domain and wavelet transformations, however, beyond the fourth piezo-step the oscillations become indistinguishable from noise. A likely explanation is that the combined effects of acoustic attenuation and acoustic impedance mismatches lead to a weakening of the high frequency phonon field within this secondary material (discussed

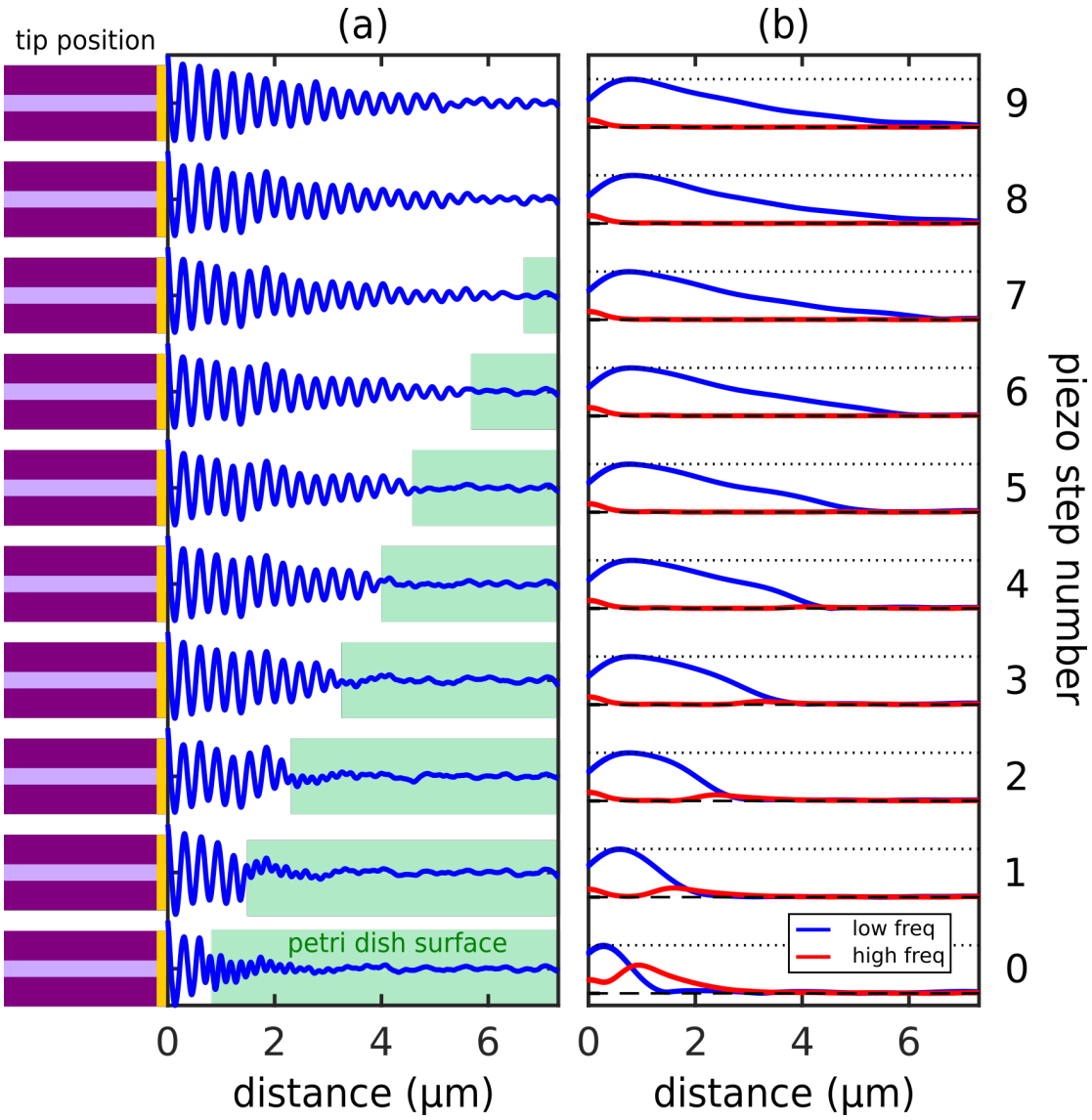


Figure 6.3: The stand-off distance between the phonon probe tip and the surface of the petri dish is used to investigate the in-depth measurement capabilities of the device. (1) The tip was initially positioned closely to the surface, (2) a TRBS signal with $1M$ averages was captured, (3) the tip was stepped away from the surface using the piezo-stage, (4) process repeated. The resulting modulation depth signals in (a) initially reveal a transition from low to high frequency which occurs progressively later in the trace as the tip moves away from the surface. This is confirmed in the plotting of the wavelet coefficients (b) for $\approx 5\ GHz$ (blue) and $\approx 8\ GHz$ (red) centre frequencies. (a) Green bars indicating the approximate position of the petri dish relative to the position of the tip (distance$= 0$) were initially estimated by eye. Dashed lines represent amplitude $A = 0$, and dotted lines represented $A = 1$.

in Section 6.3.1).

The results in Figure 6.3 imply that the phonon probe is indeed capable of responding to changes in the 1D geometry of an environment. Before this capability can be extrapolated to 2D or 3D (by scanning) for profilometry and imaging, it is necessary to define a method for extracting a quantitative in-depth measurement of the stand-off distance between the fibre-tip and the object. This will be the aim of the following section, which will make use of the experimental results attained from the petri dish proximity experiment.

6.2.2 Proximity measurement

The reference signal (when there is no boundary near the tip), and the measurement at piezo step number 2 (third from bottom in Figure 6.3) will be used as case studies for defining the distance measurement process, and are found again in figures 6.4a-b. Recall that the case without boundary will be referred to as NB, and the case where the boundary exists will be referred to as WB. The Brillouin frequency measurements attained from the respective TRBS signals (e.g. Figure 6.2b-c) were used to assign mother wavelet centre frequencies, and the resulting wavelet coefficients (normalised to $C_w(H_2O) = 1$) for each case are displayed in figures 6.4c-d.

First considering case NB (Figure 6.4c), the wavelet response for the low frequency reveals an initial rise between $z = 0 - 1\ \mu m$; this is the "blind" zone of the trace, where the mother wavelet has not fully entered the signal window and is therefore under-sampling (and under-estimating) the signal amplitude. Once the wavelet has entered the trace, and the maximum wavelet amplitude components have sampled the maximum signal amplitude, a maximum wavelet coefficient is attained (normalising to $C_w = 1$ here). This is then followed by a slow decay at the carrier frequency, which in the case of TRBS and the low NA fibre transducer, is the acoustic attenuation of the $\sim 5\ GHz$ phonon. This same sequence of events also occurs for the carrier frequency in the WB case (Figure 6.4d), until, at the onset of the petri dish boundary, a more severe decay in amplitude takes place.

In order to unambiguously delineate the natural attenuation from the boundary response, all influences of the material attenuation should be removed from the trace. This is accomplished by fitting a decaying exponential to the NB wavelet response according to the methodology outlined in 4.2.1. For this example, the exponential function which most closely matched the decay of the signal contained an attenuation coefficient of $\alpha = 0.30 \pm 0.06\ \mu m^{-1}$ and is plotted in green in Figure 6.4c (beginning at the position of maximum wavelet amplitude after the blind zone). This attenuation function is then used to normalise the WB case resulting in the (attenuation) *corrected* wavelet

response (C_w''), shown in blue in Figure 6.4f

$$C_w''(z) = \frac{C_w(z)}{e^{-\alpha z}} \tag{6.2}$$

Recall that the z vector for each signal (NB or WB) has been calculated using the experimental measurement of the signal's Brillouin frequency and therefore sound velocity

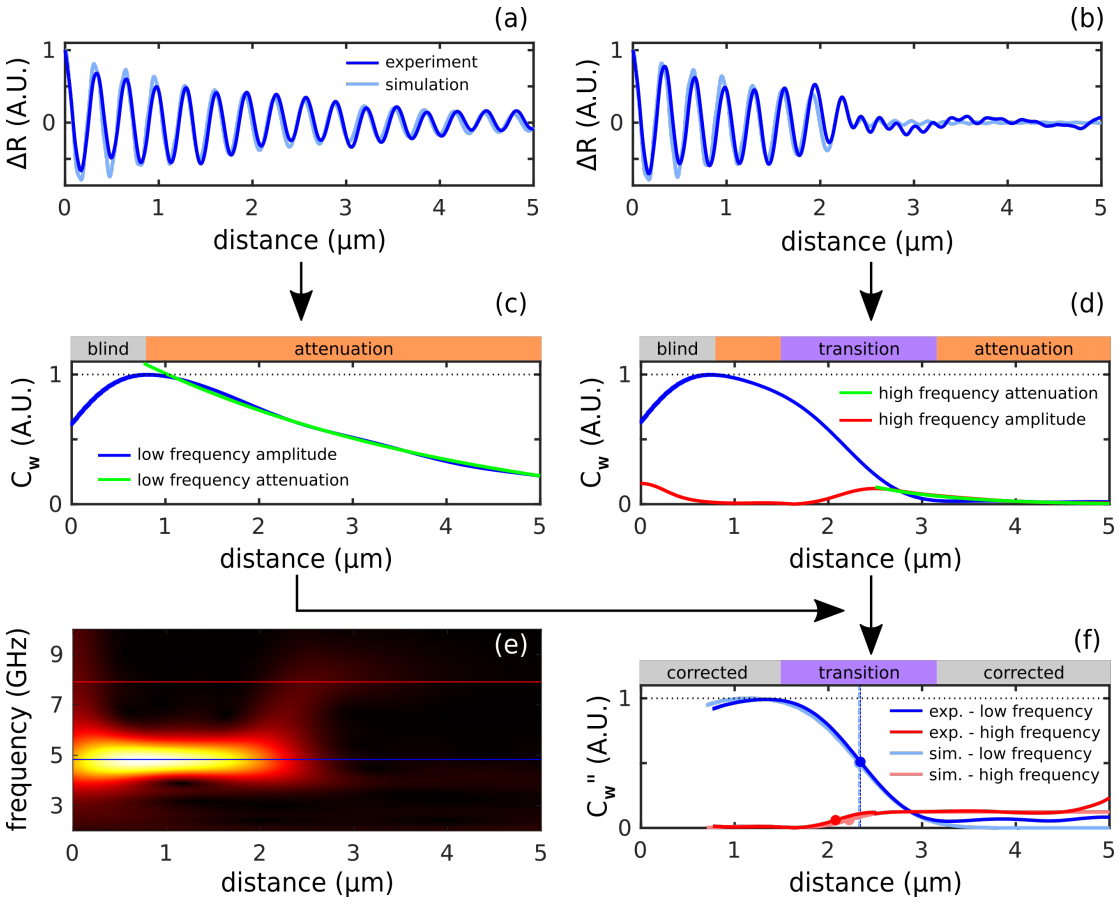


Figure 6.4: Process chain for converting a time-domain signal into a proximity measurement. (a) Acquire a reference signal (NB) where there is only water and no boundary. (b) Acquire a signal which appears to contain an additional source of signal decay (WB). (not-pictured) FFT the time-domain signals in order to characterise the component Brillouin frequencies (e.g Figure 6.2c), set the discretisation of the spatial vector, and define the mother wavelet centre frequencies ($f_{blue} \approx 4.8\ GHz$ and $f_{red} \approx 7.9\ GHz$. (c) Wavelet transform NB and fit a decaying exponential (following the initial blind zone) to characterise the signal decay produced by material attenuation (green line). (d) Wavelet transform of the WB signal; low frequency amplitude contains an additional decay event and the high frequency amplitude rises (attenuation thereafter can also be fitted in green line). (f) Normalise the wavelet response from the WB signal by the green line in (c) in order to remove the effects of material attenuation. For low frequency (blue): when wavelet is in water $C_w'' \approx 1$ and when it transitions to PS $C_w'' \approx 0$. The position of $C_w'' = 0.5$ corresponds with a measurement of the boundary proximity to the fibre-tip. Light blue and red represent the simulated analogues for all plots. (e) Time-frequency spectrum of the experimental TRBS signal in (b) where $f_{blue} \approx 4.8\ GHz$ and $f_{red} \approx 7.9\ GHz$.

(Equation 6.1).

As a result of this correction process, when the wavelet is in a medium whose Brillouin frequency matches its centre frequency (with decay α), the resulting wavelet response is flat with amplitude $A = 1$ (the couplant medium is now lossless). Conversely, when the wavelet has left this medium, an amplitude $A = 0$ occurs, therefore removing the ambiguity between material attenuation and boundary transition. In practice this will depend on the acoustic impedance mismatch, as strong acoustic reflections at a water:object boundary will result in a wave which counter-propagates in reality, but co-propagates beyond the boundary in the time-base of the signal.

At this point, it logically follows that the width of the boundary transition in the corrected wavelet response should correspond with the width of the wavelet being used. In other words, as the $f_c \sim 5\ GHz$ wavelet leaves water and enters PS, the transition from $A = 1 \rightarrow 0$ will occur within the distance spanned by the wavelet. The approximate length of the boundary transition region in Figure 6.4f is $w_\lambda \approx 1.8\ \mu m$, which is shorter than the original estimate of $w_\lambda \approx 2.5\ \mu m$ ($N_\lambda = 8$) in Figure 6.2e. The width $w_\lambda \approx 1.8\ \mu m$ does however correspond with $N_\lambda = 6$ cycles of the acoustic wavelength, which will now be used as the width of the wavelet. The discrepancy in N_λ is likely due to the outermost cycles of the wavelet (which were originally counted) not having sufficient energy to influence the response of the transformation. In any case, the position at which amplitude $A = 0.5$ occurs corresponds with the wavelet straddling the boundary between water and PS, and as such, provides a measurement of the boundary proximity to the fibre tip at $z = 0$. The experimental proximity measurement for this example was determined to be $z_e = 2.30 \pm 0.07 \mu m$.

In principle, the same measurement process can be applied to the high frequency PS wavelet response. It is less crucial to correct for the material attenuation rate of PS in this scenario, as the transition will occur before PS-attenuation has taken place. In any case an estimate of the attenuation rate can still be attained by fitting a decaying exponential to the falling edge of the PS-response after the transition has occurred (green in Figure 6.4d) and exhibits a decay rate of roughly $\alpha = 0.83 \pm 0.07\ \mu m^{-1}$. The position at which the half maximum of the PS-amplitude rise occurs was measured to be $z_e = 2.04 \pm 0.08 \mu m$. The offset between this distance measurement and that of the low frequency wavelet can be explained by the drop in signal amplitude, and therefore lower SNR of the PS oscillation. The average frequency peak position measured for the carrier frequency was identified as $f_B(H_2O) = 4.80 \pm 0.08\ GHz$, whereas the high frequency peak was characterised as $f_B(PS) = 7.9 \pm 0.3\ GHz$ and shows greater variance due to the lower SNR at this frequency. This is an effect that will also worsen with distance due to the natural attenuation of the wave (before the boundary transition occurs), therefore, in the interest of locating the boundary transition with highest possible SNR, the transition position of solely the carrier frequency will be used going

forward (blue dot in Figure 6.4f). This choice will also simplify the conversion from the time-domain to the spatial-domain, since the sound velocity of only a single material needs to be considered.

The boundary phenomena discussed thus far, and the resulting proximity measurement, can be corroborated using the analytical PLU-model (Section 2.2.2). Using the same pump and probe wavelengths, the NB case was first simulated resulting in the TRBS signal in Figure 6.4a (light blue). The proximity measurement attained using the low frequency wavelet roll-off (blue star $z_e = 2.30 \pm 0.07\ \mu m$ in Figure 6.4f) was used as the input thickness for the water layer (sandwiched between the transducer and PS layer) configured in the geometry seen in Figure 4.13a. The resulting simulated TRBS signal is showed in light blue in Figure 6.4b and appears to closely agree with the experimental trends seen in the time-domain. Attenuation-corrected wavelet coefficients for the low and high frequency wavelets were calculated using the same technique as above, and plotted in Figure 6.4f (light blue and red). The resulting agreement between the proximity measurement provided by experiment (z_e) and simulation (z_m) (without noise) (light blue star in Figure 6.4f) is on the order of $20\ nm$ indicating that wavelet analysis produces an accurate measurement of where the theoretical boundary exists.

Earlier, an amplitude threshold of $C_w'' = 0.5$ was established given the condition that the corrected wavelet response should transition from $C_w'' = 1 \rightarrow 0$ at the boundary (see Figure 6.5a). In experiment, the minimum amplitude (m_C) is unlikely to drop all the way to zero due to slight mismatches between the fitted attenuation rate and the experimental decay rate, especially as SNR worsens later in the signal. Therefore two user-defined thresholds should be established for a proximity measurement to occur:

1. τ_{min} - threshold for the maximum value permitted for the absolute minimum amplitude of the wavelet response. For example, in the ideal case of a perfect sinusoid without attenuation, this threshold should be $\tau_{min} = 0$. However, given noise and attenuation in a signal, a reasonable value for this threshold might be $\tau_{min} = 0.4$. If the minimum C_w'' (m_C) is beneath this threshold, then a measurement will be logged as in Figure 6.5b, otherwise a measurement will not be made (i.e. temporarily pin measurement to the end of the time-window z_{end}) as in Figure 6.5c.

2. τ_{half} - if the condition $m_C < \tau_{min}$ is met then the proximity measurement will be taken at the amplitude that is half-way between the m_C value and 1. For the ideal scenario with no attenuation $m_C = 0$ and $\tau_{half} = 0.5$, otherwise $\tau_{half} > 0.5$.

Using these criteria, the proximity measurement protocol (Figure 6.4) was repeated for each TRBS signal acquired from the petri dish experiment (Figure 6.3a). Recall that each TRBS signal at a piezo-step contained 100 counts of $10k$ oscilloscope averages; the attenuation correction procedure was performed on each of the 100 counts, and the Brillouin frequency for each signal was used to set the spatial mesh. In Figure

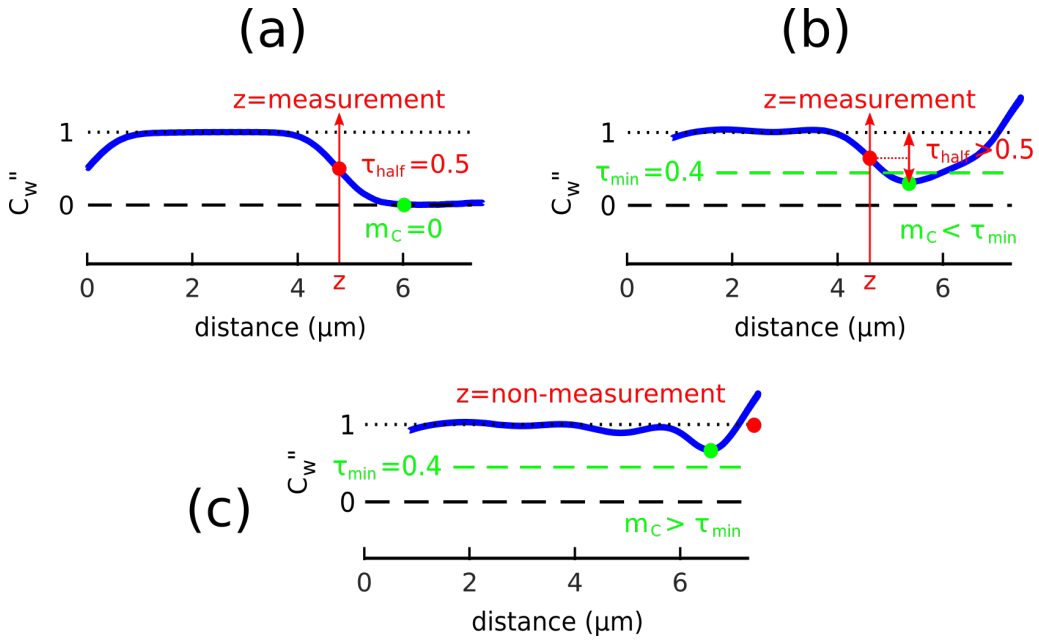


Figure 6.5: Criteria for whether a transition can be registered as a distance measurement. (a) Ideal situation: material with no attenuation transitions into another material. The corrected wavelet response (C_w'') should transition from $C_w'' = 1 \rightarrow 0$ and the distance measurement takes place at the location where $C_w'' = 0.5$ occurs (red circle). (b) In reality the minimum C_w'' value (m_C, green circle) will be greater than 0; apply an amplitude threshold τ_{min}, if $m_C < \tau_{min}$ then a measurement is valid, otherwise it is invalid (c). If a measurement is valid, then determine the amplitude value that is halfway between 1 and m_C and assign as distance measurement ((b) red circle), otherwise non-measurements are anchored to end of time-base ((c) red circle).

6.6b, the mean attenuation corrected wavelet response (C_w'') is plotted in blue and the standard deviation across measurements (at each piezo step) plotted in the dashed blue lines. Using the threshold criteria defined above, proximity measurements were extracted from the wavelet responses, and are marked by the red coloured asterisks (placed at end of signal if no measurement occurred). The output experimental proximity measurements from this process were input as the thickness of the water layer for the PLU-model, and the measurement process repeated. Figure 6.7a-b shows the result of this exercise; it is worth noting that experimental measurements from piezo-step numbers 8 and 9, were input to the model as $z = z_{end}$.

The proximity measurements from experiment and simulation can now be collated and compared as a function of piezo-step and experimental averaging (see Figure 6.8). The red line and error bars represent the average proximity measurements and standard deviations across the $N = 100$ data-points, i.e. 100 separate measurements of $10k$ averages each. Conversely, the blue line and error bars are representative of averaging the TRBS signals into $N = 2$ bins, i.e. 2 separate measurements of $500k$ averages each. The latter results in much higher precision measurements at the cost of approximately 50 times longer acquisition time. Additionally, the uncertainty increases

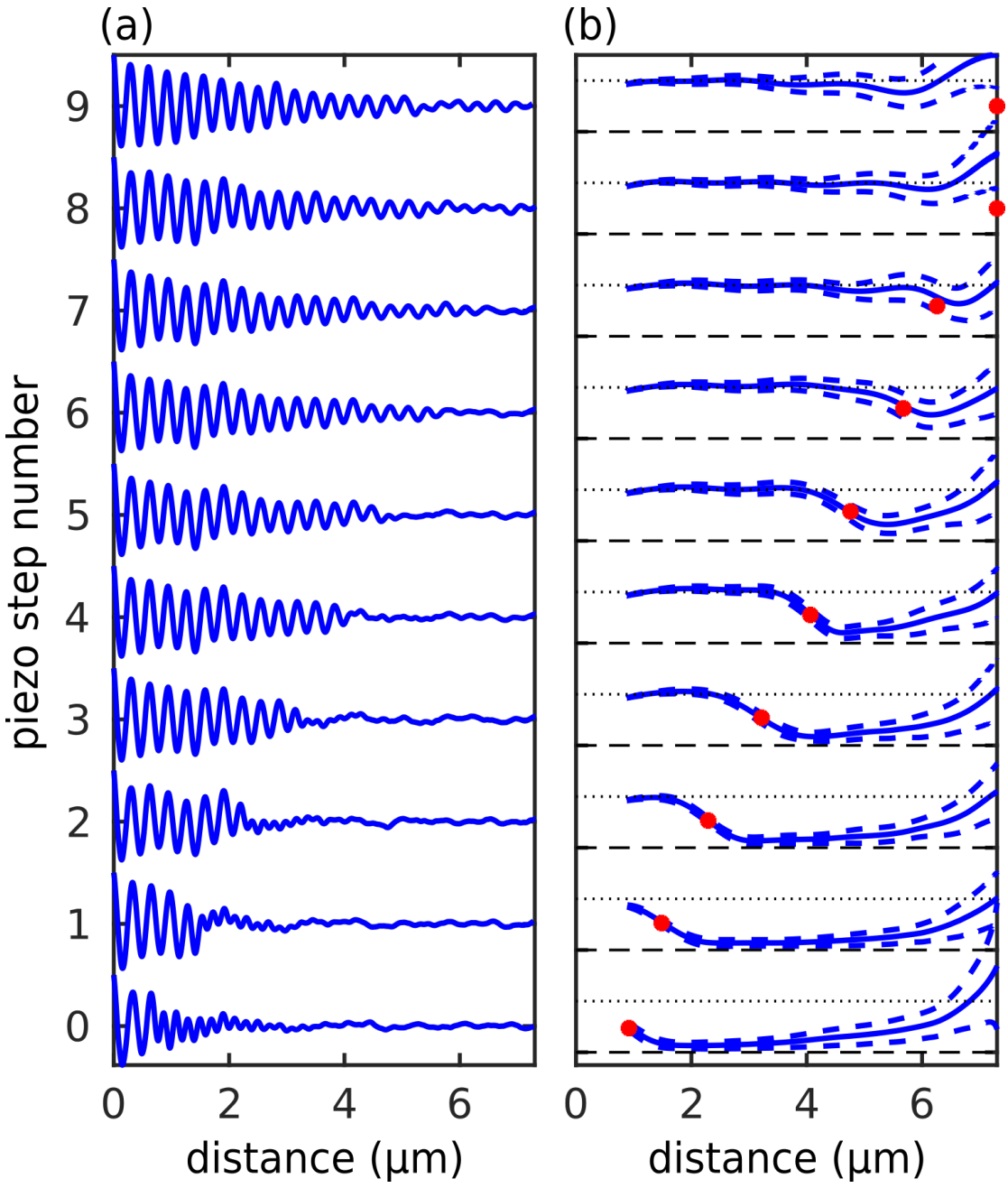


Figure 6.6: (a) Replotting of TRBS signals acquired as the phonon probe is incrementally stepped away from the surface of a petri dish filled with water (moving up the y-axis). (b) The low frequency (carrier signal in water) wavelet responses in Figure 6.3b have now been corrected (C_w'') to remove the decaying influence of material attenuation according to the methodology discussed around Figure 6.4. In theory, what's left is a trace that transitions from amplitude 1 to 0 at the boundary. Red marks indicate the proximity measurement and are determined by finding the amplitude that is halfway between the absolute minimum of the response and $C_w'' = 1$. Dotted lines outline the standard deviation of each C_w'' trace. Red marks anchored at the end of the trace represent non-measurements where the amplitude thresholds presented in Figure 6.5 have not been fulfilled.

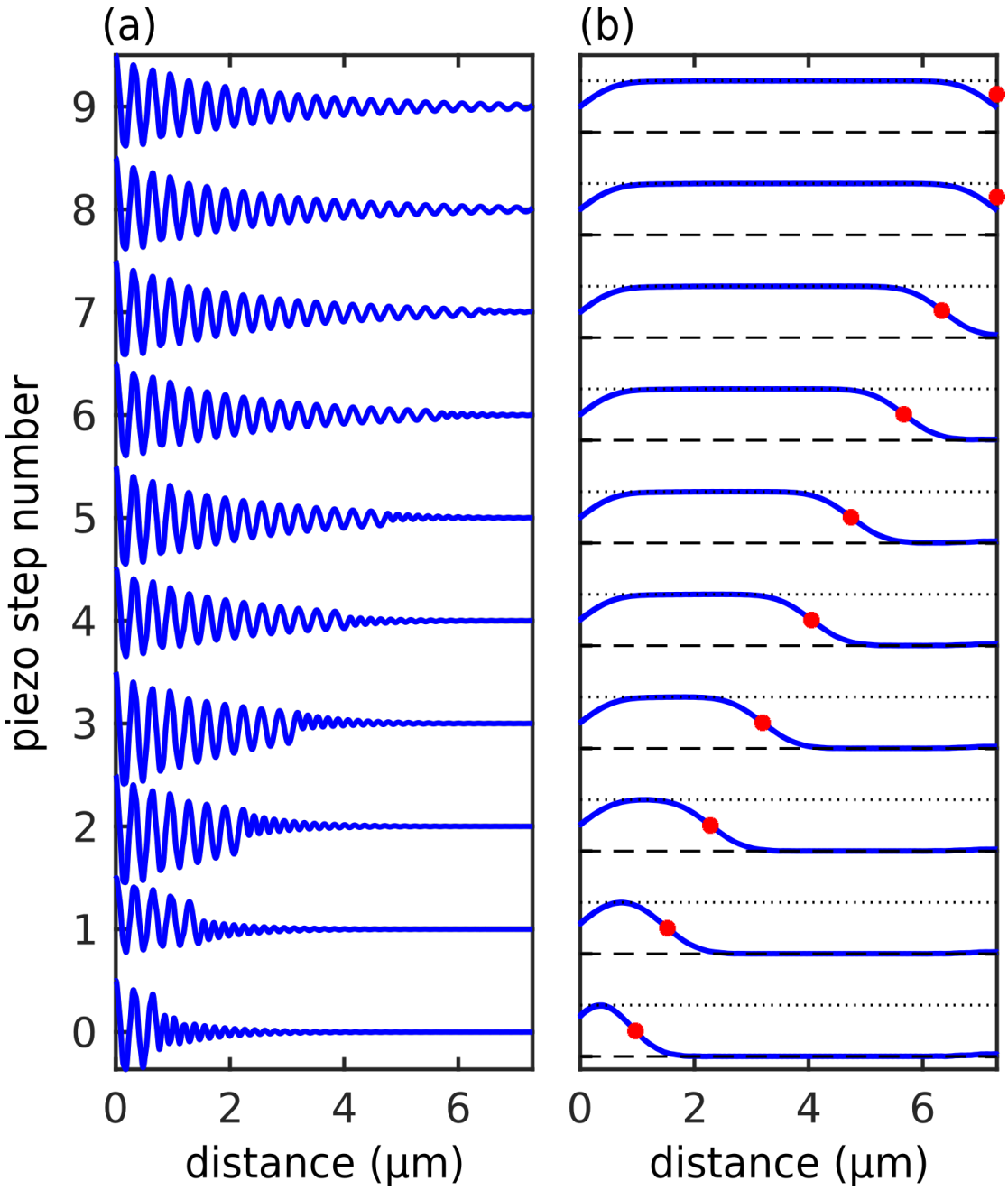


Figure 6.7: The distance measurements determined in Figure 6.6b were used as input thicknesses for the water layer between the transducer tip and the PS-object within the opto-acoustic model. (a) Resulting TRBS signals attained from the model (attenuation has been added artificially by including the factor $e^{-\alpha z}$ with a frequency dependent value of α from literature [201]). (b) Wavelet transform coefficients of the non-attenuating simulated signals in (a). The same measurement protocol was employed to produce the positions of the red marks and hence the proximity measurements. Since piezo-steps 8 and 9 produced no measurement in experiment, this was hard-coded for the simulation.

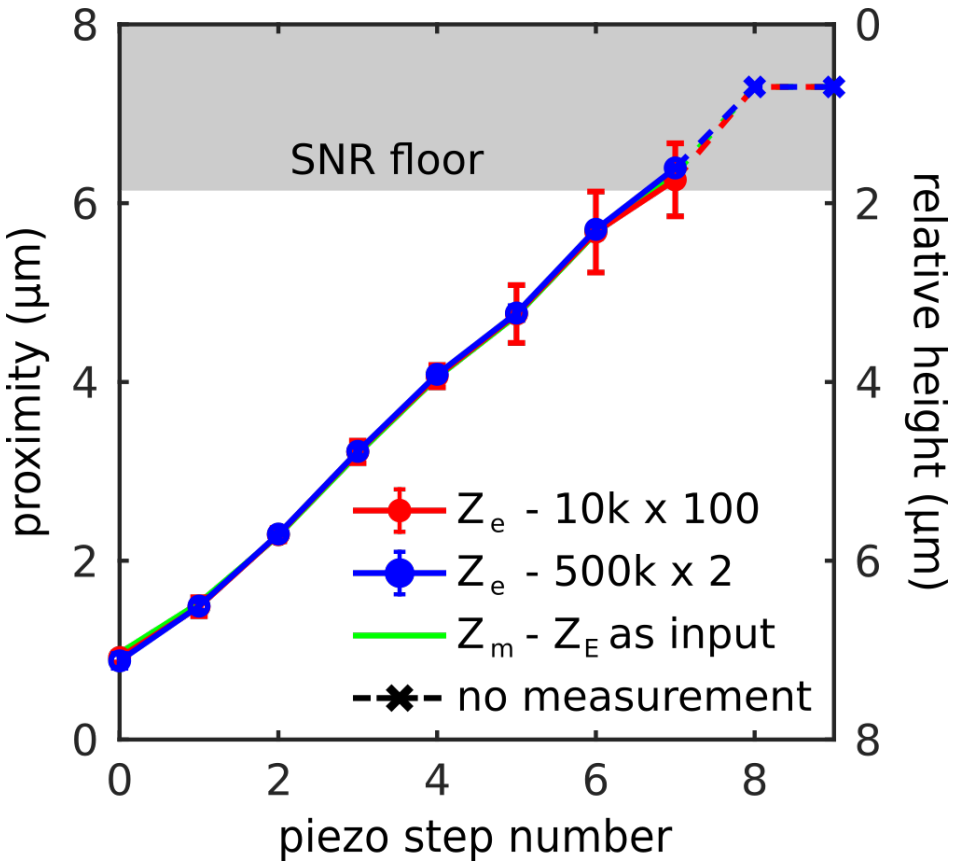


Figure 6.8: Final set of proximity measurements made as the phonon probe incrementally steps away from the surface of a petri dish. Red measurements are the average of $N = 100$ counts (per step), and the standard deviation over the N measurements. Blue measurements are the average of $N = 2$ counts where each of the two counts are themselves the average of $N = 50$ TRBS signals. The decrease in precision as a function of distance (between the fibre tip and the petri dish) is due to SNR falling with acoustic attenuation. The effect of averaging (blue) demonstrates an ability to maintain precision with distance. Green line is the simulated measurement using the red measurements as input water layer thickness to the PLU-model. Measurements which do not meet the threshold criteria presented in Figure 6.5, have been registered as non-measurements (dotted lines and x's) and define the SNR floor of the technique (at $10k$ averages). The SNR or the measurement of the physical floor can be used to invert proximity measurements into measurements of height (right y-axis).

as the measurement occurs later in the time signal, especially for the case of lower averaging (red). This is due to the SNR falling with increasing distance in the signal due to acoustic attenuation. Beyond the eighth piezo step the measurements can no longer be resolved from the noise floor (at $10k$ averages), and the non-measurements have been anchored to the end of the time-window. This establishes the effective dynamic range of the technique, which for this set of experimental parameters, is approximately $z_{DR} \approx 5.5\ \mu m$ (from blind zone to SNR floor). Increasing beam powers, additional signal averaging, a more efficient transducer, or a longer probe wavelength, will extend the dynamic range of the device; the latter two will be discussed in Section 7.

Simulated measurements are displayed along the green line in Figure 6.8 and ap-

pear to agree closely with the experimental measurements. The lone point of noticeable disagreement occurs at the first measurement (step 0). This highlights a minor limitation of the current technique: boundaries which are positioned within the blind zone of the wavelet transformation cannot be fully resolved since the measurement window is cropped to start at this position; therefore the measurement has been anchored to the beginning of cropped time window. In practice this is less of an issue since the distance of closest approach can be controlled by the user (discussed in following section), and a stand-off distance greater than $1\ \mu m$ is preferred to minimise the thermal load experienced by the imaging target due to transducer heating (see Section 5.2.2).

The slope of the experimental measurements in Figure 6.8 was calculated as $dz \approx 0.8\ \mu m$, indicating that this is the average distance the piezo moved the fibre tip away from the petri surface. As discussed at the beginning of this experiment, the piezo-stage was set to take $50\ mV$ (pre-amplified) steps which corresponds with an expected step of $dz \approx 1\ \mu m$. This offset could be due to the lack of calibration for the nanopositioner product, or due the output voltage error of the microcontroller and/or amplifier (discussed in Section 6.4.1). This systematic error from the z-piezo stage could affect the measurements of the phonon probe if the z-position is used as a free parameter in 3D scanning (but the error can be calibrated); if the z-offset between the tip and the imaging target is fixed, as will be the case in the following section, this error can be neglected.

Now that the protocol for performing a proximity measurement between the transducer tip and the target object has been established, the measurement process can be repeated across the x/y plane using mechanical stages. This ability for the phonon probe to generate proximity maps, can then be inverted to access the topographical information of the local environment. In Figure 6.8, this is exemplified by treating the SNR floor as height $h = 0$ and all measurements that are more proximal (to the fibre tip) can then be treated as a height measurement ($h > 0$) relative to the floor. The cases in which this translates to measuring the absolute height of an object will be discussed in the following section, in addition to proof of concept imaging results.

6.3 Polymer phantom imaging

In order to achieve proof of concept for using the phonon probe as a 3D imaging tool, polymer microstructures were selected as the imaging targets. Polystyrene microspheres were chosen for this project for their: (1) simple fabrication protocol, (2) relative inertness (e.g. no harsh chemicals required), (3) ability to self-assemble to some degree (and form compound structures), and (4) relatively similar optical and mechanical properties compared with biological cells, with cells being a key future imaging target for this device. This section will briefly introduce the fabrication protocol of such phan-

toms, and will introduce the first 3D images of microscopic objects using an optical fibre ultrasound probe.

Fabrication

The polystyrene microstructures were fabricated by drop-coating and melting $10\ \mu m$ diameter PS microspheres (Bangs Laboratories, Inc.) onto a special substrate. The relevant information and protocols for the fabrication process is detailed in Appendix D. The end result is a gridded landscape populated with compound PS microstructures found in Figure 6.9 (imaged using a reflection microscope). For this study, the phantoms located in the green, red, and blue boxes (in Figure 6.9) will be investigated. Figure 6.10 shows higher magnification views of these regions of interest (same colour coding). The phantoms contain the following approximate dimensions: green - $75\ \mu m \times 75\ \mu m$, red - $40\ \mu m \times 40\ \mu m$ (each), and blue - $20\ \mu m \times 20\ \mu m$. Each of the objects appear

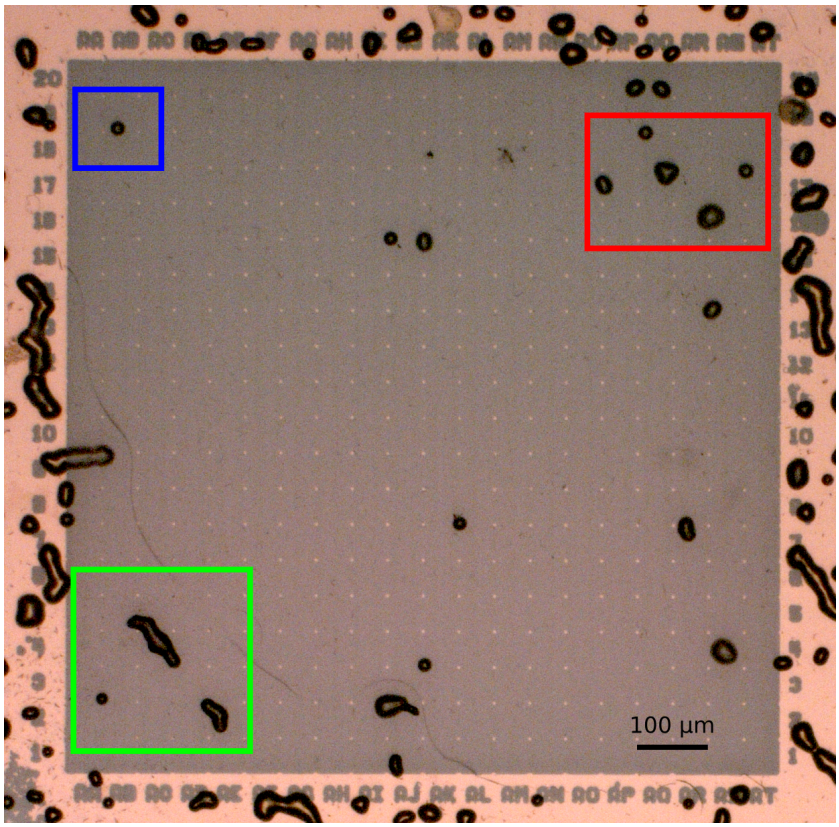


Figure 6.9: The photolithography process has created a pattern of gold (bright outline) and glass (dark background) in the shape of a square grid. This array is lined with letters and numbers to aid with locating objects within the cells of the grid. Small gold dots fill the grid which provide basic distancing and locating capabilities. The polymer phantoms were created by drop-coating PS microspheres and melting them into continuous structures. The blue, red, and green boxes designate regions that contain interesting imaging targets, due to their sizes, shapes, and possible heights. Images acquired using a reflection microscope with $5x$ magnification.

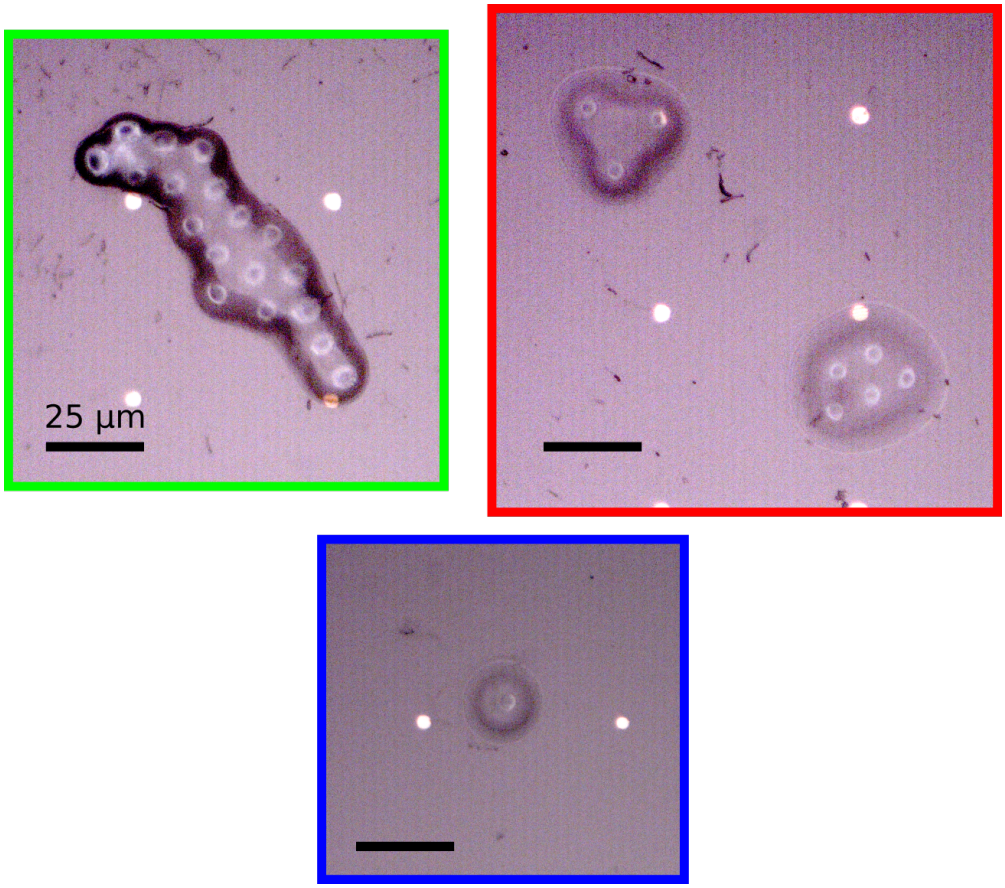


Figure 6.10: High magnification ($50x$) views of the proposed imaging targets in Figure 6.9 (same colour coding). It is estimated that the these structures contain the following dimensions: green - 75 $\mu m \times 75$ μm, red - 40 $\mu m \times 40$ μm (each), and blue - 20 $\mu m \times 20$ μm. Each phantom appears to have retained inner sphere-like structures which are likely the remnants of unmelted microspheres whose top layers have melded into a continuous surface.

to retain an inner microsphere core that is less visible with low magnification. The core features are likely subsurface since they appear most in focus when the substrate is in focus (e.g. using the gold dots as reference), and defocus when the tops of the phantoms are in focus. It is likely that this is a result of not melting the microspheres completely through, leaving an unmelted structure of seeds below. This likely allows the structures to retain some of the height from the original $h = 10$ μm diameter, but are now $h < 10$ μm as a result of partial melting. In any case, the cores clearly exhibit different optical properties compared with the rest of the structure.

With the substrate and polymer phantoms now prepared, the following section will present the basic experimental protocol and proof of concept 3D imaging results.

6.3.1 Imaging experiments

After fabricating the gridded substrate and polymer microstructures, the proximity measurement protocol outlined in Section 6.2 can now be carried out across the 2D plane

parallel to the substrate (Figure 6.11). First, the specimen substrate is placed at the sample plane of the phonon probe imaging system (Figure 6.1) such that it can be moved with high resolution in the x and y directions. The surface of the substrate is then brought into focus of the ancillary optical imaging system by adjusting the axial position of the objective lens with respect to the fixed height of the sample plane. Roughly $0.5 - 1\ mL$ of deionised water is then deposited onto the centre of the specimen in order to provide acoustic coupling between the phonon probe and the imaging objects. Then the x/y stages are adjusted to centre the grid (Figure 6.9) within the field of view of the optical imaging system.

To initiate the measurement procedure, the phonon probe is manually descended towards the sample plane using the coarse adjustment of the overhead assembly. Once the tip nears the air:water interface the z-micrometre is then used to carefully descend the probe tip into the water droplet and approach the substrate surface. Furthermore, the x and y micrometres in the overhead assembly were used to ensure that the fibre

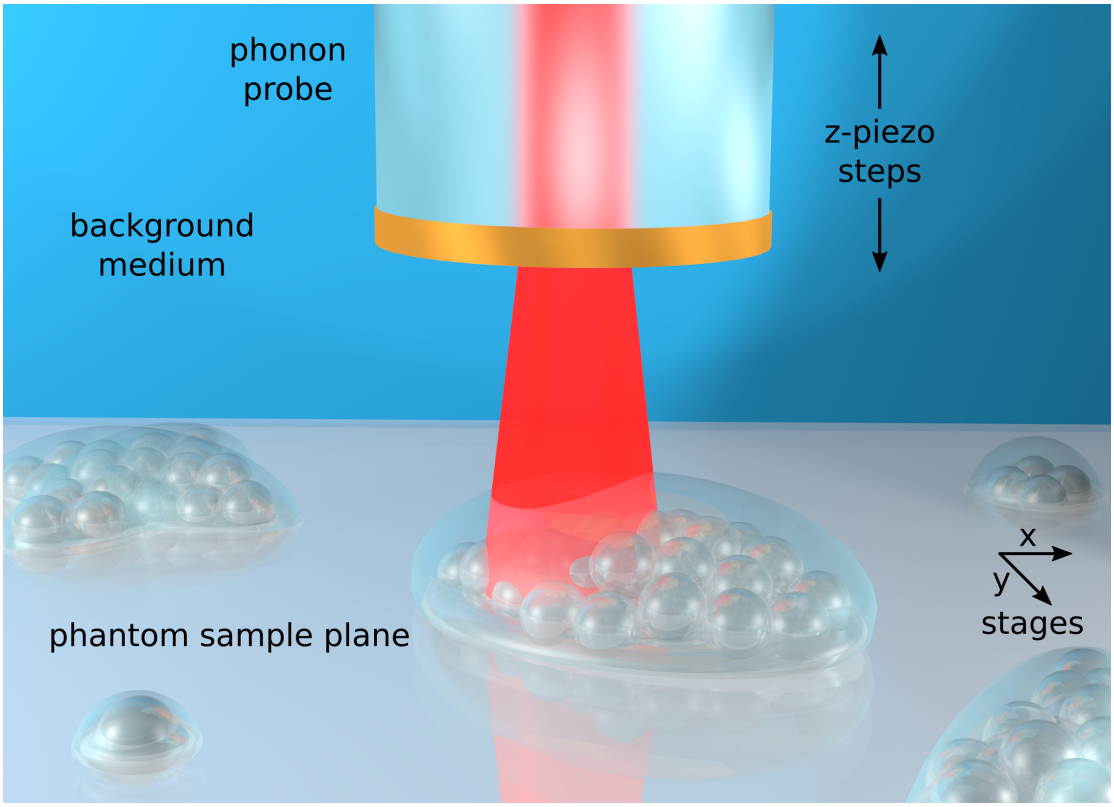


Figure 6.11: Conceptual illustration of the measurement environment when using the phonon probe as a microscopic imaging tool. The experimental configuration presented in this study will use a z-piezo stage to carefully position the tip of the phonon probe within $5\ \mu m$ of a PS phantom. The scanning action of the imaging technique will solely be performed by the x/y stages controlling the horizontal position of the specimen substrate. Water is used as an acoustic coupling medium between the probe and the phantom. As the phantom is scanned beneath the fixed fibre tip, the probe beam (pictured in red) will experience different TRBS interaction lengths as the topography of the phantom changes.

tip was centred in the field of view of the imaging system. At this point the x/y stages are used to locate a patch of substrate where there are no phantoms, which will facilitate a safe position for localising the substrate surface with respect to the positions of the z-micrometre and the z-piezo. The approach protocol used in Section 6.2.1 was employed to then bring the tip of the phonon probe towards the substrate such that it is within the dynamic range of the measurement system. Once this had been confirmed by observing a change in the TRBS signal (this piezo step + look for boundary signal process can be automated in the future), the probe tip was adjusted so that it was roughly $5\ \mu m$ away from the surface, and the positions of the z-micrometre and z-piezo were recorded.

Following the localisation of the substrate surface, the x/y stages were used to move the desired imaging target (initially green box in figures 6.9-6.10) into the centre of the optical and acoustic imaging systems; this can be confirmed optically since both the fibre tip and the phantom are within the focal plane of the imaging system (see Figure 6.12a). Before scanning the object, a series of single-point measurements were acquired at the apparent centre of the phantom while adjusting the position of the z-piezo; the piezo was disengaged once the TRBS boundary response appeared to occur at a proximity of roughly $z = 2 - 3\ \mu m$ as presented in 6.12b. This stand-off distance between the fibre tip and the phantom was selected in an attempt to maximise the signal length in which boundary transitions can be detected (before attenuation becomes too great), and also to leave enough spacing to accommodate potentially taller portions of the phantom.

From this point, the z-position of the fibre tip was left fixed and all scanning took place using the x/y stages controlling the phantom position. In the future, the z-piezo can be used as an additional degree of freedom with which the dynamic range of the technique can be extended. The phantom was then moved such that the fibre was centred at the bottom left corner of the scan area shown in green in 6.12a. The following experimental parameters were defined: scan area of $100\ \mu m \times 100\ \mu m$, x/y step size of $2\ \mu m$, $15k$ oscilloscope averages, and using the half time window ($50\ \mu s$) for better acquisition speed. The entire scan took roughly 2.8 hours with each pixel taking approximately 4 seconds to acquire. Measurements of the DC light levels were only recorded at the beginning and end of the experiment as the modulation depth of the signals is not critical to achieve proof of concept for imaging; the AC portion of the signal is sufficient for the time-frequency analysis used to make proximity measurements.

In Figure 6.13 the maximum signal amplitude is mapped across the scan area. Upon initial inspection it appears that the signal amplitude is indeed sensitive to changes in the topography of the object geometry. The magenta circle, cross, and diamond markers represent pixels which will be individually analysed in order to better understand the range of responses exhibited by the phonon probe. The diamond pixel, which

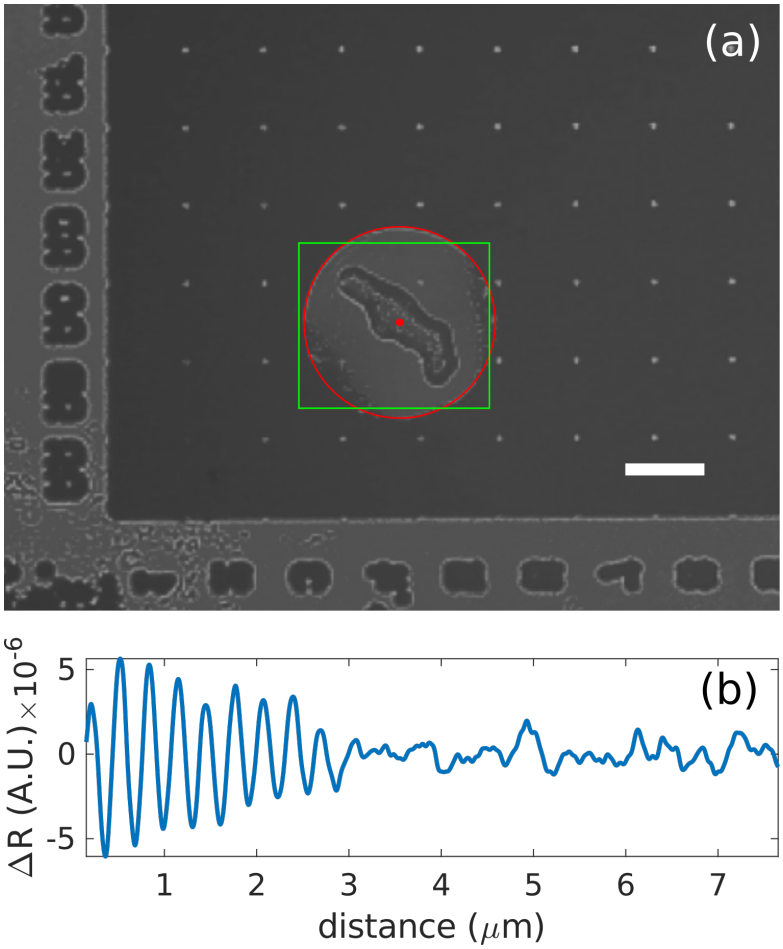


Figure 6.12: (a) Image from the ancillary optical imaging system used to locate the phantom objects and also the approximate position of the fibre tip with respect to the imaging focal plane. The phantom has been moved such that it is roughly centred beneath the fibre tip which is the light grey region outlined with red (red dot is the approximate position of the 5 μm core), and the scan area has been identified in green. (b) TRBS signal that occurs when the phonon probe is piezo stepped down to within 3 μm of the phantom-centre, confirming that the object is now within the dynamic range of the device. Scale bar is approximately 50 μm.

is located in the bottom right extreme of the scan area (well away from the phantom), does not appear to contain a fast amplitude decay which would be representative of a boundary between materials, as confirmed by the relatively flat response seen in the attenuation corrected wavelet response (C_w'' in bottom trace). This implies that the specimen substrate is beyond the penetration depth of the phonon probe at this location (non-measurement).

On the other hand, the time-domain signals at the circle and cross markers clearly reveal a sharp signal decay. At the position of the circle marker, the TRBS signal transitions from $f_B = 4.88\ GHz$ to $f_B = 8.25\ GHz$ as confirmed by the frequency spectrum. This $\sim 8\ GHz$ peak was also used to set the centre frequency for the mother wavelet resulting in the amplitude response seen in green. The proximity measurement protocol outlined in Section 6.2.2 was used to produce an experimental distance measurement

between the fibre tip and this position of the phantom, $z_e = 1.38\ \mu m$ (red star). However, just $\sim 4\ \mu m$ away (laterally) from this pixel, at the cross marker, this transition in Brillouin frequency is no longer observed, despite there being a sudden signal decay which produces a proximity measurement of $z_e = 1.86\ \mu m$.

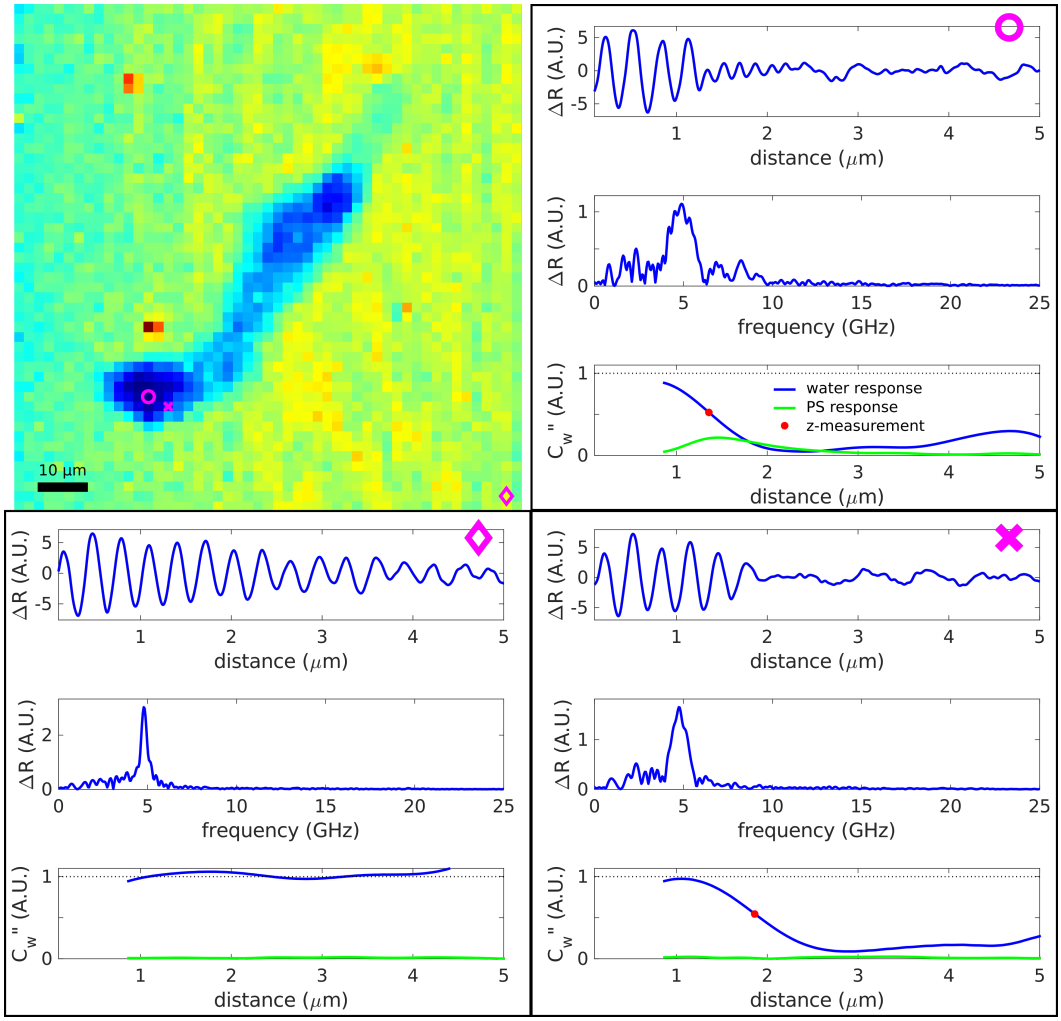


Figure 6.13: (top-left) Maximum TRBS signal amplitude map resulting from the scan of the object in green in figures 6.9, 6.10, and 6.12. Blue corresponds with minimum amplitude and red maximum amplitude. When the $5\ GHz$ frequency phonons (in water) are suddenly impeded by the phantom, a lower TRBS signal amplitude is observed, and vice versa when there is no object within the penetration depth of the phonon probe. The red dots (forming a square) are DC optical reflections from the gold dots of the gridded coverslip. Example pixels have been identified using the pink markers. (Diamond) Example of when the sample plane is beyond the dynamic range of the probe as seen by the slow attenuation of the signal (therefore flat response of corrected wavelet coefficients C_w''). (Circle) The TRBS signal transitions from the Brillouin frequency of water to that of the PS phantom as confirmed in the FFT; in the wavelet response, the signal amplitude at $f_B(PS)$ (green) increases as the amplitude at the carrier frequency decreases (blue). A proximity measurement is attained as described previously $z_e = 1.38\ \mu m$. (Cross) A similarly proximal boundary compared with that of the circle-marker, but no Brillouin mode is observed at $f_B(PS)$.

From Figure 6.13 it is apparent that not every proximity measurement event is accompanied with a frequency measurement of the imaging target. This is likely due to one of the following reasons:

1. the imaging target is not photoelastic or is weakly so
2. the acoustic impedance mismatch between the couplant and imaging object is very large preventing the acoustic field from entering the object
3. the acoustic wave has attenuated too much by the time it transmits into the imaging object
4. the topography of the imaging object is such that the sound refracts away from the optical axis of the phonon probe, and the TRBS interaction strength is reduced (discussed in Section 6.3.3).

Since PS is known to be a photoelastic object, as experimentally confirmed in this study, case $\#1$ is unlikely to be the cause. Considering case $\#2$, the acoustic impedances ($Z = \rho v$) of water and PS are relatively similar; the acoustic amplitude transmission coefficient between the two materials is given by [161]

$$T_{ac} = \frac{v_{H_2O}}{v_{PS}} \frac{2Z_{H_2O}}{Z_{H_2O} + Z_{PS}} \approx 50\% \tag{6.3}$$

which should be detectable. For case $\#3$, given the $\approx 500\ nm$ difference in axial distance between the circle and cross measurements in Figure 6.13, the amplitude decay due to acoustic attenuation will only result in a 20% decrease in amplitude; i.e., despite additional attenuation, the acoustic amplitude in the secondary object should be detectable using TRBS. Therefore, it is most likely that the lack of observed Brillouin oscillations in the secondary material is due to the geometry of the water/phantom interface scattering sound away from the optical axis of detection (case $\#4$). This concept will be revisited in the Section 6.3.3; the next Section will focus on reconstructing a 3D profile using the decay of the $f_B(H_2O)$ mode at the water/PS interface.

6.3.2 Three-dimensional profiling

Following the scanning of the PS phantom, the TRBS signal at each pixel in the image (51×51 pixels) was wavelet transformed using the same wavelet bandwidth ($N_\lambda = 6$). The criteria discussed in Figure 6.5 was used to determine whether a TRBS signal produces a proximity measurement; to briefly summarise: the absolute minimum value for the corrected wavelet response should correspond with the wavelet having fully exited the water medium ($m_C < \tau_{min}$), therefore an upper limit was placed on τ_{min} such that minor amplitude fluctuations do not register false measurements. A value of $\tau_{min} = 0.4 - 0.5$ was primarily used for this study, if the minimum value of C_w'' does

not fall below this threshold then the measurement is anchored to the end of the time window (non-measurement).

This process produces the proximity map seen in Figure 6.14a, where the experimental sound velocity (Equation 6.1) at each pixel provides the necessary time-distance conversion. Subsequently a proximity measurement threshold is assigned to create a binary mask for the phantom (Figure 6.14b) in order to separate the object from the background. This provides an opportunity to average together the lower SNR background pixels (blue pixels in Figure 6.14b), increasing the number of averages from $15k$ to $\sim 33M$ with which an ensemble measurement of the object floor (or SNR floor) can be made. Figure 6.14c shows this ensemble TRBS signal and corrected wavelet

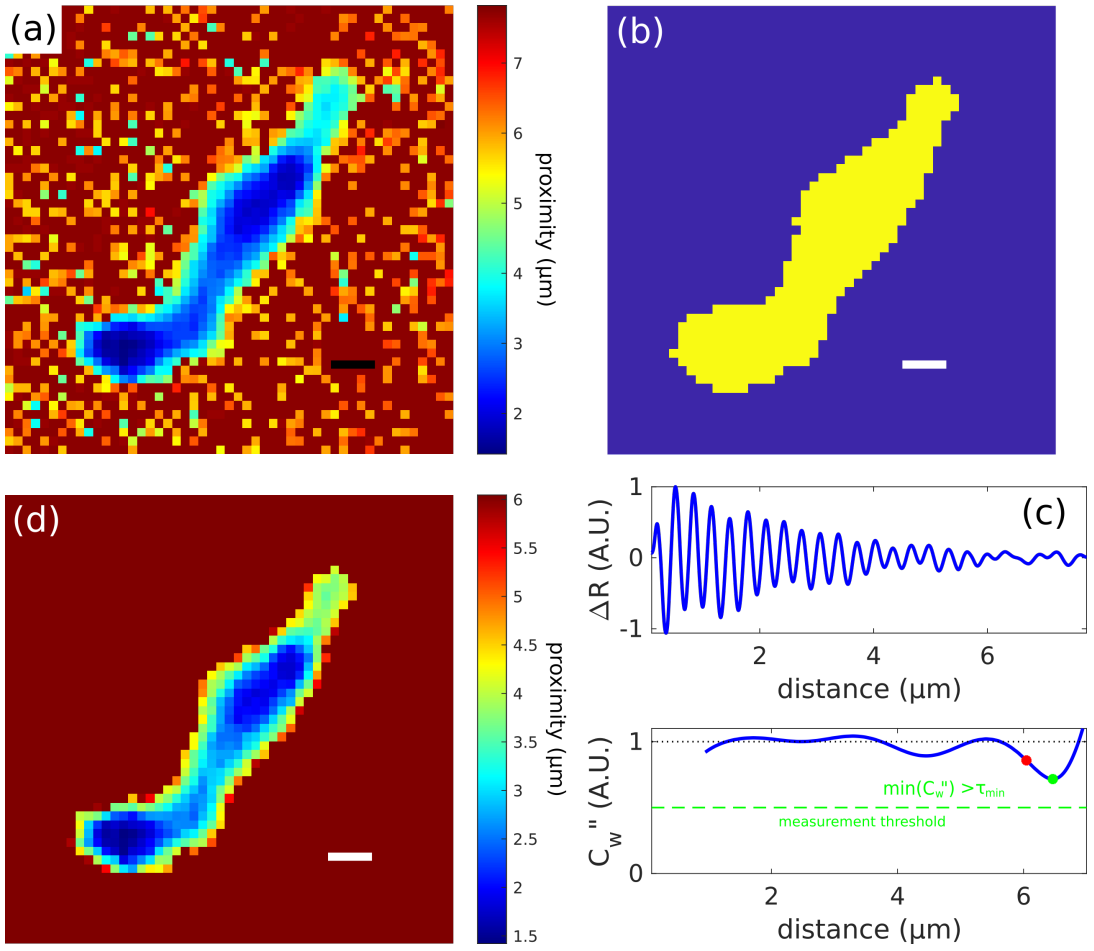


Figure 6.14: Process flow for rendering a proximity map from TRBS signals in an area scan. (a) Raw proximity measurements attained from the position of the amplitude roll-off (of the corrected wavelet response) induced by the water:phantom boundary. (b) Binary mask created by thresholding the proximity map in (a). (c) All background (blue) pixels in (b) can be combined into one high average signal ($33M$ averages) from which a potential proximity measurement of the floor can be made. In this case the wavelet response did not meet the measurement-threshold requirement ($C_w'' < \tau_{min}$) resulting in a non-measurement (red dot is an approximate position of the SNR floor). (d) Mask and background averaging applied to the original proximity map; in this instance the map provides the height contrast of the sample. All scale bars represent $10\ \mu m$.

response, however, the minimum value of the wavelet response (m_C, green marker) does not fall below the measurement threshold (green line) which renders the entire image background as a non-measurement. The z-position of the red dot is defined by the half-way point between amplitudes m_C and 1, and provides an estimate of the SNR floor with $z_{floor} \approx 6\ \mu m$ proximity to the fibre tip. Figure 6.14d reveals the masked proximity map where the background is now positioned at the SNR floor measurement. If a non-measurement is assigned to the background, it's exact numerical value is less critical since the map then only represents the proximity contrast, or relative proximity (for the non-masked region).

Now that the proximity map has been rendered, it's values can be inverted in space, $h = z_{floor} - z_{prox}$, to create a relative height map of the upper $h = 4.6\ \mu m$ of the phantom (relative to the SNR floor) and is presented in Figure 6.15c. The lateral features of the 3D image appear to reproduce the unique shape of the phantom, first observed in the optical brightfield image attained by conventional microscopy (Figure 6.15a). An optical profilometer (Zeta Optical Profiler, see Appendix E) was used to corroborate the height contrast measured by the phonon probe (see Figure 6.15b). Furthermore, a stylus profiler (see Appendix E) was also used to measure the height of the object along arbitrary cross-sections (Figure 6.15d).

Both the optical and stylus profilometers produced maximum height measurements of $h_{abs} = 7.7\ \mu m$ which further confirms that the phonon probe image is a relative measurement. However, the contours measured by the phonon probe for the top few microns of the object correlate well with those seen in the optical profilometry, albeit with lower spatial resolution. A critical difference between the optical and acoustic measurements, is that the optical inhomogeneity produced by the sub-surface defects present in the phantom appear to distort the accuracy of the height map of the optical profiler (discussed further in the Section 6.4). These artefacts do not affect the measurement from the phonon probe since the decay of the acoustic time-of-flight is unaffected by sub-surface features.

Next the phantom structures in the red boxes of figures 6.9 and 6.10 were targeted and an area scan of $120\ \mu m \times 120\ \mu m$ in $2.5\ \mu m$ steps was performed (49×49 pixels) with the same $15k$ averaging rate (per pixel). This structure presents an interesting opportunity since its absolute height $h_{abs} = 4.89\ \mu m$ (as measured by the optical profiler in Figure 6.16b) is within the $z_{DR} \approx 6\ \mu m$ dynamic range of the phonon probe (at $\lambda_{probe} = 850\ nm$ and $15k$ averages). However, the ability to measure the distance from the fibre tip to the floor of the specimen (i.e. the substrate) will also depend on how proximal the phantom-peak is to the fibre tip. In this case the position of closest approach between the fibre tip and phantom was approximately $1.96\ \mu m$, meaning that the remaining dynamic range is on the order of $z_{DR} \sim 4\ \mu m$. The averaging of the background pixels (approximately $32M$ averages) resulted in the TRBS signal seen in

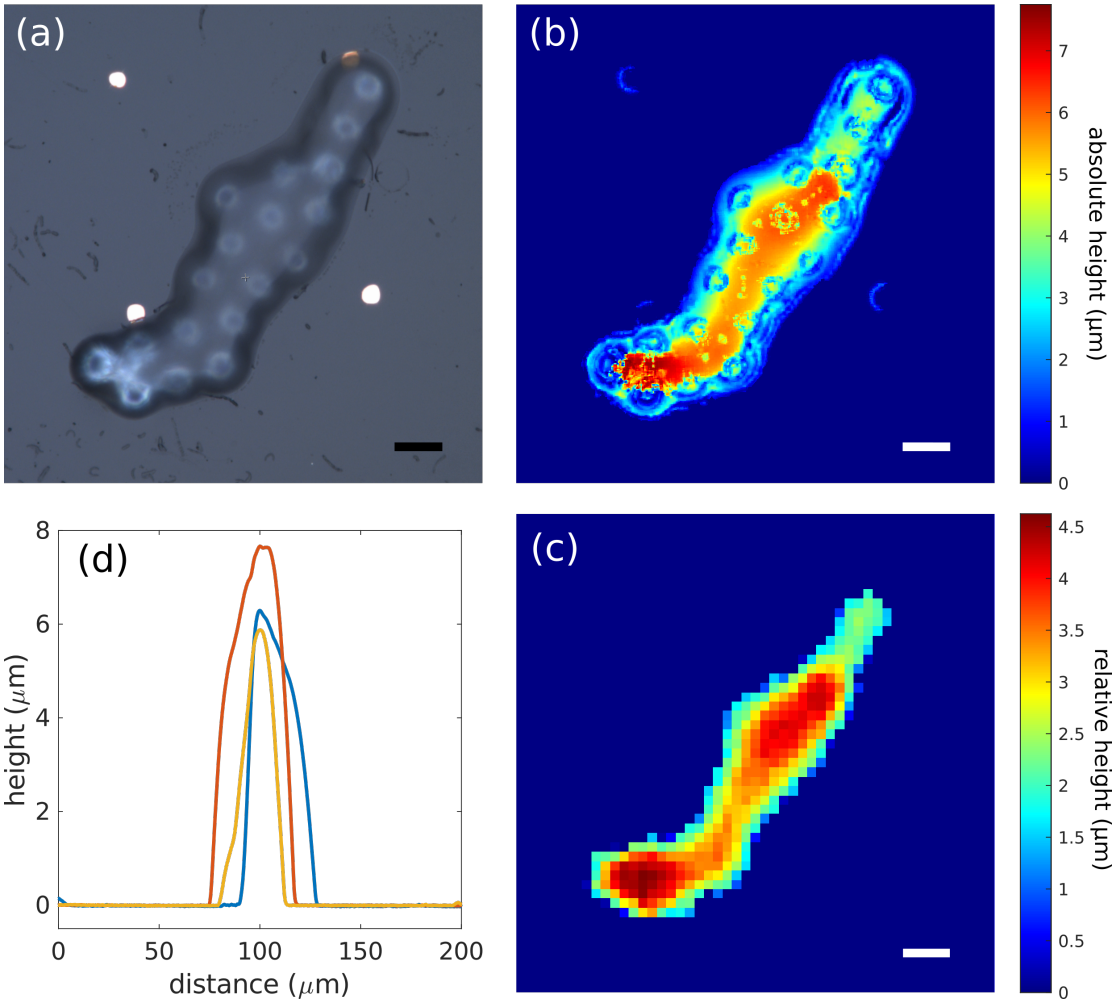


Figure 6.15: (a) Optical brightfield image of the current imaging target. (b) Absolute height map attained using an optical profiler. A maximum phantom height of $h_{abs} = 7.7\ \mu m$ was measured, however, the accuracy of the technique is limited by the optical inhomogeneity of the object (see artefacts). (c) Relative height map produced by the phonon probe (the axial inverse of the proximity map in Figure 6.14d). The maximum height measurement of $h = 4.6\ \mu m$ is relative to the position of the SNR floor since a measurement of the physical floor could not be attained with this object. (d) Further corroboration of the true phantom height using a stylus profilometer (along arbitrary cross-sections of the phantom), with a maximum height of $7.7\ \mu m$. All scale bars represent $10\ \mu m$.

Figure 6.16d; a sudden decay of the $5\ GHz$ carrier signal is seen around $\approx 6\ \mu m$ which points to the presence of a boundary (measurement). However, the measurement threshold for this signal remains ambiguous due to how low the SNR is later in the trace. In any case a boundary transition occurs centred at $z_{floor} = 5.81\ \mu m$ (red dot) was measured which can serve as the base for the relative height map (Figure 6.16c).

The maximum measurable height in this experiment was $h = 3.85\ \mu m$ compared with the $h_{abs} = 4.89\ \mu m$ measured with optical profilometry, a measurement error of $\epsilon_z = 1.04\ \mu m$. This offset between the two measurements can be explained by: (1) the $1.96\ \mu m$ closest approach which limits the dynamic range (unable to resolve the bottom

$\sim 1\ \mu m$ portion of the object), and (2) the maximum height of the object is aliased by the spatial resolution of the phonon probe. With regards to this latter effect, since the lateral resolution (discussed in Section 6.4) of the phonon probe is less than optical profilometry, the "taller" features in the phantom will be averaged with "shorter" features within the same point-spread function (PSF). Therefore the true height of the peaks in Figure 6.16b will be aliased when the height varies with spatial periods that are less than the resolution of the device.

An additional area scan was performed on the triangular phantom (bottom left) in Figure 6.16 with a higher resolution step size of $1\ \mu m$ and is found in the right-hand pink box in Figure 6.16c. As a result, there is an apparent increase in image resolution, however, since the characteristics of the probe PSF have not changed, it is instead more accurate to characterise this as an increase in the precision of the local height measurements. This is a consequence of the finer lateral step sizes causing the fibre tip

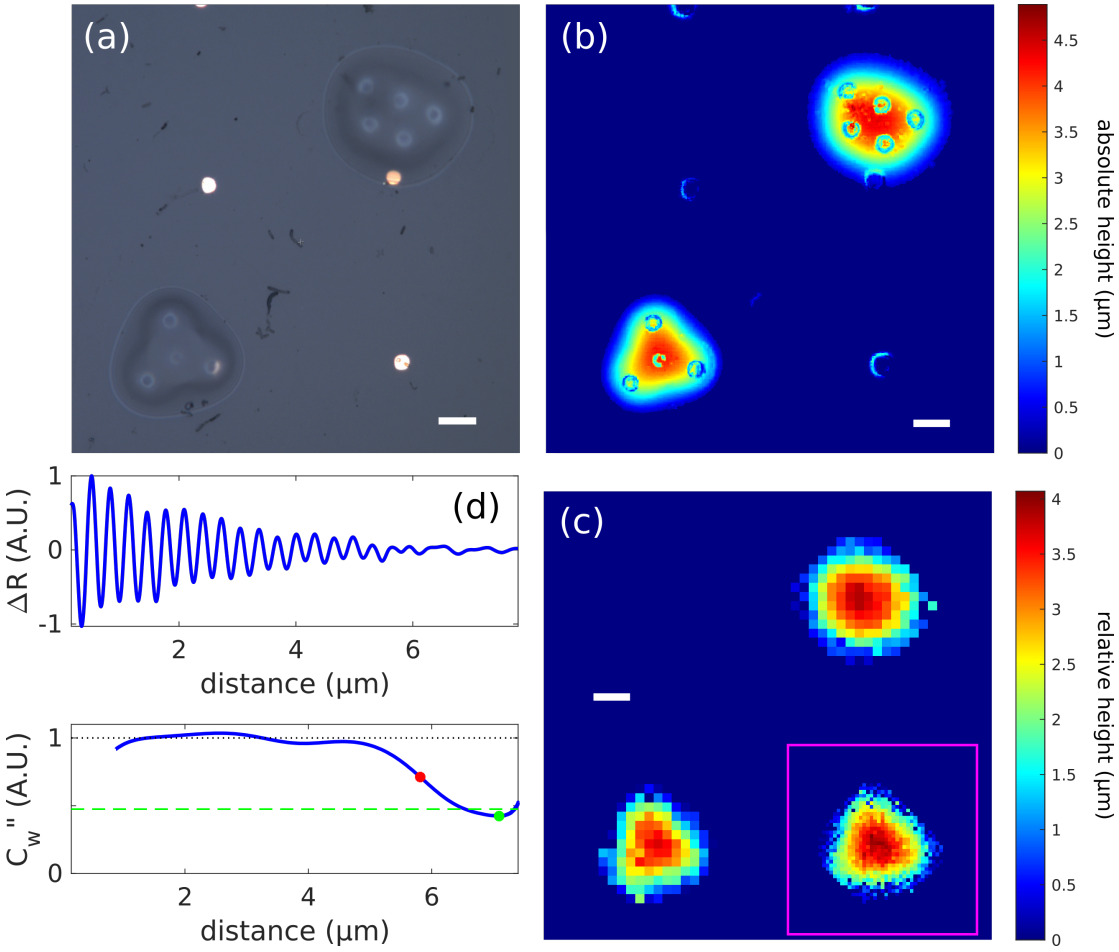


Figure 6.16: (a) Optical brightfield image of the current imaging target. (b) Height map as produced by optical profiler revealing a maximum height of $h_{abs} = 4.89\ \mu m$. (c) Height maps resulting from the area scan with the phonon probe. A maximum height of $h = 3.85\ \mu m$ was measured from the average SNR floor position found in (d) ($z_{floor} = 5.81\ \mu m$). Pink box in (c) shows a re-scan of the lower-left microstructure with finer x/y step sizes. All scale bars represent $10\ \mu m$.

to dwell (and thus average) over any given μm^2 area for longer than with coarser steps. Strategies for increasing the true lateral resolution of the technique will be discussed in the following section and Chapter 7.

A final scan was performed on the phantom outlined in blue in figures 6.9 and 6.10, and the resulting 3D images are found in Figure 6.17. Experimental parameters of $15k$ oscilloscope averages, $40\ \mu m \times 40\ \mu m$ area, and $1\ \mu m$ steps (41×41 pixels) were utilised. The tip of the fibre had a minimum proximity of $z = 2.10\ \mu m$ with the phantom, leaving $z_{DR} \sim 4\ \mu m$ of available dynamic range given the current experimental parameters. Optical profilometry and the phonon probe produced maximum height

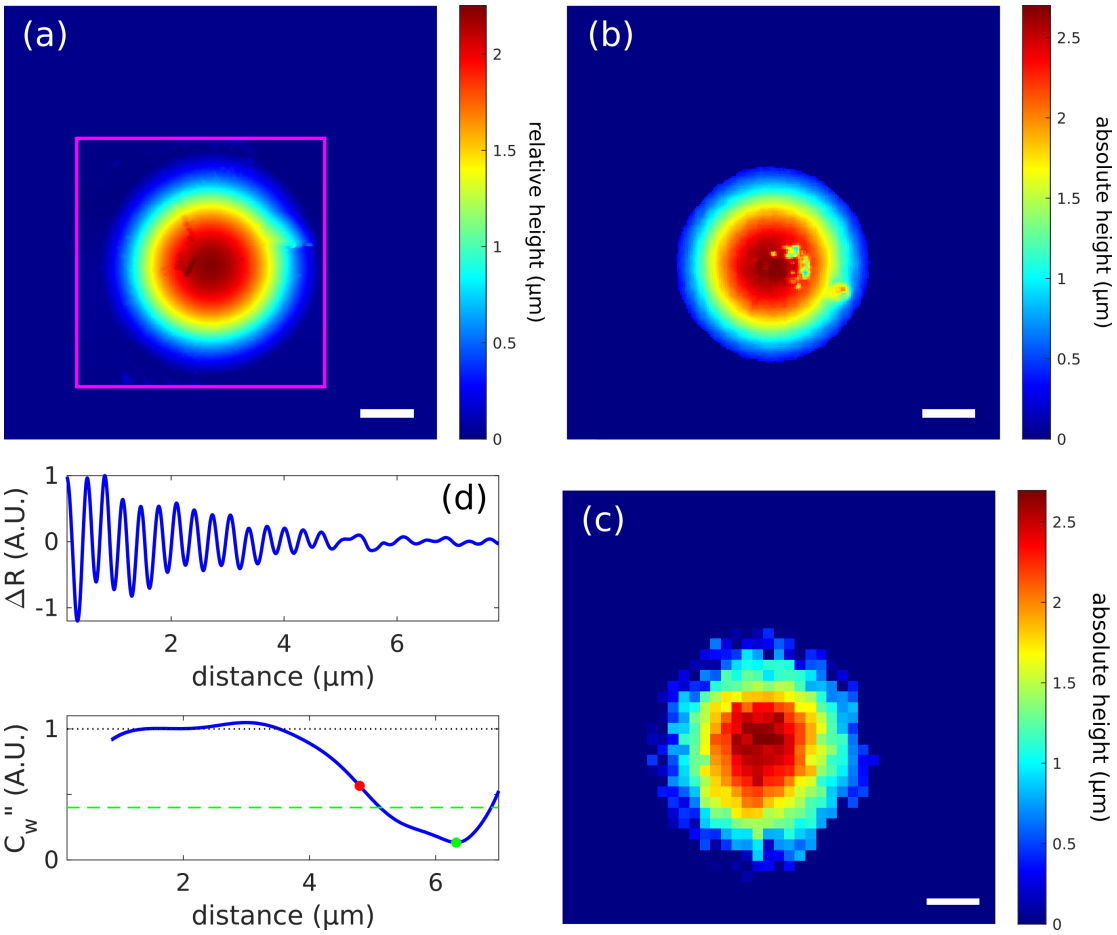


Figure 6.17: (a) AFM height map of the object shown in blue in Figure 6.10. The maximum height measured with this technique, $2.25\ \mu m$, does not corroborate that of the optical profiler (nor the phonon probe), indicating that this measurement is likely the relative height of the object. Pink square outlines the field of view encompassed by AFM measurement. (b) Optical profilometry of the object indicating a maximum height of $h_{abs} = 2.700\ \mu m$. This is corroborated by the measurement made by the phonon probe (c) $h = 2.695\ \mu m$ showing the potential for the phonon probe as a 3D imaging tool. (d) Measurement of the physical floor of the specimen. The pixels which are rejected by the mask are averaged to create a high SNR floor-pixel (top). Corrected wavelet response contains a minimum value (green marker) which approaches zero (and is well below the measurement threshold, green line), permitting an actual measurement of the fibre/substrate proximity (red star). All scale bars represent $5\ \mu m$.

measurements of $h_{abs} = 2.700\ \mu m$ and $h = 2.695\ \mu m$ respectively (figures 6.17b-c). This initial accuracy of $\epsilon_z = 5\ nm$ for the phonon probe will be discussed further in Section 6.4. The measurement of the object floor (with the phonon probe) can be seen in Figure 6.17d; the boundary-decay in the TRBS signal is clearly seen in both the acoustic time-of-flight (top) and the corrected wavelet response (bottom), and in addition, the minimum C_w'' value (green marker) is well below the measurement threshold (green line) producing an unambiguous measurement (red marker).

In addition to optical profilometry, AFM was used in attempt to further corroborate the height profile (Appendix E). However, at the time of writing the available AFM instrument did not have sufficient dynamic range to cope with structures taller than $1-2\ \mu m$. During measurement the piezo-element controlling the axial position of the AFM-probe was at the limit, confirming that the object was not being fully sampled. Consequently, the AFM height map (Figure 6.17a) appears to be a relative height measurement (of the upper $\sim 2\ \mu m$), notwithstanding the fact that the maximum height does not agree with the optical profiler nor the phonon probe.

This section has presented proof of concept that the phonon probe can be used to image objects in 3D on the micrometre scale. The following section will demonstrate the potential for the device to map the Brillouin frequency of the imaging target, which would provide access to elasticity-related information.

6.3.3 Brillouin imaging

As discussed in the Section 6.3.1, the Brillouin frequency within the PS-phantom can be measured given that acoustic impedance, acoustic attenuation, and the scattering geometry do not result in loss of sensitivity to the TRBS signal in the PS-phantom. The latter phenomenon will now be explained further. Figure 6.18a demonstrates a map of the Brillouin frequency obtained by the phonon probe for the PS-phantom shown in Figures 6.12-6.13 (produced from the same TRBS signals used for 3D profiling). The blue portion of the map represents the frequency measurement of the water medium ($\approx 5\ GHz$); when the TRBS signal amplitude (in the frequency domain) breaches a user-set amplitude threshold within the signal band of interest ($> 8\ GHz$ for PS), the frequency position at the local maximum within that band is recorded (pink pixels in Figure 6.18a). An alternative way to visualise this frequency map is by calculating the average Brillouin frequency measured in the PS: $f_B(PS) = 8.43 \pm 0.17\ GHz$. Then the maximum FFT amplitude within this frequency band is assigned as the degree of opacity in the intensity channel plotted in Figure 6.18b (overlaid onto a brightfield image).

The TRBS signals can also be directly used to visualise the changing topography; Figure 6.18c shows the absolute value of the TRBS signal along the cross-section of the phantom shown in the inset of Figure 6.18d. Here the abrupt decay of the $f_B \approx 5\ GHz$

mode (appears as 10 GHz with absolute value) follows the height profile measured through wavelet analysis. This is also the case when the TRBS signals are high-pass filtered for $f_B > 8\ GHz$ as shown in Figure 6.18d. Now the $f_B \approx 9\ GHz$ mode in the PS shows to be highly localised towards the peaks of the object, and is unresolvable as the height gradients begin to increase down the sides.

Figure 6.19a shows the height gradient map (in units of inclination angle between neighbouring pixels) of the topographic map presented in Figure 6.15c. Here the steep height gradients of the object become accentuated, as does the relatively flat ridge connecting the peaks of the structure (central black region). Using the frequency mea-

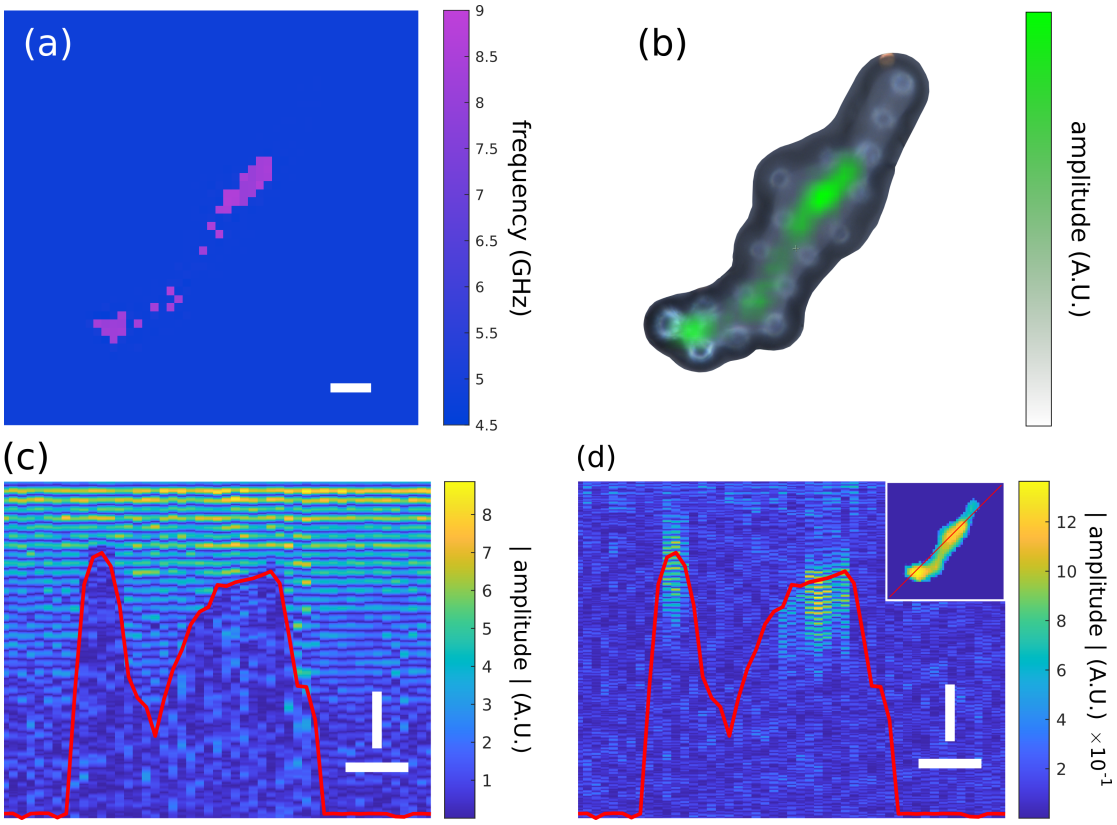


Figure 6.18: Mapping Brillouin frequency in a PS microstructure (object in Figure 6.15). (a) Map of the maximum amplitude frequency position in the frequency domain shows the pervasive $f_B \approx 5\ GHz$ mode (blue) from the couplant; when the FFT amplitude for the $f_B > 8\ GHz$ band rises above an amplitude threshold, the frequency position of the local maximum is recorded (pink pixels); scale bar 10 μm. (b) The mean Brillouin frequency measurement in the PS was calculated $f_B(PS) = 8.43 \pm 0.17\ GHz$, and the maximum FFT amplitude within this frequency band is assigned as the opacity of the intensity channel (overlaid onto brightfield image). (c) The absolute value of the TRBS signals (time of flight along the vertical direction) is plotted along a single cross-section of the phantom (inset in (d)). The 5 GHz mode attenuates at the object interface which is confirmed by the height profile measured through wavelet analysis (red). (d) When the TRBS signals are high-pass filtered for $f_B > 8\ GHz$, the $f_B(PS)$ water becomes clearly visible, however, only at the peaks of the object. Horizontal scale bars - 20 μm, vertical scale bars are approximately 1 μm.

surement information in Figures 6.18a-b, and the height gradient, the maximum angle at which $f_B(PS)$ can still be measured was calculated: $\theta_{f_B} \approx 10^\circ$. Figure 6.19b demonstrates the proportion of a single height cross-section where this angle-condition is met (grey lines indicate $\theta_{f_B} > 10^\circ$). The inset of Figure 6.19a provides visual confirmation that the regions of minimum height gradient correspond with the regions in which the Brillouin frequency can be measured.

By further inspecting a region of high gradient (orange square in Figure 6.19b) the cause of poor TRBS sensitivity can be identified. At oblique angles of incidence (due to curved object-geometry), both light and sound waves will refract at the interface according to the relative difference in acoustic and optical properties of the two media (see Figure 6.19c). Since light slows down upon entering PS, the refracted ray will bend towards the surface normal; conversely since sound speeds up upon entering PS, the refracted ray will bend away from the surface normal (Figure 6.19c). In this example, both light and sound are incident to a PS-surface that is angled by $\theta_i = \theta_{f_B} = 40^\circ$. Using Snell's law, light will refract at an angle of $\theta^L = 33^\circ$ from the surface normal ($\Delta\theta = -7^\circ$) and sound will refract at an angle of $\theta^S = 80^\circ$ ($\Delta\theta = +40^\circ$).

The end result of this interaction, is that the acoustic and optical fields lose spatial overlap, an effect which worsens with depth (and inclination angle). Recall from Equation 2.77 that TRBS signal strength is proportional to the acoustic amplitude and the probe intensity. Therefore, when the overlapping volume between the two fields is reduced, the TRBS signal amplitude will suffer. Additionally, the photon and phonon wavevectors will now differ by the relative refraction angle between them $\theta_{diff} = \theta^S - \theta^L$. Consequently, the probe beam will now sample a lower spatial frequency of the acoustic field; one which results in a measured Brillouin frequency of

$$f_B = \frac{2nv}{\lambda_{probe}} \cos\theta_{diff} \approx 3.2\ GHz$$

for the example of $\theta_i = 40^\circ$ and $\lambda_{probe} = 850\ nm$.

The above set of circumstances is unique to the case of the acoustic and optical fields travelling from water into PS. The fact that the fields diverge from each other is due to the negative velocity gradient experienced by light and the positive velocity gradient experienced by sound. However, the aggressiveness of the this divergence, particularly with respect to the acoustic field, is due to the contrast in acoustic impedance between the two materials. This is also accompanied by a 50% transmission loss across the boundary (Equation 6.3). However, if the PS-object was replaced by a material with less severe refractive index and acoustic impedance mismatches, then the phonon probe would be better able to resolve sub-surface elasticity-related information of the object since the overlap between the fields will be better optimised versus depth. One such material would be a biological cell. Using common values for the mean sound velocity, refractive index, and mass density for cells like 3T3 fibroblasts or blood cells

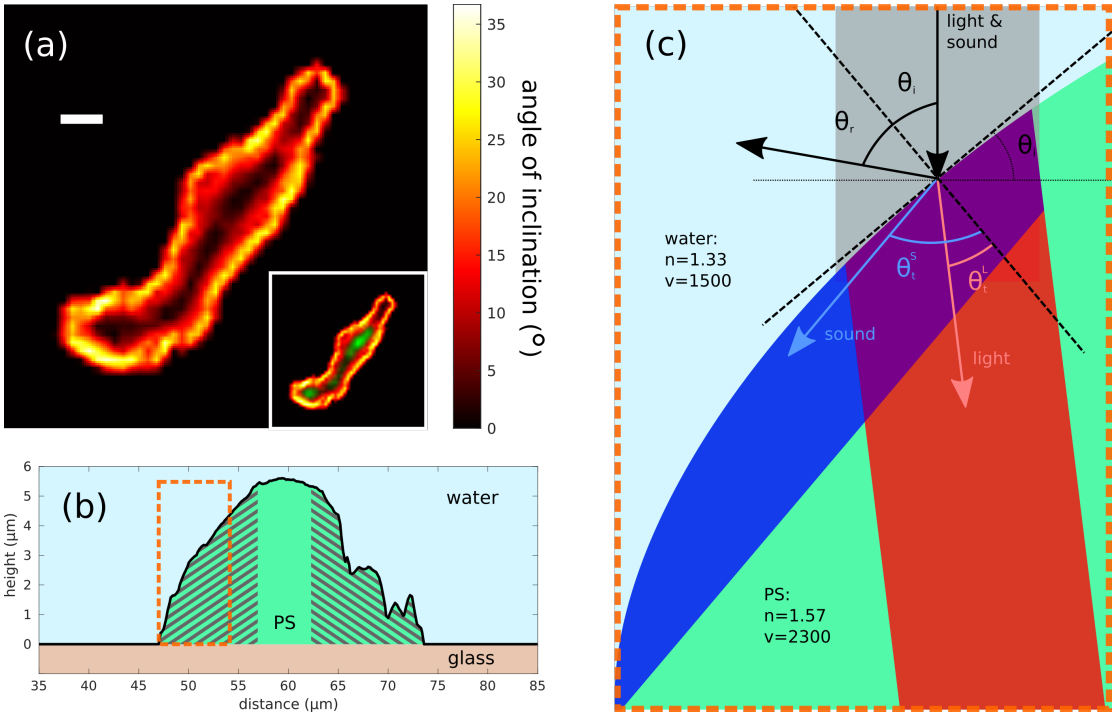


Figure 6.19: Demonstration of the effect of oblique incidence when normally incident light and sound impinge on an object with curved topography. (a) Gradient of the height map presented in Figure 6.15c (scale bar 10 μm); the height difference between two neighbouring pixels and the horizontal distance between the pixels is used to calculate the wall angle (angle of inclination). The flat (dark coloured) inner region of the phantom corresponds with positions of the Brillouin frequency measurement (Figures 6.18a-b), as confirmed by the overlay of the Brillouin amplitude map onto the height gradient (inset). From this correlation, when the height varies by more than $\theta_{f_B} \approx 10°$ the Brillouin frequency of the PS-phantom cannot be resolved. This unresolvable region is shown as the striped segment of (b) which is a cross-section of the optical profilometry taken from Figure 6.15b. Within the orange square, an area of steep height gradient ($\theta_{f_B} \approx 40°$), causes both acoustic (blue) and optical (red) refraction (c). (c) Due to the contrasting velocity gradients between sound and light (for a water to PS transition) the acoustic and optical fields refract away from each other resulting in loss of spatial overlap (purple volume) and therefore TRBS signal amplitude.

[221–223], both the optical and acoustic transmission coefficients and the corresponding refraction angles can be calculated. For example, compared with the $T_{ac} = 50\%$ transmission rate in acoustic amplitude between water and PS, the acoustic transmission rate between water and the model cell [221–223] will instead be on the order of 90%. Furthermore, for the $\theta_i = 40°$ incidence example in Figure 6.19c, both the acoustic and optical rays will now refract by less than $\theta_t < 2°$, resulting in an interaction volume (Figure 6.20) which is much greater than the analogue in Figure 6.19c. For example the ratio between the purple volumes (and the TRBS signal strength) within the fields of view in Figures 6.19-6.20 is roughly a factor of 4, a number which will continue to increase with depth. These conditions between the coupling medium and cells bodes well for applying the phonon probe to parallel cell 3D imaging and elastography.

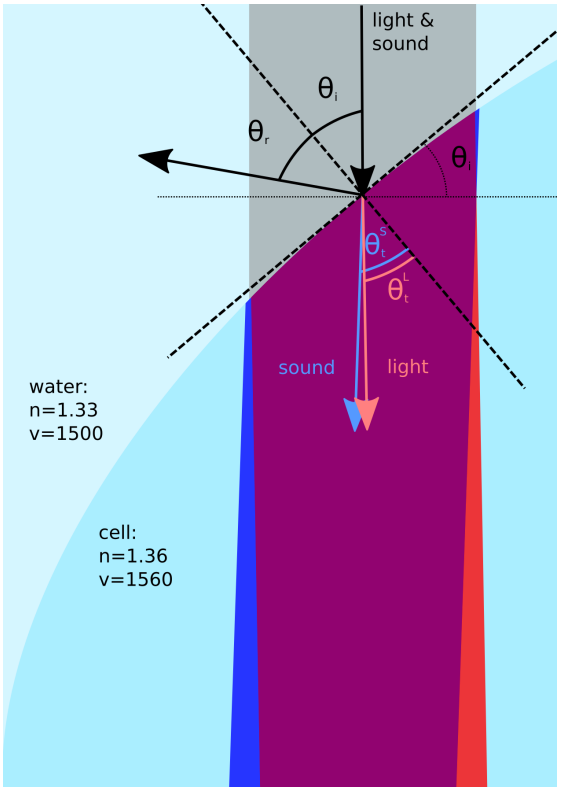


Figure 6.20: Change in the opto-acoustic scattering interaction when the imaging target contains similar refractive index, sound velocity, and mass density to the coupling medium, e.g. a 3T3 fibroblast cell. The refraction angles, 1.95° (acoustic) and 1.05° (optical), are much less severe than the case of a PS-object (Figure 6.19c) resulting in better overlap between the optical and acoustic fields in the sub-surface volume of the object. Also the similarity in acoustic parameters will result in over 90% transmission of the incident acoustic amplitude which will further increase the TRBS interaction strength. These qualities will lend themselves towards using the phonon probe to achieve effective depth sectioning of the Brillouin frequency in biological media.

6.4 Discussion

In this section the unique capabilities (and limitations) of the phonon probe will be discussed in the contexts of imaging and metrology. First the sources of measurement error will be introduced and discussed, followed by a general discussion on how the phonon probe compares with state of the art profilometry techniques. This will motivate a discussion on the resolution, both lateral and axial, provided by the device and how it might be improved in the future.

6.4.1 Sources of systematic error

There are two main sources of systematic error within the measurement system as it pertains to measuring the proximity of the fibre tip to an object or boundary: the error introduced by the high-voltage piezo amplifier (controlling the z-position of the fibre tip), and the error introduced by the temperature gradient surrounding the tip and therefore

creating a ruler with inhomogeneous tick marks. The former is only relevant when z-position is one of the degrees of freedom within the experiment, i.e. if it is kept at a fixed position throughout an area scan then it will have a null contribution to measurement error; this is the case for the 3D imaging results presented in this chapter. However, for the measurements presented in Section 6.2.2), where the z-piezo was used to vary the stand-off distance between the fibre-tip and a petri dish, this error should be considered. The PI P-721 PIFOC nanopositioner converts voltage to translation at a rate of $1\ \mu m/V$ over the voltage range of $-20\ V \rightarrow 120\ V$. Recall from Section 6.1 that this voltage is supplied by controlling the output voltage of a microcontroller over the range $0 \rightarrow 5\ V$, which is then amplified by $G = 20$ using a piezo driver amplifier. Therefore, any fluctuation in the output voltage of the microcontroller and/or the amplifier will result in error with respect to the expected translation given the user-defined voltage step and the $1\ \mu m/V$ specification of the stage. To investigate this, the microcontroller and amplifier output voltages were monitored with a multimeter. The $0 \rightarrow 5\ V$ voltage range was swept in steps of $250\ mV$, which should amount to $5\ V$ step changes for the amplifier output ($5\ \mu m$). In Figure 6.21a the measured amplifier output voltage is plotted against the measured microcontroller output voltage, showing an average slope of $G_{amp} = 19.99$ a variation of less than 1% compared with the expected amplification factor $G = 20$. However, when investigating the actual voltage step taken by the microcontroller (Figure 6.21b), small $4\ mV$ deviations are seen which feed through the amplifier resulting in a maximum deviation of $73\ mV$ (Figure 6.21c). Using the specification of the nanopositioner, these voltage fluctuations only result in a maximum positional error of $73\ nm$ (see Figure 6.21d). The values shown in Figure 6.21 are the average measurements over 3 repetitions of the voltage measurement protocol. This process for calibrating positional error will be required in the future when the z-piezo stage can be utilised to increase the dynamic range of the phonon probe.

A brief consideration is made for the error in axial distance measurement due to the optical fibre potentially sitting at an angle with respect to the target object. This situation is again limited to the scenario in which the z-piezo is utilised as a degree of freedom in the scanning protocol (not the case for the 3D images presented in this study). An angle (θ) between the surface normals of the fibre tip and the specimen can be created by the clamping mechanism (Thorlabs SM1F1-250) for the optical fibre, the specimen stage supporting the sample, or a combination of both. Figure 6.22a illustrates this scenario; it is assumed that the piezo-stage results in pure vertical motion of the fibre-clamping assembly, however, due to an angle (either created by the fibre-clamp or the sample plane) an offset (ϵ_z) will arise between the vertical step taken by the piezo-stage (z_p) and the distance measured by the phonon probe (z_e). This offset will worsen as the angle increases, and the stand-off distance increases, which is confirmed in Figure 6.22b. However, it is reasonable to consider that the fibre is unlikely to create an angle

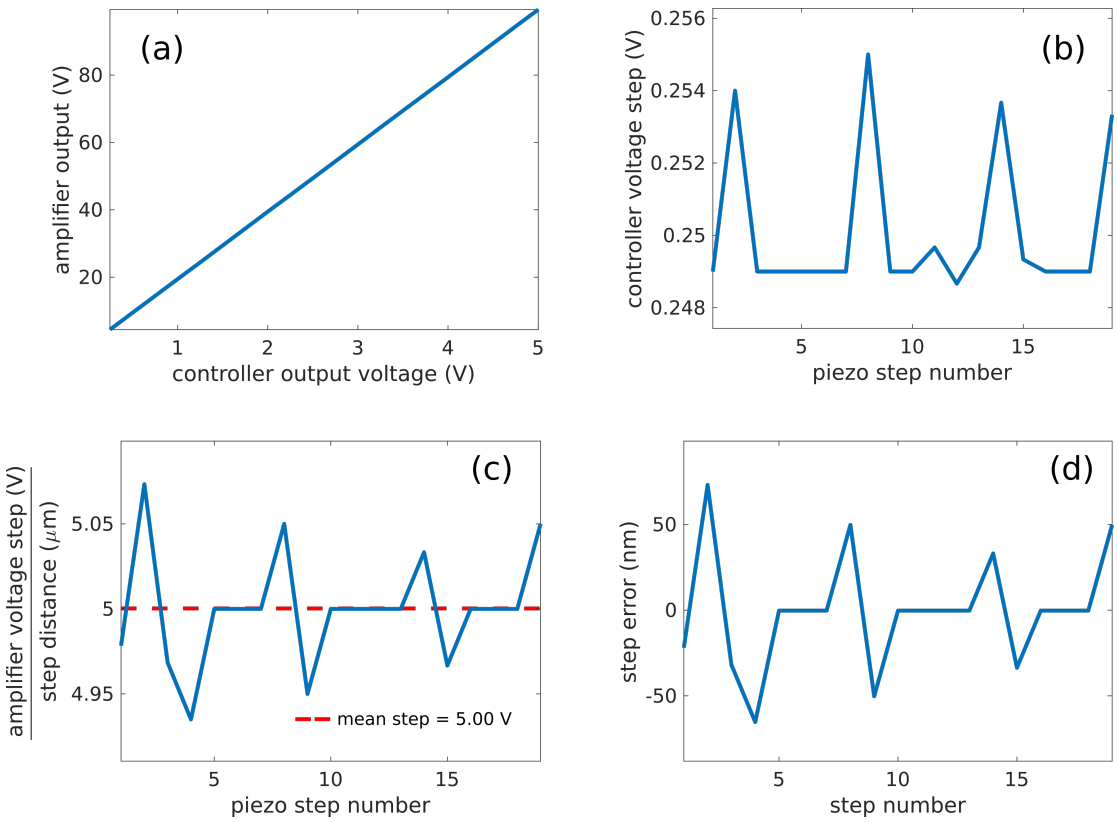


Figure 6.21: Characterisation of the z-positional error when using the z-nanopositioner to measure changes in proximity (Figure 6.8) or as a degree of freedom within the imaging set-up. (a) Measured output voltage from the PiezoDrive amplifier as a function of the measured output voltage of the Phidget microcontroller. The voltage gain (slope) is measured as 19.99 which closely agrees with the specification of the amplifier (20). (b) The microcontroller was driven in 250 mV steps (e.g. 250 mV, 500 mV, 750 mV, etc); the measured voltage steps reveal small fluctuations which are amplified by a factor of 20 by the amplifier (c). Despite $\sim$ 50 mV fluctuations, a mean step of 5 V (5 μm for the piezo stage) was still achieved by the amplifier. (d) These fluctuations translate to positional errors on the order of $\sim$ 50 nm, with a maximum error of approximately 70 nm.

of more than $\theta = 5 - 10°$ when it is placed into the channel of the fibre-clamp and the specimen stage is levelled. For the case that $\theta = 5°$, a maximum error of $\epsilon_z \approx 20$ nm is estimated at $z_p = 5$ μm; therefore, for the distances covered by the petri-dish calibration in Section 6.2.2, this source of error is less influential. Nevertheless, the phonon probe can be used to correct for this error by measuring the differences in proximity (at a fixed stand-off distance) between at least 3 vertices of a square/triangle patten. Then the stage or fibre angle can be adjusted and the measurement process repeated until the angle error has been compensated, and is similar in principle to correcting for tilt in AFM.

A key source of measurement error arises due to the TRBS signal having an instantaneous frequency which is not entirely constant across the time-of-flight. If the Brillouin frequency fluctuates as a function of axial distance, then so too does the measurement of the sound velocity (Equation 6.1) and ultimately the conversation rate from time to

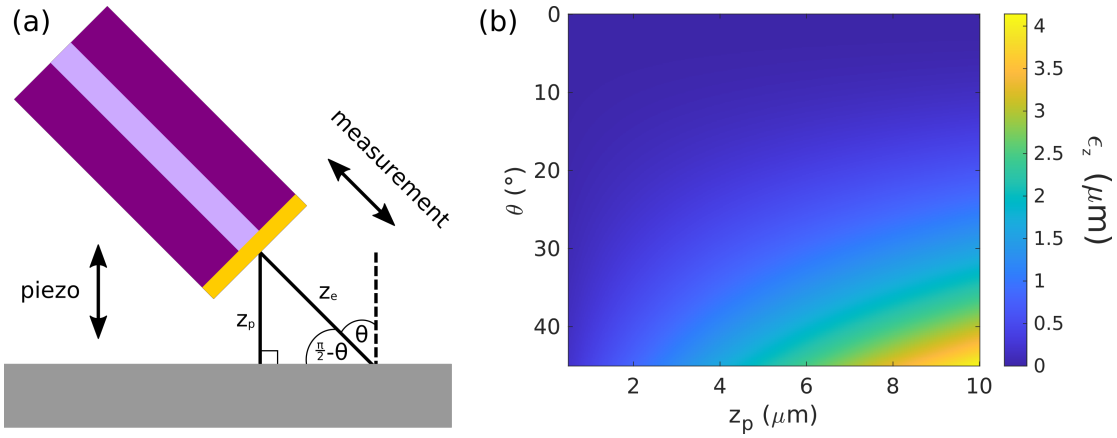


Figure 6.22: (a) Diagram illustrating the phonon probe sitting at an angle with respect to the sample plane. The deviation of the fibre from normal incidence (e.g. at angle θ) will cause a discrepancy between the direction in which the piezo-stage moves (z_p) and the distance measured by the phonon probe (z_e). (b) The offset between these quantities, ϵ_z, worsens with angle and height, however, measures are taken in the experiment to ensure that the fibre is as vertical as possible. It is likely that the experimental angle is $\theta << 10°$, implying that the error due to this effect is $\epsilon_z << 100\ nm$, especially given the stand-off distances reported in this study ($z_p < 10\ \mu m$).

space used to provide a spatial measurement. This phenomenon becomes relevant due to the fact that the fibre transducer produces heating within the measurement volume (as characterised and discussed in Section 5.2.2). Through the thermo-acoustic effect, the induced temperature gradient modulates the sound velocity within the measurement volume. Consequently, a constant sound velocity for the medium (water) - obtained from the FFT of the entire TRBS signal - can no longer assumed. For this previous case, the spatial vector is assembled using the original time-discretisation of the signal (Δt) and a constant sound velocity (v_c) measured by Equation 6.1:

$$z_c = z_i = \sum_{k=1}^{i} v_c \Delta t \tag{6.4}$$

where i denotes the i^{th} element in the spatial vector, and the uniform discretisation of the vector can be written as $\Delta z_c = \Delta z_i = v_c \Delta t$. In reality, the deviation from constant sound velocity will produce a spatial vector

$$z_T = z_i = \sum_{k=1}^{i} v_k \Delta t \tag{6.5}$$

with spacing $\Delta z_T = \Delta z_i(f_{B_i}) = v_i(f_{B_i})\Delta t$. Now, in order to estimate and compensate this positional error, the time-varying sound velocity should be characterised and included in the time-space conversion.

Two separate experimental signals (without a boundary in the measurement volume) were wavelet transformed across the Brillouin frequency-centred bandwidth $f_c =$

$4 - 6\ GHz$. The frequency which exhibited the maximum amplitude wavelet coefficient (C_w) at each time-slice is plotted in Figure 6.23a (blue and red lines); this time-varying frequency-fluctuation was then fitted using a high-order polynomial (light blue and red lines) and used to determine the time-varying sound velocity (right y-axis) assuming a constant refractive index (Equation 6.1). The assumption that the refractive index of water is constant with changes in temperature is reasonable when comparing the thermo-optic and thermo-acoustic coefficients of water. In Figures 5.10a-b these coefficients are plotted for the temperature range $20 \leq T \leq 100^{\circ}C$. Considering the maximum variation in the values over this range, the maximum percent variation in the refractive index with temperature is on the order of 1%, and the maximum percent variation in the sound velocity is on the order of 15%. Accordingly, the maximum percent variation in the theoretical Brillouin frequency over this range (Figure 5.10c) is also 15%. Therefore, since the variation in sound velocity is over an order of magnitude greater than that of refractive index, and matches the total variation in Brillouin frequency, the variation in water's refractive index with temperature can be approximated as constant $n_{H_2O} = 1.33$.

Now, the temperature-dependent sound velocity can be used to calculate Equation 6.5, and therefore redistribute the z_T ticks of the z-ruler for each experimental TRBS trace. The offset between the spatial vector calculated using a constant spacing Δz_c (single f_B value extracted from frequency spectrum) and the spatial vector calculated with spacing Δz_T results in an estimate of the positional error, ϵ_z

$$\epsilon_z = z_c - z_T \tag{6.6}$$

and is plotted for the two TRBS signals in Figure 6.23b. Despite there being subtle differences in the rate of change in instantaneous Brillouin frequency and sound velocity between the two TRBS signals - e.g. due to slight differences in beam power and therefore heating/diffusion between the two experiments - it is evident that the overall effect on the positional error remains similar.

From Figure 6.23b, the magnitude of the error is small towards the beginning of the time-vector, where the instantaneous Brillouin frequency matches the weighted average Brillouin frequency (frequency peak in FFT) of the entire signal; for the blue and red signals this average Brillouin frequency is $f_B = 4.83\ GHz$ and $f_B = 4.79\ GHz$ respectively. However, as the sound velocity fluctuates (beyond $t > 2\ ns$ in Figure 6.23a), this error will carry on and accumulate towards the end of the time-vector, seen at the end of Figure 6.23b. Therefore, the error in measuring the proximity of the floor/substrate of a specimen will be greater than measuring the peak height of the specimen, since the floor will occur later in the time-vector. Figure 6.23b can then be used to estimate the maximum positional error for the three objects imaged in Figures 6.15-6.17. For these objects the floor (or SNR floor) was localised at the $t = 3.95,\ 3.80$, and $3.14\ ns$ time

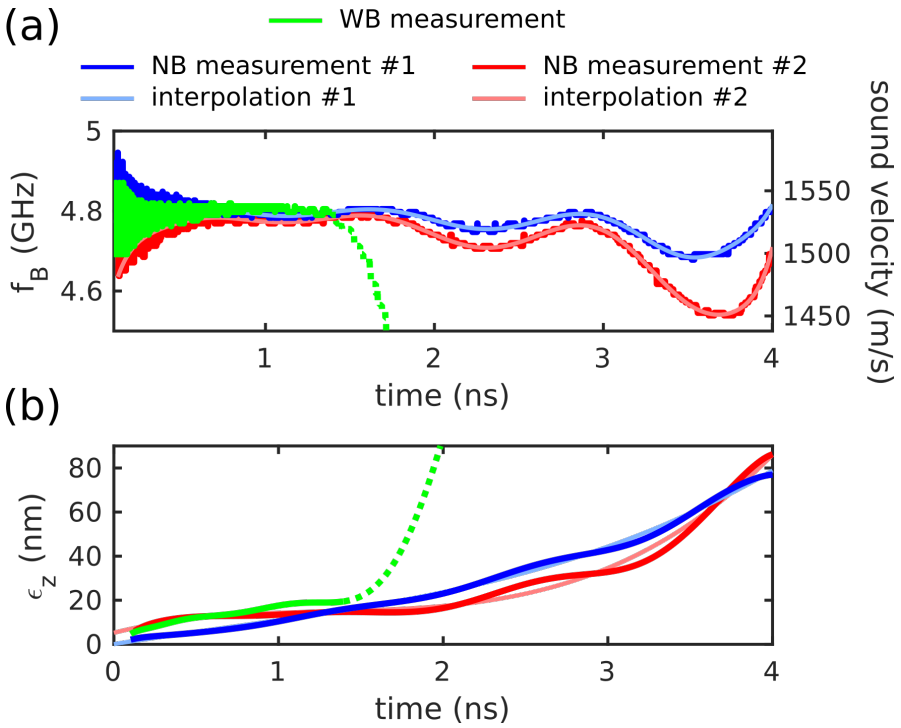


Figure 6.23: Estimation of positional error due to in-depth fluctuations of the sound velocity within the measurement volume. (a) Wavelet transformation of three TRBS signals: 1 with a boundary (WB - green), and 2 without a boundary (NB - blue and red). The frequency containing the maximum amplitude wavelet coefficient is plotted as a function of signal time. All three signals demonstrate a similar average Brillouin frequency of $f_B \approx 4.8\ GHz$, which is represented by the relatively flat region between $t = [0, 2]\ ns$. After $t = 2\ ns$ the red and blue curves begin to vary in frequency, which can be explained by temperature fluctuations within the measurement volume (see Figure 5.14). The green signal varies much more rapidly in frequency after the boundary as the TRBS oscillations attenuate drastically and sound velocity can no longer be measured (dotted green). The instantaneous frequency can be interpolated (for smoothness) (light blue and red curves) and used to calculate the instantaneous sound velocity (right axis). This is then used to build unique spatial vectors for each trace that have spacings $\Delta z_i = v_i(f_{B_i})\Delta t$. The error ϵ_z between the new spatial vectors and those calculated using a constant sound velocity is shown in (b). All three signals show close agreement before the green signal diverges (non-physical), after which the two NB responses remain in close agreement.

positions respectively. These time positions translate to positional errors of $\epsilon_z = 91,\ 73,$ and $40\ nm$ using the red error function in Figure 6.23b.

For the special case of the object in Figure 6.17, which appeared to be fully reconstructed in height by the phonon probe, the original proximity measurement of the floor $z_c = z_{floor} = 4.796\ \mu m$, can be corrected using Equation 6.6 and the ϵ_z calibration in Figure 6.23 (for $t = 3.14\ ns$):

$$z_T^{floor} = z_c - \epsilon_z = 4.796\ \mu m - 0.040\ \mu m \approx 4.756\ \mu m$$

The peak of the object occurred at time $t = 1.37\ ns$ ($z_c = 2.101\ \mu m$ original measure-

ment), corresponding to a positional error of $\epsilon_z = 16\ nm$, and a corrected measurement of

$$z_T^{peak} = z_c - \epsilon_z = 2.101\ \mu m - 0.016\ \mu m \approx 2.085\ \mu m$$

Now, using the new measurements above, the total height measured by the phonon probe can be updated to

$$h_T = z_T^{floor} - z_T^{peak} = 2.671\ \mu m$$

which compared with the absolute height measured through optical profilometry, results in an accuracy estimate of

$$\epsilon_{abs} = h_{abs} - h_T = 30\ nm$$

rather than the $5\ nm$ accuracy that was originally reported for the raw height measurement in Figure 6.17.

In this exercise the two signals without boundaries have been used to estimate the positional error for signals that *do* contain boundaries. In Figure 6.23, a signal containing a boundary (WB) has been included in green for comparison. Due to the sudden attenuation of this TRBS signal, there exists a strong low frequency component (the envelope of the attenuated waveform), which dominates the maximum amplitude frequency after the transition at $t \approx 1.4\ ns$ (dotted green in Figure 6.23a). However, the overall frequency content of the wave before it has attenuated closely matches the two NB signals, the latter two being relatively flat for the first $t \approx 2\ ns$. Consequently, the positional error for the WB waveform in Figure 6.23b does not deviate by more than $4\ nm$ compared with the average of the red and blue curves (for $t < 1.4\ ns$). This agreement indicates that the NB-cases are valid approximations whether there exists a boundary or not, and are sufficient to estimate the total positional error. This process for identifying and calibrating positional error should ideally be repeated for each new experiment; especially when conditions such as the pump and probe wavelength or beam powers have been altered, the latter producing a new steady-state heat rise (see Figure 5.12) and therefore an altered thermo-acoustic response. However, despite the red and blue measurements taking place on separate days (yet experimental parameters unchanged), and therefore slight deviations in ϵ_z, the magnitude of the error remains reproducible.

Understanding the sources of error within the phonon probe system is crucial for its future application, especially when being used in a profilometric-capacity, as demonstrated by the 3D imaging capabilities presented in this chapter. Compared with traditional stylus and optical profilometry techniques, there are clear advantages and disadvantages to using the phonon probe for this purpose. This motivates a discussion of the resolution of the phonon probe; the following section will discuss this in the context

of 3D imaging/profilometry, and highlight ways in which it can be improved in the future.

6.4.2 Resolution

The lateral resolution of the phonon probe is dictated by the mode field diameter (MFD) of the optical fibre, which is a function of the core diameter, wavelength, and core:cladding refractive indices. This is akin to the point spread function (PSF) with a traditional lens; the spatial intensity distribution that is emitted from the core will determine the minimum resolvable separation between two objects. For the 780HP type single mode fibre used in this study, this lateral resolution is $r_{PSF} \approx MFD/2 \approx 2.5\ \mu m$. However, due to the fact that the pump and probe beams are diverging away from the fibre-tip, the lateral resolution of the phonon probe will be a function of axial distance, $r_{PSF}(z)$. The axial dependence of the lateral resolution will then be a function of the fibre NA, similar to the resolving power of a lens:

$$r_{PSF} = w_0 \sqrt{1 + \left(\frac{z \cdot NA}{n \cdot w_0}\right)^2} \tag{6.7}$$

where w_0 is the beam waist radius (MFD/2) and n the refractive index of the medium [224]. Figure 6.24a shows this axially-varying resolution in water using the phonon probe; the change in lateral resolution is negligible over the axial distances covered by this study ($z < 10\ \mu m$) showing a divergence of only $\sim 100\ nm$. This is due to the low NA of the 780HP fibre, NA$= 0.13$, and thus a slow beam divergence.

For the case of axial resolution, there are two scenarios to consider: (1) *a priori* knowledge that there is only one (axial) boundary within each measurement volume, and (2) no *a priori* knowledge regarding the number of boundaries within the measurement volume. The former is most relevant to the 3D profilometry presented in this study, since the surface of an object is the imaging target. In this case, it is less relevant to discuss *resolution* as there is only one object; instead, it is more pertinent to discuss the precision with which a boundary can be located, which will primarily be a function of the SNR of the original time-domain signal.

In Figure 6.24b, a proximity measurement between the phonon probe and a petri dish was repeated 100 times (with $10k$ averages per count). The N=100 data-set was partitioned into averaged bins, each with population 10 (counts). For example, the lowest average measurement consisted of 10 individual proximity measurements ($10k$ averages for each measurement); the highest average measurement consisted of 10 proximity measurements, each of which was the average of 10 counts ($100k$ averages per measurement). The standard deviation of the average proximity measurement in each bin, σ_z, decreases (increasing precision) as the number of averages increases (see Figure 6.24b). Conversely, as the bandwidth of the wavelet is increased, i.e. increasing the number of cycles in the mother wavelet, the precision decreases. This

can be explained by the inherent trade off between precision in frequency and time when using continuous wavelet transform. As the number of cycles N_λ in the wavelet increases the precision with which frequency can be measured increases. However, this comes at the cost of being able to measure a discrete event in time with greater uncertainty. The imaging experiments presented in this paper were performed utilising a wavelet width of approximately $N_\lambda = 6$ and 15,000 oscilloscope averages which results in a height measurement uncertainty of $\sigma_z = 55\ nm$. Similar to characterising frequency, as the width of the wavelet increases, so too does the precision with which TRBS amplitude can be measured (at a single frequency) as shown in Figure 6.24c.

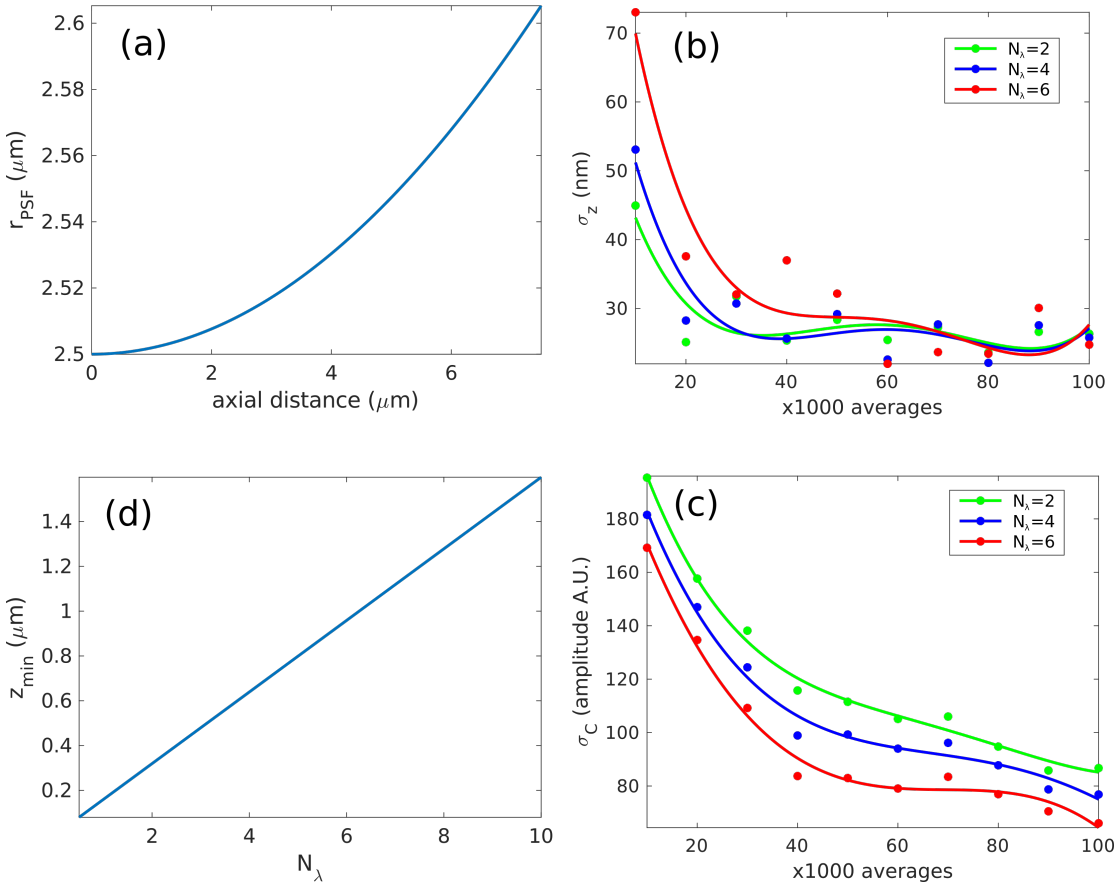


Figure 6.24: Characterisations of the resolution and precision of the phonon probe. (a) Lateral resolution is dictated by the mode field diameter of the fibre which decreases as the probe beam diverges away from the fibre-core ($NA = 0.13$). (b) The standard deviation (σ_z) of 10 separate proximity measurements as a function of signal averaging and wavelet width (N_λ). As the wavelet is widened, it more precisely samples the frequency of an oscillation, and conversely samples the timing of the oscillation with less precision. Markers indicate the measured values of σ_z and the lines represent polynomial fits. (c) Standard deviation of the wavelet amplitude (C_w") as a function of signal averaging and wavelet width. Widening the wavelet results results in a more precise sampling of the amplitude of an oscillation, as does increasing the SNR of the oscillation through signal averaging. (d) When the phonon probe is used to map the in-depth change in Brillouin frequency - e.g. as an imaging contrast mechanism - the axial resolution (temporal resolution) will worsen as the wavelet widens.

In this instance the effect of signal averaging increases the SNR of the TRBS signal amplitude and therefore enables less uncertainty in σ_C.

For the future case where the phonon probe uses the instantaneous Brillouin frequency as an imaging contrast mechanism in the axial direction, a different criterion for axial resolution with apply. In this scenario there will no longer be *a priori* information regarding the number of objects or boundaries within the TRBS signal time-of-flight, and resolution will depend on the acoustic wavelength and the effective PSF of the wavelet. The relationship between axial resolution, acoustic wavelength, and wavelet width has been empirically determined [168], with the minimum resolvable spacing between objects defined as

$$z_{min} = \frac{N_\lambda \lambda_a}{2} = \frac{N_\lambda \lambda_{probe}}{4n} \tag{6.8}$$

As N_λ increases, so too does the resolution with which frequency (f_B) can be characterised; i.e. the true frequency of an oscillation is more heavily sampled when the wavelet contains additional cycles. Again, this comes at the cost of lower axial resolution due to greater uncertainty in the time-domain; a wavelet that occupies a greater expanse in time will be unable to resolve fast changes in frequency and therefore has lower temporal resolution. This is analogous to lateral resolution: a larger PSF will overlap two nearby objects leaving them unresolved.

In any case, the phonon probe holds great potential for the 3D imaging of elasticity, e.g. in biological cells. Using the $\lambda_a = \lambda_{probe}/2n$ phonons with wavelets on the order of $N_\lambda \sim 2-6$ will allow sub-surface (photoelastic) features to be detected with axial resolutions on the order of $z_{min} \sim 0.3-1\ \mu m$. Compared with optical microscopy this would require objective lenses with $NA \sim 1-1.7+$. However, an optical system with a numerical aperture equivalent to that of the phonon probe ($NA = 0.13$) would possess an axial resolution on the order of $z_{min} = 70\ \mu m$, showing that the phonon probe is two orders of magnitude higher resolution. Additionally, compared with the highest resolution endomicroscopes (Table 1.1) and photoacoustic endoscopes (Table 1.2), the phonon probe as configured achieves 1-2 orders of magnitude improvement in axial resolution, respectively.

Compared with the gold standard of profilometry, AFM, the phonon probe is relatively low resolution (see Table 6.1). However, the phonon probe offers the following unique benefits:

- *non-contact* operation (except for contact with the couplant)
- native bio-compatibly since it uses low energy light and the effects of heating can be mitigated by thermally insulating transducer layers or increasing the stand-off distance between the specimen and the fibre tip
- sub-surface information can be extracted by the phonon probe (for semi-transparent and transparent samples)

- dynamic range on the order of $\sim$ 6 μm (for fixed z-position) with potential to approach $\sim$ 100 μm by varying the height of the fibre. Unlike AFM this does not depend on the cantilever, but exclusively on the piezo-stage (and to some degree the fibre outer diameter). The AFM-instrument available at the time of writing required a cantilever which was incapable of sampling the entire height of the phantoms presented in this study.

As constructed, the phonon probe is not equipped to match the resolution of AFM, but instead provides a supplementary set of capabilities. These benefits offer unique potential for biological specimens - which are historically non-trivial for AFM instruments [225] - while still providing cellular and sub-cellular resolutions.

In a similar vein, the optical profiler used in this study to corroborate the PS-phantom topography provides high resolution capabilities utilising white light interferometry and high-NA objective lenses. Two key properties of optical profiling, are that (1) no lateral scanning is required and the entire field of view can be acquired in one exposure, and (2) the dynamic range is only limited by the z-range of the piezo-stage; also, similar to the phonon probe it is non-contact and both compare favourably in terms of the axial resolution. However, the optical quality of the sample is critical for optical profilometry. Using the PS-phantoms as an example, the sub-surface defects in the objects result in a heterogeneous refractive index distribution (which is why the defects can be observed visually). For the interferometric optical profiler, this implicates that light scattered from the same z-slice will undergo inhomogeneous phase shifts and will distort the interferogram used to measure topography [226, 227]. These artefacts are clearly visible in the height maps of figures 6.15-6.16 and disrupt the overall accuracy of the measurement, yet do not affect the phonon probe measurements. Metallic films can be coated onto such samples in order to homogenise the reflectivity, however, this alters the natural state of the sample and would not be compatible with biological organisms.

Ultimately the phonon probe is strongly positioned as a future 3D imaging tool due

Profilometer characteristics						
Technique	lateral resolution	axial resolution	acquisition time	dynamic range	optical uniformity required?	access sub-surface?
AFM*	$\sim nm$	$< nm$	$\sim$ hour	$\sim \mu m$	no	no
Optical profiler†	$< \mu m$	$< \mu m$	$\sim$ minute	$\sim cm$	yes	yes$^{\circ}$
Phonon probe	$\sim \mu m$	$\sim$ 100 nm	$\sim$ hour	$\sim$ 6 $\mu m^{\bullet}$	no	yes$^{\$}$

Table 6.1: *Specifications for Bruker Dimension FastScan. †Specifications for KLA Zeta-20. Acquisition times were user-recorded, and are relative to the field of view and phantom heights relevant to this study, $FOV \sim 100\ \mu m \times 100\ \mu m$ and $h \leq 10\ \mu m$ respectively. $^{\circ}$Object must be optically uniform. $^{\bullet}$Given a fixed z-position; z-position can be varied up to $\sim 100\ \mu m$. $^{\$}$ Object must be partially transparent and photoelastic.

to the endoscopic nature of the system, a quality that is unique compared with profilometers. However, in the context of imaging with a single optical fibre, the phonon probe excels with both contrast and axial resolution provided by acoustics. Lateral resolution and acquisition speed are key areas of improvement for the device in order for it to be adopted within industry and the wider-research landscape. One potential way to achieve high lateral resolution would be to fabricate an acoustic micro-lens onto the tip of the fibre, Section 7 will introduce this and other strategies for optimisation.

6.4.3 Conclusions

After achieving proof of concept that the phonon probe can be used as a high resolution Brillouin spectrometer (Chapter 5), it was posited that the acoustic time-of-flight capabilities of the device could be used for 3D imaging. This chapter has showed that this is indeed possible. By controlling the position of the phonon probe (with respect to the sample) with micrometre precision in the x and y directions, and with nanometre precision in the z-direction, the phonon probe can be positioned close enough to a microscopic object to pre-empt the effects of acoustic attenuation. A signal-processing strategy was developed and utilised to observe when GHz acoustic waves either scatter from or transmit into a microscopic object, such as PS-phantoms. This system was extrapolated into a full 3D scanning imaging technique, and resulted in the first images of cell-sized objects using a single optical fibre. Furthermore, the phonon probe achieves this milestone without traditional microscopy equipment, such as high magnification objectives lenses and nanometre-tipped needles.

The lateral resolution of the phonon probe, $r_{PSF} \approx 2.5\ \mu m$, is determined by the properties of the optical fibre itself; however the axially resolving characteristics of the device are greatly improved compared with pre-existing optical and acoustic endoscopes, especially given the low numerical aperture ($NA = 0.13$). It has been shown that a boundary can be localised with a precision on the order $\sigma_z \approx 55\ nm$, which scales with averaging the TRBS signal. A close agreement in total height measured by optical profilometry and the phonon probe was demonstrated (Figure 6.17). However, this accuracy is dependent on whether or not the phonon probe is able to image the entire height of an object, otherwise only a relative measurement is possible to provide height-contrast. It can also be affected by: (1) mismatches in lateral resolution between techniques as fast-varying height features can be unresolved by the phonon probe, and (2) thermal errors on the position calculation; the contribution from the latter has been discussed and was estimated to produce an accuracy of $\epsilon_z \approx 30\ nm$ compared with optical profiling, when the full height of an object can be reconstructed.

Aside from profilometry, proof of concept was also achieved for using the phonon probe to the map elasticity of microscopic objects (Figure 6.18). Using the device in this capacity is highly dependent on maintaining spatial overlap between phonons and pho-

tons; for PS-phantoms this relationship is only preserved when the surface is relatively flat ($\theta_i \leq 10^\circ$). There exists great potential for using the phonon probe to map cellular elasticity due to the low mismatch in both optical and acoustic properties (compared with water). This and other future applications, developments, and implications of the phonon probe device will be covered in the following two chapters.

Chapter 7

Future work

This chapter will present some of the areas of future development for the phonon probe. There are no shortage of possibilities for developing a high frequency acoustic endoscopic device. Two in particular which will not be discussed at length here, but deserve mentioning are: moving beyond traditional pump-probe pulse trains in order to increase acquisition speed, and moving beyond Brillouin scattering as a detection mechanism. The latter holds promise in the following way: if an arbitrary cavity can be constructed that mechanically resonates at frequency f, the acoustic penetration depth of the system will be proportional to f^{-2}. By ensuring that this cavity resonance is sub-GHz, the acoustic field will be capable of travelling in the range of 10^2 μm therefore increasing the working distance. This will require an inline detection cavity whose optical resonance is sensitive to the mechanical vibrations (e.g. when the generated sound echoes from an object and returns back to the detection cavity). In the interest of brevity, the key themes that will be addressed in this chapter will pertain to the time-resolved Brillouin scattering mechanism of the phonon probe; this chapter will outline strategies, and even proof of concept, for how to expand the following characteristics of the device: field of view, SNR, penetration depth, and lateral resolution.

7.1 Phonon imaging bundle

The phonon probe is a single-fibre, single-pixel device. It only achieves spatial resolution by scanning the fibre tip in the x/y plane (and z using the time-of-flight and the piezo-stage). A natural evolution of this device is to group together many individual fibre transducers to create a multi-pixel phonon imaging system. Then, the scanning mechanism of the device can in part be transferred from the distal end (side of the fibre containing the transducer where the measurement is made) to the proximal end (side of the fibre containing the light source), by way of scanning the pump-probe beam spots across and into each individual fibre core. When *bundling* multiple fibres together to create a pixel array, the lateral resolution of the tool will be dictated by the pixel spac-

ing, i.e. the distance between fibre cores; if a group of 780HP single-mode fibres (used throughout this study) were bundled together, the resolution would be given by the outer cladding diameter of a $125\ \mu m$.

To avoid such low resolution, the industry standard is to create a bundle of cores all sharing a common cladding, and is commonly referred to as an imaging bundle or a fibre bundle. In this way the $125\ \mu m$ distance between cores can be reduced to an arbitrarily small distance allowing bundling of up to $\sim 100,000$ cores. Consider light propagating down a single channel of such an imaging bundle. As the cladding space between cores shrinks, the non-guided cladding modes will begin to increasingly couple into neighbouring cores and therefore be converted into guided modes [228] (e.g. when neighbouring core is within the radial distance shown in Figure 3.2). To counteract this the contrast between the refractive index of the core and cladding is increased. As seen in Equation 3.4, the numerical aperture of any given core is dependent on the refractive index contrast; therefore, in order to prevent cladding leakage the core NA must increase. In addition to the refractive index contrast, the increase in NA has the effect of rendering the core multi-modal as dictated by the changes in the acceptance cone and critical angle.

In order to investigate the compatibility between the phonon probe system and an imaging bundle, a Schott Leached Fiber Bundle was used (Figure 7.1a); this product is a *coherent* fibre bundle, meaning that there is a one-to-one spatial mapping between pixels on the proximal and distal ends. The product contains the following specifications: $1.65 \times 1350\ mm$ (diameter and length respectively), $11.6\ \mu m$ core diameter, 18,000 cores, core $NA = 0.393$, and the transmission spectrum seen in Figure 7.1b. With these parameters, and a probe wavelength of $\lambda_{probe} = 780\ nm$, the approximate number of modes supported by a core in the bundle is $V^2/2 \approx 168$ (Equation 3.10).

The experimental set-up was adapted in order to vary the spatial position of the

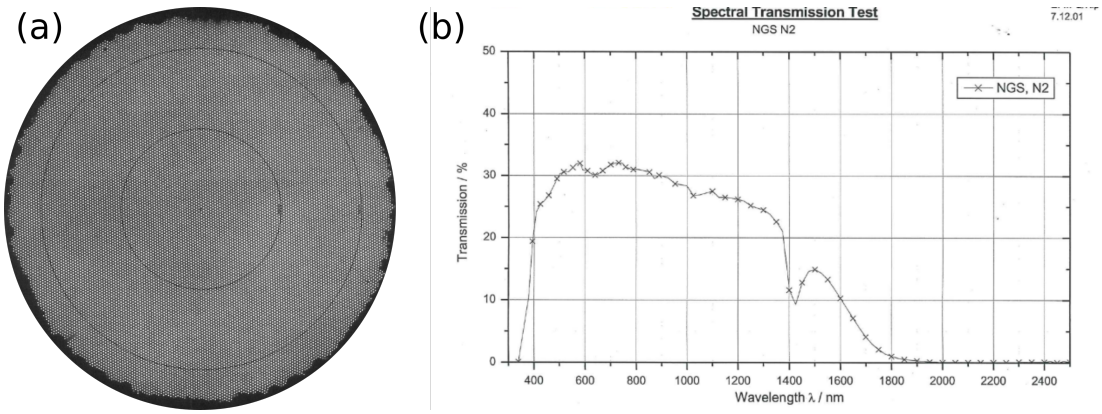


Figure 7.1: (a) Photograph of the distal end of a coherent imaging bundle similar to the one used in this study, containing 18,000 cores surrounded by a common cladding. (b) Transmission spectrum for the imaging bundle in (a) showing $> 20\%$ transmission across the NUV-NIR wavelength range.

pump and probe spots, such that each core can be excited individually. This was accomplished by fixing the proximal end of the bundle to high resolution x/y stages (proximal facet facing the normal of stage) and within the focal plane of a microscope objective lens, as presented in Figure 7.2a-b. Both the pump and probe wavelengths were set to $\lambda = 780\ nm$, however, both beams are effectively pump and probe (will discuss below). The pump and probe spots are focused into a single core, as monitored with a CCD. Then at the distal end, the familiar process of optical absorption, ultrasonic generation, and Brillouin scattering takes place, followed by the back-scattered beams re-coupling into the bundle and eventually the preceding free-space system, before being directed onto a photodiode with a 50/50 beamsplitter (see Figure 7.2a-c). An additional detector was arranged along the optical axis of the distal bundle-tip to allow

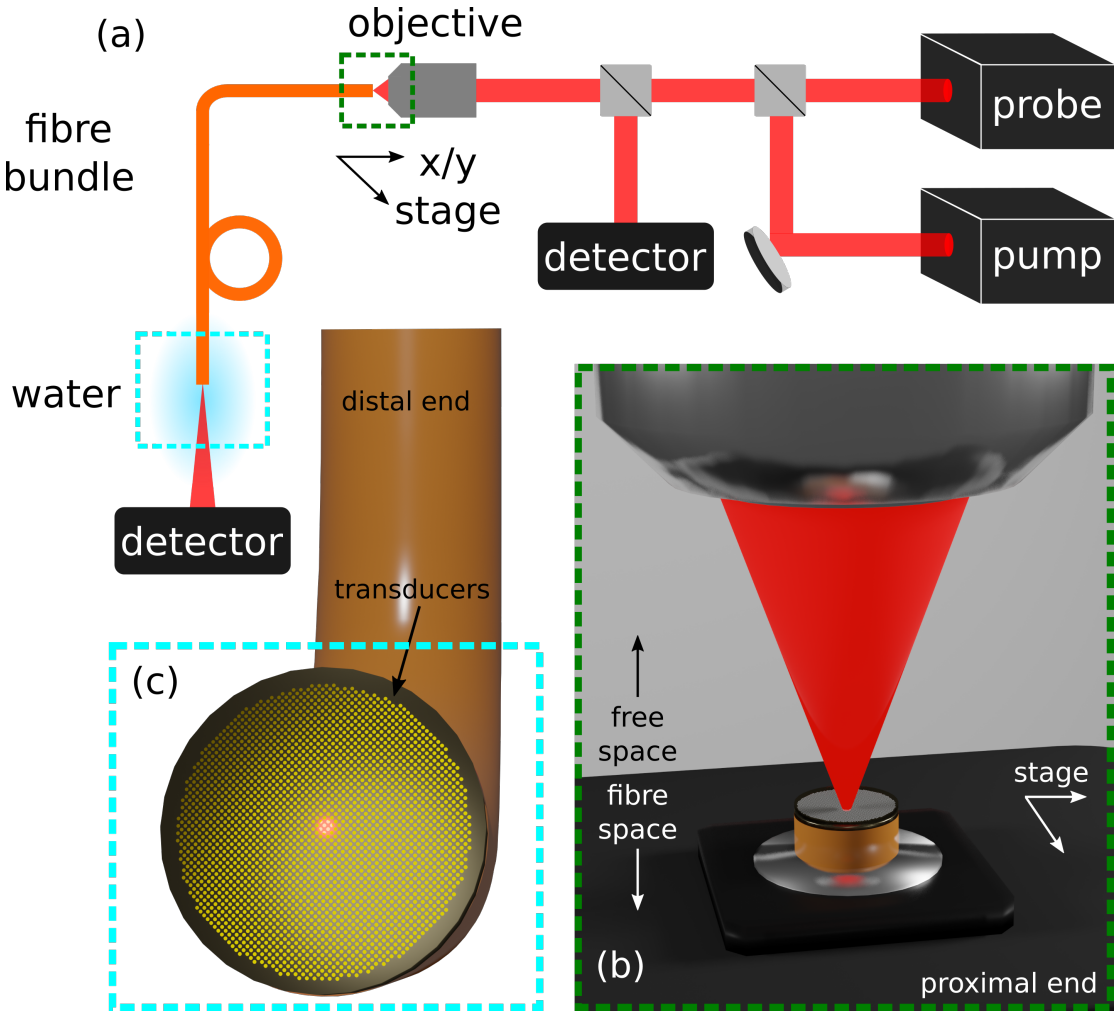


Figure 7.2: (a) Modified phonon probe system for the imaging bundle; instead of using FiberPorts to couple from free-space to fibre, an objective lens is used to focus the NIR pump-probe beams into a single core of the fibre. (b) Each core can be sequentially illuminated by scanning the position of the proximal end-face using high resolution x/y stages. (c) On the distal end of the bundle, $15 - 20\ nm$ of gold has been deposited to create 18,000 transducers. TRBS signals for this configuration are detectable in transmission and reflection beam paths.

allow detection of the transmitted Brillouin scattered light.

Initially the distal facet of the imaging bundle was sputter-coated with $15 - 20\ nm$ for thermo-elastic generation of ultrasound. Following this, the distal end of the bundle was immersed in water, the pump and probe beams were directed into a single core, and $500k$ averages of the TRBS signal was attained (Figure 7.3). This core in the bundle was capable of facilitating a spectroscopic measurement in water of $f_B = 5.28 \pm 0.03\ GHz$, which is expected for this wavelength and medium. Following this proof of concept that TRBS can be performed in a multi-mode imaging bundle, the pump and probe beams were simultaneously scanned over an $80\ \mu m \times 80\ \mu m$ area in steps of $2\ \mu m$. The oscilloscope was set to record $20,000$ averages at each position in the

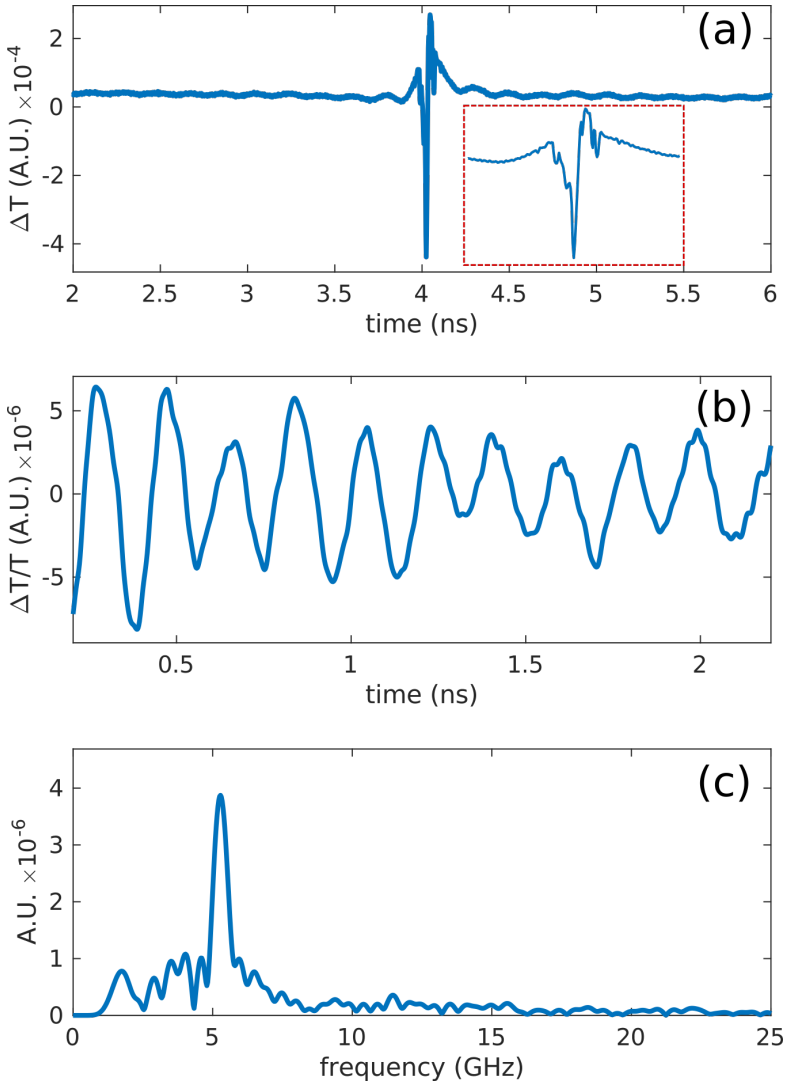


Figure 7.3: (a) Raw unprocessed signal from a single core of the imaging bundle transducer immersed in water. (inset) The coincidence peak appears to show multiple spikes which could correlate with parasitic coincidence peaks carried by higher order modes that are time-delayed from the fundamental mode. (b) Processed modulation depth of the signal in (a) (portion of the signal travelling from $t = 4 \rightarrow 6\ ns$). (c) FFT of the modulation depth which produces a spectroscopic measurement of $f_B = 5.28 \pm 0.03\ GHz$.

scan which took 4 hours to complete. Figures 7.4a-b show the maximum modulation depth amplitude maps for the transmission (a) and reflection (b) TRBS signals. The time-resolved signal at each pixel was processed in the same way described in Section 4.2.1, resulting in the Brillouin frequency maps found in figures 7.4c-d.

The blue-coloured space in between cores represents the pump-probe spots impinging the cladding and this dead-space significantly lengthens the time of the experiment. In order to avoid unnecessary scan-time the following protocol was established: (1) perform an area scan across the desired field of view while only acquiring the DC intensity at each pixel (Figure 7.5a); (2) from (a) locate the centroid and approximate diameter of each core (Figure 7.5b); (3) perform an area scan in which the pump-probe beams are only directed to the x/y positions of each centroid in (b). In addition, the DC map in Figure 7.5a provides an opportunity to empirically determine the mode field

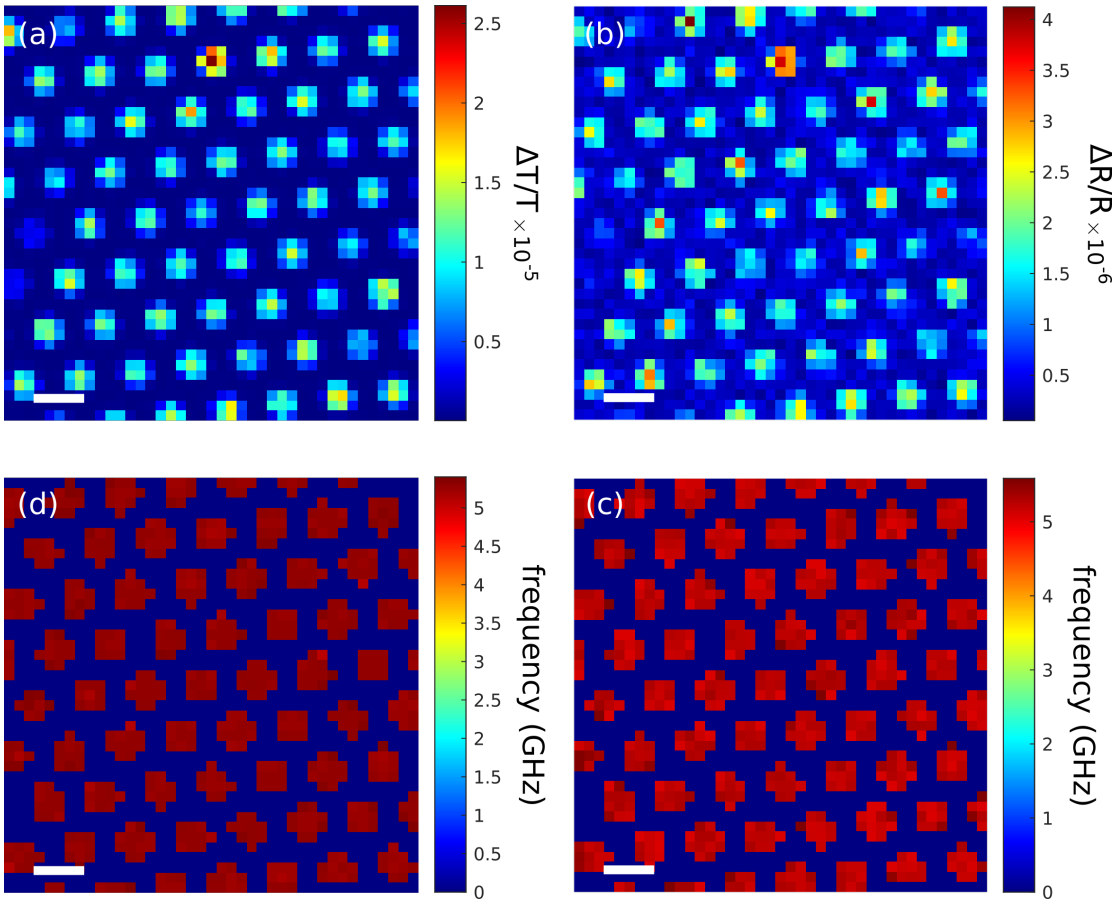


Figure 7.4: (a-b) Maximum amplitude of the modulation depth at each pixel for the transmission and reflection paths, respectively. The variation in coupling efficiency across cores is apparent as some cores may be damaged. The difference in maximum amplitude between transmission and reflection signals can be explained by the additional optical attenuation that occurs for the round trip through the bundle in the reflection path. (c-d) Brillouin frequency maps attained from the signals at each pixel in (a-b), which demonstrate that a stationary bundle can be used to acquire spatially resolved elastic information. Time duration of the scan is 4 hours and scale bars are 10 μm.

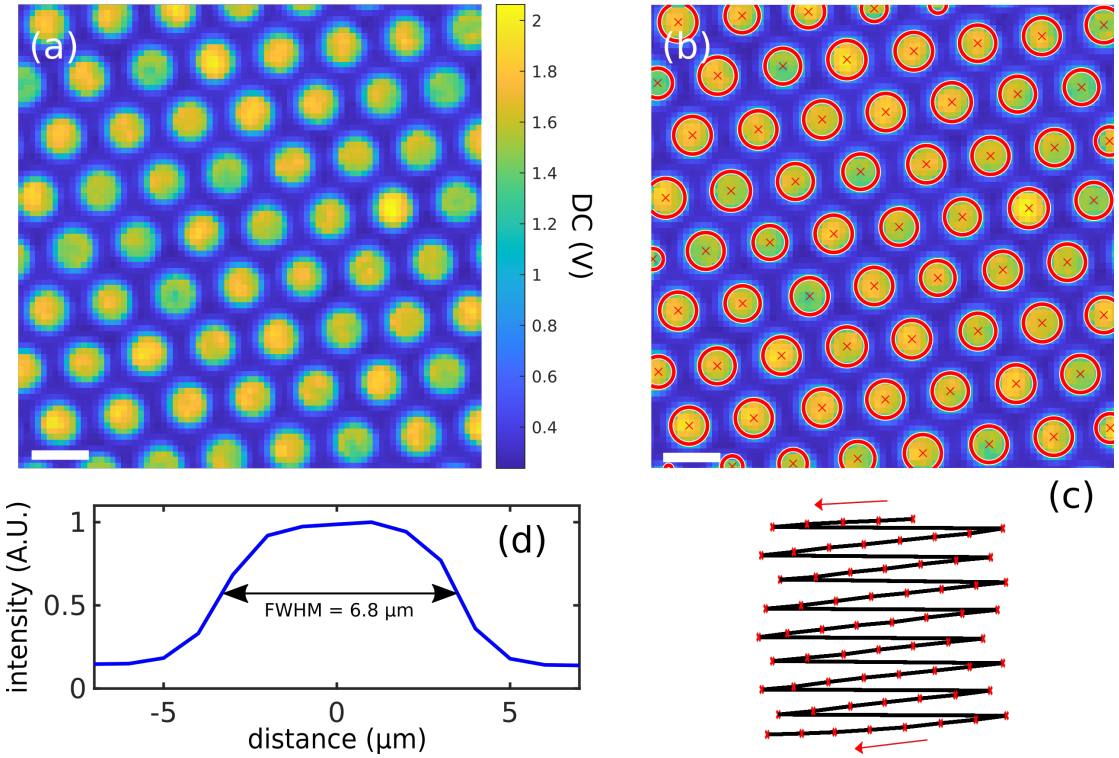


Figure 7.5: Process chain for a new scanning protocol in which pump/probe beams hop from core to core when neighbouring cores are in arbitrary directions. (a) Area scan of the field of view shown in Figure 7.4 where only the DC optical intensity is acquired at each scan-position. (b) The centroid of each high intensity core is calculated in addition to the approximate core-diameter. (c) A new set of scan coordinates, for a future AC/DC scan are established from the centroid positions acquired in (b). (d) Intensity profile for a single core in (a) revealing an effective spot size of $6.8\ \mu m$. Scale bars are $10\ \mu m$.

diameter and core-core spacing of the imaging bundle. Figure 7.5d shows the optical intensity distribution of a cross-section of a single core and reveals a full-width half-maximum of $FWHM = 6.8\ \mu m$ and a core-core distance of $\approx 11.3\ \mu m$.

The above procedure was carried out in the same field of view as Figure 7.4 reducing the acquisition time from 4 hours to 4 minutes, however, with $\approx 11.3\ \mu m$ lateral resolution. The core-calibration scan (which preceded this 4 minute scan) took approximately 20 minutes, yet only needs to be performed once provided that the bundle remains fixed in its position for subsequent scans. Figure 7.6 presents the signal amplitude and frequency maps attained with the new scan-technique. It is worth noting that there are fluctuations in DC-level and SNR across some cores, which is observable in both experiments (figures 7.4-7.5), and is a likely cause for the slight frequency variations found in Figure 7.6c-d. This could be due to damaged cores, imperfections in the cores, a thickness gradient from the gold layer, or mismatches between the scan location and actual core-location (spatially and angularly).

In the raw unprocessed signal in Figure 7.3, it is apparent that there exists both a forward (travelling from $t = 4 \rightarrow 6\ ns$) and backward propagating (travelling from

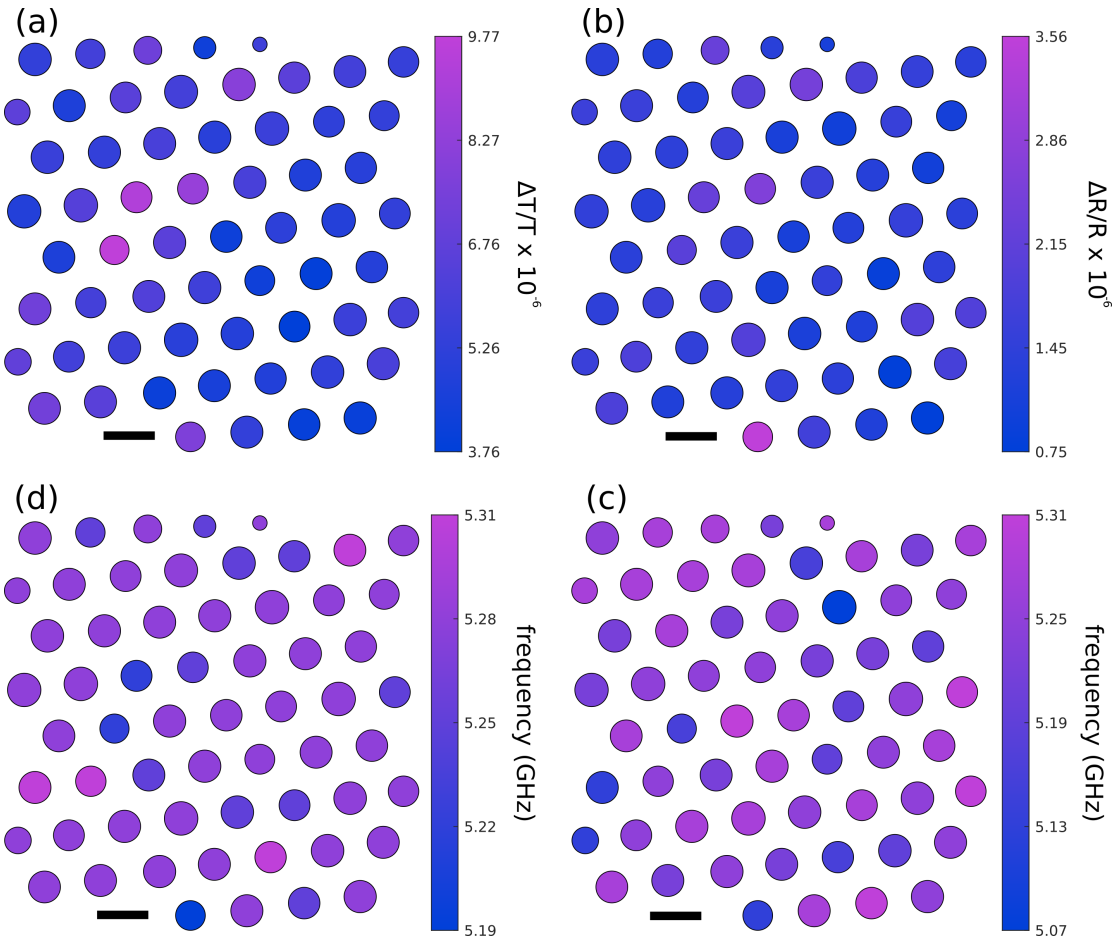


Figure 7.6: The combined pump-probe spot is now scanned directly from core to core, thus avoiding the dwell-time in the cladding space. Compared with the rectilinear scan performed in Figure 7.4 which took 4 hours, this new protocol only requires 4 minutes, since the spots can scan from any arbitrary point to another (e.g. core to core). (a-b) Modulation depth amplitude map for the transmitted and reflected probe signals respectively. (c-d) Corresponding Brillouin frequency maps for the core-signals associated with the amplitudes in (a-b). Scale bars 10 μm.

$t = 4 \rightarrow 2\ ns) \sim 5\ GHz$ wave. This can be explained by considering that a portion of each beam is being absorbed by the transducer (acting as the pump), and each beam is participating in Brillouin scattering and terminates at the detector (acting as the probe). The caveat is that one "probe" samples the acoustic wave moving forward in time, and the other samples it moving backward in time. This phenomenon is inherent to the pump-probe technique, yet the influence of one beam (e.g. the pump) is often filtered from the detector (e.g. which is placed in the probe path) through dichroic filters used to initially combine the beams into a common path. Since the experiments presented here have equivalent pump and probe wavelengths, and a 50/50 beamsplitter is used to combine the beams, the effect is registered by the detector. If each counter-propagating signal can be extracted, the sum of the aligned signals will increase the signal strength according to the relative weighting of the beam powers. Figure 7.7 shows this signal folding and alignment process: (1) the signal from each side of the coincidence peak is

selected (a), (2) crop one signal to align the phases (optional, not pictured), and (3) sum the two aligned oscillations (c). Comparing the maximum amplitudes at the Brillouin frequency for the pre-summed and summed signals (figures 7.7b and d respectively), this process results in a doubling in signal amplitude (double since the pump and probe optical powers are equal).

This proof of concept experiment was performed with a microscope objective of numerical aperture NA=0.45. Despite using a lens with comparable NA to that of each core, and thus exciting undesirable higher order modes, the multi-mode bundle proved compatible with the TRBS detection scheme. As mode order increases in the waveguide, so too does the effect of inter-modal dispersion. In other words, since each mode within the core roughly corresponds to an infinitesimal angle within the acceptance cone, the high angle higher order modes travelling longer path lengths and thus disperse in time with respect to the fundamental mode. For the imaging bundle used in this study, the original $100\ fs$ pulse is dispersed into a train of higher order mode pulses

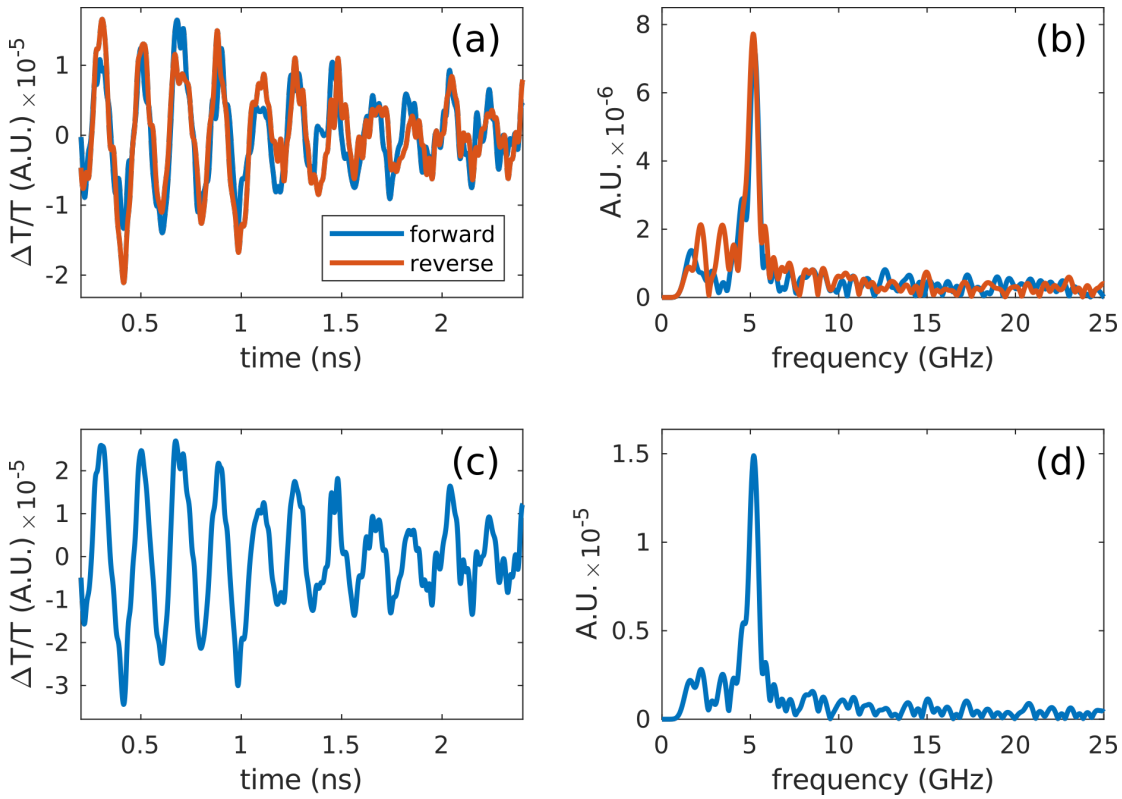


Figure 7.7: (a) Beginning with a TRBS signal from a single core in Figure 7.6a, which is similar in form to that in Figure 7.3a, the Brillouin oscillations travelling in the forward and reverse time directions can both be extracted and summed to increase signal amplitude. (b) FFT of each signal with both providing a frequency measurement of $f_B = 5.2\ GHz$ and containing an amplitude of $\sim 7.5 \times 10^{-6}$. The two signals can be aligned in phase by iteratively cropping one with respect to the other (not shown) and then summed resulting in a new signal (c). (d) The FFT of the new signal reveals a frequency peak at $f_B = 5.2\ GHz$ with an amplitude $\sim 1.5 \times 10^{-5}$.

which have spread in time by [15, 229]

$$\Delta\tau = \frac{L}{c}\frac{n_{core} - n_{clad}}{2n_{core}} \approx 80\ ps \tag{7.1}$$

The result is that each sub-pulse now acts as a pump and probe in their own regard which reduces the energy carried by the signal in the fundamental (non-dispersed) mode. However, the acoustic wave encoded by each sub-pulse will contain a random phase (compared with the stationary phase of the fundamental) as the path length of that mode changes, e.g. by bending the fibre. This has the consequence of raising the noise floor of the technique, and is potentially witnessed in the form of multiple coincidence peaks in Figure 7.3a; however, more investigation is required to confirm that such modes are unambiguously detectable in the TRBS signals. The effect of attenuation through the fibre will also reduce the effects of inter-modal dispersion in addition to the signal decay. Again, for the length of fibre utilised in this study, the total attenuation is approximately 0.2 dB according to the specifications and therefore can be neglected. The reduction in detection bandwidth due to material dispersion is not readily available for this product, however, it is likely not limiting the signal band that is of interest ($f < 50\ GHz$).

In any case, the fact that the imaging bundle is capable of producing well behaving TRBS signals is a sign that the negative effects described above are relatively insubstantial in the current configuration of the experiment. There are a number of ways in which this fibre bundle probe can be optimised:

1. utilising a lower NA objective lens (compared with the NA of a core) could reduce the effects of intermodal dispersion, however likely at the cost of lower coupling efficiency due to mode mismatch.

2. the 50/50 beamsplitter used to divert the signal light from the incident light could be replaced with a fibre optic circulator to avoid a loss of 3 dB.

3. higher lateral resolution can be achieved by using an imaging bundle with both smaller core diameters and lower core-to-core separation.

It is worth noting that $\#3$ (above) is an imperfect way to increase resolution, since both reduced core sizes and separations will increase the cross-talk between channels. Cross-talk occurs when the mode field (for a single core) spatially overlaps with a neighbouring core(s), resulting in power-transfer between cores, leading to decreased resolution, contrast, SNR, and spatial accuracy [228, 230]. Possible ways of mitigating these effects (without decreasing resolution) include: reducing the mode order (e.g. using lower NA illumination) [231, 232], using shorter wavelengths [228], or, interestingly, fabricating bundles with nonuniform core diameters [228]. With respect to the latter, it has been shown through simulation and experiment that standard commercial bundle

products contain $7-15\%$ variation in core diameter when fabricating small core sizes (e.g. $\sim 2\ \mu m$). This has the effect of reducing the inter-core coupling efficiency and therefore can suppress cross-talk and increase pixel accuracy [228].

Achieving microscopic resolution using the single-fibre phonon probe is heavily dependent on the ability to control and articulate the x, y, and z position of the fibre-tip with sub-micron precision. This does not affect its potential for *in vivo* spectroscopy or *ex vivo* imaging, but is a major hurdle for its application to cellular imaging in an *in vivo* environment (until endoscopic mechanical technology is sufficiently developed). The imaging bundle greatly alleviates this complication by only mandating that the distal end be controlled in z and held steady in x/y, which is also a requirement for state of the art commercial endocytoscopy [17]. Therefore, the phonon imaging bundle has great potential for contact tissue imaging and spectroscopy with resolution set by the core-core spacing. Future work will focus on developing the bundle - according to the ways listed above and also in a manufacturing capacity - and testing its compatibility with biological tissue, with the future aim to inspect elasticity of diseased tissue.

7.2 Fabry-Pérot transducer

In Chapter 3, a single metallic layer transducer was proposed to achieve proof of concept for the phonon probe system. A range of metals and thicknesses were simulated from the perspective of TRBS signal strength and damage threshold (from optical absorption-based heating), in order to identify a relatively optimum design of Au $= 15\ nm$. This design facilitated ease-of-fabrication as it only required the calibration of a single highly-sputterable material. However, replacing the single-layer with an optical cavity (see Figure 2.8 in Chapter 2), i.e. a Fabry-Pérot cavity, provides an opportunity to increase both the absorbance (pump) and transmittance (probe) as radiation resonates within the cavity (higher quality factor); ultimately this correlates with increased thermo-elastic generation and Brillouin scattering interaction strength (see Equation 2.77). Generally speaking, when the length of the cavity is an integer multiple of the optical wavelength, constructive interference between round trips permits a strong optical resonance and therefore a maximum in transmission [16].

The PLU-model (Section 2.2.2) was used to simulate the output reflection modulation depth (TRBS signal strength) over a range of cavity dimensions. The following parameters were designated for the simulation: pump and probe wavelengths were both fixed at $\lambda = 780\ nm$ to reduce the number of free-variables in the simulation, and an architecture of glass/gold/ITO/gold/water was used due to ease of fabrication with these materials (gold and ITO) and precedent for performance [166, 173]. The mirror dimensions of the cavity were iterated from 5 to $30\ nm$, and the cavity layer dimension was varied from 100 to $200\ nm$. In order to quantify the TRBS signal strength at each

transducer dimension, the simulated reflected modulation depth signal (Figure 7.8c) was extracted ($TRBS$), Fourier transformed, and the maximum amplitude at $f_B(H_2O)$ was recorded (A_{TRBS}).

Figure 7.8a presents the result of this simulation and points towards Au/ITO/Au

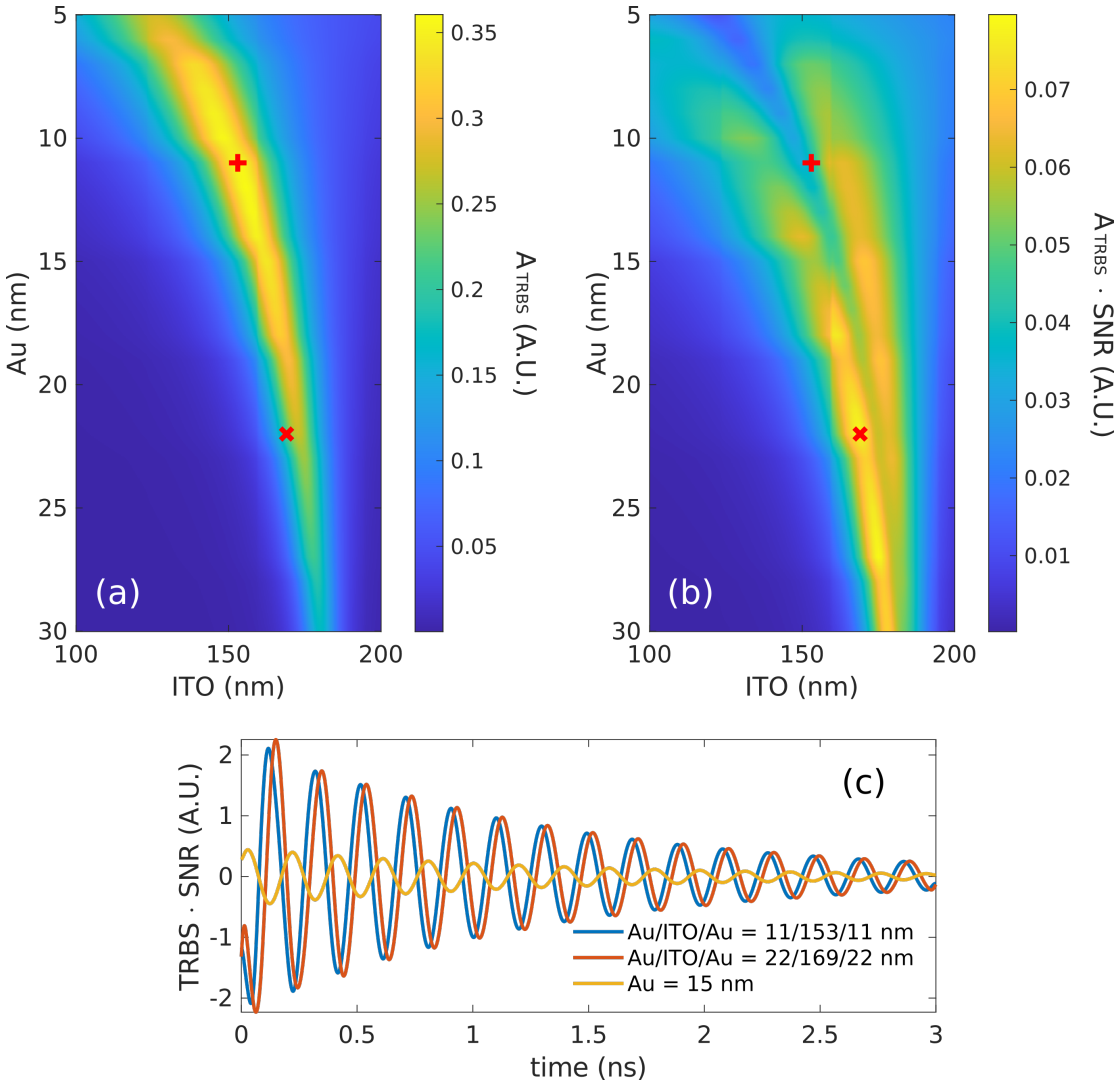


Figure 7.8: (a) Simulation of the TRBS signal strength (A_{TRBS}) in water at $f_B \approx 5\ GHz$, for a Fabry-Pérot cavity design, as a function of mirror layer thickness (gold) and cavity length (ITO), and with $\lambda_{pump} = \lambda_{probe} = 780\ nm$. An optimum cavity dimensions of Au/ITO/Au = $11/153/11\ nm$ (red plus sign) was identified with regard to this metric. However, the total reflectance of the cavity must also be considered as this dictates the SNR of the final signal. Since the SNR scales with $\sim \sqrt{I_{probe}}$ (Equation 2.78), the signal amplitude A_{TRBS} should be scaled by the total cavity reflectance R_0 ($\sqrt{R_0}$) which is shown in (b). Now a different cavity dimension appears optimum Au/ITO/Au = $22/169/22\ nm$ (red cross) due to the higher reflectance of this position compared with the previous dimension (red plus sign) which occurs at a reflectance minimum (i.e. transmittance maximum, dark band in middle). (c) The TRBS signals from these two cavity dimensions are plotted and scaled by the SNR for each cavity and increase signal amplitude by a factor of 5 compared with the performance of the single gold layer transducer.

= $11/153/11$ nm (red plus sign) as the optimal dimensions given these optical wavelengths and materials. However, since the SNR of the final TRBS signal (see Equation 2.78) will also be a function of the probe light intensity that has been directly reflected by the transducer (and not just Brillouin scattered with the sample), the total reflectance (R_0) of the structures must also be considered. Similar to Figure 3.8d where $SNR \sim \sqrt{R_0}$ was used to scale the TRBS signal amplitude, Figure 7.8b reveals the $TRBS \cdot SNR$ performance over the range of possible cavity dimensions. Here it is evident that the optimum design, Au/ITO/Au = $22/169/22$ nm (red cross), is now deviated from the previous band of high TRBS signal amplitude in Figure 7.8a (see red cross in Figure 7.8a). This central bright band (in Figure 7.8a) has now turned dark in Figure 7.8a since these are the dimensions producing maximum optical transmission, and therefore minimum reflectance (relative minimum SNR).

In Figure 7.8c the TRBS signals from the marked regions in Figure 7.8a are plotted and scaled by the SNR of the cavity. For comparison the $TRBS \cdot SNR$ performance of single $Au = 15$ nm layer transducer used throughout this study was also simulated. Using the comparison between Au = 15 nm and Au/ITO/Au = $22/169/22$ nm as an example, the total absorbance increases from 9% to 40%, and the transmittance increases from 38% to 47%. Overall the Fabry-Pérot cavities demonstrate an improvement in signal strength by a factor of 5 compared with the single gold layer. Ultimately this factor of 5 improvement can be leveraged for increasing SNR which can be utilised for increasing the precision either for resolving small frequency shifts in spectroscopy, or for measuring the axial position of objects in imaging. Alternatively, the improvement in SNR can be used to increase acquisition speed per-mW of input optical power, and therefore increase the practicality of the phonon probe system. The process outlined above, can also be repeated for other optimum transducer materials, such as copper and silver (discussed in Chapter 3.2), and also different pump-probe wavelength combinations in order to press further the signal efficiency of the transducers. As with the signal gold layer proof of concept presented in Chapter 5.2.2, the thermal performance of these cavities will also require close investigation and simulation, especially for the context of future imaging applications.

7.3 IR Brillouin scattering

In Brillouin scattering, if the wavelength of scattering light is varied, so too is the sampled acoustic wavelength: $\lambda_{ac} \sim \lambda_{probe}$. This the analogue to the scenario of a Bragg grating undergoing a shift in its grating period, e.g. under the influence of stress, therefore preferentially scattering a different optical wavelength. In this way, the user has a degree of freedom in selecting the desired acoustic mode, $f_B \sim \lambda_{probe}^{-1}$, to detect in a given material (with unchanging parameters such as temperature, salinity, etc.). One of

the central frequency-dependent properties in acoustics is the attenuation of the acoustic field, which in water is proportional to $\alpha \sim f_B^2$ [201]. The reciprocal of this statement then describes the penetration depth, or working distance (z_{WD}), of the acoustic field, i.e. $z_{WD} \sim f^{-2}$.

This study has demonstrated that a working distance on the order of $z_{WD} \approx 6\ \mu m$ is sufficient to perform 3D imaging and elastography of microscopic objects. However, the future utility of the phonon probe will be subject to relaxing the requirement that the tip of the device be brought infinitesimally close to the imaging target. Therefore, it is proposed that the working distance of the phonon probe can be increased by using a longer wavelength probe beam. For example, if the probe wavelength was doubled from $\lambda_{probe} = 780\ nm$ to $\lambda_{probe} = 1550\ nm$, thereby halving the detected acoustic frequency from $f_B \approx 5\ GHz$ to $f_B \approx 2.5\ GHz$, the working distance of the device will increase by a factor of 4. An additional consideration is the optical attenuation that occurs, e.g. optical absorption, as the optical wavelength increases in water [233]. Figure 7.9a

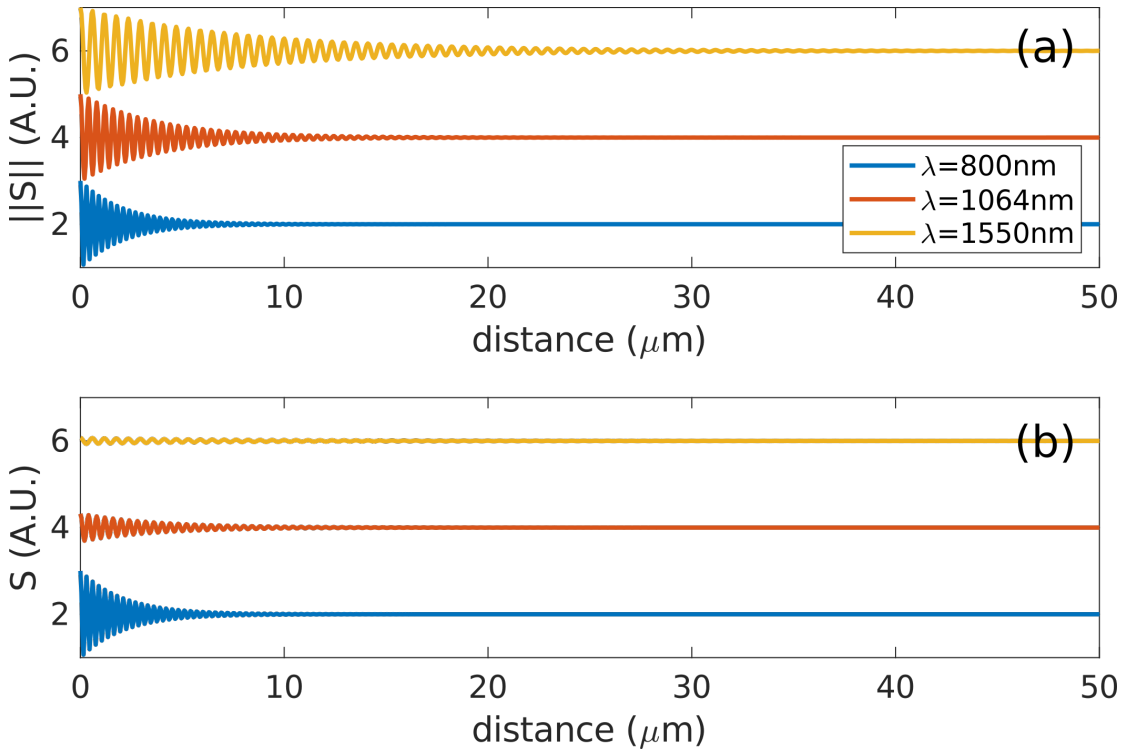


Figure 7.9: (a) TRBS signals simply approximated as decaying sinusoids, with frequency $f_B = 2nv/\lambda_{probe}$ and decay rate $\alpha = \alpha_{optical}\alpha_{acoustic}$, as functions of the optical probe wavelength. Optical attenuation is a function of the extinction coefficient (dispersive) in the medium, and acoustic attenuation is a proportional to f_B^2. As wavelength lengthens the penetration depth increases, as confirmed by the 1/e distances for the signals: 2 μm, 4 μm, and 9 μm for $\lambda = 800\ nm$, 1064 nm, and 1550 nm respectively. (b) When changing the probe wavelength one must consider the change in the Brillouin scattering cross-section, which is proportional to λ^{-4}. This factor was used to scale the amplitude of the signals in (a) revealing that more power will be required to benefit from greater working distances.

shows a simplified model of the TRBS signal using a decaying sinusoid - considering both acoustic and optical attenuation - as a function of probe wavelength in a water medium, and with maximum amplitude normalised to 1. As an approximate measure of the working distance, the 1/e distances were calculated: $2\ \mu m$, $4\ \mu m$, and $9\ \mu m$ for wavelengths of $800\ nm$, $1064\ nm$, and $1550\ nm$ respectively, revealing the additional penetration depth attained with longer wavelengths.

A potential caveat for this strategy is that the Brillouin scattering cross-section decreases proportional to the fourth power of the optical wavelength, i.e. $\sigma_B \sim \lambda_{probe}^{-4}$ [149, 234]. In other words, the same phenomenon which preferentially scatters NUV light rendering the sky blue, will adversely effect the TRBS interaction as the optical probe wavelength lengthens. Figure 7.9b demonstrates the scaling of the simplified TRBS signal amplitude as a function of this wavelength factor. The effect can be compensated by increasing optical power, however, this will result in additional heating. Furthermore, the axial resolution of the phonon probe would decrease, e.g. by a factor of 2 between $\lambda_{probe} = 780\ nm$ and $1550\ nm$. Therefore, it appears that a trade-off exists between working distance and signal amplitude (and axial resolution). This reality is not typically discussed in the context of coherent Brillouin scattering, since these techniques actively pump the sample with strain pulses. As the strength of the strain waves increases, so too does the photoelastic modulation in refractive index of the medium [161, 163], a quantity which increases the scattering cross-section [234]. Nonetheless, the prevalence of this effect within the field of TRBS is difficult to encapsulate - despite the widespread use of both NUV and NIR probe wavelengths - since not everyone reports signal amplitude in terms of the normalised quantity, modulation depth.

In the context of coherent Brillouin scattering techniques, this study is the first to decouple the direct physical contact between the transducer and the target object. However, when operating within the NUV-NIR probe spectrum, all such techniques will be fundamentally limited to a working distance on the order of $10\ \mu m$. This is the cost of achieving both optical resolution and high scattering efficiency. There is potential for sacrificing axial resolution in order to achieve more practical penetration depths, e.g. by designing mechanical cavities which resonate in the $> 100\ MHz$ frequency range. Such cavities would require a non-Brillouin detection mechanism, for example using the optical sensitivity of a separate cavity to measure pulse-echo events within the sample medium. However, more investigation is required to identify and optimise materials and cavity dimensions which stably resonate in this frequency band.

7.4 Super-resolution acoustic lens

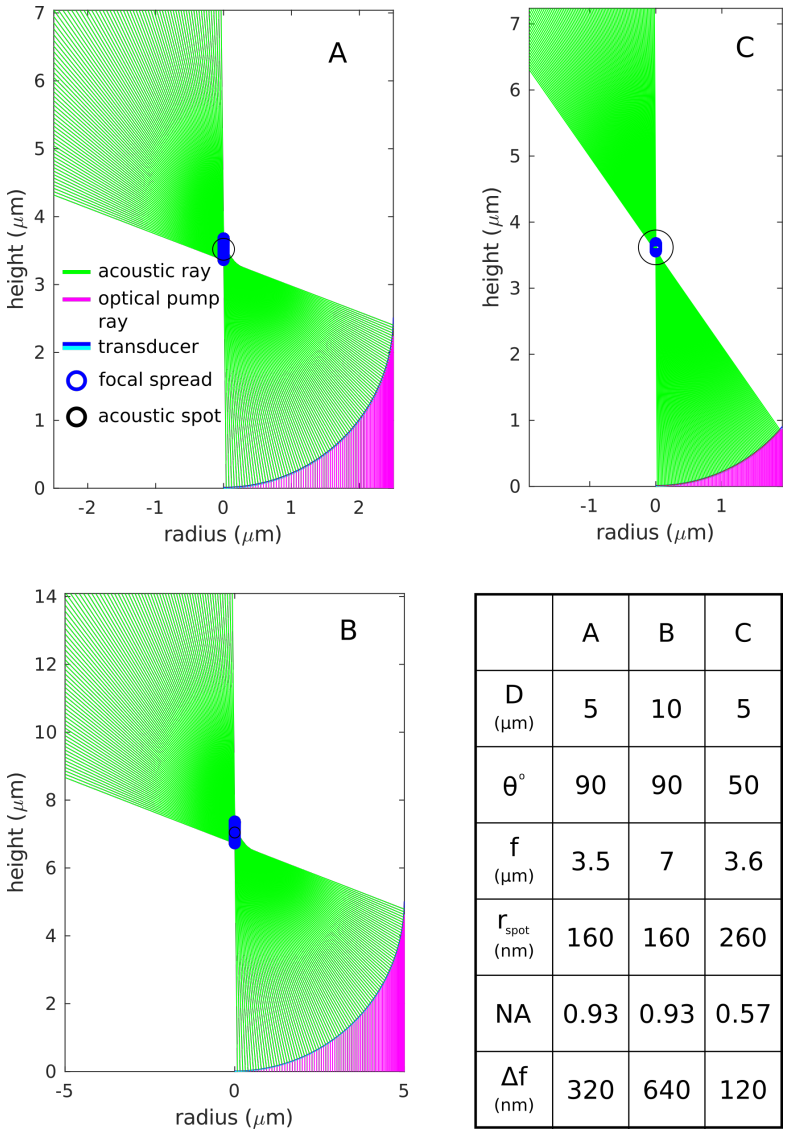
Currently, the phonon probe is primarily limited in lateral resolution by the mode field diameter of the optical fibre. Furthermore, the resolving capabilities of the device are

dependent on controlling the x/y position of the fibre tip with micrometre resolution. Increasing the lateral resolution of the phonon probe would allow its performance to match that of high magnification microscope lenses and imaging systems. In the field of optical fibre-based imaging there are numerous pathways towards increasing the native resolution of an optical fibre, such as 3D-printed micro-lenses [34], novel high NA fibres [235], and even computational super-resolution methodology [36]. However, aside from the latter, pathways to higher optical resolution are limited by diffraction. If a similar route to high (optical) resolution was considered for the phonon probe, the depth of focus for the probe beam must remain on the order of the acoustic penetration depth, otherwise there will be insufficient photon-phonon scattering for detection.

The phonon probe achieves super-optical axial resolution as a result of the acoustic wavelength being a factor $1/2n$ shorter than the optical probe wavelength. In theory this same principle can be used to create an acoustic spot, whose lateral dimension is sub-optical by the same factor, given an equivalent numerical aperture between acoustics and optics. Widespread proof of concept on this idea has already been achieved within the greater landscape of acoustics - serving as the basis for scanning acoustic microscopy [82] - and generally involves a concave surface from which acoustic waves refract towards a focus. More recently, this concept of concave acoustic lenses has been revitalised in the more practically viable field of laser ultrasound. A planar transducer containing a nano-indented lens has proven capable of $r \approx 100\ nm$ resolution which was achieved using picosecond laser ultrasound, $10\ GHz$ phonons, and pulse-echo detection [236]. Furthermore, the curved outer diameter of a tapered optical fibre was transformed into a concave acoustic lens which was capable of focusing $44\ GHz$ acoustic waves to a $r \approx 150\ nm$ spot using TRBS as the detection mechanism [237].

Now with the breakthrough of the phonon probe, the long-anticipated concepts described above can finally be realised in pragmatic way, with a probe-device that is compact, flexible, and already capable of imaging. Figure 7.10 presents a series of designs for a concave acoustic lens that would be deposited onto the tip of the phonon probe (centred at the fibre-core). The curvature for the acoustic lens is assigned to the glass substrate (i.e. the fibre core) upon which $15\ nm$ of chromium is deposited for thermo-elastic generation. It is anticipated that a curved substrate can be prepared using techniques such as two-photon polymerisation or focused ion-beam milling.

An opto-acoustic ray-tracing model was written under the following assumptions: normal incidence for the pump beam (incident from beneath the lens), an initial eccentricity of zero (spherical lens), and that each material is acoustically non-dispersive. The optical portion of the ray-tracing model was included in order to account for the unwanted effect that pump rays may experience total internal reflection when their incidence angle (with the curved surface) exceeds the critical angle. Furthermore, the lenses were simulated given a background medium of water, and an optical pump



	A	B	C
D (µm)	5	10	5
θ°	90	90	50
f (µm)	3.5	7	3.6
r_{spot} (nm)	160	160	260
NA	0.93	0.93	0.57
Δf (nm)	320	640	120

Figure 7.10: Designs for concave spherical acoustic lenses constructed of curved glass and a top layer of 15 nm of chromium in an external medium of water (only half of the lens geometry shown for simplicity). A ray-tracing approach was employed to determine the angles of refraction at the various interfaces, resulting in the green acoustic rays propagating towards the vertical axis of the lens. The average height above the lens at which the acoustic rays cross $r = 0$ was designated as the focal point of the lens (f), and the range of f values (blue markers) was considered to be an estimation of the degree of longitudinal spherical aberration (Δf). Lens diameter (D) and angular extent (θ) were varied between A, B, and C. Lens (A) produced a maximum NA of 0.93 and corresponding acoustic spot size of $r_{spot} = 160$ nm (black circles), yet with a focal length that is still within the acoustic penetration depth of 5 GHz phonons.

wavelength of $\lambda = 780$ nm. For this theoretical exercise, only two parameters were varied: the diameter of the lens (D) and the half arc angle of the sphere (θ). Figures 7.10a-b demonstrate that when the lens is composed of the same range of angles, the same range of spatial frequencies will be produced resulting in a common $NA \approx 0.9$ and acoustic spot radius $r_{spot} \approx 160$ nm. Numerical aperture was approximated as

$NA \approx \sin\theta_{max}$ where θ_{max} is the maximum angle produced by the lens, and the spot size was estimated as $r_{spot} \approx \lambda_{acoustic}/2NA$. However, the increase in the radius of the lens results in a shift to longer focal lengths, which was determined by calculating the mean distance at which the rays cross the vertical axis at $r = 0$. When the radius of the lens is kept fixed, but the range of angles produced by the lens is reduced, as in figures 7.10a-c, the NA of the lens reduces yet the focal length remains the same.

There is a degree of rigidity to applying the above acoustic lens designs to the phonon probe, as it will effectively be rendered into a fixed working distance device. Furthermore, the fabrication, performance characterisation, and signal processing pertaining to the device concept will all require considerable innovation. Further work will also be required to more unambiguously define the lateral resolution of TRBS techniques - which is typically defined using the smallest spot size between the pump and probe. The acoustic focal volume will be much smaller than the probe spot, and the overlap between these two spots will act as the source of the highest amplitude Brillouin oscillations, but may require additional treatment to realise the maximum resolution. There may also be the challenge of ensuring that the timing of thermo-elastic generation between the lowest and highest spatial frequencies does not vary to such a degree that the two acoustic waves are no longer in phase; however, the lens is applicable beyond Brillouin detection schemes as demonstrated by [236].

This simple model is not an exhaustive simulation of the full wave mechanics of the lens, but still provides basic insight on the key parameters that may enable a super-optical resolution phonon probe. Due to the sphericity of this lens design, the effect of spherical aberration will distort the spot sizes reported in Figure 7.10. The parameter Δf has approximated the amount of longitudinal spherical aberration by determining the range of distances at which the different spatial frequencies cross the $r = 0$ plane (blue circles in centre). For future designs spherical aberration can be lessened by selecting aspherical curvatures, such as ellipsoids and hyperbolas, or even creating compound lens layers/structures. The design presented here represents a classical paradigm for lens construction; more exotic structures such as Fresnel zone plates or acoustic meta-surfaces may also offer intriguing routes to super-optical resolution. Ultimately, an acoustic lens which provides any approximation of the specifications simulated here would bring the phonon probe a step closer to the resolving power of a microscope.

Part IV

Conclusion

Chapter 8

Conclusion

For over two centuries, endoscopes have made human eyesight portable. Optical fibres have played the most critical role in this history of endoscopy; for the first time light could be conveyed in a channel with the dimensions, and flexibility, of a strand of human hair. One of the great challenges in the last half century, has been devising strategies for making endoscopes, and by extension optical fibres, as powerful as the optical microscope. Key breakthroughs which have begun to unlock this potential are miniaturised lens systems, miniature scanning equipment, and bundles of hundreds of thousands of optical fibre pixels [18]. These developments have finally afforded new techniques - such as confocal laser endomicroscopy and endocytoscopy - the ability to inspect diseases such as oesophageal squamous cell carcinoma, ulcerative colitis, and Barrett oesophagus at a cellular level *in vivo* [10, 12].

Reproducing this same developmental trajectory using acoustic waves is highly desirable; in conventional settings, using ultrasound instead of light offers benefits such as: non-destructive energy, long penetration depth, and fluorophore-free contrast. However, realising acoustic technology in a high resolution fashion has been a persistent challenge beginning with the advent of scanning acoustic microscopy (SAM) [82]. Techniques such as endoscopic ultrasound [75] and photoacoustic endoscopy [105] have set a path towards high resolution and portable ultrasonics. Ultimately this path narrows: high frequency acoustic waves experience tremendous attenuation, high frequency piezoelectric transducers are fragile, and complex endoscopic payloads are required.

Within the last decade a new path to high resolution opto-acoustic endoscopy has begun to emerge: all-optical acoustics. These techniques excite ultrasound through the photoacoustic effect, and then listen for the sound optically using an optical cavity or interferometry [100]. Furthermore, the photoacoustic excitation process can be carried out by the specimen itself (if it is optically absorbing), or by a dedicated transducer used to thermo-elastically generate ultrasound. Thus far these approaches have resulted in successful proof of concept imaging of biologically relevant samples such embryonic

duck vasculature [113] and swine cardiac tissue [119].

This thesis has sought to expand upon these all-optical approaches to high frequency and high resolution acoustics. In doing so, the mechanisms of picosecond laser ultrasonics (PLU) and Brillouin scattering were identified. PLU utilises highly absorbing metals with nanometric thickness to convert light pulses into $\sim 0.1\ THz$ bandwidth coherent acoustic fields via the photoacoustic effect. The century-old phenomenon of Brillouin scattering - whereby acoustic phonons scatter incident light waves - can be used as a non-contact detection mechanism for high frequency ultrasound. Prototype Brillouin endoscopes which are sensitive to naturally occurring low amplitude thermal phonons in aqueous media have only just emerged, and due to low sensitivity have only proven capable of 1D line scanning [153]. However, the principles of PLU can be applied to Brillouin scattering: time resolved Brillouin scattering (TRBS). This technique accesses the same fundamental information as spontaneous Brillouin scattering, yet with greater amplitude acoustic waves and superior axial resolution set by the acoustic wavelength. Multiple TRBS-based microscopes have now been developed which utilise these principles for opto-acoustic cell imaging [172, 173, 177]. The result of combining PLU and TRBS onto the payload of an optical fibre, is the *phonon probe* presented here; unlike spontaneously scattering counterparts, this device can be implemented with a basic single optical fibre. With the phonon probe proof of concept, the qualities of an acoustic microscope have finally been transferred to the portable landscape of an optical fibre. The following is a review of the work presented in this thesis, and the future outlook on this new technology.

8.1 Summary of thesis

Phonon probe design

At the core of the phonon probe is a single-mode optical fibre with $125\ \mu m$ outer cladding diameter, $5\ \mu m$ core diameter, $NA = 0.13$, and a single-mode bandwidth of $\lambda = 730 - 970\ nm$. Due to the attenuation of sound liquids in the GHz frequency range, techniques which utilise PLU and TRBS are inherently near-field, in that the acoustic wave typically propagates less than $z = 20\ \mu m$ before extinction. This aspect of PLU restricts the use of focusing fibre-optical elements, such as GRIN lenses, which extend working distance beyond which there is usable acoustic amplitude. For this reason, the choice in the small $5\ \mu m$ diameter core fibre is crucial since it dictates the resolution of the device when using the optical fibre as an imaging pixel.

In order to generate broadband ($> 100\ GHz$) and coherent acoustic fields from the tip of the optical fibre, a nanometric transducer thin-film must be deposited onto the optical fibre substrate. The transducer acts as a photoacoustic source: the absorption of a pulse of light results in the generation of thermal stress within the transducer and

relaxes in the form of strain pulses. The pulsed nature of the optical excitation is a key component of this thermo-elastic generation process; after the finite pulse has been absorbed, the transducer has the opportunity to relax and therefore radiate mechanical waves into its surroundings.

A number of single-layer transducer designs were considered, consisting of different metallic elements and layer thicknesses. Four key parameters were prioritised for designing the transducer: TRBS signal strength, SNR, thermal stability, and fabrication throughput. Ultimately the design of $15\ nm$ of gold was selected as it optimised all four characteristics. One of the main benefits of this thickness, is that it is partially transparent in the NIR portion of the electromagnetic spectrum. By choosing a probe wavelength in this range, the light will be able to transmit through the transducer, participate in Brillouin (reflection) scattering with the mechanically excited sample, and transmit back through the transducer before travelling to the detector.

The desired transducer thin-film was fabricated using DC magnetron sputtering. A custom fibre-assembly was designed such that the optical fibres could be easily sputter coated in the vacuum chamber. In order to characterise the thin-film thickness a white light spectrometer was constructed which enabled the optical transmissivity of the deposited layer to be measured. The transmission spectrum could then be compared with the theoretical Fresnel transmission coefficients for a range of layer thicknesses with the best fitting layer providing the lowest residual with the experimental spectrum.

Experimental system

The experimental system driving the phonon probe is based on two 100 femtosecond pulse-width lasers with a tuning range of $\lambda = 700 - 900\ nm$. One laser produces a pump pulse used for photoacoustic excitation, and the second laser produces a probe pulse used for detection through time resolved Brillouin scattering. The pump and probe pulses are synchronised using the concept of asynchronous optical sampling. In this ASOPS configuration the pump excites ultrasound through transducer absorption in periodic intervals. Following each pump absorption event, a time-delayed probe pulse samples the optical properties of the acoustically excited region; this time-delay increases from $t = 0$ until the end of the acquisition window (e.g. $t = 12.5\ ns$). In this way ASOPS enables picosecond temporal resolution and $\sim THz$ detection bandwidth, while achieving orders of magnitude acquisition speeds compared with mechanically scanning alternatives.

A series of fibre-optic elements were introduced to enable conventional PLU and TRBS measurements to be performed with an optical fibre substrate. Namely, an optical fibre coupler and a wavelength division multiplexer (WDM) allowed the pump and probe pulses to be combined into the channel of a single optical fibre. The WDM was selected such that its dichroic element strongly transmits one wavelength band

and strongly reflects a separate wavelength band. Pump and probe wavelengths of $\lambda_{pump} < 740\ nm$ and $\lambda_{probe} > 740\ nm$ were chosen to meet this criterion, and also to ensure single-mode propagation within the fibre bandwidth. Ultimately, the fibre-coupler can be replaced with a fibre-optic circulator which will drastically lower the loss experienced by the probe beam as it propagates to the detector; this will have the consequence of increasing signal to noise ratio given a fixed input optical power.

To enable imaging in three dimensions, the optical fibre-based transducer was placed into a nanopositioner which controls the height of the fibre-tip with nanometre resolution over a range of $\sim 100\ \mu m$. Spatial resolution in the lateral dimensions was achieved using 2 linear stages with $< 1\ \mu m$ resolution to control the position of the sample plane with respect to the fixed lateral position of the phonon probe.

Signal processing

The phonon probe detects the modulation of optical reflectance due to the presence of strain, through the process of time-resolved Brillouin scattering. In order to extract the acoustic time-of-flight information that is sampled through TRBS, the raw optical reflectance signal is post-processed using a series of Matlab scripts. Features within the signal such as the coincidence peak, and the thermal relaxation are removed to reveal the acoustic time-of-flight. The frequency of the wave is related to the elastic properties of the sample, and is measured through fast Fourier transform. The viscosity of the medium in which the wave is travelling, is related to the attenuation of the TRBS signal, which can be measured by fitting a decaying exponential to the signal.

When a GHz frequency acoustic wave encounters a boundary of acoustic impedance, it will be partially transmitted and reflected. Due to the fixed optical probe wavelength, the transmission of an acoustic wave from one medium to another will result in a shift in detected Brillouin frequency, because of the change in refractive index and sound velocity. The signal-time position at which this change in frequency occurs presents an opportunity to localise the boundary itself. The time-frequency analysis technique of continuous wavelet transformation was used to measure the position of these transitions events by searching for when the acoustic wave amplitude attenuates quicker than its natural decay rate.

Brillouin spectroscopy

Initially, proof of concept was demonstrated using the phonon probe in a spectroscopic capacity. This was accomplished by immersing the optical fibre tip containing the transducer into a liquid medium, and measuring the Brillouin spectrum of the environment. Furthermore, this can be achieved without complicated mechanical/scanning equipment: simply by placing the fibre into the medium. The unique combination of a ma-

terial's refractive index and sound velocity serve as the spectroscopic signature captured by the phonon probe, measured as the Brillouin frequency. Unique signatures were measured for the cases of water, glycerol, liquid polystyrene, blood plasma, and gelatin, and agreed well with the expected values of the Brillouin frequency reported in literature. These experiments were carried out using $10,000$ oscilloscope averages per signal resulting in a $\approx 3\ s$ acquisition speed, and were repeated 100 or more times to increase the signal SNR. The probe was also tested all the way down to $1,000$ oscilloscope averages, an acquisition speed of $\approx 0.4\ s$, and still proved capable of sensing a dynamic environment.

To further demonstrate the capabilities of the phonon probe, it was placed in aqueous environments with varying temperature and salinity. Through the thermo-optic, thermo-acoustic, salino-optic, and salino-acoustic effects, the changes in refractive index and sound velocity gave rise to changes in the Brillouin frequency detected by the probe. Using thermo-optic and thermo-acoustic constants of water, the experimental Brillouin frequency was used to produce an experimental readout of the changing water temperature. These measurements were in close agreement with an external measurement of water temperature. The device was able to measure changes in temperature with a sensitivity of $\Delta f_B/\Delta T = 2.5 \pm 0.6\ MHz/^{\circ}C$. A similar process was performed to provide experimental measurements of salt concentration that were in agreement with the known concentrations poured into the medium, and were accomplished with a sensitivity of $\Delta f_B/\Delta C = 41 \pm 3\ MHz/\%wt$, and a minimum resolvable frequency shift of $\Delta f_B = 9 \pm 2\ MHz$ ($\Delta C = 0.23\ \%wt$ salt).

Parallel profilometry and spectroscopy

Before showing that the phonon probe was capable of 3D imaging, it's in-depth measurement capability was first demonstrated. This was accomplished by using the z-nanopositioner to position the tip of the fibre to within $z = 10\ \mu m$ of a common laboratory petri dish (PS) filled with water. The water is key to the technique, as it provides ultrasonic coupling between the transducer-source and the imaging target. At a critical proximity between the fibre-tip and petri-dish, the TRBS signal produced a clear shift in Brillouin frequency from that of the water-couplant $f_B(H_2O) = 4.8\ GHz$ to that of the PS dish $f_B(PS) = 7.9\ GHz$. The position in signal-time at which the amplitude of the $f_B(H_2O)$ mode decayed by 50% (after taking into account material attenuation) was located through wavelet analysis. This time-position was then converted into axial distance by multiplying the sound velocity measured through the Brillouin frequency, therefore providing a proximity measurement to the petri dish. This process was varied over a series of fibre/petri-dish distances, and an SNR floor of $z_{DR} \approx 5.5\ \mu m$ was identified which sets the effective dynamic range of the instrument.

The above procedure was then extended to 3D profilometric imaging; the phonon

probe remained within $10\ \mu m$ vertically of the sample plane, and the specimen stage was scanned in x and y to achieve spatial resolution. At each x/y position the proximity between the phonon probe was measured, then the device was scanned to the adjacent x/y position and the process repeated to build an image. If the floor of the object is within the dynamic range of the system, then the proximity measurement of this floor acts as height $h = 0$ and the inversion of the proximity map produces a map of the object height. However, if the proximity of the object floor cannot be measured, then only a relative height map can be attained; this scenario of relative measurements is similar to the case of dynamic range in atomic force microscopy (AFM).

Using this imaging principle, the topographies of 3 PS-microstructures were imaged. These structures were fabricated through drop-coating and melting, and ranged in size from $20\ \mu m$ to $75\ \mu m$ in diameter. For the two taller objects, the phonon probe was capable of measuring the upper $h = 4.6\ \mu m$ and $h = 3.9\ \mu m$ portions. Optical profilometry was performed on these objects, resulting in absolute height measurements of $h_{abs} = 7.7\ \mu m$ and $h_{abs} = 4.9\ \mu m$ (respectively), confirming that the phonon probe was indeed measuring relative height. However, a third shorter PS-phantom was scanned with the phonon probe and a height measurement of $h = 2.695\ \mu m$ was obtained, compared with the $h_{abs} = 2.700\ \mu m$ measurement made with optical profilometry.

Proof of concept was also achieved for using an optical fibre-based probe to map the Brillouin frequency of an object in two-dimensional space, a world first. Since light slows down upon entering PS (from water), and sound speeds up, the optical-probe and acoustic fields will refract in different directions (away from each other). This effect worsens as the height gradient of the object increases (angle of incidence becomes more severe). Consequently, the optical and acoustic fields lose overlap which results in a decay in TRBS signal amplitude. The maximum inclination angle for the height gradient of a PS-object, for which the Brillouin frequency can still be measured, was measured as $\theta_i \approx 10^\circ$. On the other hand, many biological media, such as 3T3 fibroblast cells, contain similar optical and acoustic refractive indexes compared with water, and therefore should enhance the phonon probe's sensitivity to detecting sub-surface Brillouin scattering in microscopic objects.

Sources of systematic error when using the z-nanopositioner as a degree of freedom were discussed, and a maximum value of $\epsilon_z \approx 70\ nm$ was identified. A key source of systematic error for 3D imaging (with a fixed z-offset between fibre tip and imaging plane) was identified in the variation in sound velocity along the TRBS signal time-of-flight, likely due to the temperature gradient surrounding the transducer. This ultimately results in an error on converting from the time-domain to the 1D spatial-domain, the latter providing the basis for a proximity measurement. The impact of this error was quantified; for the three imaging objects, maximum positional errors of $\epsilon_z = 91,\ 73$, and $40\ nm$ were reported. After considering the temperature error, the total height measure-

ment of the smallest object was estimated to be within $\epsilon_z = 30\ nm$ accuracy compared with optical profilmetry; this was made possible by the stand-off distance between the fibre and the object being within the dynamic range of the instrument.

The lateral resolution of the phonon probe is provided by the $r_{PSF} = 2.5\ \mu m$ mode field radius of the optical fibre. This spatial resolution is enabled by the $\sim 1\ \mu m$ resolution of the x/y stages which articulate the sample with respect to the fibre-tip. If the phonon probe uses the measure of the instantaneous Brillouin frequency (along the axial direction) as a contrast mechanism, then the axial resolution is determined by the acoustic wavelength and the width of the wavelet used for time-frequency analysis; in the case of this study, the theoretical axial resolution would be $z_{min} \approx 1\ \mu m$. When the phonon probe is being used strictly for profilometry, the concept of axial precision is more pertinent, since within each voxel, only a single "object" is being resolved. From this perspective, the configuration of the phonon probe (and wavelet processing) in this report was capable of $\sigma_z = 55\ nm$ axial precision, a quantity which can be further improved with increasing SNR.

The performance metrics for the phonon probe discussed in this thesis are collated in Table 8.1.

Phonon probe performance							
min acq. speed	sensitivity	freq. res.	lateral res.	axial res.	dynamic range	in-depth precision	in-depth accuracy
$0.4\ s$	$2.5\ \frac{MHz}{^\circ C}$ † $41\ \frac{MHz}{\%wt}$ †	$9\ MHz$†	$2.5\ \mu m$•	$1\ \mu m$•	$5.5\ \mu m$†	$55\ nm$†	$30\ nm$†

Table 8.1: †quantities which improve with signal averaging. •not verified experimentally.

Future work

The future developments for the phonon probe were discussed, particularly those related to the field of view, SNR/acquisition speed, dynamic range, and lateral resolution. Proof of concept was demonstrated that the fundamental TRBS mechanism of the phonon probe, is also compatible with a optical fibre imaging bundle. This is also in spite of the reality that cores of the bundle channels no longer support a single spatial mode, and therefore produce intermodal dispersion which ultimately affects the detection bandwidth of the phonon probe.

Next, a Fabry-Pérot optical cavity was proposed as a possible solution for increasing TRBS signal amplitude. The PLU analytical-model was used to demonstrate that approximately one order of magnitude improvement in TRBS signal strength can be obtained (compared with $15\ nm$ of gold), due to the high quality factor of the optical cavity which leads to greater optical absorption (strain generation) and transmission

(for Brillouin scattering).

Additionally, a method for increasing the $z_{DR} \approx 5.5\ \mu m$ dynamic range of the phonon probe was discussed. Compared with the NIR probe wavelengths used in this report, a probe wavelength in the IR (e.g. $\lambda = 1550\ nm$) would enable approximately four times greater acoustic penetration depth (e.g. $z_{DR} \approx 20\ \mu m$). Through the Bragg condition, a $\lambda = 1550\ nm$ probe wavelength would scatter constructively with a $\lambda_a \approx 600\ nm$ phonon ($f_B = 2.5\ GHz$). Since acoustic attenuation (α) is proportional to the square of the acoustic frequency, the phonon probe would gain dynamic range at the rate $z_{DR} \propto \alpha^{-1} \propto f_B^{-2} \propto \lambda_{probe}^2$.

As the probe is further developed to image deeper, additional effects such as optical diffusion may become more relevant, especially for living specimens which can be considered dynamic scatterers of light. For example, in biological tissue it has been shown that an incident wavefront will decorrelate as a function of tissue thickness and experiment time (fluctuating speckle fields) [238]. However, for the length scales probed in this thesis ($z \sim 10\ \mu m$), the probe photons can be treated as ballistic resulting in decorrelation times on the order of several hours or more [239]. Nonetheless, future deep imaging will necessitate faster imaging speeds to avoid significant variations in refractive index required to measure Brillouin frequency.

Finally, a strategy for increasing the $r_{PSF} = 2.5\ \mu m$ lateral resolution of the phonon probe was devised. Introducing a concave acoustic lens onto the tip of the fibre - similar to the acoustic lenses originally developed for scanning acoustic microscopy - will allow the generated ultrasound to refract towards a focus, dictated by the lens radius of curvature. Since a $\sim 5\ GHz$ acoustic wave propagates with a wavelength on the order of $\sim 300\ nm$, high spatial resolution can be achieved while still remaining non-destructive, unlike the equivalent optical wavelength.

8.2 Outlook

The future prospects for using the phonon probe in a purely spectroscopic capacity are promising. The qualities of nearly real-time acquisition speed ($0.4\ s$) and high spectral resolution ($9\ MHz$) that have been demonstrated here, provide utility for a wide range of situations in which monitoring dynamic processes or minute fluctuations are required. Both qualities are also scalable as the SNR of the device improves, e.g. using optimised transducer designs. Without the requirements of micron-precision motion control and bulky scanning equipment (for spectroscopy alone), the full compactness and flexibility of the fibre-spectrometer can be realised. For example, the fibre could be easily deployed down the bore of a needle (over a wide range of needle gauges), catheter, endoscope, or any space greater than $125\ \mu m$. Consequently, the spectroscopy feature of this device could conceivably be used for applications related to: *in situ* liquid mon-

itoring, *in vivo* alternatives to biopsies and tissue diagnostics, or surgical guiding (e.g. in epidural procedures). *In vivo* biopsies would be a particularly interesting application for the technology, especially for biopsy-types which are primarily liquid-based such as fine needle aspiration. Conventional microscope-based Brillouin spectrometers have already shown promise for differentiating between healthy and diseased cerebrospinal fluid in liquid-biopsy screening for bacterial meningitis (*in vitro*) [240].

Among the potential applications for using the phonon probe as a high resolution imaging tool, perhaps the most exciting are those associated with cellular resolution bio-imaging. The finer structure of the biological world is a complex environment which is not always easily navigated by large optical microscopes or low-resolution ultrasound. Having an ultrasonic endoscope-style tool which accesses this regime with high contrast and resolution will broaden the tool-box with which biology can be investigated. Using the phonon probe as a bio-friendly profilometer will be a key application moving forward, and will set a path towards being able to image the more complex architectures of biological tissue. The requirement of a water coupling medium with the phonon probe is ultimately a benefit for application to cell profilometry since the specimens can remain in culture and therefore a living/undisturbed state.

As it pertains to future cell imaging applications with the phonon probe, one promising topic may be the endoscopic inspection of neuronal processes [241]. Although typically studied for their electrical properties, recent work has begun to reveal that mechanical properties and behaviours of neuron cells are closely related to the electrical activity that defines the action potential [242, 243]. Furthermore, viscoelasticity is emerging as a key biomarker for detecting and tracking the progression of neurodegenerative diseases such as Alzheimer's, multiple sclerosis, and amyotrophic lateral sclerosis [244–246] and warrants further investigation on the cellular scale. Time resolved Brillouin scattering has recently demonstrated compatibility with individual neuron cells [176, 247], and now with the phonon probe is now poised to supplement conventional elastographic techniques such as atomic force microscopy [243, 248] and magnetic resonance elastography [244, 245].

Tissue samples are inherently challenging for transducer-substrate-reliant PLU techniques, due to turbidity and the inability for GHz frequency ultrasound to penetrate through thick tissue. However, with the mobility of the phonon probe, and now the phonon imaging bundle, the devices can be introduced to the top surface of tissue (with a couplant and likely with contact) for spectroscopy, profilometry, and imaging of superficical layers without need for a microscope. To this end, a promising application for the phonon probe is to act as an *in situ* monitoring tool for the rapidly accelerating field of 3D bioprinting and tissue engineering [249]. The $125\ \mu m$ footprint of the phonon probe could be integrated to pre-existing needle-like print-heads and extruders.

In the context of biological imaging, the phonon probe will achieve low specificity un-

less the environment is well calibrated and constituents are known *a priori*, or another imaging modality is used for specification. Therefore there is significant interest in pairing the phonon probe technology with high specificity techniques such as endoscopic fluorescence and molecular imaging [18, 22, 250]; similar complementarity between these modalities has already been demonstrated for conventional Brillouin microscopy [246]. Due to the partial transparency of the phonon probe, it is possible to integrate the requisite wavelengths for TRBS and fluorescence imaging into the same channel - e.g. in a fibre bundle core. Alternatively, the two modalities can be separated, either by occupying different channels of the same fibre bundle, or by utilising separate optical fibres for each modality - e.g. using a NUV single-mode fibre for fluorescence excitation and a neighbouring phonon probe for TRBS and fluorescence collection (or vice-versa for two-photon fluorescence). This concept could also be carried out with other near-field endoscopic techniques, such as endoscopic Raman spectroscopy, which itself provides molecular and highly specific information [251].

Many fluorescence endoscopy devices utilise some form of focusing to increase the working distance of the device. One possibility for overcoming the mismatch in working distance between these devices and phonon endoscopy is to relocate the transducer from the fibre-tip to the specimen itself. This could be made possible by using metallic nanoparticles as TRBS contrast agents (photoacoustic absorbers for the pump beam) in tissue; then pump and probe beams could be focused from the far-field (e.g. using a GRIN lens) and epi-detection can be achieved through Brillouin scattering or optical sensitivity to mechanical vibrations of the particle [252].

As endoscopic procedures become increasingly automated and roboticised [253, 254], the phonon probe (single-fibre or bundle) could act as the first sub-cellular resoution ultrasonic endocytoscope. Ideally as the technology continues to develop, the acquisition speed can be increased to video rates at which point machine intervention is less critical. Perhaps label-free *phonon endomicroscopy* will continue to mature to the point where it is an additional modality for pre-existing confocal laser endomicroscopy-based endoscopes, by converting the viewing window into a laser ultrasonic transducer as shown in Figure 8.1. Even at this young stage of the phonon probe, this technological combination is a natural pairing because CLE already relies on contact between the viewing window and the specimen, and also is restricted to near-field penetration depths ($< 50\ \mu m$) [22]. This perhaps will lead to using elasticity as a novel histological metric for minimally invasive and high throughput *in vivo* diagnostics.

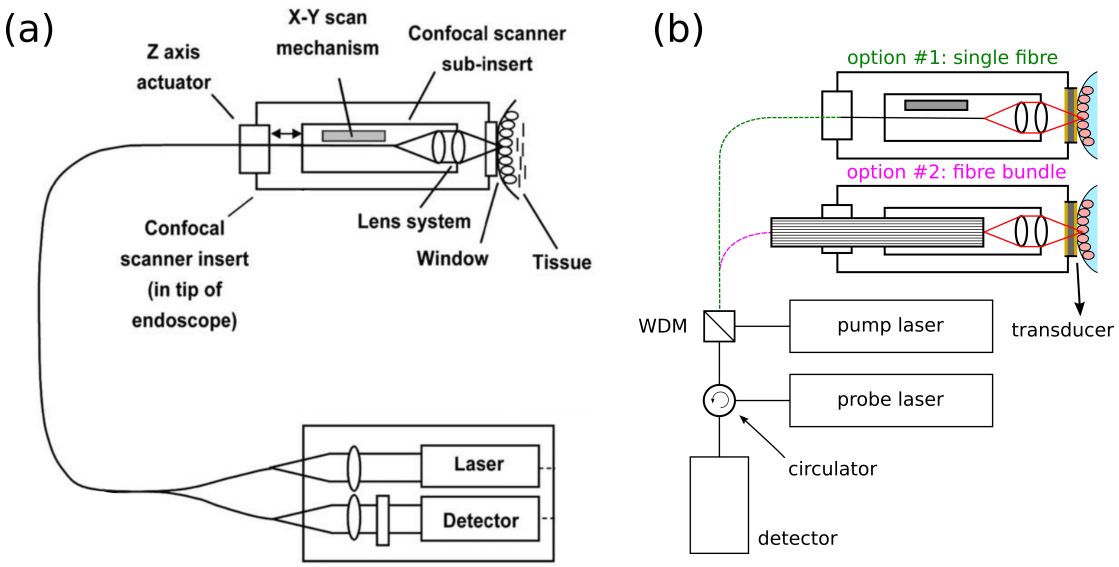


Figure 8.1: Future device concept for phonon endomicroscopy. (a) Current state-of-the-art confocal laser endomicroscope developed for Pentax; a single-fibre is scanned in x, y, and z across the back focal plane of a miniaturised imaging system which is capable of $1\ \mu m$ lateral resolution [24]. (b) Concept for using the viewing window as a transducer for high frequency ultrasound. Spatial resolution can be achieved through the same scanning mechanism as (a), or by integrating a fibre bundle with illumination raster scanned across the proximal end. (a) Reprinted from Gastrointestinal Endoscopy, 62, Adrian L. Polglase, Wendy J. McLaren, Stewart A. Skinner, et al., A fluorescence confocal endomicroscope for in vivo microscopy of the upper- and the lower-GI tract, 686-695, Copyright (2005), with permission from Elsevier.

Appendix A

Green's function

This Appendix provides additional information for solving electric fields within a perturbed medium, which was initially derived in Section 2.2.2. Recall that the inhomogeneous wave equation in Equation 2.69

$$\Big[\frac{\partial^2}{\partial z^2} + k^2\epsilon_h(z)\Big]E(z) = -k^2\epsilon_{ih}(z)E(z) \tag{A.1}$$

must be solved in order to solve for an electric field given an inhomogeneous source $\epsilon_{ih}(z)$ (source of a perturbation in permittivity). Recall from Equation 2.70 that this wave equation can be rewritten in terms of a *Green's function* $G(z, z')$:

$$\Big[\frac{\partial^2}{\partial z^2} + k^2\epsilon_h(z)\Big]G(z, z') = -\delta(z - z') \tag{A.2}$$

or using the differential operator, $\mathcal{L}$,

$$\mathcal{L}G(z, z') = -\delta(z - z') \tag{A.3}$$

where the source (in this case $\epsilon_{ih}(z)$) is treated as a delta function centred at position z' (position of the strain pulse). By first solving for the Green's function ($G(z, z')$), the original inhomogeneity ϵ_{ih} can then be treated as a distribution of delta functions at position z',

$$\delta(z - z')\left[k^2\epsilon_{ih}(z')E(z')\right]$$

which when integrated over space yields the solution for the field:

$$\mathcal{L}E(z) = -k^2\epsilon_{ih}(z)E(z) = -\int \delta(z-z')k^2\epsilon_{ih}(z')E(z')dz' = \int \mathcal{L}G(z, z')k^2\epsilon_{ih}(z')E(z')dz' \tag{A.4}$$

Since the operator $\mathcal{L}$ is not a function of the strain position z' (see LHS of Equation A.1), it can be removed from the integral on the far RHS and cancelled with its equivalent on

the far left to yield the final solution:

$$E(z) = \int G(z, z')k^2\epsilon_{ih}(z')E(z')dz' \tag{A.5}$$

with the RHS being referred to as a Green's integral. One of the valid solutions to both Equation A.1 and A.3 is the case for no perturbation $\epsilon_{ih} = \delta(z - z') = 0$, i.e. the homogeneous component of the solution. The linear combination of the homogeneous and inhomogeneous fields then gives the total field:

$$E(z) = E_0(z) + \int G(z, z')k^2\epsilon_{ih}(z')E(z')dz' \tag{A.6}$$

$$E_0(z) = A_0e^{ik_0z} + B_0e^{-ik_0z} \tag{A.7}$$

where the unperturbed field amplitudes are solved using TMM.

In order to solve for the field, the Green's function $G(z, z')$ must be solved. In order to achieve this, a unique feature of delta functions is utilised. The fact that the area under the curve of delta function is 1

$$\int_{-\infty}^{\infty} \delta(z - z')dx = 1 \tag{A.8}$$

imposes a restriction on the possible values of the Green's function. With this identity, the process proceeds in a similar manner to solving a homogeneous normal electric field (Equations 2.40-2.44): (1) the forward and backward propagating fields on each side of the delta function are treated independently, (2) continuity of the fields (i.e. the Green's functions) is imposed at the perturbation $z = z'$, and (3) continuity of the derivatives of the fields at the perturbation. However, due to the fact that Equation A.8 holds for a delta function, the derivatives on each side of the delta function will be discontinuous by 1 [161]. Combining these conditions allows for the Green's function to be solved. For the case that the optical detector is placed in a position where it collects the light reflected by the transducer ($z < 0 < z'$), the following Green's function solves the set of linear differential equations [161]

$$G(z, z') = \frac{ie^{-ik_0z}}{2k_0A_0}E_0(z') \tag{A.9}$$

which is then applied to Equation A.6 and ultimately the complete set of field equations within the multi-layer structure (Equation 2.74 in main text).

Appendix B

Finite element thermal model

In Figure 5.12, Chapter 5.2.2, the temperature rise in the water medium surrounding the fibre-transducer was simulated using finite element method (FEM). The temperature rise is a result of the energy exchanged from the optical fields to the metallic thin-film through optical absorption. In this section, the FEM model utilised to investigate this phenomenon will be discussed.

This model was performed using the software, COMSOL, which finds approximate solutions to systems of partial differential equations (PDEs) within a computational space that has been discretised into computational sub-spaces called *elements* whose vertices are defined by *nodes*. Similar to other numerical methods, such as finite difference, a set of material properties and initial conditions are defined at discrete positions in the spatial mesh, and the initial conditions are propagated through the system (e.g. in time, space, or both) according to the PDEs; when material interfaces and the like are encountered, boundary conditions such as the conservation of energy are then utilised to ensure continuity. For systems with complex geometries or many independent variables, exact analytical solutions are often unobtainable or are computationally impractical. FEM addresses this issue by using the initial conditions and various numerical methods to guess/interpolate the values of the unknown nodes until the collection of node-values approximately solves the relevant PDEs and boundary conditions [255].

In order to approximate the temperature rise in the water medium induced by the irradiated gold transducer, the Heat Transfer module was used in Comsol. This module takes an input heat source Q_{in}, a set of initial conditions (e.g. $T_0 = 273^\circ$ at all points) and solves for the temperature of a system as a function of space and time. This is achieved by the solving the heat equation which is the thermodynamic equivalent of an expression of energy conservation: the work done on the system (by source Q_{in}) results in the rise of thermal energy, i.e. temperature (T)

$$\rho C\left(\frac{\partial T}{\partial t} + \mathbf{v}\cdot\nabla T\right) + \nabla\cdot\mathbf{q} = Q_{in} \tag{B.1}$$

where ρ is the density of the material, C its specific heat capacity, and $\mathbf{v}$ is the velocity vector of the material [256]. Equation B.1 can be interpreted in the following way: term 1 is variation in thermal energy (e.g. at one node) over time, the second term is change in energy due to forced convection (material flowing at rate v), and the third term is the change in energy due to heat conduction (energy flux density) which is defined using Fourier's law: $\mathbf{q} = -K\nabla T$ where K is the thermal conductivity [53, 256].

For each individual optical pulse absorbed by the transducer, a separate temperature rise/heating event will occur followed by thermal diffusion. As this is happening 80 million times per second, the heat accumulation by the transducer means that the transducer will eventually reach a steady-state temperature where the energy consumption by the transducer is equivalent to the energy diffusion (thermal equilibrium). For pulsed lasers this equilibrium state is typically reached on length scales $t << 1\ s$ [257]. Therefore, given the exposure times utilised in this report, $t \sim 80 - 7200\ s$, for all intents and purposes the beam can be treated as effectively continuous wave (CW) with average power P. Under these circumstances the time-dependence in Equation B.1 becomes null, and the model is said to be *stationary*. Furthermore, since the water medium is at rest, the term for forced convection disappears for zero velocity. What's left is the simplified equation for the steady-state temperature rise in the environment due to conduction:

$$-K\nabla^2 T = Q_{in} \tag{B.2}$$

The steady-state stationary model was then run with the following parameters:

- a geometry based on the cylindrical dimensions of a single mode optical fibre (250 μm diameter cladding) and the surrounding environment: 250 μm x 200 μm volume (radius and height respectively) of fibre, a 250 μm x 15 nm volume gold transducer, and a 250 μm x 200 μm volume of water.
- with the following material properties:

  water: $\rho = 1004\ kg/m^3$, $C = 4217\ J/(kg \cdot K)$, and $K = 0.556\ W/(m \cdot k)$

  glass: $\rho = 2203\ kg/m^3$, $C = 703\ J/(kg \cdot K)$, and $K = 1.38\ W/(m \cdot k)$

  gold: $\rho = 19300\ kg/m^3$, $C = 129\ J/(kg \cdot K)$, and $K = 317\ W/(m \cdot k)$
- cylindrical axial symmetry was used utilised about the $r = 0$ axis in order to increase computation speed ($T(z < 0) = T(z > 0)$) (red line in Figure B.1).
- initial temperature of $T = 273\ K$ everywhere.
- thermally insulating boundaries ($T = 273\ K$) were defined as boundary conditions away from the central heated region (blue edges in Figure B.1).
- under the steady-state assumption, the heat source Q_{in} is approximated by the average optical power (CW) absorbed by the gold transducer. This was solved

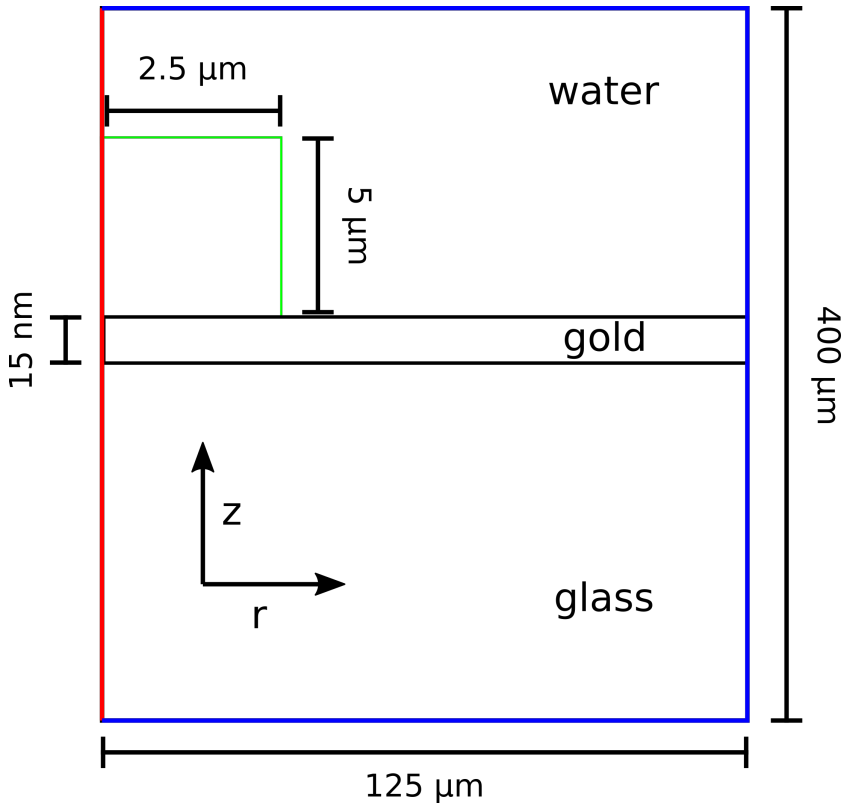


Figure B.1: Demonstration of the geometry and initial conditions utilised to model the steady-state temperature of the irradiated transducer and its surroundings. The computational space comprised a 250 μm x 400 μm (radius and height) volume cylinder containing half glass (optical fibre) and half water, in between these two materials along $z = 0$ exists a gold transducer layer with thickness 15 nm. The red edge of the geometry designates axial symmetry about $r = 0$ and the blue edges designate the constant thermally insulating boundary condition of $T = 273$ K. The green volume indicates the volume in which the average temperature rise was measured. Dimensions in drawing are not to scale.

using the transfer matrix method (TMM) to solve for the Fresnel coefficients of the gold transducer surrounded by glass (beneath) and water (above). Then the experimental powers in Figure 5.12 were multiplied by the absorbance $A = 1-R-T$ calculated from the TMM resulting in the absorbed average power $P = 2$ mW, and the heat source of $Q_{in} = P/V$ where V is the 5 μm x 15 nm volume where the optical fibre core meets the transducer.

- the 5 x 5 x 5 μm volume outlined in green was designated as a volume within which the average temperature is calculated, based on the core radius and the typical axial distance covered by TRBS signal.

The output of this simulation resulted in the temperature map plotted in Figure 5.12 in the manuscript, which contained an average temperature rise - within the 5 x 5 x 5 μm volume surrounding the core/transducer interface - of $\Delta T \approx 55°$.

Appendix C

Fluence damage threshold

In Figure 3.9, Chapter 3.2, the ability for a single metallic thin-film to withstand laser pulse absorption and melting was discussed. This investigation was carried out using an analytical thermal diffusion model [189] to estimate the absorbed optical fluence required to heat a metallic thin-film to its melting temperature as a function of film thickness, and will be described in brief here. The thermal diffusion model begins with the heat equation; as discussed in Appendix B, the heat equation is a PDE which describes the exchange of thermal energy over space and time between a heat source and the surrounding environment. With the assumption that the heat transfer due to convective processes is limited compared with conduction, Equation B.1 is rewritten:

$$\rho C \frac{\partial T}{\partial t} - K\nabla^2 T = Q_{in} \tag{C.1}$$

Instead of applying a heat source directly, the optical fluence was used in the following way. In order to raise the temperature of the metal from its initial temperature (T_0) to melting (T_m), an energy density of

$$F_m = C_v(T_m - T_0)L_d \tag{C.2}$$

is required, where C_v is now the *volumetric* heat capacity and L_d is defined as the thermal diffusion length [258]. F_m can then be considered the optical fluence required to raise the temperature of the metal to T_m degrees, or in terms of the melting temperature:

$$T_m = \frac{F_m}{C_v L_d} \tag{C.3}$$

where for $T_m >> T_0$ (e.g. in metals). Furthermore, Equation C.2 can be converted into the *incident* fluence by dividing by the absorbance of the metallic film $A = 1 - R - T$:

$$F_m = C_v(T_m - T_0)L_d A \tag{C.4}$$

Instead of using a heat source, Equation C.4 was used to make the melting temperature the initial condition of the solution to the heat equation:

$$\rho C \frac{\partial T}{\partial t} - K\nabla^2 T = 0 \tag{C.5}$$

Using the initial condition for $T_f(z = 0) = T_m$ in the metal film (with light incident at $z = 0$), and the requirement for continuity at the boundary between the metal film and a substrate placed a distance d from the light incidence (metal film thickness d), Equation C.5 can be solved in integral form as demonstrated in [189, 259]. The analytical solution at the position of maximum temperature ($z = 0$), and the time at which the pulse of width τ has traversed the metal interface ($t = \tau$) is then written:

$$F_m = \frac{T_m L_f C_f}{A} \cdot \frac{(1+b)(e^{d/L_f} - 1) + (1-b)(e^{-d/L_f} - 1)}{(b-1)e^{-d/L_f} + (b+1)e^{d/L_f}} + \frac{2T_m L_s C_s b}{A(b-1)e^{d/L_f}} \tag{C.6}$$

where the diffusion length L_i and the constant b are defined as

$$L_i = \sqrt{\frac{2K_i\tau}{C_i}} = \sqrt{2D_i\tau} \qquad\qquad b = \sqrt{\frac{K_f C_f}{K_s C_s}}$$

and the index i corresponds with the relevant index for the metal film (f) or the substrate (s) [189]; note that the quantity K_i/C_i is further defined as the thermal diffusivity of the material.

This expression for the fluence damage threshold as a function of metal material f of thickness d is the basis for the theoretical damage thresholds presented in Figure 3.9. The specific heat capacity, density, and melting temperatures for the metals Au, Ag, Cu, Cr, Al, Ti, and the fused silica (glass) substrate were collated (Table C.1) and the metal thickness was varied over the range $d = 1 \rightarrow 50\ nm$. To calculate the optical absorbance the transfer matrix method was used to solve for the Fresnel coefficients of each metal film using a wavelength of $\lambda = 780\ nm$.

It is important to note that a pulse width of $\tau = 100\ fs$ was utilised in the implementation of this analytical model, which is only valid for ns pulses. In the ns regime, the hot electrons within the metal remain in thermal equilibrium with the lattice [165]. However, for the case of fs radiation, this equilibrium is no longer preserved and the heat equation must be solved simultaneously for the temperatures of the hot electrons and the lattice. In this regime the influence of the *electron* heat capacity (C_e), the electron diffusion length (L_e), and the electron-phonon coupling rate (g) become significant [258]. Simulating these coupled effects is non-trivial, and conventionally is performed numerically using a two-temperature model (TTM) which is without the analytical solution in Equation C.6.

Despite using a pulse width that is beyond the limits of the model, the general trends observed for $\tau = 100\ fs$ are still within general agreement of equivalent inves-

tigations in the fs-regime performed previously with TTM [165]. The same effects are still observed: (1) as metal thickness decreases so does the damage threshold, and (2) noble metals such possess greater damage thresholds than transition metals. In the fs-regime this discrepancy actually worsens due to the greater electron-phonon coupling strength demonstrated by transition metals; i.e. the lattice couples to the thermal energy of the hot electron bath more quickly and thus becomes damaged more rapidly. Since noble metals have much weaker $e-ph$ coupling, the damage thresholds between the ns- and fs-regimes are rather similar [165]. Therefore the simulations presented in this study are meant to provide first-order approximation for thin-film damage.

Damage threshold material parameters			
Material	C_v $[10^6 J/(m^3 \cdot K)]$	K_i $[W/(m \cdot K)]$	T_m $[K]$)
Au	2.49	314	1337
Ag	2.46	419	1235
Cr	3.36	94	2180
Cu	3.43	401	1358
Ti	2.43	22	1941
Al	0.07	234	934
glass	1.55	1.4	1923

Table C.1: Material parameters for the metals and glass substrate used to simulate the damage threshold through optical absorption as a function of metal film thickness.

Appendix D

Polymer phantom fabrication

This Appendix is in reference to the fabrication procedure for Polystyrene microspheres mentioned at the beginning of Section 6.3. Before preparing the polymer microstructures, a specimen substrate was prepared that would enable the user to easily locate structures of interest, both for imaging with the phonon probe and other ancillary imaging techniques such as brightfield microscopy and profilometry. This was achieved by creating a quasi-grid pattern (with alpha-numeric labelling) onto a microscope slide using photolithography and was performed according to the following protocol:

1. clean a blank microscope slide using a series of organic solvents and an ultrasonic bath
2. spin coat a positive photoresist (BPRS 150) layer onto the substrate - 4000 rpm for 30 seconds which gives approximately $1.3\ \mu m$ thickness
3. bake slide to evaporate residual solvents - 90° for 5 minutes
4. cool slide down to room temperature
5. exposure - use a Karl Suss MJB3 Mask Aligner to expose the sample to the desired pattern of UV light (mercury lamp, $7\ mW/cm^2$) - 8 seconds exposure
6. development - gently stir substrate in a 1:8 solution of developer (AZ400K) and deionised water for roughly 20 seconds - wash with water and dry the substrate with N_2 gas
7. coating - use sputter coating facility to deposit $20\ nm$ of gold followed by $10\ nm$ of ITO
8. lift-off of undesired gold - warm a beaker of acetone at 60° for 10 minutes, then immerse substrate for 10 minutes while in ultrasonic bath
9. wash with organic solvents and dry with N_2.

Once the gridded substrate was prepared the PS microstructures were fabricated. The precursor for the structures was a concentrated pot of $10\ \mu m$ diameter PS microspheres (Bangs Laboratories, Inc.) which was diluted to a volume ratio of 1:500 with deionised water. Approximately $250\ \mu L$ of diluted solution was drop coated into the centre of the gridded coverslip, and the sample was baked for $\approx 35 - 40$ minutes at $245°C$. As a result of the baking, the microspheres, which start as conglomerates of individual spheres (see cyan box in Figure D.1), are eventually melted into joint structures (magenta box in Figure D.1). Following this procedure, a gridded landscape populated with complex polymer microstructures was achieved, and is shown in Figure 6.9 in the main manuscript. The small bright dots that fill the gridded area are $5\ \mu m \times 20\ nm$ spots of gold spaced $50\ \mu m$ apart, which are residual from the lift-off procedure in photolithography. Letters and numbers along the periphery of the grid aid in locating and recording the positions of imaging targets.

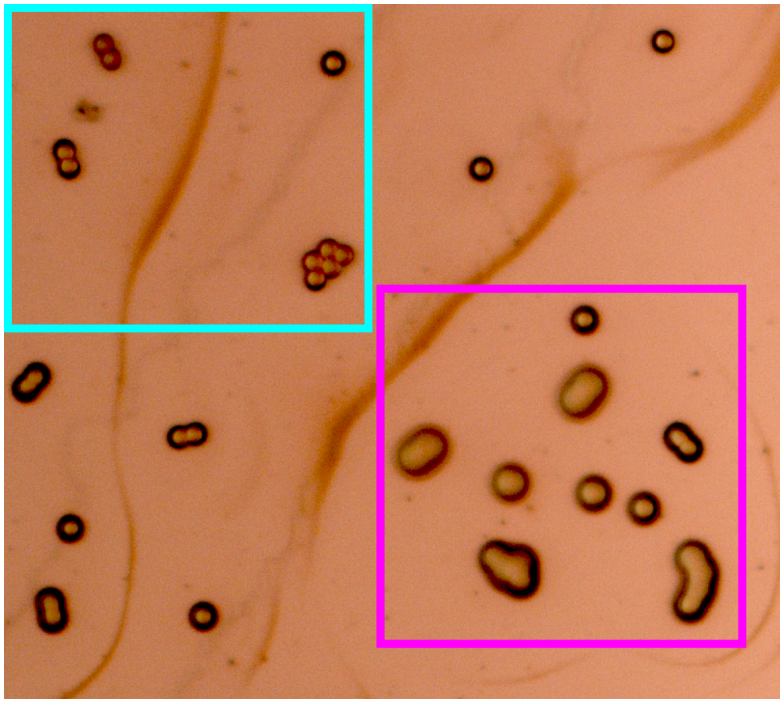


Figure D.1: PS microspheres with diameters of $10\ \mu m$ were drop coated onto the surface of the gridded coverslip. In order to imitate the size and shape of a biological cell, the microspheres were oven-baked to melt the individual spheres into compound continuous structures. Inside the cyan box, unmelted microspheres can be seen, some of which have adhered together. The magenta box shows the effect of melting as the discrete spheres have now begun to meld forming a continuous structure.

Appendix E

Profilometry methodologies

This section will briefly explain the three forms of profilometry used in this study: a stylus profiler, an optical profiler, and atomic force microscopy. These techniques and instruments were used to provide corroborative profile measurements of the PS phantoms used as 3D imaging targets for the phonon probe. Additionally the basic protocols for using the instruments will be reviewed.

Stylus profilometry

Stylus profilometry is a contact technique which drags a stylus-tipped cantilever across the topography of a sample. A force is applied to the cantilever such that any change in the height of the sample is counteracted by the downward force of the stylus. When the tip is displaced by a change in height of the sample an electrical signal is registered which is proportional to the degree of displacement. This process is repeated as the stylus is scanned along the specimen in a series of 1D lines.

The profilometer used in this study was a KLA-Tencor AlphaStep D-120 Stylus Profiler. The machine is capable of $55\ mm$ maximum scan lengths, contains a dynamic range for height measurements of $1.2\ mm$, and sub-angstrom axial resolution. The following protocol was utilised to operate the instrument:

1. glass microscope slide containing the PS phantom was placed in the specimen stage of the instrument and secured in place using a vacuum contact.

2. the x/y stages were manually adjusted until the phantom was within the field of view of the optical imaging system of the instrument (which was brought into focus).

3. the sample was positioned such that it was not directly beneath the silhouette of the stylus. Then the stylus tower was automatically descended until the stylus produced a force on the substrate that was consistent with the instrument calibration.

4. with the stylus raised, the centre of x/y stages were then zeroed at the apparent centre of the PS phantom.

5. scan parameters of $900\ \mu m$ travel (length of line scan), in $100\ nm$ steps, and a cantilever force of $5\ mg$ were established and run by the instrument.

6. in post-processing the tilt of the surface was fitted and removed, with the minimum measurement then assigned to the height $h = 0$.

This process was repeated three times for only a single phantom (the object in Figure 6.15d) along three different cross-sections. Only a single object was scanned due to the instrument's lack of 2D scanning capability (which would require stitching many individual line scans together). The profiler registered a maximum height measurement of $h = 7.7\ \mu m$ which was also in agreement with the maximum height from the same phantom measured through optical profiling which will be discussed next.

Optical profilometry

In general optical profilers are scanning microscopes which operate through the principle of low coherence interferometry. Incident broadband light is split into a reference path and the object path. Due to the low coherence length of the broadband light source, equal path lengths will result in an interference pattern with maximum intensity contrast [226]. As the optical path length of the system is scanned (e.g. by moving the objective lens or specimen with a piezo z-stage), a depth-resolved interferogram is generated for each pixel in x/y; the position of maximum intensity for this interference envelope then provides a height measurement for the given pixel and allows construction of a 3D image.

The optical profiler used in the work was the KLA Zeta-20 Optical Profiler. An objective lens with numerical aperture $NA = 0.9$ was used resulting in a lateral resolution of $r = 370\ nm$. The interferometric nature of the depth resolving mechanism permits a z-resolution for height measurements of $15\ nm$. The dynamic range of the instrument is determined by the travel range of the piezo z-stage used for axial scanning, which is $40\ mm$. The instrument operates very similarly to a standard brightfield or confocal microscope, with the following protocol being utilised

1. place microscope slide with PS phantom onto the specimen stage of the microscope.

2. manually scan the x/y stages until the object is centred within the field of view.

3. use the software to adjust the focus of the imaging system. The brightness of the light source can also be adjusted.

4. to initiate 3D profilometry, the z-scan range limits must be defined. First, a 2D grating is projected onto the focal plane, and the piezo z-stage is adjusted until the grating and the substrate are both in focus: then alert the software that this is the *floor* of the measurement.

5. repeat the above process to localise the top of the PS phantom, i.e. when the grating and the object peak are the only objects in focus.

6. now that the floor and peak positions of the object have been assigned in the software, only two scan parameters need defining: x/y discretisation of $180\ nm$, and a scan area of $173\ \mu m$ x $129\ \mu m$.

This process was repeated for each of the three PS phantoms presented in this study (Figures 6.15-6.17) using the same objective lens ($NA = 0.9$) and x/y discretisation. Optical profilometry is a powerful technique which offers nanometric profiling resolution, optical lateral resolution, fast acquisition speeds (less than a minute), non-contact operation, and high dynamic range. For these reasons it provided the most convenient 3D profiling measurements for corroborating the phonon probe measurements. For additional discussion on this technology refer to Section 6.4.2 in the main text.

Atomic force microscopy

Atomic force microscopy (AFM) is the gold standard of high resolution profilometric imaging. The technique generally operates by dragging or resonantly tapping a cantilever with a needle tip across the varying topography of a specimen. A detection laser is fixed in space away from the oscillating cantilever, with the light incident onto the end of the cantilever (just above the tip). As the tip is displaced due to changes in specimen topography, this displacement causes the detection laser to change its reflection angle with the cantilever; this deflection angle is then recorded by a photodetector and correlated with a measurement of specimen topography [225]. AFM achieves lateral resolution using the $\sim nm$ diameter of the probe tip and sub-nm axial resolution.

The AFM instrument utilised in this study was the Bruker Dimension FastScan. This device is capable of $20\ pm - 5\ nm$ lateral resolution which depends on both the radius of curvature of the probe tip and the deformability of the imaging object; e.g. a greater portion of the arc length of the probe tip will come into contact with a highly deformable object. In the axial direction, the instrument contains a dynamic range of $\sim 2\ \mu m$, however the deflection of the cantilever can be tracked with a resolution of $\sim 30\ pm$. In order to corroborate the height measurement of the phonon probe, the FastScan was used based on the following protocol:

1. the sample substrate was placed onto the specimen stage of the instrument and secured with a vacuum contact.

2. the x/y stages and optical microscope portions of the instrument were manually adjusted until the PS phantom appeared within the field of view and in focus.

3. the cantilever assembly was engaged to approach the substrate surface.

4. at a position adjacent to the imaging object, the position of the piezo z-stage controlling the cantilever height was calibrated by performing line scans across objects of known height: e.g. the 20 nm tall gold dots that populate the gridded substrate (see Figures 6.9-6.10).

5. with the tip disengaged, the x/y stages were then zeroed to the apparent position of the PS phantom centre. A scan was set up with the following parameters: scan area of ≈ 23.4 μm x 23.4 μm in steps of ≈ 92 nm, and a scan rate of 0.2 Hz (final scan taking roughly 30 minutes).

6. the tilt of the profile measurement was corrected in the post-process of the AFM scan, and the minimum height of the measurement array was set to $h = 0$.

Due to the low dynamic range of this particular instrument, measurements were only attainable for the shortest of the three PS phantoms imaged in this report (Figure 6.17). Since the absolute height of this object (measured through optical profilometry) was still taller than the dynamic range of the AFM, only a relative height measurement of the upper 2.25 μm could be obtained. For additional discussion and comparison between AFM and the phonon probe, see Section 6.4.2.

Bibliography

[1] I.M. Modlin. *Brief history of endoscopy (A)*. Nexthealth, 2000.

[2] Irvin M. Modlin, Mark Kidd, and Kevin D. Lye. From the Lumen to the Laparoscope. *Archives of Surgery*, 139(10):1110–1126, October 2004.

[3] Patsy Gerstner. The American Society for Gastrointestinal Endoscopy: a history. *Gastrointestinal Endoscopy*, 37:S1–S26, March 1991.

[4] H. H. Hopkins and N. S. Kapany. A Flexible Fibrescope, using Static Scanning. *Nature*, 173(4392):39–41, January 1954.

[5] T. Yamada, D.H. Alpers, A.N. Kalloo, N. Kaplowitz, C. Owyang, and D.W. Powell. *Atlas of Gastroenterology*. Wiley, 2009.

[6] https://www.olympus-europa.com/medical/en/products-and-solutions/products/product/evis-x1.html?olycmp=sea_evisx1_brand_olympus_ad01&gclid=cj0kcqjwuh6brdqarisai3i-ueuokhxj7wwmqngbnhvql26_g4yq0b7-efwlqcgp0lwktr5ew0tpxsaai-8ealw_wcb.

[7] Cadman L. Leggett and Kenneth K. Wang. Computer-aided diagnosis in GI endoscopy: looking into the future. *Gastrointestinal Endoscopy*, 84(5):842–844, November 2016.

[8] Thomas D. Wang and Jacques Van Dam. Optical biopsy: A new frontier in endoscopic detection and diagnosis. *Clinical Gastroenterology and Hepatology*, 2(9):744–753, September 2004.

[9] Louis Michel Wong Kee Song, Douglas G. Adler, Jason D. Conway, David L. Diehl, Francis A. Farraye, Sergey V. Kantsevoy, Richard Kwon, Petar Mamula, Betsy Rodriguez, Raj J. Shah, and William M. Tierney. Narrow band imaging and multiband imaging. *Gastrointestinal Endoscopy*, 67(4):581–589, April 2008.

[10] Martin Goetz, Nisar P. Malek, and Ralf Kiesslich. Microscopic imaging in endoscopy: endomicroscopy and endocytoscopy. *Nature Reviews Gastroenterology & Hepatology*, 11(1):11–18, January 2014.

[11] Metin N. Gurcan, Laura E. Boucheron, Ali Can, Anant Madabhushi, Nasir M. Rajpoot, and Bulent Yener. Histopathological Image Analysis: A Review. *IEEE Reviews in Biomedical Engineering*, 2:147–171, 2009.

[12] Adriana Vaz Safatle-Ribeiro, Elisa Ryoka Baba, Sheila Friedrich Faraj, Juliana Trazzi Rios, Marcelo Simas de Lima, Bruno Costa Martins, Sebastian Naschold Geiger, Caterina Pennacchi, Carla Gusman, Fbio Shiguehissa Kawaguti, Ricardo Sato Uemura, Evandro Sobroza de Melo, Ulysses Ribeiro, and Fauze Maluf-Filho. Diagnostic accuracy of probe-based confocal laser endomicroscopy in Lugol-unstained esophageal superficial lesions of patients with head and neck cancer. *Gastrointestinal Endoscopy*, 85(6):1195–1207, June 2017.

[13] J. Hecht. *City of Light: The Story of Fiber Optics*. Oxford University Press paperback. Oxford University Press, 2004.

[14] K C Kao. Dielectric-fibre surface waveguides for optical frequencies. 113(7):8, 1966.

[15] Govind P. Agrawal. *Fiber-Optic Communication Systems*, volume 222 of *Wiley Series in Microwave and Optical Engineering Ser.* John Wiley & Sons, Incorporated, 4 edition, 2010.

[16] Eugene Hecht. *Optics*. Addison Wesley, San Francisco USA, 4 edition, 2002.

[17] https://www.olympus-europa.com/medical/en/products-and-solutions/products/product/endocyto.html.

[18] Benjamin A. Flusberg, Eric D. Cocker, Wibool Piyawattanametha, Juergen C. Jung, Eunice L. M. Cheung, and Mark J. Schnitzer. Fiber-optic fluorescence imaging. *Nature Methods*, 2(12):941–950, December 2005.

[19] https://www.maunakeatech.com/en/cellvizio.

[20] Thomas D. Wang, Shai Friedland, Peyman Sahbaie, Roy Soetikno, PeiLin Hsiung, Jonathan T. C. Liu, James M. Crawford, and Christopher H. Contag. Functional Imaging of Colonic Mucosa With a Fibered Confocal Microscope for Real-Time In Vivo Pathology. *Clinical Gastroenterology and Hepatology*, 5(11):1300–1305, November 2007.

[21] Prateek Sharma, Alexander R. Meining, Emmanuel Coron, Charles J. Lightdale, Herbert C. Wolfsen, Ajay Bansal, Monther Bajbouj, Jean-Paul Galmiche, Julian A. Abrams, Amit Rastogi, Neil Gupta, Joel E. Michalek, Gregory Y. Lauwers, and Michael B. Wallace. Real-time increased detection of neoplastic tissue in Barrett's esophagus with probe-based confocal laser endomicroscopy: final

results of an international multicenter, prospective, randomized, controlled trial. *Gastrointestinal Endoscopy*, 74(3):465–472, September 2011.

[22] Gyungseok Oh, Euiheon Chung, and Seok H. Yun. Optical fibers for high-resolution in vivo microendoscopic fluorescence imaging. *Optical Fiber Technology*, 19(6, Part B):760–771, December 2013.

[23] https://pdf.medicalexpo.com/pdf/pentax/confocal-endomicroscopy/70880-70744.html.

[24] Adrian L. Polglase, Wendy J. McLaren, Stewart A. Skinner, Ralf Kiesslich, Markus F. Neurath, and Peter M. Delaney. A fluorescence confocal endomicroscope for in vivo microscopy of the upper- and the lower-GI tract. *Gastrointestinal Endoscopy*, 62(5):686–695, November 2005.

[25] Youngwoon Choi, Changhyeong Yoon, Moonseok Kim, Taeseok Daniel Yang, Christopher Fang-Yen, Ramachandra R. Dasari, Kyoung Jin Lee, and Wonshik Choi. Scanner-Free and Wide-Field Endoscopic Imaging by Using a Single Multimode Optical Fiber. *Physical Review Letters*, 109(20):203901, November 2012.

[26] Alex J. Thompson, Carl Paterson, Mark A. A. Neil, Chris Dunsby, and Paul M. W. French. Adaptive phase compensation for ultracompact laser scanning endomicroscopy. *Optics Letters*, 36(9):1707–1709, May 2011.

[27] Tom imr and Kishan Dholakia. Exploiting multimode waveguides for pure fibre-based imaging. *Nature Communications*, 3(1):1027, January 2012.

[28] Martin Plschner, Tom Tyc, and Tom imr. Seeing through chaos in multimode fibres. *Nature Photonics*, 9(8):529–535, August 2015.

[29] Victor Tsvirkun, Siddharth Sivankutty, Karen Baudelle, Rmi Habert, Graud Bouwmans, Olivier Vanvincq, Esben Ravn Andresen, and Herv Rigneault. Flexible lensless endoscope with a conformationally invariant multi-core fiber. *Optica*, 6(9):1185–1189, September 2019.

[30] Seok H. Yun, Guillermo J. Tearney, Benjamin J. Vakoc, Milen Shishkov, Wang Y. Oh, Adrien E. Desjardins, Melissa J. Suter, Raymond C. Chan, John A. Evans, Ik-Kyung Jang, Norman S. Nishioka, Johannes F. de Boer, and Brett E. Bouma. Comprehensive volumetric optical microscopy in vivo. *Nature Medicine*, 12(12):1429–1433, December 2006.

[31] Pilhan Kim, Euiheon Chung, Hiroshi Yamashita, Kenneth E. Hung, Atsushi Mizoguchi, Raju Kucherlapati, Dai Fukumura, Rakesh K. Jain, and Seok H. Yun. In vivo wide-area cellular imaging by side-view endomicroscopy. *Nature Methods*, 7(4):303–305, April 2010.

[32] D. Yelin, I. Rizvi, W. M. White, J. T. Motz, T. Hasan, B. E. Bouma, and G. J. Tearney. Three-dimensional miniature endoscopy. *Nature*, 443(7113):765–765, October 2006.

[33] Hamid Pahlevaninezhad, Mohammadreza Khorasaninejad, Yao-Wei Huang, Zhujun Shi, Lida P. Hariri, David C. Adams, Vivien Ding, Alexander Zhu, Cheng-Wei Qiu, Federico Capasso, and Melissa J. Suter. Nano-optic endoscope for high-resolution optical coherence tomography in vivo. *Nature Photonics*, 12(9):540–547, September 2018.

[34] Timo Gissibl, Simon Thiele, Alois Herkommer, and Harald Giessen. Two-photon direct laser writing of ultracompact multi-lens objectives. *Nature Photonics*, 10(8):554–560, August 2016.

[35] Jiawen Li, Simon Thiele, Bryden C. Quirk, Rodney W. Kirk, Johan W. Verjans, Emma Akers, Christina A. Bursill, Stephen J. Nicholls, Alois M. Herkommer, Harald Giessen, and Robert A. McLaughlin. Ultrathin monolithic 3D printed optical coherence tomography endoscopy for preclinical and clinical use. *Light: Science & Applications*, 9(1):124, July 2020.

[36] Lyubov V. Amitonova and Johannes F. de Boer. Endo-microscopy beyond the Abbe and Nyquist limits. *Light: Science & Applications*, 9(1):81, May 2020.

[37] W. Zhong, J. P. Celli, I. Rizvi, Z. Mai, B. Q. Spring, S. H. Yun, and T. Hasan. In vivo high-resolution fluorescence microendoscopy for ovarian cancer detection and treatment monitoring. *British Journal of Cancer*, 101(12):2015–2022, December 2009.

[38] Juergen C. Jung, Amit D. Mehta, Emre Aksay, Raymond Stepnoski, and Mark J. Schnitzer. In Vivo Mammalian Brain Imaging Using One- and Two-Photon Fluorescence Microendoscopy. *Journal of Neurophysiology*, 92(5):3121–3133, November 2004.

[39] H. Neumann, F. S. Fuchs, M. Vieth, R. Atreya, J. Siebler, R. Kiesslich, and M. F. Neurath. Review article: in vivo imaging by endocytoscopy. *Alimentary Pharmacology & Therapeutics*, 33(11):1183–1193, 2011.

[40] Geoffrey M. Cooper. The Molecular Composition of Cells. *The Cell: A Molecular Approach. 2nd edition*, 2000.

[41] Malte Renz. Fluorescence microscopy - A historical and technical perspective. *Cytometry Part A*, 83(9):767–779, 2013.

[42] Stefan W. Hell and Jan Wichmann. Breaking the diffraction resolution limit by stimulated emission: stimulated-emission-depletion fluorescence microscopy. *Optics Letters*, 19(11):780–782, June 1994.

[43] Eric Betzig, George H. Patterson, Rachid Sougrat, O. Wolf Lindwasser, Scott Olenych, Juan S. Bonifacino, Michael W. Davidson, Jennifer Lippincott-Schwartz, and Harald F. Hess. Imaging Intracellular Fluorescent Proteins at Nanometer Resolution. *Science*, 313(5793):1642–1645, September 2006.

[44] Michael Eisenstein. Helping cells to tell a colorful tale. *Nature Methods*, 3(8):647–655, August 2006.

[45] Ellen C. Jensen. Use of Fluorescent Probes: Their Effect on Cell Biology and Limitations. *The Anatomical Record*, 295(12):2031–2036, 2012.

[46] Ram Dixit and Richard Cyr. Cell damage and reactive oxygen species production induced by fluorescence microscopy: effect on mitosis and guidelines for non-invasive fluorescence microscopy. *The Plant Journal*, 36(2):280–290, 2003.

[47] Bernard F. Godley, Farrukh A. Shamsi, Fong-Qi Liang, Stuart G. Jarrett, Sallyanne Davies, and Mike Boulton. Blue Light Induces Mitochondrial DNA Damage and Free Radical Production in Epithelial Cells. *Journal of Biological Chemistry*, 280(22):21061–21066, June 2005.

[48] Johnathan Donaldson Craik, Delilah Khan, and Reda Afifi. The Safety of Intravenous Indigo Carmine to Assess Ureteric Patency During Transvaginal Uterosacral Suspension of the Vaginal Vault. *Female Pelvic Medicine & Reconstructive Surgery*, 15(1):11–15, February 2009.

[49] Scott S. Auerbach, Douglas W. Bristol, John C. Peckham, Gregory S. Travlos, Charles D. Hbert, and Rajendra S. Chhabra. Toxicity and carcinogenicity studies of methylene blue trihydrate in F344N rats and B6C3F1 mice. *Food and Chemical Toxicology*, 48(1):169–177, January 2010.

[50] Raphael Alford, Haley M. Simpson, Josh Duberman, G. Craig Hill, Mikako Ogawa, Celeste Regino, Hisataka Kobayashi, and Peter L. Choyke. Toxicity of Organic Fluorophores Used in Molecular Imaging: Literature Review. *Molecular Imaging*, 8(6):7290.2009.00031, November 2009.

[51] Alisha V. DSouza, Huiyun Lin, Eric R. Henderson, Kimberley S. Samkoe, and Brian W. Pogue. Review of fluorescence guided surgery systems: identification of key performance capabilities beyond indocyanine green imaging. *Journal of Biomedical Optics*, 21(8):080901, August 2016.

[52] Tim J. Mellow. Elsevier Science & Technology, Oxford, 2012.

[53] Charles Kittel. W. H. Freeman and Company, San Francisco, 1980.

[54] Robert H. Randall. Dover Publications, 2005.

[55] D. Kane, W. Grassi, R. Sturrock, and P. V. Balint. A brief history of musculoskeletal ultrasound: From bats and ships to babies and hips. *Rheumatology*, 43(7):931–933, July 2004.

[56] Amir Manbachi and Richard S. C. Cobbold. Development and application of piezoelectric materials for ultrasound generation and detection. *Ultrasound*, 19(4):187–196, November 2011.

[57] Joseph H. Holmes, Douglass H. Howry, Gerald J. Posakony, and C. Richard Cushman. The Ultrasonic Visualization of Soft Tissue Structures in the Human Body. *Transactions of the American Clinical and Climatological Association*, 66:208–225, 1955.

[58] Floyd A. Firestone. The Supersonic Reflectoscope, an Instrument for Inspecting the Interior of Solid Parts by Means of Sound Waves. *The Journal of the Acoustical Society of America*, 17(3):287–299, January 1946.

[59] Qifa Zhou, Sienting Lau, Dawei Wu, and K. Kirk Shung. Piezoelectric films for high frequency ultrasonic transducers in biomedical applications. *Progress in Materials Science*, 56(2):139–174, February 2011.

[60] Joseph H. Holmes. Diagnostic ultrasound during the early years of A.I.U.M. *Journal of Clinical Ultrasound*, 8(4):299–308, 1980.

[61] Monique Moderiano, Maureen McEvoy, Jessie Childs, and Adrian Esterman. Safety of Ultrasound Exposure: Knowledge, Attitudes, and Practices of Australasian Sonographers. *Journal of Diagnostic Medical Sonography*, 34(5):357–367, September 2018.

[62] Section 7discussion of the mechanical index and other exposure parameters. American Institute of Ultrasound in Medicine. *Journal of Ultrasound in Medicine*, 19(2):143–148, 2000.

[63] Qinghua Huang and Zhaozheng Zeng. A Review on Real-Time 3D Ultrasound Imaging Technology. *BioMed Research International*, March 2017.

[64] D B Downey and A Fenster. Vascular imaging with a three-dimensional power Doppler system. *American Journal of Roentgenology*, 165(3):665–668, September 1995.

[65] P. R. Hoskins, P. J. Fish, W. N. McDicken, and C. Moran. Developments in cardiovascular ultrasound. Part 2: Arterial applications. *Medical and Biological Engineering and Computing*, 36(3):259–269, May 1998.

[66] Yidan Li, Yidan Wang, Zhenguo Zhai, Xiaojuan Guo, Yuanhua Yang, and Xiuzhang Lu. Real-Time Three-Dimensional Echocardiography to Assess Right Ventricle Function in Patients with Pulmonary Hypertension. *PLOS ONE*, 10(6):e0129557, June 2015.

[67] P. Forouhi, J. S. Walsh, T. J. Anderson, and U. Chetty. Ultrasonography as a method of measuring breast tumour size and monitoring response to primary systemic treatment. *BJS (British Journal of Surgery)*, 81(2):223–225, 1994.

[68] N. Goyal, N. Jain, V. Rachapalli, D. L. Cochlin, and M. Robinson. Non-invasive evaluation of liver cirrhosis using ultrasound. *Clinical Radiology*, 64(11):1056–1066, November 2009.

[69] Juan Luis Alczar and Matas Jurado. Three-dimensional ultrasound for assessing women with gynecological cancer: A systematic review. *Gynecologic Oncology*, 120(3):340–346, March 2011.

[70] Valma J. Robertson and Kerry G. Baker. A Review of Therapeutic Ultrasound: Effectiveness Studies. *Physical Therapy*, 81(7):1339–1350, July 2001.

[71] ALI S. Alavi, MARK S. Soloway, ANIL Vaidya, CHARLES M. Lynne, and EDWARD L. Gheiler. LOCAL ANESTHESIA FOR ULTRASOUND GUIDED PROSTATE BIOPSY: A PROSPECTIVE RANDOMIZED TRIAL COMPARING 2 METHODS. *The Journal of Urology*, 166(4):1343–1345, October 2001.

[72] Steven L. Garrett. Attenuation of Sound. In Steven L. Garrett, editor, *Understanding Acoustics: An Experimentalists View of Sound and Vibration*, Graduate Texts in Physics, pages 673–688. Springer International Publishing, Cham, 2020.

[73] K. R. Waters, J. Mobley, and J. G. Miller. Causality-imposed (Kramers-Kronig) relationships between attenuation and dispersion. *IEEE Transactions on Ultrasonics, Ferroelectrics, and Frequency Control*, 52(5):822–823, May 2005.

[74] Thomas L. Szabo and Junru Wu. A model for longitudinal and shear wave propagation in viscoelastic media. *The Journal of the Acoustical Society of America*, 107(5):2437–2446, April 2000.

[75] Eugene P. DiMagno and Matthew J. DiMagno. Endoscopic Ultrasonography: From the Origins to Routine EUS. *Digestive Diseases and Sciences*, 61(2):342–353, February 2016.

[76] Steven M. Shaw and Michael B. Kimmey. General principles of endoscopic ultrasonographic imaging. *Techniques in Gastrointestinal Endoscopy*, 2(2):50–55, April 2000.

[77] Larissa L. Fujii and Michael J. Levy. Basic techniques in endoscopic ultrasound-guided fine needle aspiration for solid lesions: Adverse events and avoiding them. *Endoscopic Ultrasound*, 3(1):35–45, 2014.

[78] E. P. Dimagno, P. T. Regan, J. E. Clain, E. M. James, and J. L. Buxton. Human endoscopic ultrasonography. *Gastroenterology*, 83(4):824–829, October 1982.

[79] Thomas Rsch, Reinhard Lorenz, Christine Braig, Stefan Feuerbach, Jrg Rudiger Siewert, Volker Schusdziarra, and Meinhard Classen. Endoscopic ultrasound in pancreatic tumor diagnosis. *Gastrointestinal Endoscopy*, 37(3):347–352, May 1991.

[80] Faris M. Murad, Sri Komanduri, Barham K. Abu Dayyeh, Shailendra S. Chauhan, Brintha K. Enestvedt, Larissa L. Fujii-Lau, Vani Konda, John T. Maple, Rahul Pannala, Nirav C. Thosani, and Subhas Banerjee. Echoendoscopes. *Gastrointestinal Endoscopy*, 82(2):189–202, August 2015.

[81] Hideo Yanai, Hiroshi Fujimura, Munetaka Suzumi, Shinjiro Matsuura, Nobuhilo Awaya, Takayoshi Noguchi, Mikio Karita, Masahiro Tada, Kiwamu Okita, and Tsuyoshi Aibe. Delineation of the gastric muscularis mucosae and assessment of depth of invasion of early gastric cancer using a 20-megahertz endoscopic ultrasound probe. *Gastrointestinal Endoscopy*, 39(4):505–512, January 1993.

[82] R. A. Lemons and C. F. Quate. Acoustic microscopescanning version. *Applied Physics Letters*, 24(4):163–165, February 1974.

[83] J. Heiserman, D. Rugar, and C. F. Quate. Cryogenic acoustic microscopy. *The Journal of the Acoustical Society of America*, 67(5):1629–1637, May 1980.

[84] R N Johnston, A Atalar, J Heiserman, V Jipson, and C F Quate. Acoustic microscopy: resolution of subcellular detail. *Proceedings of the National Academy of Sciences of the United States of America*, 76(7):3325–3329, July 1979.

[85] J. A. Hildebrand, D. Rugar, R. N. Johnston, and C. F. Quate. Acoustic microscopy of living cells. *Proceedings of the National Academy of Sciences*, 78(3):1656–1660, March 1981.

[86] A. Jakob, M. Bender, T. Knoll, R. Lemor, T. Lehnert, M. Koch, M. Veith, Q. Zhou, B. P. Zhu, J. X. Han, and K. K. Shung. Comparison of different piezoelectric materials for GHz acoustic microscopy transducers. In *2009 IEEE International Ultrasonics Symposium*, pages 1722–1725, September 2009.

[87] Alexander Graham Bell. The Production of Sound by Radiant Energy. *Science*, 2(48):242–253, 1881.

[88] Léon Brillouin. Diffusion de la lumière et des rayons X par un corps transparent homogène: Influence de l'agitation thermique. *Ann. Phys.*, 9(17):88–122, 1922.

[89] C. V. Raman and N. S. Nagendra Nathe. The diffraction of light by high frequency sound waves: Part I. *Proceedings of the Indian Academy of Sciences - Section A*, 2(4):406–412, October 1935.

[90] H. K. Wickramasinghe, R. C. Bray, V. Jipson, C. F. Quate, and J. R. Salcedo. Photoacoustics on a microscopic scale. *Applied Physics Letters*, 33(11):923–925, December 1978.

[91] Eric M. Strohm, Elizabeth S. L. Berndl, and Michael C. Kolios. High frequency label-free photoacoustic microscopy of single cells. *Photoacoustics*, 1(3):49–53, December 2013.

[92] Junjie Yao, Lidai Wang, Joon-Mo Yang, Konstantin I. Maslov, Terence T. W. Wong, Lei Li, Chih-Hsien Huang, Jun Zou, and Lihong V. Wang. High-speed label-free functional photoacoustic microscopy of mouse brain in action. *Nature Methods*, 12(5):407–410, May 2015.

[93] Konstantin Maslov, Gheorghe Stoica, and Lihong V. Wang. In vivo dark-field reflection-mode photoacoustic microscopy. *Optics Letters*, 30(6):625–627, March 2005.

[94] Eric M. Strohm, Michael J. Moore, and Michael C. Kolios. Single Cell Photoacoustic Microscopy: A Review. *IEEE Journal of Selected Topics in Quantum Electronics*, 22(3):137–151, May 2016.

[95] Junjie Yao and Lihong V. Wang. Photoacoustic microscopy. *Laser & Photonics Reviews*, 7(5):758–778, 2013.

[96] Joon-Mo Yang, Christopher Favazza, Ruimin Chen, Junjie Yao, Xin Cai, Konstantin Maslov, Qifa Zhou, K. Kirk Shung, and Lihong V. Wang. Simultaneous functional photoacoustic and ultrasonic endoscopy of internal organs in vivo. *Nature Medicine*, 18(8):1297–1302, August 2012.

[97] P. C. Beard and T. N. Mills. Characterization of post mortemarterial tissue using time-resolved photoacoustic spectroscopy at 436, 461 and 532 nm. *Physics in Medicine and Biology*, 42(1):177–198, January 1997.

[98] Wolfgang Bost, Frank Stracke, Eike C. WeiB, Sankar Narasimhan, Michael C. Kolios, and Robert Lemor. High frequency optoacoustic microscopy. In *2009 Annual International Conference of the IEEE Engineering in Medicine and Biology Society*, September 2009.

[99] Min Rui, Sankar Narashimhan, Wolfgang Bost, Frank Stracke, Eike Weiss, Robert Lemor, and Michael C. Kolios. Gigahertz optoacoustic imaging for cellular imaging. In *Photons Plus Ultrasound: Imaging and Sensing 2010*, volume 7564, page 756411. International Society for Optics and Photonics, February 2010.

[100] Georg Wissmeyer, Miguel A. Pleitez, Amir Rosenthal, and Vasilis Ntziachristos. Looking at sound: optoacoustics with all-optical ultrasound detection. *Light: Science & Applications*, 7(1):53, August 2018.

[101] W. F. Cheong, S. A. Prahl, and A. J. Welch. A review of the optical properties of biological tissues. *IEEE Journal of Quantum Electronics*, 26(12):2166–2185, December 1990.

[102] Eric M. Strohm, Michael J. Moore, and Michael C. Kolios. High resolution ultrasound and photoacoustic imaging of single cells. *Photoacoustics*, 4(1):36–42, March 2016.

[103] Amos Danielli, Konstantin I. Maslov, Alejandro Garcia-Uribe, Amy M. Winkler, Chiye Li, Lidai Wang, Yun Chen, Gerald W. Dorn Ii, and Lihong V. Wang. Label-free photoacoustic nanoscopy. *Journal of Biomedical Optics*, 19(8):086006, August 2014.

[104] Shriram Sethuraman, Salavat R. Aglyamov, James H. Amirian, Richard W. Smalling, and Stanislav Y. Emelianov. Intravascular photoacoustic imaging using an IVUS imaging catheter. *IEEE Transactions on Ultrasonics, Ferroelectrics, and Frequency Control*, 54(5):978–986, May 2007.

[105] Joon-Mo Yang, Konstantin Maslov, Hao-Chung Yang, Qifa Zhou, K. Kirk Shung, and Lihong V. Wang. Photoacoustic endoscopy. *Optics Letters*, 34(10):1591–1593, May 2009.

[106] Bo Wang, Jimmy L. Su, Andrei B. Karpiouk, Konstantin V. Sokolov, Richard W. Smalling, and Stanislav Y. Emelianov. Intravascular Photoacoustic Imaging. *IEEE Journal of Selected Topics in Quantum Electronics*, 16(3):588–599, May 2010.

[107] Joon-Mo Yang, Chiye Li, Ruimin Chen, Qifa Zhou, Koping Kirk Shung, and Lihong V. Wang. Catheter-based photoacoustic endoscope. *Journal of Biomedical Optics*, 19(6):066001, June 2014.

[108] Joon-Mo Yang, Chiye Li, Ruimin Chen, Bin Rao, Junjie Yao, Cheng-Hung Yeh, Amos Danielli, Konstantin Maslov, Qifa Zhou, K. Kirk Shung, and Lihong V. Wang. Optical-resolution photoacoustic endomicroscopy in vivo. *Biomedical Optics Express*, 6(3):918–932, March 2015.

[109] Heng Guo, Ying Li, Weizhi Qi, and Lei Xi. Photoacoustic endoscopy: A progress review. *Journal of Biophotonics*, October 2020.

[110] Hailong He, Georg Wissmeyer, Saak V. Ovsepian, Andreas Buehler, and Vasilis Ntziachristos. Hybrid optical and acoustic resolution optoacoustic endoscopy. *Optics Letters*, 41(12):2708–2710, June 2016.

[111] Heng Guo, Chaolong Song, Huikai Xie, and Lei Xi. Photoacoustic endomicroscopy based on a MEMS scanning mirror. *Optics Letters*, 42(22):4615–4618, November 2017.

[112] Cameron M. Lee, Christoph J. Engelbrecht, Timothy D. Soper, Fritjof Helmchen, and Eric J. Seibel. Scanning fiber endoscopy with highly flexible, 1 mm catheterscopes for wide-field, full-color imaging. *Journal of Biophotonics*, 3(5-6):385–407, 2010.

[113] Rehman Ansari, Edward Z. Zhang, Adrien E. Desjardins, and Paul C. Beard. All-optical forward-viewing photoacoustic probe for high-resolution 3D endoscopy. *Light: Science & Applications*, 7(1):75, October 2018.

[114] Guangyao Li, Zhendong Guo, and Sung-Liang Chen. Miniature Probe for Forward-View Wide-Field Optical-Resolution Photoacoustic Endoscopy. *IEEE Sensors Journal*, 19(3):909–916, February 2019.

[115] Terence T. W. Wong, Ruiying Zhang, Chi Zhang, Hsun-Chia Hsu, Konstantin I. Maslov, Lidai Wang, Junhui Shi, Ruimin Chen, K. Kirk Shung, Qifa Zhou, and Lihong V. Wang. Label-free automated three-dimensional imaging of whole organs by microtomy-assisted photoacoustic microscopy. *Nature Communications*, 8(1):1386, November 2017.

[116] Terence T. W. Wong, Ruiying Zhang, Pengfei Hai, Chi Zhang, Miguel A. Pleitez, Rebecca L. Aft, Deborah V. Novack, and Lihong V. Wang. Fast label-free multilayered histology-like imaging of human breast cancer by photoacoustic microscopy. *Science Advances*, 3(5):e1602168, May 2017.

[117] JeanPierre Monchalin. LaserUltrasonics: From the Laboratory to Industry. *AIP Conference Proceedings*, 700(1):3–31, February 2004.

[118] Richard J. Colchester, Edward Z. Zhang, Charles A. Mosse, Paul C. Beard, Ioannis Papakonstantinou, and Adrien E. Desjardins. Broadband miniature optical ultrasound probe for high resolution vascular tissue imaging. *Biomedical Optics Express*, 6(4):1502–1511, April 2015.

[119] Malcolm C Finlay, Charles A Mosse, Richard J Colchester, Sacha Noimark, Edward Z Zhang, Sebastien Ourselin, Paul C Beard, Richard J Schilling, Ivan P

Parkin, Ioannis Papakonstantinou, and Adrien E Desjardins. Through-needle all-optical ultrasound imaging in vivo: a preclinical swine study. *Light: Science & Applications*, 6(12):e17103–e17103, December 2017.

[120] Sacha Noimark, Richard J. Colchester, Ben J. Blackburn, Edward Z. Zhang, Erwin J. Alles, Sebastien Ourselin, Paul C. Beard, Ioannis Papakonstantinou, Ivan P. Parkin, and Adrien E. Desjardins. Carbon-NanotubePDMS Composite Coatings on Optical Fibers for All-Optical Ultrasound Imaging. *Advanced Functional Materials*, 26(46):8390–8396, 2016.

[121] C. Thomsen, J. Strait, Z. Vardeny, H. J. Maris, J. Tauc, and J. J. Hauser. Coherent phonon generation and detection by picosecond light pulses. *Physical Review Letters*, 53(10):989–992, September 1984.

[122] Barry R. Masters. Lord Rayleigh: A Scientific Life, 2009.

[123] Thomas Schneider. *Nonlinear Optics in Telecommunications*. Springer-Verlag, Berlin, DE, 2004.

[124] Joseph Larmor. XV. The principle of molecular scattering of radiation. *The London, Edinburgh, and Dublin Philosophical Magazine and Journal of Science*, 37(217):161–163, January 1919.

[125] Elsa Garmire. Perspectives on stimulated Brillouin scattering. *New Journal of Physics*, 19(1):011003, January 2017.

[126] J. G. Dil. Brillouin scattering in condensed matter. *Reports on Progress in Physics*, 45(3):285, March 1982.

[127] Giuliano Scarcelli and Seok Hyun Yun. Confocal Brillouin microscopy for three-dimensional mechanical imaging. *Nature Photonics*, 2(1):39–43, January 2008.

[128] David J. Griffiths. *Introduction to Electrodynamics*. Prentice Hall, Upper Saddle River, NJ, 3 edition, 1999.

[129] Karsten Rottwitt and Peter Tidemand-Lichtenberg. *Nonlinear optics : principles and applications*. Optical sciences and applications of light. CRC Press, Boca Raton ; London, 2015.

[130] Peter E Powers and Joseph W. Haus. *Fundamentals of nonlinear optics*. CRC Press, Boca Raton ; London, 2nd ed. edition, 2017.

[131] Robert Prevedel, Alba Diz-Muoz, Giancarlo Ruocco, and Giuseppe Antonacci. Brillouin microscopy: an emerging tool for mechanobiology. *Nature Methods*, 16(10):969–977, October 2019.

[132] Wonshik Choi, Christopher Fang-Yen, Kamran Badizadegan, Seungeun Oh, Niyom Lue, Ramachandra R. Dasari, and Michael S. Feld. Tomographic phase microscopy. *Nature Methods*, 4(9):717–719, September 2007.

[133] Sadra Bakhshandeh, Hubert M. Taeb, Raimund Schller, Kyoohyun Kim, Timon Beck, Anna Taubenberger, Jochen Guck, and Amaia Cipitria. Optical quantification of intracellular mass density and cell mechanics in 3D mechanical confinement. *Soft Matter*, 17(4):853–862, February 2021.

[134] Kyoohyun Kim and Jochen Guck. The Relative Densities of Cytoplasm and Nuclear Compartments Are Robust against Strong Perturbation. *Biophysical Journal*, 119(10):1946–1957, November 2020.

[135] Giuseppe Antonacci, Timon Beck, Alberto Bilenca, Jrgen Czarske, Kareem Elsayad, Jochen Guck, Kyoohyun Kim, Benedikt Krug, Francesca Palombo, Robert Prevedel, and Giuliano Scarcelli. Recent progress and current opinions in Brillouin microscopy for life science applications. *Biophysical Reviews*, 12(3):615–624, June 2020.

[136] S. M. Lindsay, M. W. Anderson, and J. R. Sandercock. Construction and alignment of a high performance multipass vernier tandem FabryPerot interferometer. *Review of Scientific Instruments*, 52(10):1478–1486, October 1981.

[137] K. J. Koski, J. Mller, H. D. Hochheimer, and J. L. Yarger. High pressure angle-dispersive Brillouin spectroscopy: A technique for determining acoustic velocities and attenuations in liquids and solids. *Review of Scientific Instruments*, 73(3):1235–1241, March 2002.

[138] K. J. Koski and J. L. Yarger. Brillouin imaging. *Applied Physics Letters*, 87(6):061903, August 2005.

[139] Giuliano Scarcelli and Seok Hyun Yun. In vivo Brillouin optical microscopy of the human eye. *Optics Express*, 20(8):9197, April 2012.

[140] Pei-Hsun Wu, Dikla Raz-Ben Aroush, Atef Asnacios, Wei-Chiang Chen, Maxim E. Dokukin, Bryant L. Doss, Pauline Durand-Smet, Andrew Ekpenyong, Jochen Guck, Nataliia V. Guz, Paul A. Janmey, Jerry S. H. Lee, Nicole M. Moore, Albrecht Ott, Yeh-Chuin Poh, Robert Ros, Mathias Sander, Igor Sokolov, Jack R. Staunton, Ning Wang, Graeme Whyte, and Denis Wirtz. A comparison of methods to assess cell mechanical properties. *Nature Methods*, 15(7):491–498, July 2018.

[141] Giuliano Scarcelli, Sebastien Besner, Roberto Pineda, Patricia Kalout, and Seok Hyun Yun. In Vivo Biomechanical Mapping of Normal and Keratoconus Corneas. *JAMA Ophthalmology*, 133(4):480, April 2015.

[142] Jérémie Margueritat, Angélique Virgone-Carlotta, Sylvain Monnier, Hélène Delanoë-Ayari, Hichem C. Mertani, Alice Berthelot, Quentin Martinet, Xavier Dagany, Charlotte Rivière, Jean-Paul Rieu, and Thomas Dehoux. High-frequency mechanical properties of tumors measured by Brillouin light scattering. *Physical Review Letters*, 122(1), January 2019.

[143] Giuseppe Antonacci, Ryan M. Pedrigi, Avinash Kondiboyina, Vikram V. Mehta, Ranil de Silva, Carl Paterson, Rob Krams, and Peter Trk. Quantification of plaque stiffness by Brillouin microscopy in experimental thin cap fibroatheroma. *Journal of The Royal Society Interface*, 12(112):20150843, November 2015.

[144] Giuliano Scarcelli, William J. Polacheck, Hadi T. Nia, Kripa Patel, Alan J. Grodzinsky, Roger D. Kamm, and Seok Hyun Yun. Noncontact three-dimensional mapping of intracellular hydromechanical properties by Brillouin microscopy. *Nature Methods*, 12(12):1132–1134, December 2015.

[145] Raimund Schlüßler, Stephanie Möllmert, Shada Abuhattum, Gheorghe Cojoc, Paul Müller, Kyoohyun Kim, Conrad Möckel, Conrad Zimmermann, Jürgen Czarske, and Jochen Guck. Mechanical Mapping of Spinal Cord Growth and Repair in Living Zebrafish Larvae by Brillouin Imaging. *Biophysical Journal*, 115(5):911–923, September 2018.

[146] Carlo Bevilacqua, Hèctor Sánchez-Iranzo, Dmitry Richter, Alba Diz-Muñoz, and Robert Prevedel. Imaging mechanical properties of sub-micron ECM in live zebrafish using Brillouin microscopy. *Biomedical Optics Express*, 10(3):1420–1431, March 2019.

[147] Jitao Zhang, Raksha Raghunathan, Justin Rippy, Chen Wu, Richard H. Finnell, Kirill V. Larin, and Giuliano Scarcelli. Tissue biomechanics during cranial neural tube closure measured by Brillouin microscopy and optical coherence tomography. *Birth Defects Research*, 111(14):991–998, 2019.

[148] Xinrong Hu, Qiang Sun, Jing Li, Chun Li, Ying Liu, and Jianzhong Zhang. Spectral dispersion modeling of virtually imaged phased array by using angular spectrum of plane waves. *Optics Express*, 23(1):1–12, January 2015.

[149] Milos Nikolic and Giuliano Scarcelli. Long-term Brillouin imaging of live cells with reduced absorption-mediated damage at 660nm wavelength. *Biomedical Optics Express*, 10(4):1567, April 2019.

[150] Francesca Palombo and Daniele Fioretto. Brillouin Light Scattering: Applications in Biomedical Sciences. *Chemical Reviews*, 119(13):7833–7847, July 2019.

[151] Itay Remer, Roni Shaashoua, Netta Shemesh, Anat Ben-Zvi, and Alberto Bilenca. High-sensitivity and high-specificity biomechanical imaging by stimulated

Brillouin scattering microscopy. *Nature Methods*, 17(9):913–916, September 2020.

[152] Irina V. Kabakova, YuChen Xiang, Carl Paterson, and Peter Török. Fiber-integrated Brillouin microspectroscopy: Towards Brillouin endoscopy. *Journal of Innovative Optical Health Sciences*, 10(06):1742002, August 2017.

[153] YuChen Xiang, Carin Basirun, Joshua Chou, Majid E. Warkiani, Peter Trk, Peter Trk, Yingying Wang, Shoufei Gao, and Irina V. Kabakova. Background-free fibre optic Brillouin probe for remote mapping of micromechanics. *Biomedical Optics Express*, 11(11):6687–6698, November 2020.

[154] C. Thomsen, H. T. Grahn, H. J. Maris, and J. Tauc. Surface generation and detection of phonons by picosecond light pulses. *Physical Review B*, 34(6):4129–4138, September 1986.

[155] Vitalyi E. Gusev and Pascal Ruello. Advances in applications of time-domain Brillouin scattering for nanoscale imaging. *Applied Physics Reviews*, 5(3):031101, July 2018.

[156] C. Thomsen, H. T. Grahn, H. J. Maris, and J. Tauc. Picosecond interferometric technique for study of phonons in the brillouin frequency range. *Optics Communications*, 60(1):55–58, October 1986.

[157] O. B. Wright and T. Hyoguchi. Ultrafast vibration and laser acoustics in thin transparent films. *Optics Letters*, 16(19):1529–1531, October 1991.

[158] O. B. Wright and K. Kawashima. Coherent phonon detection from ultrafast surface vibrations. *Physical Review Letters*, 69(11):1668–1671, September 1992.

[159] B Perrin, C Rossignol, B Bonello, and J. C Jeannet. Interferometric detection in picosecond ultrasonics. *Physica B: Condensed Matter*, 263-264:571–573, March 1999.

[160] O. B. Wright. Laser picosecond acoustics in double-layer transparent films. *Optics Letters*, 20(6):632–634, March 1995.

[161] O. Matsuda and O. B. Wright. Reflection and transmission of light in multilayers perturbed by picosecond strain pulse propagation. *JOSA B*, 19(12):3028–3041, December 2002.

[162] M. Claudia Troparevsky, Adrian S. Sabau, Andrew R. Lupini, and Zhenyu Zhang. Transfer-matrix formalism for the calculation of optical response in multilayer systems: from coherent to incoherent interference. *Optics Express*, 18(24):24715–24721, November 2010.

[163] Osamu Matsuda, Maria Cristina Larciprete, Roberto Li Voti, and Oliver B. Wright. Fundamentals of picosecond laser ultrasonics. *Ultrasonics*, 56:3–20, February 2015.

[164] J. Hohlfeld, S.-S. Wellershoff, J. Güdde, U. Conrad, V. Jähnke, and E. Matthias. Electron and lattice dynamics following optical excitation of metals. *Chemical Physics*, 251(1-3):237–258, January 2000.

[165] S.-S. Wellershoff, J. Hohlfeld, J. Güdde, and E. Matthias. The role of electron-phonon coupling in femtosecond laser damage of metals:. *Applied Physics A Materials Science & Processing*, 69(S1):S99–S107, December 1999.

[166] Richard J. Smith, Fernando Perez Cota, Leonel Marques, Xuesheng Chen, Ahmet Arca, Kevin Webb, Jonathon Aylott, Micheal G. Somekh, and Matt Clark. Optically excited nanoscale ultrasonic transducers. *J. Acoust. Soc. Am.*, 137(1):219–227, January 2015.

[167] Richard J. Smith, Salvatore La Cavera, Fernando Prez-Cota, Leonel Marques, and Matt Clark. Thickness measurement of polymer thin films with high frequency ultrasonic transducers. *AIP Conference Proceedings*, 2102(1):040015, May 2019.

[168] Fernando Pérez-Cota, Richard J. Smith, Emilia Moradi, Leonel Marques, Kevin F. Webb, and Matt Clark. High resolution 3D imaging of living cells with sub-optical wavelength phonons. *Sci. Rep.*, 6(1), December 2016.

[169] C. Rossignol, N. Chigarev, M. Ducousso, B. Audoin, G. Forget, F. Guillemot, and M. C. Durrieu. In Vitro picosecond ultrasonics in a single cell. *Applied Physics Letters*, 93(12):123901, September 2008.

[170] B. Audoin, C. Rossignol, N. Chigarev, M. Ducousso, G. Forget, F. Guillemot, and M. C. Durrieu. Picosecond acoustics in vegetal cells: Non-invasive in vitro measurements at a sub-cell scale. *Ultrasonics*, 50(2):202–207, February 2010.

[171] T. Dehoux, M. Abi Ghanem, O. F. Zouani, J.-M. Rampnoux, Y. Guillet, S. Dilhaire, M.-C. Durrieu, and B. Audoin. All-optical broadband ultrasonography of single cells. *Scientific Reports*, 5(1):8650, August 2015.

[172] Sorasak Danworaphong, Motonobu Tomoda, Yuki Matsumoto, Osamu Matsuda, Toshiro Ohashi, Hiromu Watanabe, Masafumi Nagayama, Kazutoshi Gohara, Paul H. Otsuka, and Oliver B. Wright. Three-dimensional imaging of biological cells with picosecond ultrasonics. *Applied Physics Letters*, 106(16):163701, April 2015.

[173] Fernando Pérez-Cota, Richard J. Smith, Emilia Moradi, Leonel Marques, Kevin F. Webb, and Matt Clark. Thin-film optoacoustic transducers for subcellular Brillouin oscillation imaging of individual biological cells. *Applied Optics*, 54(28):8388, October 2015.

[174] T. Dehoux and B. Audoin. Non-invasive optoacoustic probing of the density and stiffness of single biological cells. *Journal of Applied Physics*, 112(12):124702, December 2012.

[175] Liwang Liu, Alexis Viel, Guillaume Le Saux, Laurent Plawinski, Giovanna Muggiolu, Philippe Barberet, Marco Pereira, Cdric Ayela, Herv Seznec, Marie-Christine Durrieu, Jean-Marc Olive, and Bertrand Audoin. Remote imaging of single cell 3D morphology with ultrafast coherent phonons and their resonance harmonics. *Scientific Reports*, 9(1):6409, April 2019.

[176] Alexis Viel, Emmanuel Pronne, Ocane Snpart, Loc Becerra, Claire Legay, Fannie Semprez, La Trichet, Thibaud Coradin, Ahmed Hamraoui, and Laurent Belliard. Picosecond ultrasounds as elasticity probes in neuron-like cells models. *Applied Physics Letters*, 115(21):213701, November 2019.

[177] Liwang Liu, Laurent Plawinski, Marie-Christine Durrieu, and Bertrand Audoin. Label-free multi-parametric imaging of single cells: dual picosecond optoacoustic microscopy. *Journal of Biophotonics*, 12(8):e201900045, 2019.

[178] Fernando Prez-Cota, Rafael Fuentes-Domnguez, Salvatore La Cavera, William Hardiman, Mengting Yao, Kerry Setchfield, Emilia Moradi, Shakila Naznin, Amanda Wright, Kevin F. Webb, Alan Huett, Claire Friel, Virginie Sottile, Hany M. Elsheikha, Richard J. Smith, and Matt Clark. Picosecond ultrasonics for elasticity-based imaging and characterization of biological cells. *Journal of Applied Physics*, 128(16):160902, October 2020.

[179] Omar F. Zouani, Thomas Dehoux, Marie-Christine Durrieu, and Bertrand Audoin. Universality of the network-dynamics of the cell nucleus at high frequencies. *Soft Matter*, 10(43):8737–8743, October 2014.

[180] Fernando Pérez-Cota, Richard J. Smith, Hany M. Elsheikha, and Matt Clark. New insights into the mechanical properties of Acanthamoeba castellanii cysts as revealed by phonon microscopy. *Biomedical Optics Express*, 10(5):2399–2408, May 2019.

[181] Jiang-Lai Wu, Yi-Qing Xu, Jing-Jiang Xu, Xiao-Ming Wei, Antony CS Chan, Anson HL Tang, Andy KS Lau, Bob MF Chung, Ho Cheung Shum, Edmund Y. Lam, Kenneth KY Wong, and Kevin K. Tsia. Ultrafast laser-scanning time-stretch imag-

ing at visible wavelengths. *Light: Science & Applications*, 6(1):e16196–e16196, January 2017.

[182] Anthony E. Siegman. *Lasers*. University Science Books, Mill Valley, California, 1986.

[183] H Kogelnik and T Li. Laser Beams and Resonators. page 18.

[184] Arkadiusz Ciesielski, Lukasz Skowronski, Marek Trzcinski, Ewa Grecka, Pawe Trautman, and Tomasz Szoplik. Evidence of germanium segregation in gold thin films. *Surface Science*, 674:73–78, August 2018.

[185] Arkadiusz Ciesielski, Lukasz Skowronski, Marek Trzcinski, and Tomasz Szoplik. Controlling the optical parameters of self-assembled silver films with wetting layers and annealing. *Applied Surface Science*, 421:349–356, November 2017.

[186] Aleksandar D. Raki, Aleksandra B. Djurii, Jovan M. Elazar, and Marian L. Majewski. Optical properties of metallic films for vertical-cavity optoelectronic devices. *Applied Optics*, 37(22):5271–5283, August 1998.

[187] S. Preuss, E. Matthias, and M. Stuke. Sub-picosecond UV-laser ablation of Ni films. *Applied Physics A*, 59(1):79–82, July 1994.

[188] S. Preuss, A. Demchuk, and M. Stuke. Sub-picosecond UV laser ablation of metals. *Applied Physics A*, 61(1):33–37, July 1995.

[189] J. Siegel. UV-laser ablation of ductile and brittle metal films. *Applied Physics A: Materials Science & Processing*, 64(2):213–218, January 1997.

[190] Dmitry I. Yakubovsky, Yury V. Stebunov, Roman V. Kirtaev, Georgy A. Ermolaev, Mikhail S. Mironov, Sergey M. Novikov, Aleksey V. Arsenin, and Valentyn S. Volkov. Ultrathin and Ultrasmooth Gold Films on Monolayer MoS2. *Advanced Materials Interfaces*, 6(13):1900196, 2019.

[191] Hui Chen, Michael Buric, Paul R. Ohodnicki, Jinichiro Nakano, Bo Liu, and Benjamin T. Chorpening. Review and perspective: Sapphire optical fiber cladding development for harsh environment sensing. *Applied Physics Reviews*, 5(1):011102, February 2018.

[192] Cary Hill, Dan Homa, Zhihao Yu, Yujie Cheng, Bo Liu, Anbo Wang, and Gary Pickrell. Single Mode Air-Clad Single Crystal Sapphire Optical Fiber. *Applied Sciences*, 7(5):473, 2017.

[193] C. Hoberg, P. Balzerowski, and M. Havenith. Integration of a rapid scanning technique into THz time-domain spectrometers for nonlinear THz spectroscopy measurements. *AIP Advances*, 9(3):035348, March 2019.

[194] Paul A. Elzinga, Fred E. Lytle, Yanan Jian, Galen B. King, and Normand M. Laurendeau. Pump/probe spectroscopy by asynchronous optical sampling. *Applied Spectroscopy*, 41(1):2–4, January 1987.

[195] Paul A. Elzinga, Ronald J. Kneisler, Fred E. Lytle, Yanan Jiang, Galen B. King, and Normand M. Laurendeau. Pump/probe method for fast analysis of visible spectral signatures utilizing asynchronous optical sampling. *Applied Optics*, 26(19):4303–4309, October 1987.

[196] R. Paschotta. Noise of mode-locked lasers (Part II): timing jitter and other fluctuations. *Applied Physics B*, 79(2):163–173, July 2004.

[197] D.H. Hurley, O.B. Wright, O. Matsuda, V.E. Gusev, and O.V. Kolosov. Laser picosecond acoustics in isotropic and anisotropic materials. *Ultrasonics*, 38(1-8):470–474, March 2000.

[198] O. Matsuda, O. B. Wright, D. H. Hurley, V. E. Gusev, and K. Shimizu. Coherent Shear Phonon Generation and Detection with Ultrashort Optical Pulses. *Physical Review Letters*, 93(9):095501, August 2004.

[199] Jitao Zhang, Farid Alisafaei, Milo Nikoli, Xuefei A. Nou, Hanyoup Kim, Vivek B. Shenoy, and Giuliano Scarcelli. Nuclear Mechanics within Intact Cells Is Regulated by Cytoskeletal Network and Internal Nanostructures. *Small*, 16(18):1907688, May 2020.

[200] Fernando Pérez-Cota, Salvatore La Cavera III, Shakila Naznin, Rafael Fuentes-Domínguez, Richard J. Smith, and Matt Clark. Apparent attenuation by optoacoustic defocus in phonon microscopy. *Photoacoustics*, 19:100180, September 2020.

[201] F Yang, T Atay, C H Dang, T J Grimsley, S Che, J Ma, Q Zhang, A V Nurmikko, and H J Maris. Study of phonon propagation in water using picosecond ultrasonics. *J. Phys. Conf. Ser.*, 92:012024, December 2007.

[202] Ronald L Allen and Duncan Mills. *Signal Analysis: Time, Frequency, Scale, and Structure: Time, Frequency, Scale, and Structure*. John Wiley & Sons, 2004.

[203] Yu-Ping Wang, Jie Chen, Qiang Wu, and Kenneth R. Castleman. Fast Frequency Estimation by Zero Crossings of Differential Spline Wavelet Transform. *EURASIP Journal on Advances in Signal Processing*, 2005(8):624376, May 2005.

[204] Haddad Richard A. Akansu, Ali N. 5.3.1 the continuous wavelet transform, 1992.

[205] P. F. Ribeiro. *Time-Varying Waveform Distortions in Power Systems*. John Wiley & Sons, 2010.

[206] J. Rheims, J. Köser, and T. Wriedt. Refractive-index measurements in the near-IR using an Abbe refractometer. *Measurement Science and Technology*, 8(6):601–605, June 1997.

[207] F. A. A. Fergusson, E. W. Guptill, and A. D. MacDonald. Velocity of sound in glycerol. *J. Acoust. Soc. Am.*, 26(1):67–69, January 1954.

[208] K. J. Zhang, M. E. Briggs, R. W. Gammon, J. V. Sengers, and J. F. Douglas. Thermal and mass diffusion in a semidilute good solvent-polymer solution. *The Journal of Chemical Physics*, 111(5):2270–2282, August 1999.

[209] Jeffrey C. Heine and William J. Snyder. Ultrasonic velocity in polystyrene-toluene solutions. *Journal of Chemical & Engineering Data*, 29(2):175–178, April 1984.

[210] Martina Meinke, Gerhard Mller, Jrgen Helfmann, and Moritz Friebel. Optical properties of platelets and blood plasma and their influence on the optical behavior of whole blood in the visible to near infrared wavelength range. *Journal of Biomedical Optics*, 12(1):014024, 2007.

[211] https://itis.swiss/virtual-population/tissue-properties/database/acoustic-properties/speed-of sound/.

[212] Alexey N. Bashkatov and Elina A. Genina. Water refractive index in dependence on temperature and wavelength: a simple approximation. In *Saratov Fall Meeting 2002: Optical Technologies in Biophysics and Medicine IV*, volume 5068, pages 393–395. International Society for Optics and Photonics, October 2003.

[213] F. Yang, T. J. Grimsley, S. Che, G. A. Antonelli, H. J. Maris, and A. V. Nurmikko. Picosecond ultrasonic experiments with water and its application to the measurement of nanostructures. *Journal of Applied Physics*, 107(10):103537, May 2010.

[214] Iago Pereiro, Anna Fomitcheva Khartchenko, Lorenzo Petrini, and Govind V. Kaigala. Nip the bubble in the bud: a guide to avoid gas nucleation in microfluidics. *Lab on a Chip*, 19(14):2296–2314, July 2019.

[215] Xiaohong Quan and Edward S. Fry. Empirical equation for the index of refraction of seawater. *Applied Optics*, 34(18):3477–3480, June 1995.

[216] Kenneth V. Mackenzie. Discussion of sea water sound-speed determinations. *J. Acoust. Soc. Am.*, 70(3):801–806, September 1981.

[217] Cary Hill, Dan Homa, Zhihao Yu, Yujie Cheng, Bo Liu, Anbo Wang, and Gary Pickrell. Single mode air-clad single crystal sapphire optical fiber. *Applied Sciences*, 7(5):473, May 2017.

[218] K. König, P. T. C. So, W. W. Mantulin, and E. Gratton. Cellular response to near-infrared femtosecond laser pulses in two-photon microscopes. *Optics Letters*, 22(2):135–136, January 1997.

[219] N. Sultanova, S. Kasarova, and I. Nikolov. Dispersion Properties of Optical Polymers. *Acta Physica Polonica A*, 116(4):585–587, October 2009.

[220] *https://www.olympus-ims.com/en/ndt-tutorials/thickness-gage/appendices-velocities/*.

[221] Yoshifumi Saijo, Joe Shikama, Koki Yoshida, Ryo Nagaoka, Mototaka Arakawa, and Kazuto Kobayashi. Multiparametric characterization of a single cell by an ultrasound and optical combined microscope. In *2014 IEEE International Ultrasonics Symposium*, pages 727–730, September 2014.

[222] Benjamin Rappaz, Pierre Marquet, Etienne Cuche, Yves Emery, Christian Depeursinge, and Pierre J. Magistretti. Measurement of the integral refractive index and dynamic cell morphometry of living cells with digital holographic microscopy. *Optics Express*, 13(23):9361–9373, November 2005.

[223] Nazila Norouzi, Heran C. Bhakta, and William H. Grover. Sorting cells by their density. *PLOS ONE*, 12(7):e0180520, July 2017.

[224] Miguel A. Bandres and Julio C. Gutirrez-Vega. InceGaussian beams. *Optics Letters*, 29(2):144, January 2004.

[225] Yves F. Dufrłne, Toshio Ando, Ricardo Garcia, David Alsteens, David Martinez-Martin, Andreas Engel, Christoph Gerber, and Daniel J. Mller. Imaging modes of atomic force microscopy for application in molecular and cell biology. *Nature Nanotechnology*, 12(4):295–307, April 2017.

[226] Akiko Harasaki, Joanna Schmit, and James C. Wyant. Offset of coherent envelope position due to phase change on reflection. *Applied Optics*, 40(13):2102–2106, May 2001.

[227] Conor O Mahony, Martin Hill, Magali Brunet, Russell Duane, and Alan Mathewson. Characterization of micromechanical structures using white-light interferometry. *Measurement Science and Technology*, 14(10):1807–1814, October 2003.

[228] Kristen Lantz Reichenbach and Chris Xu. Numerical analysis of light propagation in image fibers or coherent fiber bundles. *Optics Express*, 15(5):2151–2165, March 2007.

[229] Bahaa E. A. Saleh. *Fundamentals of photonics / Bahaa E.A. Saleh, Malvin Carl Teich.* Wiley series in pure and applied optics. John Wiley & Sons, Inc., third edition. edition, 2019.

[230] Kristen Lantz Reichenbach and Chris Xu. Analysis and measurement of light propagation in coherent fiber bundles. In *2007 Conference on Lasers and Electro-Optics (CLEO)*, pages 1–2, May 2007.

[231] Tuqiang Xie, David Mukai, Shuguang Guo, Matthew Brenner, and Zhongping Chen. Fiber-optic-bundle-based optical coherence tomography. *Optics Letters*, 30(14):1803–1805, July 2005.

[232] Kunimasa Saitoh and Shoichiro Matsuo. Multicore Fiber Technology. *Journal of Lightwave Technology*, 34(1):55–66, January 2016.

[233] George M. Hale and Marvin R. Querry. Optical Constants of Water in the 200-nm to 200-m Wavelength Region. *Applied Optics*, 12(3):555–563, March 1973.

[234] Donald A. McQuarrie. Harper's chemistry series. Harper & Row, Publishers, Inc., New York, 1976.

[235] Ivo T. Leite, Sergey Turtaev, Xin Jiang, Martin iler, Alfred Cuschieri, Philip St. J. Russell, and Tom imr. Three-dimensional holographic optical manipulation through a high-numerical-aperture soft-glass multimode fibre. *Nature Photonics*, 12(1):33–39, January 2018.

[236] S. Che, P. R. Guduru, A. V. Nurmikko, and H. J. Maris. A scanning acoustic microscope based on picosecond ultrasonics. *Ultrasonics*, 56:153–159, February 2015.

[237] Thomas Dehoux, Kenichi Ishikawa, Paul H. Otsuka, Motonobu Tomoda, Osamu Matsuda, Masazumi Fujiwara, Shigeki Takeuchi, Istvan A. Veres, Vitalyi E. Gusev, and Oliver B. Wright. Optical tracking of picosecond coherent phonon pulse focusing inside a sub-micron object. *Light: Science & Applications*, 5(5):e16082–e16082, May 2016.

[238] K. M. Yoo, Feng Liu, and R. R. Alfano. When does the diffusion approximation fail to describe photon transport in random media? *Physical Review Letters*, 64(22):2647–2650, May 1990.

[239] Joshua Brake, Mooseok Jang, and Changhuei Yang. Analyzing the relationship between decorrelation time and tissue thickness in acute rat brain slices using multispeckle diffusing wave spectroscopy. *JOSA A*, 33(2):270–275, February 2016.

[240] Zachary Steelman, Zhaokai Meng, Andrew J. Traverso, and Vladislav V. Yakovlev. Brillouin spectroscopy as a new method of screening for increased CSF total protein during bacterial meningitis. *Journal of Biophotonics*, 8(5):408–414, 2015.

[241] Sebastian A. Vasquez-Lopez, Raphal Turcotte, Vadim Koren, Martin Plschner, Zahid Padamsey, Martin J. Booth, Tom imr, and Nigel J. Emptage. Subcellular spatial resolution achieved for deep-brain imaging in vivo using a minimally invasive multimode fiber. *Light: Science & Applications*, 7(1):110, December 2018.

[242] Ahmed El Hady and Benjamin B. Machta. Mechanical surface waves accompany action potential propagation. *Nature Communications*, 6(1):6697, March 2015.

[243] Yun-Bi Lu, Kristian Franze, Gerald Seifert, Christian Steinhuser, Frank Kirchhoff, Hartwig Wolburg, Jochen Guck, Paul Janmey, Er-Qing Wei, Josef Ks, and Andreas Reichenbach. Viscoelastic properties of individual glial cells and neurons in the CNS. *Proceedings of the National Academy of Sciences*, 103(47):17759–17764, November 2006.

[244] Tonia Munder, Anna Pfeffer, Stefanie Schreyer, Jing Guo, Juergen Braun, Ingolf Sack, Barbara Steiner, and Charlotte Klein. MR elastography detection of early viscoelastic response of the murine hippocampus to amyloid accumulation and neuronal cell loss due to Alzheimer's disease. *Journal of Magnetic Resonance Imaging*, 47(1):105–114, 2018.

[245] Jens Wuerfel, Friedemann Paul, Bernd Beierbach, Uwe Hamhaber, Dieter Klatt, Sebastian Papazoglou, Frauke Zipp, Peter Martus, Jrgen Braun, and Ingolf Sack. MR-elastography reveals degradation of tissue integrity in multiple sclerosis. *NeuroImage*, 49(3):2520–2525, February 2010.

[246] Giuseppe Antonacci, Valeria de Turris, Alessandro Rosa, and Giancarlo Ruocco. Background-deflection Brillouin microscopy reveals altered biomechanics of intracellular stress granules by ALS protein FUS. *Communications Biology*, 1(1):1–8, September 2018.

[247] Ahmed Hamraoui, Ocane Snpart, Maxime Schneider, Sophie Malaquin, Emmanuel Pronne, Loc Becerra, Fannie Semprez, Claire Legay, and Laurent Belliard. Correlative Imaging of Motoneuronal Cell Elasticity by Pump and Probe Spectroscopy. *Biophysical Journal*, 120(3):402–408, February 2021.

[248] Elise Spedden, James D. White, Elena N. Naumova, David L. Kaplan, and Cristian Staii. Elasticity Maps of Living Neurons Measured by Combined Fluorescence and Atomic Force Microscopy. *Biophysical Journal*, 103(5):868–877, September 2012.

[249] Sean V Murphy and Anthony Atala. 3D bioprinting of tissues and organs. *Nature Biotechnology*, 32(8):773–785, August 2014.

[250] Timothy J. Muldoon, Mark C. Pierce, Dawn L. Nida, Michelle D. Williams, Ann Gillenwater, and Rebecca Richards-Kortum. Subcellular-resolution molecular imaging within living tissue by fiber microendoscopy. *Optics Express*, 15(25):16413–16423, December 2007.

[251] Joannie Desroches, Michael Jermyn, Michael Pinto, Fabien Picot, Marie-Andre Tremblay, Sami Obaid, Eric Marple, Kirk Urmey, Dominique Trudel, Gilles Soulez, Marie-Christine Guiot, Brian C. Wilson, Kevin Petrecca, and Frdric Leblond. A new method using Raman spectroscopy for in vivo targeted brain cancer tissue biopsy. *Scientific Reports*, 8(1):1792, January 2018.

[252] Rafael Fuentes-Domnguez, Fernando Prez-Cota, Shakila Naznin, Richard J. Smith, and Matt Clark. Super-resolution imaging using nano-bells. *Scientific Reports*, 8(1):16373, November 2018.

[253] Brian S. Peters, Priscila R. Armijo, Crystal Krause, Songita A. Choudhury, and Dmitry Oleynikov. Review of emerging surgical robotic technology. *Surgical Endoscopy*, 32(4):1636–1655, April 2018.

[254] Ivo Bokoski and Guido Costamagna. Endoscopy robotics: Current and future applications. *Digestive Endoscopy*, 31(2):119–124, 2019.

[255] Singiresu S RAO and Singiresu S Rao. *The Finite Element Method in Engineering*. Oxford, 2010.

[256] Hana Charvtov and Martin Zlek. Computer Application for Simulation of Temperature Distribution Inside the Room. *MATEC Web of Conferences*, 210:04036, 2018.

[257] Ying Xu, Ruizhe Wang, Shaojie Ma, Lei Zhou, Y. Ron Shen, and Chuanshan Tian. Theoretical analysis and simulation of pulsed laser heating at interface. *Journal of Applied Physics*, 123(2):025301, January 2018.

[258] J. Gdde, J. Hohlfeld, J. G. Mller, and E. Matthias. Damage threshold dependence on electronphonon coupling in Au and Ni films. *Applied Surface Science*, 127-129:40–45, May 1998.

[259] J.A. Juregui and E. Welsch. Treatment of thermal gratings in the time and frequency domain. *Journal of Modern Optics*, 40(11):2173–2198, 1993.